Life-Extending Control for a Highly Maneuverable Flight Vehicle

Si-bok Yu
Old Dominion University

Life Extending Control for a

Highly Maneuverable Flight Vehicle

by

Si-bok Yu
B.S. February 1997, University of Ulsan, (R.O.K.)
M.S. December 1999, Old Dominion University

A Dissertation Submitted to the Faculty of
Old Dominion University in Partial Fulfillment of the
Requirement for the Degree of

DOCTOR OF PHILOSOPHY

AEROSPACE ENGINEERING

OLD DOMINION UNIVERSITY

December 2003

Approved by:

Brett A. Newman (Director)

Chuh Mei (Member)

Jen-Kuang Huang (Member)

Thomas E. Alberts (Member)

ABSTRACT

Life Extending Control for a Highly Maneuverable Flight Vehicle

Si-bok Yu
Old Dominion University, December 2003
Director: Dr. Brett A. Newman

This dissertation investigates the feasibility and potential of life extension control logic for reducing fatigue within aerospace vehicle structural components. A key underpinning of this control logic is to exploit nonintuitive, optimal loading conditions which minimize nonlinear crack growth behavior, as predicted by analytical fatigue models with experimentally validated behavior. A major simplification in the development of life extension control logic is the observation and justification that optimal stress loading conditions, as described by overload magnitude ratio and application interval, are primarily independent of crack length and therefore, component age. This weak relationship between optimal stress loading and structural age implies the life extension control logic does not require tight integration with real-time health monitoring systems performing crack state estimation from measurement and model simulation. At a fundamental level, the life extension control logic conducts load alleviation and/or amplification tailoring of external and internal excitations to optimally exploit nonlinear crack retardation phenomenon. The life extension control logic is designed to be a simple, practical modification applied to an existing flight control system. A nonlinear autopilot for the nonlinear F-16 dynamics, coupled with a separate flexible F-16 wing model and a state space crack growth model, are used to demonstrate the life extension control concept. Results indicate that significant structural life savings is obtained by integrating life extending control logic dedicated for critical structural

components to the existing flight control system. On the other hand, some components under life extending control showed minor reductions of structural life, particularly when the components are located in a low stress region where fatigue damage is of lower concern. Further, to achieve enhanced long-term structural integrity with life extending control, tradeoffs with flight system stability and performance may be required. Careful consideration is thus necessary when applying life extending logic to the aircraft flight control system. Although life extending control appears feasible with significant potential, full implementation of the concept requires further study.

Members of Advisory Committee: Dr. Chuh Mei

Dr. Jen-Kuang Huang

Dr. Thomas E. Alberts

ACKNOWLEDGEMENT

I would like to express my deep appreciation to my advisor, Dr. Brett Newman for his continuous encouragement and well-planned guidance. He always did his best to spend his time with me, and he helped me to make every important breakthrough in my research. I also appreciate continuous financial support from the Department of Aerospace Engineering. Special acknowledgement should be expressed to Dr. Chuh Mei for giving me continuous supervising and advise, and another acknowledgement for Dr. Donald Kunz for helping me with structural modeling. I also received valuable help from my officemate, Salim.

Another acknowledgement is given to my father and mother who let me continue my educational training in the U.S. and who provided me with continuous support. I also want say thanks to my wife, Kwisun, for her support and for helping me to overcome all the hardships we have faced together.

TABLE OF CONTENTS

LIST OF TABLES

TABLE Page

LIST OF FIGURES

FIGURE Page

NOMENCLATURE

English Symbols

A	Height of model wing main box spar
A_i	i'th coefficient for crack opening equation
A_y	Aircraft lateral load factor
a_{N}	Notch half-width of the specimen
A, B	Aircraft characteristic matrices for state equation
B	Width of model wing main box spar
b	Wing span
B, C	Elliptic hole dimensions
C, D	Aircraft characteristic matrices for measurement equation
C	Crack length in width direction, Mean chord, and Damping matrix of wing dynamics equation
C'	Effective elastic crack half length
C_0	Empirical constant
C_1	Positive constant
C_0, C_1	Constants computing optimal overload ratio
C_{c}	Critical crack length
C_{d}	Minimal detectable crack length
C_{final}	Final crack length
C_{initial}	Initial crack length
$C_{\mathrm{i,j}}$	Damping constant of i^{th} spar element
C_{i}^{j}	Integration constants

$C^{\theta}_{i,j}$	Rotational damping constant of i^{th} spar element
$C_{l,t}$, $C_{m,t}$, $C_{n,t}$	Total aerodynamic moment coefficient in X, Y, and Z
$C_{x,t}$, $C_{y,t}$, $C_{z,t}$	Total aerodynamic force coefficient in X, Y, and Z
c_i	Initial crack length and Constants related to the aircraft mass moment of inertia
dC/dN	Crack growth rate
d_{i_ex2cg}	Distance from elastic axis to center of gravity
E	Young's modulus
e	Distance from wing root to force acting on wing spar
F	Geometric factor, Nonlinear functionality related to P loop, Force acting on the wing spar, and External force
F_a	Aileron control force
F_{ag}	Aileron control force after roll command gradient
$F_{Dowling}$	Geometric factor calculated from Dowling's equation
F_e	Elevator control force
F_{eg}	Elevator control force after pitch command gradient
F_r	Rudder control force
F_{rg}	Rudder control force after rudder command gradient
F_x ,F_y, F_z	Force acting on the aircraft in x, y, z axis
G	Plant transfer function matrix, Nonlinear functionality related to α'
g	Gravitational acceleration
H_e	Aircraft engine spin moment
h	Aircraft altitude

h_N	Notch height of the specimen
$h_{\_c}$	Altitude command
I_{mi}	Mass moment inertia of i^{th} wing spar station
I_s	Mass moment inertia of model wing spar
I_x, I_y, I_{xz}	Mass moment inertia of aircraft
l_i	Distance from root of wing to i^{th} wing spar station
J, J_z	Polar second moment of inertia
K, K_t	Stress concentration factor and Stiffness matrix of wing dynamics equation
K_0	Stress intensity factor associated with crack opening stress
K_{Fe}	Gain for Life Extending Control logic
K_i	Autopilot control gain for U loop
K_{i_h}	Autopilot control gain for altitude loop
K_{i_h2}	Autopilot control gain for altitude loop
K_{i_phi}	Autopilot control gain for ϕ loop
K_{i_th}	Autopilot control gain for θ loop
K_p	Autopilot control gain for U loop
K_{p_h}	Autopilot control gain for altitude loop
K_{p_h2}	Autopilot control gain for altitude loop
K_{p_psi}	Autopilot control gain for ψ loop
K_{p_sb}	Autopilot control gain for speed break loop
K_{Qi}	Autopilot control gain for Q loop
K_{max}	Maximum stress intensity factor

$K_{\min}$	Minimum stress intensity factor
$k^{\theta}_{i,j}$	Rotational spring constant of i^{th} spar element
$k_{i,j}$	Spring constant of i^{th} spar element
L	Characteristic length and Moment in vehicle X axis
M	Moment acting on the structure and Mach number
M, M_i	Moment in vehicle Y axis
$\overline{M}$	Inertia matrix of wing dynamics equation
m	Positive constant
m_i	Mass of i^{th} wing span station
N	Number of cycle and Moment in vehicle Z axis
N_1	Number of σ_{max1} applied cycles (Overload Interval, P_{ov})
N_2	Number of σ_{max2} applied cycles
N_3	Number of σ_{max3} applied cycles
N_i	Number of load cycles at σ_i required for failure and Control gain for aircraft Flight Control System
N_{if}	Cycle where brittle fracture occur
N_p	Inspection interval in cycle
N_z	Aircraft vertical load factor
n	Empirical constant
n_i	Number of load cycles occurring at stress level σ_i
n_y	Load factor in Y_b axis
n_z	Load factor in Z_b axis
P	Perturbation value in crack growth equation and Roll rate

P_1	Aircraft engine power command to engine
P_2	Intermediate aircraft engine power command
P_3	Current aircraft engine power
P_{E}	Aircraft location in east
P_{N}	Aircraft location in north
P_{ov}	Overload interval
P_{ov}^{fixed}	Pre-defined optimal overload interval
P_{ov}^*	Optimal overload interval
P_{Trim}	Roll trim
psi_c	Yaw command
Q	Pitch rate
Q_{cr}	Threshold pitch rate
Q_{max}	Maximum pitch rate of the pitch maneuver
Q_{Trim}	Pitch trim
Q_accm	Vector of accumulated pitch rate over critical pitch rate
q	Dynamic pressure
$\mathcal{R}$	Ratio between constant amplitude crack opening stress and maximum stress ($\sigma_{0\mathrm{CA}}/\sigma_{\mathrm{max}}$)
R	Stress ratio ($\sigma_{\mathrm{min}}/\sigma_{\mathrm{max}}$), Radius of curvature and Radial distance from crack tip and Pitch rate
R'	Modified stress ratio parameter
R_{ov}	Overload ratio
R_{ov}^*	Optimal overload ratio

R_{Sub}	Sub-optimal weight
R_{Trim}	Yaw trim
r_y	Radius of plastic region
S	Stress and Wing area
S_0	Crack opening stress
S_{max}	Crack opening stress
S_{max1}^{m}	Intermediate parameter for Life Extending Control logic
S_{max1}^{new}	Intermediate parameter for Life Extending Control logic
S_{max2}^{hu}	Intermediate parameter for Life Extending Control logic
S_{yi}	Constants related to inertia coupling of transversal equations of motion
s	Laplace variable
T	Thrust and Height of model wing main box spar flange
T_{idle}	Engine idle thrust
T_{max}	Maximum engine thrust
T_{mil}	Engine military thrust (maximum thrust without after burner)
t	Thickness of specimen and Time
t_p	Panel thickness
U, u	Aircraft forward speed
$\overline{U}$	Input vector for aircraft model
U_d	Desired aircraft forward speed
$U_{\_c}$	Aircraft forward speed command
V	Aircraft side speed and Shear stress
V_T	Total flight velocity

W	Half-width of the specimen, Aircraft vertical speed, and Width of model wing main box spar flange
X	Vector of state variables
X_b	X in body axis coordinate
X_c	Safety factor
x, y, z	Elemental structural axes
x, z	Airframe structural axes
x_1, z_2	Airframe structural axes
x_i	Deflection of i^{th} wing span station
Y	Output vector
Y_b	Y in body axis coordinate
Z	Intermediate variable in crack growth equation and Damping matrix
Z_b	Z in body axis coordinate
z	Deflection of the specified position on the beam

Greek Symbols

α	Loading condition factor
α	Angle of attack
α'	Modified angle of attack
α_g	Gust angle of attack
β	Side slip angle
$\Delta C_{i,j}$	Increment or correction of aerodynamic coefficient
ΔK	Stress intensity factor range
ΔK_e, ΔK_{eff}	Effective stress intensity factor range
δ	Pilot input and Crack opening displacement
δ_a	Differential flaperon deflection
δ_e	Elevator deflection
δ_{Fa}	Differential flaperon deflection (= δ_a)
δ_h	Horizontal tail deflection
δ_{ha}	Differential horizontal tail deflection (= δ_h)
δ_{lef}	Leading Edge Flap deflection
δ_r	Rudder deflection
δ_{sb}	Speed break deflection
ϕ	Roll angle
Γ	Intermediate property related to the mass moment of inertia
η, η_1, η_2	Positive empirical constants determined from testing
θ	Pitch angle and Angular distance from crack tip

θ_{th}	Throttle position
θ_i	Rotational deflection of i^{th} wing span station
λ	Variable function of various stress and crack length values
ρ	Air density
σ	Far field stress loading
σ_a	Stress amplitude
σ_{flow}	Average value of material ultimate tensile strength and the yield stress
σ_i	Stress loading at cycle i
σ_{ij}, σ_i	Stress acting on surface where $i, j = x, y, z$
σ_m	Mean stress
σ_{max}	Applied maximum stress in the cycle
σ_{max1}	Applied maximum stress before the overload is applied
σ_{max2}	Overload stress
σ_{max3}	Applied maximum stress after the overload is applied
σ_{min}	Applied minimum stress in the cycle
σ_{min}'	Modified minimum stress
σ_0	Crack opening stress
$\sigma_{0\ CA}$	Crack opening stress for constant amplitude loading
$\sigma_{0\ old}$	Crack opening stress from previous cycle
σ_r	Stress range
σ_u	Material ultimate tensile strength
σ_y	Yield stress and Normal stress along Y axis

$\sigma_{max2} / \sigma_{max1}$	Overload ratio (R_{ov})
σ_{max2}^{Sub}	Sub-optimal overload stress
τ_T	Engine time constant
Ω	Natural frequency matrix
ψ	Yaw angle

CHAPTER 1

INTRODUCTION

1.1 Motivation and Formulation

Over the past decade and for the foreseeable future, flight operations within the defense sector and commercial airline domains have experienced severe financial and budgetary pressures. Military services and civil aviation corporations are interested in extending the life of current aircraft wings and fleets through lower cost upgrades and retrofit packages, as opposed to direct investment of large amounts of capital to purchase new airframes. In particular, these organizations are experiencing a historically difficult period under increasing cost of fuel, increasing maintenance labor cost, and reduced governmental funding and market revenue. Since these external factors are problematic and cannot be easily influenced, one area having potential for reducing maintenance expense is consideration of advanced, breakthrough concepts and technologies lessening the need for maintenance. The focus of this dissertation is to reduce the requirement for maintenance processing and extend structural life while maintaining current safety levels by utilizing flight control logic to exploit and optimize nonlinear fracture mechanics phenomena.

The most significant factor in loss of aircraft structural integrity is fatigue. Studies show that the largest source of mechanical failure in the aircraft industry is fatigue with a significant contribution of 61% to all failures.[1] As a comparison, the largest source of mechanical failure in all industries is corrosion at 29%, with mechanical failure by

---

Journal model for this dissertation is the Journal of Guidance, Control and Dynamics fatigue close behind at 25%. Fatigue crack growth in aircraft components requires routine monitoring of crack size, stop drilling treatment, replacement of parts, tear down and build up of complex structures, and many other labor intense processes. Commercial aviation support including repair, parts, and maintenance for fatigue related damage

Table 1.1 Average Fleet Age for Selected Air Carriers in the United States (June 2002)[3]

Airline	Average Age [yr]	Fleet Size
AirTran	15.21	63
Alaska	9.37	103
American	10.46	836
Continental	7.35	379
Delta	11.22	594
Midwest	26.83	36
Northwest	20.19	431
Southwest	9.23	370
United	8.76	561
US Airway	11.42	241

Table 1.2 Fleet Age Distribution for a Major Airline (December 2000)[4]

Aircraft Type	Owned	Leased		Total	Average Age [yr]
		Capital	Operating		
B-727-200	72	-	10	82	22.4
B-737-200	1	45	8	54	16.1
B-737-300	-	3	23	26	14.1
B-737-800	40	-	-	40	0.9
B-757-200	77	-	41	118	9.5
B-767-200	15	-	-	15	17.6
B-767-300	4	-	24	28	10.9
B-767-300ER	49	-	8	57	5.0
B-767-400	12	-	-	12	0.2
B-777-200	7	-	-	7	1.3
L-1011-1	6	-	-	6	19.7
L-1011-250	5	-	-	5	18.1
L-1011-500	4	-	-	4	19.9
MD-11	8	-	7	15	6.9
MD-88	63	-	57	120	10.5
MD-90	16	-	-	16	5.1
EMB-120	49	-	11	60	10.6
ATR-72	4	-	15	19	6.5
CRJ-100/200	23	-	124	147	2.8
Total	455	48	328	831	9.6

reached $47.5 billion in 1999.[2] To compound the problem, commercial air carriers are facing age of their airframe fleets. Average fleet age of major United States air carriers are around 10 years old while some specific airlines show over 20 years of average fleet age. Table 1.1 shows the average fleet age for selected air carriers in the United States.[3] The age distribution across a single fleet for a specific major airline is also shown in Table 1.2.[4] This particular airline uses 15 L-1011 aircraft of various models whose average age is well over 15 years. Note that large commercial aircraft are usually designed for 20-25 years of service.

During flight, dynamic motion of the aircraft generates cyclic loading on structural components. Depending on the mission, aircraft structures are exposed to a series of varying loads. A specific mission can be assumed to generate highly similar load series in each flight.[5] These series of loads are repeated flight after flight over the lifetime of the aircraft structure. A representative profile for a tactical aircraft conventional

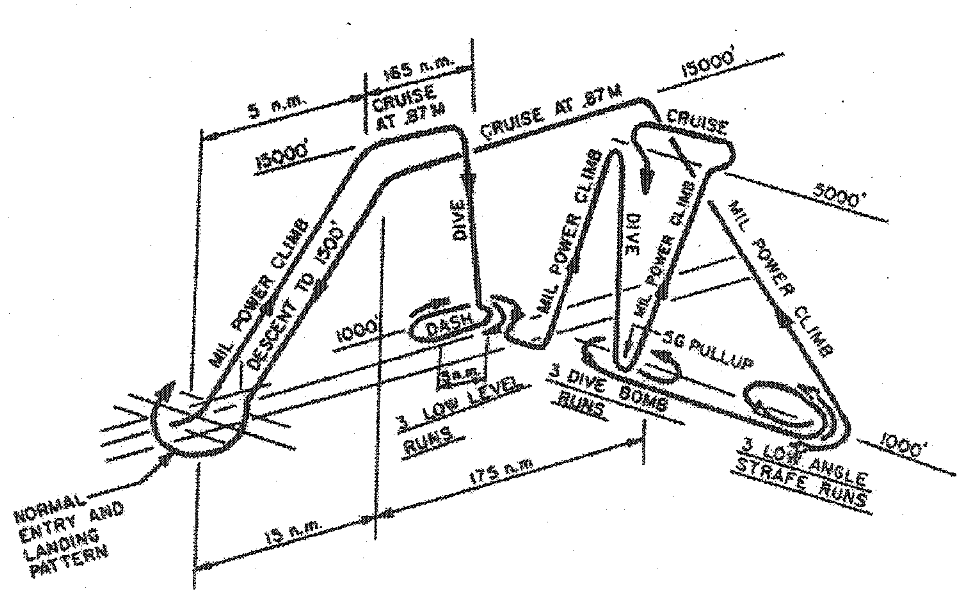

Figure 1.1 Profile for a Tactical Ordinance Delivery Mission[6]

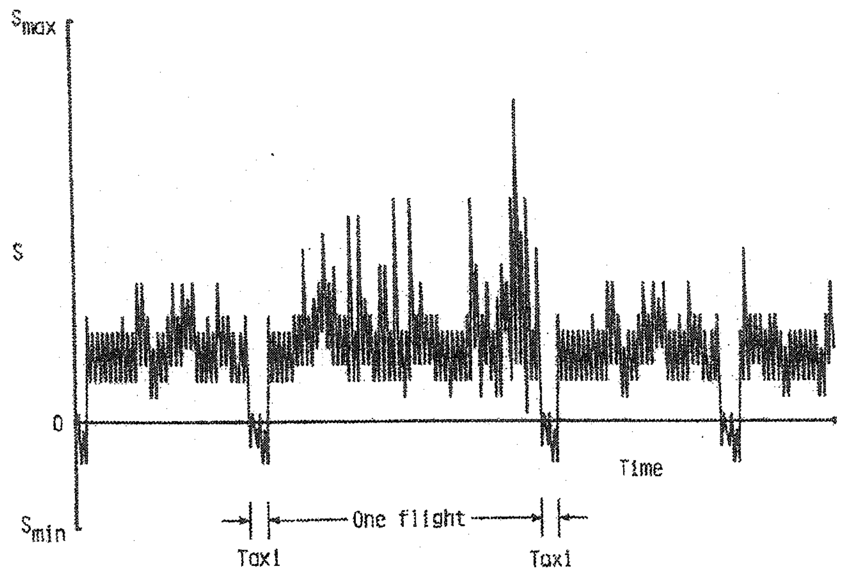

Figure 1.2 Simplified Load of a Transport Wing[7]

ordinance delivery mission is shown in Figure 1.1.[6] A simplified load acting on an airframe wing root in this application is shown in Figure 1.2.[7] In addition to this nominal cyclic loading, random, infrequent high stress loads can be experienced. The source of such atypical transients could be emergency traffic collision avoidance maneuvers or flight through severe energetic weather conditions, for example. These transients are uncommon on a per flight basis, but over the full life span of the aircraft, they are quite common. Under the flight loading described above, airframe materials show fatigue and fracture behavior resulting in weakened structural integrity and reduced life cycle.

References 6 and 8 provide a summary of common practices and newer methodologies for modeling and predicting the fracture mechanics of such systems. Newer methodologies provide significant improvement in understanding nonlinear crack growth behavior, although structural life prediction under fatigue is still a stochastic process showing large spreads in test results. Recent experimental and theoretical development for simple structural specimens has focused on characterizing and modeling nonlinear crack growth behavior including acceleration, deceleration, and complete stoppage of crack propagation due to overload application. In addition, recent investigations show the existence of non-intuitive optimal overload strength and interval parameters that minimize crack growth.[6,8] Existence of these optimal overload conditions is due to the crack retardation phenomenon that is based on the plastic behavior of metal.

These observations imply significant extension of structural life and large reduction of maintenance related operational cost may be possible by facilitating optimal overload conditions in flight. A mechanism for achieving these favorable conditions is utilization of flight control technology, and any such investigations in this concept should be considered as a systems phenomenon related to the motion of the entire vehicle and any on board systems. Since reduced loading does not directly correlate to maximum structural life, the flight control system shall have to perform load tailoring functions, including both alleviation and amplification, of internal/external excitations in order to maintain the optimal overload stress conditions. Note that the load amplification function may generate conceptual resistance from conservative operational and managerial perspectives. A system of this type could be thought of as a generalization to typical gust and maneuver load alleviation systems widely used in commercial and military aircraft today. These traditional load alleviation systems are based on the intuitive but not necessarily correct perspective that minimum structural load corresponds to maximum structural life.

A recent study provided a preliminary investigation into this concept. In this study, the potential influence on long-term airframe structural integrity from a flight control system was addressed. A large flexible airframe with an associated control system was coupled to a dynamic model of crack growth. The control system was originally designed for flying qualities and structural mode suppression objectives, and its logic and architecture were not altered to directly support structural life enhancement and crack growth minimization. A large number of cases involving control gain adjustment and loading parameter variations was considered to expose any significant trends and trades between long-term structural integrity and flight dynamic characteristics. Although not directly considered in this study, results supported the conclusion that dedicated flight control logic optimizing crack growth behavior through load tailoring provides significant leverage on structural life extension. Conclusions from this study motivate the deeper investigation undertaken here.

This dissertation investigates the feasibility and potential of life extension control (LEC) logic for reducing fatigue within aerospace vehicle structural components. Reduced fatigue damage shall be addressed by exploiting nonlinear crack retardation behavior through load tailoring with a flight control system. A full envelope model of a highly maneuverable rigid aircraft with separate flexible wing model and control system coupled to a dynamic crack growth model is used in the investigation. A complete mission from just after take off to just prior to landing is simulated to provide a realistic structural loading environment. The control system consists of a baseline component providing stability augmentation and autopilot functions, and a separate component for load tailoring to increase structural life. Several practical implementation issues are addressed in the research. Objectives of the dissertation research are to 1) explore feasibility of the LEC concept, 2) quantify potential enhancement to structural integrity from the LEC concept, 3) identify practical implementation for the LEC concept, and 4) assess stability and performance loss with the LEC concept.

1.2 Literature Review

Structural components are often subjected to repeated or cyclic loads, and the resulting stress can lead to microscopic physical damage within the materials involved. Even at stresses well below a given material's ultimate strength, this microscopic damage can accumulate with continuous cycling until it develops into a crack or other macroscopic damage that leads to component failure. This damage process and failure mechanism due to cyclic loading is called "fatigue."[5] Fatigue degradation of structural materials has been studied experimentally for over 150 years. The first major recognition of mechanical failure by fatigue was observed in the railway industry in the 1840s.[11] The label fatigue was introduced sometime between 1840 and 1850 to describe failures occurring from repeated stress. In the early 1900s, Ewing and Humfrey[12] used the optical microscope to pursue the study of fatigue mechanisms. Localized slip lines and slip bands leading to the formation of microcracks were observed. Figure 1.3 describes a microscopic view of the fatigue mechanism.[11] A schematic edge view of coarse slip with static loading is shown in Figure 1.3.a. Figure 1.3.b shows the fine slip occurring from cyclic loading. Progressive development of an extrusion/intrusion pair under cyclic loading is shown in Figure 1.3.c.

Basquine in 1910 showed that alternating stress (S or σ) versus number (N) of cycles to failure in the finite life region could be represented as a log-log linear relationship.[13] If the stress-strain curve is taken to be the most fundamental description of static material behavior, the stress-load cycle curve (or "S-N" curve) is the counterpart for describing fundamental dynamic fatigue material behavior.[14] Figure 1.4 shows an example stress-load cycle curve for unnotched 7075-T6 aluminum alloy.[14] The characteristic data is generated from exhaustive fatigue testing of material specimens. The specimen is subjected to cyclic constant amplitude tensile-tensile or tensile-compressive loading until failure. The corresponding values for stress and number of load

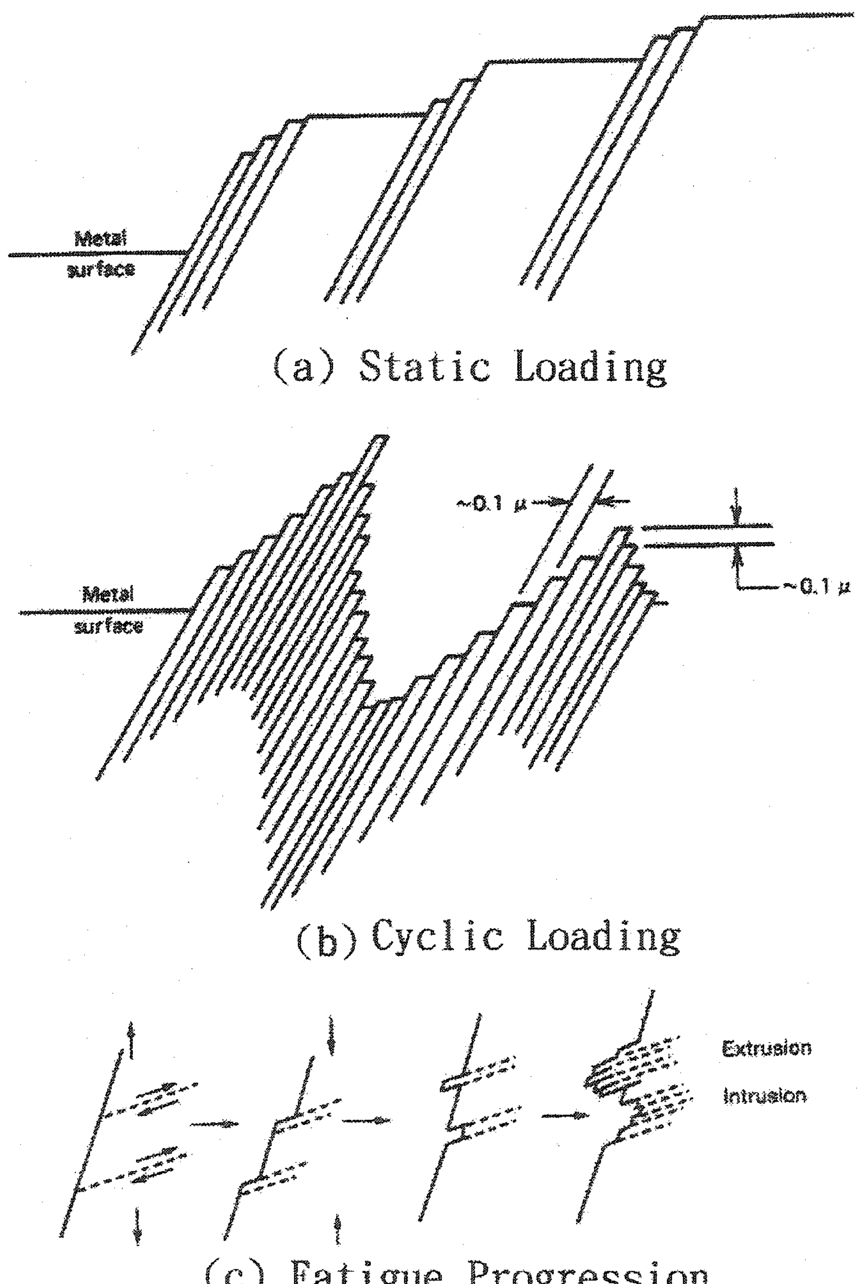

Figure 1.3 Schematic of Slip due to External Loads[11]

cycles are recorded and become one data point in Figure 1.4. The parameter R in Figure 1.4 is defined as the ratio of minimum to maximum stress ($R = \sigma_{min}/\sigma_{max}$) during the cyclic loading, and Figure 1.5 illustrates common loading terminology.

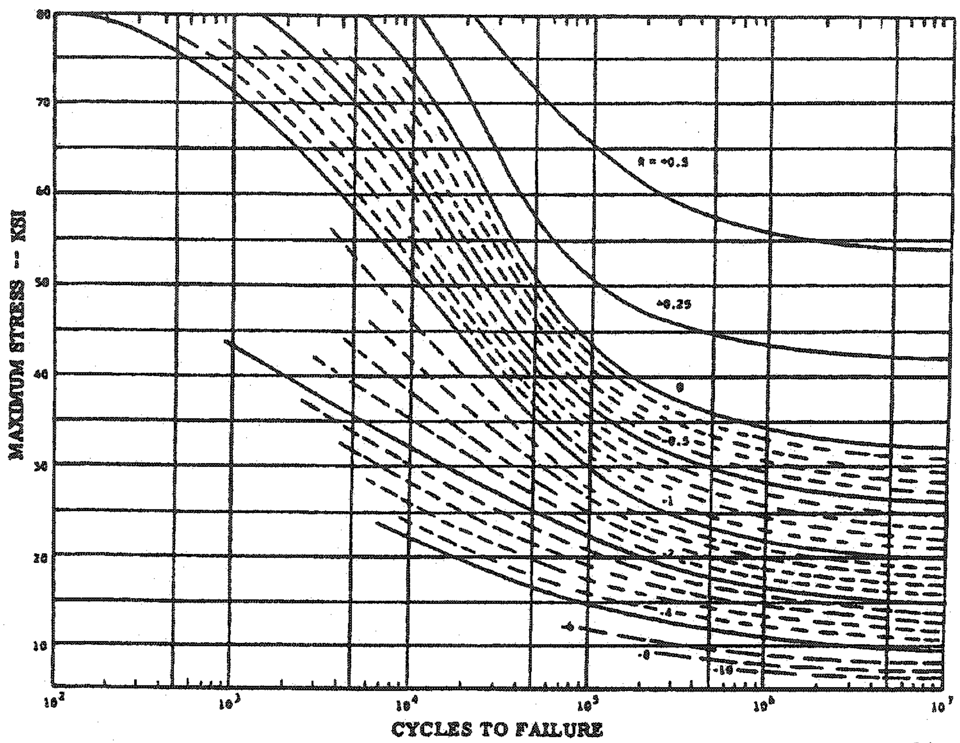

Figure 1.4 S-N Curve for Unnotched 7075-T6 Aluminum Alloy[14]

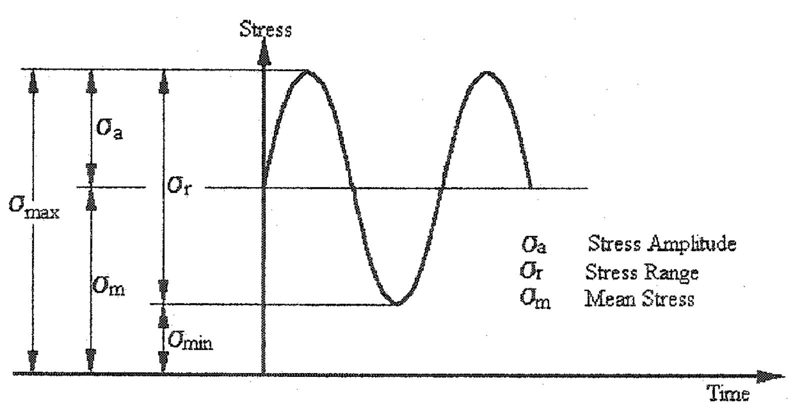

Figure 1.5 Nomenclature for Loading

Although fundamental in nature, the data in Figure 1.4 is only remotely applicable for predicting useful remaining life in aircraft structural components.[1] Two major reasons for this inapplicability include the widely variable stress concentration characteristics and loading traits associated with flight structures, which are simply not captured in Figure 1.4, or other similar data. Aircraft structural components often consist of complex geometries including holes, notches, fillets, taper, curvature, corners, edge discontinuities, rivets, welds, fasteners and many others. The stress field near these regions will be high and can significantly influence fatigue life. For example, Figure 1.6 shows a stress-load cycle curve for both notched and unnotched 7075-T6 aluminum specimens.[14] The structural life of the notched specimens are drastically reduced relative to the pure specimen. Further, the loading environment during flight is highly variable and includes both deterministic and stochastic traits associated with load mean, cyclic amplitude, overload strength, load sequence and frequency. These loadings also originate from various sources including once per flight events, maneuvering and atmospheric turbulence. The loading is not easily modeled by constant amplitude sinusoidal signals.

Even in the face of such difficulties, basic stress-load cycle curves are still used in an engineering design context. A common practice is to equate a complex built-up structural component to a notched material specimen having an equivalent stress concentration behavior.[14] Of course, validation testing for these critical components is necessary. Further, unnotched stress-load cycle curves have a common usage in predicting the fatigue life for an overall built-up structure via cumulative damage theories such as the Palmgren-Miner rule.[6] This rule states that the summation of fractional life

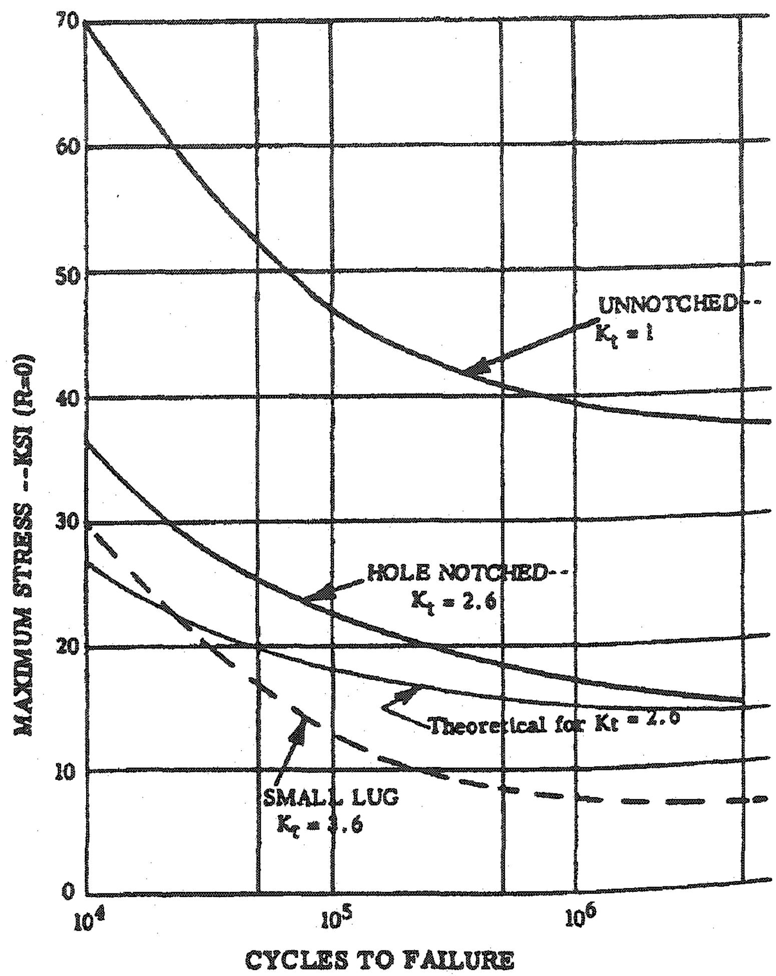

Figure 1.6 S-N Curve for Notched and Unnotched 7075-T6 Aluminum Alloy[14]

components of a structure must equal unity, or

$$\sum_{i=1}^{m} \frac{n_i}{N_i} = 1 \tag{1.1}$$

In Equation (1.1), n_i is the number of load cycles occurring at stress level σ_i and N_i is the total number of load cycles at σ_i required for failure, as obtained from an unnotched S-N curve. This rule is an approximate theory, but is in common usage. Note, the Palmgren-Miner rule does not reflect the effect of load amplitude sequencing. As a result, the summation term within Equation (1.1) shows large scatter usually between 1 and 4 depending on the application. Further efforts on predicting structural life under different sequencing of load amplitude have been considered. Among such efforts, Marco-Starkey rule, Henry's rule, Gatts' rule, Corten-Dolan rule, and Manson Double Linear Damage rule are well known, and can be found in many areas of the literature. Load-N curves are another variation of the S-N curve which are in common use for both overall structure or material components.[14]

To advance the understanding and knowledge of fatigue mechanisms, considerable analytical, or analytical-empirical, research focusing on the formation and propagation of cracks has been conducted. Over the last half century, efforts have also focused on analysis and design techniques addressing the nonlinear fatigue phenomenon. References 6 and 14, and the many references contained therein, provide detailed summaries of important developments in this field through 1975. Supplements from the post-1975 period provide more recent developments and breakthroughs in this field. These advancements have yielded considerable insights for improving the fatigue life of aircraft structures and are discussed below.

In practice, cracks are often observed to form near high stress concentration regions within a structure. Therefore, a discussion of stress concentration, or stress intensification is warranted. Figure 1.7 shows the longitudinal stress field near an elliptic hole in an infinite uniform sheet under uniform tension.[6] Application of elasticity theory[15, 16] to this situation reveals stress near the edge of the hole is amplified relative to the far field value by a factor of one plus two multiplied by the hole slenderness ratio (C/B). For a slenderness ratio of two, the edge stress is five times the nominal value. Note that a thin crack can be thought of as an elliptic hole with slenderness ratio approaching a very large value in the limit (see Figure 1.7). In this case, the crack tip stress becomes nearly unbounded. The material cannot support such a high stress level and goes under yielding thus forming small plastic regions near the crack tip. With this insight, it is clear why cracks tend to originate from rivet holes and other high stress concentration regions.

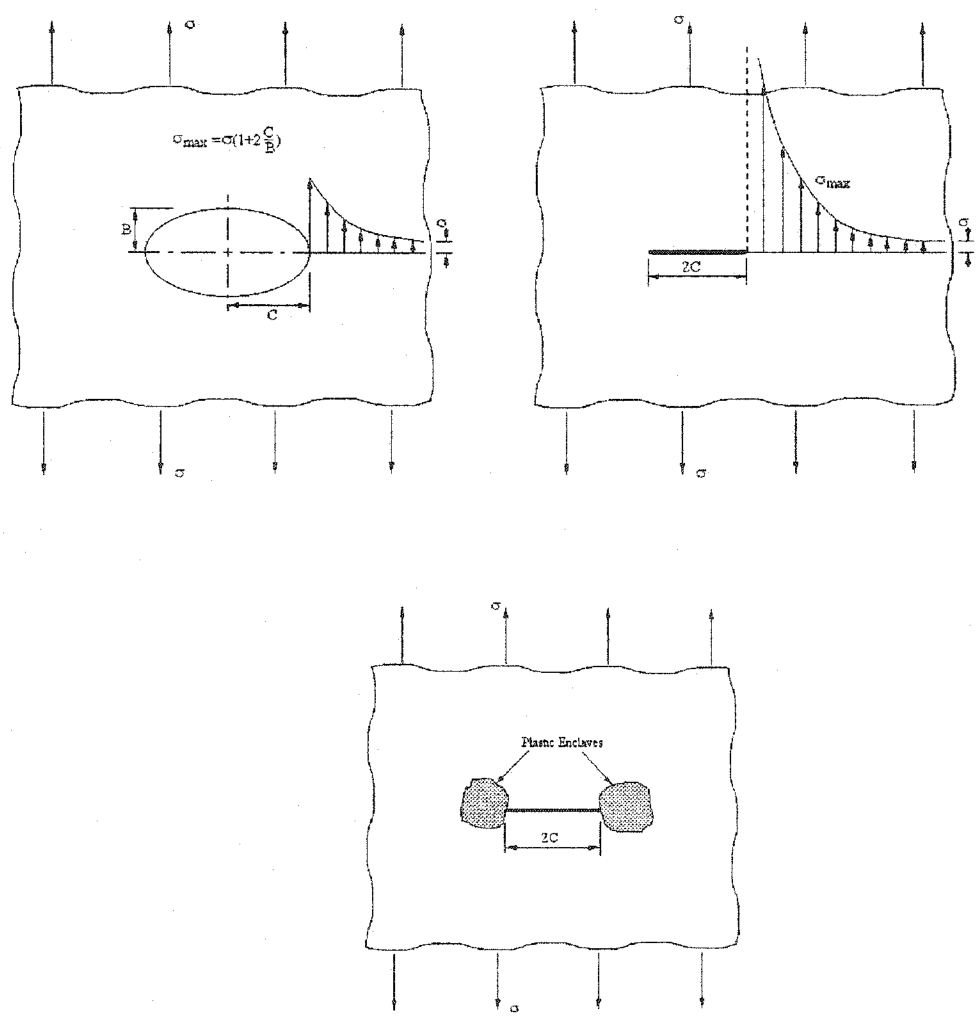

Figure 1.7 Stress Distribution Near a Slender Hole[6]

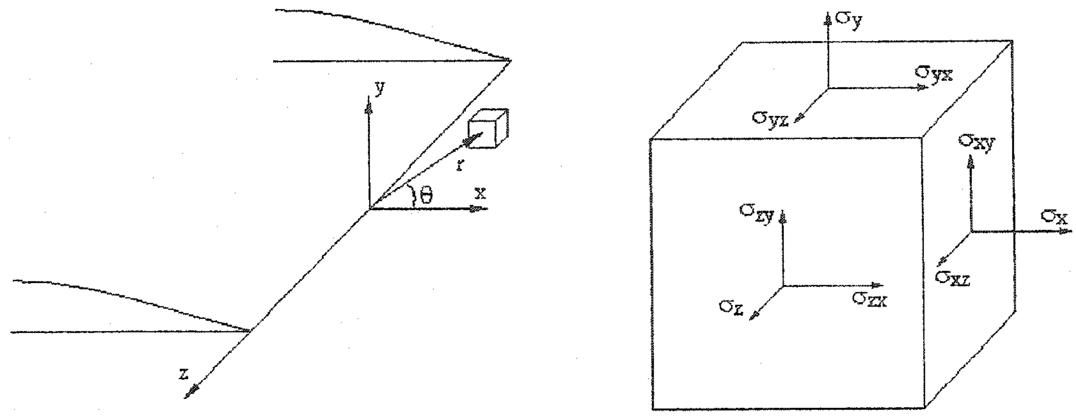

Figure 1.8 Crack Tip Geometry and Elemental Stress Notation[6]

The first rigorous treatment of a static relationship between crack length and stress utilizing elastic theory was completed by Irwin in 1957. This approach is often called Linear Elastic Fracture Mechanics (LEFM), and References 17-18 and many others provide detail information. Figure 1.8 illustrates the crack tip geometry. The crack is assumed to have a sharp-edged tip which is straight. The structural component is an infinite, thin sheet of homogeneous and isotropic nature. The component is loaded in tension along the y axis at the infinite boundary. In this plane stress situation, normal stress along the y axis (σ_y) near the crack tip, when expressed in an infinite series, is

$$\sigma_y = \frac{K}{\sqrt{2\pi r}}\cos\frac{\theta}{2}\left[1+\sin\frac{\theta}{2}\sin 3\frac{\theta}{2}+\cdots\right] \qquad (1.2)$$

In Equation (1.2), K represents a positive multiplying factor which only depends on the boundary condition loading and the crack size. This parameter is referred to as the stress concentration (or stress intensity) factor.

According to Equation (1.2), the spatial stress variation is inversely proportional to square root of the radial distance from the crack tip and is infinite at the tip itself.

However, the individual stress state for various structural configurations is captured solely by the stress intensity factor. An exact solution from the boundary conditions for the infinite sheet with thin crack is

$$K = \sqrt{\pi C}\sigma \tag{1.3}$$

where C is the crack half length and σ is the far field stress value. Equation (1.3) represents the crack length-stress relationship at the equilibrium condition for the infinite sheet with thin crack. Reference 6 contains a summary of other similar relationships for various geometries. Reference 6 also documents many refinements to this theory such as techniques to correct the solution results for the presence of small plastic regions near the crack tip as shown in Figure 1.7.

From Equation (1.3), the parameter $(K/\sigma_y)^2$ is often considered as a measure of fatigue resistance since it is proportional to crack length. In this context, note that σ_y is taken as the material yield stress. Another popular measure of fatigue resistance, which is based on consideration of small plastic regions near the crack tip, is the crack opening displacement (δ) which is illustrated in Figure 1.9. This concept was first considered in References 19-20. The plastic tip region is approximated by a circle of radius r_y where $r_y = 1/2\pi(K/\sigma_y)^2$.[6] As shown in Figure 1.9, the actual elastic-plastic crack is replaced by an effective fully elastic crack of half length $C' = C + r_y$. The crack opening displacement is the height of the effective crack at the elastic-plastic boundary of the actual crack. Utilizing the displacement equation along the y direction corresponding to Figure 1.8,[6] the crack opening displacement (COD) is

$$\delta = \frac{4}{\pi}\frac{K^2}{E\sigma_y} \tag{1.4}$$

where E denotes the material modulus of elasticity. Equation (1.4) represents the crack opening displacement relationship at the equilibrium condition.

Results in Equation (1.3)-(1.4) describe only static fracture mechanics relationships. To capture the fundamental behavior of crack growth, considerable research has addressed dynamic relationships, in particular crack growth rate laws such as

$$\frac{dC}{dN} = f(C, K, R, \cdots) \tag{1.5}$$

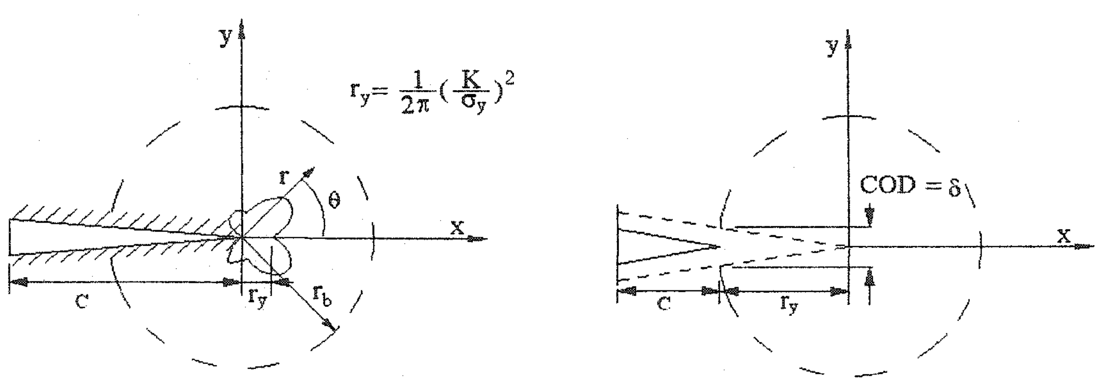

(a) Crack Tip

(b) Replacement of Actual Crack and Plastic Zone by Effective Elastic Crack ($C' = C + r_y$)

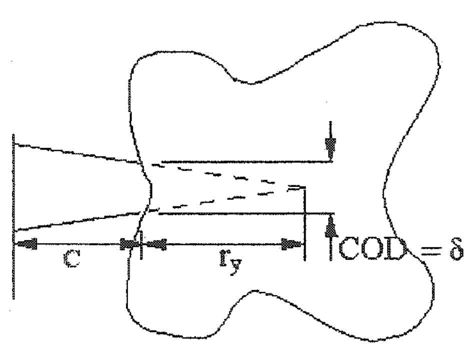

(c) COD: Effective Crack Height at Elastic-Plastic Boundary

Figure 1.9 Crack Opening Displacement[6]

With such relationships and applicable loading characteristics, analytical or numerical integration can be performed to project crack length vs. service life behavior. Conceptually, engineering predictions of this sort can be used to reduce expensive validation and verification testing activities, to lessen structural maintenance inspection efforts and optimize the scheduling thereof, and to address improved structural fatigue design considerations. Note, Equation (1.5) is nothing more than a state space model for crack growth, although this interpretation was not made until recently.[21] References 6 and 8 indicate fatigue life is characterized by three distinct phases:

1) Crack initiation,

2) Crack growth, and

3) Crack failure (rapid).

Relationships such as in Equation (1.5) only describe phase 2 while up to 50% of the service life can be spent in phase 1.[8]

Theoretic-based growth laws suffer from various inaccuracies, but most results contain the factor $\sqrt{C}\sigma$ (see Equation (1.3)). Therefore, the most widely accepted technique for growth law development is a semi-empirical approach built around the factor $\sqrt{C}\sigma$. Paris and Erdogen (References 22-23) recommend a growth law such as

$$\frac{dC}{dN} = C_0(K)^n \tag{1.6}$$

where C_0 and n are empirical constants and K is interpreted as the maximum stress intensity factor for constant amplitude cyclic loading. A modified version of this law was quickly developed as

$$\frac{dC}{dN} = C_0(\Delta K)^n \tag{1.7}$$

$$\Delta K = K_{max} - K_{min}$$

where ΔK denotes the stress intensity factor range, and K_{max} and K_{min} correspond to the maximum and minimum stress intensity factors for a variable amplitude loading.[24] This law was found to fit a wide range of materials, geometries and loadings. Reference 6 discusses many variants of this methodology to encompass an even broader range of materials and characteristics such as multi-slope behavior, threshold behavior and sensitivity to load mean and ratio, material properties and stress state. An example reference describing some of these detail effects is Reference 25.

With the development and utilization of crack propagation laws for fatigue life prediction, a significant issue arises in the selection of proper loading signatures which will be representative of operational flight environments. This selection is also important for testing purposes. Constant amplitude cyclic loading is often utilized but not very applicable as a substitute for actual flight loads. Common variable amplitude loads consist of programmed blocks of cyclic signals of various maximum/minimum amplitudes and frequency.[6] Random loadings of both broad band and narrow band spectra are also utilized.[6] Flight simulation blocks utilizing load exceedence charts/tables, flight test measurements and historical data can also be considered.[6,8] Reference 26 provides a good example of the variable amplitude loadings and their sequencing and interacting effects on crack growth. An example of maneuver loads is shown in Figure 1.10.[7] Accumulation of maneuver loads of this sort allows generation of the maneuver load spectra as shown in Figure 1.11.[6] An example gust load is shown in Figure 1.12.[7] Similarly, gust load spectra can be generated from accumulated gust load data as shown in Figure 1.13. [6] Figure 1.11 and 1.13 indicate the distribution of inflight load strength across the expected number of occurrences at those load strength levels.

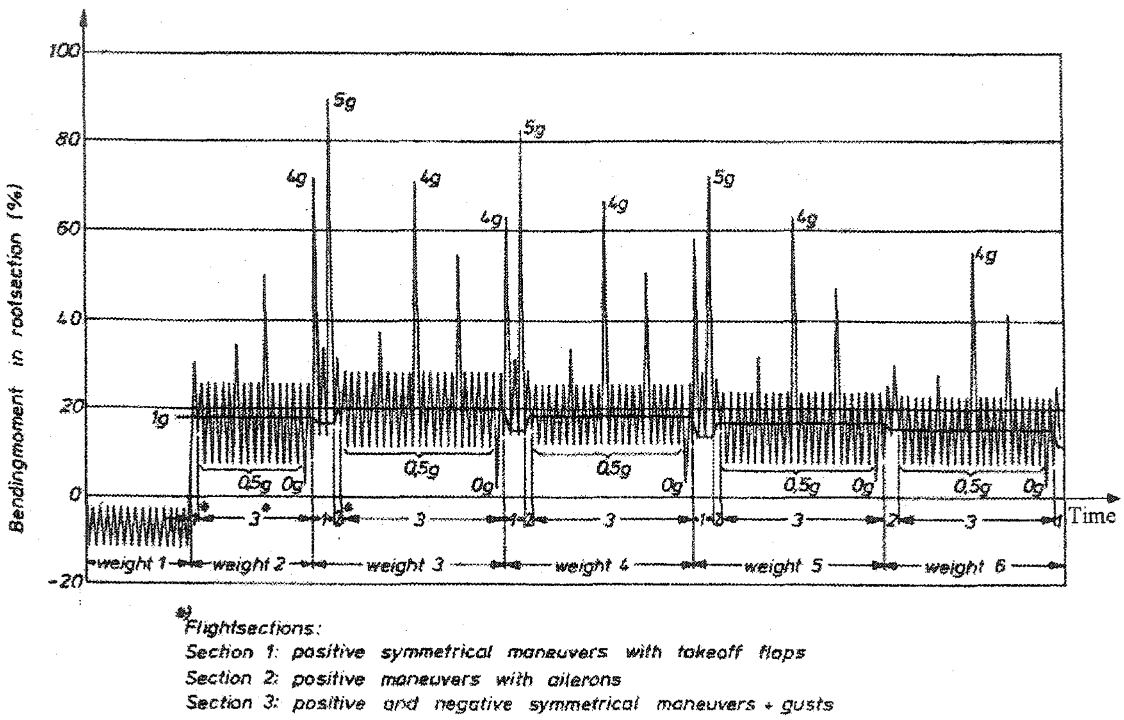

Figure 1.10 Example Maneuver Load[7]

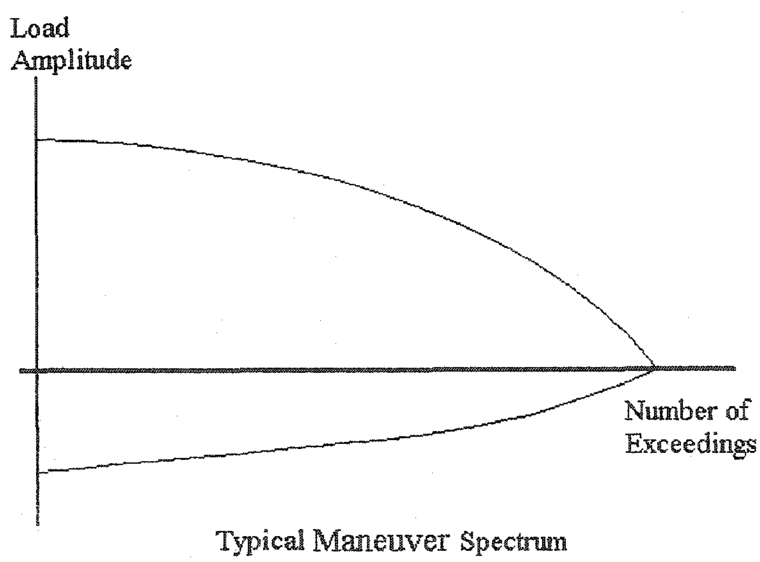

Figure 1.11 Typical Maneuver Load Spectrum[6]

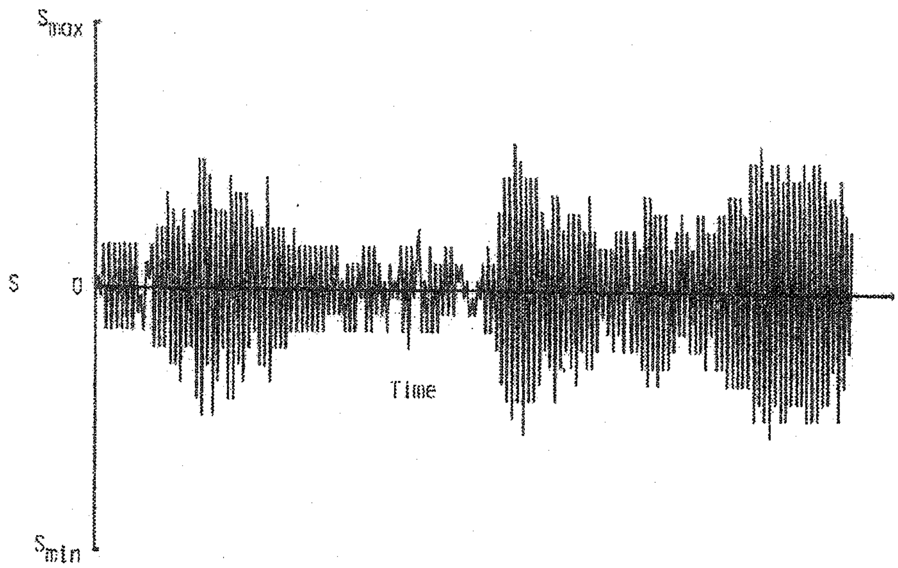

Figure 1.12 Example Gust Load[6]

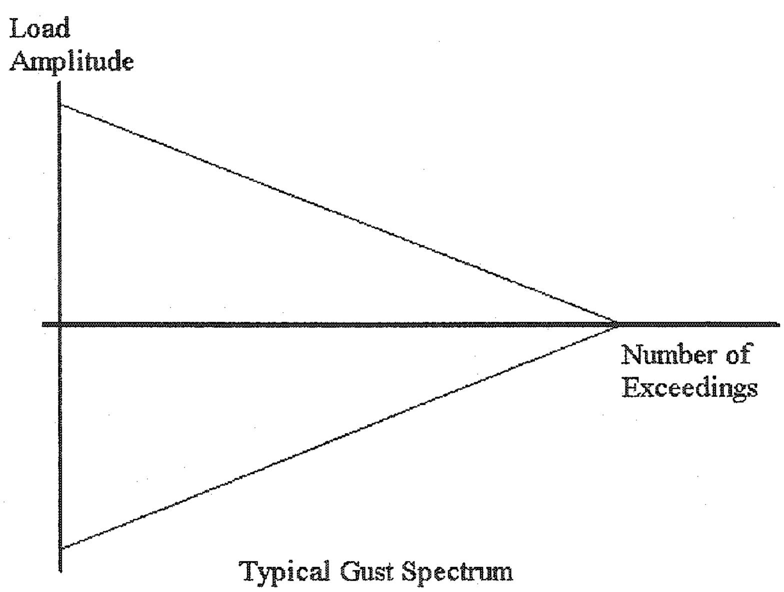

Figure 1.13 Typical Gust Load Spectrum[6]

Constant amplitude cyclic loading with a single applied overload during test has shown that crack propagation immediately following the overload, and for many cycles thereafter, is highly reduced or near zero.[27-28] Apparently, the overload introduces a large region of plasticity at the crack tip which is temporally under compression from the surrounding elastic material, thus retarding growth.[7] Figure 1.14 shows the nonlinear effect of this repeated overload on crack growth behavior during constant amplitude loading. This highly anti-intuitive and desirable behavior is of great interest to the fracture mechanics discipline. Figure 1.14 also shows the degraded behavior for a combined overload-underload situation. Note, symbol "a" in Figure 1.14 denotes crack size, and the applied nominal stress consists of mean stress S_m and stress amplitude S_a. S_{max} and S_{min} denote the corresponding overload and underload stress applied to the specimen. In addition to Figure 1.4, excessive overloads have been shown to accelerate crack growth,[29] thus indicating the presence of an optimum overload value for minimal crack growth. These relationships are exploited in the dissertation.

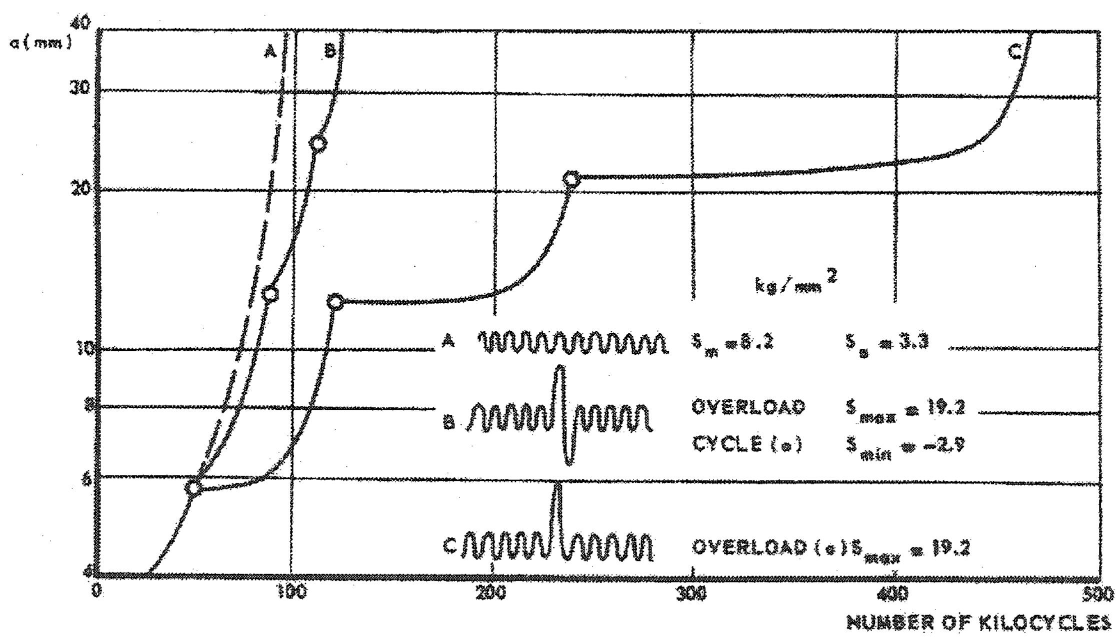

Figure 1.14 Overload and Underload Effect[29]

Until recently, the crack growth retardation effect due to overload was not accounted for in crack growth rate expressions, such as in Equation (1.7). To model this behavior, such relationships must incorporate stress state memory functionality.[6] A significant breakthrough in this area is development of the crack closure and crack

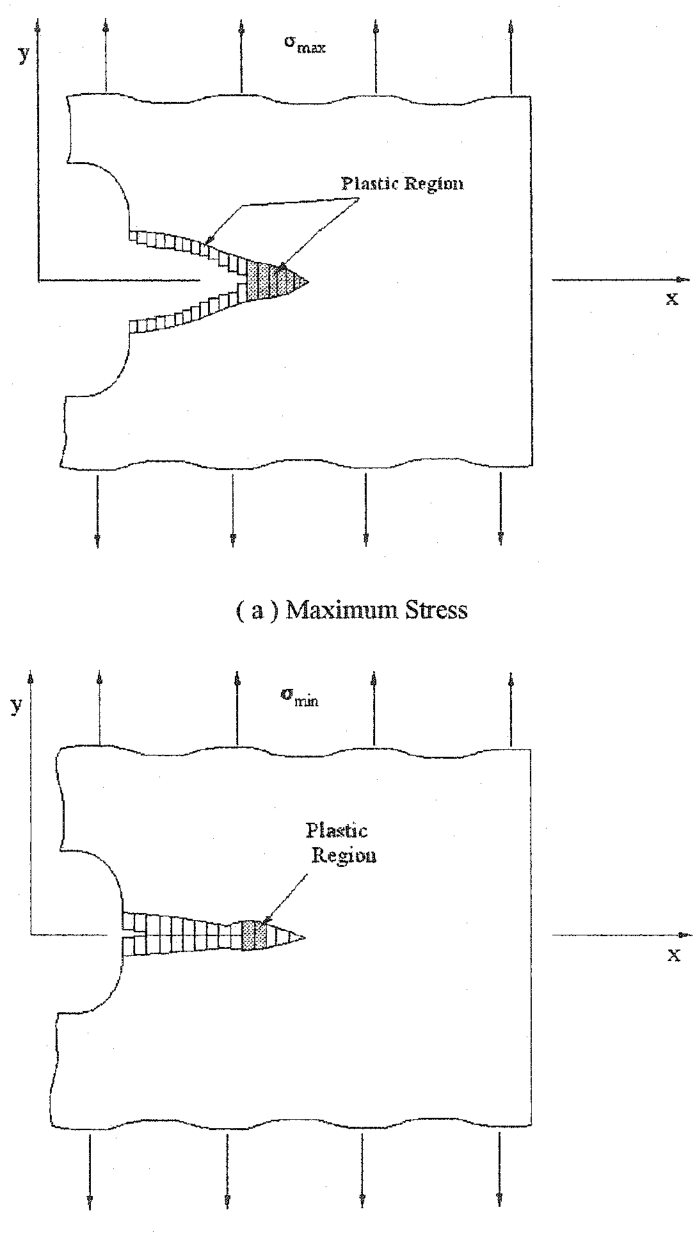

(a) Maximum Stress

(b) Minimum Stress

Figure 1.15 Schematic of Crack Closure Model under Cyclic Loading[6] opening stress concepts. The phenomenon was first recognized by Elber[30] and later formalized and refined by many others, such as in References 31-32. Fatigue crack closure is caused by residual plastic material left in the wake of an advancing crack on the upper and lower surfaces, as shown in Figure 1.15. Under heavy loading (σ_{max}), the crack is fully opened and normal fatigue mechanisms are in affect. However, under light loads (σ_{min}), the crack is not fully opened and the upper and lower plastic regions behind the crack front are still in contact. This contact mechanism retards crack growth under small loading. Crack opening stress (S_0 or σ_0) is defined as the required stress level to fully open the crack. The crack opening stress has been found to have strong dependency on the stress ratio and maximum stress. With this insight, the crack propagation law in Equation (1.7) is modified to become

$$\frac{dC}{dN} = C_0(\Delta K_e)^n \tag{1.8}$$

$$\Delta K_e = K_{max} - K_0$$

where ΔK_e is the effective stress intensity factor range. K_0 is the stress intensity factor associated with the crack opening stress level. Only that portion of the load cycle for which the crack is open leads to crack propagation.

Several attempts to calculate crack opening stress, in order to develop analytical models of crack closure, have been investigated. The Dugdale model[33] or strip-yield models, modified to leave plastically-deformed materials in the wake of the advancing crack, are the primary basis for these advanced crack closure models. These two dimensional models show that the crack opening stress is a function of stress ratio (R) and stress level (S_{max}). Crack opening stress is also known to be a function of specimen thickness. The most well known and widely used crack opening stress model was developed by J. C. Newman.[34] In his expressions, the crack opening stress is a function of stress ratio, stress level, and a three dimensional constraint factor α which represents the effect of thickness. The equations for the crack opening stress to maximum stress ratio are

$$S_0 / S_{max} = A_0 + A_1 R + A_2 R^2 + A_3 R^3 \qquad \text{for } R \geq 0 \tag{1.9}$$

and

$$S_0 / S_{max} = A_0 + A_1 R \qquad \text{for } -1 \leq R < 0 \tag{1.10}$$

when $S_0 \geq S_{min}$. The coefficients of Eq. (1.9) – (1.10) are

$$A_0 = \left(C_1 + C_2\alpha + C_3\alpha^2\right)\left[\cos\left(\pi S_{max} / 2\sigma_0\right)\right]^{1/\alpha} \tag{1.11}$$

$$A_1 = \left(C_4 + C_5\alpha\right)S_{max} / \sigma_0 \tag{1.12}$$

$$A_2 = 1 - A_0 - A_1 - A_3 \tag{1.13}$$

$$A_3 = 2A_0 + A_1 - 1 \tag{1.14}$$

The crack opening stress σ_0 can be determined experimentally by conducting a compression test. When the material yields under compression, the applied stress is defined as $-\sigma_0$, and crack opening stress σ_0 is computed from this basis. Also, constraint factor α can be estimated from a tensile test by defining the yield stress under the tensile load as $\alpha\sigma_0$. Testing can be used to calibrate the C_i coefficients. Using Equations (1.9) to (1.14), the effective stress intensity factor range can be calculated as

$$\Delta K_e = \left[\left(1 - S_0 / S_{max}\right)/\left(1 - R\right)\right]\Delta K \tag{1.15}$$

This type of propagation law is capable of modeling growth retardation and acceleration behavior following overload and underload applications. Stress state memory is included through the crack opening stress value, and will be fully explained in the next chapter.

Research by Ray has taken such crack growth models and interpreted them as state space models, thus providing a link between the disciplines of fracture mechanics and dynamic systems and control.[35] Both deterministic and stochastic models have been developed.[36] These state space crack growth models have been used in life extension and reliability enhancement strategies utilizing high-level supervisory control logic. This new concept is called damage mitigating control. Applications have included mechanical systems and aerospace propulsion component subsystems, for example.[35, 37] A more detailed description of the damage mitigating control concept is introduced shortly. This concept of employing feedback control to leverage long-term structural integrity is central to the dissertation.

Modern aircraft rely heavily upon computerized flight control systems to satisfy mission goals, provide acceptable handling qualities, stabilize relaxed stability airframes, and for suppression of flutter and structural vibrations.[38, 39] The first autopilot was implemented in 1914 by the Sperry brothers. Although not computerized, the system demonstrated that an aircraft could be controlled without frequent monitoring from a pilot-in-the-loop. After refinements, simple autopilots of this sort were utilized for many decades to assist pilots in performing basic tasks such as holding a course heading at a specified altitude.

In the post-World War II era, unprecedented advancements in speed, altitude, maneuverability, and operational envelopes were achieved with breakthroughs in aerodynamic, structural, and propulsive technologies, and in innovative aircraft design concepts. The basic dynamic characteristics of these vehicles, however, were often deficient for manual control. Flight control stability augmentation systems were relied upon to influence and improve these basic dynamic characteristics. With the advent of digital computer technologies, nearly every modern aircraft concept under consideration today incorporates a flight control system as an essential component for success.[40, 41]

Among the category of modern, highly maneuverable aircrafts, the F-16 is a primary example of a relaxed stability airframe requiring artificial stability supplements from control. The pitch stability of this vehicle is heavily dependent upon a flight control system (FCS) to the extent that the vehicle cannot be manually stabilized and flown without the digital fly-by-wire system. The control system changes fundamental response behaviors to task tailored response types appropriate for various flight phases such as take-off and landing, high-altitude cruise, low-altitude terrain contour following, air refueling, etc. The control system is every bit as important as the aerodynamic shape and structural layout in achieving overall vehicle performance.

Linear point-design control methods for flight control are numerous and are typically classified as being either conventional-based or contemporary-based. Conventional-based methods include the ubiquitous Nyquist, Bode, Nichols and Evans techniques, and variations thereof such as quantitative feedback theory (QFT), sequential loop closure, generalized gain/root loci, and singular value loop shaping.[42-52] Some of the more popular contemporary-based techniques include linear quadratic regulator / linear quadratic gaussian / loop transfer recovery (LQR/LQG/LTR), infinity norm control (H_∞), mu synthesis, eigenspace assignment and model following.[48, 53-58] Each technique has its own strengths and weakness with no one technique being satisfactory in all areas of interest. Important factors of interest when selecting a design technique include ability to address interacting loops, portrayal of insight, ease of implementation, architectural simplicity, robustness to uncertainties, controller order, achievable performance, design effort, etc.

Most of the literature specifically associated with flight control, such as References 9-10, is directed toward applications where the aircraft dynamic model is approximated reasonably well by a rigid-body model. Emphasis is typically given to stability augmentation systems and command augmentation systems such as pitch and yaw dampers, pitch rate command systems, roll rate command systems, and autopilot hold systems. Rigidity assumptions and approximations work reasonably well for a majority of the problems faced by flight control engineers. Rigorously speaking, however, rigid modeling assumptions cannot be used to investigate flight control leverage on fatigue damage, since the latter is only exhibited by flexible airframes.

One particular class of flight control systems closely related to the dissertation research subject is commonly referred to as maneuver and gust load alleviation systems.[10,59] Maneuver load alleviation is a technique of redistributing the spanwise lift profile on a wing, for example, with multiple aerodynamic control surfaces so as to reduce the structural loads during a maneuver. If a maneuver does not fully saturate the actuation performance capability of the vehicle, inboard surfaces can be used to initiate the maneuver and to shift the lift distribution inward, thus reducing wing root bending loads. Gust load alleviation is a technique of suppressing rigid-body and/or structural motions excited by gust encounters with multiple control surfaces so as to reduce structural loads or passenger/pilot discomfort during the transient motions. If a vertical gust is encountered, fore and aft surfaces could deflect to cancel or dampen the ensuing accelerations, for example. Several references describing such systems include References 60-66.

When the vehicle becomes so flexible that structural dynamics contribute significant percentages to the total accelerations, and when significant coupling exists between rigid-body and structural motions, highly specialized flight control systems are required to provide acceptable dynamic characteristics. These types of control systems are commonly referred to as ride control systems, structural mode control systems, and more generally aeroelastic flight control systems. Design of such aeroelastic flight control systems which include possibly separate but interacting subsystems for traditional stability augmentation and for structural dynamics suppression is a complex multivariable problem requiring an integrated synthesis perspective. Some significant research and applications are listed in References 67-71. Other recent studies have also been conducted on control of highly flexible vehicles.[72-75]

Although low risk load alleviation systems and higher risk integrated structural mode control systems provide significant benefit, the logic is based on the conservative conjecture that lighter transient motion and lower stress level correspond to maximum structural life. Since existence of anti-intuitive, optimal loads has been shown to exist, new control logic generalizing the load alleviation system to an aggressive load augmentation system performing both alleviation and amplification functions appears to be a research topic warranting exploratory investigations. In terms of flight control, there appears to be very little past work on direct control of crack growth and fatigue damage reduction. References 10 and 59 briefly discuss this type of control system and objective, but indicate very little research has been conducted on this topic. Reduction of crack growth and fatigue damage in overall airframe structures is achieved indirectly, to some extent, by structural mode control systems. Reference 76 briefly describes the level of fatigue damage reduction that might be expected with such systems. However, a dedicated flight control system for optimizing the loading environment to yield minimal fatigue damage has not been seriously considered until recently.

Such control concepts have been considered for other systems prior to flight control applications. The concept of damage mitigating control (DMC), developed by Ray and others, was proposed and conceptually demonstrated for life extension of systems such as the space shuttle rocket engine[77] and a fossil fuel power plant.[78] For the fossil power plant, structural durability of the main steam header was the focus. In the DMC concept, selected plant outputs are fed into the structural models of plant components under consideration. Structural loads are then computed from the component model, and a damage model computes the instantaneous damage and accumulated damage of the component. Based on the damage information, the control systems engineer determines the trade off between system performance and structural life of the component.

Literature reviews indicate only three previous attempts to apply active flight control to the nonlinear dynamic crack growth behavior in structural aviation systems. Early work was done by Rozak, and Rozak and Ray in 1995[79] and 1997. [80] A robust controller was developed for a helicopter to minimize the damage to the control horn of the main rotor and to provide acceptable handling qualities for the pilot. Because of the operating condition of the horn, the load acting on the component was based purely on mechanical forces and did not consider any aerodynamic force. A second follow on application by Caplin and Ray considered robust control for the structural component of a wing, as well as flying qualities.[81] Particular interest was on a component representing the wing main spar located at the wing root. A linear rigid body model of a highly maneuverable aircraft was used, and the aircraft and control system was modeled for one particular point within the flight envelope. An aeroelastic model of the wing was considered and includes aerodynamic forces and dynamic forces of the wing structure. The wing is simplified and modeled as a pair of beams, and subjected to bending and torsion motion. Several robust controllers were designed and tested for several short term maneuver responses, and the performance of the DMC system was evaluated. The DMC logic demonstrated a large influence on structural life benefit. While such a methodology could be used to design new controllers for existing helicopters or aircraft, the main application of this work is anticipated to be in the aircraft design phase.[82]

The third investigation covering application of structural life extension to aircraft by flight control technology was by Yu and Newman in 1998.[79] A linear model for a highly flexible version of the B-1 aircraft with control system was used. The longitudinal motion of the model and control system was considered, and a fuselage stringer component located near the cockpit was of interest. An integrated stability augmentation and structural mode control system for the vehicle dynamics was considered. The model and control system was developed for one point in the flight envelope, and again, selected motion of the vehicle was studied. Design of a dedicated control system for structural life extension was not conducted, but the effect of control parameters on structural life, dynamic stability, and transient performance was investigated. An important result from that body of research influencing this dissertation is the discovery of the significant potential that exists for life extension of structural components through applying optimal structural loading.

Although investigation of such systems demonstrated great advantage on structural life, direct implementation of this strategy within aircraft flight control systems is not yet feasible. In-flight estimation and measurement of small crack size states, detection and sensing of large turbulent wind fields and sudden emergency maneuvers looming in the near term,[83, 84] real-time simulation of long-term crack life cycle scenarios, and localized-isolated actuation and augmentation of specific structural components or subsystems will be required to fully achieve active control based structural life extension. However, two recent simplifying developments show a near term possibility for in-flight implementation. First, identification and characterization of optimal overload invariance to structural age (or crack size) has been discovered.[85] This discovery allows life extension control logic to be designed and applied independently from the structural component age. Tremendous savings result in terms of crack size measurement and crack life simulation. Second, formulation of an optimal overload strength to overload interval relationship has been considered. This relationship provides an efficient computational procedure for the desired load in each flight state and each life extending control compute cycle. Therefore, the life extending control logic can be designed without monitoring the structural age or crack size within each component of interest. Tremendous savings result in terms of control architecture and computational processing.

In light of the literature review, this dissertation focuses on developing life extending control (LEC) logic which can be directly implemented with current FCS. The new LEC logic will tailor the motion behavior of the vehicle into a desired state for structural life extension whenever necessary during flight as long as mission objectives are not compromised. In order to develop such LEC logic, a realistic nonlinear model of a highly maneuverable fighter aircraft and its nonlinear control system is developed for a large area of the flight envelope. The closed-loop aircraft model allows realistic maneuvering of the vehicle over large areas of the flight envelope facilitating consideration of a complete mission that can be studied over the airframe lifecycle. These features capture the most significant factors of the LEC concept, thus providing a solid basis for making engineering projections and associated conclusions.

1.3 Research Contributions

To the author's knowledge, this dissertation is a unique attempt to design a dedicated closed loop control logic that monitors critical motion behavior of flight vehicle, and issues control commands to drive the motion behavior of the aircraft to the desired optimal or sub-optimal motion which results maximum possible structural life. The Life Extending Control (LEC) logic extends structural life of selected components. Also, this dissertation evaluates the effect of such control logic on multiple structural components. Life Extending Control (LEC) logic is developed for a F-16 fighter aircraft. As a baseline of LEC development, a highly realistic nonlinear model of F-16 aircraft is developed, and nonlinear flight control system of the fighter aircraft is also developed. Crack growth behavior, age dependency of the crack retardation phenomenon are investigated. An autopilot system to operate the vehicle for the desired mission, and flexible wing model of the aircraft was developed. This dissertation demonstrates great possibility of life extension control through additional LEC logic added to the existing flight control system.

1.4 Dissertation Outline

An outline of this dissertation is given below. In Chapter 2, description of an analytic state space model of crack growth will be considered. After this description, the crack growth model is numerically exercised in order to uncover and expose fundamental crack growth behavior. To characterize crack growth behavior, both "short-term" laboratory specimen test type inputs and "long-term" operational flight type inputs will be considered. Crack retardation phenomenon after overload application and its dominant factors will be summarized. In Chapter 3, age dependency in crack growth behavior is investigated. This chapter will be focused on characterizing any dependencies of optimal overload ratio and interval on crack size, where crack size directly represents the age of the structural component. Since the optimal load condition is strongly related to the crack retardation phenomenon, age dependency of the crack retardation phenomenon will be emphasized. Chapter 4 will describe development of a nonlinear dynamic rigid-body model of the F-16 aircraft. The model is based on the nonlinear aerodynamic data for a large area of the flight envelope. Development of the equilibrium condition and step response of the vehicle are addressed. A linear dynamic flexible model of the F-16 aircraft wing is also described in Chapter 4. The flexible wing model allows precise calculation of stress response based on the aerodynamic and structural force/moment response of the rigid-body vehicle model. Description of a simplified inner loop, stability augmentation digital flight control system for the F-16 aircraft is offered in Chapter 5. Nonlinear features such as limiters, position saturation, rate saturation, and nonlinear gains are included in the FCS. Longitudinal and lateral directional FCS logic are discussed, and closed-loop time responses of the augmented rigid-body vehicle are shown. Also in Chapter 5, an outer loop, nonlinear autopilot system for the augmented F-16 aircraft is developed. The autopilot system consists of velocity hold, altitude hold, and heading hold functions. Time response behavior of the overall system including vehicle, stability augmentation system, and autopilot system are presented. Before the aircraft model performs the actual mission, the flight envelope is expanded in order to represent flight conditions. In Chapter 6, a realistic mission of the F-16 aircraft is defined. Vehicle motion response for the planned mission, and associated stress response of the wing is presented. Finally, development of life extending control logic is discussed in Chapter 7. In this chapter, design objectives of the LEC logic are identified. LEC logic is designed based on the nonlinear relationship between the vehicle state and resulting stress. LEC logic and LEC activating logic are discussed in detail. Crack growth with and without LEC logic is compared and contrasted in order to evaluate the performance of LEC logic, as well as the effect of the logic on multiple components within the wing and on nominal system stability and performance. Conclusions and recommendations are formulated in Chapter 8.

CHAPTER 2

CRACK GROWTH BEHAVIOR

2.1 Analytic Crack Growth Model

The crack growth model considered throughout this research was developed by Professor Asok Ray from Pennsylvania State University. This model is based on theoretical crack growth characterizations developed by Dr. James Newman at the National Aeronautics and Space Administration Langley Research Center. Reference 21 provides detailed information about the crack model which is summarized and highlighted here. Figure 2.1 illustrates a typical structural component that is associated with the analytical crack model. The specimen is a thin rectangular plate containing a notch. The notch could represent a rivet hole or access for carry-through supporting structure, for example. The plate is symmetric and axially loaded. Parameters describing the plate geometry include the half-width W, thickness t, notch half-width a_N, and notch height h_N. The far field stress loading is denoted by σ with a convention of positive values for tension. Figure 2.1 indicates the presence of cracks near both ends of the notch. The crack length (one side only) is denoted by the symbol C.

From Reference 21, the analytic state space model describing crack growth within the specimen depicted in Figure 2.1 can be written as

$$\frac{dC}{dN} = C_1 \left\{ F(\sigma_{\max} - \sigma_0)\sqrt{\pi C} \right\}^m \qquad \text{for} \qquad \sigma_{\max} \geq \sigma_0 \tag{2.1}$$

$$\frac{dC}{dN} = 0 \qquad \text{for} \qquad \sigma_{\max} < \sigma_0 \tag{2.2}$$

where

$$F = \frac{1}{\sqrt{\cos\left(\frac{\pi}{2}\frac{C}{W}\right)}} \tag{2.3}$$

$$\sigma_0 = f(\sigma_{max}, \sigma_{min}, C) \tag{2.4}$$

In Equation (2.1), N denotes number of load cycles, σ_{max} denotes the maximum stress during the load cycle, σ_0 denotes the crack opening stress, and F denotes a boundary condition correction factor. The parameters C_1 and m are positive constants and can be identified from experimental data. Equation (2.3) shows the explicit dependency of the boundary condition factor on the crack length. Equation (2.4) implies the crack opening stress is a function of the maximum and minimum stress occurring during the load cycle and of the crack length. The functionality represented by Equation (2.4) will be presented shortly.

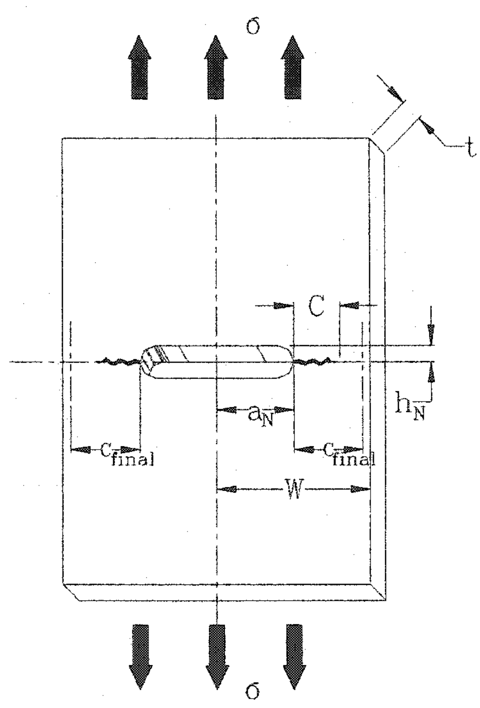

Figure 2.1 Structural Component Specimen

The crack model in Equations (2.1)-(2.2) is nothing more than a first order differential equation for C in terms of N, where dC/dN represents the rate of crack growth. If crack growth is interpreted as a dynamic system, then Equation (2.1)-(2.2) is simply a state space description of this system. Even though the crack growth rate in Equations (2.1)-(2.2) is initially expressed as a continuous differential equation, the independent temporal variable N is discrete. When performing simulation on a digital computer, the continuous derivative is replaced with a discrete derivative and the inconsistency is eliminated. Note the crack model described above is highly nonlinear: C and σ_{max} raised to a power, trigonometric functions of C, hard on-off behavior dependent on the sign of $\sigma_{max} - \sigma_0$, and crack opening stress functionality in terms of C, σ_{max} and σ_{min}. In addition to the above observations, Equations (2.1)-(2.2) indicate crack growth rate is always nonnegative and hence, crack length is a monotonically increasing function.

The crack opening stress function in Equation (2.4) is expressed below in Equations (2.5) through (2.24) in Table 2.1 with the indicated logic. In Equation (2.17), the crack opening stress for constant amplitude loading (σ_{0CA}) is computed from the product of σ_{max} and $\mathcal{R}$ where the parameter $\mathcal{R}$ denotes the ratio $\sigma_{0CA}/\sigma_{max}$. Note the similarity between parameter $\mathcal{R}$ as defined here and parameter R defined in Chapter 1. $\mathcal{R}$ is given by Equation (2.15) in terms of coefficients A_i and a modified ratio parameter R'. Depending upon the value of σ_{max}, the coefficients A_i and parameter R' are computed by either Equations (2.5)-(2.6) or (2.7)-(2.14). For the case $\sigma_{max} > 0$, the modified ratio R' is computed from a modified minimum stress (σ'_{min}) given in Equation (2.7) where $\sigma_{min\ old}$ is the minimum stress from the previous load cycle. Note the coefficients A_0 and A_1 for this case are functions of the current crack length through the intermediate variable Z and the boundary condition factor F. Further, α is a constant parameter describing the specimen loading condition somewhere between plane stress ($\alpha = 1$) and plane strain ($\alpha = 3$), and σ_{flow} is the average value between the material ultimate tensile strength (σ_u) and the yield strength (σ_y), or $\sigma_{flow} = ½(\sigma_u+\sigma_y)$.

The general crack opening stress for a variable amplitude loading (σ_0) is computed in Equation (2.24). σ_0 is calculated from the crack opening stress value associated with the previous loading cycle ($\sigma_{0\ old}$) and a perturbation value P where P is

Table 2.1 Crack Opening Stress Model

If $\sigma_{max} \leq 0$

$$R' = 0 \tag{2.5}$$

$$A_0 = A_1 = A_2 = A_3 = 0 \tag{2.6}$$

If $\sigma_{max} > 0$

$$\sigma'_{min} = \frac{\sigma_{min} + \alpha\sigma_{min\,old}}{1+\alpha} \tag{2.7}$$

$$R' = \sigma'_{min} / \sigma_{max} \tag{2.8}$$

$$Z = F\,(\sigma_{max}/\sigma_{flow}) \tag{2.9}$$

$$A_0 = (0.825\text{-}0.34\alpha+0.05\alpha^2)\left\{\cos\left(\frac{\pi}{2}Z\right)\right\}^{1/\alpha} \tag{2.10}$$

$$A_1 = (0.415\text{-}0.71\alpha)Z \tag{2.11}$$

If $R' < 0$

$$A_2 = A_3 = 0 \tag{2.12}$$

Table 2.1 Crack Opening Stress Model (Continued)

If $R' \geq 0$

$$A_2 = 2 - 3A_0 - 2A_1 \quad (2.13)$$

$$A_3 = -1 + 2A_0 + A_1 \quad (2.14)$$

$$\mathcal{R} = A_0 + A_1 R' + A_2 R'^2 + A_3 R'^3 \quad (2.15)$$

If $\sigma_{max} > 0$ & $\mathcal{R} < R'$

$$\mathcal{R} = R' \quad (2.16)$$

$$\sigma_{0CA} = \mathcal{R}\sigma_{max} \quad (2.17)$$

If $\sigma_{0\,old} \geq \sigma_{0CA}$

$$\lambda = 0 \quad (2.18)$$

If $\sigma_{0\,old} > \sigma_{max}$

$$\eta = \eta_1 \quad (2.19)$$

If $\sigma_{0\,old} \leq \sigma_{max}$

$$\eta = \eta_2 \quad (2.20)$$

If $\sigma_{0\,old} < \sigma_{0CA}$

$$\lambda = \left(1 + e^{\frac{2t}{C-W}}\right)\frac{\sigma_{max} - \sigma'_{min}}{\sigma_{max} - \sigma_{min\,old}} \quad (2.21)$$

$$\eta = \eta_2 \quad (2.22)$$

$$P = \lambda\{\sigma_{0CA}(1+\eta) - \sigma_{0\,old}\} + \eta\sigma_{0CA} \quad (2.23)$$

$$\sigma_0 = \frac{\sigma_{0old} + P}{1+\eta} \quad (2.24)$$

dependent on $\sigma_{0\ old}$ and σ_{0CA} and is given by Equation (2.23). In Equation (2.23), and depending on the value of $\sigma_{0\ old}$ relative to σ_{0CA} and σ_{max}, the parameter η (= η_1 or η_2) is a positive empirical constant determined from testing. Also, depending on the case, the variable λ in Equation (2.23) can be a function of the various stresses and the crack length (see Equation (2.21)).

With the complete analytic model for crack growth laid bare, several insightful observations concerning crack growth behavior are noted below. In Equation (2.1)-(2.2), the factor σ_{max} - σ_0 plays the role of an input to the dynamic system. During any load cycle where $\sigma_{max} > \sigma_0$, the crack will have a positive growth rate. If the difference between σ_{max} and σ_0 remains roughly constant during repeated loading, then the crack length will tend to increase with a power relationship ($\sqrt{C}^m$) as N increases. This growth behavior is noted in much of the fracture mechanics literature such as in References 6 and 14. On the other hand, if σ_{max} falls below σ_0, then no growth occurs. In other words, the loading is not sufficient to fully open the crack due to the presence of plastic material left behind the advancing crack tip (see Chapter 1 and Reference 87). In this case, the crack tip and surrounding material are not being "worked" by the loading. This behavior is the situation observed to occur immediately following application of an overload (see References 6, 14, 87, and Chapter 1). The mechanism leading to $\sigma_0 > \sigma_{max}$ will be discussed shortly. An additional insight into the crack growth behavior can be had by taking $\sigma_0 = 0$. In this case, Equations (2.1)-(2.2) indicate that for tension loading ($\sigma_{max} >$ 0), positive growth rate occurs, but for compression loading ($\sigma_{max} < 0$), the growth rate is zero.

Now consider the crack opening stress behavior following the application of an overload. With large σ_{max}, the product $\mathcal{R}\,\sigma_{max}$ in Equation (2.17) induces a large but somewhat less than σ_{max} value for σ_{0CA}. Note that $\mathcal{R}$ is typically dominated by the A_0 term in Equation (2.15) and the other A_i terms can be considered small higher order effects. Further, for $1 \le \alpha \le 3$ and $0 \le C/W \le 2/\pi \cos^{-1}\{(\sigma_{max}/\sigma_{flow})^2\}$, the value of A_0 lies in the region $0 \le A_0 \le 0.535$. Therefore, depending on the specific loading case and crack state, the constant amplitude crack opening stress value σ_{0CA} can be increased up to approximately half of the overload stress value σ_{max}.

In the initial pass through the crack opening stress model following the overload, $\sigma_{0old} < \sigma_{0CA}$ and Equation (2.21) is activated with $\lambda \neq 0$. Assuming constant σ_{min} and small t/W and C/W (i.e., less than 0.25), Equation (2.21) indicates λ can approach a value of 2. Typically $\eta = \eta_2$ is a very small number relative to 1. Therefore, the perturbation value P which is added to σ_{0old} in Equation (2.24) is approximately $P \approx 2(\sigma_{0CA} - \sigma_{0old})$. If σ_{0old} is small relative to σ_{0CA}, it can be deduced that P could approach the value of the overload stress in the maximum case. The actual crack opening stress value is given by Equation (2.24). In the initial pass, σ_0 could thus approach an approximate maximum value that is on the order of the overload stress. In the second pass through the crack opening stress model following the overload, σ_{0CA} will be reduced because σ_{max} is of a lower value in Equation (2.17). In this second pass, σ_{0old} is now larger than σ_{0CA} and λ = 0 and $\eta = \eta_1$, according to Equations (2.18)-(2.19). The parameter η_1 is also typically very small relative to 1. Therefore, the perturbation value $P = \eta_1 \sigma_{0CA}$ is quite small when added to σ_{0old}. Recall, σ_{0old} is a large stress value resulting from the initial pass. Division by $1+\eta_1$ incrementally reduces the crack opening stress value σ_0. σ_0 will be gradually reduced by this effect on repeated passes through the model. Finally note that when σ_{0old} falls below σ_{max}, the division factor changes to $1+\eta_2$ (see Equation (2.20)).

In summary, the above observations encompass both crack acceleration and retardation behavior observed in experiments. Application of a sizable overload initially leads to a large value for $\sigma_{max} - \sigma_0$ which, through Equation (2.1), directly results in high growth rate. The crack length accelerates as the material near the crack tip is "torn" in the overload process. Immediately following this event, the crack opening stress value σ_0 rises sharply as σ_{max} falls off to its nominal level. Therefore, through Equation (2.1)-(2.2), a zero growth rate ensues. Crack growth is retarded as the crack is not fully opened and the material near the crack tip is unloaded. As the specimen is repetitively loaded following the overload, but at a reduced level, the crack opening stress value is gradually reduced until it falls below the σ_{max} threshold. At this point, a positive growth rate returns as the material near the crack tip is once again "worked."

2.2 Short-Term Crack Growth Behavior

To further expose characteristics and behaviors of the analytic crack growth model, MATLAB[#] software implementing Equations (2.1)-(2.24) is exercised with various stress input cases. In this section, the input loading template is representative of a short-term laboratory type test conducted on a material specimen. This type of input is common in the literature concerning experimental characterization of crack growth. A baseline input trace will be considered initially. Following this baseline case, other cases obtained by varying the input template parameters will be considered.

The short-term input loading is illustrated in Figure 2.2. The loading consists of an initial constant amplitude repetitive load with minimum stress σ_{min} and maximum stress σ_{max1}. This loading is repeated for N_1 cycles. This initial portion of the overall load is called phase 1. After phase 1 is complete, a single cycle overload is applied to the

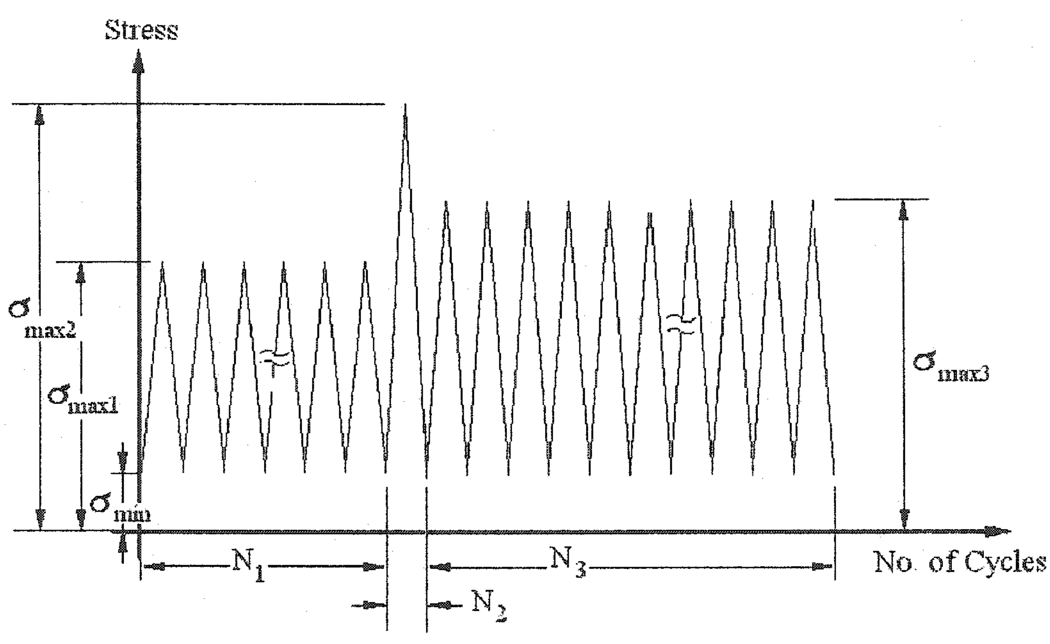

Figure 2.2 Short-Term Load Template

crack model. This component is called phase 2 and the associated parameters are σ_{min}, σ_{max2} and N_2 (= 1 *cyc*). The phase 3 portion of the overall load again consists of constant amplitude repetitive loading with σ_{min}, σ_{max3} and N_3 as the parametric description. Note that each loading phase has a common minimum stress level but distinct maximum stress levels and cycle numbers.

The geometry of the material specimen with the internal crack, whose model is being exercised here, is illustrated in Figure 2.1. The dimensions, material properties, and emperical constants for this specimen are listed below.

$$t = 1.016\,mm,\ W = 76.2\,mm,\ \sigma_y = 520\,MPa,\ \sigma_u = 575\ \text{MPa},\ m = 3.8\ \ \alpha = 1.7,$$

$$C_1 = 7\times10^{-11}\left[\frac{m}{cyc}\frac{1}{\left(MPa\sqrt{m}\right)^m}\right],\ \eta_1 = 0.8\times10^{-5},\ \eta_2 = 2.5\times10^{-4} \tag{2.25}$$

These values correspond to a small specimen consisting of an advanced metallic alloy. These values are used throughout the dissertation research. Figures 2.3-4 show crack growth and crack opening stress behavior for the loading in Figure 2.2 with $\sigma_{min} = 0.345\ MPa$, $\sigma_{max1} = \sigma_{max3} = 68.9\ MPa$, $\sigma_{max2} = 137.8\ MPa$, $N_1 = 17{,}000\ cyc$, and $N_3 = 40{,}000\ cyc$. Note the phase 1 and phase 3 maximum stress levels are equal, the phase 2 overload stress value is double that for phase 1 and phase 3, and the minimum stress level is nearly zero. The initial crack length was set at 12.7 *mm*.

As seen from Figure 2.3, the crack growth shows a monotonically increasing, highly nonlinear behavior. During the phase 1 loading ($1 \le N \le N_1\,cyc$), the constant amplitude repetitive stress continually "works" the material near the crack tip and the crack undergoes elongation governed by a power relationship. During this loading phase,

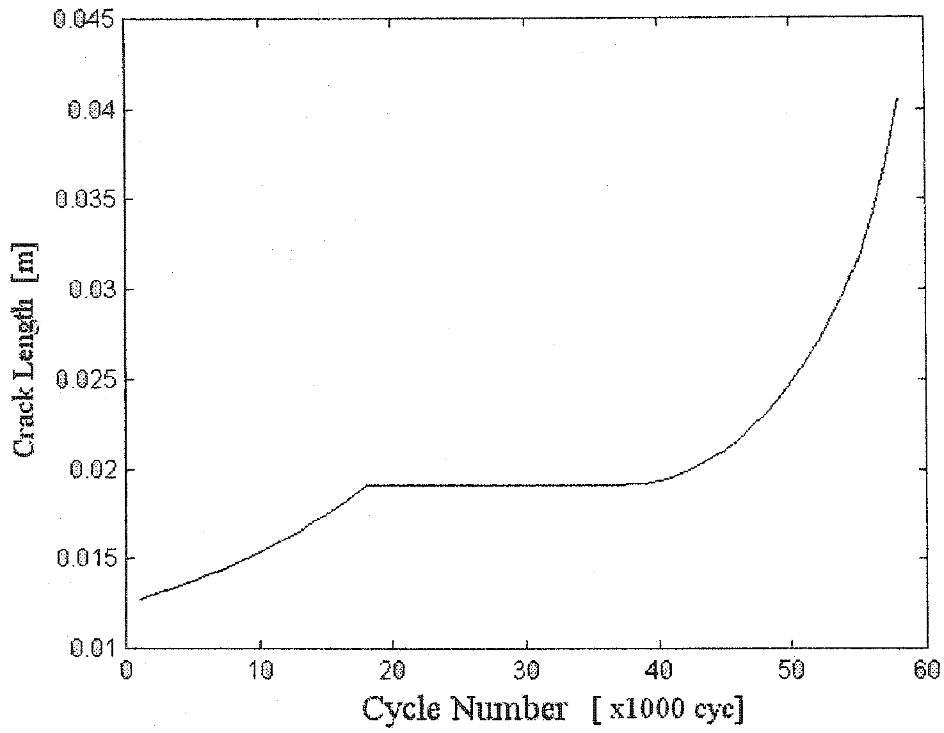

Figure 2.3 Crack Growth Behavior for Nominal Short-Term Input

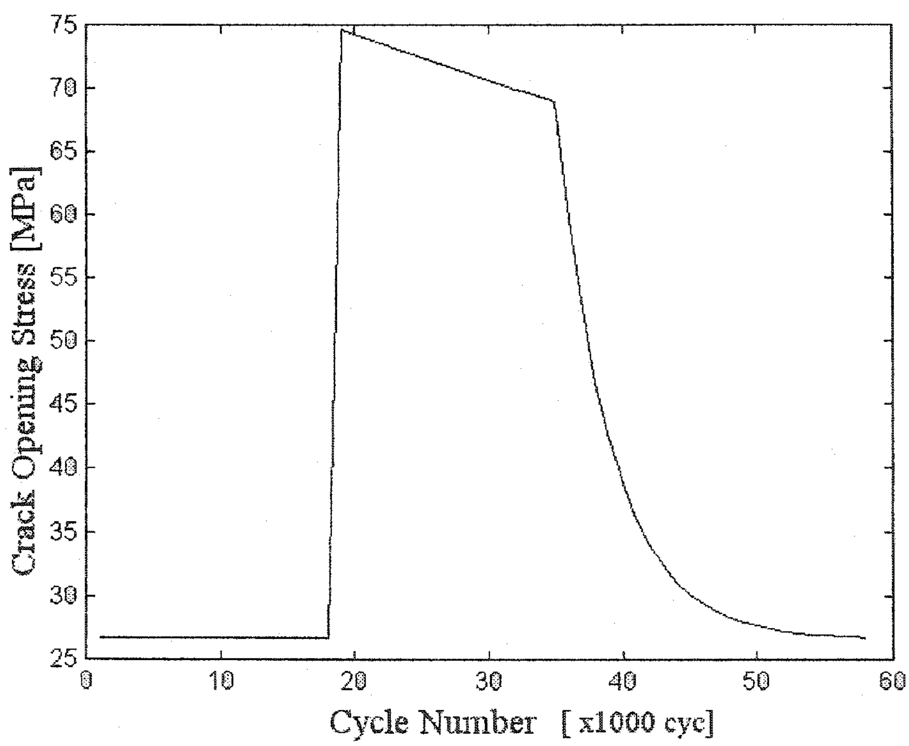

Figure 2.4 Crack Opening Stress Behavior for Nominal Short-Term Input

the crack opening stress remains nearly constant at a value of 26.5 *MPa* (see Figure 2.4), which is well below the 68.9 *MPa* maximum stress load value. After 17,000 *cyc*, the crack length is approximately 19 *mm*. During phase 2 ($N = N_1 + N_2\,cyc$) and the initial portion of phase 3 ($N_1 + N_2 + 1 \le N < N_1 + N_2 + 18{,}000\,cyc$), the crack growth is arrested and corresponds to the flat region in Figure 2.3. This behavior is the unexpected crack retardation effect noted in the literature: application of higher stress leads to reduced crack growth due to load plasticity.[6] Note that in Figure 2.4 the overload stress σ_{max2} = 137.8 *MPa* has resulted in a sudden rise in the σ_0 value (approximately 75 *MPa*). Even though the maximum applied stress immediately returns to σ_{max3} = 68.9 *MPa*, the crack opening stress remains high and only gradually drops off. In other words, $\sigma_0 > \sigma_{max}$ and the crack is not fully opened due to excessive build up of plastic material.[34] As a result, the material at the crack tip is not loaded and crack growth ceases although the crack opening stress gradually drops off. At approximately 35,000 *cyc*, the crack opening stress value falls below the threshold value of σ_{max3} = 68.9 *MPa* and changes its characteristic drop off rate. Beyond 35,000 *cyc*, $\sigma_{max} > \sigma_0$ and the crack begins to experience additional growth governed by a power relationship. After the total $N_1 + N_2 + N_3$ loading cycles, the crack length has grown to a value near 40 *mm*.

To further study the behavior of the crack growth model, several loading parameters in Figure 2.2 are varied. These parameters include σ_{max1}, σ_{max2}, σ_{max3} and σ_{min}. Each of these paremeters are varied in separate cases. All other parameters are held at their nominal values except N_3, which may be increased to illustrate various features in the results for a specified final crack length.

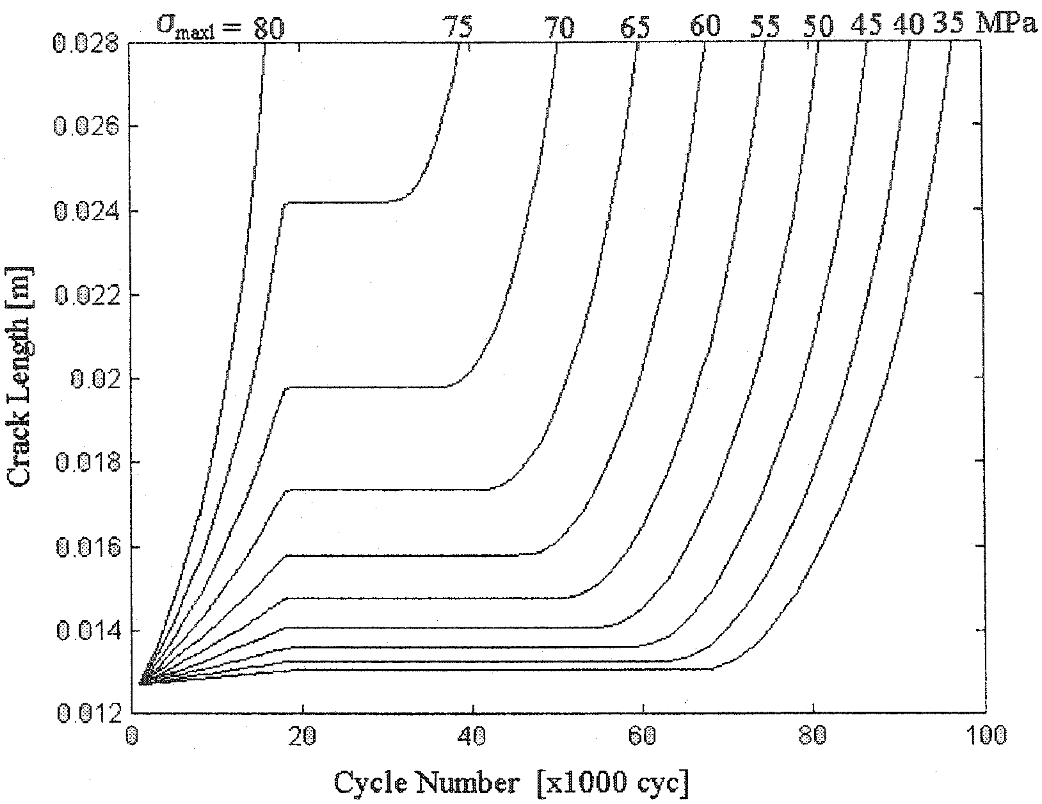

Figure 2.5 Short-Term Crack Growth Behavior – Variable σ_{max1}

First, the effects of variable σ_{max1} are considered. Figure 2.5 shows the crack growth behavior for a range of values lying between 35 and 80 *Mpa*. The data shows two important features. First, increased repetitive loading σ_{max1} results in higher rates of crack growth in phase 1. For the σ_{max1} = 35 *MPa* curve at the completion of N_1 cycles, the crack length is only 12.9 *mm* while for the σ_{max1} = 75 *MPa* case, the crack length has grown to 24 *mm*. Second, the ratio $\sigma_{max2}/\sigma_{max1}$ influences the duration of the zero growth region in the initial portion of phase 3. Increased ratios result in longer periods of crack stopage. Note for the σ_{max1} = 35 *MPa* curve the overload ratio $\sigma_{max2}/\sigma_{max1}$ = 4 is "large" and halts crack propogation until about 70,000 *cyc*. In contrast, for the σ_{max1} = 75 *MPa* case the ratio $\sigma_{max2}/\sigma_{max1}$ = 1.9 is "small" and crack growth stoppage occurs only out to near 30,000 *cyc*. Collectively, the 75 *MPa* case has higher overall crack growth, relative to the 35 *MPa* case, due to 1) an initially higher growth rate and 2) a reduced retardation period.

Second, the effects of variable σ_{max2} are considered. Figure 2.6 shows the crack growth behavior for a range of values lying between 70 and 525 *MPa*. The data shows two very interesting features. First, the duration of the zero growth rate region following the overload initially lengthens as overload stress increases, but eventually the trend is reversed and duration shortens as σ_{max2} is increased further. For the 245 *MPa* curve, the crack retardation period occurs out to approximately 130,000 *cyc*, while for a 350 *MPa* overload the retardation extends to 155,000 *cyc*, and for 455 *MPa* the value reduces back

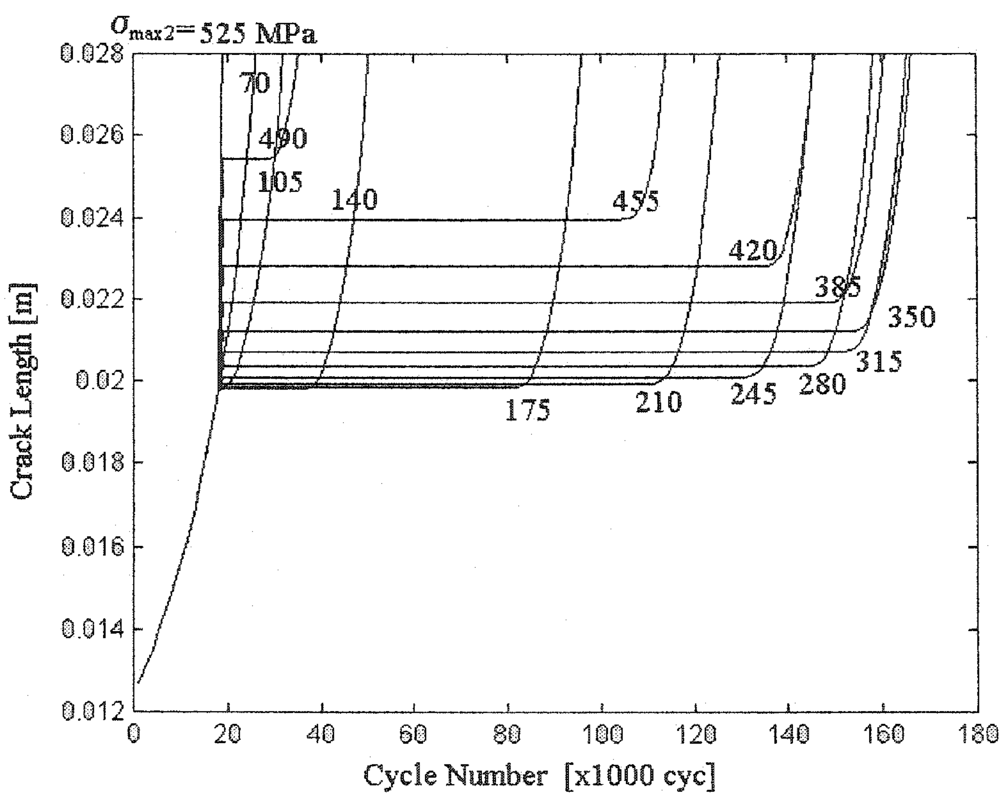

Figure 2.6 Short-Term Crack Growth Behavior - Variable σ_{max2}

to 105,000 *cyc*. Second, note the static crack length value during the dormant region due to crack acceleration imediately following the overload is higher for increased values of σ_{max2}. For the 245 *MPa* curve, the crack acceleration increment is very small and on the order of 0.2 *mm*, while for the 350 *MPa* overload the increment is significant and equal to 1.3 *mm*, and for 455 *MPa* the value jumps to 4.1 *mm*. These features combine to yield an unexpected optimal value for σ_{max2} corresponding to minimal overall crack growth. An approximate overload value of σ_{max2} = 350 *MPa* corresponds to minimal overall crack growth.

Third, the effects of variable σ_{max3} are considered. Figure 2.7 shows the crack growth behavior for a range of values lying between 35 and 80 *MPa*. Data generally shows that increased repetitive loading σ_{max3} results in higher growth rates once the crack breaks out of the retardation period. As an example, the σ_{max3} = 35 *MPa* curve requires approximately 125,000 cycles after break out to reach a crack length of 28 *mm*, while for the σ_{max3} = 75 *MPa* case only about 5,000 cycles are needed to attain the same length. Further, the ratio $\sigma_{max2}/\sigma_{max3}$ influences the duration of the zero growth region. Increased ratios result in longer periods of crack stopage. Note the 75 *MPa* curve ($\sigma_{max2}/\sigma_{max3}$ = 1.9) breakes out from retardation at 25,000 *cyc*, but the 35 *MPa* case ($\sigma_{max2}/\sigma_{max3}$ = 4) departs at the much larger value of 150,000 *cyc*.

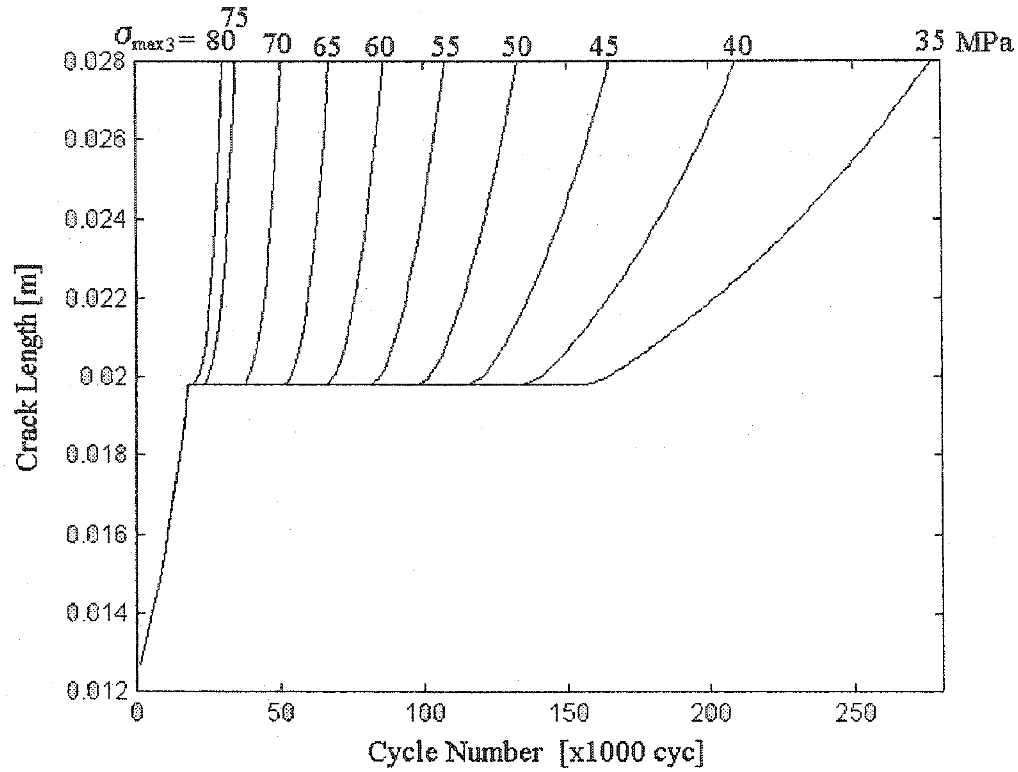

Figure 2.7 Short-Term Crack Growth Behavior – Variable σ_{max3}

Fourth, the effects of variable σ_{min} are considered. Figure 2.8 shows the crack growth behavior for a range of values lying between 1 and 19 *MPa*. In overall terms, Figures 2.5 and 2.8 have similar appearance. The data indicates that a larger spread between σ_{max} and σ_{min} corresponding to higher growth rates. As an example, the σ_{min} = 19 *MPa* case corresponds to σ_{max} - σ_{min} = 49.9 *MPa* and shows significantly slower growth when compared with the σ_{min} = 1 *MPa* case corresponding to σ_{max} - σ_{min} = 67.9 *MPa*.

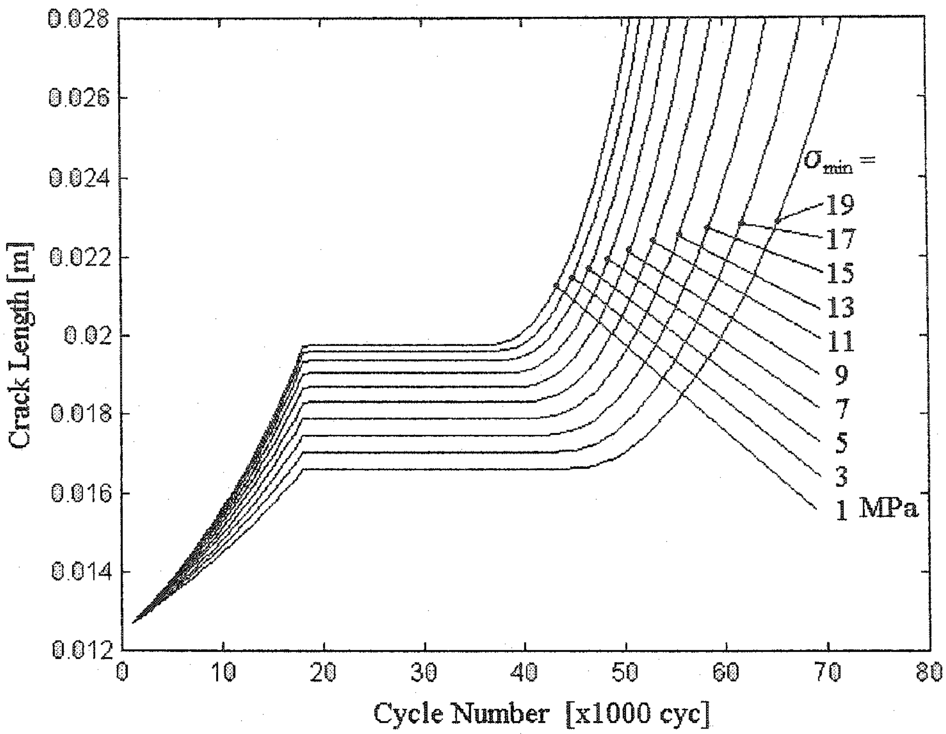

Figure 2.8 Short-Term Crack Growth Behavior - Variable σ_{min}

2.3 Long-Term Crack Growth Behavior

Now consider a long-term load template depicted in Figure 2.9 which roughly approximates in-flight loadings. The loading consists of a constant amplitude repetitive load (σ_{max1}, N_1) and a single overload (σ_{max2}, N_2=1 *cyc*) sequence continuously repeated. Note each load cycle has a common minimum stress (σ_{min}). The crack model parameters listed in Equation (2.5) are again used here.

Figure 2.10 shows the crack growth behavior for the loading in Figure 2.9 with σ_{min} = 0.345 *MPa*, σ_{max1} = 70 *MPa*, $80 \le \sigma_{max2} \le 360$ *MPa*, and N_1 = 1,000 *cyc*. For all cases, the repeated sequence input results in exponential crack growth with atypical behavior. During the initial increase in the overload stress ($80 \le \sigma_{max2} \le 140$ *MPa*), a corresponding decrease in crack growth rate can be seen. As the overload stress value is further increased, this trend reverses direction. For the range $180 \le \sigma_{max2} \le 360$ *MPa*, the

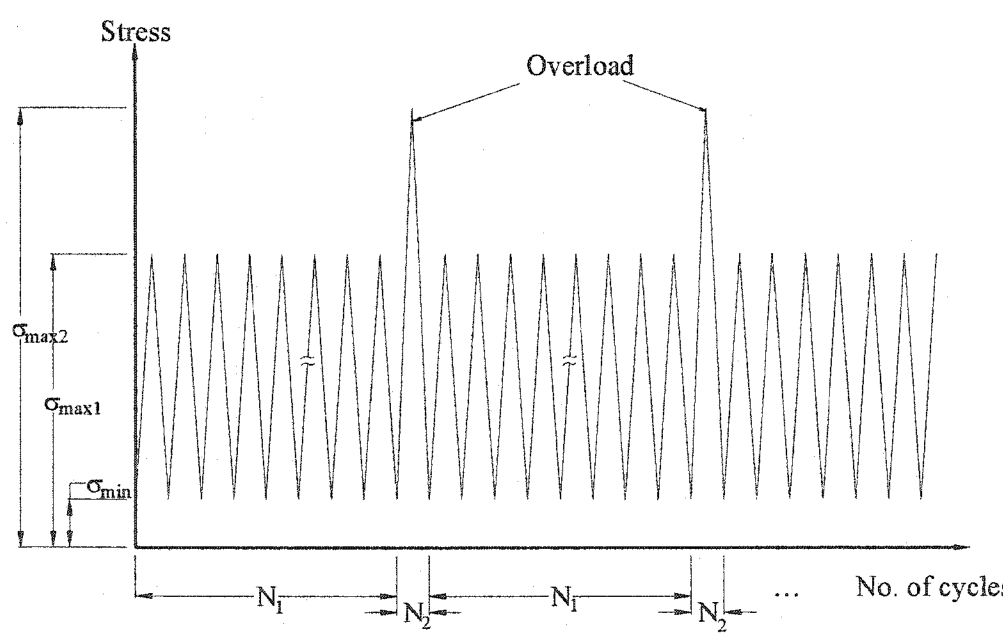

Figure 2.9 Long-Term Load Template

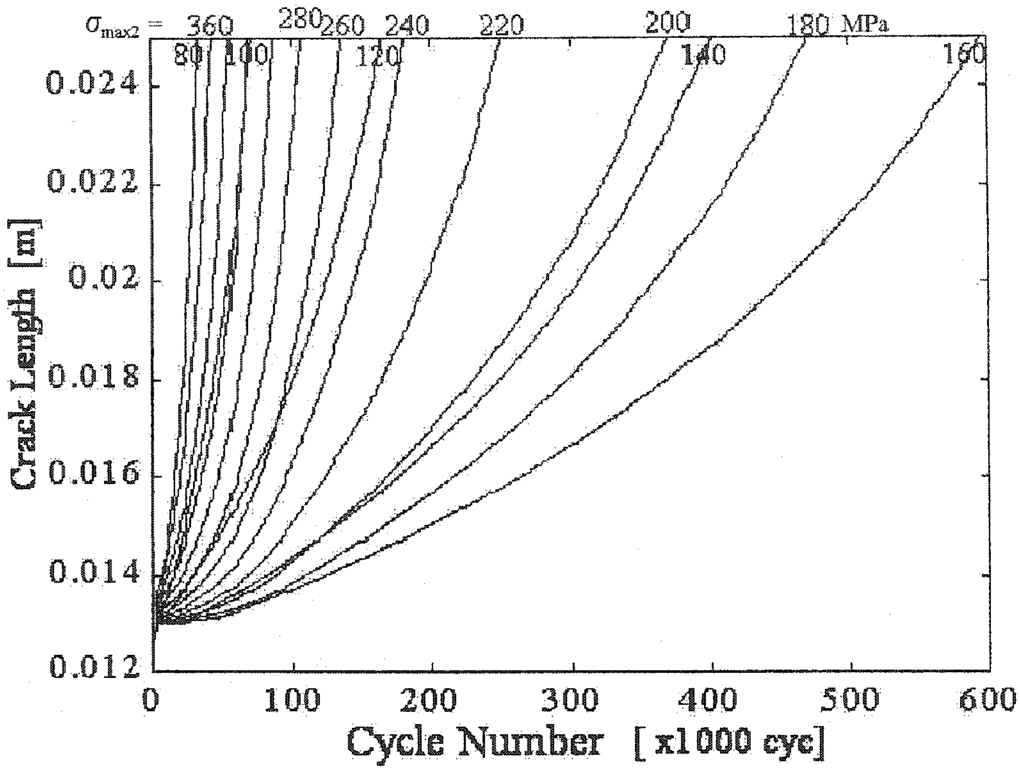

Figure 2.10 Long-Term Crack Growth Behavior – Variable σ_{max2}

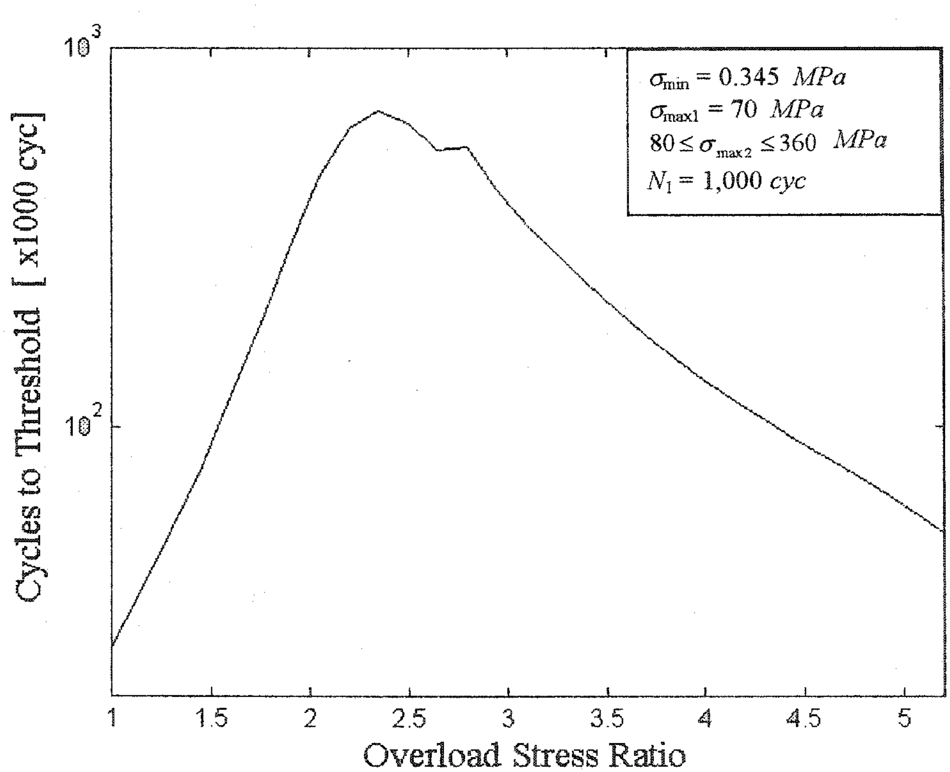

Figure 2.11 Cycles to Threshold Summary – Effect of Overload Ratio

crack growth rate picks up. An approximate value of σ_{max2} = 160 *MPa* corresponds to minimal overall crack growth. Thus, minimum crack growth does not correspond to the minimum overload stress. It is important to note that after each overload application, a crack retardation segment appears, but can not be observed in Figure 2.10 due to the axis scaling.

The optimum overload ratio $\sigma_{max2}/\sigma_{max1}$ in Figure 2.10 which yields minimal growth is just above a value of 2. Overload ratios above and below this value lead to longer cracks in the same number of cycles, or shorter cycles to reach a specfied crack length. Information of this sort can be used to construct a cycles to failure summary chart

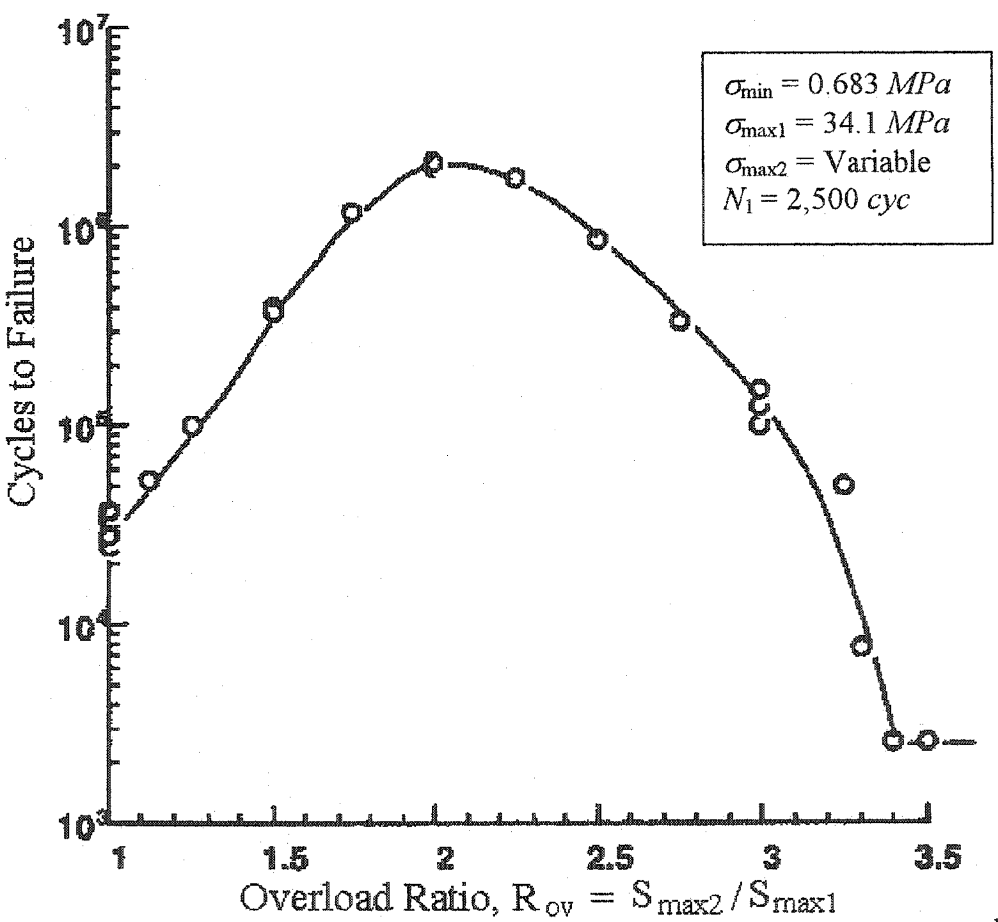

Figure 2.12 Experiment Result from Dawicke – Effect of Overload Ratio[12]

in Figure 2.11. If C = 25 *mm* is taken as the crack length threshold beyond which immediate repair is necessary, the final points from each curve in Figure 2.10 are used to construct Figure 2.11. Figure 2.11 indicates the optimum ratio is near 2.25. The structural life can be substantially enhanced (by an order of magnitude) if the overloading inherently occures at this value, or a control system such as LEC tailored the loading to achieve this value.

To validate this highly nonintuitive behavior, experimental results from Reference 29 are offered in Figure 2.12. Figure 2.12 shows a cycles to threshold summary chart based on actual test data for a specimen and loading which is similar but not identical to the analytical case presented previously. In this test, the overload was applied every 2,500 *cyc*. The curves in Figures 2.11-2.12 exhibit similar behavior showing maximum structural life for an overload ratio near 2 with significant loss in life on either side of this desirable value. In some sense, Figure 2.12 validates the analytical model predictions given in this research. Note the number of cycles at threshold for the test data in Figure 2.12 are much higher than the corresponding values in Figure 2.11 because the testing was carried through to actual failure while the analytically generated data was terminated at an artificial threshold point.

Further investigation revealed the overload application interval significantly influenced the shape of the cycles to threshold summary chart. The interval between overload applications in Figure 2.9 is parameterized by N_1. A large family of load cases with varying σ_{max2} and N_1 were inputted to the MATLAB crack model. Results from these cases are displayed in Figure 2.13 in the form of cycles to threshold summary charts. The varying load parameters were distributed according to $70 \le \sigma_{max2} \le 360$ *MPa* and $1{,}000 \leq N_1 \leq 7{,}000\,cyc$. Figure 2.13 shows that for increasing interval between overload application, the optimum overload stress ratio also increases. For the indicated input runs, this ratio can vary from 2 to 3. Therefore, maximal structural life is dependent on both overload strength and overload interval.

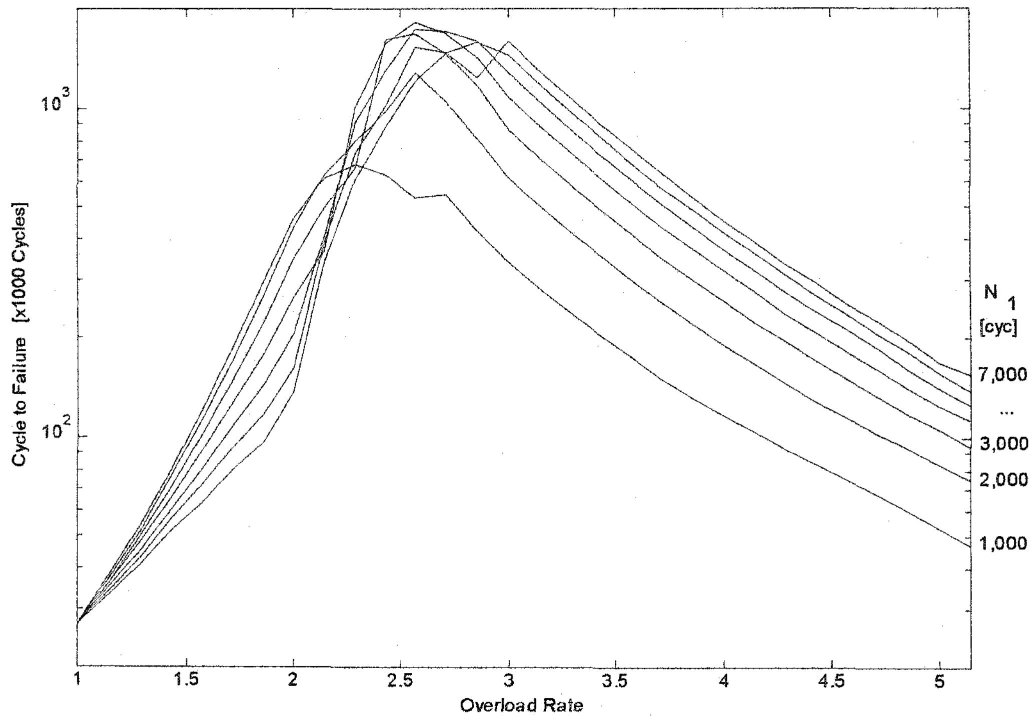

Figure 2.13 Cycles to Threshold Summary – Effect of Overload Interval

CHAPTER 3

AGE DEPENDENCY IN THE CRACK RETARDATION PHENOMENON

3.1 Age Dependency Implications for Control Implementation

Age dependency implications on optimal stress management within life extending control (LEC) logic are an important matter. In practical development and implementation of LEC logic, two difficulties arise due to crack growth dependency on length or size of the crack. Note crack size and the age of the structural component are synonomous. First, size data for all cracks within all critical components is not realistically available from sensor measurement for LEC processing in real-time, in-flight operations. Second, individual cracks in different components, or cracks within the same component, are of different lengths implying each individual component or crack requires its own optimal stress level. However, if dependency of the crack retardation phenomenon on structural age can be shown to be weak and negligible, a tremendous simplification can be realized which makes LEC a near term feasibility. A weak relationship between age of the structural component and the crack retardation behavior, and hence the required optimal stress, implies that health monitoring systems employing on-line crack measurement or on-line crack model simulation would not require tight integration to the LEC logic. Further, load tailoring for individual cracks would be unnecessary. An argument supporting the existence of weak dependency of crack retardation behavior on structural age is presented in this chapter. A cornerstone of the argument is that future aircraft employing LEC systems will still undergo periodic inspections of their structure, followed up with preventive maintence or part replacement. Under such maintence procedures, maximum crack length experienced during flight is bounded. With a finite window for crack length, age dependency is shown to be negligible. This argument involves both analytical consideration and computer simulation. Note that without the inspection and maintence assumption, the argument may breakdown. However, the assumption is repesentative of actual flight systems.

3.2 Damage Tolerance and Safety Maintenance Concepts

The presence of cracks can significantly reduce the strength of structural components, leading to brittle fracture. However, it is unusual for a component to be fabricated with an initial crack having a dangerous size. The common situation is that an initial microscopic flaw develops into a crack and then grows over time until it reaches the critical crack size (C_c) where brittle fracture occurs. Modern damage tolerance design philosophy works under the principle that components may contain cracks, but there is no crack approximately larger than the refurbish crack length (C_r). This principle is a result of periodic inspections conducted under a rigorous safety maintenance program that can identify any crack larger than the minimal detectable crack length (C_d). In the aircraft industry, various inspection methods and associated technologies establish the value of C_d as the crack size that can be found with 90% probability at a confidence level of 95%. Note the usual definition for C_d is the depth of a surface crack or half width of an internal crack.[5] The value of C_r is established from an estimate of C_c and a specified safety factor X_{bf} against sudden brittle fracture defined as

$$X_{bf} = \frac{N_c}{N_r} \tag{3.1}$$

In Equation (3.1), N_c denotes the cycle where crack length equals C_c and brittle fracture occurs, and N_r denotes the cycle where crack length corresponds to C_r. The inspection period N_p is determined from

$$N_p = N_r - N_d \tag{3.2}$$

where N_d denotes the cycle when crack length equals C_d for the expected fastest growing crack.

Figure 3.1 illustrates these various parameters and the damage tolerance and safety maintenance concepts just presented. For the component with the fastest growing crack, once the crack becomes detectable at $N = N_d$, the structure is allowed to operate for another N_p cycles. After this period, the structure is again inspected and the crack size will be approximately equal to C_r at which time the component is refurbished. As the refurbished component is utilized further and inspected every N_p cycles, a new crack appears and eventually becomes detectable when its length is near C_d. After N_p cycles of additional usage, the component will again require refurbishment. For other components experiencing slower rates of crack growth, once detected, they are monitored at each inspection period until after several of these periods, their crack size is near C_r and the component is refurbished. If an unexpectedly fast growing crack arises, the safety margin between C_r and C_c will facilitate avoidance of brittle fracture.

It is unlikely that future aircraft employing an LEC system will fully eliminate the need for a damage tolerance and system maintenance process such as illustrated in Figure 3.1. However, an LEC system will reduce the dC/dN slopes in Figure 3.1, and thereby save large amounts of capital by extending the inspection period N_p. Assuming continuance of design methodologies and maintenance procedures as these, the maximum crack length expected during in-flight operations will be approximately C_r. A key observation exploited in the next sections to investigate the strength of age dependency factors is that crack length is bounded and will lie within the region $0 \le C \le C_r$.

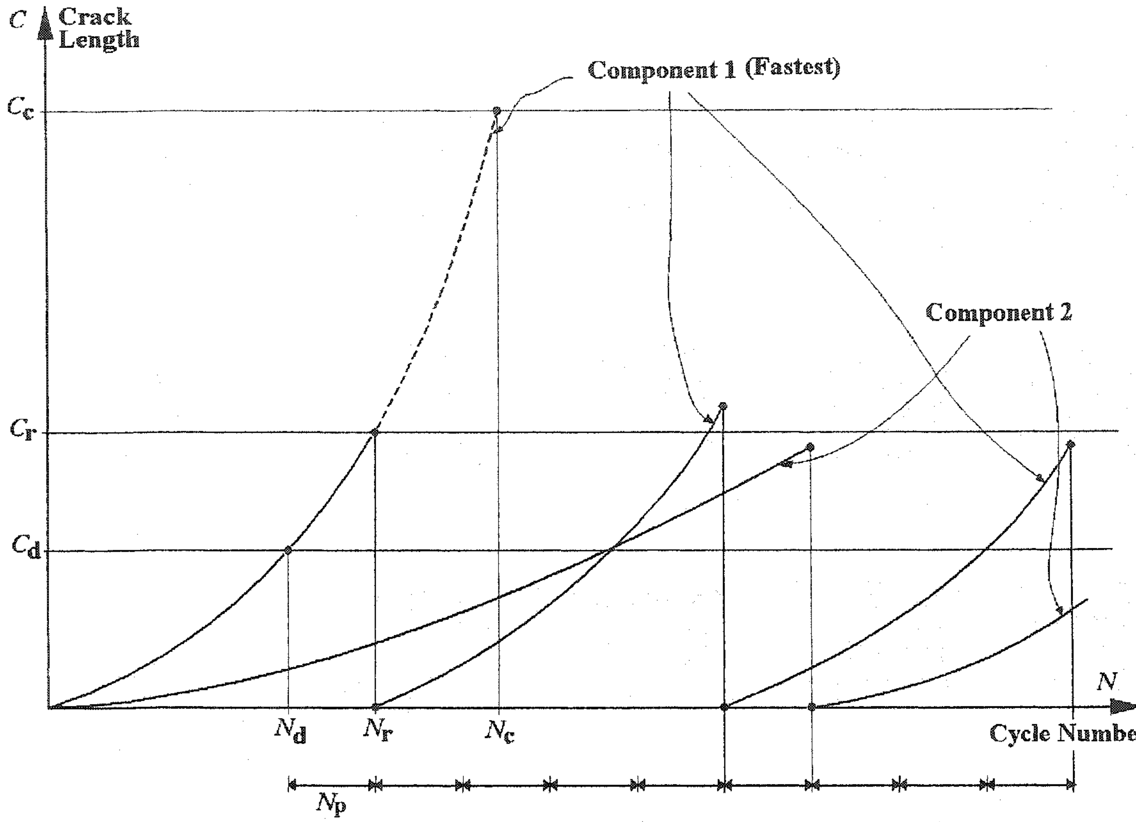

Figure 3.1 Structural Inspection and Maintenance Illustration

For the crack model used in this dissertation, C_c can be computed from the following equation[5]

$$C_C = \frac{1}{\pi}\left(\frac{K_c}{F\sigma_{\max}}\right)^2 \tag{3.3}$$

where K_c is the fracture toughness value at $C = C_c$ where sudden brittle failure is expected. The geometric factor F is taken as a constant, and σ_{max} denotes the constant amplitude loading. The critical crack length for the specimen illustrated in Figure 2.1 and quantified in Equation (2.25) is calculated here. C_c computed from Equation (3.3) is 39.54 *mm*. Applying a safety factor of X_{bf} = 1.27 gives the refurbish crack length of about C_r = 25 *mm*. In order to generalize the applicability of the crack model, non-dimensional crack size C/W will be used throughout the study. In terms of non-dimensional crack length, these values are $C_c/W = 0.52$ and $C_r/W = 0.33$. Therefore, a practical range for C/W values for the specimen under consideration is restricted to approximately $0 \leq C/W \leq 0.33$. Note that behavior of the plastic zone at the crack tip depends on component thickness. Use of non-dimensional crack size allows the dissertation results to be applied to general components with other geometries. However, the effect of thickness must also be captured through the thickness-related parameter α before applying any results presented here to other geometries.

3.3 Analytical Based Age Dependency Investigation

Figure 3.2 shows the single curve from Figure 2.6 for $\sigma_{max2} = 455\ MPa$. Features within Figure 3.2 indicate there are three clearly identifiable phases of crack growth before, during and after an overload: $1 \le N \le 17{,}000$, $N = 17{,}001$, and $17{,}002 \le N \le 105{,}000$ *cyc*. The crack propagation phase corresponds to exponential growth under cyclic loading before the overload ($\sigma_{max} = \sigma_{max1} > \sigma_0$). The crack acceleration phase corresponds to immediate crack expansion during the overload application and mainly depends on overload strength ($\sigma_{max} = \sigma_{max2} > \sigma_0$). The crack static phase corresponds to zero growth during cyclic loading after the overload ($\sigma_{max} = \sigma_{max3} < \sigma_0$). The combined affect from the acceleration and static phases is referred to as the retardation phenomenon.

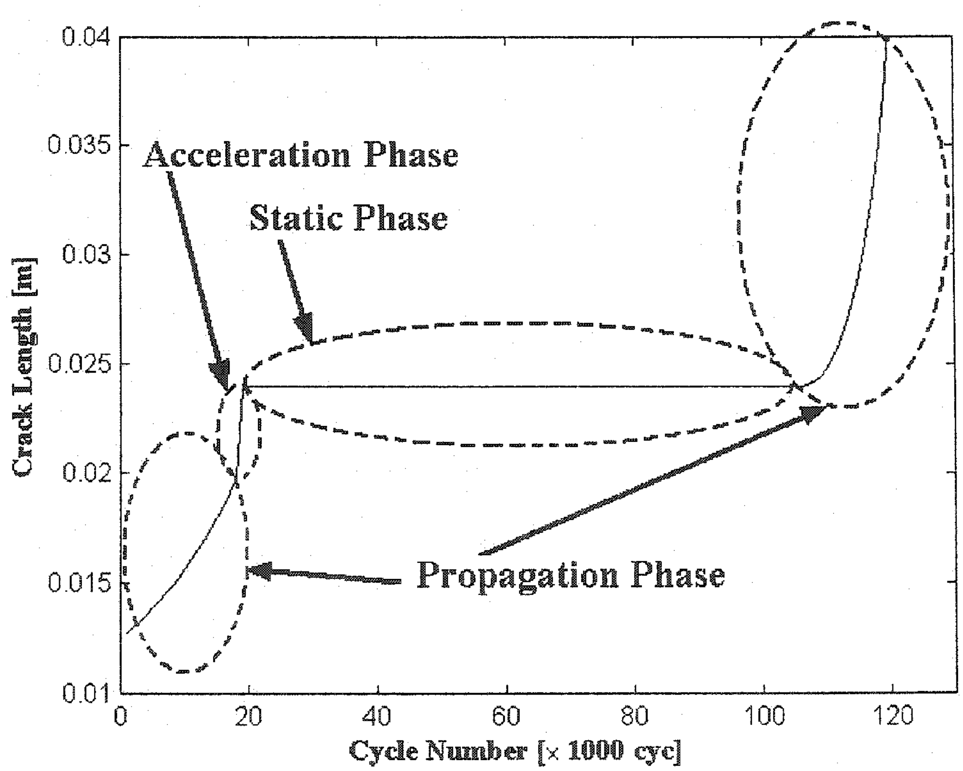

Figure 3.2 Three Phases of Crack Growth Near an Overload

The three phases of crack growth highlighted in Figure 3.2 originate within the analytical crack growth model presented in Equations (2.1)-(2.24). In general, the crack growth rate *dC/dN* for this model depends on structural age through functional dependency on C. Growth rate is directly proportional to $C^{m/2}$ from Equation (2.1). Growth rate is also indirectly a function of C through the geometry factor F in Equation (2.3). The effect of these two mechanisms is clearly observable in the propagation phase in Figure 3.2. The dC/*dN* slope steepens as the component ages, and the effect is quite significant. During this phase, the only way to improve structural life is to lower the cyclic maximum stress amplitude (see Equation (2.1)). This process is the fundamental control strategy underlying typical load alleviation systems.

In contrast, the LEC strategy is inherently related to the acceleration and static phases in Figure 3.2. Specifically, LEC logic seeks optimal overload conditions which maximize the overall retardation phenomenon across the acceleration and static phases. Rapid build-up and gradual drop-off of crack opening stress σ_0 during these two phases are the key factors. Application of the optimal overload to the structural component can be thought of as generating the best σ_0 profile that minimizes growth. If crack opening stress, and hence the optimal overload conditions, show a weak dependence on structural component age, then LEC can be greatly simplified. Characterization of this relationship is the primary focus of this chapter.

Equation (2.4) indicates σ_0 dependency on C, and Table 2.1 contains the detail functionality of Equation (2.4). In Table 2.1, there are only two occurrences of C: 1) within F in Equation (2.9) and 2) within λ in Equation (2.21). Figure 3.3 illustrates the influence paths from F and λ to σ_0, for both the acceleration phase and static phase. In

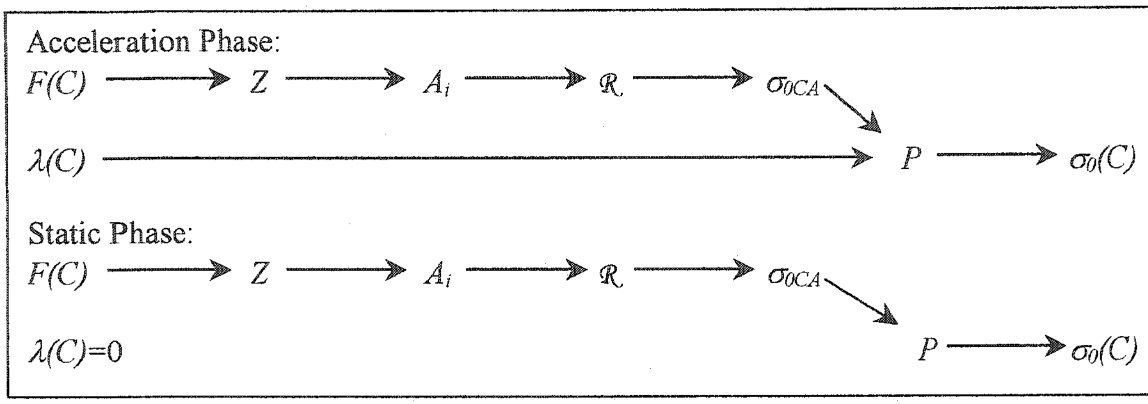

Figure 3.3 Crack Opening Stress Dependency on Crack Size

the acceleration phase during the rapid build-up of σ_0, both $F(C)$ and $\lambda(C)$ influence the σ_0 value. The intermediate variable Z is influenced by crack size through F, and Z in turn contributes to the coefficients A_0, A_1, A_2, and A_3. These coefficients are used to compute the ratio parameter $\mathcal{R}$., and $\mathcal{R}$ is used to determine the crack opening stress for constant amplitude loading σ_{0CA}. Finally parameter λ and σ_{0CA} are used to compute P, and P partially determines σ_0. In the static phase during gradual drop-off of σ_0, only the influence path from F to σ_0 is active since λ is fixed at zero. The F influence path here is identical to that for the acceleration phase. The variation of these influence paths under the bounded crack size condition ($0 \le C \le C_r$) are analyzed in the next sections.

Before considering this analysis, note the crack opening stress model in Table 2.1 has various cases depending on the sign of σ_{max} and R', on the relative size of $\mathcal{R}$ and R', and on the relative size of σ_{0old} and σ_{0CA}. To first order, fatigue damage is invariant to nominal compressive loading and this is consistent with Equations (2.5)-(2.6) where R' and A_i are zero for the case $\sigma_{max} < 0$. In this case, the $F \rightarrow \sigma_0$ influence path is completely independent of C. This case will not be considered. Following this same reasoning, before applying a stress cycle to the crack model in Chapter 6-7, compressive stress will be reset to zero. Such processing is consistent with computations in References 86 and 87, and through σ_{min}, Equations (2.7)-(2.8) imply nonnegative R'. Therefore, case $R' < 0$ will also not be considered. In the case where $\mathcal{R} < R'$, Equation (2.16) implies the $F \rightarrow \sigma_0$ influence path is also nondependent on C and will not be considered. Finally, when $\sigma_{0old} > \sigma_{0CA}$, Equation (2.18) implies the influence path $\lambda \rightarrow \sigma_0$ is invariant to C. Case $\sigma_{0old} > \sigma_{0CA}$ will thus not be considered. In summary, the only scenarios left for analysis in the next sections are $\sigma_{max} > 0$, $\mathcal{R} > R' > 0$, and $\sigma_{0old} < \sigma_{0CA}$.

3.3.1 Acceleration Phase

During this phase, the maximum stress loading becomes the overload ($\sigma_{max} = \sigma_{max2}$) resulting in sudden expansion of crack size. Consider the $F \rightarrow \sigma_{0CA}$ influence path initially. Substituting Equation (2.3) into Equation (2.9) gives

$$Z = \frac{\sigma_{\max 2}}{\sigma_{flow}} \frac{1}{\sqrt{\cos\left(\frac{\pi}{2}\frac{C}{W}\right)}} \tag{3.4}$$

Further substitution of Equation (3.4) into coefficients A_0 and A_1 results in

$$A_0 = (0.825 - 0.34\alpha + 0.05\alpha^2)\left[\cos\left\{\frac{\pi}{2}\frac{\sigma_{\max 2}}{\sigma_{flow}}\frac{1}{\sqrt{\cos\left(\frac{\pi}{2}\frac{C}{W}\right)}}\right\}\right]^{\frac{1}{\alpha}} \tag{3.5}$$

$$A_1 = (0.415 - 0.71\alpha)\frac{\sigma_{\max 2}}{\sigma_{flow}}\frac{1}{\sqrt{\cos\left(\frac{\pi}{2}\frac{C}{W}\right)}} \tag{3.6}$$

and A_2 and A_3 are expressed as functions of A_0 and A_1

$$A_2 = 2 - 3A_0 - 2A_1 \tag{3.7}$$

$$A_3 = -1 + 2A_0 + A_1 \tag{3.8}$$

The stress ratio parameter $\mathcal{R}$ is expressed as

$$\mathcal{R} = A_0 + A_1 R' + A_2 R'^2 + A_3 R'^3 \tag{3.9}$$

and $\mathcal{R}$ is used to compute σ_{0CA} as

$$\sigma_{0CA} = \mathcal{R}\sigma_{max2} \tag{3.10}$$

Finally, if Equation (3.10) is expanded, one finds the explicit dependence of σ_{0CA} on C.

$$\sigma_{0CA} = \sigma_{\max 2}\left[\left(0.825 - 0.34\alpha + 0.05\alpha^2\right)\left[\cos\left\{\frac{\pi}{2}\frac{\sigma_{\max 2}}{\sigma_{flow}}\frac{1}{\sqrt{\cos\left(\frac{\pi}{2}\frac{C}{W}\right)}}\right\}\right]^{\frac{1}{\alpha}}\left(1 - 3R'^2 + 2R'^3\right)\right.$$

$$\left. + \left[\left(0.415 - 0.71\alpha\right)\frac{\sigma_{\max 2}}{\sigma_{flow}}\frac{1}{\sqrt{\cos\left(\frac{\pi}{2}\frac{C}{W}\right)}}\right]\left(R' - 2R'^2 + R'^3\right) + \left(2R'^2 - R'^3\right)\right] \tag{3.11}$$

Now consider the $\sigma_{0CA}/\lambda \rightarrow P$ influence path. In the acceleration phase, overload results in sudden increase of σ_{0CA}, and the condition $\sigma_{0old} < \sigma_{0CA}$. Therefore, λ adheres to

$$\lambda = \left(1 + e^{\frac{2t}{C-W}}\right)\frac{\sigma_{\max 2} - \sigma'_{\min}}{\sigma_{\max 2} - \sigma_{\min old}} \tag{3.12}$$

and η becomes η_2. Now P in Equation (2.23) is expressed as

$$P = \{\lambda\,(1+\eta_2)+\eta_2\}\ \sigma_{0CA} - \lambda\sigma_{0old} \tag{3.13}$$

and upon substitution for λ and σ_{0CA}, the C dependency is transparent.

$$P = \left\{\left[\left(1+e^{\frac{2t}{C-W}}\right)\frac{\sigma_{\max 2}-\sigma'_{\min}}{\sigma_{\max 2}-\sigma_{\min old}}\right](1+\eta_2)+\eta_2\right\}$$

$$\times\left\{\sigma_{\max 2}\left[\left(0.825-0.34\alpha+0.05\alpha^2\right)\left[\cos\left\{\frac{\pi}{2}\frac{\sigma_{\max 2}}{\sigma_{flow}}\frac{1}{\sqrt{\cos\left(\frac{\pi}{2}\frac{C}{W}\right)}}\right\}\right]^{\frac{1}{\alpha}}\left(1-3R'^2+2R'^3\right)\right.\right.$$

$$\left.\left.+\left[(0.415-0.71\alpha)\frac{\sigma_{\max 2}}{\sigma_{flow}}\frac{1}{\sqrt{\cos\left(\frac{\pi}{2}\frac{C}{W}\right)}}\right]\left(R'-2R'^2+R'^3\right)+\left(2R'^2-R'^3\right)\right]\right\}$$

$$-\left[\left(1+e^{\frac{2t}{C-W}}\right)\frac{\sigma_{\max 2}-\sigma'_{\min}}{\sigma_{\max 2}-\sigma_{\min old}}\right]\sigma_{0old} \tag{3.14}$$

The complete path is had from Equation (2.24), or

$$\sigma_0 = \frac{\sigma_{0old}+P}{1+\eta_2} \tag{3.15}$$

where P is given by Equation (3.14).

Consider the variation in the $\sqrt{\cos(\pi/2\ C/W)}$ term in Equation (3.14) over the range $0 \le C \le C_r$.

$$\sqrt{\cos\left(\frac{\pi}{2}\frac{C}{W}\right)} = 1 \qquad \text{for} \qquad \frac{C}{W} = 0 \tag{3.16}$$

$$\sqrt{\cos\left(\frac{\pi}{2}\frac{C}{W}\right)} = 0.93 \qquad \text{for} \qquad \frac{C}{W} = 0.33 \tag{3.17}$$

A variation of 7% is observed over the $0 \le C \le C_r$ range. In a similar fashion, focus on the $e^{2t/C-W}$ term.

$$e^{\frac{2t}{C-W}} = 0.97 \qquad \text{for} \qquad \frac{C}{W} = 0 \tag{3.18}$$

$$e^{\frac{2t}{C-W}} = 0.96 \qquad \text{for} \qquad \frac{C}{W} = 0.33 \tag{3.19}$$

A variation of only 1% is noted here. These small variations suggest crack opening stress has a weak dependency on crack size during the acceleration phase, under all assumptions alluded to earlier.

To further illustrate this argument, Table 3.1 summarizes the variations in each parameter in Figure 3.3 along the paths from F and λ to σ_0 for specified values of α, η_2, t, W, R', σ_{0old} and $\sigma_{max2}/\sigma_{flow}$ over the range $0 \le C \le C_r$. $\sigma_{max2}/\sigma_{flow}$ is taken as about 1/4 for computing the parameters for Table 3.1. Note the level of $\sigma_{max2}/\sigma_{flow}$ is related to the load spectra and design criteria of aircraft, and the above value is considered according to

Table 3.1 Influence of Crack Size on Crack Opening Stress Parameters – Acceleration Phase

Parameter	$C/W = 0$	$C/W = 0.33$	Percent Variation [%]
F	1.0	1.0720	6.95
Z	0.2557	0.2741	6.95
A_0	0.3729	0.3701	0.75
A_1	0.0753	0.0807	6.95
A_2	0.7309	0.7285	0.34
A_3	-0.1790	-0.1792	0.09
$\mathcal{R}$	0.3730	0.3703	0.75
σ_{0CA} $[MPa]$	52.227	51.838	0.75
λ	1.9737	1.9611	0.64
P $[MPa]$	50.421	49.335	2.18
σ_0 $[MPa]$	77.102	76.016	1.42

References 21 and 29. When overload is applied, R' becomes 0.0025 which is about half of nominal value under considered load condition. Note the contribution of R' becomes significantly lower when R' is significantly higher, while the contribution incerases as R' becomes lower. This fact can be derived from S-N curve since the stress amplitude which shows opposite behavior of R' is a major factor of fatigue crack growth. The crack opening stress of previous cycle σ_{0old} is taken as 26.7 MPa concerning the nominal value before overload is applied.

3.3.2 Static Phase

During this phase, the maximum stress loading returns to the nominal level ($\sigma_{max} = \sigma_{max3}$) resulting in cessation of crack growth. The $F \rightarrow \sigma_{0CA}$ influence path from the previous section is again applicable with no change except σ_{max3} replaces σ_{max2}. Equation (3.11) describes the relationship between C and σ_{0CA}. In the early portion of the static phase, σ_{0old} is significantly larger than σ_{0CA} , and σ_{max3} is smaller than σ_{0old}. Equation (2.18) requires $\lambda = 0$ and the $\lambda \rightarrow \sigma_0$ path is eliminated here. Equation (2.19) also requires $\eta = \eta_1$. Parameter P in Equation (2.23) simplifies to

$$P = \eta_1 \sigma_{0CA} \tag{3.20}$$

and crack opening stress is expressed as

$$\sigma_0 = \frac{\sigma_{0old} + P}{1 + \eta_1} \tag{3.21}$$

where P and σ_{0CA} are obtained from above.

In this phase, $\sqrt{\cos(\pi/2\ C/W)}$ is the only crack length term affecting σ_0. Variation of this term across $0 \le C \le C_r$ again yields a small 7% change (see Equation (3.16)-(3.17)). Table 3.2 summarizes the variations for each parameter highlighted in the influence path in Figure 3.3. Note 77 *MPa* is used as σ_{0old} for computing parameters of Table 3.2. To construct this table, values for α and η_l are consistent with information from Chapter 2. In the static phase, reasonable expected values for R' and $\sigma_{max3}/\sigma_{flow}$ are 0.005 and 0.126.[21] The conclusion from Table 3.2 is that crack opening stress also has weak dependency on crack size during the static phase, under all assumptions stated previously.

Since the geometric factor $F = 1/\sqrt{\cos(\pi/2\ C/W)}$ is a major term in the weak

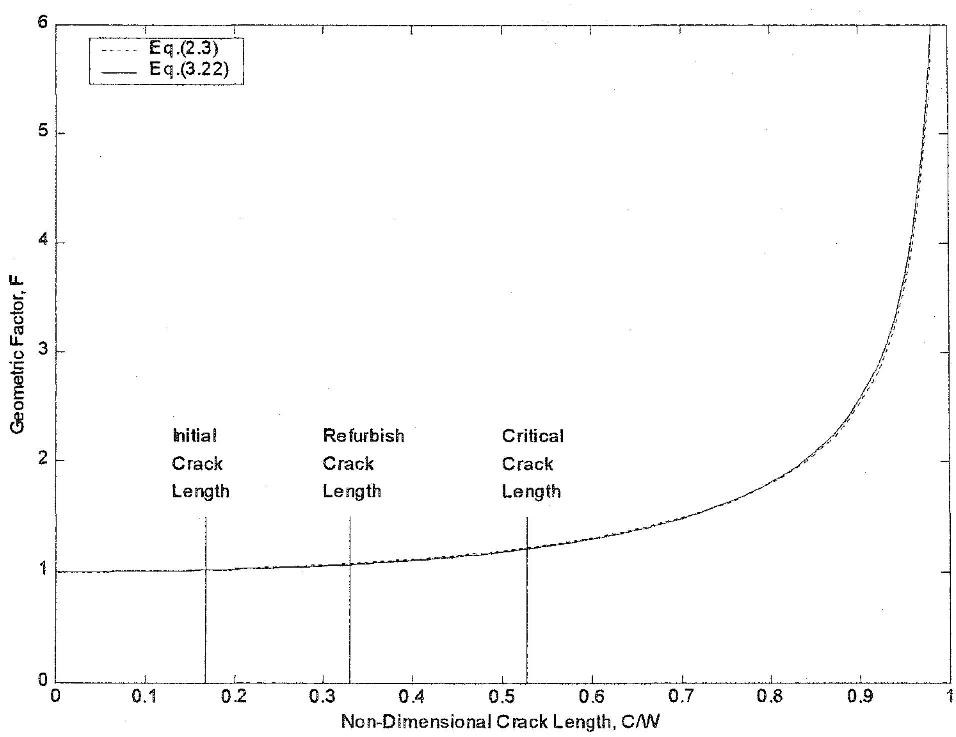

Figure 3.4 Comparison of Geometric Factor Behavior

dependency argument, another formulation for F from Reference 5 is presented in Equation (3.22) for comparison with Equation (2.3).

$$F_{Dowling} = \frac{1 - 0.5\frac{C}{W} + 0.32\left(\frac{C}{W}\right)^2}{\sqrt{1 - \frac{C}{W}}} \tag{3.22}$$

Figure 3.4 illustrates the behavior of the geometric factors computed using Equation (2.3) and Equation (3.22). Observations from Figure 3.4 indicate the two geometric factors match well without significant difference. Further, note the value for F is essentially constant over the range of expected crack sizes. Applying the expected range of F from Figure 3.4 to Equation (3.11) under nominal constant amplitude loading gives σ_{0CA} =

Table 3.2 Influence of Crack Size on Crack Opening Stress Parameters - Static Phase

Parameter	$C/W = 0$	$C/W = 0.33$	Percent Variation [%]
F	1.0	1.0720	6.95
Z	0.1279	0.1371	6.95
A_0	0.3869	0.3862	0.18
A_1	0.0376	0.0403	6.95
A_2	0.7642	0.7609	0.44
A_3	-0.1887	-0.1873	0.70
$\mathfrak{R}$	0.3871	0.3864	0.18
σ_{0CA} $[MPa]$	27.094	27.046	0.18
λ	1.9737	1.9611	0.64
P $[MPa]$	0.0002	0.0002	0.18
σ_0 $[MPa]$	77.000	77.000	0.00

27.09 MPa at the zero crack length and $\sigma_{0CA} = 27.05$ MPa at the refurbish crack length. A difference of only 0.18 % results.

3.4 Computational Based Age Dependency Investigation

The previous section implied optimal overload conditions for $\sigma_{max2}/\sigma_{max1}$ and N_1 can be regarded as generating the minimizing crack opening stress profile, and hence optimum $\sigma_{max2}/\sigma_{max1}$ and N_1 values are approximately invariant to structural age. To confirm this suggestion, several computer simulation cases generating optimal overload conditions with variable structural age are considered. For notational convenience, symbols R_o and I_o are defined as the overload stress $\sigma_{max2}/\sigma_{max1}$, and overload application interval N_1, respectively. Optimum overload values will be denoted by R_o^* and I_o^*.

3.4.1 Single Overload with Varying Age

Referring back to Section 2.2, consider constant amplitude cyclic loading ($\sigma_{max1} = \sigma_{max3}$) with a single overload applied at different points throughout the structural life. Simulations are generated with the single overload application point ranging between 50 and 20,000 *cyc*. Note the overload strength is also varied in these simulations. For 17,000 cyc, a family of results would appear as in Figure 2.6. Initial crack length is set to 12.7 *mm*, and the assumed final crack length is 28 *mm* which is approximately equal to C_r. A cycles to threshold summary chart is constructed and presented in Figure 3.5 for 100, 1,000, and 10,000 *cyc*. Further, 24 different overload application points were investigated, and the optimum $\sigma_{max2}/\sigma_{max1}$ overload ratios are shown in Figure 3.6. Note the optimum overload ratio is very near a value of 5 for all application points. Therefore, optimal $\sigma_{max2}/\sigma_{max1}$ overload ratio shows no age dependency under the assumptions considered.

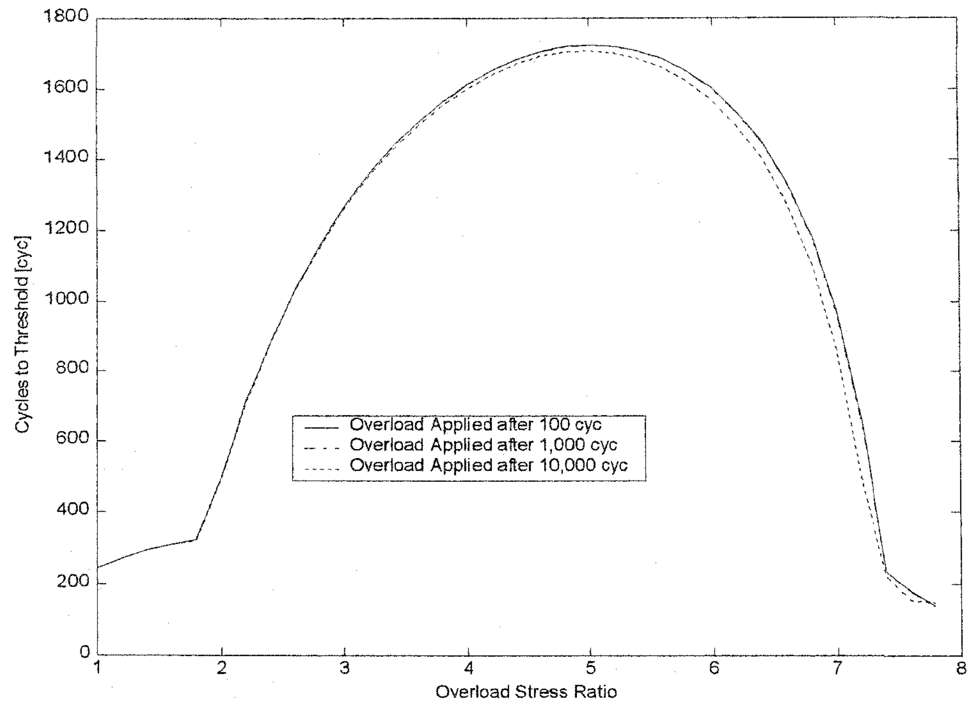

Figure 3.5 Cycles to Threshold - Single Overload

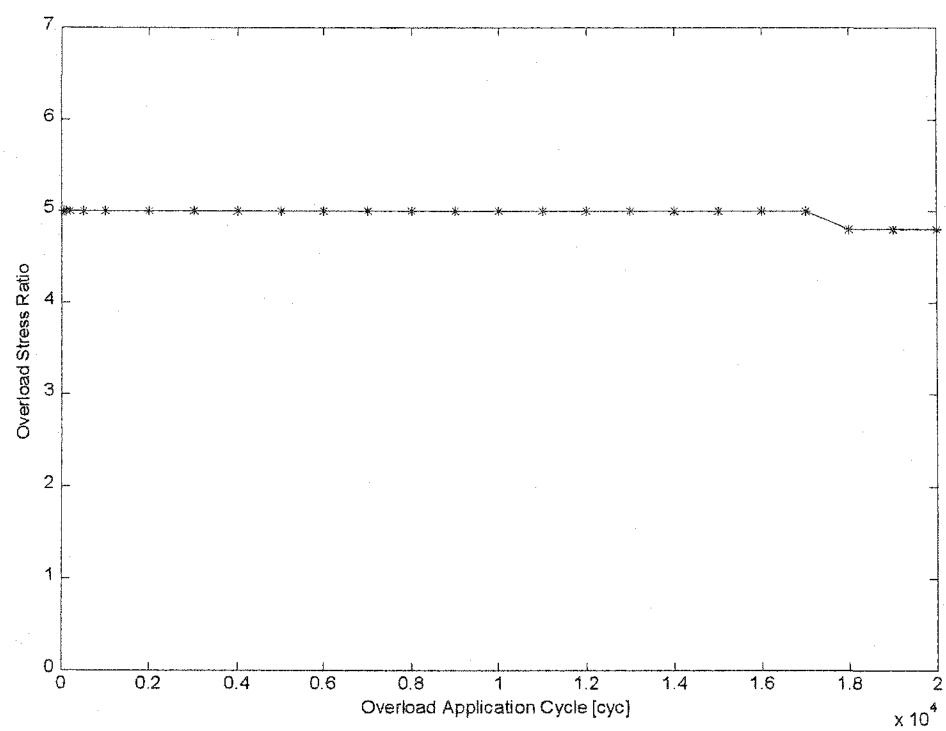

Figure 3.6 Optimal Overload Ratio with Overload Application cycle Variable

3.4.2 Periodic Overload with Varying Initial Age

Refer back to Section 2.3 and consider constant amplitude cyclic loading with a periodically applied overload with varying initial crack length. The initial crack size is varied from 13 to 20 *mm*. The overload interval is also varied from 50 to 20,000 *cyc*. Note the overload strength is also varied in these simulations. For N_I = 1,000 *cyc*, a family of results would appear as in Figure 2.10 for initial crack length equal to 13 *mm*. Figure 3.7 shows the cycles to threshold summary chart for a final crack length of 28 *mm* and for N_I = 200 *cyc* with 8 different initial crack lengths. Similar information is shown in Figure 3.8 for N_I = 3,000 *cyc*. These figures show that optimal overload stress ratio is practically constant against the initial age variation.

Figure 3.9 shows a plot of the optimal ratios against initial crack size for the two cases N_I = 200 *cyc* and N_I = 3,000 *cyc*. Weak dependency on initial crack size is again noted for the best $\sigma_{max2}/\sigma_{max1}$, but observe the optimum $\sigma_{max2}/\sigma_{max1}$ value depends on the overload interval N_I. To characterize this relationship, the averaged optimum overload ratios with respect to initial crack size are plotted against the corresponding overload intervals in Figure 3.10. The data in Figure 3.10 is noted to have a logarithmic characteristic and should be accurately represented with a simple linear curve using a I_o log scale. A least squares method is used to fit a logarithmic function to the data in Figure 10 yielding

$$\frac{\sigma_{\max 2}}{\sigma_{\max 1}} = 0.49 \times \log_{10} N_1 + 0.93 \tag{3.28}$$

The dotted line in Figure 3.10 represents the curve-fitted values which are in close agreement to the exact values. Equation (3.28) can be directly implemented in the LEC logic to simplify logical and computational processing, regardless of the age of the structural components. However, the effects from thickness and underload need to be further investigated.

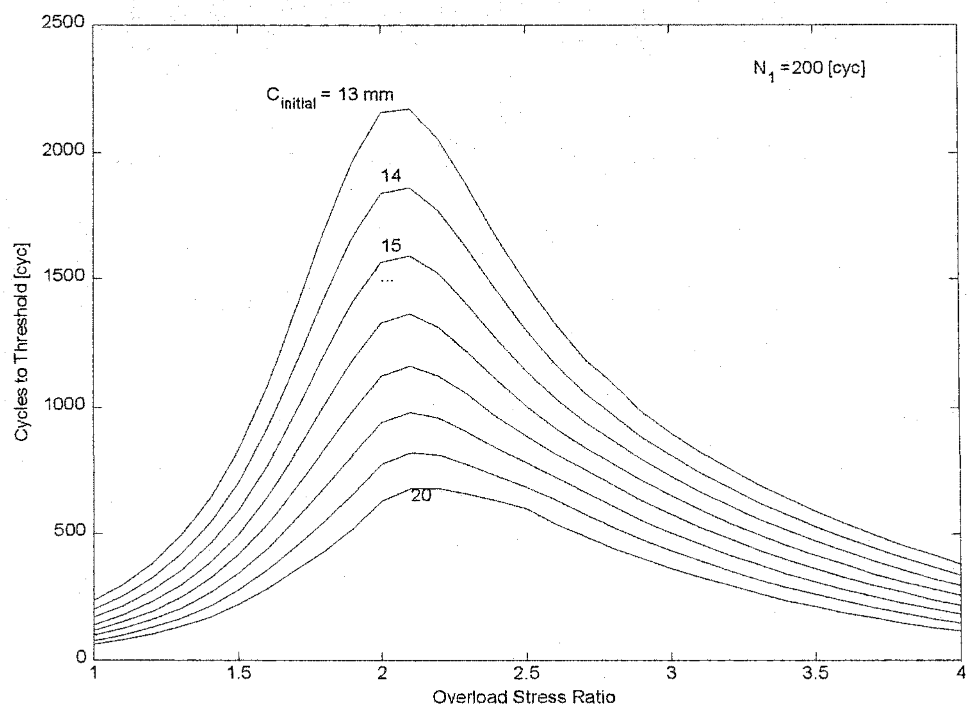

Figure 3.7 Cycles to Threshold - Periodic Overload ($N_1 = 200\ cyc$)

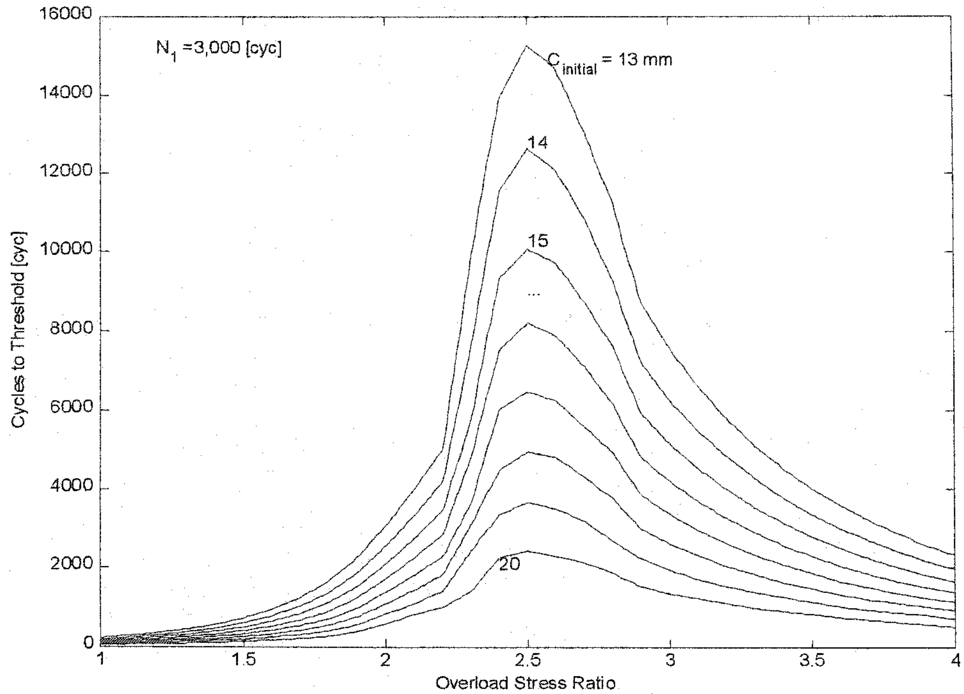

Figure 3.8 Cycles to Threshold - Periodic Overload ($N_1 = 3{,}000\ cyc$)

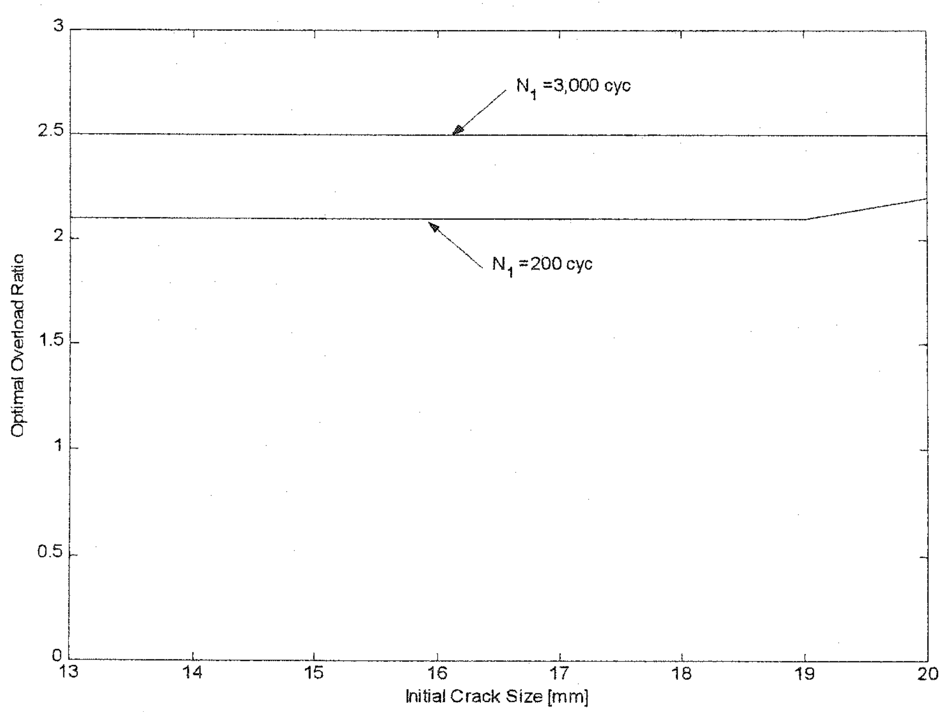

Figure 3.9 Optimal Overload Ratio with Initial Crack Length Variable

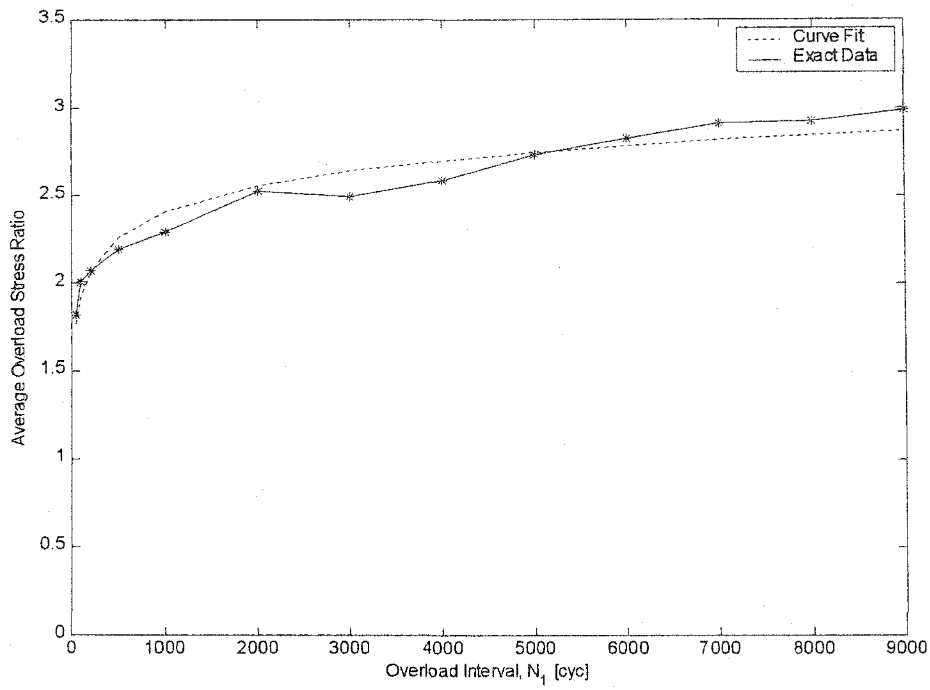

Figure 3.10 Overload Ratio and Interval Relationship

CHAPTER 4

RIGID AND FLEXIBLE DYNAMIC MODELS OF F-16 AIRCRAFT

4.1 Vehicle Model Overview

A fully nonlinear model of a highly maneuverable aircraft, the F-16 aircraft, is developed and used throughout this dissertation. A 3-directional view of the F-16 aircraft is shown in Figure 4.1. This aircraft is a small single engined fighter having a swept wing integrated with fuselage strakes and conventional aft horizontal tail and single vertical tail. Aerodynamic control surfaces include symmetric horizontal stabilizer, leading edge flap, aileron, rudder, differential horizontal stabilizer, and speed break. The propulsion system is controlled by the throttle setting. The airframe is statically unstable in the pitch axis at low speeds. Further, the airframe is highly maneuverable, with capability to generate large moments in all three axis for rapid angular motion at large aerodynamic attitudes.

Numerical aerodynamic data for the nonlinear aircraft model is obtained from Reference 88. The main purpose of the engineering project described in Reference 88 was to develop an aircraft model appropriate for the study of stall and post-stall characteristics through simulation. The aerodynamic data for the aircraft model was derived from the result of low-speed ($M = 0.1 \sim 0.2$) static and dynamic (forced-oscillation) tests conducted in several wind tunnel facilities and is in a table look up format. The aerodynamic data scaling and coefficient build-up procedure details are provided in Reference 88. Inertial and propulsion data are derived from the actual F-16

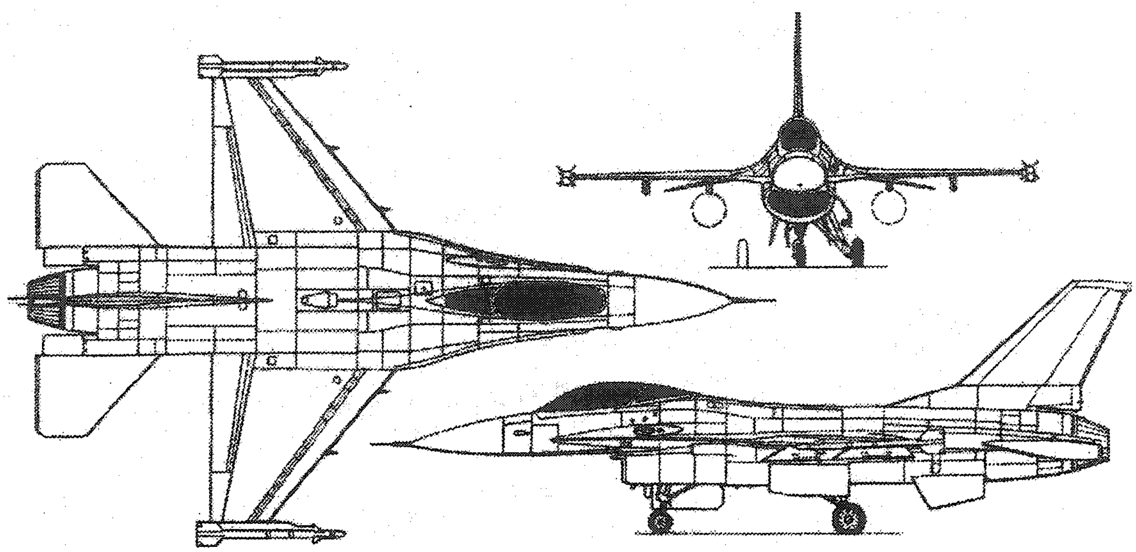

Figure 4.1 F-16 Aircraft[92]

aircraft. This data is integrated with the flight dynamics equations of motion in nonlinear state space form, which can be solved using a numerical integration technique.

A linear structural wing model for the F-16 aircraft is also developed and used throughout the dissertation research. A 3-dimensional view of the F-16 wing structure is shown in Figure 4.2. The wing structure is of conventional design with a thin, aluminum multi-box layout utilizing numerous spars and ribs with honeycomb, load bearing surface panels. The cantilevered wing is swept and includes near full span leading and trailing edge control surfaces.

A numerical model of this structure is available and is based on properties presented in Reference 89. Specifically the wing model is a 20% scaled representation of the actual F-16 wing and corresponds to a constructed wing used in wind tunnel tests at the Air Force Institute of Technology's low speed 5*ft* wind tunnel. The original wing model in Reference 89 was developed as a low speed aeroelastic model for investigations of the Active Flexible Wing (AFW) concept applied to an F-16 derivative.[90] The AFW concept utilizes increased wing flexibility and multiple control surfaces to initiate increasingly agile maneuvers. Increase in control power obtained through use of aeroelastic deformations are tested. Detail of the model development can be found in Reference 89. Because the original model is a down scaled model, the full size wing characteristics need to be recovered from the original model, and this process is presented in a later section. This flexible wing model will be integrated to the rigid flight model, which can also be solved for deflections and stresses using numerical integration techniques.

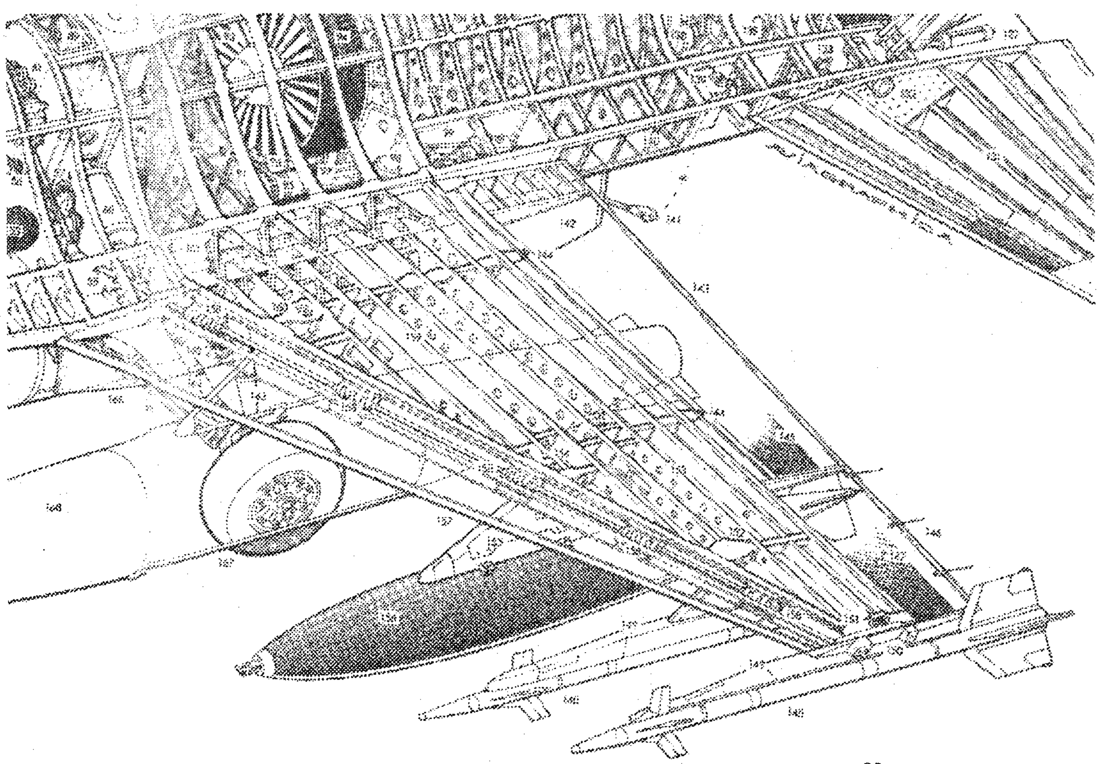

Figure 4.2 Wing Structure of F-16 Aircraft[92]

4.2 Equations of Motion for Rigid Flight Model

The full set of equations of motion for the aircraft model includes 3 force equations, 3 moment equations, 3 kinematics equations, and 3 navigation equations. Derivation of these twelve differential equations for flight over a stationary flat earth can be found in Reference 1. Other major assumptions include infinite aircraft rigidity, constant aircraft mass and inertia, and constant gravitational acceleration. These equations describe the body axes 6 degree of freedom dynamics of the rigid aircraft. The force equations and moment equations are given in Reference 88, and the kinematics equations and navigational equations are given in Reference 6. Table 4.1 lists the 12 scalar nonlinear equations of motion. Note the equations are in first order, state space form.

State variables included in the differential equations are

$$\vec{X} = [U \; V \; W \; \phi \; \theta \; \psi \; P \; Q \; R \; P_N \; P_E \; h]^T \tag{4.1}$$

where $\vec{X}$ demotes the state vector. Variables U, V, W, P, Q, and R denote translational velocities and angular velocities in the x_b, y_b, z_b body frame axes which are attached to and move with the aircraft. Also, roll angle ϕ, pitch angle θ, yaw angle ψ, position in north direction P_N, east direction P_E, and altitude h in the vertical direction are included. The aircraft model has 6 inputs listed in the control vector $\vec{U}$, or

$$\vec{U} = [\theta_{th} \;\; \delta_h \;\; \delta_a \;\; \delta_r \;\; \delta_{sb} \;\; \delta_{lef}]^T \tag{4.2}$$

where θ_{th} denotes throttle position in percentage of maximum throttle, and δ_h denotes symmetric horizontal stabilizer deflection angle in terms of degree. Also, aileron deflection angle δ_a, rudder deflection δ_r, speed break deflection δ_{sb}, and leading edge flap deflection δ_{lef} are included in the input vector in terms of degree. The throttle input

θ_{th} varies from 0 to 100%. Horizontal stabilizer deflection limitation is ± 25°, and maximum leading edge flap deflection is 25°. The actual roll-control system uses both

Table 4.1. Flat-Earth, Body Axes 6-DOF Equations

Force Equations

$$\dot{U} = RV - QW - g\sin\theta + \frac{F_x}{m} + \frac{T}{m} \tag{4.3}$$

$$\dot{V} = -RU + PW + g\sin\phi\cos\theta + \frac{F_y}{m} \tag{4.4}$$

$$\dot{W} = QU - PV + g\cos\phi\cos\theta + \frac{F_z}{m} \tag{4.5}$$

Kinematic Equations

$$\dot{\phi} = P + \tan\theta(Q\sin\phi + R\cos\phi) \tag{4.6}$$

$$\dot{\theta} = Q\cos\phi - R\sin\phi \tag{4.7}$$

$$\dot{\psi} = \frac{Q\sin\phi + R\cos\phi}{\cos\theta} \tag{4.8}$$

Moment Equations

$$\dot{P} = (c_1R + c_2P)Q + c_3L + c_4N + c_5H_eQ \tag{4.9}$$

$$\dot{Q} = c_6PR - c_7(P^2 - R^2) + c_8M - H_eR \tag{4.10}$$

$$\dot{R} = (c_9P - c_2R)Q + c_4L + c_{10}N + c_{11}H_eQ \tag{4.11}$$

Navigation Equations

$$\dot{P}_N = U\cos\theta\cos\psi + V(-\cos\phi\sin\psi + \sin\phi\sin\theta\cos\psi) + W(\sin\phi\sin\psi + \cos\phi\sin\theta\cos\psi) \tag{4.12}$$

$$\dot{P}_E = U\cos\theta\sin\psi + V(\cos\phi\cos\psi + \sin\phi\sin\theta\sin\psi) + W(-\sin\phi\cos\psi + \cos\phi\sin\theta\sin\psi) \tag{4.13}$$

$$\dot{h} = U\sin\theta - V\sin\phi\cos\theta - W\cos\phi\cos\theta \tag{4.14}$$

aileron and differential-tail deflections at a ratio of 4° of δ_a per 1° of δ_d. The surface deflection limits are $\pm 5.38°$ and $\pm 21.5°$ for differential tail and ailerons, respectively. The rudder deflection angle has a limitation of ± 30°, and maximum speed break deflection is 60°.

In the moment equations (Equations (4.9)-(4.11)), the constants c_i are defined in terms of the moments and products of inertia. The constants are defined as

$$c_1 = \frac{(I_y - I_z)I_z - I_{xz}^2}{\Gamma} \qquad c_2 = \frac{(I_x - I_y + I_z)I_{xz}}{\Gamma}$$

$$c_3 = \frac{I_z}{\Gamma} \qquad c_4 = \frac{I_{xz}}{\Gamma} \qquad c_5 = \frac{I_{xz} I_z}{\Gamma}$$

$$c_6 = \frac{I_z - I_x}{I_y} \qquad c_7 = \frac{I_{xz}}{I_y} \qquad c_8 = \frac{1}{I_y}$$

$$c_9 = \frac{(I_x - I_y)I_x + I_{xz}^2}{\Gamma} \qquad c_{10} = \frac{I_x}{\Gamma} \qquad c_{11} = \frac{I_x I_z}{\Gamma} \tag{4.15}$$

where

$$\Gamma = I_x I_z - I_{xz}^2 \tag{4.16}$$

and I_x, I_y and I_z are moments of inertia and I_{xz} is a product of inertia. Note inertia symmetry is assumed ($I_{xy} = I_{yz} = 0$). The parameter H_e appearing in the moment equations represents engine angular momentum which is variable and corresponds to a value of 160 *slug ft²/s* for $\theta_h = 1$. Note the engine spin momentum will be eliminated in the autopilot development phase in Chapter 5, but the original aircraft model has non-zero engine spin momentum. The term g denotes gravitational acceleration, where g = 32.17 ft/s^2, and m represents vehicle mass.

The aerodynamic forces and moments acting on the aircraft, F_x, F_y, F_z, L, M, and N can be obtained from the following equations

$$F_x = q\,S\,C_{x,t} \qquad F_y = q\,S\,C_{y,t} \qquad F_z = q\,S\,C_{z,t}$$

$$L = q\,S\,b\,C_{l,t} \qquad M = q\,S\,c\,C_{m,t} \qquad N = q\,S\,b\,C_{n,t} \tag{4.17}$$

where dynamic pressure q is described as

$$q = \frac{1}{2}\rho V_t^2 \tag{4.18}$$

In Equations (4.17)-(4.18), b denotes wing span, c denotes mean wing chord length, V_t denotes total velocity, and ρ denotes atmospheric density. Finally T in Equation (4.3) denotes engine thrust.

The total aerodynamic coefficients $C_{x,t}$, $C_{y,t}$, $C_{z,t}$, $C_{l,t}$, $C_{m,t}$, and $C_{n,t}$ are computed from nonlinear aerodynamic data tables in Reference 88. These aerodynamic coefficients are usually expressed as a baseline component, plus increment or correction terms which are indicated by the symbol Δ. Typically, the baseline component is primarily a function of angle of attack α, sideslip angle β, and Mach number M. The available aerodynamic data was over the ranges -20° to 90° for α, and -30° to 30° for β. Mach dependence can be removed from the baseline component and treated as a correction term in the case of data for subsonic speeds. As the wind tunnel tests were conducted at subsonic flow conditions for subsonic flight studies, the effect of Mach number is neglected. In this model, the aerodynamic data shows strong dependency on horizontal stabilizer deflection δ_h, so δ_h is also included as an independent variable for the baseline component.

The component build up equations to compute total aerodynamic coefficients are listed below. For the x_b - axis force coefficient,

$$C_{x,t} = C_x(\alpha,\beta,\delta_h) + \Delta C_{x,lef}\left(1-\frac{\delta_{lef}}{25^\circ}\right) + \Delta C_{x,sb}(\alpha)\left(\frac{\delta_{sb}}{60^\circ}\right) + \frac{cQ}{2V_t}\left[C_{x_Q}(\alpha) + \Delta C_{x_Q,lef}(\alpha)\left(1-\frac{\delta_{lef}}{25^\circ}\right)\right] \quad (4.19)$$

where

$$\Delta C_{x,lef} = C_{x,lef}(\alpha,\beta) - C_x(\alpha,\beta,\delta_h = 0^\circ) \quad (4.20)$$

For five different horizontal stabilizer deflection δ_h, the force coefficient C_x is provided in tabular form with independent variables α and β. The provided δ_h are –25°, -10°, 0°, 10°, 25°, and the expression of $C_x(\alpha,\beta,\delta_h = 0^\circ)$ in Equation (4.20) indicates the C_x table when δ_h is 0°. Similar expression within following equations can be interpreted in the same manner. For the z_b - axis force coefficient,

$$C_{z,t} = C_z(\alpha,\beta,\delta_h) + \Delta C_{z,lef}\left(1-\frac{\delta_{lef}}{25^\circ}\right) + \Delta C_{z,sb}(\alpha)\left(\frac{\delta_{sb}}{60^\circ}\right) + \frac{cQ}{2V_t}\left[C_{z_Q}(\alpha) + \Delta C_{z_Q,lef}(\alpha)\left(1-\frac{\delta_{lef}}{25^\circ}\right)\right] \quad (4.21)$$

where

$$\Delta C_{z,lef} = C_{z,lef}(\alpha,\beta) - C_z(\alpha,\beta,\delta_h = 0^\circ) \quad (4.22)$$

For the pitching moment coefficient,

$$C_{m,t} = C_m(\alpha,\beta,\delta_h)\eta_{\delta_h}(\delta_h) + C_{z,t}(X_{cg,ref} - X_{cg}) + \Delta C_{m,lef}\left(1-\frac{\delta_{lef}}{25^\circ}\right) + \Delta C_{m,sb}(\alpha)\left(\frac{\delta_{sb}}{60^\circ}\right)$$

$$+\frac{cQ}{2V_t}\left[C_{m_Q}(\alpha) + \Delta C_{m_Q,lef}(\alpha)\left(1-\frac{\delta_{lef}}{25^\circ}\right)\right] + \Delta C_m(\alpha) + \Delta C_{m,ds}(\alpha,\delta_h) \quad (4.23)$$

where

$$\Delta C_{m,lef} = C_{m,lef}(\alpha,\beta) - C_m(\alpha,\beta,\delta_h = 0) \quad (4.24)$$

The horizontal stabilizer effectiveness factor $\eta_{\delta_h}(\delta_h)$ is provided in tabular form as a function of δ_h. The strength of this term reduces near the maximum deflection angle of the horizontal stabilizer. For the y_b - axis force coefficient,

$$C_{y,t} = C_y(\alpha,\beta) + \Delta C_{y,lef}\left(1-\frac{\delta_{lef}}{25^\circ}\right) + \left[\Delta C_{y,\delta_a=20^\circ} + \Delta C_{y,\delta_a=20^\circ,lef}\left(1-\frac{\delta_{lef}}{25^\circ}\right)\right]\left(\frac{\delta_a}{20^\circ}\right) + \Delta C_{y,\delta_r=30^\circ}\left(\frac{\delta_r}{30^\circ}\right)$$

$$\frac{b}{2V_t}\left\{\left[C_{y_R}(\alpha) + \Delta C_{y_R,lef}(\alpha)\left(1-\frac{\delta_{lef}}{25^\circ}\right)\right]R + \left[C_{y_P}(\alpha) + \Delta C_{y_P,lef}(\alpha)\left(1-\frac{\delta_{lef}}{25^\circ}\right)\right]P\right\} \quad (4.25)$$

where

$$\Delta C_{y,lef} = C_{y,lef}(\alpha,\beta) - C_y(\alpha,\beta) \quad (4.26)$$

$$\Delta C_{y,\delta_a=20^\circ} = C_{y,\delta_a=20^\circ}(\alpha,\beta) - C_y(\alpha,\beta) \quad (4.27)$$

$$\Delta C_{y,\delta_a=20^\circ,lef} = C_{y,\delta_a=20^\circ,lef}(\alpha,\beta) - C_{y,lef}(\alpha,\beta) - \left[C_{y,\delta_a=20^\circ}(\alpha,\beta) - C_y(\alpha,\beta)\right] \quad (4.28)$$

$$\Delta C_{y,\delta_r=30^\circ} = C_{y,\delta_r=30^\circ}(\alpha,\beta) - C_y(\alpha,\beta) \quad (4.29)$$

For the yawing moment coefficient,

$$C_{n,t} = C_n(\alpha,\beta,\delta_h) + \Delta C_{n,lef}\left(1-\frac{\delta_{lef}}{25^\circ}\right) + C_{y,t}(X_{cg,ref} - X_{cg})\frac{c}{b}$$

$$+\left[\Delta C_{n,\delta_a=20^\circ} + \Delta C_{n,\delta_a=20^\circ,lef}\left(1-\frac{\delta_{lef}}{25^\circ}\right)\right]\left(\frac{\delta_a}{20^\circ}\right) + \Delta C_{n,\delta_r=30^\circ}\left(\frac{\delta_r}{30^\circ}\right)$$

$$+\frac{b}{2V_t}\left\{\left[C_{n_R}(\alpha) + \Delta C_{n_R,lef}(\alpha)\left(1-\frac{\delta_{lef}}{25^\circ}\right)\right]R + \left[C_{n_P}(\alpha) + \Delta C_{n_P,lef}(\alpha)\left(1-\frac{\delta_{lef}}{25^\circ}\right)\right]P\right\}$$

$$+\Delta C_{n_\beta}(\alpha)\beta \quad (4.30)$$

where

$$\Delta C_{n,lef} = C_{n,lef}(\alpha,\beta) - C_n(\alpha,\beta,\delta_h = 0^\circ) \quad (4.31)$$

$$\Delta C_{n,\delta_a=20^\circ} = C_{n,\delta_a=20^\circ}(\alpha,\beta) - C_n(\alpha,\beta,\delta_h = 0^\circ) \quad (4.32)$$

$$\Delta C_{n,\delta_a=20^\circ,lef} = C_{n,\delta_a=20^\circ,lef}(\alpha,\beta) - C_{n,lef}(\alpha,\beta) - \left[C_{n,\delta_a=20^\circ}(\alpha,\beta) - C_n(\alpha,\beta,\delta_h = 0^\circ)\right] \quad (4.33)$$

$$\Delta C_{n,\delta_r=30^\circ} = C_{n,\delta_r=30^\circ}(\alpha,\beta) - C_n(\alpha,\beta,\delta_h = 0^\circ) \quad (4.34)$$

For the rolling moment coefficient,

$$C_{l,t} = C_l(\alpha,\beta,\delta_h) + \Delta C_{l,lef}\left(1-\frac{\delta_{lef}}{25°}\right) + \left[\Delta C_{l,\delta_a=20°} + \Delta C_{l,\delta_a=20°,lef}\left(1-\frac{\delta_{lef}}{25°}\right)\right]\left(\frac{\delta_a}{20°}\right)$$

$$+ \Delta C_{l,\delta_r=30°}\left(\frac{\delta_r}{30°}\right) + \frac{b}{2V_t}\left\{\left[C_{l_R}(\alpha) + \Delta C_{l_R,lef}(\alpha)\left(1-\frac{\delta_{lef}}{25°}\right)\right]R\right.$$

$$\left. + \left[C_{l_P}(\alpha) + \Delta C_{l_P,lef}(\alpha)\left(1-\frac{\delta_{lef}}{25°}\right)\right]P\right\} + \Delta C_{l_\beta}(\alpha)\beta \tag{4.35}$$

where

$$\Delta C_{l,lef} = C_{l,lef}(\alpha,\beta) - C_l(\alpha,\beta,\delta_h = 0°) \tag{4.36}$$

$$\Delta C_{l,\delta_a=20°} = C_{l,\delta_a=20°}(\alpha,\beta) - C_l(\alpha,\beta,\delta_h = 0°) \tag{4.37}$$

$$\Delta C_{l,\delta_a=20°,lef} = C_{l,\delta_a=20°,lef}(\alpha,\beta) - C_{l,lef}(\alpha,\beta) - \left[C_{l,\delta_a=20°}(\alpha,\beta) - C_l(\alpha,\beta,\delta_h = 0°)\right] \tag{4.38}$$

$$\Delta C_{l,\delta_r=30°} = C_{l,\delta_r=30°}(\alpha,\beta) - C_l(\alpha,\beta,\delta_h = 0°) \tag{4.39}$$

The aerodynamic moment coefficients are obtained with reference to a center of gravity position of $X_{cg,ref} = 0.35c$ and the desired center of gravity position was coincident ($X_{cg} = 0.35c$) in the coefficient equations. The angle of attack and sideslip angle are defined in terms of body axis velocity components as

$$\alpha = \tan^{-1}\left(\frac{W}{U}\right), \qquad \beta = \sin^{-1}\left(\frac{V}{V_t}\right) \tag{4.40}$$

where

$$V_t = \sqrt{U^2 + V^2 + W^2} \tag{4.41}$$

Aerodynamic coefficient tables can be found in Reference 88.

The F-16 is powered by an afterburning turbofan jet engine. The thrust response to throttle inputs is computed by using the mathematical model described in Figure 4.3. This model is a variable time constant, first order system representing spool up and spool

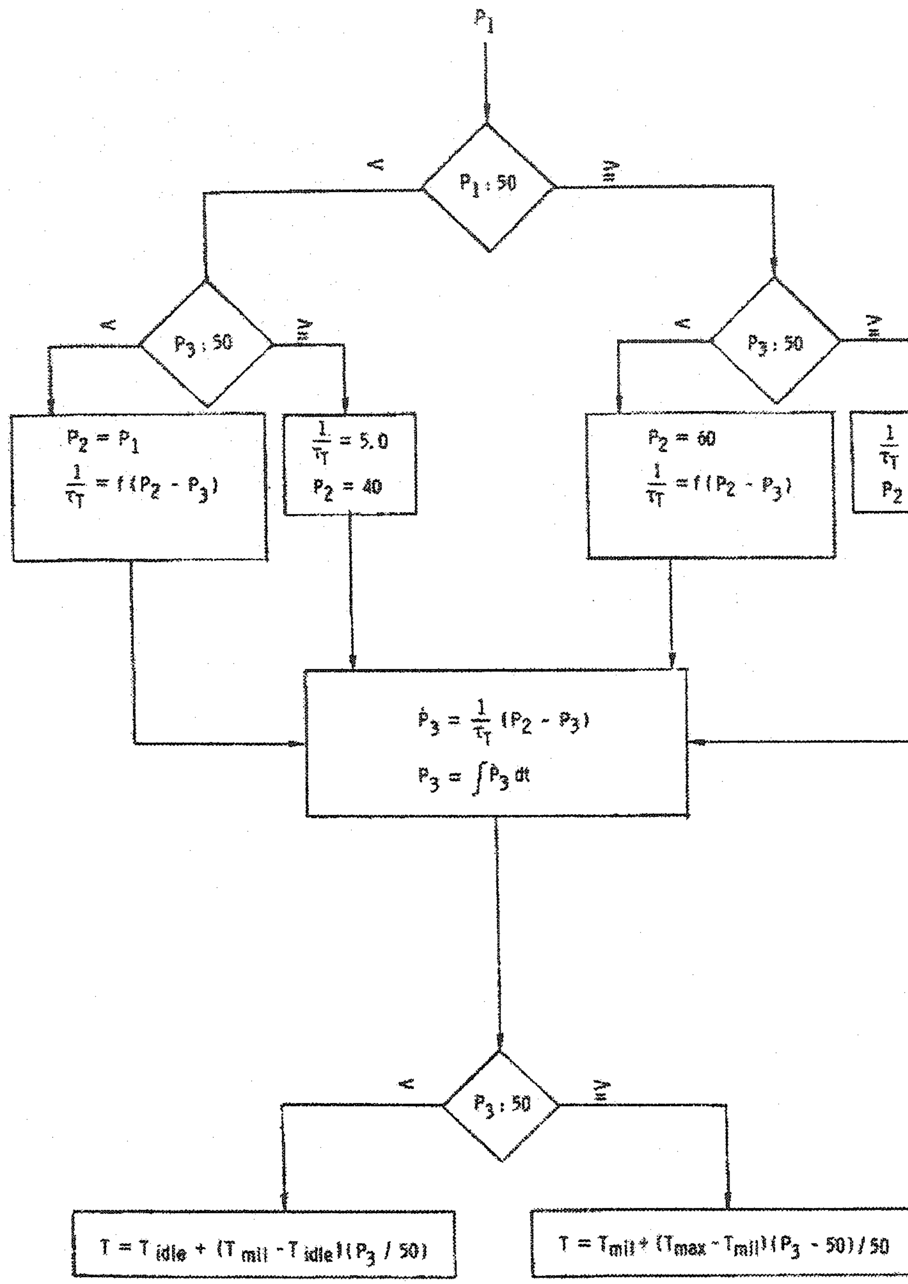

Figure 4.3 Logic Diagram for Thrust Dynamic Model[88]

down lags in the turbine engine. The engine power command based on throttle position P_1 is obtained from Figure 4.4. Figure 4.4 describes the throttle command gearing which generates P_1 at the corresponding θ_{th}. Variable P_2 denotes intermediate power command to the engine, and P_3 denotes current engine power which is a state representing the time delay in engine response. The power command terms P_1 , P_2 and P_3 are represented as percent of maximum power. $1/\tau_T$ represents decay rate of the turbine engine. T_{mil} denotes the military thrust representing thrust generated at the normal operating condition, T_{idle} denotes idle thrust representing thrust generated at the idle condition, and T_{max} denotes maximum thrust representing thrust generated with afterburner engaged condition. If the engine power command P_1 is over 50%, the engine model checks if the current engine power P_3 is over 50%. If P_3 is over 50%, the decay rate is fixed at 5.0 $1/s$, and P_2 is taken as P_1. If P_3 is less than 50%, the decay rate is obtained from P_2 and P_3 using Figure 4.5, and P_2 is taken as 60%. If the engine power command P_1 is less than 50%, the engine model checks if the current engine power P_3 is over 50%. Again, if P_3 is over 50%, the delay rate is fixed at 5.0 $1/s$, and P_2 is taken as 40%. If P_3 is less than 50%, the decay rate is also obtained from P_2 and P_3 using Figure 4.5, and P_2 is taken as P_1. Now, based on the computed P_2 and $1/\tau$ values, the time lag is applied to the engine through P_3. When the current engine power P_3 indicates over 50% of throttle, the engine dynamic model uses the T_{mil} and T_{max} to compute the engine power command. If P_3 does not exceed 50%, T_{idle} and T_{mil} are used to compute the engine power command. A 4th order Runge-Kutta method is again employed to integrate the first order engine state space equation. The thrust values are presented as function of altitude and Mach number in Reference 88. The thrust table is consisted of the thrust values for idle, military, and maximum thrust levels. Engine gyroscopic effects were simulated by representing the engine momentum at a fixed value of 160 $slug\,ft^2/sec$.

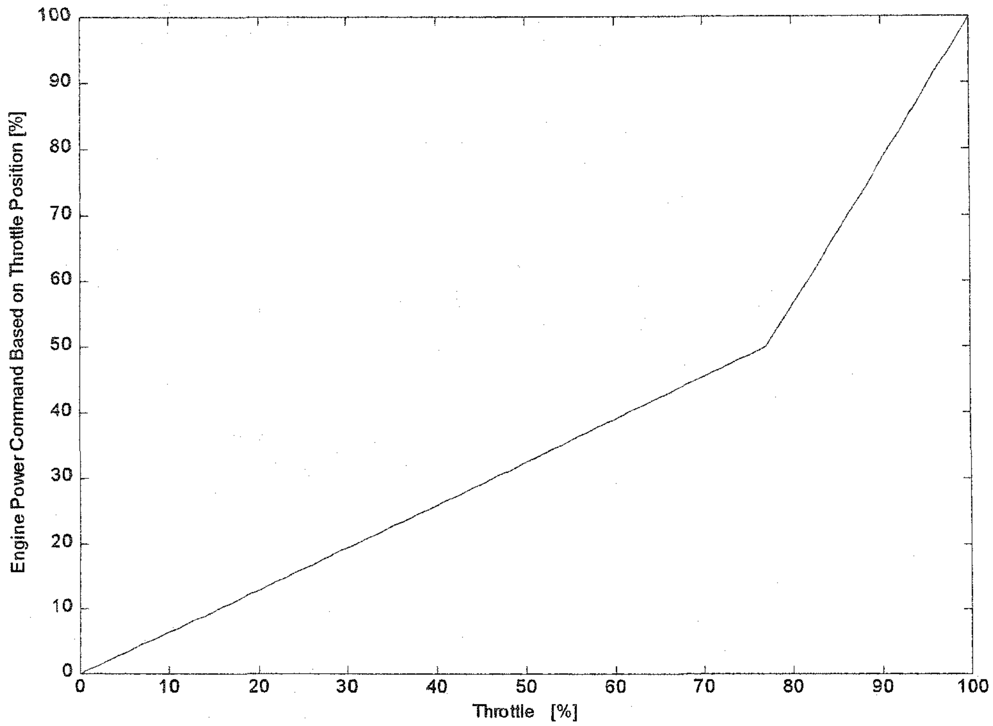

Figure 4.4 Power Variation with Throttle Position

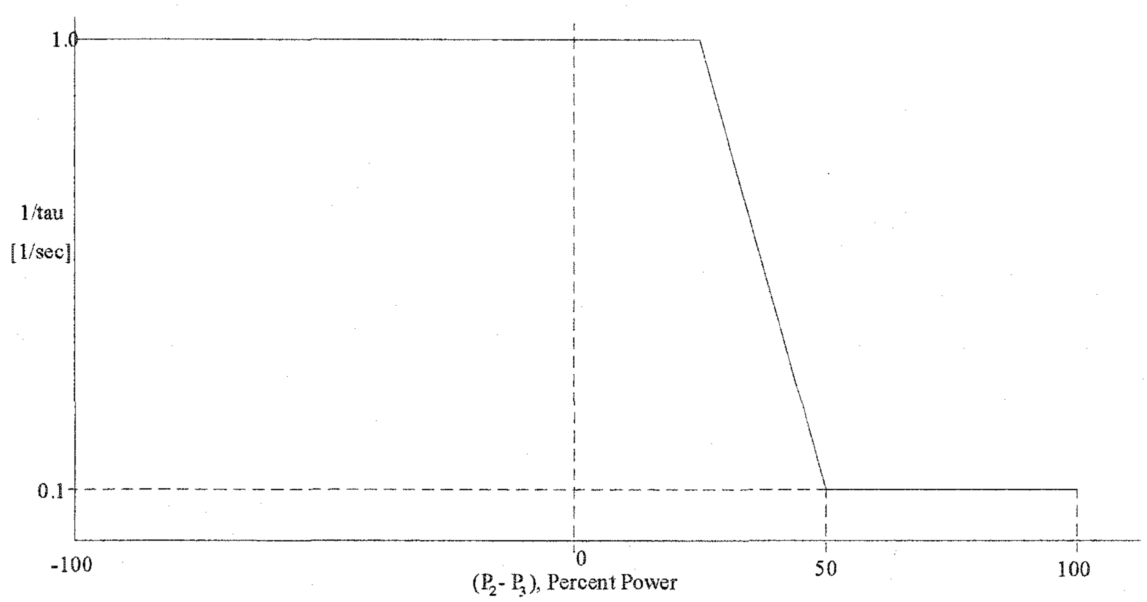

Figure 4.5 Variation of Thrust Decay Rate with Incremental Power Command

4.3 Equilibrium Flight Condition and Time Response

The equations for developing steady rectilinear symmetric level equilibrium flight conditions are derived, and the numerical computation of a single equilibrium condition and the corresponding step input time responses are presented as a demonstration of the nonlinear model. In this equilibrium condition, angle of attack is constant (α = constant) with no sideslip angle ($\beta = 0\,^{\circ}$). Velocity components U, V, and W are all constant, and V is precisely zero. Also, the angular rates P, Q, and R should be all zero. Roll angle ϕ is zero, pitch angle θ is a constant value, and yaw angle ψ is specified as zero. In level flight, pitch angle is equal to angle of attack ($\theta = \alpha$). For the control inputs, throttle position θ_{th} and horizontal stabilizer deflection δ_h are constants. Also, aileron deflection δ_a and rudder deflection δ_r are identically zero, and speed break deflection δ_{sb} and leading edge flap deflection δ_{lef} are set to zero for convenience in this phase. The center of gravity is at the referenced center of gravity position ($0.35c$), and unchanged during the simulation.

By applying the straight and level flight condition mentioned above, Equations (4.42)-(4.44) can be derived from Equations (4.3)-(4.14).

$$-g\sin\theta + \frac{F_x(h, V_t, \alpha, \delta_h)}{m} + \frac{T(\theta_{th})}{m} = 0 \tag{4.42}$$

$$g\cos\theta + \frac{F_z(h, V_t, \alpha, \delta_h)}{m} = 0 \tag{4.43}$$

$$M(h, V_t, \alpha, \delta_h) = 0$$

(4.44)

where

$$\alpha = \theta = \tan^{-1}\left(\frac{W}{U}\right), \; V_t = \sqrt{U^2 + W^2} \tag{4.45}$$

Equations (4.42)-(4.44) represent three equations with five independent unknown variables h, V_t, α, δ_h, and θ_{th} which describe the equilibrium condition to be calculated. Two of the unknown variables will be specified leaving three unknowns. In finding the equilibrium solution points, the Newton-Raphson iteration method[2] is used.

Altitude and total velocity will be specified here. For an equilibrium condition at h = 3,000 *ft* and V_t = 500 *ft/s*, the calculated state and control inputs are

$$[\alpha, \; \delta_h, \; \theta_{th}] \;=\; [2.3210^\circ \quad -0.1250^\circ \quad 13.3650\%] \tag{4.46}$$

Using θ_{th}, the engine power command to engine and current engine power variables P_2 and P_3 can be estimated, and correspond to

$$[P_2, \; P_3] \;=\; [8.8\% \quad 8.7\%] \tag{4.47}$$

Time responses for initial conditions and control inputs corresponding to this equilibrium flight condition are illustrated in Figures 4.6-4.9. In finding the time responses, the 4th order Runge-Kutta numerical integration method[2] is used. As shown in Figures 4.6-4.8, the three velocity components are constant, and the angular velocity components also have nearly constant null behavior as shown in Figure 4.9. These simulated responses validate, in some sense, the equilibrium and simulation computations.

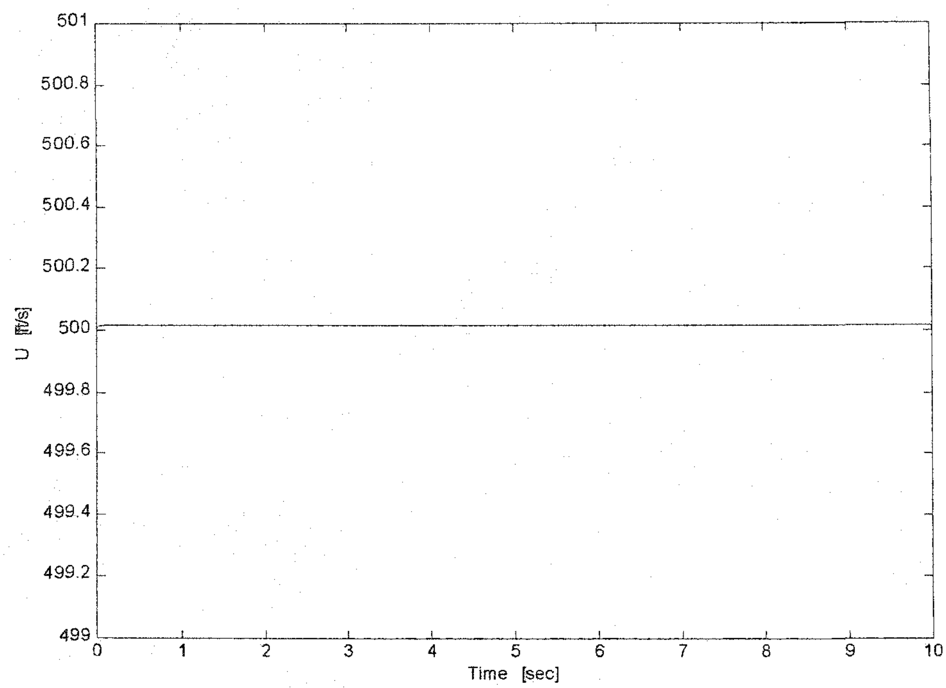

Figure 4.6 *U* Response at Straight and Level Flight Condition

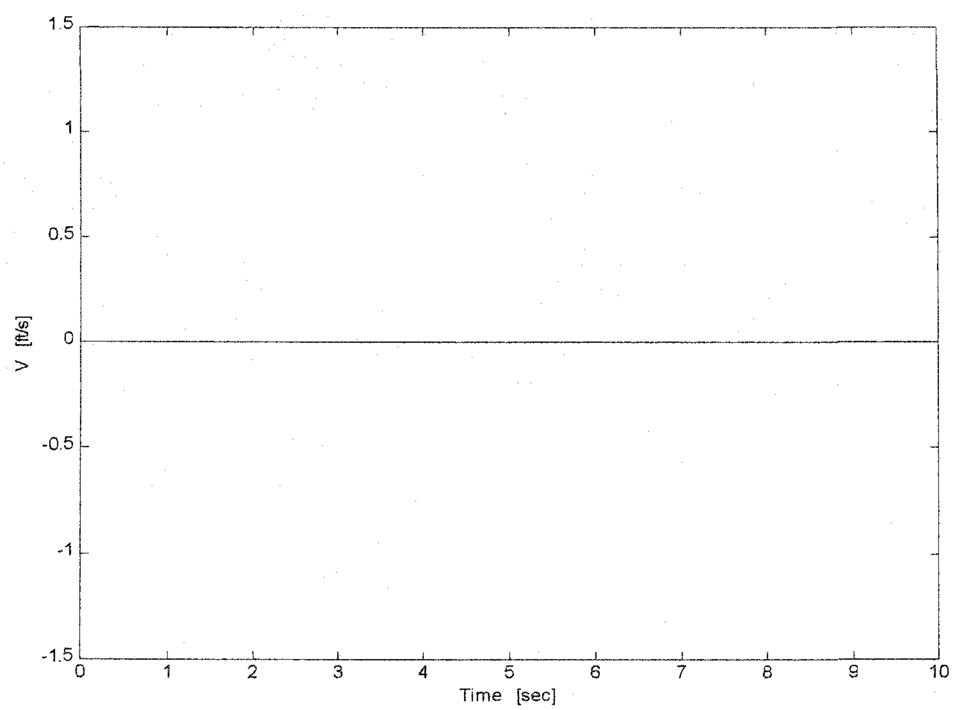

Figure 4.7 *V* Response at Straight and Level Flight Condition

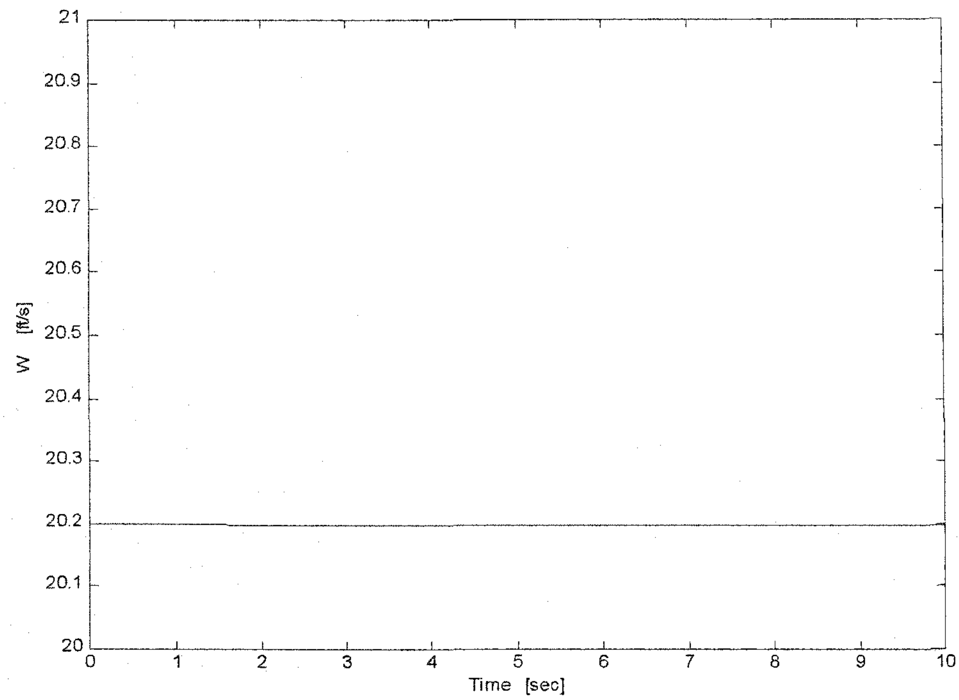

Figure 4.8 *W* Response at Straight and Level Flight Condition

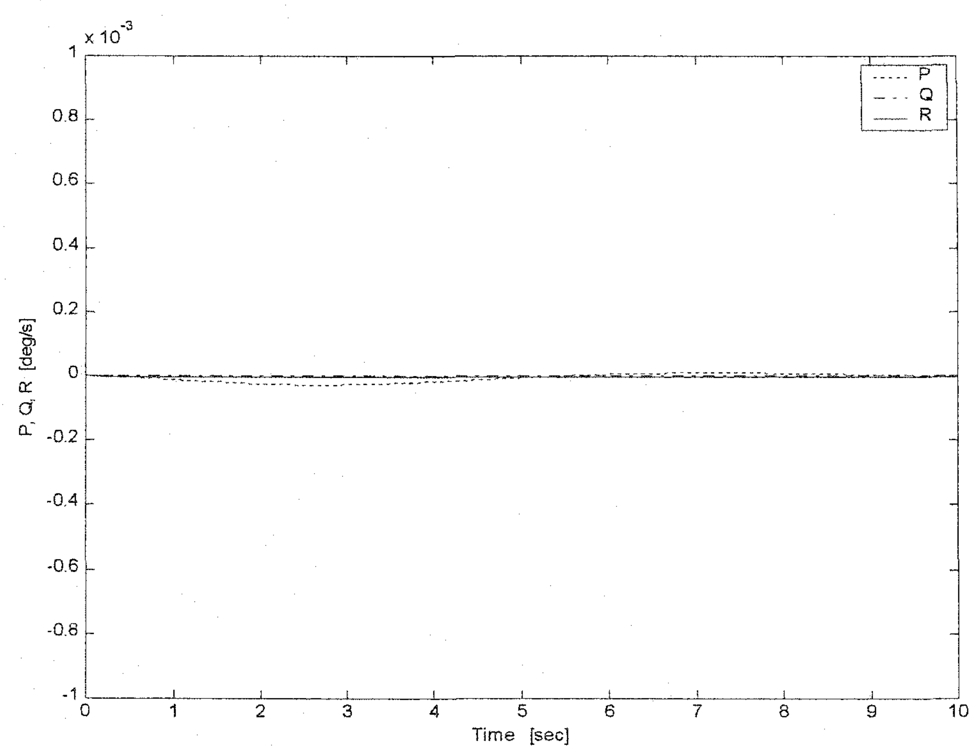

Figure 4.9 Roll, Pitch, and Yaw Rate Response at Straight and Level Flight Condition

To further demonstrate the nonlinear aircraft characteristics, step responses at the equilibrium condition are presented. Three different simulations are conducted. The vehicle motion responses are generated under step input of symmetric horizontal stabilizer only, aileron only, and rudder only cases. Throttle input cases show velocity build up behavior with very little coupling into the attitude responses, since the thrust vector approximately passes through the gravity center, and are thus not shown. Simulation starts from the equilibrium condition (see Equations (4.46)-(4.47)) at time equal to zero, and the step input in each case is applied 1 *s* after the simulation start. First, the horizontal stabilizer step input is given to the vehicle model as shown in Figure 4.10. Generated motion responses are shown in Figures 4.11-4.15. Note the velocity U gradually drops as the vehicle climbs after 1 *sec* as a result of horizontal stabilizer change. P and R are excited after the step input indicating the coupling through engine spin moment term in moment equations.

Second, the aileron step input as shown in Figure 4.16 is given to the vehicle model. Motion responses are shown in Figures 4.17-21. Unlike the horizontal stabilizer step response, the vehicle rolls and turns gradually, and maintains stable lateral behavior. The vehicle roll rate changes from negative to positive resulting in a stable turn. Coupling from the pitch instability starts to appear after about 3 *s*. Finally, the rudder step input is applied to the vehicle (see Figure 4.22), and the response is shown in Figures 4.23 -4.27. High oscillation of pitch and yaw are observed at the beginning of the simulation in Figure 4.26.

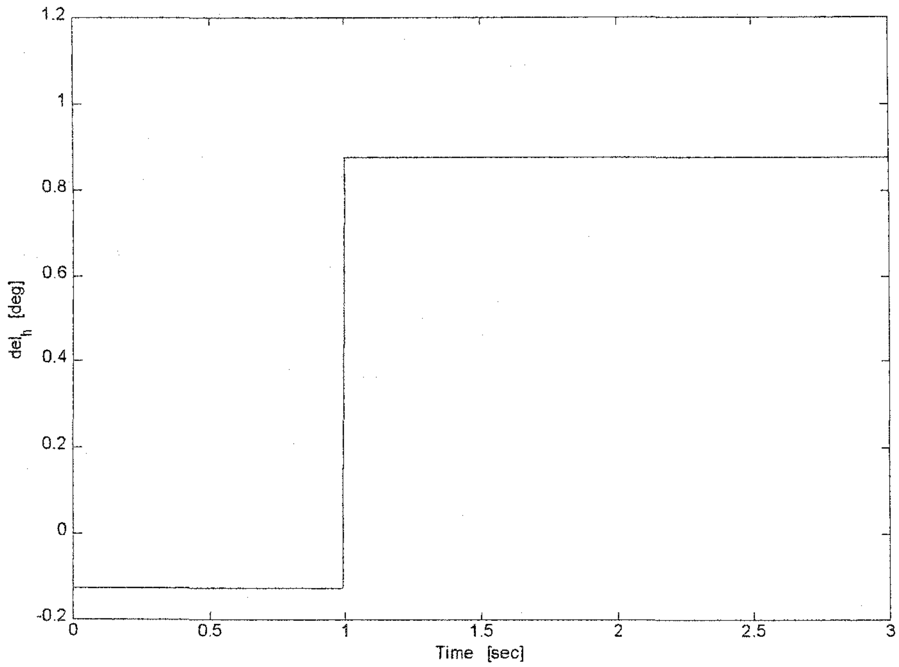

Figure 4.10 Horizontal Stabilizer Step Input

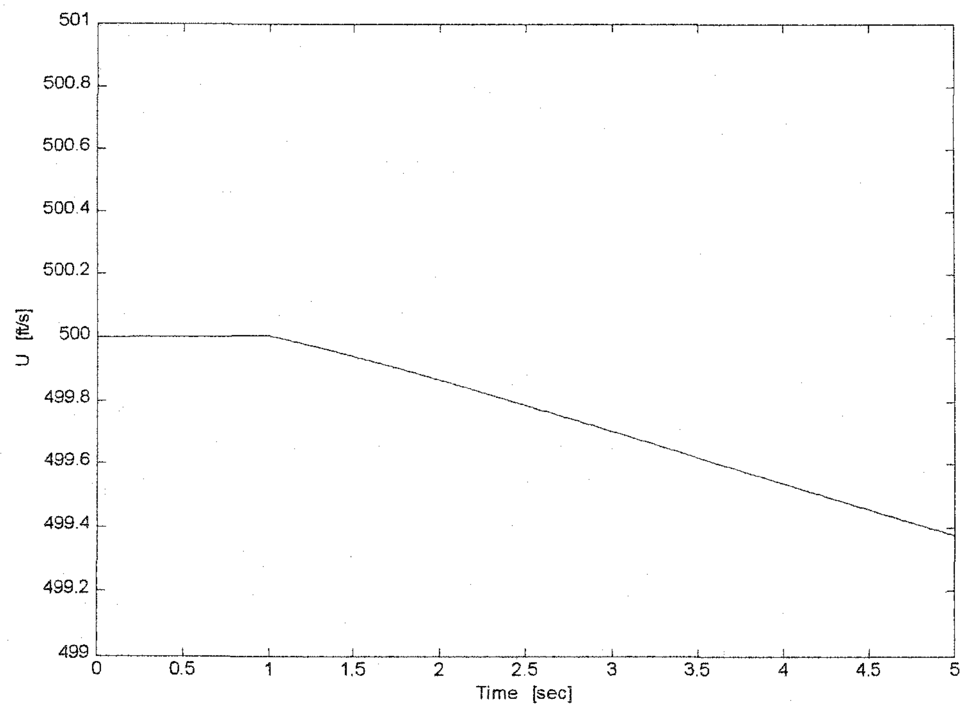

Figure 4.11 *U* Response under Horizontal Stabilizer Step Input

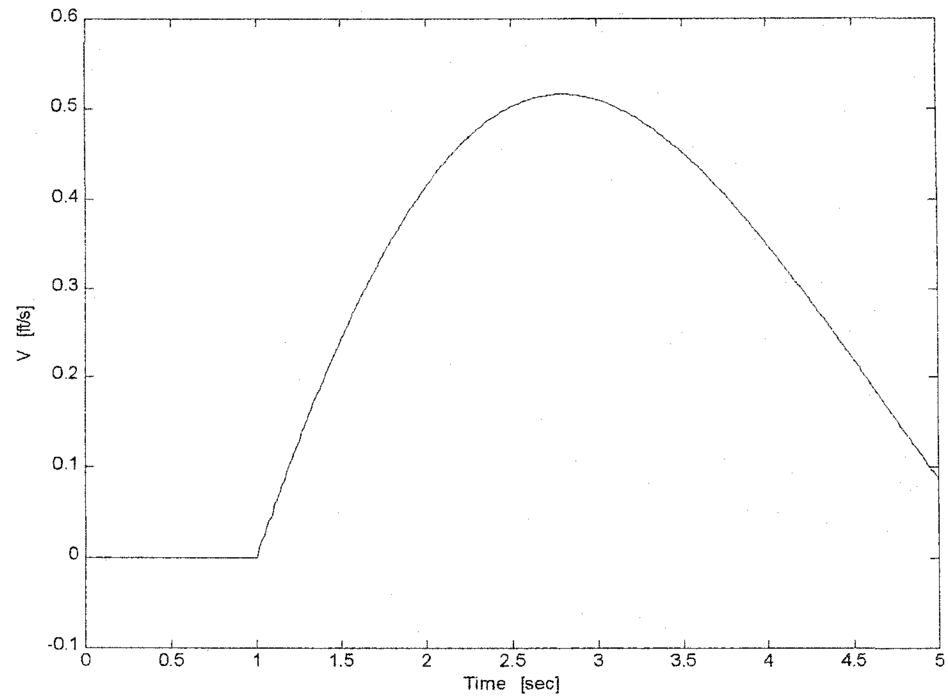

Figure 4.12 V Response under Horizontal Stabilizer Step Input

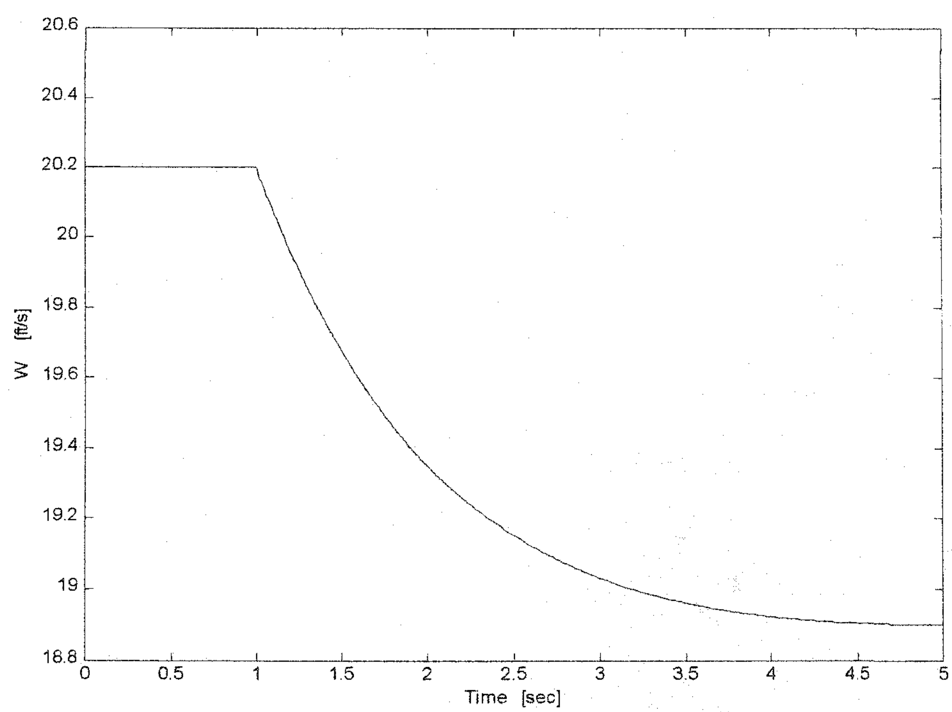

Figure 4.13 W Response under Horizontal Stabilizer Step Input

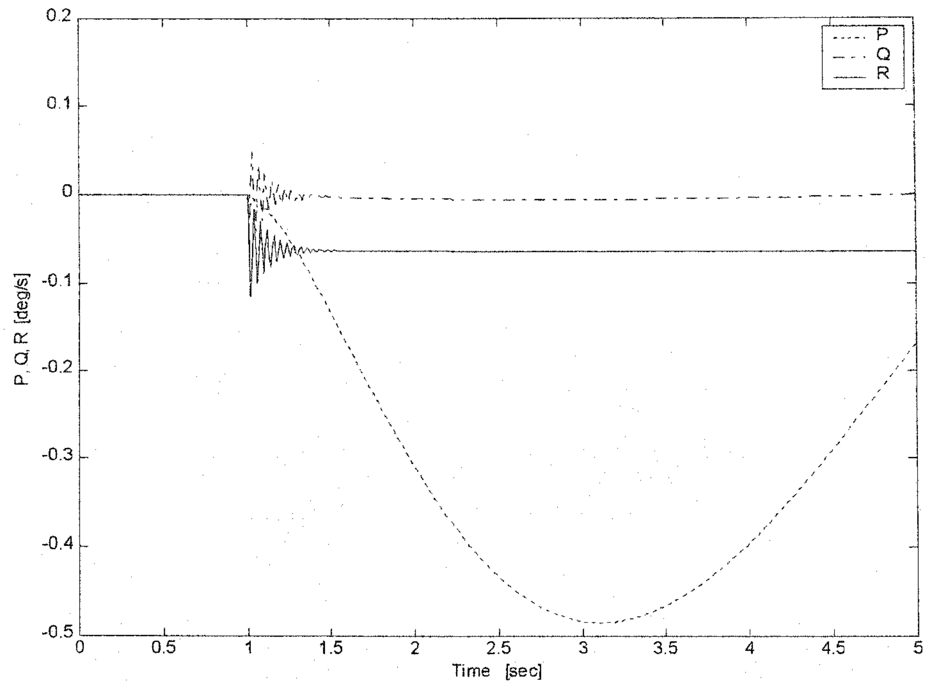

Figure 4.14 Pitch, Roll, Yaw Rate Response under Horizontal Stabilizer Step Input

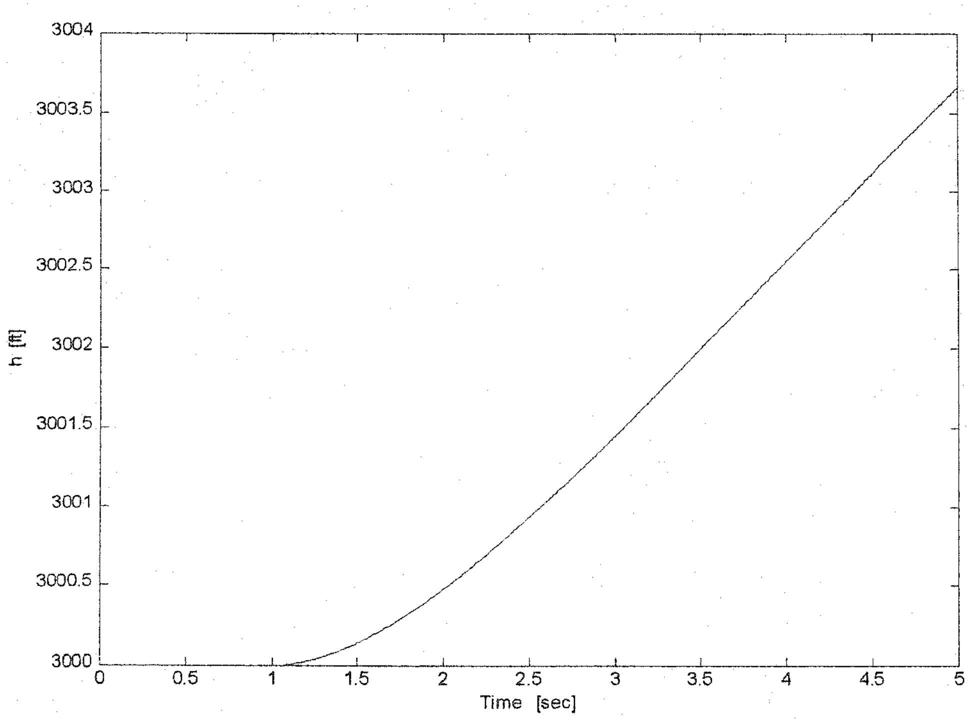

Figure 4.15 Altitude Response under Horizontal Stabilizer Step Input

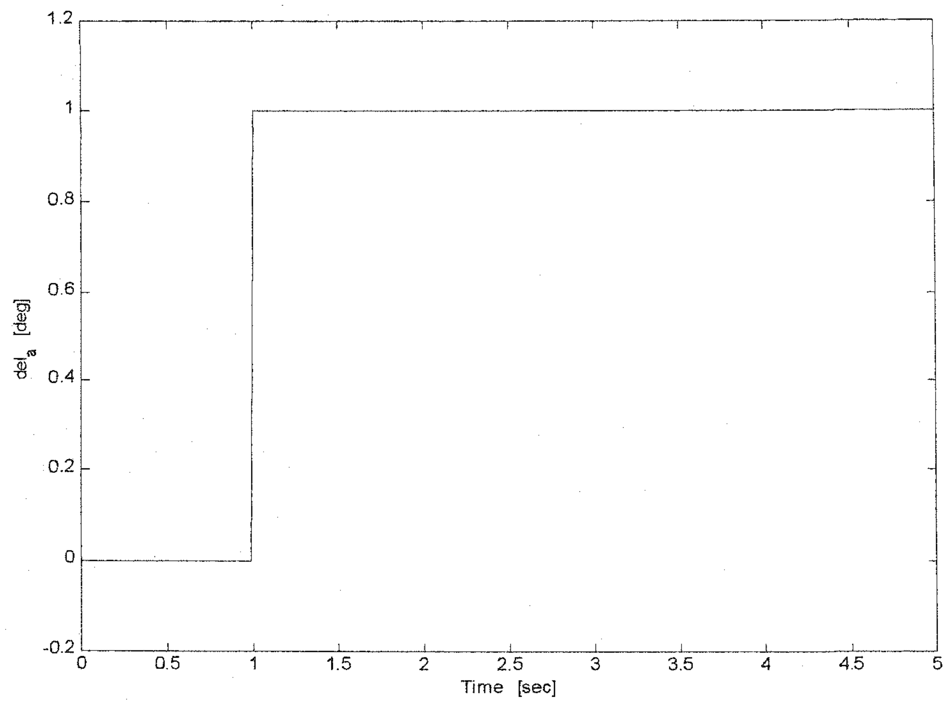

Figure 4.16 Aileron Step Input

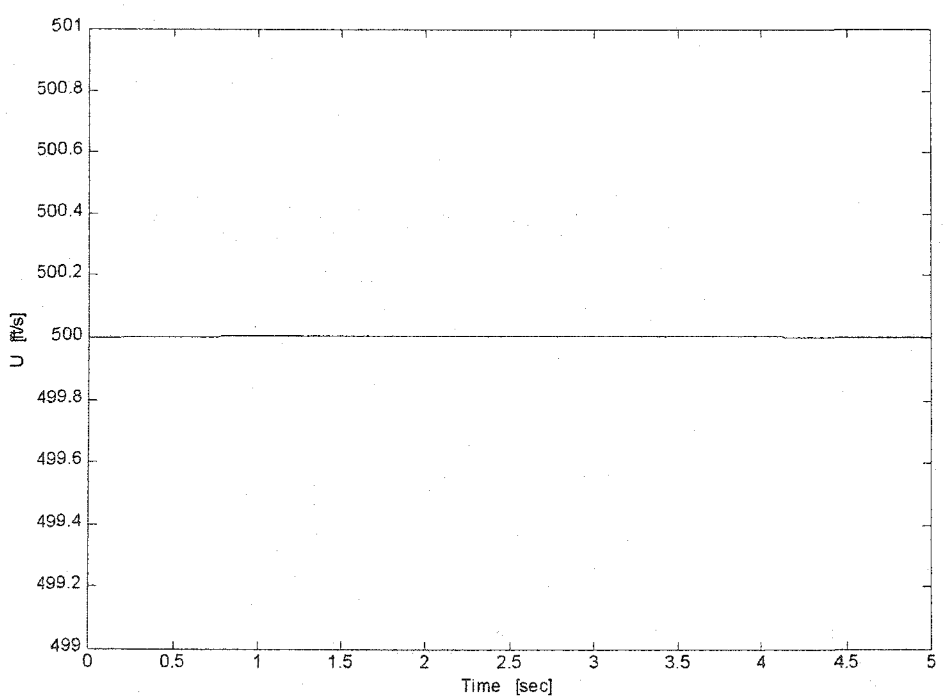

Figure 4.17 *U* Response under Aileron Step Input

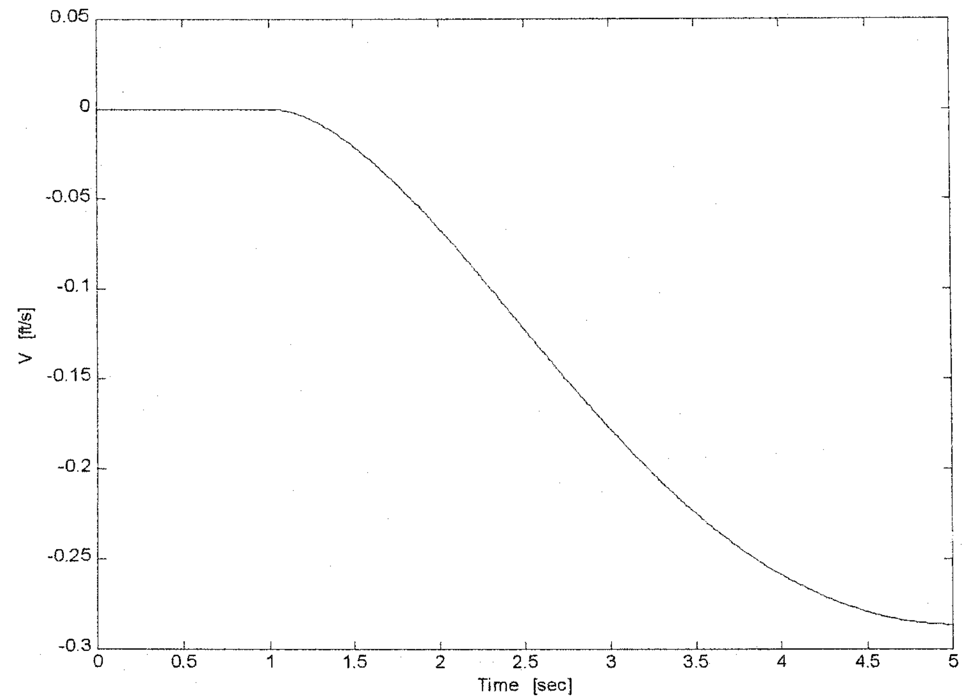

Figure 4.18 *V* Response under Aileron Step Input

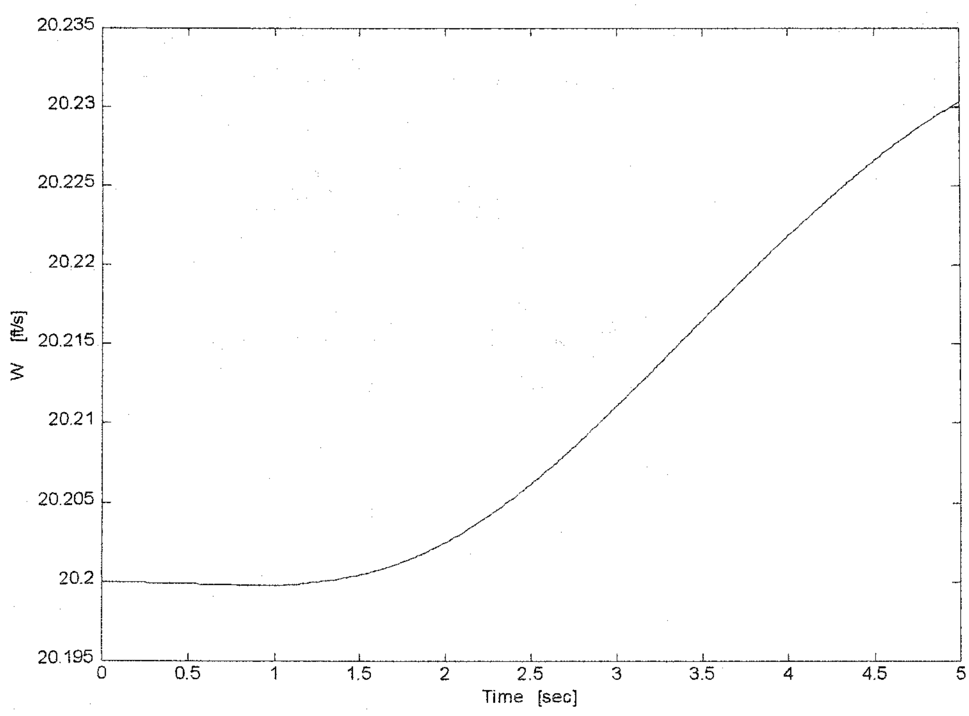

Figure 4.19 *W* Response under Aileron Step Input

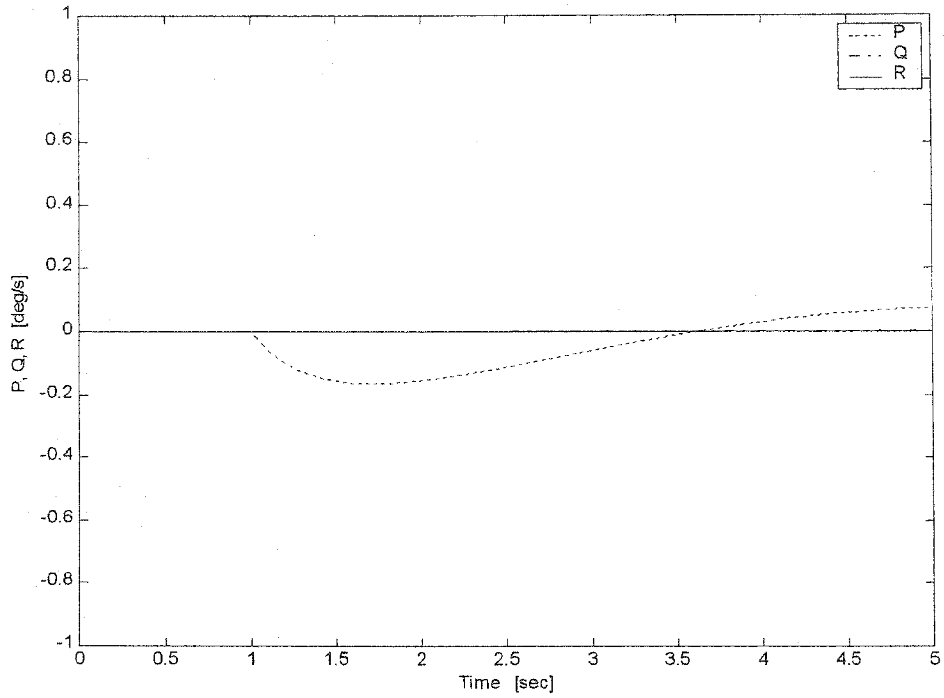

Figure 4.20 Roll, Pitch, and Yaw Rate Response under Aileron Step Input

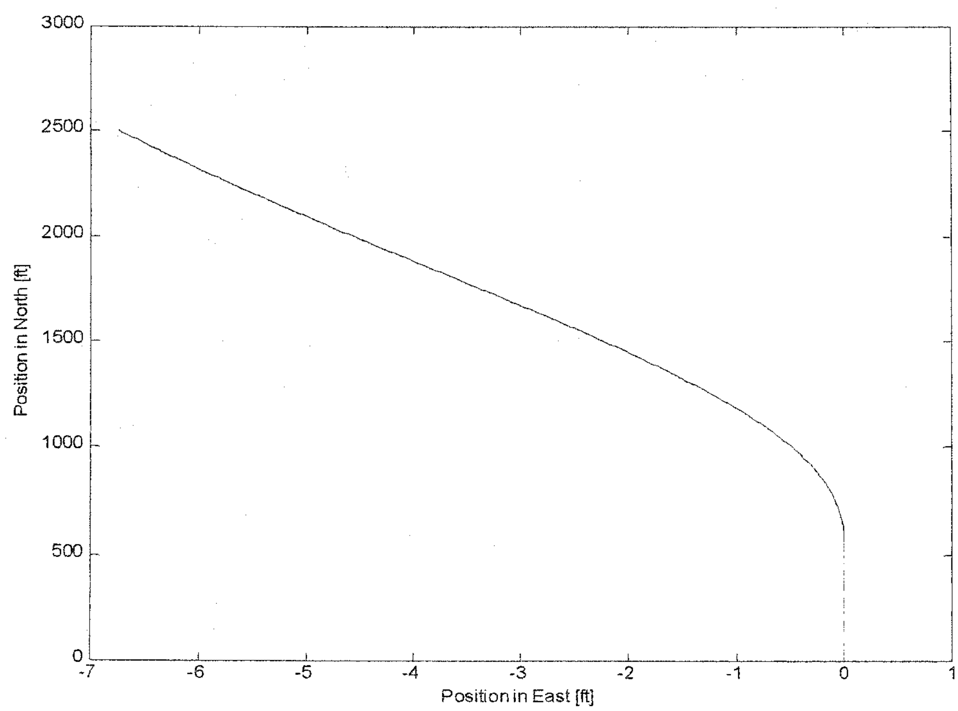

Figure 4.21 Plane Motion Response under Aileron Step Input

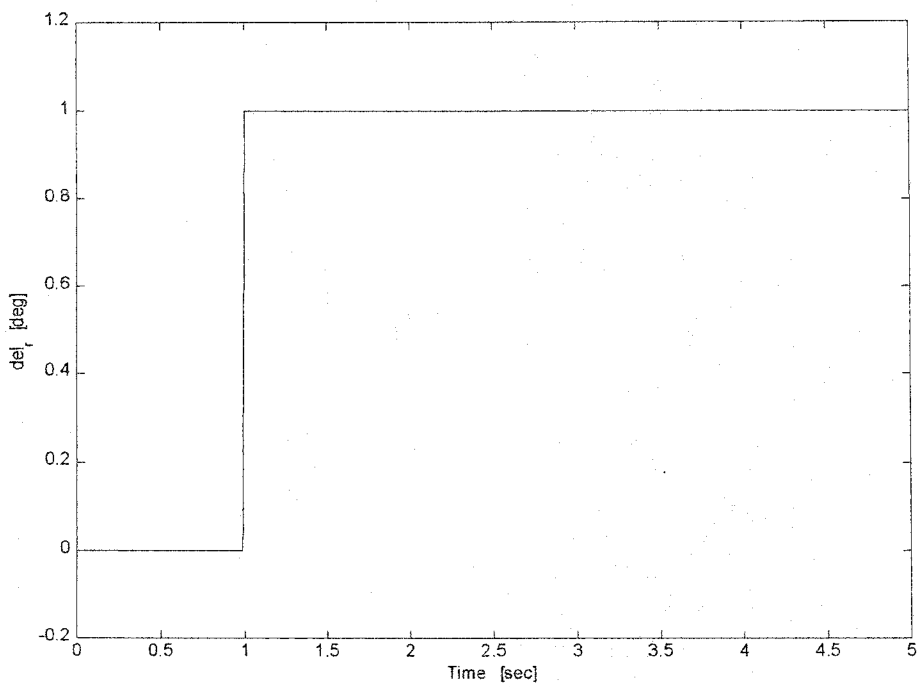

Figure 4.22 Rudder Step Input

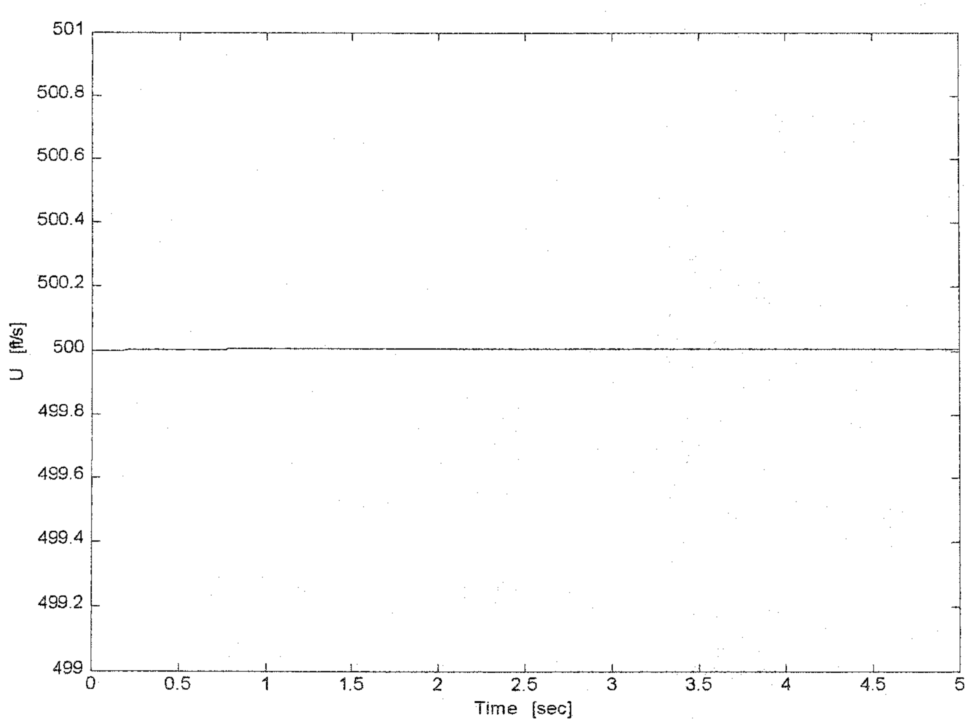

Figure 4.23 *U* Response under Rudder Step Input

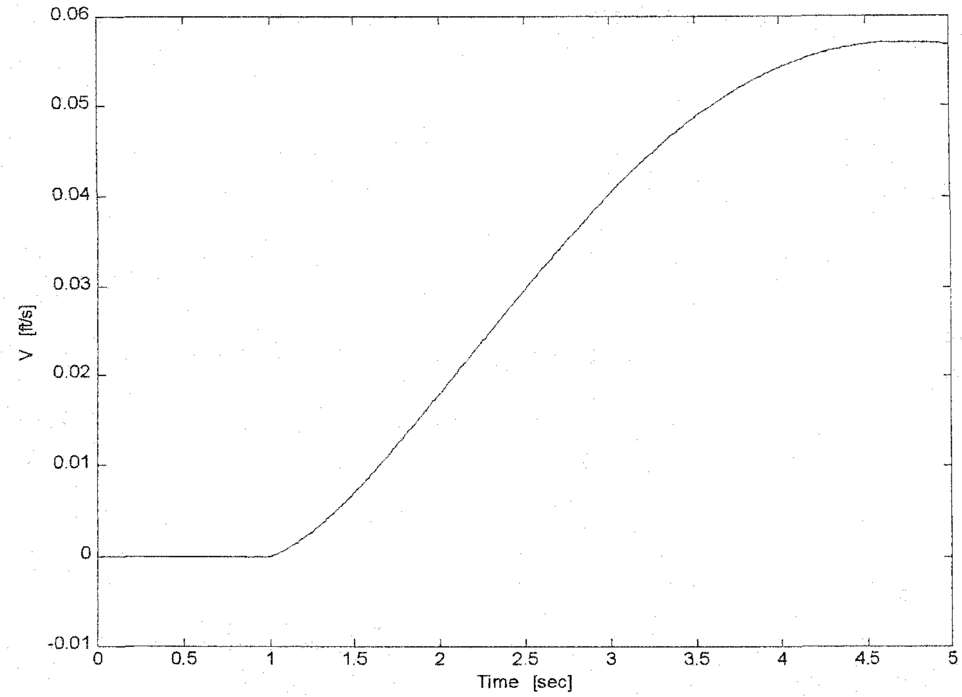

Figure 4.24 *V* Response under Rudder Step Input

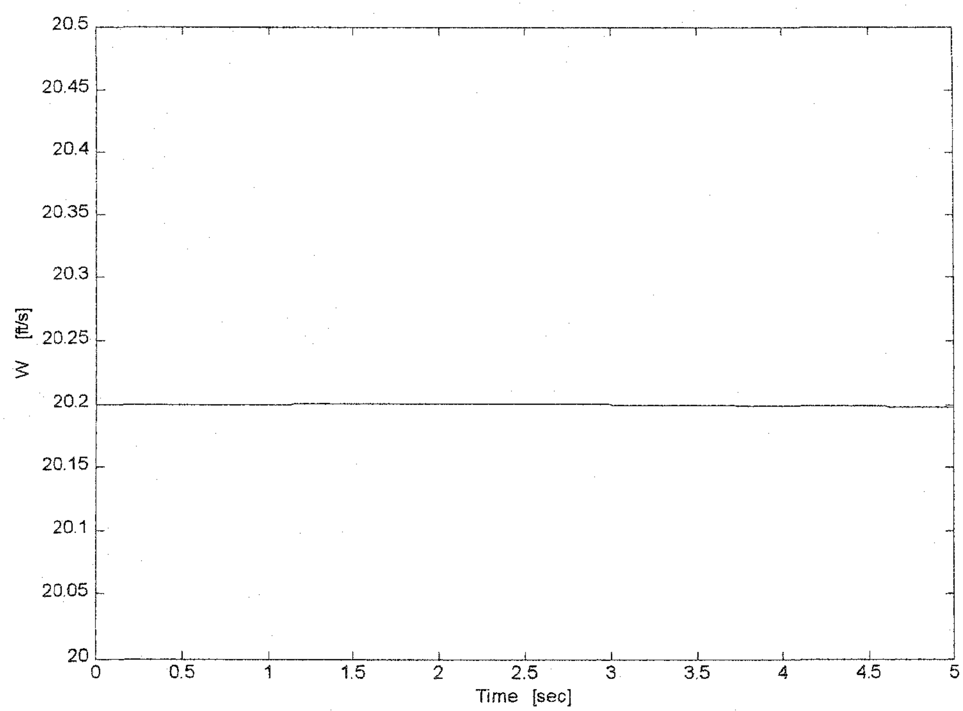

Figure 4.25 *W* Response under Rudder Step Input

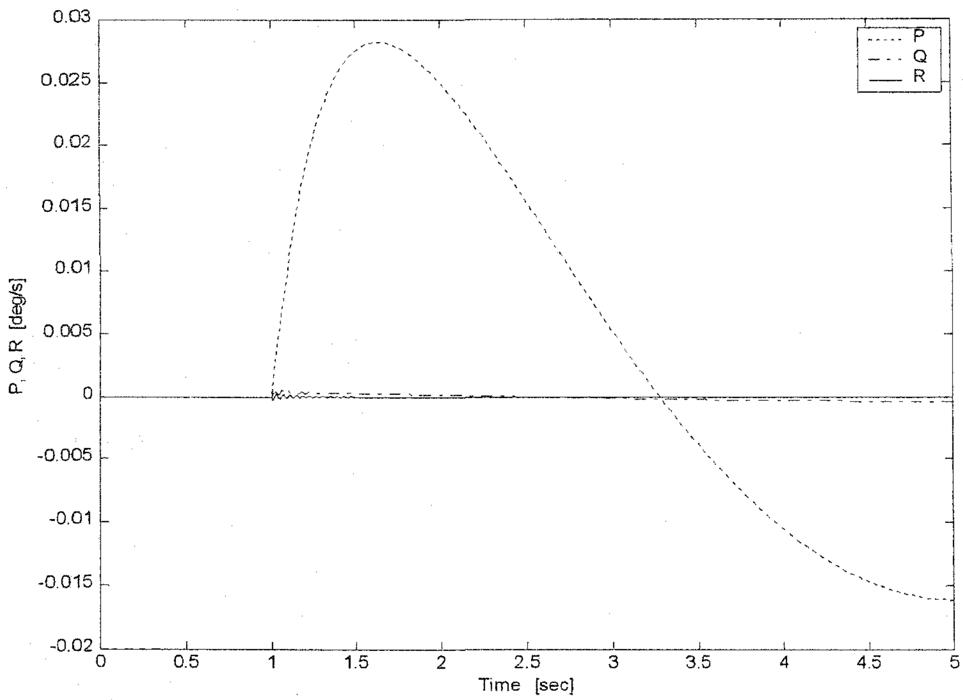

Figure 4.26 Roll, Pitch, and Yaw Rate Response under Rudder Step Input

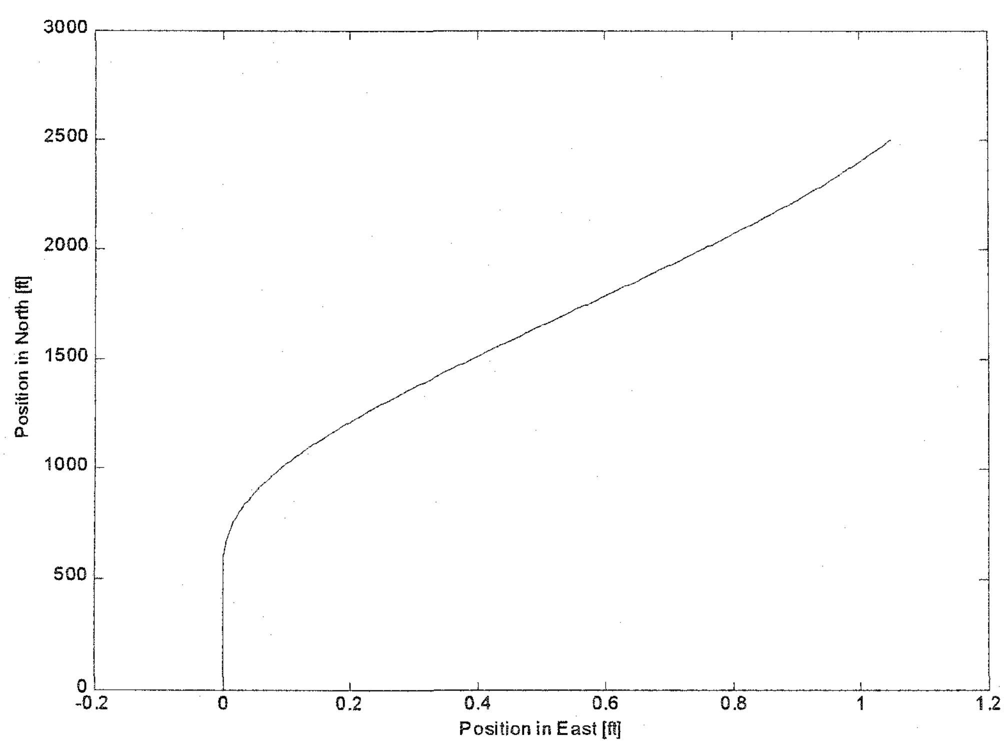

Figure 4.27 Plane Motion Response under Rudder Step Input

4.4 Wing Model Properties

In this section, there are three mathematical wing models under consideration which include a full scale finite element NASTRAN model representing the actual F-16 wing, a simplified 1/5 reduced scale model representing a wind tunnel test wing, and an approximate full-scale model recovered from the reduced-scaled model, which will be further simplified and used in the LEC research simulations. The phrase "approximate" is used to denote the fact that all properties of the full scale NASTRAN model are not recoverable. Properties of the reduced-scale model are fully available in Reference 89, while only partial full-scale model properties are available. To circumvent any confusion, consistent wing model terminology will be used throughout this section.

The low speed test wing was designed based on mass, stiffness, and planform data presented in the full-scale NASTRAN finite element description of the F-16 wing.[91] Figure 4.28 shows the layout of this finite element wing model. In the original development of the test wing, the F-16 wing is scaled so that testing could be

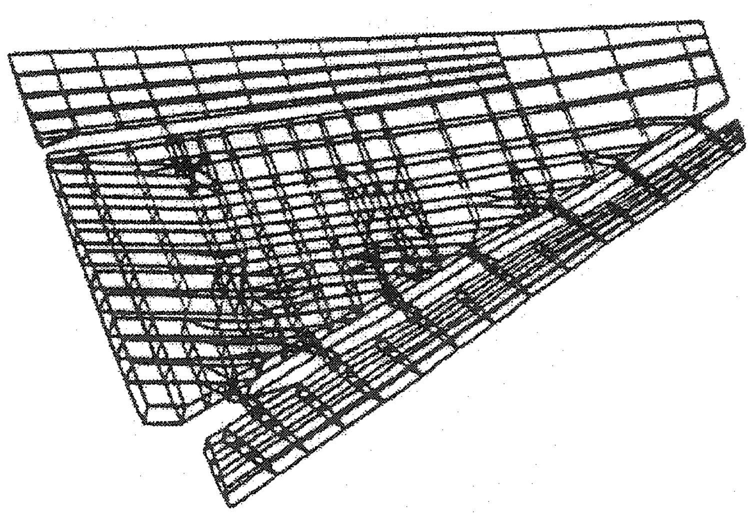

Figure 4.28 Full-Scale NASTRAN Model of F-16 Wing[89]

accomplished in a 5 *ft* wind tunnel section. Full-scale recovered model properties are compared with the available full-scale NASTRAN model properties for validation purpose. In developing the reduced-scale model, the velocity ratio was chosen so that the aeroelastic reversal point for the test trailing edge outboard surface is near the top of the wind tunnel speed envelope. The selected geometric scale factor was 0.2 such that a representation of the 183.5 *in* full size semispan F-16 wing can fit into the 5 *ft* test section as shown in Figure 4.29.

All test wing scale factors are listed in Table 4.2. In Table 4.2, geometric, velocity, density, dynamic pressure, acrodynamic-structural, frequency, inertial, and elastic scale factors are defined. Except for the inertial properties, constant units are

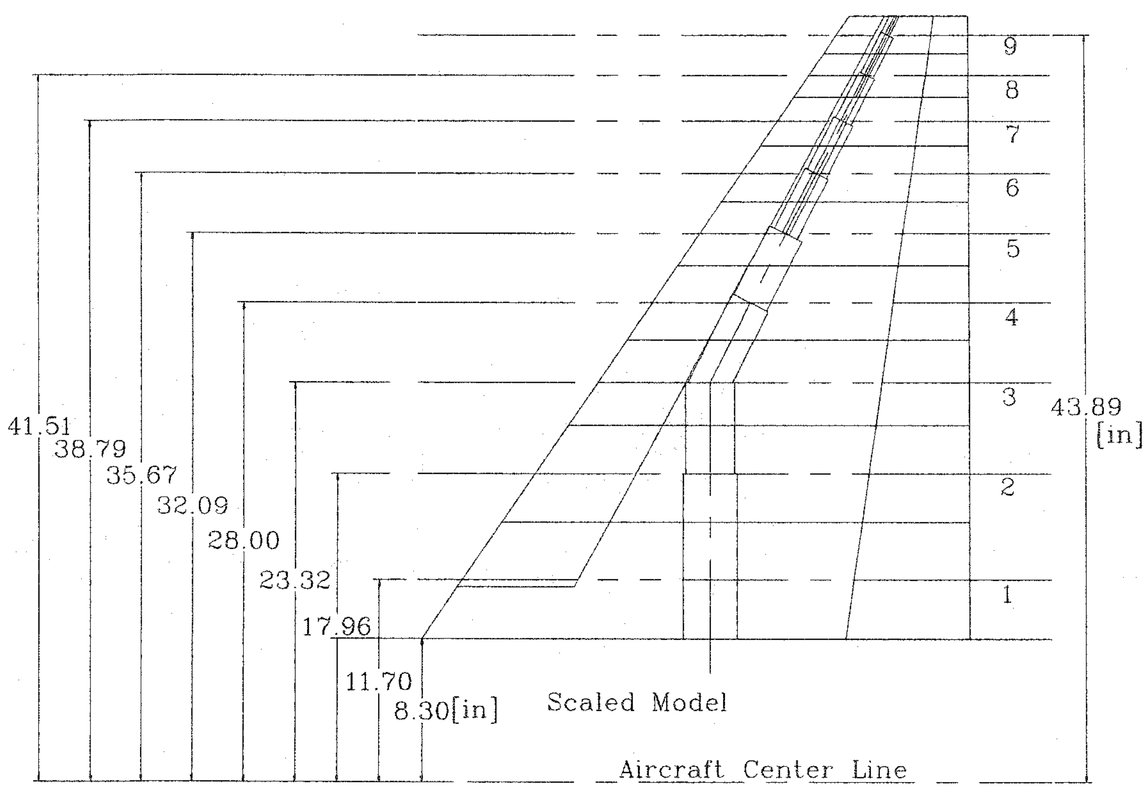

Figure 4.29 Plan View of the Test Wing and Reduced Scale Model[89]

invoked in the scaling process. For the inertial properties, the F-16 wing is described in pound mass (lb_m) while the test wing is expressed with grams (g). Relative test wing geometry was uniformly scaled proportional to the F-16 wing. Test wing dimensions are reduced to one fifth of the full size structure. Vehicle center line to wing tip distance for the F-16 wing is 225 *in*, and it was reduced to 45 *in*. The aspect ratio was kept at 3.75, the taper ratio based on tip and fuselage centerline chords was kept at 0.218, and the thickness to chord ratio was also kept constant at 3.8%. Sweep angle of the leading edge was preserved at 34.3° while the trailing edge was kept unswept.

In order to minimize unwanted bending and torsional stiffness contributions to the test wing from the aerodynamic sleeve, the test article airfoil was designed and constructed in sections. The wing box of the wind tunnel tested model consisted of nine aluminum reinforced balsa sections, and each of the leading edge and trailing edge control surfaces also consisted of nine aluminum reinforced balsa sections. The wing sections are attached to a single wing spar, and the control surface sections were attached to four separate control surface spars. Springs, simulating both actuators

Table 4.2 Scale Factors for Low Speed Wind Tunnel Test Wing[93]

Test Section Design Conditions						
Parameters	Geometric	Velocity	Density	Dynamic Pressure	$V/(b\omega)$	Frequency
Scale Factors	0.200	0.152	1.00	0.023	1.0	0.76

Mass Properties			
Parameters	Mass Total	Static Unbalance	Moment of Inertia
Scale Factors	3.6320 [*g/lb*]	0.72640 [*g in/lb in*]	0.14528 [$g\ in^2/lb\ in^2$]

Elastic Properties			
Parameters	Translational Stiffness	Bending Stiffness	Torsional Stiffness
Scale Factors	4.62×10^{-3}	3.69×10^{-5}	3.69×10^{-5}

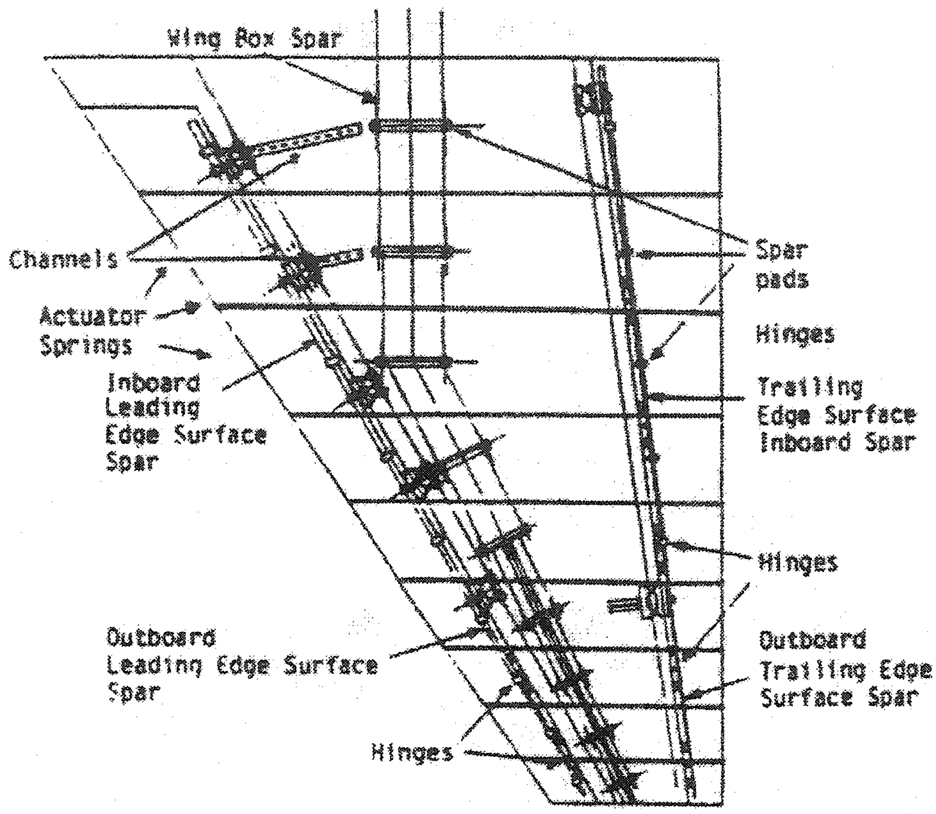

Figure 4.30 Spars and Hinges of the Scaled Wing[89]

and hinges, were used to attach each of the control surface spars to the wing box sections. Figure 4.30 shows the spanwise box section layout of the scaled aeroelastic test wing.

Bending (*EI*) and torsional stiffness (*GJ*) for the reduced-scale model are characterized with cantilever beam equations. A pitching moment was applied at the test wing tip and points of zero deflection were taken as the effective elastic axis. The reduced scale model spar was placed to match the observed elastic axis as close as possible to ensure modeling fidelity while keeping the design simple enough to permit

Table 4.3 Full-Scale and Reduced Scale Model Stiffness Distribution[89]

Full-Scale Span Station [*in*]	Full-Scale *EI* [*lb in*^{2}]	Full-Scale *GJ* [*lb in*^{2}]	Reduced-Scale Span Station [*in*]	Reduced-Scale Wing Box *EI* [*lb in*^{2}]	Reduced-Scale Wing Box *GJ* [*lb in*^{2}]
41.5	140.00×10^8	228.00×10^8	8.30	439040.0	715008.0
51.2	40.00×10^8	69.00×10^8	10.24	125440.0	216384.0
108.1	40.00×10^8	55.00×10^8	21.62	125440.0	172480.0
133.0	16.70×10^8	34.00×10^8	26.60	52371.2	106624.0
162.0	9.54×10^8	16.00×10^8	32.40	29917.4	50176.0
199.2	3.44×10^8	3.01×10^8	39.84	10787.8	9439.4
225.0	0.79×10^8	0.865×10^8	45.00	2477.4	2712.6

low cost construction. For this reason, the kinked spar layout is shown as in Figure 4.29-4.30. Stiffness characteristics of the aluminum, kinked spar were provided by the spar's flanged rectangular cross section, shown in Figure 4.31. Spar dimensions and properties were determined according to the formulas listed in Reference 94 based on the full-scale model stiffness distribution shown in Table 4.3. The dimensions of the test wing spar are listed in Table 4.4. In Table 4.3-4.4, E and G denote normal and torsional elasticity module, while I and J denote the cross sectional and polar area moments. Note that the properties of first spar element is assumed to be same as the second spar element because

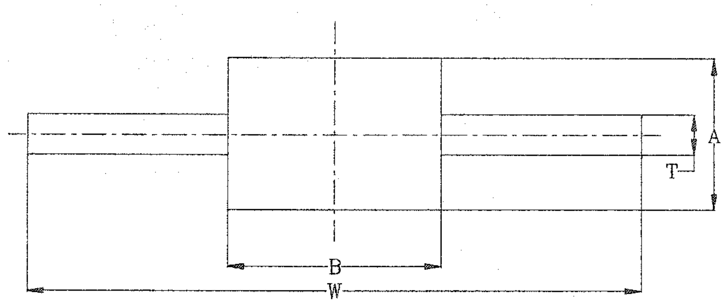

Figure 4.31 Solid Spar Cross Section Geometry[89]

Table 4.4 Test Wing Spar Dimensions[89]

Test Wing Model Span Station [*in*]	Aluminum Spar Designs [*in*]				I [in^4]	J [in^4]
	A	B	T	W		
8.3-11.7	0.354	3.19	0.0	0	11.7×10^{-3}	43.8×10^{-3}
11.7 - 17.96	0.354	3.19	0.0	0	11.7×10^{-3}	43.8×10^{-3}
17.96 - 23.32	0.323	2.91	0.0	0	8.17×10^{-3}	30.4×10^{-3}
23.32 - 28.00	0.262	2.36	0.0	0	3.54×10^{-3}	13.1×10^{-3}
28.00 - 32.09	0.239	2.15	0.0	0	2.44×10^{-3}	9.09×10^{-3}
32.09 - 35.67	0.297	0.430	0.08	1.5	0.984×10^{-3}	2.39×10^{-3}
35.67 - 38.79	0.293	0.424	0.08	1.25	0.924×10^{-3}	2.24×10^{-3}
38.79 - 41.51	0.226	0.302	0.08	1.0	0.320×10^{-3}	0.789×10^{-3}
41.51-43.89	0.208	0.270	0.08	0.8	0.225×10^{-3}	0.555×10^{-3}

the first and second spar elements show the same spar sectional dimensions.

In the reduced-scale model, mass properties are assumed to be lumped on the wing main spar, leading edge spar, and trailing edge spar of each wing section. Torsional stiffness of leading and trailing edge spars were computed through evaluating influence coefficients followed by scaling to reduced-scale conditions. The torsional stiffness properties of the leading and trailing edge spars for the reduced-scaled model are listed in Table 4.5. Note the description of box spar height A and width B in Table 4.5 can be found in Figure 4.31. Note the properties of the first leading edge spar element is assumed to be zero since the first leading edge spar element starts from the second span station. Also, the first trailing edge spar properties are assumed from Table 4.3 such that the ratio between the first and the second element of wing box (= 1.81) is same as the ratio between the first and the second element of trailing edge spar. Bending stiffness for

Table 4.5 Reduced-Scale Torsional Stiffness of Leading Edge and Trailing Edge Spars[89]

Reduced Scale Model Span Station [*in*]	Leading Edge Spar		Trailing Edge Spar	
	B/A	$J\ [in^4]$	*B/A*	$J\ [in^4]$
8.3-11.7	0	0	1.0	59.3×10^{-5}
11.7 - 17.96	1.0	500.0×10^{-5}	1.0	32.7×10^{-5}
17.96 - 23.32	1.0	295.3×10^{-5}	1.0	18.8×10^{-5}
23.32 - 28.00	1.0	180.2×10^{-5}	1.0	10.4×10^{-5}
28.00 - 32.09	1.0	108.9×10^{-5}	1.0	5.09×10^{-5}
32.09 - 35.67	1.0	67.2×10^{-5}	1.0	1.63×10^{-5}
35.67 - 38.79	1.0	36.9×10^{-5}	1.0	0.773×10^{-5}
38.79 - 41.51	1.0	12.2×10^{-5}	1.0	0.497×10^{-5}
41.51-43.89	1.0	8.11×10^{-5}	1.0	0.386×10^{-5}

full-scale leading and trailing edge control surfaces were not modeled in Reference 89. Therefore this extra control surface stiffness contribution is included that next section.

The wing model presented above is a reduced scale model consistent with the test wing designed for wind tunnel test. Now, the reduced scale model is re-scaled to provide full size wing properties appropriate for integrating with the rigid flight model and LEC development activities. Geometry, stiffness, and mass properties are computed from the reduced scale model based on the scale factors in Table 4.2. The full scale model geometry can be obtained by simply dividing the scaled wing geometry by the geometric scale factor. Figure 4.32 shows the dimension of the full scale wing model.

Stiffness properties, I and J are calculated from the scaled model stiffness using scale factor. The stiffness properties of full scale wing are shown in Table 4.6. Note, the area moment of inertia I for leading edge spar and trailing edge spar are not provided in

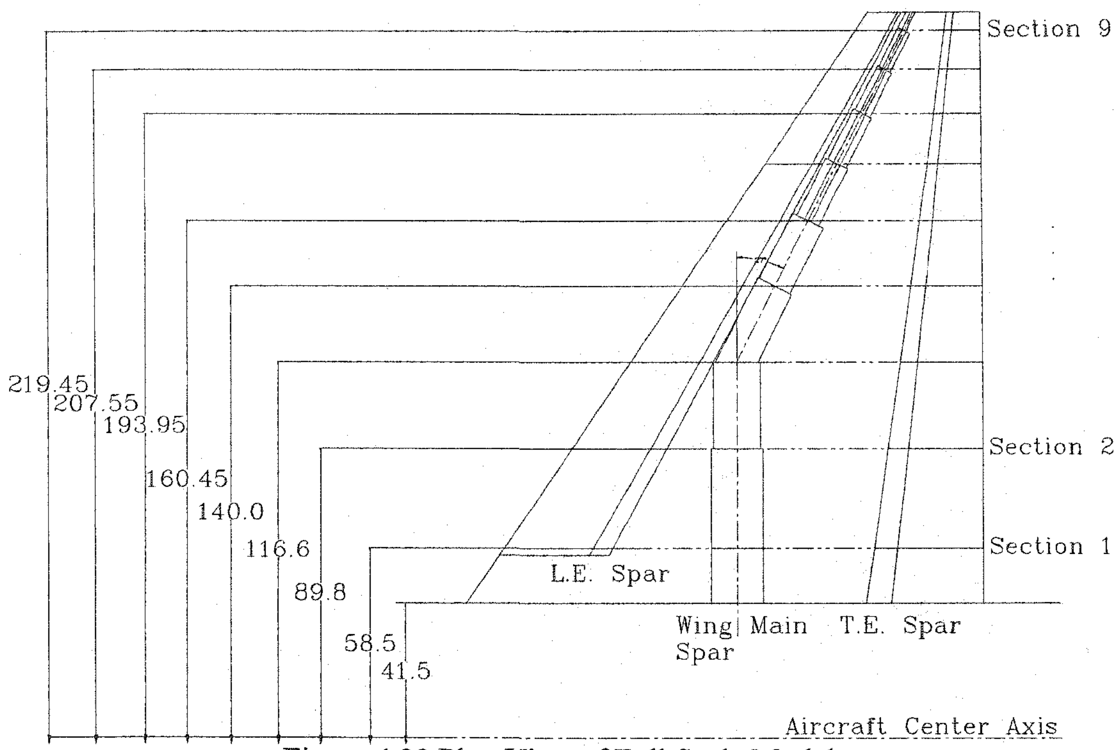

Figure 4.32 Plan View of Full Scale Model

the original model, and need to be calculated based on the properties in Table 4.4. The second moment of inertia I can be obtained from the polar second moment of inertia J. Polar second moment of inertia is defined as

$$J_z = \int_{\tilde{A}} r^2 d\tilde{A} = \int_{\tilde{A}} x^2 d\tilde{A} + \int_{\tilde{A}} y^2 d\tilde{A} = I_y + I_x \tag{4.51}$$

where, $\tilde{A}$ denotes spar sectional area, and I_x and I_y denote area moment of inertia for x and y asix, respectively. In this section, x axis corresponds to chord-wise direction, y axis corresponds to vertical direction, and z axis corresponds to spanwise direction. For rectangular sectional beam with width B and height A, area moment of inertia is defined as

$$I_x = \int_{\tilde{A}} y^2 d\tilde{A} = \frac{BA^3}{12} \tag{4.52}$$

and, polar moment of inertia is rewritten as

$$J_z = I_y + I_x = \frac{AB^3}{12} + \frac{BA^3}{12} \tag{4.53}$$

Recall that the cross section of leading edge spar and trailing edge spar are square (B = A). Therefore, the area moment of inertia I_x can be obtained from polar moment of inertia J.

$$I_x = \frac{AB^3}{12} + \frac{BA^3}{12} = \frac{B^4}{6} = \frac{1}{2} J_z \tag{4.54}$$

The area moment of inertia is computed, and listed in Table 4.6 as well as the polar moment of inertia for spars. Note the leading edge spar stiffness of first segment is zero because the first spar is located in the second span station.

Table 4.6 Stiffness of Wing Box, Leading Edge and Trailing Edge Spar

Wing Span Station	Wing Box Spar		Leading Edge Spar		Trailing Edge Spar	
	I [in^4]	J [in^4]	I [in^4]	J [in^4]	I [in^4]	J [in^4]
58.50 ~ 89.80	1.32×10^3	5.70×10^3	0	0	8.03×10^0	1.61×10^1
89.80 ~ 116.60	3.17×10^2	1.19×10^3	6.78×10^1	1.36×10^2	4.43×10^0	8.86×10^0
116.60 ~ 140.00	2.21×10^2	8.24×10^2	4.00×10^1	8.00×10^1	2.55×10^0	5.09×10^0
140.00 ~ 160.45	9.59×10^1	4.09×10^2	2.44×10^1	4.88×10^1	1.41×10^0	2.82×10^0
160.45 ~ 178.35	6.61×10^1	2.46×10^2	1.48×10^1	2.95×10^1	6.90×10^{-1}	1.38×10^0
178.35 ~ 193.95	2.67×10^1	6.48×10^1	9.11×10^0	1.82×10^1	2.21×10^{-1}	4.42×10^{-1}
193.95 ~ 207.55	2.50×10^1	6.07×10^1	7.71×10^0	1.54×10^1	1.05×10^{-1}	2.09×10^{-1}
207.55 ~ 219.45	8.67×10^0	2.14×10^1	1.65×10^0	3.31×10^0	6.73×10^{-2}	1.35×10^{-1}

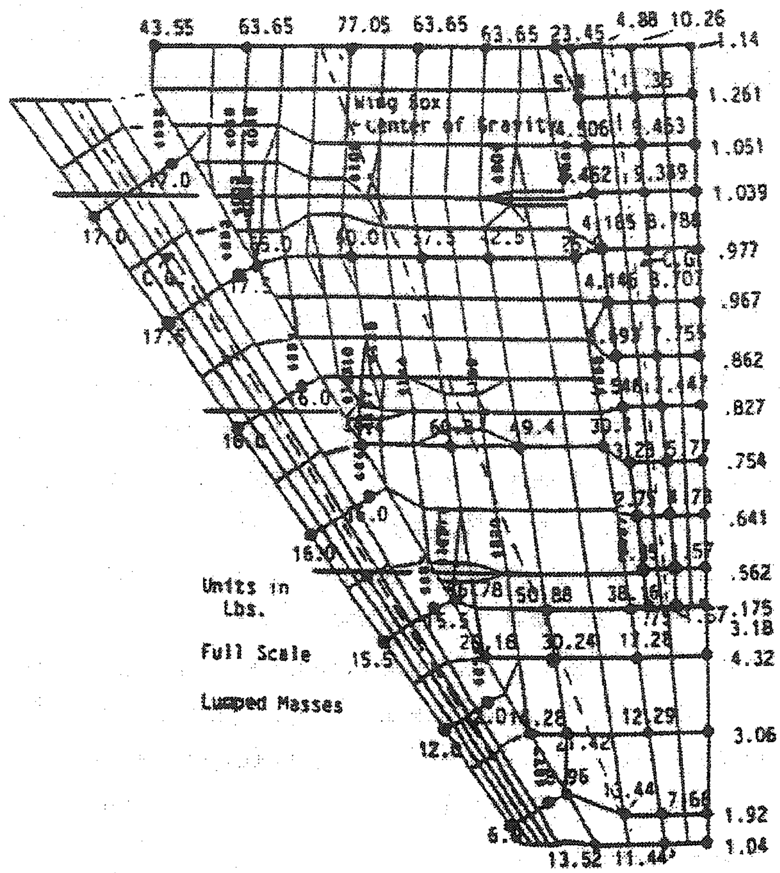

Figure 4.33 Lumped Mass Distribution of NASTRAN Model[89]

Now, mass and inertia properties are considered. The chord-wise wing section target values for total mass, static unbalance, and moment of inertia for the reduced scale model are determined though the full-scale NASTRAN model.[91] The mass distribution of the full scale model was given at specified spanwise locations as shown in Figure 4.33. These masses were used to determine the wing section chord-wise mass (M) values in Table 4.7. The dimensions and moment of inertia ($\bar{I}_y$) for each spar element are found in Reference 89. Mass properties are also computed using the scale factor and mass properties provided in Table 4.7. The computed mass and mass moment of inertia values are listed in Table 4.8. For validation, full scale lumped mass in Figure 4.32 is compared

Table 4.7 Reduced-Scale Model Sectional Mass and Moment Inertia Properties

Reduced-Scale Span Station [*in*]	Wing Box Spar		Leading Edge Spar		Trailing Edge Spar	
	M [g]	$\bar{I}_y$ [$g\ in^2$]	M [g]	$\bar{I}_y$ [$g\ in^2$]	M [g]	$\bar{I}_y$ [$g\ in^2$]
11.7	708.2+751.8*	22530	179.1	1971	186.4	1160
17.96	566.6	13439	138.1	1215	128.2	596
23.32	475.8	8437	110.8	787	91.2	318
28.00	395.9	5232	89.4	516	63.9	167
32.09	335.6+148.9*	3293	73.0	344	43.6	85
35.67	284.0	2022	59.2	230	28.7	182
38.79	152.9	815	48.3	156	17.8	84
41.51	98.8	385	39.6	107	10.2	35
43.89	59.7	169	32.1	75	51.	15

* : Additional Mass on the Main Spar Station

Table 4.8 Recovered Full Scale Model Mass and Inertia Properties

Recovered Model Span Station	Wing Box Spar		Leading Edge Spar		Trailing Edge Spar	
	M [*lb*]	$\bar{I}_y$ [$lb\ in^2$] $\times 10^4$	M [*lb*]	$\bar{I}_y$ [$lb\ in^2$]	M [*lb*]	$\bar{I}_y$ [$lb\ in^2$]
58.50	401.98	1.55×10^5	49.31	1.36×10^4	51.32	7.98×10^3
89.80	156.00	9.25×10^4	38.02	8.36×10^3	35.30	4.10×10^3
116.60	131.00	5.81×10^4	30.51	5.42×10^3	25.11	2.19×10^3
140.00	109.00	3.60×10^4	24.61	3.55×10^3	17.59	1.15×10^3
160.45	133.40	2.27×10^4	20.10	2.37×10^3	12.00	5.85×10^2
178.35	78.19	1.39×10^4	16.30	1.58×10^3	7.90	1.25×10^3
193.95	42.10	5.61×10^3	13.30	1.07×10^3	4.90	5.78×10^2
207.55	27.20	2.65×10^3	10.90	7.37×10^2	2.81	2.41×10^2
219.45	16.44	1.16×10^3	9.11	5.16×10^2	1.40	1.03×10^2

to the recovered mass properties in Table 4.8. The summation of full scale lumped mass shows 1,465.8 *lb* while the summation of recovered mass value is 1,390.5 *lb*. The difference of such is 5.3% indicating acceptable scaling error.

Now, the wing model is more simplified into a single cantilever beam having various cross sections with transversal and rotational motion. A concentrated mass and combined stiffness are computed. The inertia properties in Table 4.8 is assumed to be located in each span station of the wing. These combined inertia and stiffness properties are listed in Table 4.9. The stiffness properties of full scale NASTRAN model in Table

Table 4.9 Mass and Inertia Properties of Simplified Wing

Recovered Model Span Station	Recovered Wing Mass		Recovered Stiffness	
	M [*lb*]	$\bar{I}_y$ [*lb in*^{2}] $\times 10^4$	Full-Scale *EI* [*lb in*^{2}]	Full-Scale *GJ* [*lb in*^{2}]
58.50	502.6	5.04×10^5	140.85×10^8	228.64×10^8
89.80	229.3	2.04×10^5	41.26×10^8	53.25×10^8
116.60	186.6	1.33×10^5	27.98×10^8	36.36×10^8
140.00	151.2	9.15×10^4	12.91×10^8	18.43×10^8
160.45	165.5	4.42×10^4	8.65×10^8	11.09×10^8
178.35	102.4	2.41×10^4	3.82×10^8	3.34×10^8
193.95	60.3	1.05×10^4	3.48×10^8	3.05×10^8
207.55	40.9	4.98×10^3	1.10×10^8	0.99×10^8
219.45	27.0	2.39×10^3	0.77×10^8	0.69×10^8

4.3 can be compared to the properties of Table 4.9. Note the fair match of stiffness properties are observed although the properties in Table 4.3 are taken from different wing stations. Next, elastic axis and the distances from the elastic axis to spars are computed, and listed in Table 4.10.

Table 4.10 Center of Mass and Elastic Axis Location

Wing Span Station	1	2	3	4	5	6	7	8	9
Elastic Axis to Wing Box Spar [*in*]	-17.16	6.94	1.71	-7.29	-2.30	1.32	1.71	0.96	0.99
Center of Mass to Elastic Axis [*in*]	17.46	-3.69	3.79	10.98	3.99	-0.15	-1.17	-1.22	-2.05

4.5 Equations of Motion for Flexible Wing Model

The equations of motion are derived from the simplified model. Figure 4.34 illustrates the cantilever beam with lumped mass representing the simplified wing. l_i denotes the distance from the wing root to i^{th} wing span station where i^{th} concentrated mass is placed. Corresponding equations are listed from Equations (4.55)-(4.57) and (4.59)-(4.61). Nine equations for transversal motion are

$$m_1\ddot{x}_1 - S_{y1}\ddot{\theta}_1 - (C_{11}\dot{x}_1 + C_{12}\dot{x}_2 + \cdots + C_{19}\dot{x}_9) - (k_{11}x_1 + k_{12}x_2 + \cdots + k_{19}x_9) + L_1 - m_1\ddot{x}_0 - m_1\dot{P}l_1 = 0 \quad (4.55)$$

$$m_2\ddot{x}_2 - S_{y2}\ddot{\theta}_2 - (C_{21}\dot{x}_1 + C_{22}\dot{x}_2 + \cdots + C_{29}\dot{x}_9) - (k_{21}x_1 + k_{22}x_2 + \cdots + k_{29}x_9) + L_2 - m_2\ddot{x}_0 - m_2\dot{P}l_2 = 0 \quad (4.56)$$

$$\vdots \qquad\qquad \vdots$$

$$m_9\ddot{x}_9 - S_{y9}\ddot{\theta}_9 - (C_{91}\dot{x}_1 + C_{92}\dot{x}_9 + \cdots + C_{99}\dot{x}_9) - (k_{91}x_1 + k_{92}x_2 + \cdots + k_{99}x_9) + L_9 - m_9\ddot{x}_0 - m_9\dot{P}l_9 = 0 \quad (4.57)$$

In above equations, m_i denotes a mass, and x_i implies beam deflection while θ_i implies beam rotational deflection angle of i^{th} wing span station. C_{ij} and k_{ij} are damping constant and spring constant, respectively. L_i denotes the lift force acting on the i^{th} wing span station, and the overall vehicle roll rate is denoted as P. The inertia coupling term S_{yi} can be expressed as

$$S_{yi} = m_i \times d_{i\_ex2cg} \quad (4.58)$$

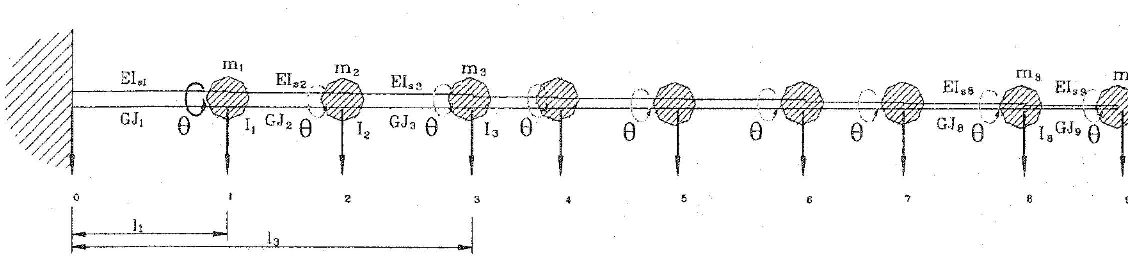

Figure 4.34 Simplified Wing Model

where, d_{i_ex2cg} denotes the distance between elastic axis and center of mass. The other nine equations for rotational motion are

$$I_{m1}\ddot{\theta}_1 - S_{y1}\ddot{x}_1 - (C^{\theta}{}_{11}\dot{\theta}_1 + C^{\theta}{}_{12}\dot{\theta}_2 + \cdots + C^{\theta}{}_{19}\dot{\theta}_9) - (k^{\theta}{}_{11}\theta_1 + k^{\theta}{}_{12}\theta_2 + \cdots + k^{\theta}{}_{19}\theta_9) + M_1 - I_{m1}\dot{Q} = 0 \quad (4.59)$$

$$I_{m2}\ddot{\theta}_2 - S_{y2}\ddot{x}_2 - (C^{\theta}{}_{21}\dot{\theta}_1 + C^{\theta}{}_{22}\dot{\theta}_2 + \cdots + C^{\theta}{}_{29}\dot{\theta}_9) - (k^{\theta}{}_{21}\theta_1 + k^{\theta}{}_{22}\theta_2 + \cdots + k^{\theta}{}_{29}\theta_9) + M_2 - I_{m2}\dot{Q} = 0 \quad (4.60)$$

$$\vdots \qquad\qquad \vdots$$

$$I_{m9}\ddot{\theta}_9 - S_{y9}\ddot{x}_9 - (C^{\theta}{}_{91}\dot{\theta}_1 + C^{\theta}{}_{92}\dot{\theta}_2 + \cdots + C^{\theta}{}_{99}\dot{\theta}_9) - (k^{\theta}{}_{91}\theta_1 + k^{\theta}{}_{92}\theta_2 + \cdots + k^{\theta}{}_{99}\theta_9) + M_9 - I_{m9}\dot{Q} = 0 \quad (4.61)$$

In equations (4.59)-(4.61), I_{mi} denotes a mass moment of inertia at i^{th} wing span station. $C^{\theta}{}_{ij}$ and $k^{\theta}{}_{ij}$ are rotational damping and rotational spring constant, respectively. M_i denotes the aerodynamic moment acting on the i^{th} wing span station, and the overall vehicle pitching rate is denoted as Q.

The spring constants of the beam can be calculated from the flexibility matrix. The flexibility matrix can be computed through applying unit force and moment to each wing span station as shown in Figure 4.35. As an example, assuming the unit force is applied to span station 3, the beam can be considered in two cases. In case 1, the moment is gradually reduced as the distance y from the wing root toward wing tip is increased.

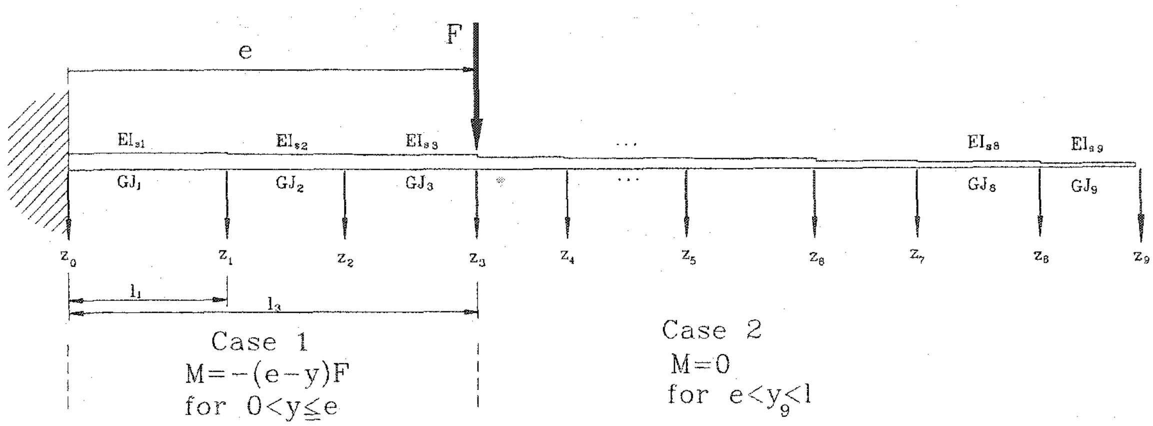

Figure 4.35 Force Applied Wing Model

For case 2, moment due to P is zero. This relationship is shown in Figure 4.35. Deriving equations to calculate deflection of each span station starts from the moment equation in Equation (4.62).

$$M = -EIx'' = -(e-y)F \tag{4.62}$$

Integrating Equation (4.62) about x yields the slope equation.

$$x' = -\frac{F}{2EI}y^2 + \frac{Fe}{EI}y + C_1^1 \tag{4.63}$$

Now, the deflection of each span station is considered. Deflection of span station 1, x_1 can be obtained from

$$x_1 = -\frac{F}{6EI_1}y_1^3 + \frac{Fe}{2EI_1}y_1^2 + C_1^1 y_1 + C_2^1 \tag{4.64}$$

where, C_1^1 and C_2^1 are constants that can be found from the boundary conditions. Applying boundary conditions $(\dot{x}_{y=0} = 0, x_{y=0} = 0)$ yield the integration constants C_1^1 and C_2^1 are both zero. Therefore, the deflection of span station 1 is

$$x_1 = -\frac{F}{6EI_1}y_1^3 + \frac{Fe}{2EI_1}y_1^2 \tag{4.65}$$

, and the slope at span station 1 is

$$x_1' = -\frac{F}{2EI_1}y_1^2 + \frac{Fe}{EI_1}y_1 \tag{4.66}$$

Similarly, slope of the second span station can be expressed as

$$x' = -\frac{F}{2EI_2}y^2 + \frac{Fe}{EI_2}y + C_1^2 \tag{4.67}$$

Applying the slope of span station 1 from Equation (4.66) to Equation (4.67) yields

$$C_1^2 = \left(-\frac{F}{2EI_1}y_1^2 + \frac{Fe}{EI_1}y_1\right) - \left(-\frac{F}{2EI_2}y_1^2 + \frac{Fe}{EI_2}y_1\right) \tag{4.68}$$

Deflection of second segment of the beam can be obtained from

$$x = -\frac{F}{6EI_2}y^3 + \frac{Fe}{2EI_2}y^2 + C_1^{\ 2}y + C_2^{\ 2} \qquad (4.69)$$

Applying boundary condition at y_1 yields

$$C_2^{\ 2} = \left(-\frac{F}{6EI_1}y_1^{\ 3} + \frac{Fe}{2EI_1}y_1^{\ 2}\right) - \left(-\frac{F}{6EI_2}y_1^{\ 3} + \frac{Fe}{2EI_2}y_1^{\ 2} + C_1^{\ 2}y_1\right) \qquad (4.70)$$

Substituting Equations (4.68) and (4.60) into Equation (4.69) gives the deflection of second wing span station, x_2. The deflection of third wing span station, x_3 can be obtained in the exactly similar manner.

Now, consider case 2 where moment is zero. At fourth span station, new moment equation is applied.

$$M = -EIx'' = 0 \qquad (4.71)$$

So, the slope of span station 4 is constant

$$x' = C_1^{\ 4} \qquad (4.72)$$

, and slope boundary condition at span station 3 gives

$$C_1^{\ 4} = -\frac{F}{2EI_3}y_3^{\ 2} + \frac{Fe}{EI_3}y_3 + C_1^{\ 3} = x'(y_3) \qquad (4.73)$$

where $C_1^{\ 3}$ can be calculated from third segment of the beam. The deflection of span station 3 from Equation (4.72) is

$$x_3 = C_1^{\ 4}y_3 + C_2^{\ 4} \qquad (4.75)$$

, and the boundary condition from third segment of the beam is

$$x_3 = -\frac{F}{6EI_3}y_3^{\ 3} + \frac{Fe}{2EI_3}y_3^{\ 2} + C_1^{\ 3}y_3 + C_2^{\ 3} \qquad (4.75)$$

Therefore, the constant $C_2^{\ 4}$ of Equation (4.74) yields

$$C_2^{\,4} = \left(-\frac{F}{6EI_3}y_3^{\,3} + \frac{Fe}{2EI_3}y_3^{\,2} + C_1^{\,3}y_3 + C_2^{\,3}\right) - \left(C_1^{\,4}y_3\right) \tag{4.75}$$

Substituting Equations (4.73) and (4.75) gives the deflection of each span station. The equation is expressed as following

$$x_i = C_1^{\,4}y_i + C_2^{\,4} \tag{4.76}$$

A computer program is coded, and the flexibility matrix is computed. The stiffness matrix can be calculated by computing the inverse of the flexibility matrix.

The Equations (4.55)-(4.57) and (4.59)-(4.61) can be rewritten in matrix form using inertia matrix M, damping matrix C, and stiffness matrix K.

$$\overline{M}\ddot{\vec{X}} + C\dot{\vec{X}} + K\vec{X} = \vec{F} \tag{4.77}$$

where $\vec{X}$ denotes state vector representing transversal and rotational deflection of each spar station and $\vec{F}$ denotes external excitation vector. The elements of Equation (4.77) can be expanded as

$$\begin{bmatrix} m_1 & 0 & \cdots & 0 & -S_{y1} & 0 & \cdots & 0 \\ 0 & m_2 & \cdots & 0 & 0 & -S_{y2} & \cdots & 0 \\ \vdots & \vdots & \ddots & \vdots & \vdots & \vdots & \ddots & \vdots \\ 0 & 0 & \cdots & m_9 & 0 & 0 & \cdots & -S_{y9} \\ -S_{y1} & 0 & \cdots & 0 & I_{m1} & 0 & \cdots & 0 \\ 0 & -S_{y2} & \cdots & 0 & 0 & I_{m2} & \cdots & 0 \\ \vdots & \vdots & \ddots & \vdots & \vdots & \vdots & \ddots & \vdots \\ 0 & 0 & \cdots & -S_{y9} & 0 & 0 & \cdots & I_{m9} \end{bmatrix} \begin{Bmatrix} \ddot{x}_1 \\ \ddot{x}_2 \\ \vdots \\ \ddot{x}_9 \\ \ddot{\theta}_1 \\ \ddot{\theta}_2 \\ \vdots \\ \ddot{\theta}_9 \end{Bmatrix} - \begin{bmatrix} C_{11} & C_{12} & \cdots & C_{19} & 0 & 0 & \cdots & 0 \\ C_{21} & C_{22} & \cdots & C_{29} & 0 & 0 & \cdots & 0 \\ \vdots & \vdots & \ddots & \vdots & \vdots & \vdots & \ddots & \vdots \\ C_{91} & C_{92} & \cdots & C_{99} & 0 & 0 & \cdots & 0 \\ 0 & 0 & \cdots & 0 & C^{\theta}_{11} & C^{\theta}_{12} & \cdots & C^{\theta}_{19} \\ 0 & 0 & \cdots & 0 & C^{\theta}_{21} & C^{\theta}_{22} & \cdots & C^{\theta}_{29} \\ \vdots & \vdots & \ddots & \vdots & \vdots & \vdots & \ddots & \vdots \\ 0 & 0 & \cdots & 0 & C^{\theta}_{91} & C^{\theta}_{92} & \cdots & C^{\theta}_{99} \end{bmatrix} \begin{Bmatrix} \dot{x}_1 \\ \dot{x}_2 \\ \vdots \\ \dot{x}_9 \\ \dot{\theta}_1 \\ \dot{\theta}_2 \\ \vdots \\ \dot{\theta}_9 \end{Bmatrix}$$

$$- \begin{bmatrix} k_{11} & k_{12} & \cdots & k_{19} & 0 & 0 & \cdots & 0 \\ k_{21} & k_{22} & \cdots & k_{29} & 0 & 0 & \cdots & 0 \\ \vdots & \vdots & \ddots & \vdots & \vdots & \vdots & \ddots & \vdots \\ k_{91} & k_{92} & \cdots & k_{99} & 0 & 0 & \cdots & 0 \\ 0 & 0 & \cdots & 0 & k^{\theta}_{11} & k^{\theta}_{12} & \cdots & k^{\theta}_{19} \\ 0 & 0 & \cdots & 0 & k^{\theta}_{21} & k^{\theta}_{22} & \cdots & k^{\theta}_{29} \\ \vdots & \vdots & \ddots & \vdots & \vdots & \vdots & \ddots & \vdots \\ 0 & 0 & \cdots & 0 & k^{\theta}_{91} & k^{\theta}_{92} & \cdots & k^{\theta}_{99} \end{bmatrix} \begin{Bmatrix} x_1 \\ x_2 \\ \vdots \\ x_9 \\ \theta_1 \\ \theta_2 \\ \vdots \\ \theta_9 \end{Bmatrix} = \begin{bmatrix} -P_1 & m_1 & m_1 l_1 & 0 & 0 \\ -P_2 & m_2 & m_2 l_2 & 0 & 0 \\ \vdots & \vdots & \vdots & \vdots & \vdots \\ -P_9 & m_9 & m_9 l_9 & 0 & 0 \\ 0 & 0 & 0 & P_1 & I_{m1} \\ 0 & 0 & 0 & P_2 & I_{m2} \\ \vdots & \vdots & \vdots & \vdots & \vdots \\ 0 & 0 & 0 & P_9 & I_{m9} \end{bmatrix} \begin{Bmatrix} L \\ \ddot{x}_0 \\ \dot{P} \\ M \\ \dot{Q} \end{Bmatrix} \tag{4.78}$$

The inertia matrix $\overline{M}$ can be decomposed as

$$\overline{M} = \begin{bmatrix} M_1 & S_y \\ S_y & I_1 \end{bmatrix} \tag{4.79}$$

The diagonal terms of M_1 which are denoted as m_i in Equation (4.78) and the diagonal terms of I_1 which are denoted as I_{mi} are listed in Table 4.10.

Table 4.11 Inertia Properties of the Simplified Wing Model

Mass [*lb*]		Mass Moment of Inertia [$lb\ in^2$]	
m_1	502.6156	I_{m1}	5.0376
m_2	229.3227	I_{m2}	2.0409
m_3	186.6189	I_{m3}	1.3288
m_4	151.2115	I_{m4}	0.9145
m_5	165.5011	I_{m5}	0.4419
m_6	102.3954	I_{m6}	0.2406
m_7	60.2974	I_{m7}	0.1053
m_8	40.9141	I_{m8}	0.0498
m_9	26.9548	I_{m9}	0.0239

The stiffness matrix can be also decomposed as

$$K = \begin{bmatrix} K_1 & 0 \\ 0 & K_2 \end{bmatrix} \tag{4.80}$$

where, the elements of matrix K_1 and K_2 are

$$K_1 = \begin{bmatrix} 1.2248e{+}007 & -2.2787e{+}006 & 7.1158e{+}005 & -1.4396e{+}005 & 3.5761e{+}004 & -7.9996e{+}003 & 2.0799e{+}003 & -3.7947e{+}002 & 6.5194e{+}001 \\ -2.2787e{+}006 & 1.6678e{+}006 & -1.0094e{+}006 & 3.3972e{+}005 & -8.4390e{+}004 & 1.8878e{+}004 & -4.9083e{+}003 & 8.9549e{+}002 & -1.5385e{+}002 \\ 7.1158e{+}005 & -1.0094e{+}006 & 1.1238e{+}006 & -7.1125e{+}005 & 2.6321e{+}005 & -5.8879e{+}004 & 1.5309e{+}004 & -2.7930e{+}003 & 4.7984e{+}002 \\ -1.4396e{+}005 & 3.3972e{+}005 & -7.1125e{+}005 & 8.4381e{+}005 & -5.5717e{+}005 & 2.0747e{+}005 & -5.3942e{+}004 & 9.8414e{+}003 & -1.6908e{+}003 \\ 3.5761e{+}004 & -8.4390e{+}004 & 2.6321e{+}005 & -5.5717e{+}005 & 6.7954e{+}005 & -4.7191e{+}005 & 1.7864e{+}005 & -3.2592e{+}004 & 5.5994e{+}003 \\ -7.9996e{+}003 & 1.8878e{+}004 & -5.8879e{+}004 & 2.0747e{+}005 & -4.7191e{+}005 & 5.8460e{+}005 & -3.8115e{+}005 & 1.2710e{+}005 & -2.1836e{+}004 \\ 2.0799e{+}003 & -4.9083e{+}003 & 1.5309e{+}004 & -5.3942e{+}004 & 1.7864e{+}005 & -3.8115e{+}005 & 4.5718e{+}005 & -2.8771e{+}005 & 7.5472e{+}004 \\ -3.7947e{+}002 & 8.9549e{+}002 & -2.7930e{+}003 & 9.8414e{+}003 & -3.2592e{+}004 & 1.2710e{+}005 & -2.8771e{+}005 & 2.9132e{+}005 & -1.0585e{+}005 \\ 6.5194e{+}001 & -1.5385e{+}002 & 4.7984e{+}002 & -1.6908e{+}003 & 5.5994e{+}003 & -2.1836e{+}004 & 7.5472e{+}004 & -1.0585e{+}005 & 4.7948e{+}004 \end{bmatrix}$$

$$K_2 = \begin{bmatrix} 1.7058e{+}009 & -1.6963e{+}008 & 0 & 0 & 0 & 0 & 0 & 0 & 0 \\ -1.6963e{+}008 & 3.0755e{+}008 & -1.3791e{+}008 & 0 & 0 & 0 & 0 & 0 & 0 \\ 0 & -1.3791e{+}008 & 2.0920e{+}008 & -7.1290e{+}007 & 0 & 0 & 0 & 0 & 0 \\ 0 & 0 & -7.1290e{+}007 & 1.2135e{+}008 & -5.0057e{+}007 & 0 & 0 & 0 & 0 \\ 0 & 0 & 0 & -5.0057e{+}007 & 6.4483e{+}007 & -1.4426e{+}007 & 0 & 0 & 0 \\ 0 & 0 & 0 & 0 & -1.4426e{+}007 & 3.0261e{+}007 & -1.5835e{+}007 & 0 & 0 \\ 0 & 0 & 0 & 0 & 0 & -1.5835e{+}007 & 2.2246e{+}007 & -6.4116e{+}006 & 0 \\ 0 & 0 & 0 & 0 & 0 & 0 & -6.4116e{+}006 & 1.1566e{+}007 & -5.1541e{+}006 \\ 0 & 0 & 0 & 0 & 0 & 0 & 0 & -5.1541e{+}006 & 5.1541e{+}006 \end{bmatrix} \tag{4.81}$$

The damping matrix C can be obtained by assuming the damping ratio as 0.02.

$$C = MU2Z\Omega U^T M \tag{4.82}$$

where, U denotes modal matrix, and Ω can be formed by diagonal matrix of natural frequencies. U and Ω can be computed from M and K matrices through modal analysis.

The right hand side of Equation (4.78) represents the external force and moment acting on the vehicle. The vertical displacement of vehicle x_0, external force L, moment M, roll rate P, and pitch rate Q are computed based on the vehicle model simulation. For lift L and wing pitching moment M, elliptical lift and moment distribution is considered when computing forces and moment of each wing section. The third column of Table

Table 4.12 Lift and Moment Distribution Considering Area and Elliptic Lift Distribution

Wing Span Segment	Area of Wing Segments $[in^2]$	Elliptic Wing Lift Distribution [%]	Life and Moment Fraction [%]
Segment 1	5.0786×10^3	23.4557	41.1324
Segment 2	3.6589×10^3	19.1223	24.1595
Segment 3	2.7317×10^3	15.8096	14.9125
Segment 4	2.0327×10^3	12.7474	8.9473
Segment 5	1.5135×10^3	10.0777	5.2665
Segment 6	1.1186×10^3	7.7060	2.9763
Segment 7	0.8163×10^3	5.5845	1.5741
Segment 8	0.5967×10^3	3.7272	0.7679
Segment 9	0.4310×10^3	1.7696	0.2634

4.11shows the percent portion of each wing segment when concerning elliptic distribution. Area portion of wing is also considered when distributing lift and moment of wing to each wing segment. Fraction of lift and moment distribution considering both area and elliptic lift distribution is listed in fourth column of Table 4.11.

The natural frequencies of first four modes are compared with the original F.E.M. full scale model and scaled model for wind tunnel of Reference 93. The model natural frequencies match fairly well with the measured model values.

Table 4.13 Natural Frequency of the Wing Model

Mode	F.E.M. Full Scale Aircraft[85] [Hz]	Scaled Model (Sine Dwell)[89] [Hz]	Simplified Wing Model Result [Hz]
1st Bending	7.25	5.6	5.55
2nd Bending	25.3	20.6	19.18
1st Torsion	33.5	28.8	26.32
2nd Torsion	58.9	41.3	41.38

CHAPTER 5

AUGMENTATION AND AUTOPILOT CONTROL SYSTEMS FOR F-16 AIRCRAFT

5.1 Stability Augmentation Control System Description

The flight control system (FCS) introduced in this section is a simplified version of the Block 25 F-16 Digital Flight Control System. The basis for this FCS can be found in Reference 95 where the focus was to develop a system for a fixed altitude and Mach number. In contrast to Reference 95, variable gains allowing simulation at any altitude and Mach number inside of flight envelope. Many operational mode of the full system, such as landing, gunnery, high angle of attack, and refueling, are not taken into account here. This FCS is a 3-axis stability augmentation system and serves as inner loops for autopilot functions considered in Section 5.2. The airframe pitch instability and the lightly damped yaw-roll oscillation noted in Chapter 4 are corrected by this system. Because the vehicle model is nonlinear, nonlinear behavior in the FCS is employed.

The stability augmentation is divided into longitudinal and lateral-directional modes of operation. The block diagrams of the longitudinal and lateral-directional systems are shown in Figure 5.1 and Figure 5.2, respectively. The longitudinal FCS consists of pitch rate and normal acceleration (N_z) feed back. Various leading and washout filters are included in these feedback paths. Stick pitch commands (F_{ec}) excites these loops and operate though a proportional-integral controller in the forward loop path providing an horizontal stabilizer deflection. The lateral FCS employs roll rate feedback to the aileron and differential horizontal stabilizer. The rudder and an aileron-rudder interconnection use a combination of lateral acceleration and yaw rate feed back. The command gradients are shown in Figures 5.3-5.5. The linear parts of the FCS are computed using numerical methods such as numerical integrations, differentiations, and multiplications of signals. The variable gain schedules are shown in

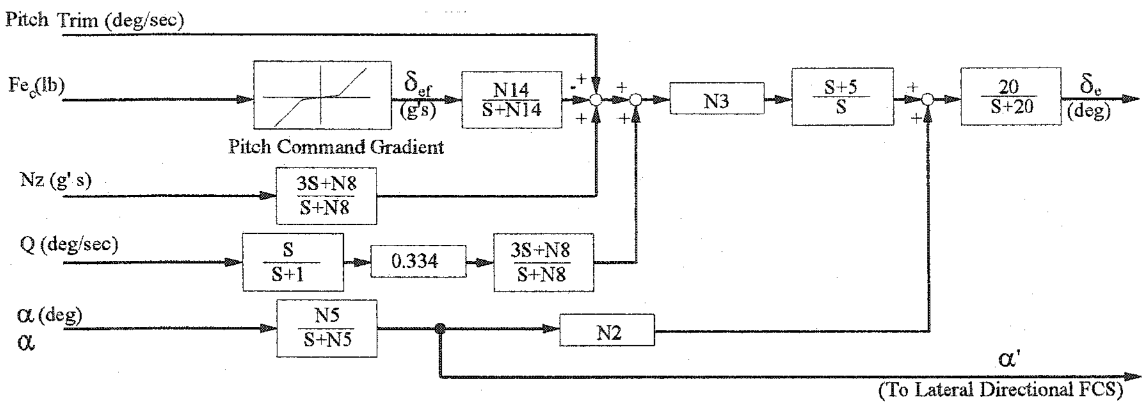

Figure 5.1 Longitudinal Stability Augmentation Control System

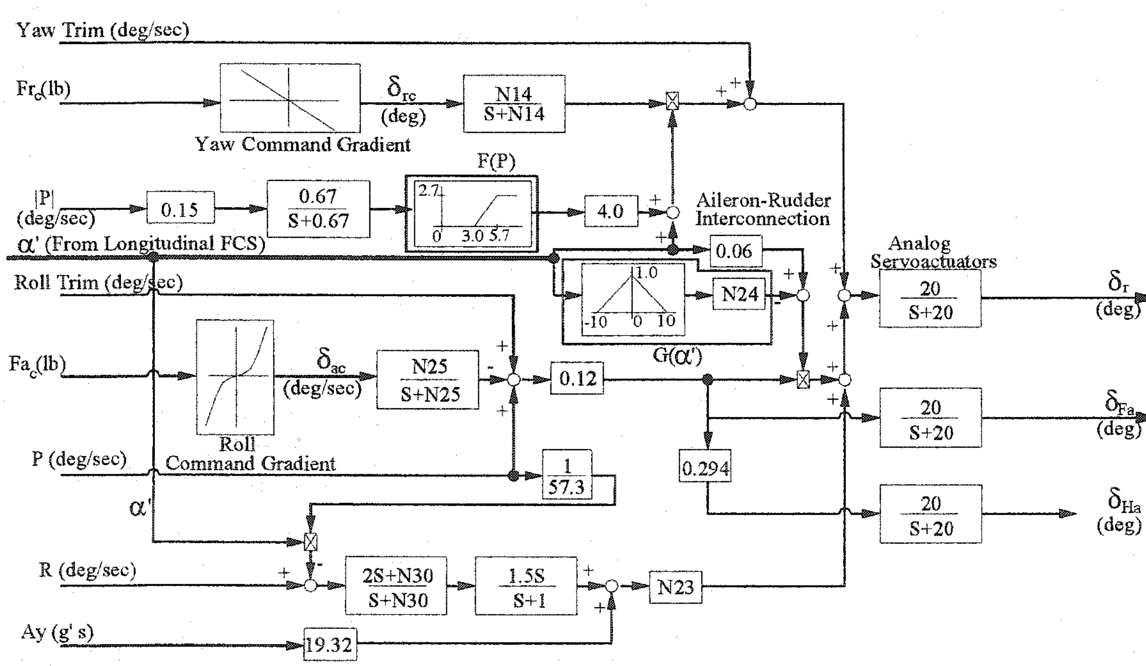

Figure 5.2 Lateral Stability Augmentation Control System

Figures 5.6-5.13. Note, N_5 is 0.909 in NOTE 2 condition or 10.0 otherwise, and N_{25} is 2.5 in any condition. The control gain N_8 can be expressed as summation of N_{8A} and N_{8B} ($N_8 = N_{8A} + N_{8B}$).

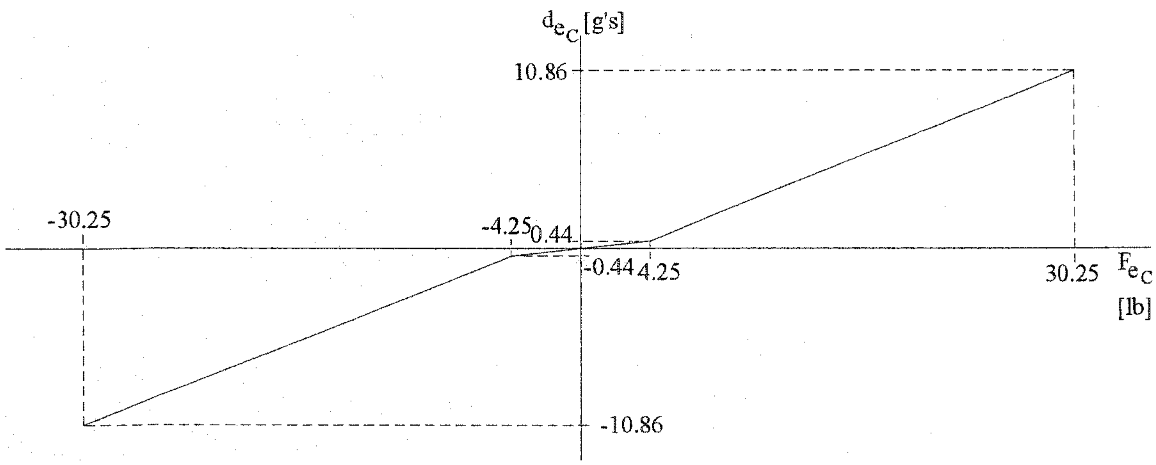

Figure 5.3 Pitch Command Gradient

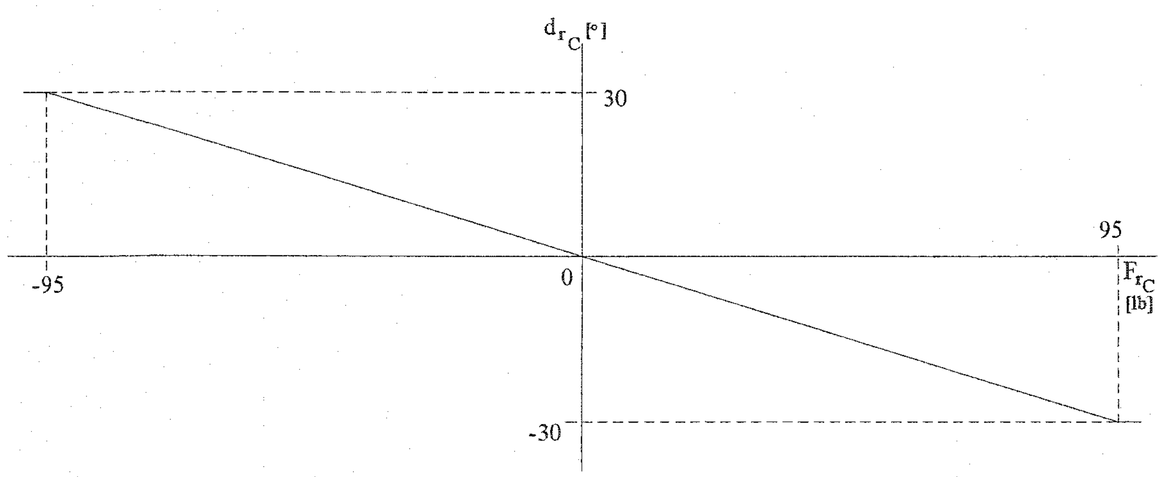

Figure 5.4 Yaw Command Gradient

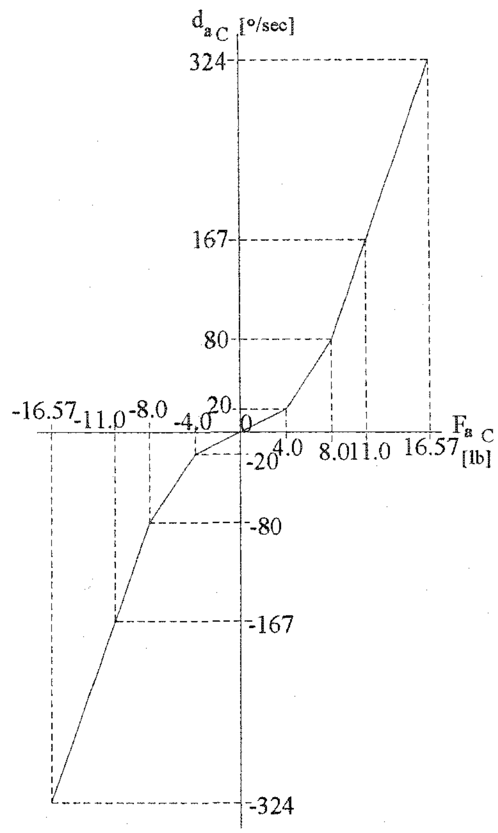

Figure 5.5 Roll Command Gradient

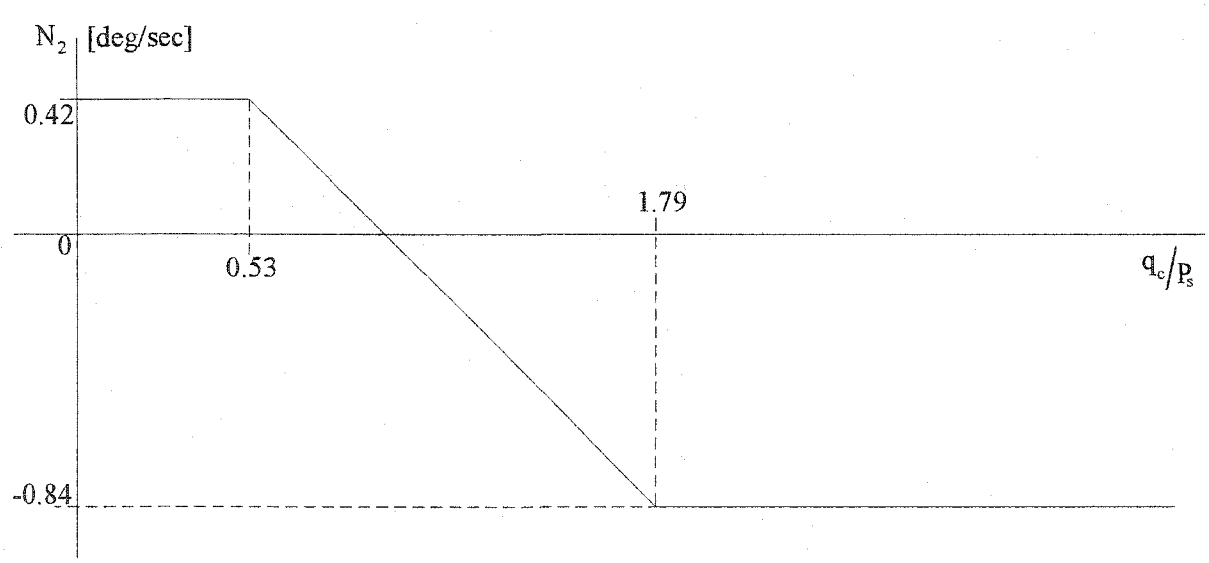

Figure 5.6 FCS Gain Functions for Longitudinal Control (N_2)

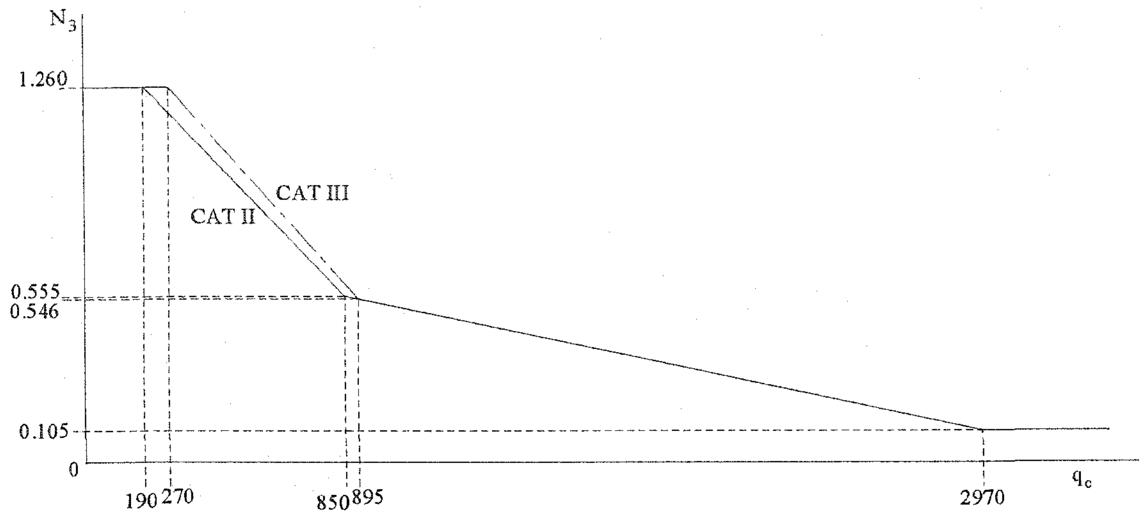

Figure 5.7 FCS Gain Functions for Longitudinal Control (N_3)

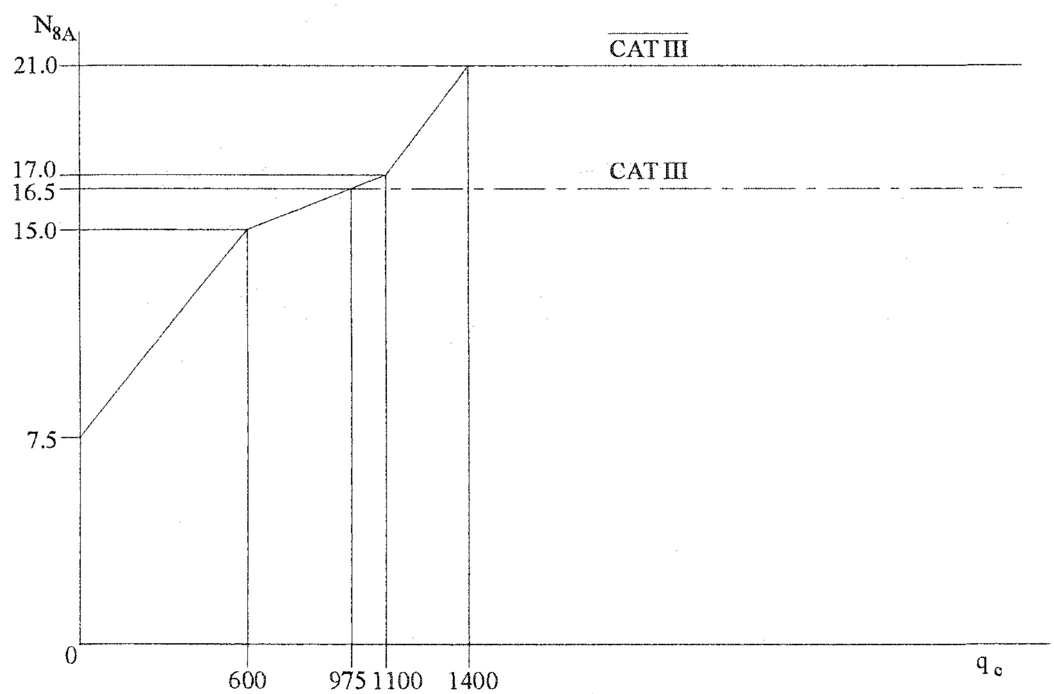

Figure 5.8 FCS Gain Functions for Longitudinal Control (N_{8A})

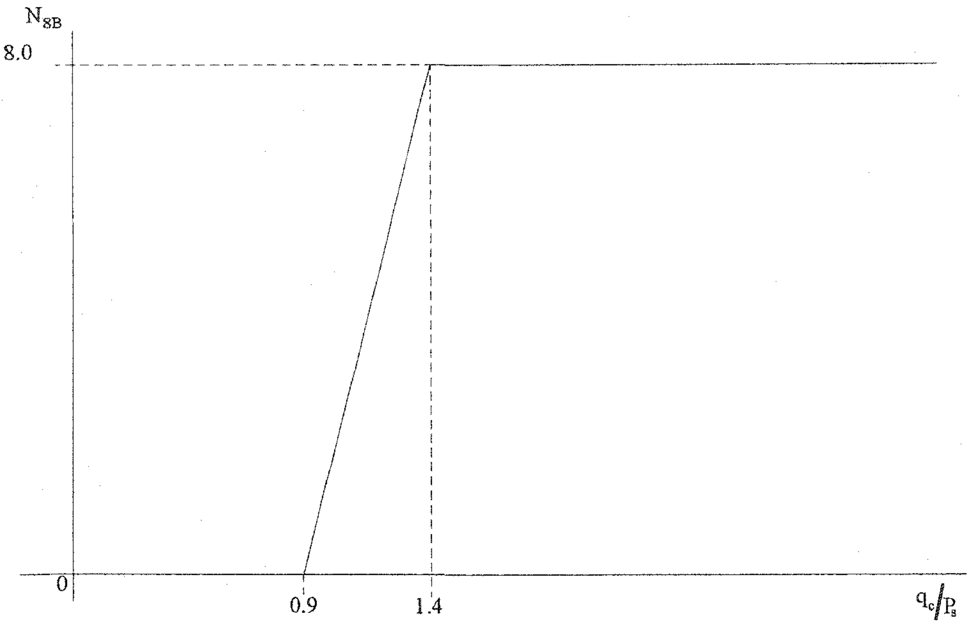

Figure 5.9 FCS Gain Functions for Longitudinal Control (N_{8B})

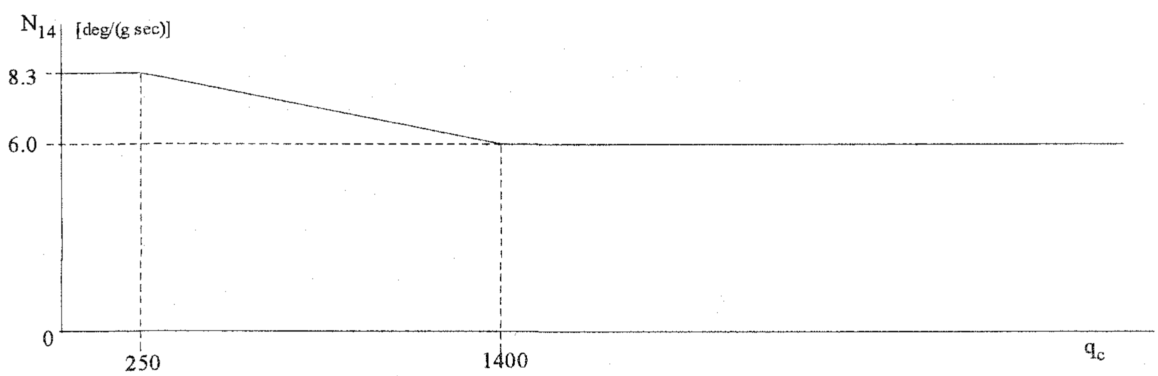

Figure 5.10 FCS Gain Functions for Longitudinal Control (N_{14})

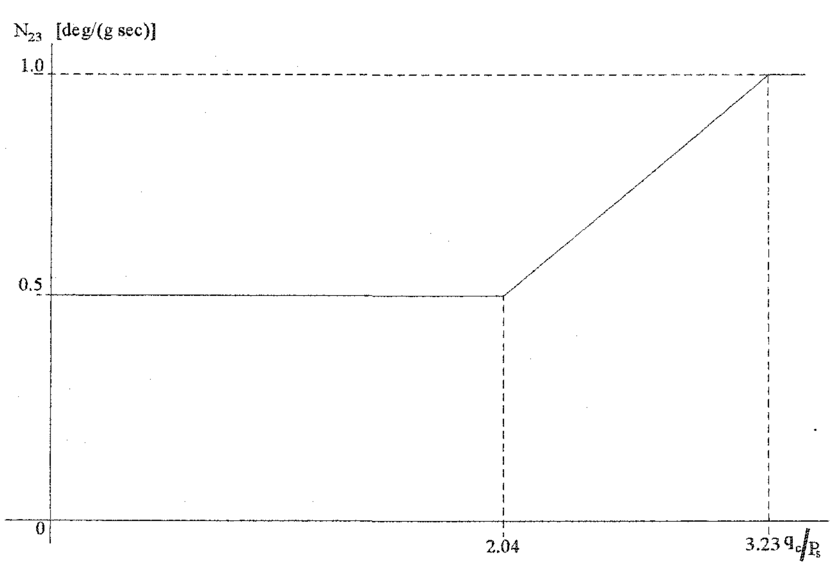

Figure 5.11 FCS Gain Functions for Lateral Control (N_{23})

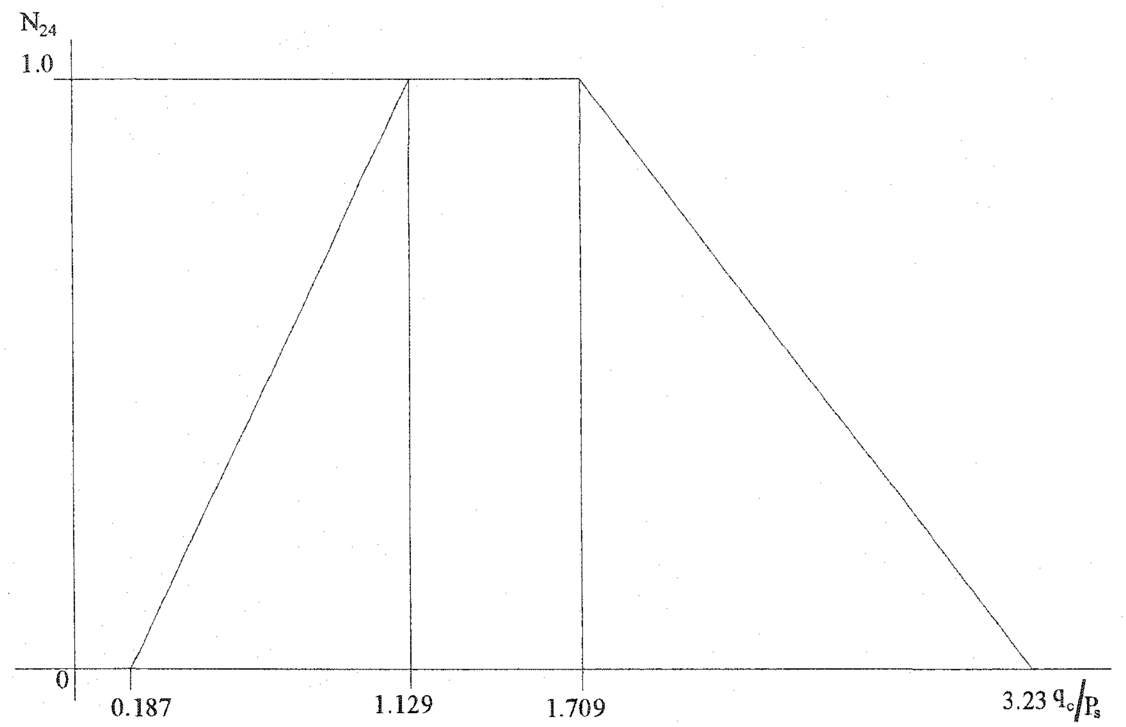

Figure 5.12 FCS Gain Functions for Lateral Control (N_{24})

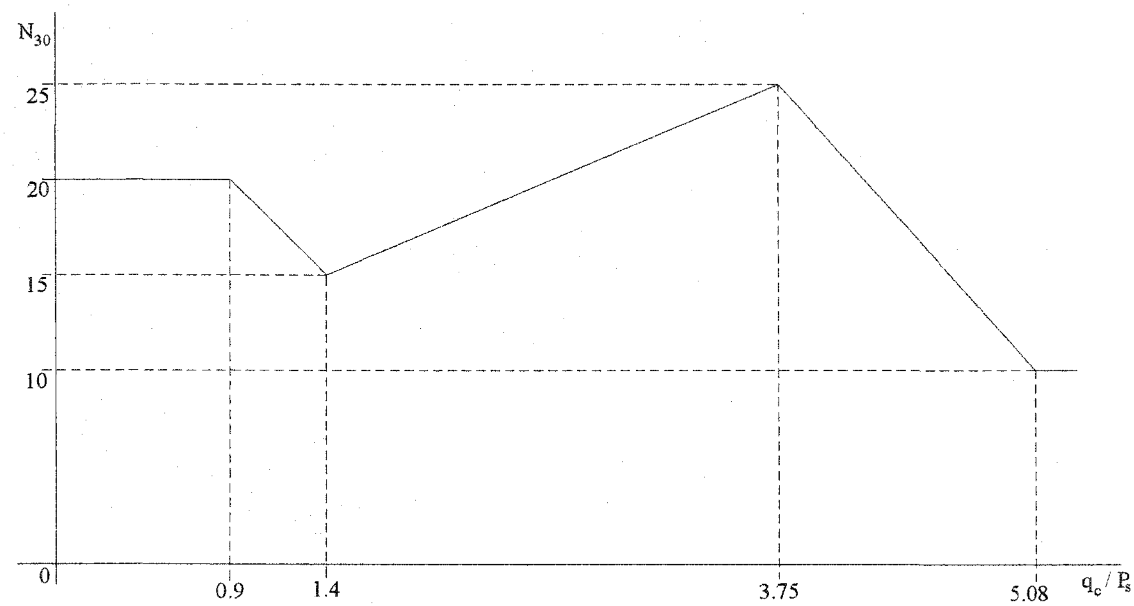

Figure 5.13 FCS Gain Functions for Lateral Control (N_{30})

Now, the transfer functions for linear part of FCS are developed. These transfer functions will be converted to the linear state space form. Through numerical integration of the state space equations using Runge-Kutta method,[2] the time domain response is calculated. Inputs from pilot and nonlinear functions are considered separately in time domain, and fed into the state space form as inputs. The longitudinal directional FCS includes pitch loop (Q), angle of attack loop (α), and vertical acceleration loop (N_z). For the longitudinal FCS, input is pilot pitch command force, and output is horizontal stabilizer deflection angle δ_e. Pitch trim is set to zero. Because of the non-linearity of the pitch command gradient function, the functionality between F_{ec} and δ_e cannot be expressed as a transfer function. Therefore, the output of pitch command gradient is regarded as a nonlinear function of F_{ec}, and expressed as δ_{ef} in following equations. The functionality of δ_{ef} is computed separately. The transfer functions for each output are derived from the block diagram of the FCS in Figures 5.1 and 5.2. The longitudinal transfer functions are listed from Equations (5.1) to (5.6).

$$\frac{\delta_e}{Q_{Trim}} = \frac{N_3 s + 5N_3}{s^2 + 20s} \tag{5.1}$$

$$\frac{\delta_e}{\delta_{ef}} = -\frac{20N_3N_{14}s + 100N_3N_{14}}{s^3 + (20 + N_{14})s^2 + 20N_{14}s} \tag{5.2}$$

$$\frac{\delta_e}{N_z} = \frac{60N_3s^2 + 20N_3(15 + N_8)s + 100N_3N_8}{s^3 + (20 + N_8)s^2 + 20N_8 s} \tag{5.3}$$

$$\frac{\delta_e}{Q} = \frac{0.334 \times 20N_3\left(3s^2 + (15 + N_8)s + 5N_8\right)}{s^3 + (21 + N_8)s^2 + (20 + 21N_8)s + 20N_8} \tag{5.4}$$

$$\frac{\delta_e}{\alpha} = \frac{20N_2N_5}{s^2 + (20 + N_5)s + 20N_5} \tag{5.5}$$

$$\frac{\alpha'}{\alpha} = \frac{N_5}{s + N_5} \tag{5.6}$$

where α' is a modified angle of attack.

The lateral directional FCS includes roll loop (P), yaw loop (R), modified angle of attack loop (α'), and lateral directional acceleration loop (A_y). Inputs are pilot roll and yaw command force, and outputs are differential flaperon deflection angle δ_{Fa} (= δ_a), differential horizontal tail deflection angle δ_{Ha} (= δ_h), and rudder deflection angle δ_r. Roll and Yaw trims are set to be zero. Again, the non-linearity of the FCS is expressed as functions of its input values, and calculated separately before computing overall transfer functions. Lateral directional transfer functions are listed below.

$$\frac{\delta_{Fa}}{P_{Trim}} = \frac{0.12 \times 20}{s + 20} \tag{5.6}$$

$$\frac{\delta_{Fa}}{P} = \frac{0.12 \times 20}{s + 20} \tag{5.7}$$

$$\frac{\delta_{Fa}}{\delta_{ac}} = \frac{0.12 \times 20N_{25}}{s^2 + (20 + N_{25})s + 20N_{25}} \tag{5.8}$$

where, F_{ag} is a command signal after roll command gradient.

$$\frac{\delta_{Ha}}{P_{Trim}} = \frac{0.294 \times 0.12 \times 20}{s + 20} \tag{5.9}$$

$$\frac{\delta_{Ha}}{P} = \frac{0.294 \times 0.12 \times 20}{s + 20} \tag{5.10}$$

$$\frac{\delta_{Ha}}{\delta_{ac}} = \frac{0.294 \times 0.12 \times 20N_{25}}{s^2 + (20 + N_{25})s + 20N_{25}} \tag{5.11}$$

$$\frac{\delta_r}{\delta_{rc}(4.0F(P) + \alpha')} = \frac{20 \times 15}{s^2 + (20 + 15)s + 20 \times 15} \tag{5.12}$$

where, δ_{rc} is a command signal after yaw command gradient, and *F(P)* represents the function after saturation of $|P|$ signal in Figure 5.2.

$$\frac{\delta_r}{R_{Trim}} = \frac{20}{s+20} \tag{5.13}$$

$$\frac{\delta_r}{(P+P_{Trim})(0.06\alpha' + G(\alpha'))} = \frac{0.12 \times 20}{s+20} \tag{5.14}$$

where, $G(\alpha')$ represents the multiplication of N_{24} and the nonlinear function response of α' as indicated in Figure 5.2.

$$\frac{\delta_r}{\delta_{ac}(0.06\alpha' + G(\alpha'))} = -\frac{0.12 \times 20 \times N_{25}}{s^2 + (20 + N_{25})s + 20N_{25}} \tag{5.15}$$

$$\frac{\delta_r}{\left(R - \frac{1}{57.3}P\alpha'\right)} = \frac{60N_{30}s^2 + 30N_{25}N_{30}s}{s^3 + (21 + N_{30})s^2 + (20 + 21N_{30})s + 20N_{30}} \tag{5.16}$$

$$\frac{\delta_r}{A_y} = \frac{19.32 \times 20N_{23}}{s+20} \tag{5.17}$$

The simplified FCS provides good performance without significant model degradation for the flight conditions simulated around flight envelope. Since the FCS is not a stand-alone system, the evaluation of the FCS will be conducted combination with autopilot system.

5.2 Autopilot System Description

The nonlinear model and corresponding FCS of the F-16 aircraft are developed in Chapter 4 and Section 5.1. A nonlinear autopilot system is designed in this chapter. Development of LEC logic requires the interconnection between vehicle motion and corresponding stress output. In order to generate a set of realistic simulation that represent the motion of the real fighter aircraft in service, a mission is developed in next chapter. The autopilot system described in this chapter acquires three commands in each time step, and the system generates horizontal stabilizer, aileron and throttle command signals that replace pilot commands. The autopilot system receives these three commands from the mission generating logic which provides altitude, velocity, and heading angles. In each time step, these three commands are calculated from the flight path while the flight path is generated based on the required vehicle motion of each section of the mission. While generating the flight path, the flight path is filtered to eliminate sharp motions that are not feasible as vehicle motion. For the results presented, the acceleration limit on climb and descent is ± 40 *ft/sec*^{2}. Heading angle acceleration is limited within ± 0.004 *rad/sec*^{2} and the heading angle rate is limited within ± 0.027 *rad/sec*. The velocity change is limited automatically by engine dynamics. Detailed description of the mission command is the topic of the next chapter.

The autopilot system consists of velocity (U) hold, altitude (h) hold, and heading hold (ψ hold). The gains of autopilot system are listed in Table 5.1, and the overall aircraft system including aircraft model, FCS, autopilot system, and connections among these systems is illustrated in Figures 5.14 (a)-(c). The vehicle simulation demonstrates various types of maneuvers. In each demonstration, the simulation starts from the same equilibrium condition. The starting conditions are prescribed in Equations (5.18) – (5.21).

$$h = 3{,}000\,ft \tag{5.18}$$

$$[U,\ V,\ W] = [471.4427 \quad 0 \quad 22.8082] \quad (ft/s), \tag{5.19}$$

thrust parameters are

$$[\theta_{th},\ P_2,\ P_3] = [15.1546 \quad 9.8332 \quad 9.8332] \quad (\%), \tag{5.20}$$

and pitch angle at the equilibrium condition is

$$\theta = 2.7698\,^{\circ} \tag{5.21}$$

Note these starting conditions are used throughout this chapter unless otherwise indicated. Altitude and velocity components are

Table 5.1 Gains for Autopilot System

Gains	Gain Values
K_{Q1}	250 [*1/sec*]
K_{Q2}	0.1 [*deg/deg*]
K_{Q3}	20 [*1/sec*]
K_{p}	30 [*%sec/ft*]
K_{i}	3 [*%/ft*]
K_{p_sb}	10 [*ft/deg sec*]
K_{i_th}	3,000 [*lb/deg*]
K_{p_h}	0.0001 [*deg/ft*]
K_{i_h}	0.001 [*deg/ft sec*]
K_{p_h2}	1
K_{i_h2}	0.01 [*1/sec*]
K_{i_phi}	200 [*lb/deg*]
K_{p_psi}	10 [*deg/deg*]

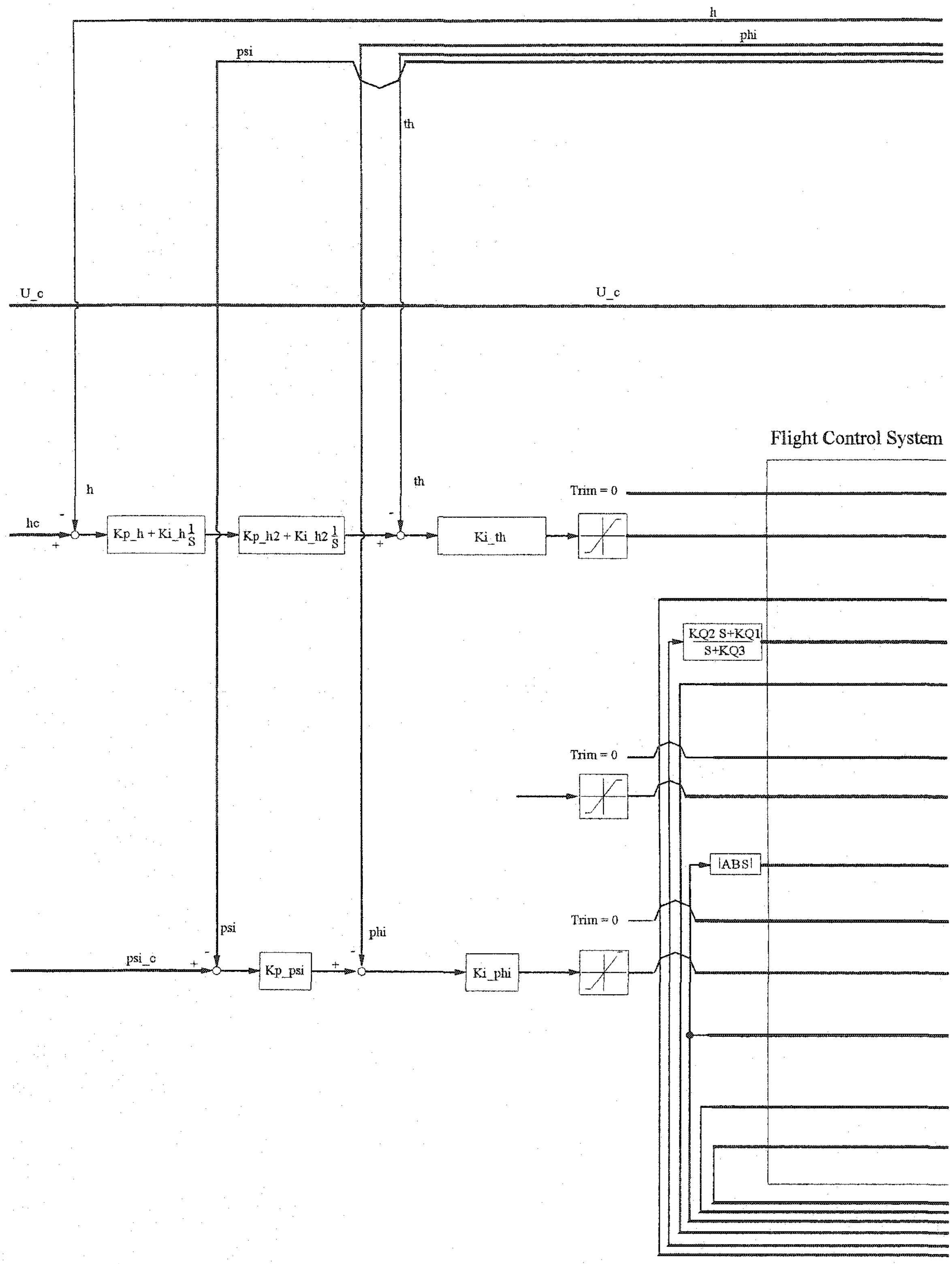

Figure 5.14.a Overall Aircraft System with Autopilot and FCS

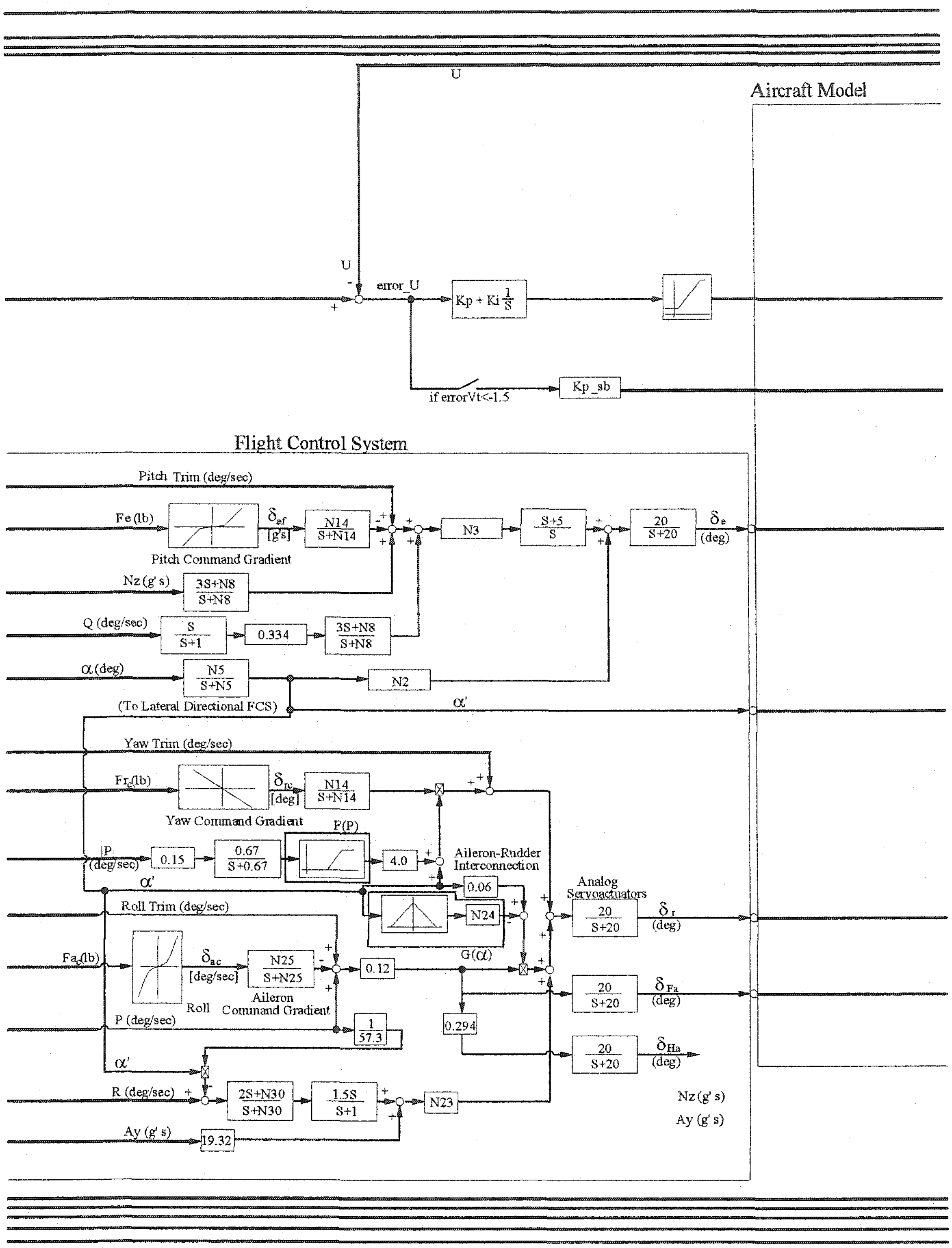

Figure 5.14.b Overall Aircraft System with Autopilot and FCS (Continued)

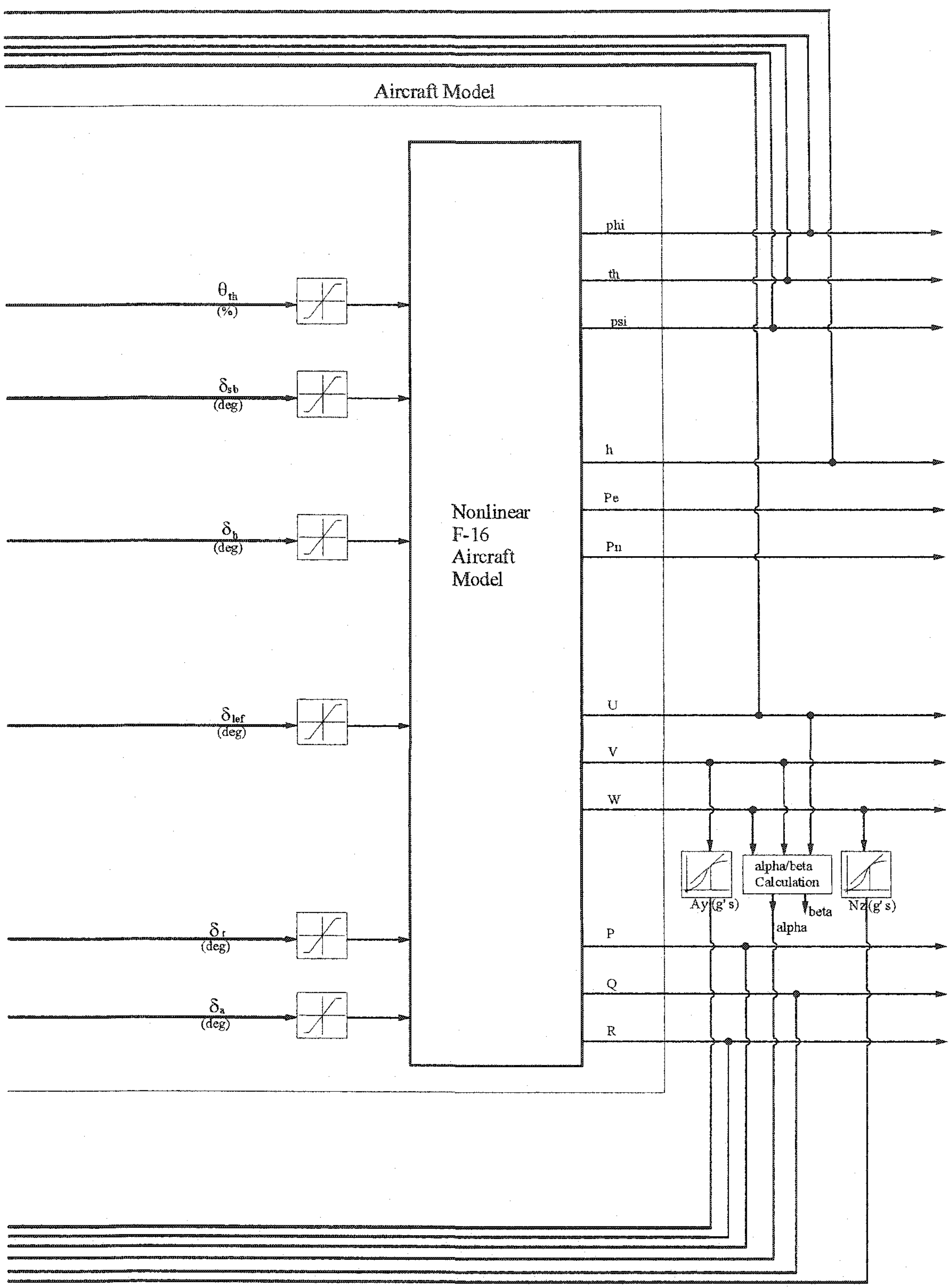

Figure 5.14.c Overall Aircraft System with Autopilot and FCS (Continued)

The overall aircraft system illustrated in Figure 5.14 consists of the base aircraft model which is illustrated as a long rectangular box in Figure 5.14 (c), FCS which is illustrated as another box with dotted outline in Figure 5.14 (b), autopilot system mainly shown outside of these two boxes, and surrounding interconnections. The vehicle model receives six inputs that are throttle position θ_{th}, speed break deflection δ_{sb}, horizontal stabilizer deflection angle δ_h, leading edge flap deflection δ_{lef}, rudder deflection δ_r, and aileron deflection angle δ_a as discussed in Chapter 4. The saturation and rate saturation of six inputs for vehicle model are included in the nonlinear model developed in Chapter 4. The outputs of the vehicle model are twelve states. These are velocities and angular velocities in x_b, y_b, z_b axis which are U, V, W, P, Q, and R, roll angle ϕ, pitch angle θ, yaw angle ψ, position in north p_N, position in east p_E, and altitude h. From these outputs, the angle of attack α and side slip angle β are calculated. Also, vertical acceleration N_z and lateral directional acceleration A_y are calculated through numerical integration of vertical velocity W and lateral directional velocity V.

Among six inputs required for the vehicle model, two inputs - throttle position θ_{th}, speed break deflection δ_{sb} - are directly fed from the autopilot system, and the other four inputs are computed from the FCS. A detailed description of the FCS is found in Section 5.1. The feedback states for the autopilot system are forward velocity U, altitude h, pitch angle θ, yaw angle ψ, and roll angle ϕ. Note that lead-lag control logic is added to the Q loop for adjusting longitudinal stability. A detailed description of each part of autopilot system follows.

5.3 Mach Hold

The Mach hold loop is designed to maintain the desired velocity using engine throttle and speed break. Through employing proportional-integral (*PI*) control logic in *U* feedback loop, the vehicle is controlled to maintain the velocity command U_c. Although total velocity of body frame has components *U*, *V*, and *W*, the Mach hold loop controls only *U* because vertical velocity *W* and side velocity *V* may vary due to flight condition such as climb or turning. In addition to the throttle loop, the speed break is employed to improve deceleration response of the aircraft system. The speed break is engaged when the velocity error (U-U_d) is less than −1.5 *ft/sec* where U_d represents the desired *U*. By employing the speed break, deceleration performance is significantly improved. As an example of Mach hold, the time response of Mach holder for 5% of *U*

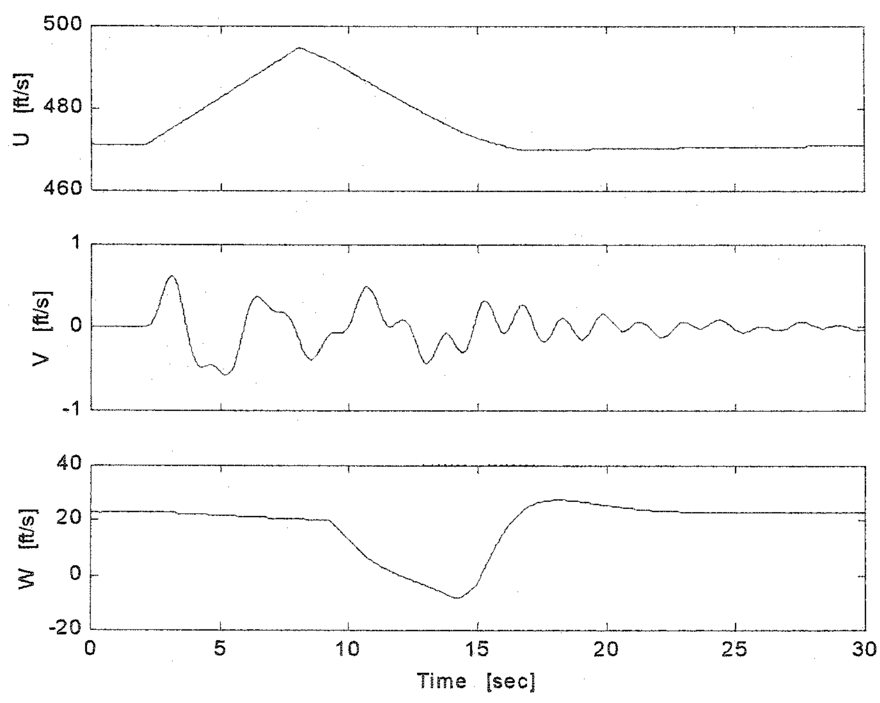

Figure 5.15 *U*, *V*, and *W* Response

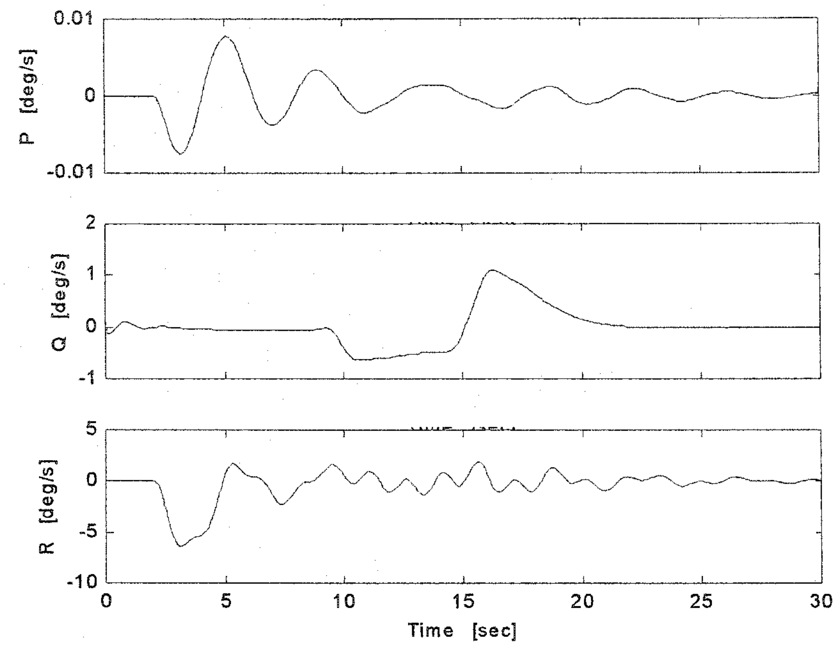

Figure 5.16 P, Q, and R Response

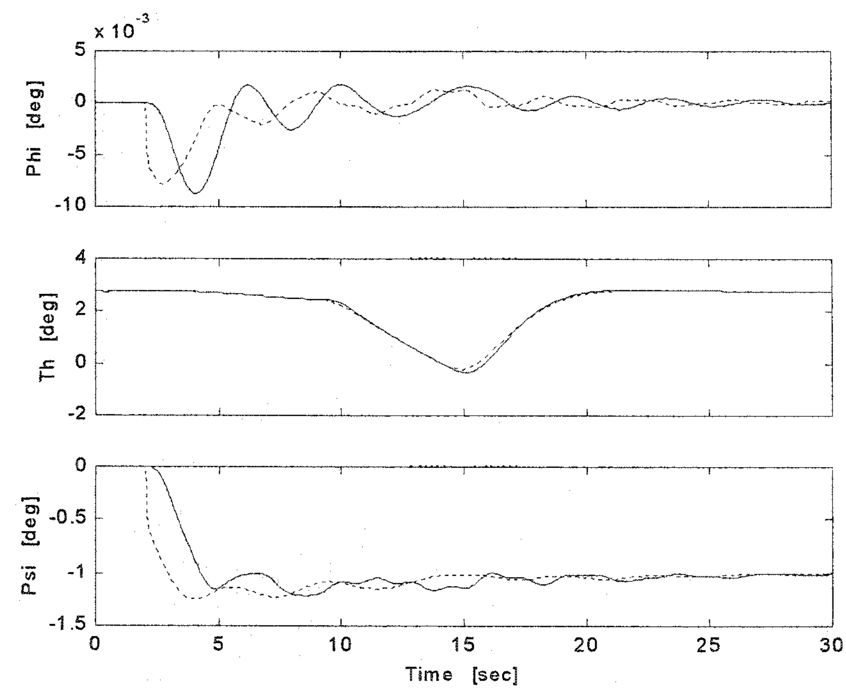

Figure 5.17 ϕ, θ, and φ Response

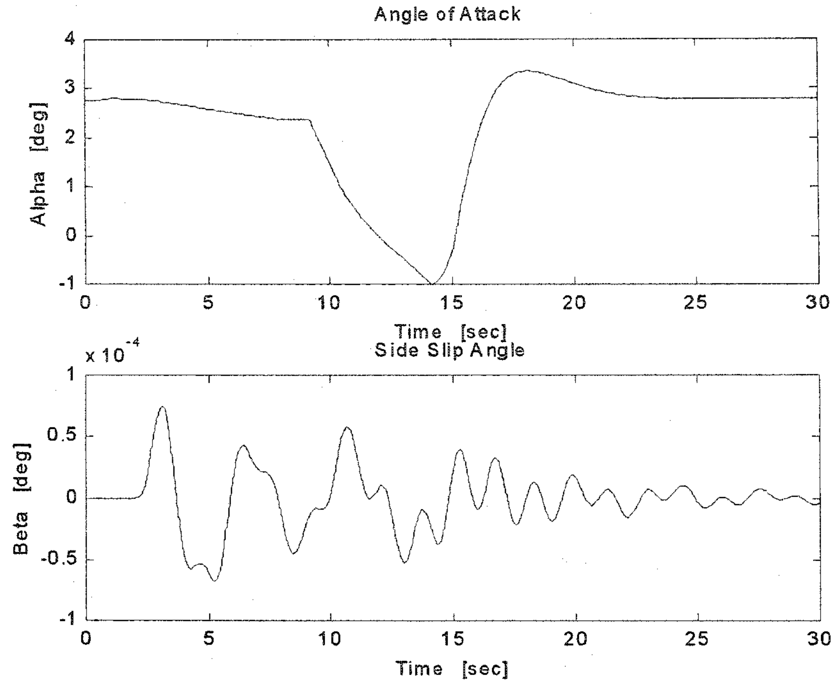

Figure 5.18 α and β Response

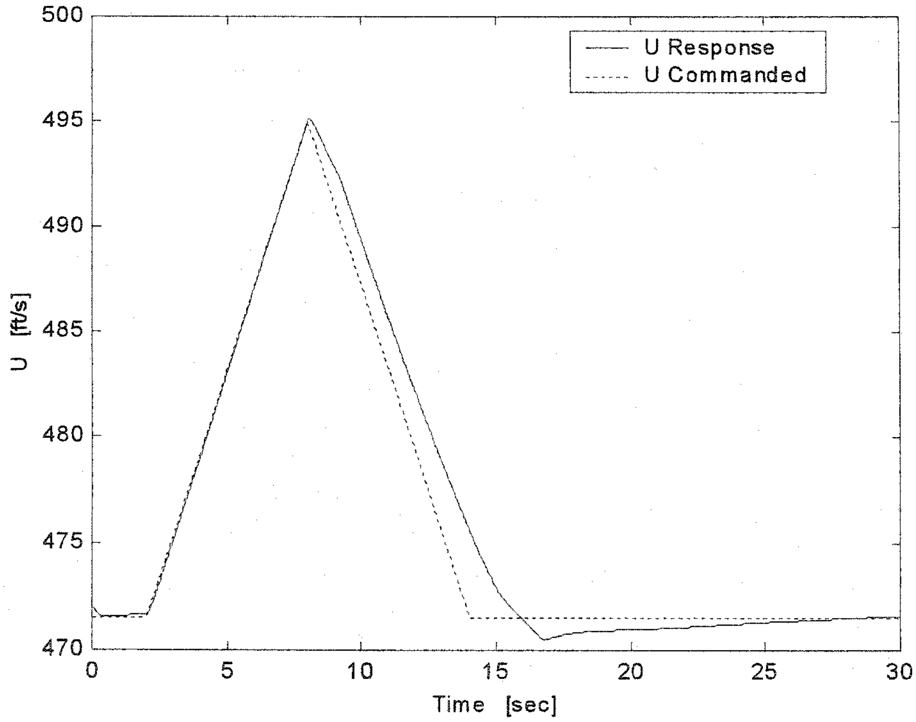

Figure 5.19 U Command and Vehicle Response

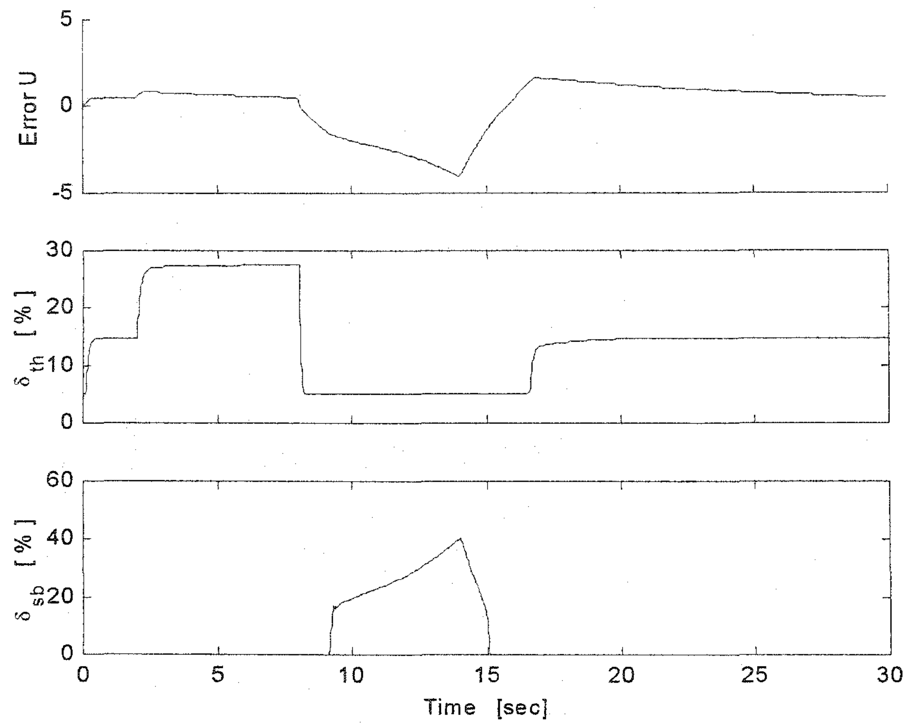

Figure 5.20 Throttle θ_{th} and Speed Break δsb Response

change is shown in Figures 5.15-5.20. The dotted line in Figure 5.19 corresponds to the desired velocity, U_d and the solid line corresponds to U response. The thrust has been increased to about 27% at the acceleration phase, but decreased to 5% at the deceleration phase. Note the thrust is limited between 5% and 100%. The lower limit of the thrust is employed to prevent the engine shut down during deceleration. Note that the speed break is driving deceleration (from 8 to 15 *sec*) showing a small offset in the velocity response value. This is because the speed break activates only when velocity error is less than −1.5 *ft/sec*. The lateral directional motion is due to the small change of heading angle (0.01°) that is generated from flight path calculation logic. The lateral directional response of this amount is negligible, and the corresponding autopilot will be discussed shortly. The change of W in Figure 5.15 indicates small change of altitude, but the altitude comes back to the original as the altitude hold which will be introduced in the next section activates its control logic after small delay. The error behavior in Figure 5.20 indicates that the velocity hold accurately follows the command, but the vehicle can have large velocity error due to time lag in deceleration.

5.4 Altitude Hold and Pitch Hold

The primary function of altitude hold is to maintain the desired altitude through generating a necessary horizontal stabilizer command signal for the FCS. The inherent instability due to the relaxed longitudinal stability of F-16 made the design process highly time consuming. Note that the vehicle is longitudinally unstable without the FCS. Before the discussion of the altitude feedback loop, an inner loop of the altitude hold loop, pitch hold feedback loop is designed. Also, a lead-lag compensator is added to Q loop to regain longitudinal stability after removing the engine spin moment from the aircraft model. The engine spin moment is eliminated to remove lateral-longitudinal directional coupling in straight level flight condition as well as design convenience of autopilot. The pitch hold operates through a proportional controller providing the F_e command signal. Note a rate saturator is added to limit the rate of the pitch command force to be within ± 0.1571 *lb/sec*. Also, the pitch command force is limited within ± 31 *lb* by an additional limiter. Altitude hold is designed to have two *PI* controllers in the altitude hold loop because a single *PI* controller did not provide enough longitudinal stability.

The result of a 300 *ft* altitude increase is shown in Figures 5.21-5.26 as an example. The time to reach the desired altitude is automatically calculated based on the acceleration limit and climb rate limit mentioned in the beginning of this chapter, and the corresponding command trajectory is generated by the flight path calculation logic which will be described in Chapter 6. The dotted line in Figure 5.26 corresponds to the command trajectory and the solid line corresponds to the vehicle response. Note, the simulation starts from the equilibrium condition mentioned in the beginning of this chapter. The altitude change command is given 2 *sec* after the simulation starts, and the response settles at 9.1 *sec* with small overshoot. The delay of the response at the settling time is about 2.5 *sec*, but the steady state error is reasonably small (about 1.7%). The solid line in Figure 5.23 corresponds to the pitch response of the vehicle, and dotted line corresponds to the pitch command generated at the altitude hold controller. Again, the lateral directional motion is generated from the flight path calculation logic due to the minor change of heading angle.

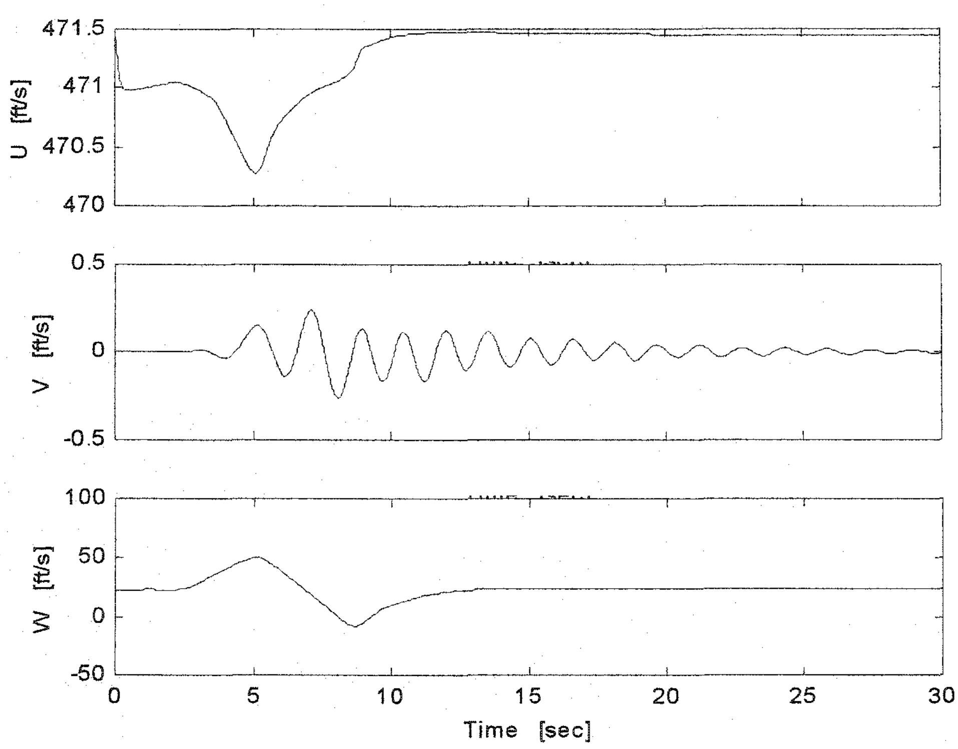

Figure 5.21 *U*, *V*, and *W* Response

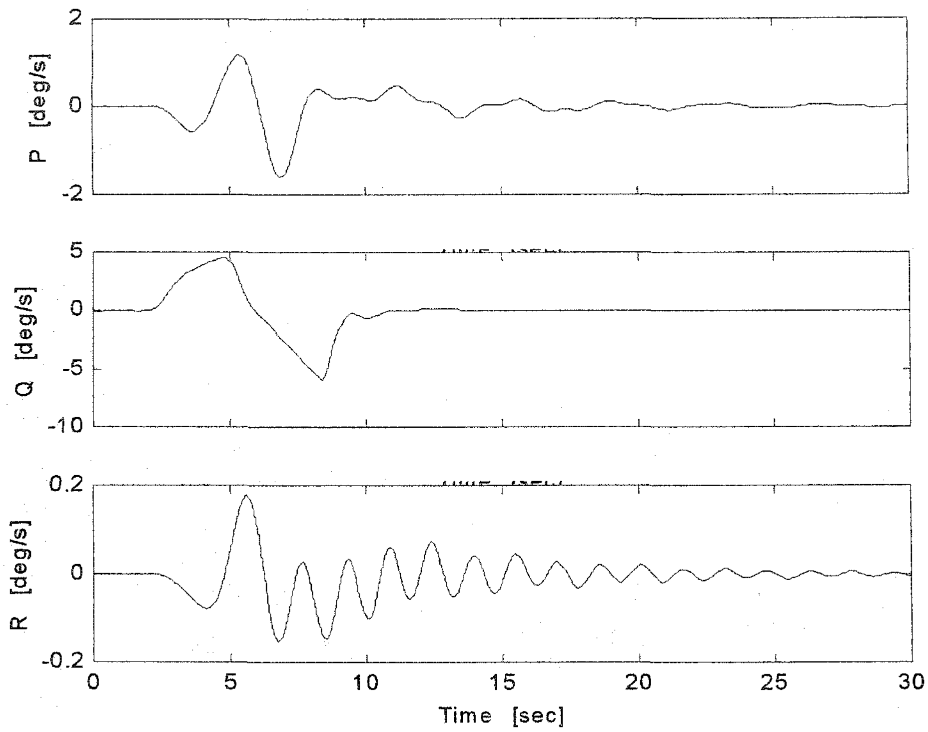

Figure 5.22 P, Q, and R Response

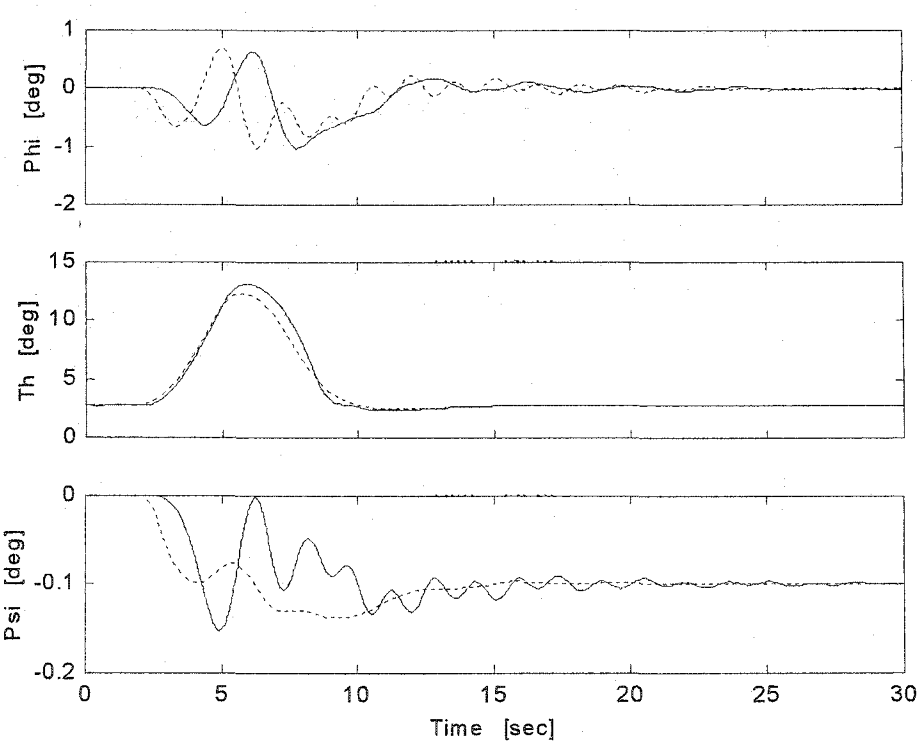

Figure 5.23 ϕ, θ, and φ Response

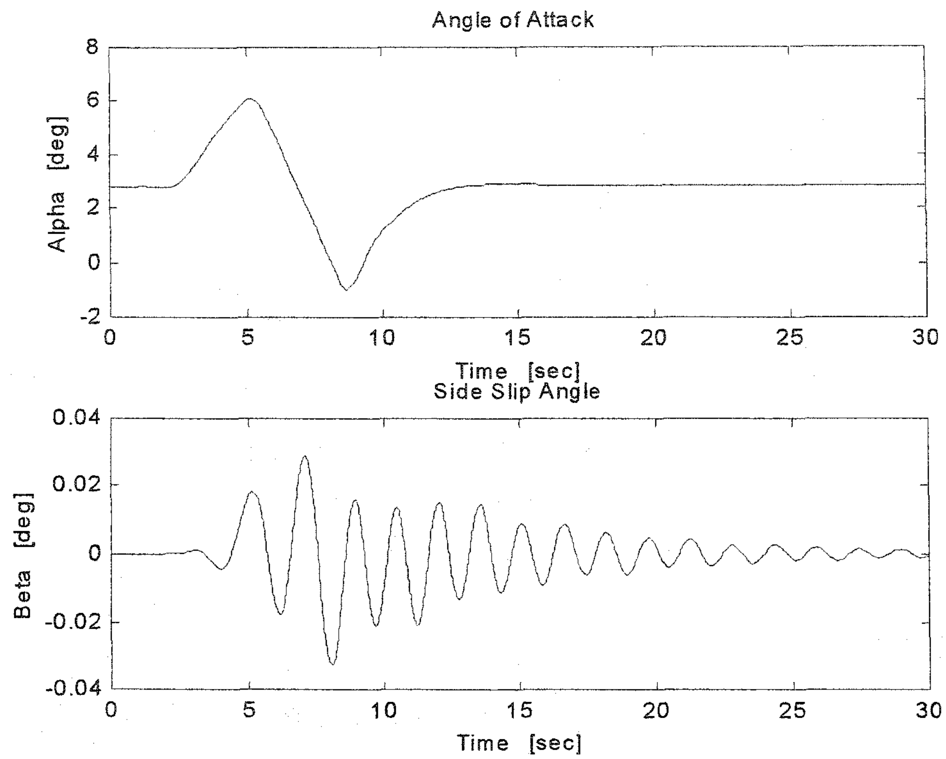

Figure 5.24 α and β Response

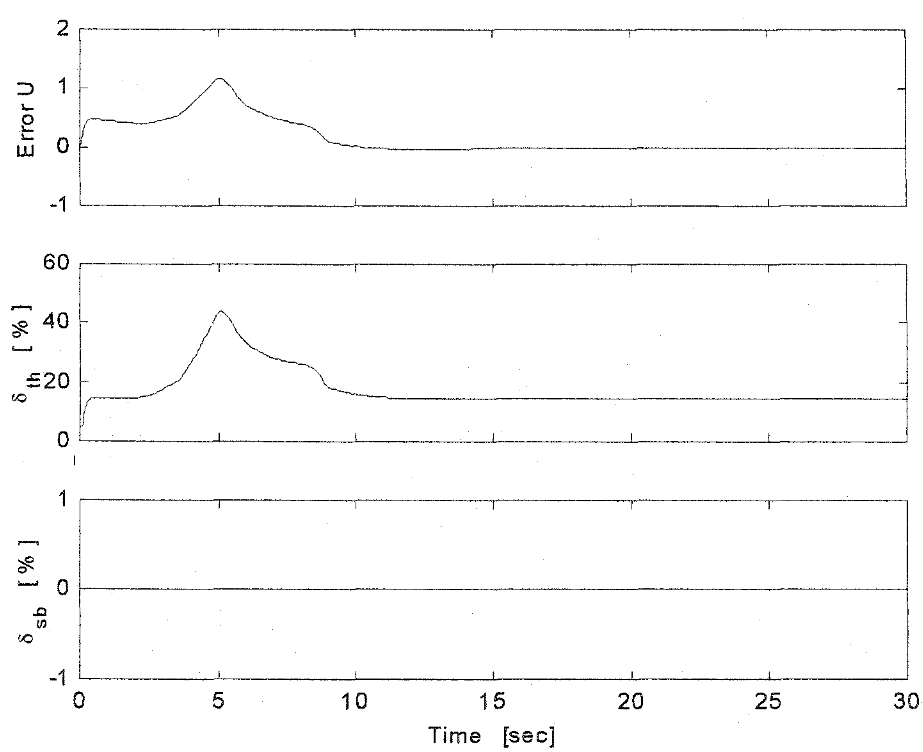

Figure 5.25 θ_{th} and δsb Response

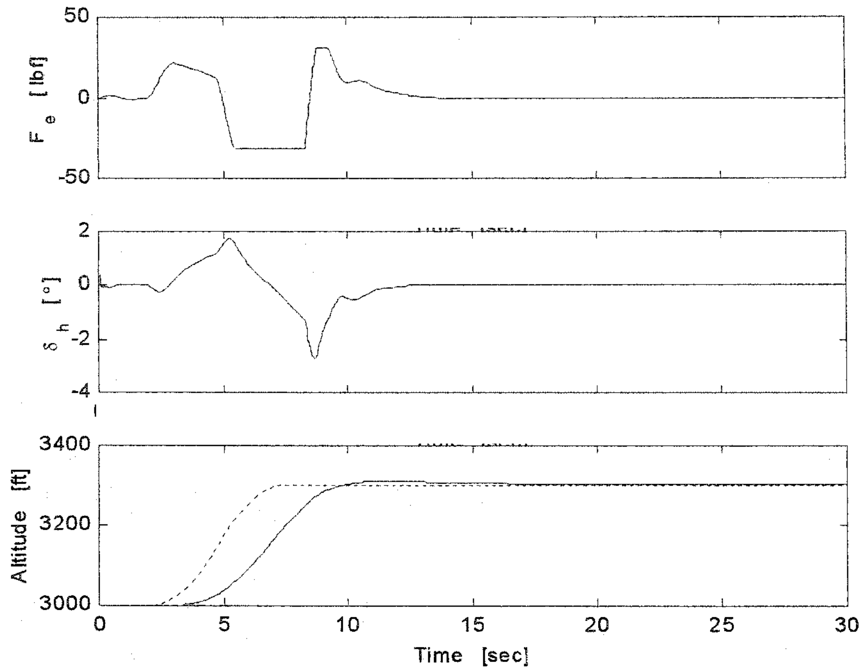

Figure 5.26 Altitude h, F_e, δ_e and Response

5.5 Heading Angle Hold

In the lateral directional autopilot, heading angle hold consists two loops that are nose hold and bank angle hold. First, bank angle hold is closed providing roll command force for the FCS through a proportional controller. Similar to the pitch loop case, the roll command force is limited within ± 16.57 *lb*. Second, a yaw loop is closed through a proportional controller providing the required roll angle for bank angle hold. The nose heading angle ψ is computed clockwise assuming north is 0 °.

As an example, time responses for a 90 ° turn is shown in Figures 5.27-5.35. The simulation starts from a equilibrium condition which are 7,000 *ft* altitude and 400 *knot* speed. From the equilibrium condition, heading angle change command is given from 15 *sec*, and the vehicle turns 90 ° clockwise. The time delay for the ψ loop is about 2.3 *sec*. Unlike the linear simulation, in this case the settling time and time delay vary due to flight conditions. Roll and yaw response in Figure 5.29 are illustrated in solid lines, and angle commands generated from corresponding outer loops are also shown in dotted lines. Note, the delay in inner loop is relatively small compared to the corresponding outer loop.

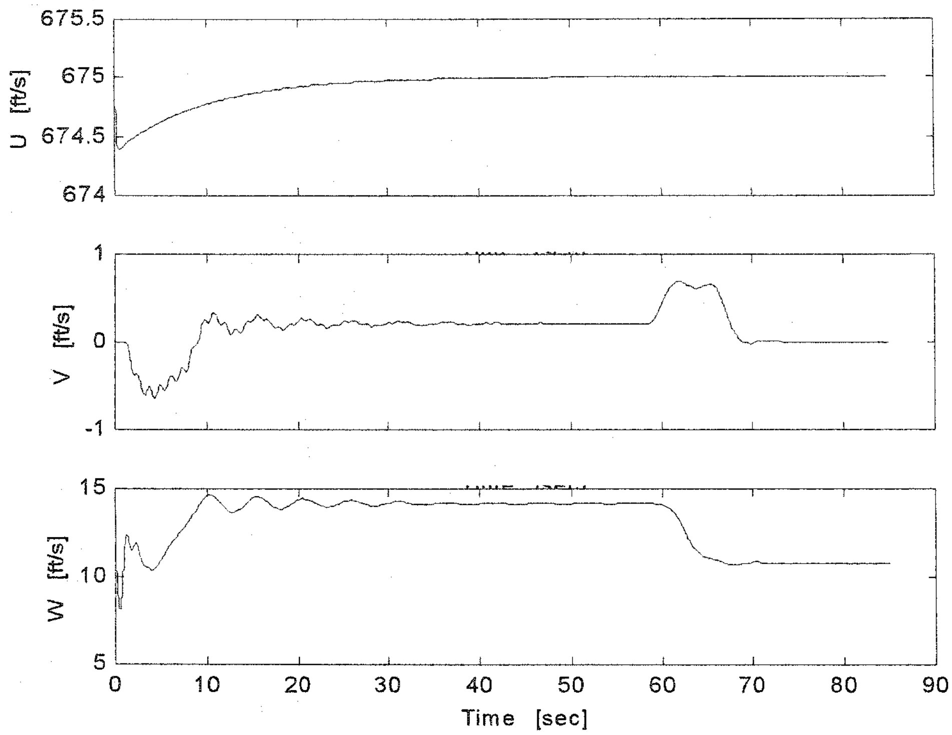

Figure 5.27 *U, V,* and *W* Response

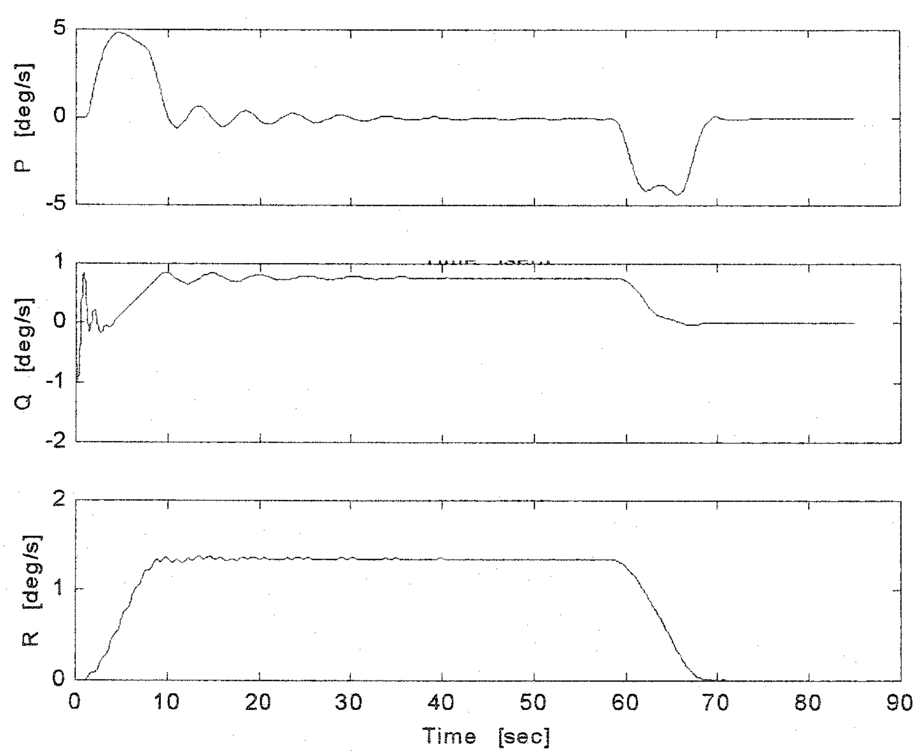

Figure 5.28 *P, Q,* and *R* Response

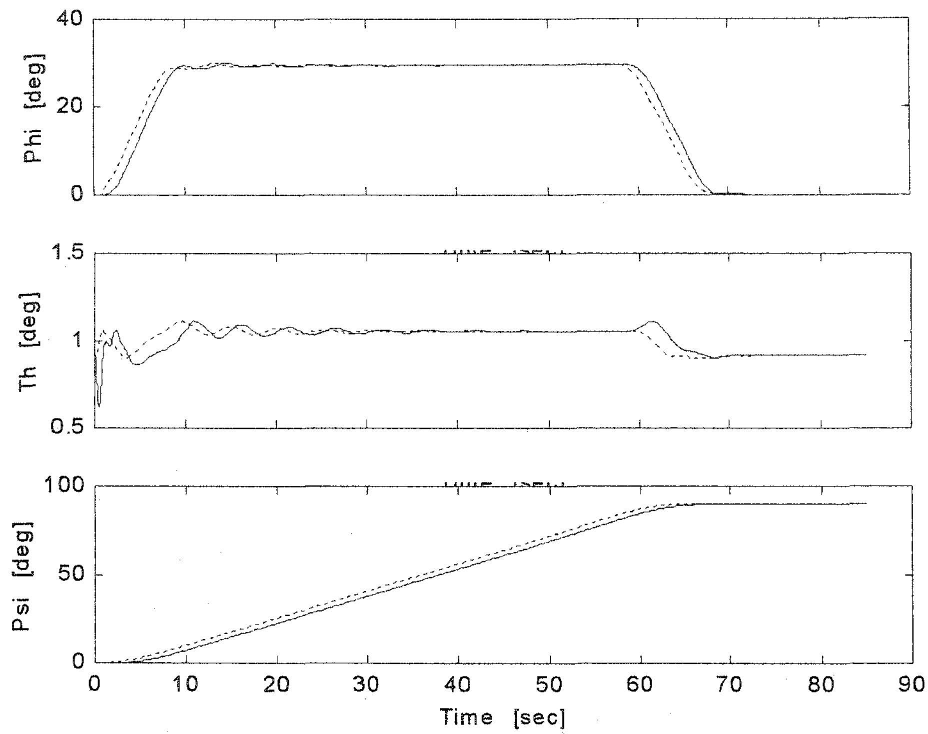

Figure 5.29 ϕ, θ, and φ Response

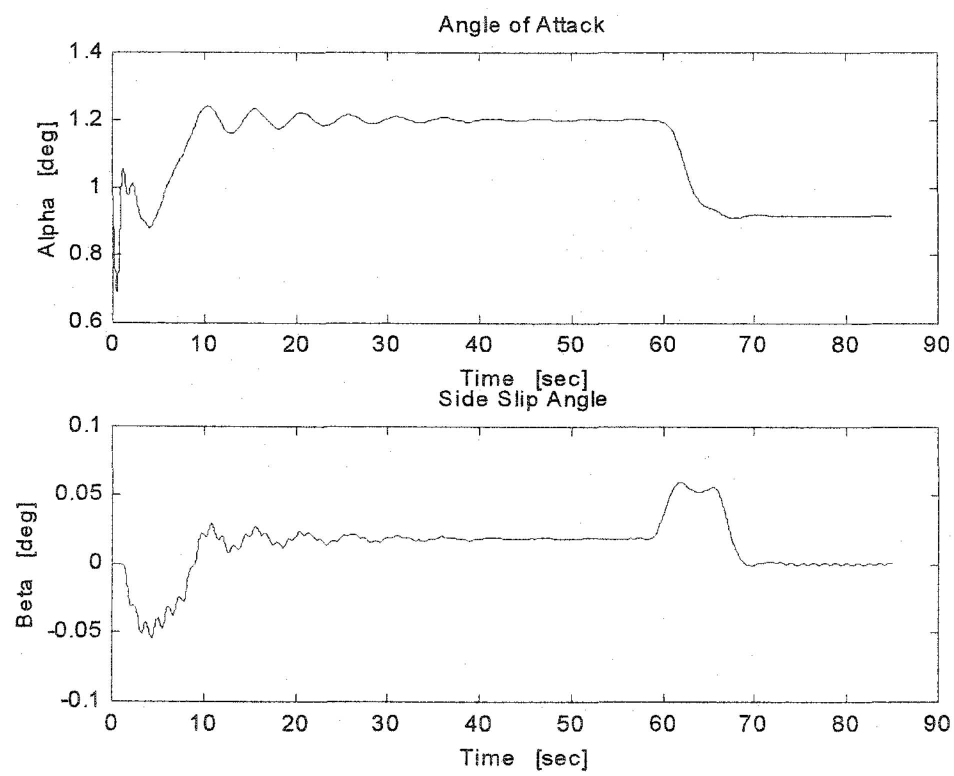

Figure 5.30 α and β Response

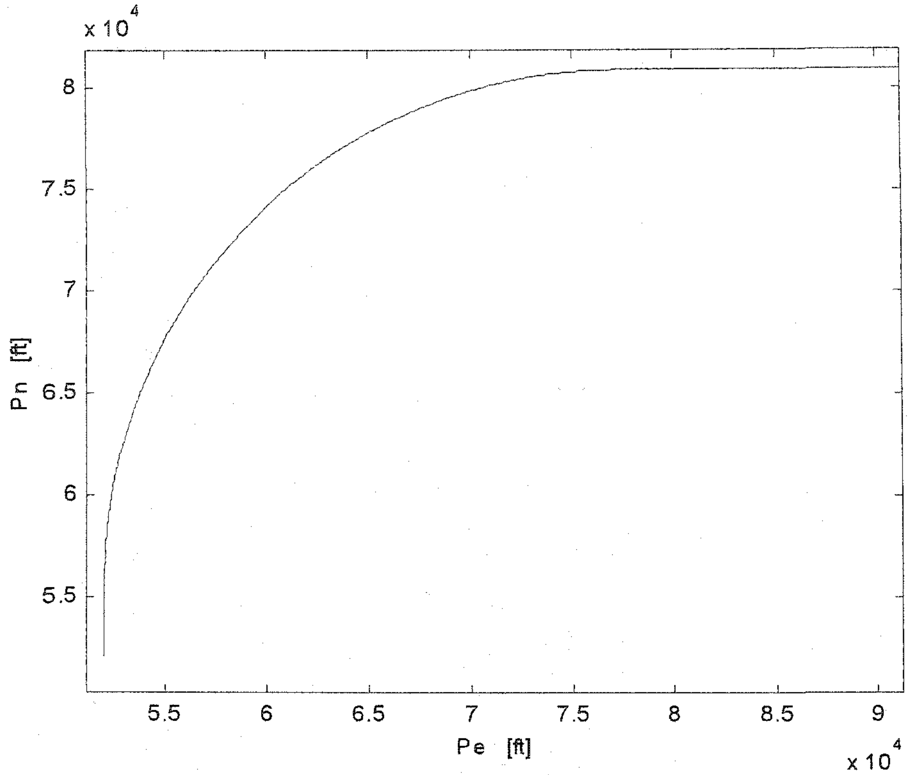

Figure 5.31 Plan movement of the Aircraft (P_e and P_n)

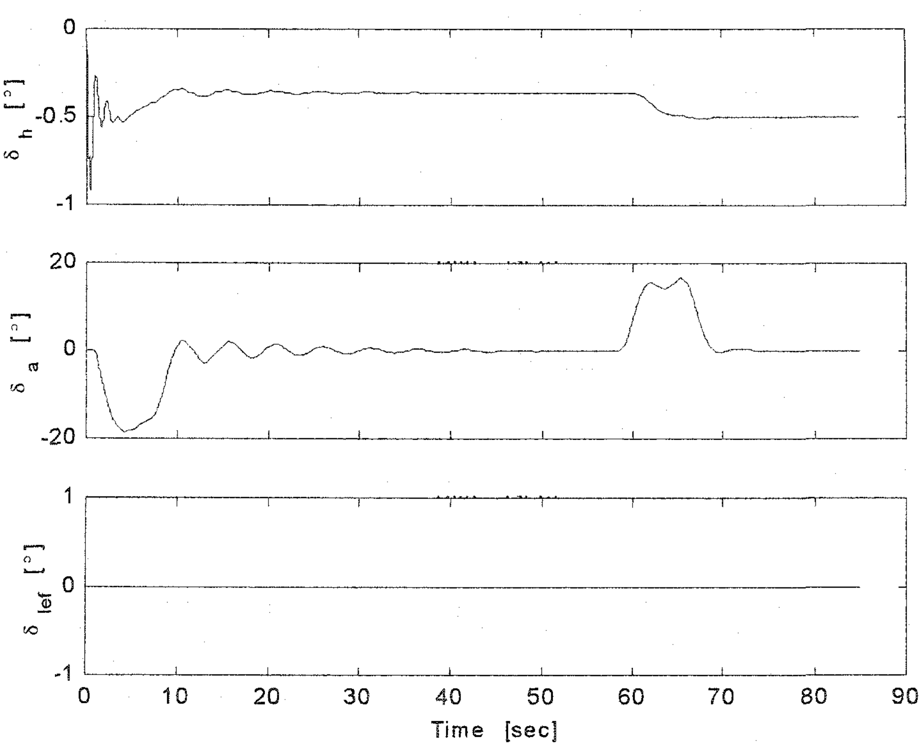

Figure 5.32 δ_h, δ_a, and δ_{lef} Response

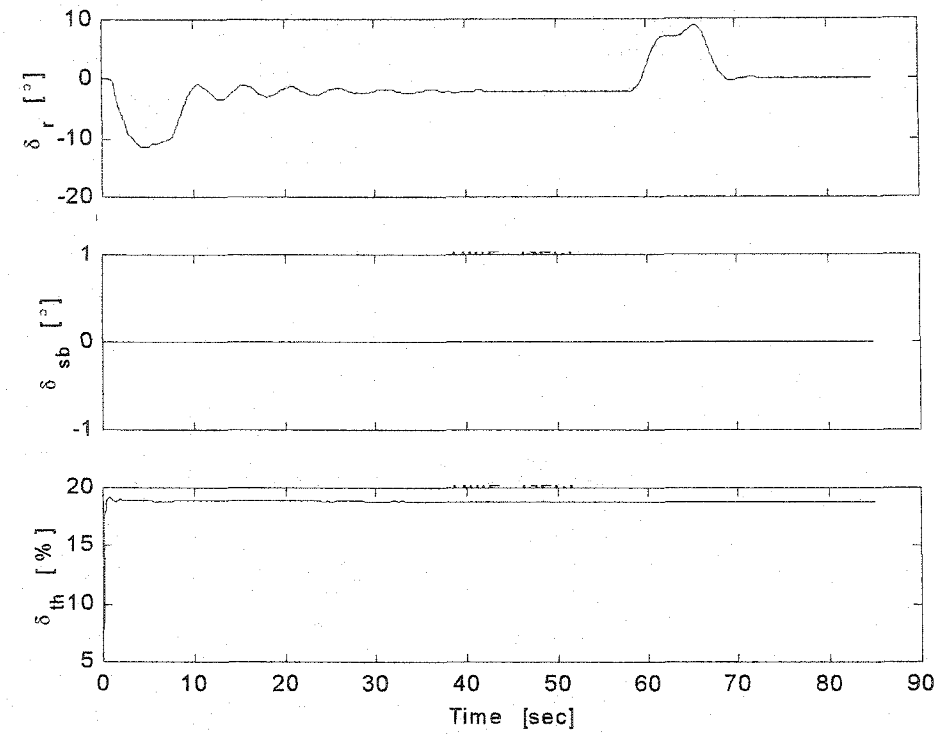

Figure 5.33 δ_r, δ_{sb}, and θ_{th} Response

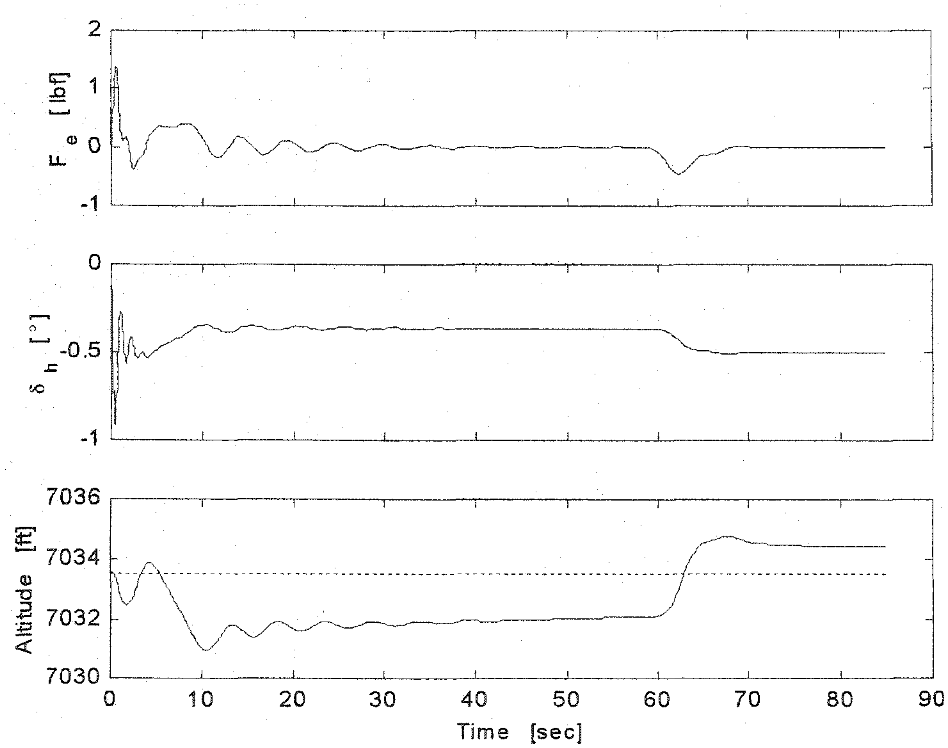

Figure 5.34 Altitude h, F_e, δ_e and Response

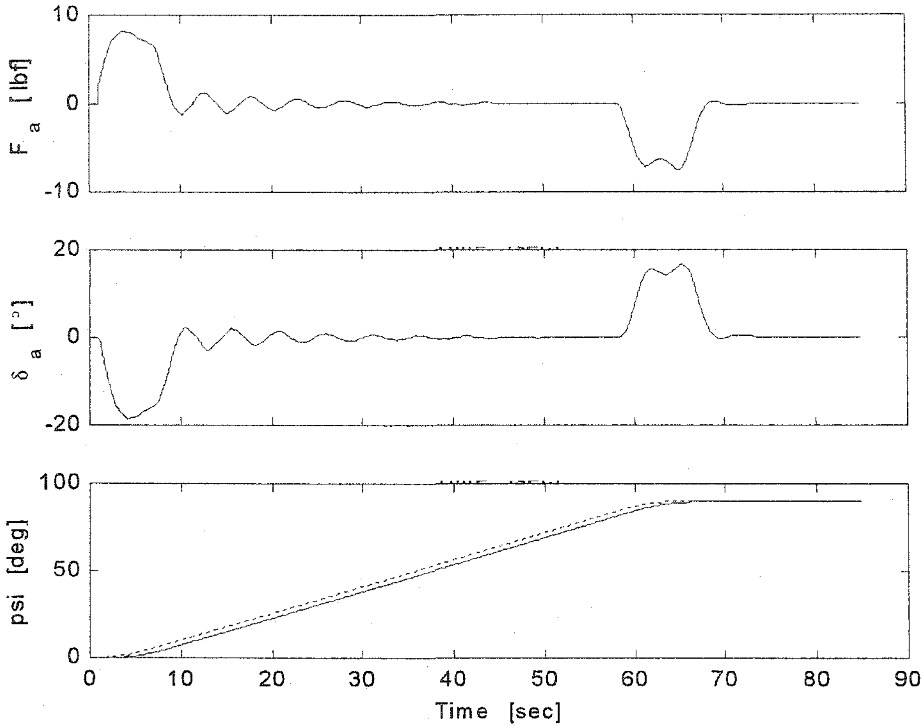

Figure 5.35 Heading Angle ψ, F_a, and δ_a Response

5.6 Expansion of the Flight Envelope for Autopilot Integrated System

In this section, the flight envelope of the overall vehicle system including FCS and autopilot is explored. Flight envelope is used to indicate flight conditions under which the vehicle can be operated. As shown in Figure 5.36, the x axis of the flight envelope is vehicle speed, and y axis of the figure is altitude. The thick solid lines with arrows indicate the simulation cases conducted. For example, the line from 600 *ft* to 7,000 *ft* at 150 *knot* indicates that the run from 600 *ft* to 7,000 *ft* at constant speed, 150 *knot* is simulated without showing unstable vehicle behavior. Similarly, many other flight conditions are tested, and the simulation cases are listed in Table 5.2. Note, the shaded area is surrounded by simulated flight conditions, and this implies that the vehicle is stable in any flight condition inside of the shaded area. For the test cases lying outside of

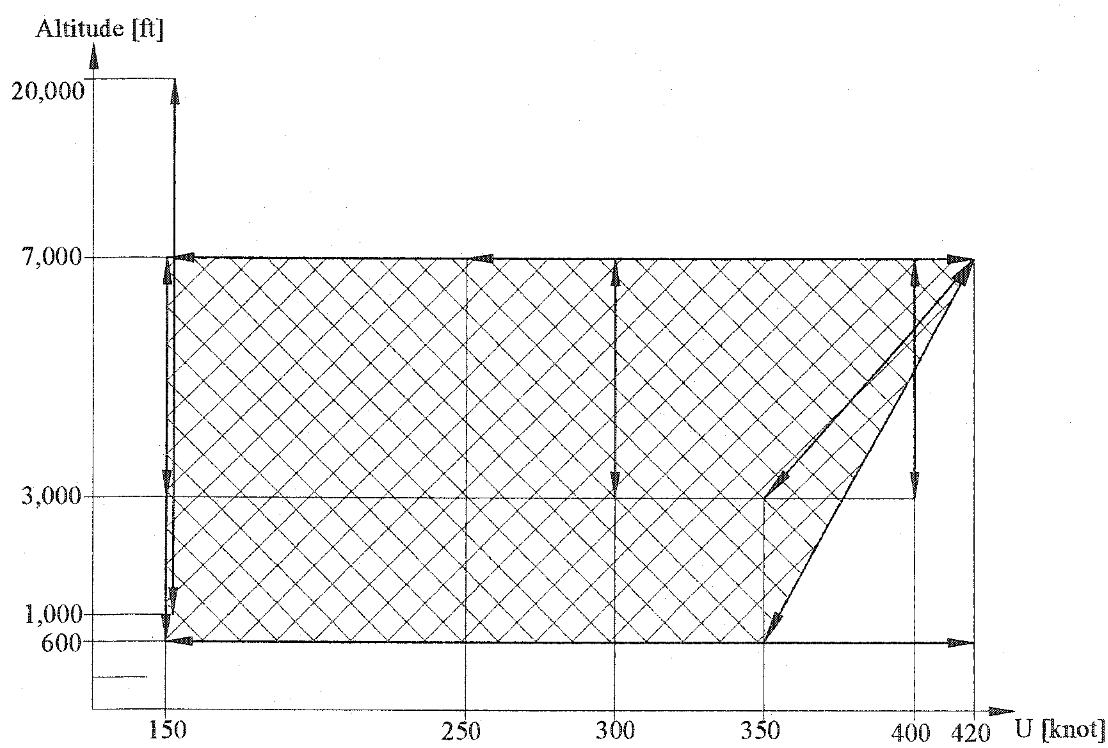

Figure 5.36 Flight Envelope of Overall Vehicle System

the shaded area, only limited flight conditions are tested. The simulation results of case 9 of Table 5.2 are shown in Figures 5.37-5.39 as example.

Table 5.2 Conducted Simulation Cases for Expansion of Flight Envelope

	Start Condition		End Condition	
	Altitude [*ft*]	Speed [*knot*]	Altitude [*ft*]	Speed [*knot*]
Case 1	7,000	150	7,000	420
Case 2	600	150	600	420
Case 3	600	150	7,000	150
Case 4	3,000	150	7,000	150
Case 5	3,000	300	7,000	300
Case 6	3,000	350	7,000	420
Case 7	600	350	7,000	420
Case 8	3,000	400	7,000	400
Case 9	1,000	430	20,000	430

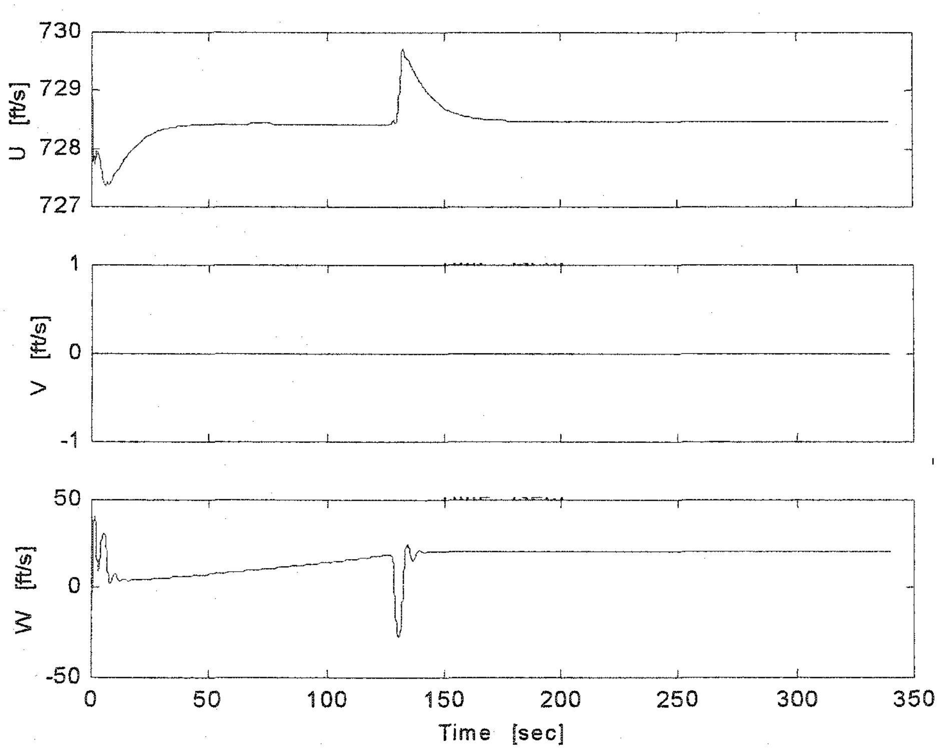

Figure 5.37 *U, V,* and *W* Response

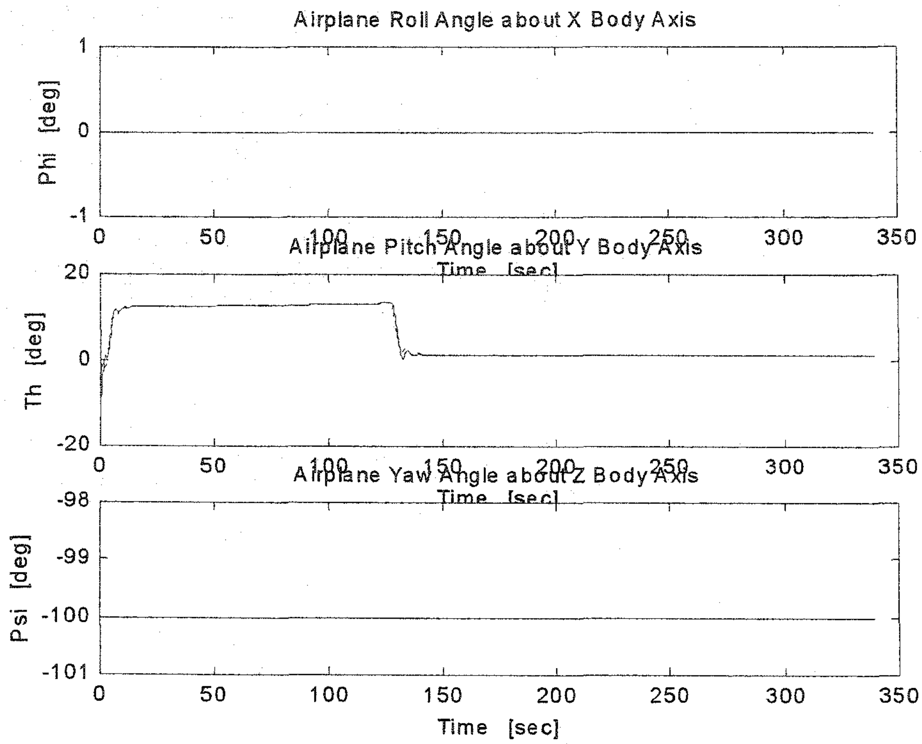

Figure 5.38 ϕ, θ, and φ Response

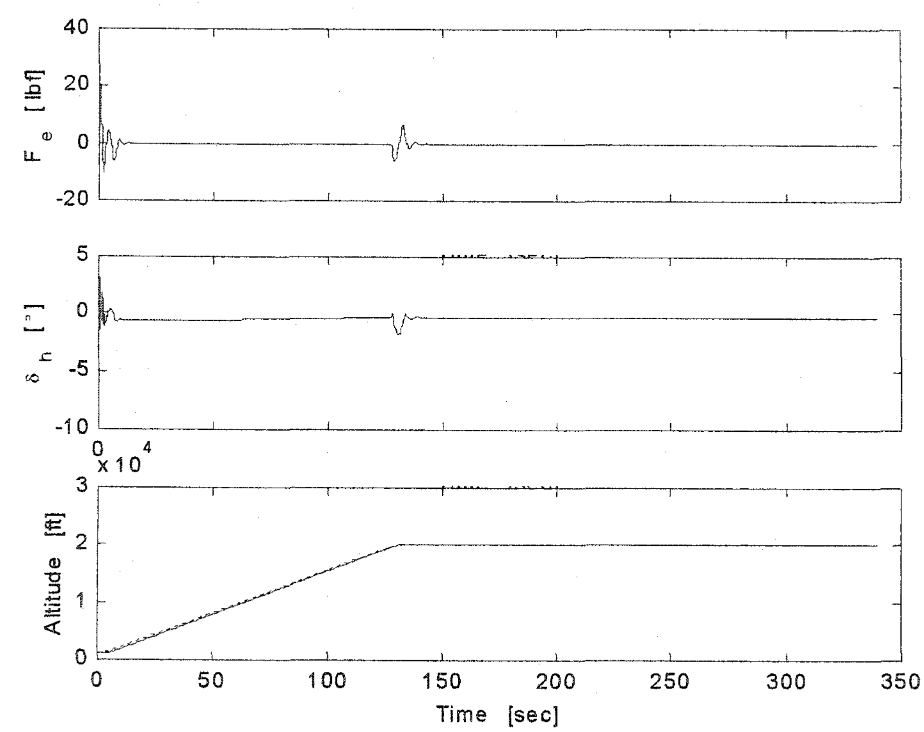

Figure 5.39 Altitude h, F_e, δ_e and Response

CHAPTER 6

Design of Mission Profile & Calculation of Load for Crack Model from the Rigid Body Motion Response

6.1 Generating Stress History from the Rigid Body Motion

This chapter discusses design of the mission profile and data process from the vehicle motion response to load input for structural life prediction, using the dynamic crack growth model. Construction of load data that can be direct input for the dynamic crack growth model introduced in Chapter 2 requires several steps. First, a realistic mission should be prepared for the vehicle model. This step includes mission design and construction of flight path connecting each steering point of the mission segments. Second, the vehicle model generates the time domain motion response according to the planned mission. The autopilot system developed in Chapter 5 will automatically guide the vehicle to perform the necessary maneuver in order to follow the given flight path. Because the vehicle is considered as a rigid body, the motion response does not contain any information on the stress of structural components. Therefore, a flexible wing model discussed in Chapter 4 will be utilized to generate the stress response of the wing spar. Fourth, the stress response data in terms of time will be processed into load data in terms of cycle through several steps. The stress response is in time domain, and this data also contains a number of unnecessary data points, so this data is improper as a direct input for the crack model. This chapter discusses the first step and the last step of such process.

A simple mission is constructed for the vehicle model. The rigid-body model follows the flight path using the autopilot system, and generates rigid body motion of the overall vehicle. The motion response is applied to the wing structural model as external forces and moments. These are vertical acceleration of the vehicle $\ddot{x}_0$, lift L, moment M, roll acceleration $\dot{P}$, and pitch acceleration $\dot{Q}$, respectively. The vertical acceleration $\ddot{x}_0$ is computed through numerical differentiation of vertical velocity w, and $\dot{P}$ and $\dot{Q}$ are also calculated through numerical differentiation of roll rate P and pitch rate Q. Lift L and pitching moment M are distributed to each segment of the half-span-wing as discussed in Chapter 4. Now, the wing structural model generates the stress response, and the stress response is fed into the crack growth model as input data. It also takes several steps to process original time domain wing stress response into the cyclic load which can be the direct input for the crack growth model. These processes include elimination of compressive stress, elimination of non-effective points, and time scale into cycle conversion.

6.2 Development of a Mission Profile

An air-to-surface mission for a fixed target is planned. This mission represents a simple striking mission that can be either training or real mission. The mission profile is developed based on a mission presented in Reference 96. Because the research objective is not to develop variety of missions, only this mission is assumed to be repeated throughout the structural life of the vehicle. For the same reason, effect of different missions on structural components is not considered in this phase of research. The mission consists of climb, cruise, descent, releasing bomb, climb, cruise, descent, and steering of each necessary point. The overall mission runs about 30 *min*. Figure 6.1 illustrates a plane view of the mission, and Figure 6.2 and Table 6.1 provide the altitude and speed information at each steering point. Note, the effect of wind and gust are not considered in the mission, and those parameters can be considered in the next phase of the research.

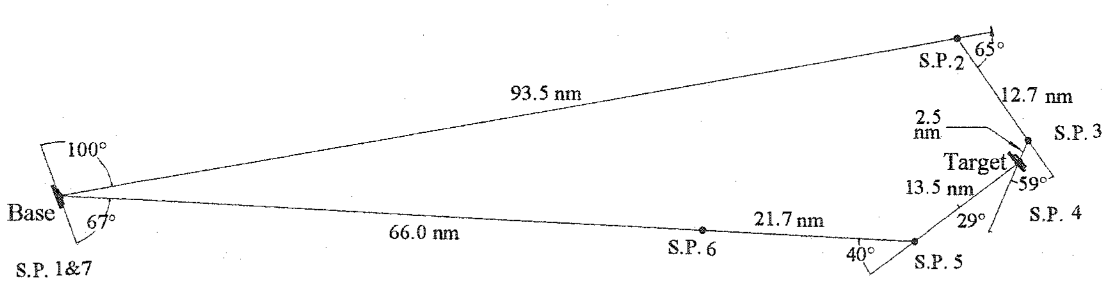

Figure 6.1 Plan View of The Mission

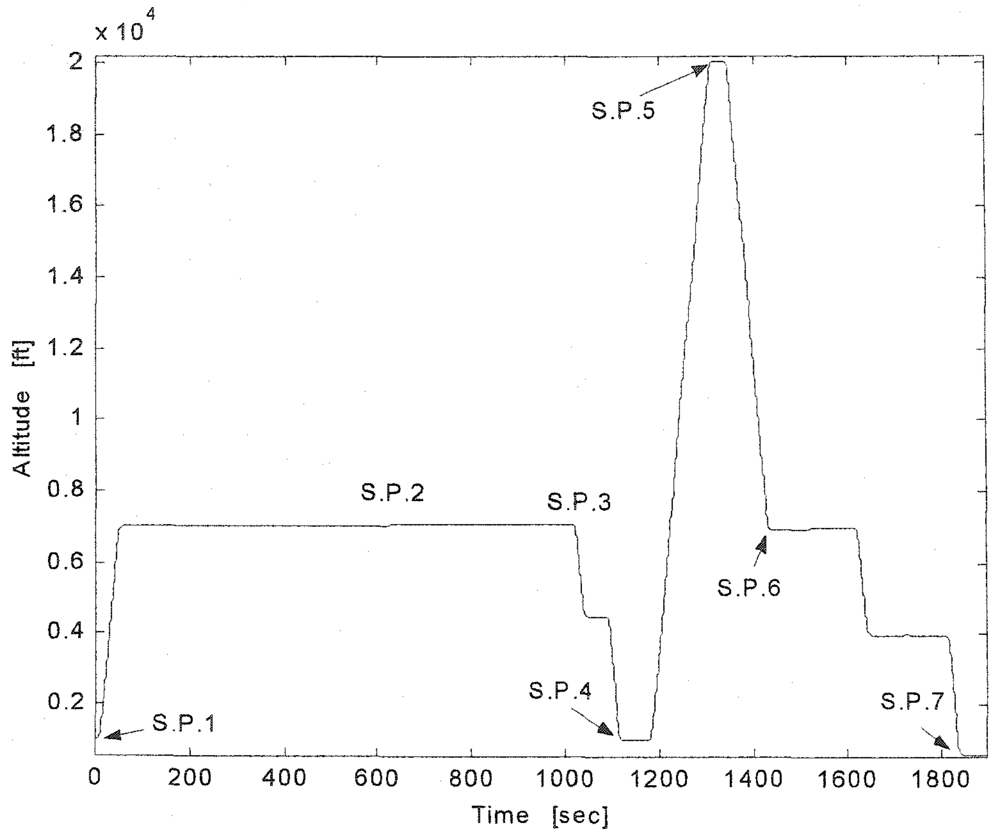

Figure 6.2 Altitude of the Mission Profile

Table 6.1 Altitude, Velocity, and Heading Angle at each Steering Point

	Altitude [*ft*]	Velocity [*knot*]	Heading [°]
Steering Point 1	1,000	320	0
Steering Point 2	7,100	400	100
Steering Point 3	7,100	410	165
Steering Point 4	1,000	410	224
Steering Point 5	20,000	430	253
Steering Point 6	7,000	420	293
Steering Point 7	600	160	0

The target is in an air base which is 98.175 *nm* away from the take off base and 2° off to the east. The altitude of the base airfield is assumed to be 500 *ft*. The usual cruise condition of F-16 is known to be 7,000 *ft* altitude at 400 *knot* speed.[96,97] The simulation starts from just after take off condition at 1,000 *ft* altitude, and finishes at little lower than 600 *ft* altitude. Note, take off and landing speed of the F-16 are usually 150 *knot* and 160 *knot*, respectively. Note, take off and landing are not included in the mission because the flight control system developed in Chapter 5 does not include such functions. After take off, the vehicle climbs to the cruise altitude, 7,000 *ft*, and makes a 100 ° turn. At Steering Point 2, altitude is increased to 7,100 *ft*, and makes a 65 ° turn. Steering for the final target approach is made at Steering Point 3, and altitude is dropped to 1,000 *ft* which is the bomb release altitude. When releasing the bomb, the CCIP (Continuously Computed Impact Point) delivery mode is considered. As soon as the bomb is released, the vehicle rapidly increases its altitude to 20,000 *ft* (Steering Point 5) to avoid any anti-aircraft fire. After Steering Point 6, altitude is returned to the cruising condition, and the vehicle approaches the original base.

The continuous flight path is generated based on the mission profile. The flight path consists of sets of three commands – velocity, altitude, and heading angle – at every time step. These sets of commands are direct input for the aircraft autopilot system described previously. The autopilot system will follow the flight path command through generation of necessary maneuvers for the vehicle. In generating the flight path, four limitations are applied. Altitude and heading angle path are computed within acceleration and velocity limits. In other words, climb/descent rate and its acceleration were limited to within ± 150 *ft/s* and ± 40 *ft/sec*^{2}, respectively. Also, the heading rate is limited within ± 0.027 °*/s* and angular acceleration of heading angle is limited within ± 0.004 °*/sec*^{2}. The change of velocity is automatically limited by engine dynamics.

Now, the F-16 model is driven by the autopilot system following the mission profile developed above. The simulation result is displayed in Figures 6.3-6.14. Because speed break engagement/disengagement causes a sudden increase of unexpected stress on the wing, the speed break is deactivated, and deceleration performance is lowered as shown in Figure 6.12.

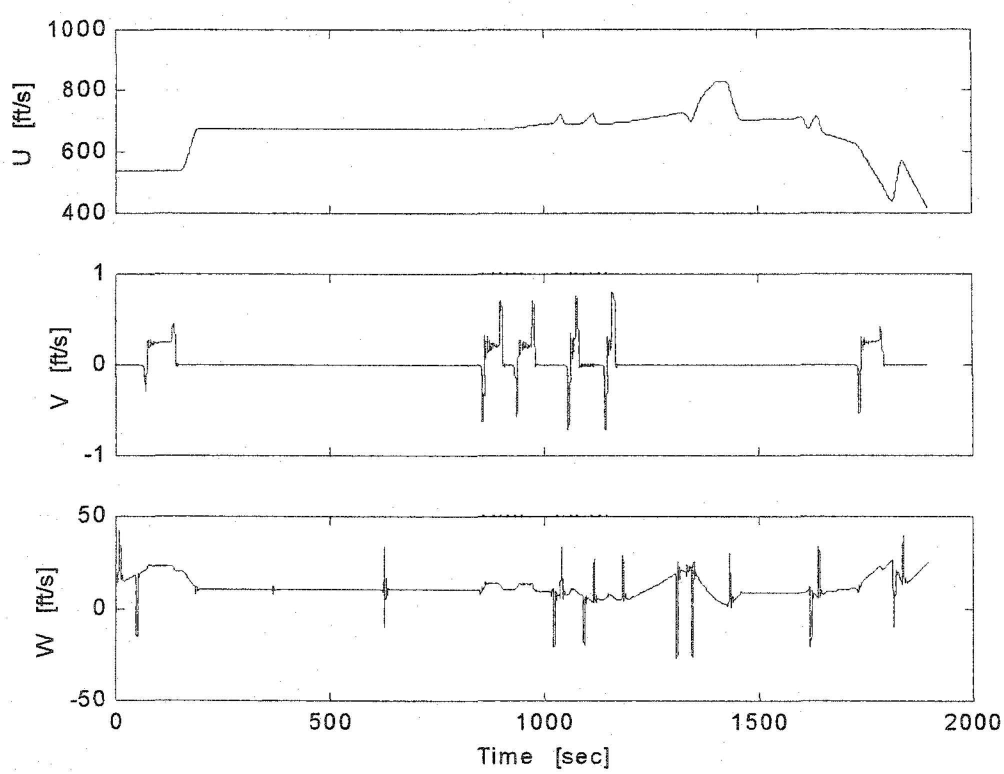

Figure 6.3 *U*, *V*, and *W* Response

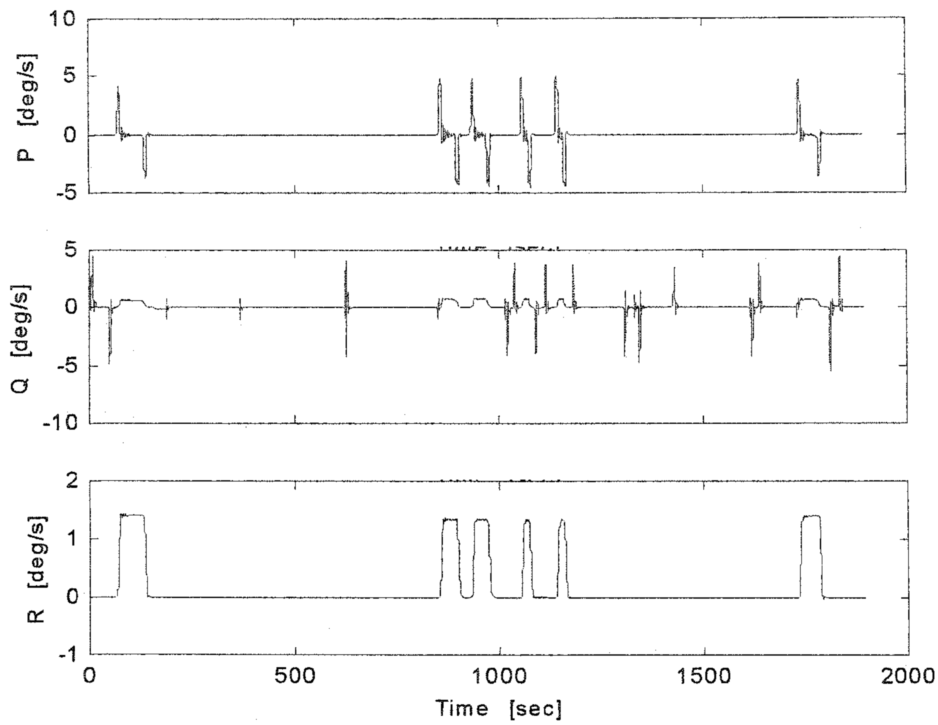

Figure 6.4 P, Q, and R Response

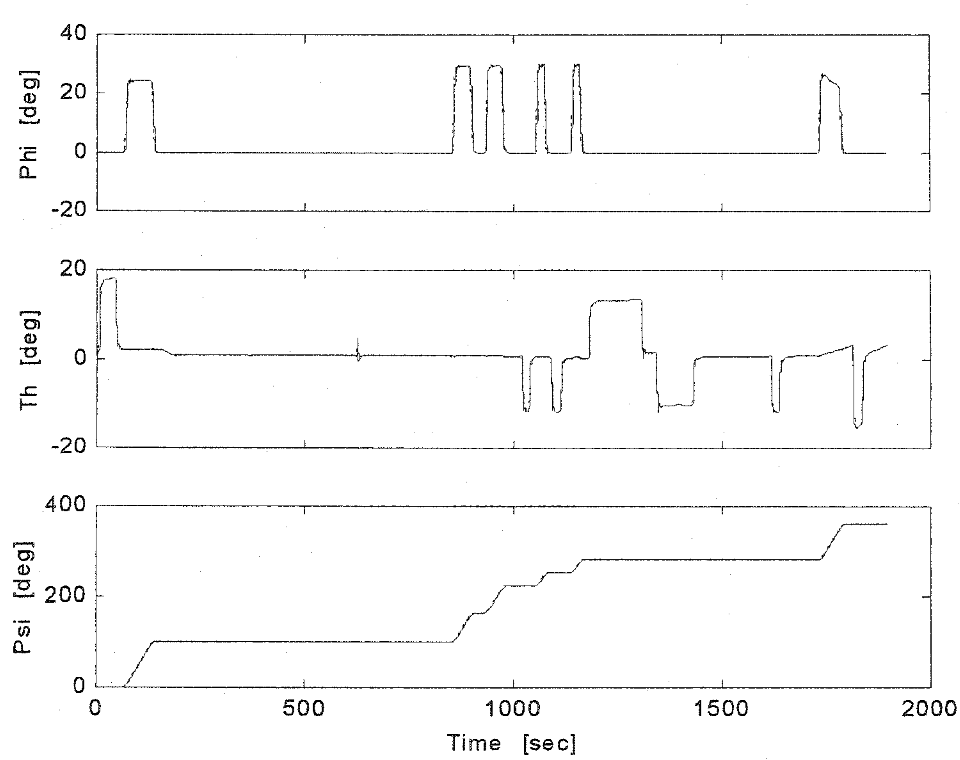

Figure 6.5 ϕ, θ, and φ Response

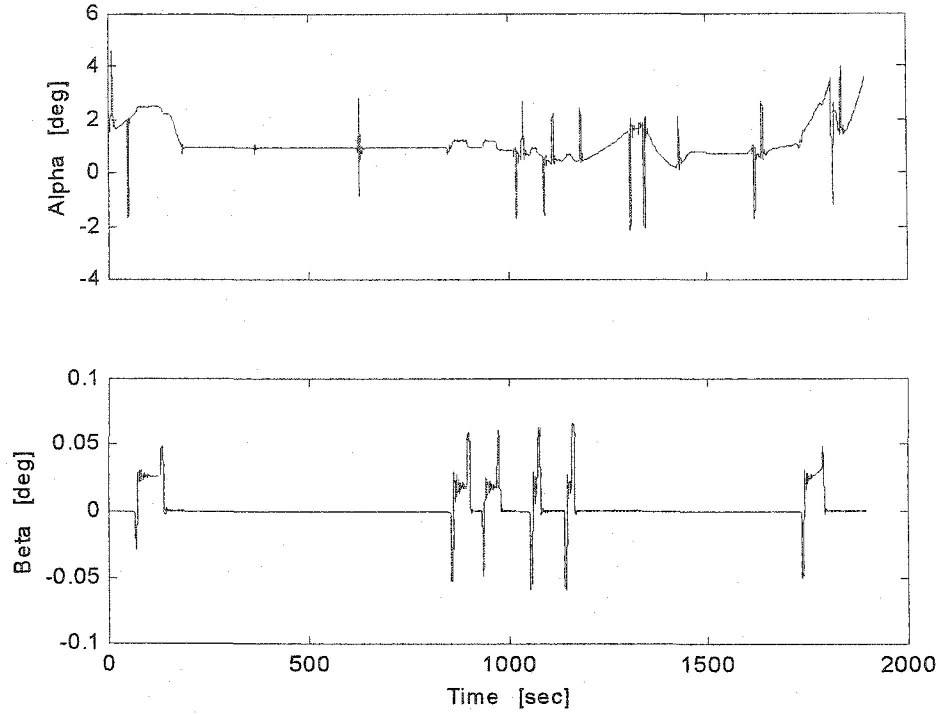

Figure 6.6 α and β Response

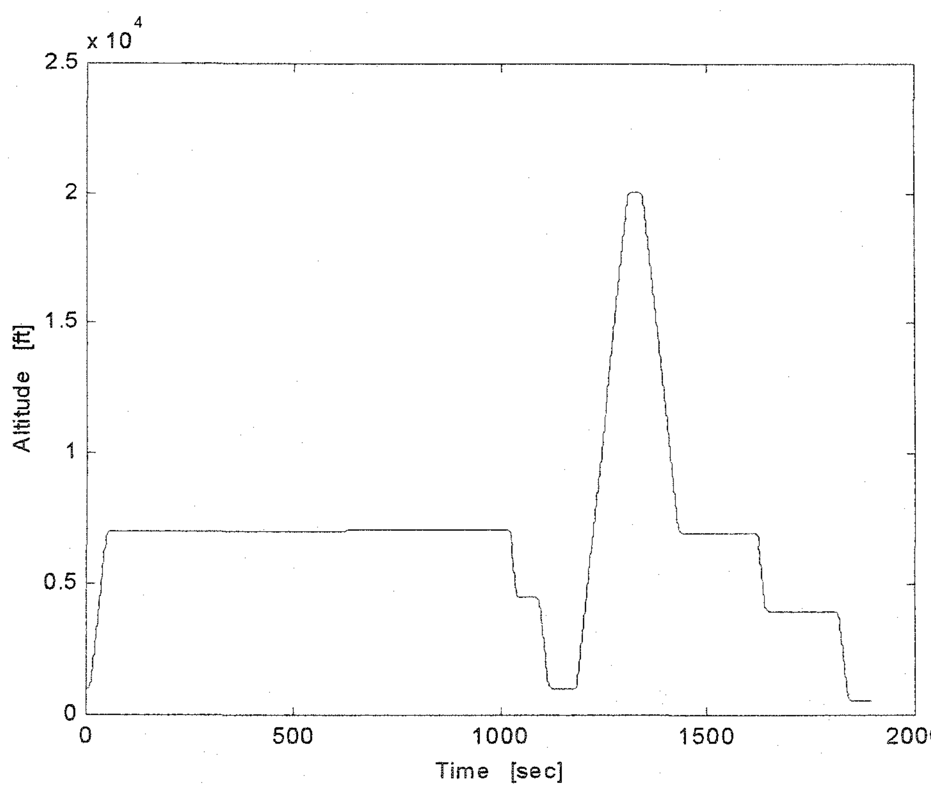

Figure 6.7 Altitude of the Aircraft (h)

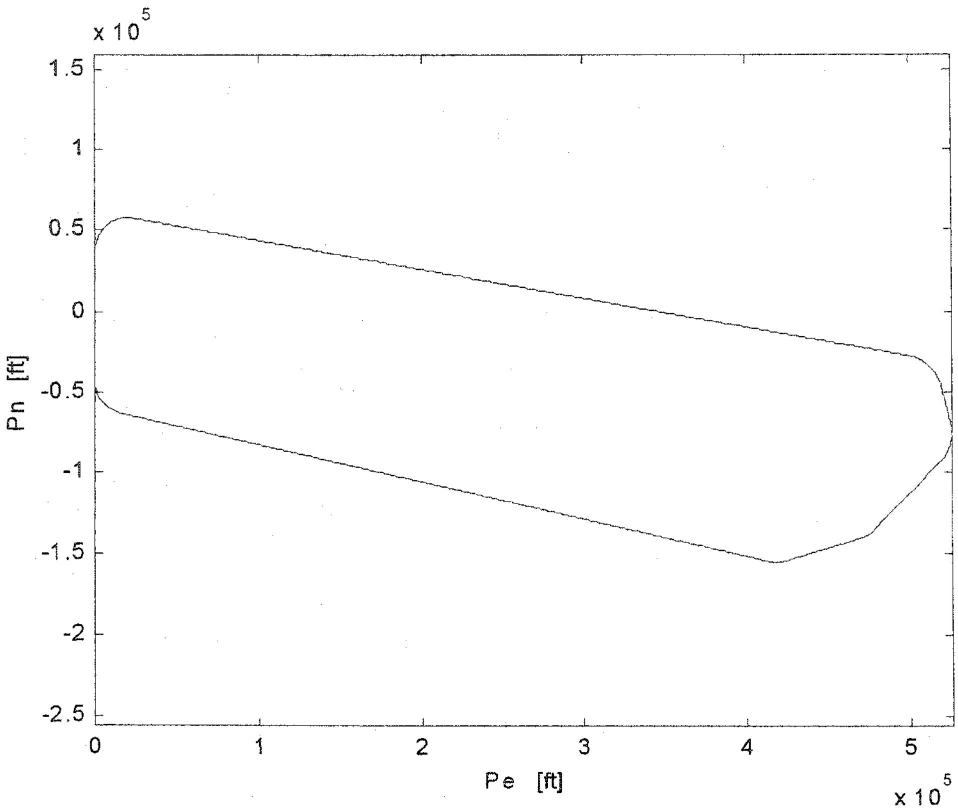

Figure 6.8 Plan View of Aircraft Motion (P_e and P_n)

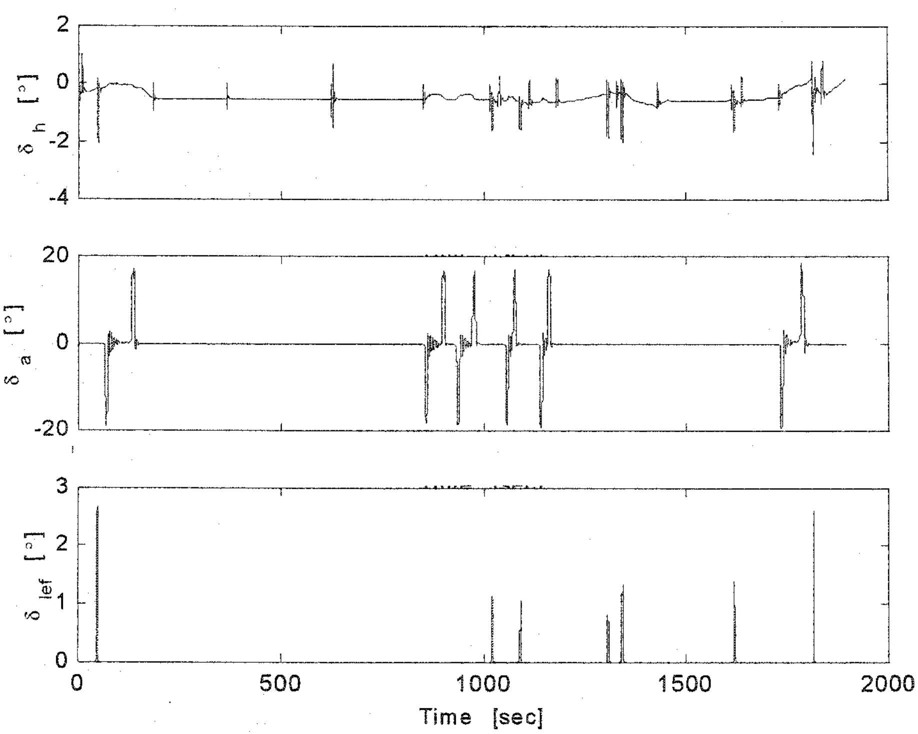

Figure 6.9 δ_h , δ_a , and δ_{lef} Response

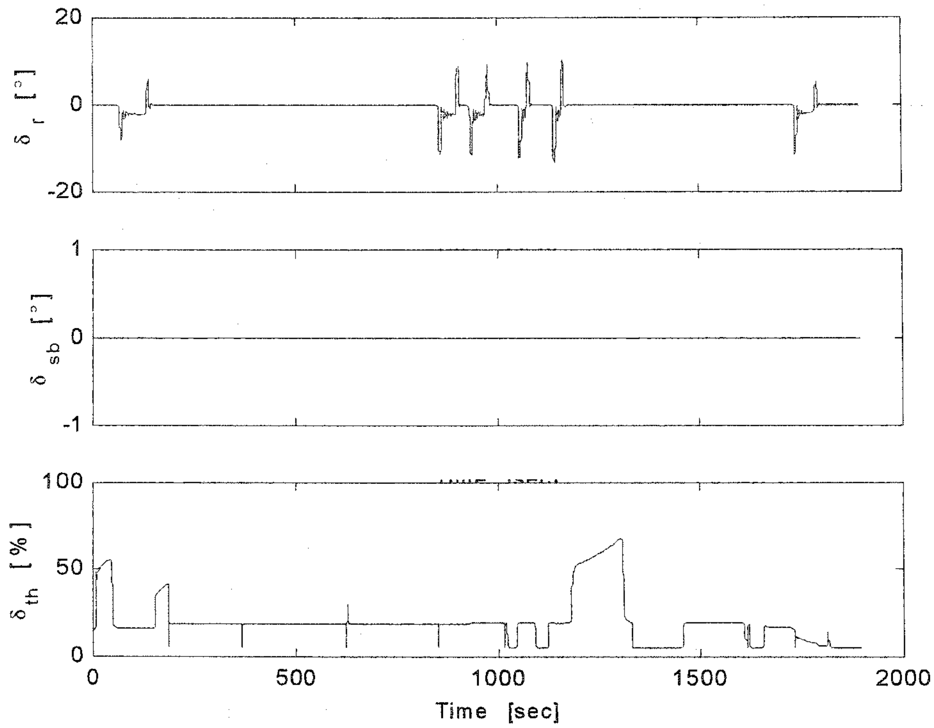

Figure 6.10 δ_r , δ_{sb} , and δ_{th} Response

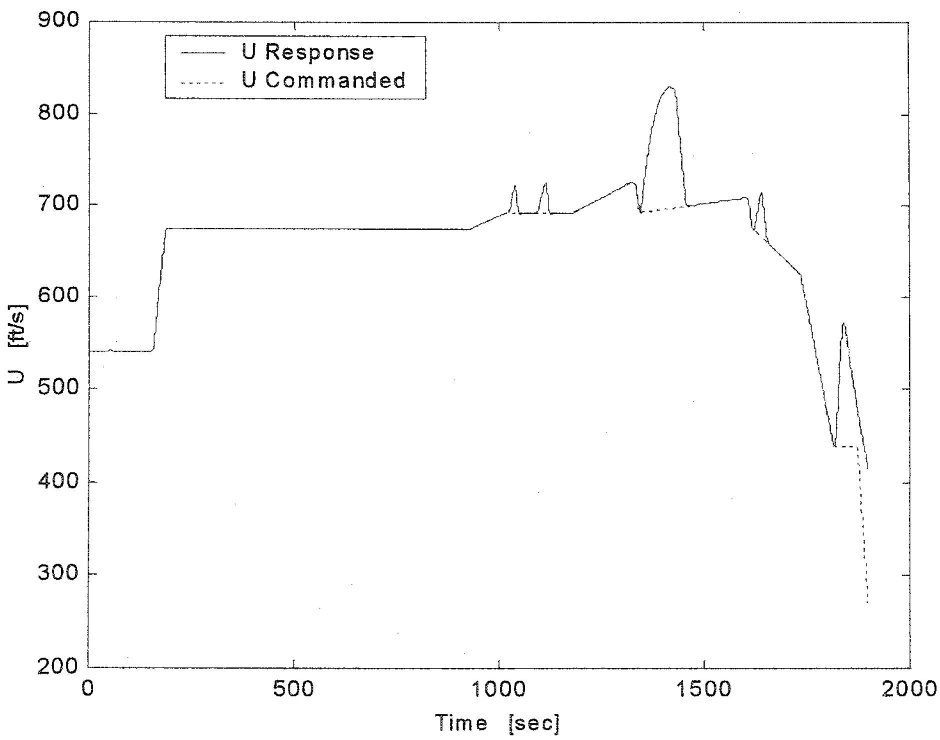

Figure 6.11 Desired Velocity U_c and U Response

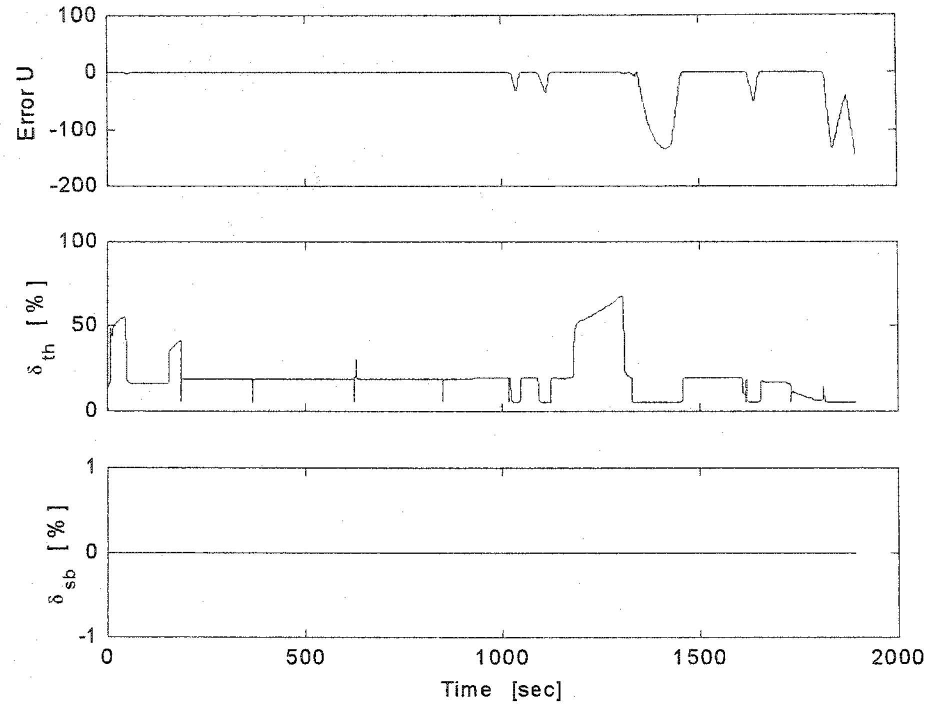

Figure 6.12 U_{error}, δ_{th}, and δ_{sb}, Response

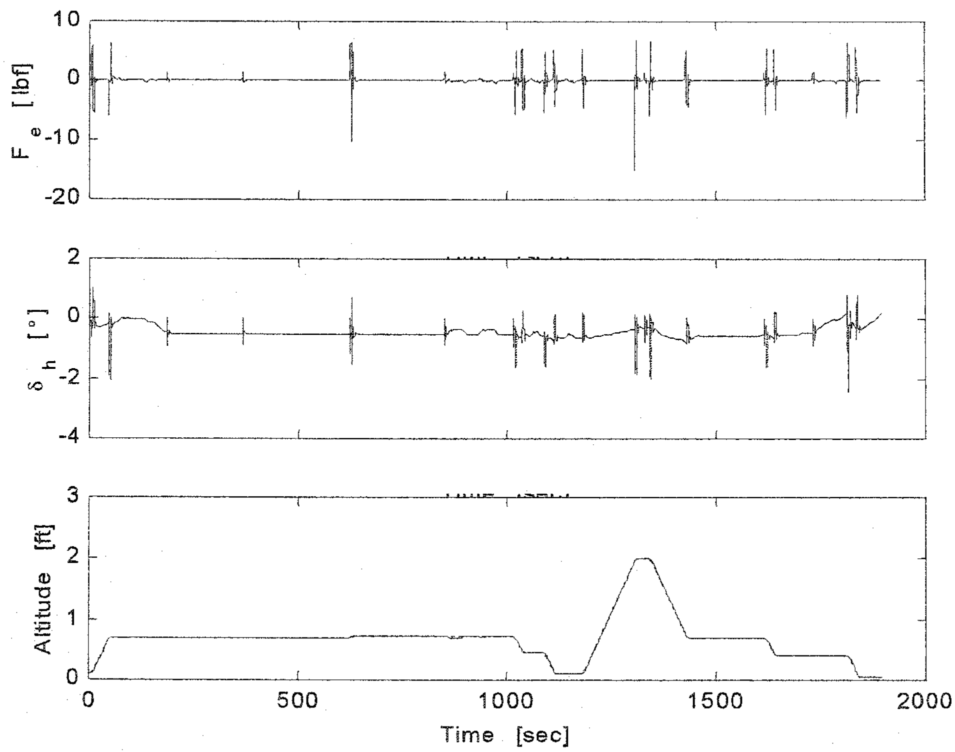

Figure 6.13 Altitude h, F_e, and δ_e Response

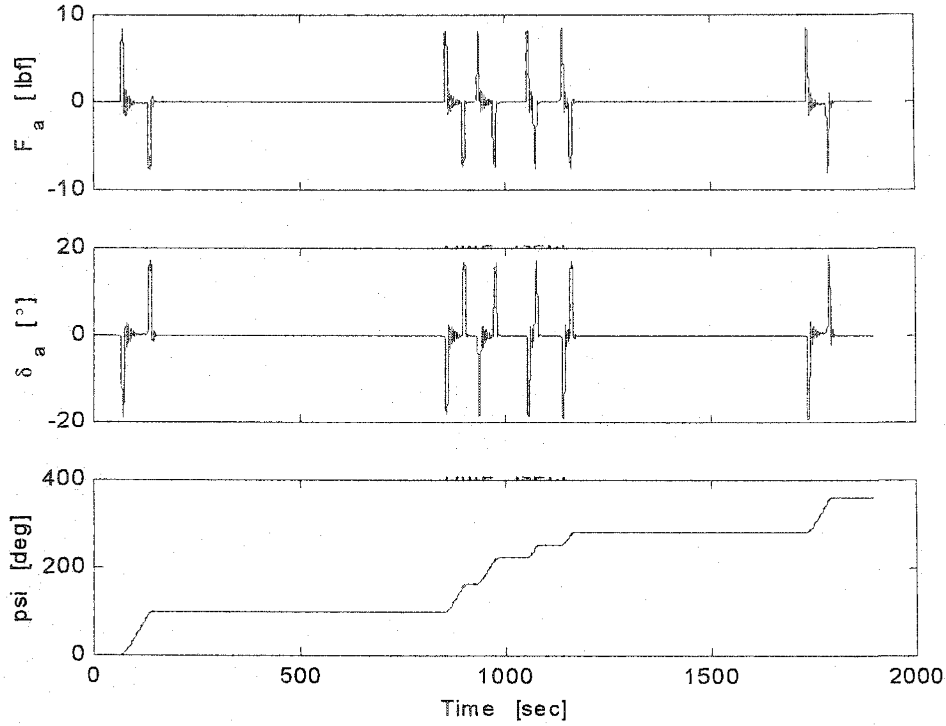

Figure 6.14Heading Angle ψ, F_a, and δ_a Response

6.3 Data Process from Stress Response to Load

Now, the vehicle motion response is applied to the wing structural model as a external excitation. Recall that the excitation needed includes the vertical acceleration of the vehicle $\ddot{x}_0$, lift L, moment M, roll acceleration $\dot{P}$, and pitch acceleration $\dot{Q}$. These four terms can be computed from the vehicle motion response. The deflection of the wing spar at different span stations is shown in Figure 6.15 and 6.16. Note each line in Figure 6.15 represents the deflection of different span station at the corresponding time. Figure 6.16 gives better understanding of Figure 6.15. In Figure 6.16, each line represents the deflection of each span station while time is varying.

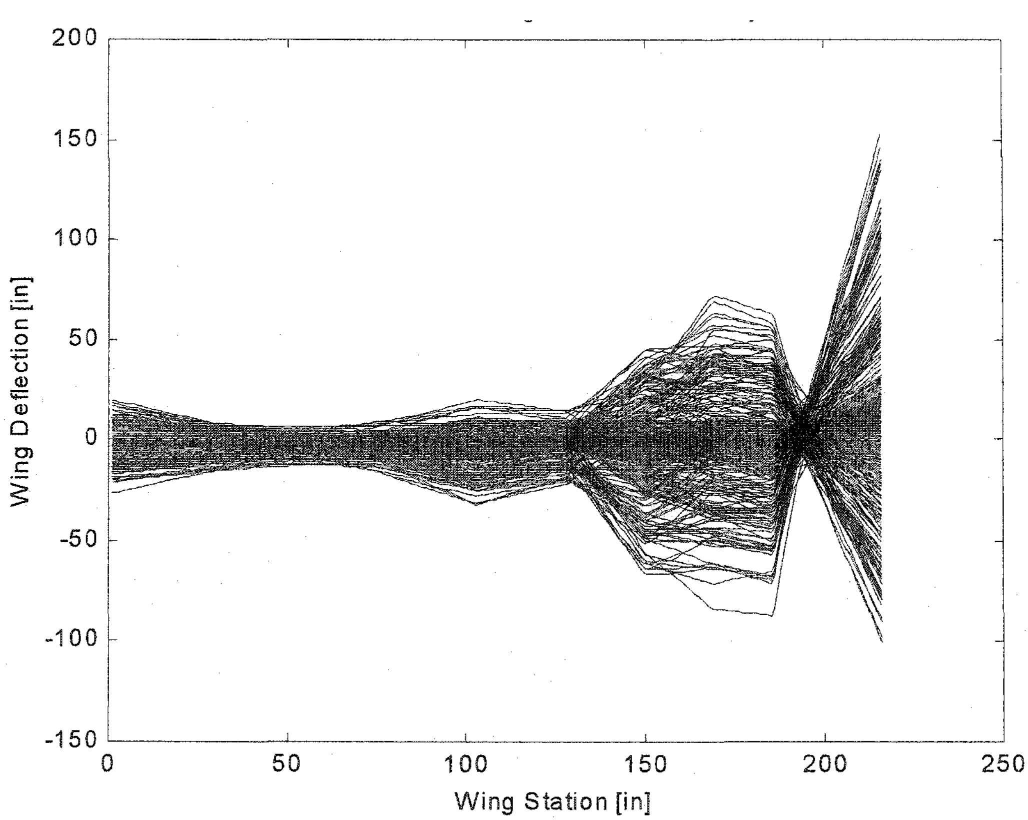

Figure 6.15 Deflection of Wing Spar; Spanwise

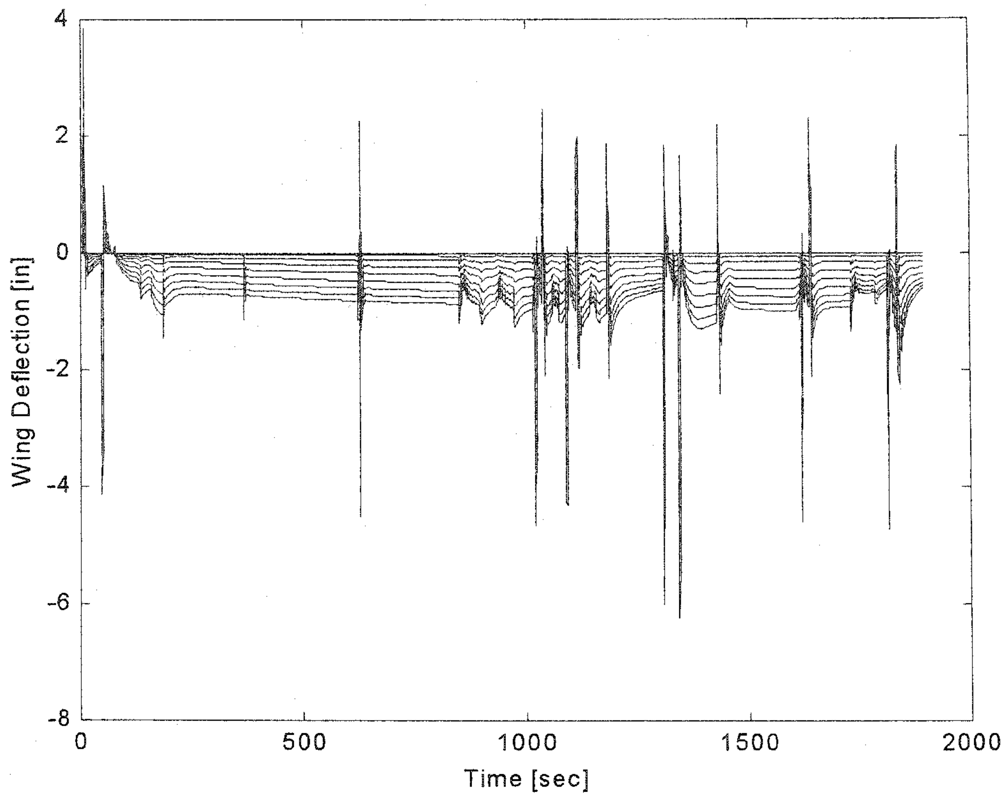

Figure 6. 16 Deflection of Wing Spar; Timewise

Now, the stress can be calculated from the deflection of the wing. A conventional beam stress state associated with the wing spar is considered. The moment of a spar can be expressed as following

$$M = \int_{x_1}\int_{x_2} -\sigma x_2 dx_1 dx_2 \tag{6.1}$$

In Equation (6.1), x_1- x_2 denotes spar cross sectional area, M denotes bending moment, and σ denotes stress. The stress σ can be derived from Equation (6.1) as

$$\sigma = -Ex_2 \frac{d^2 z}{dx^2} \tag{6.2}$$

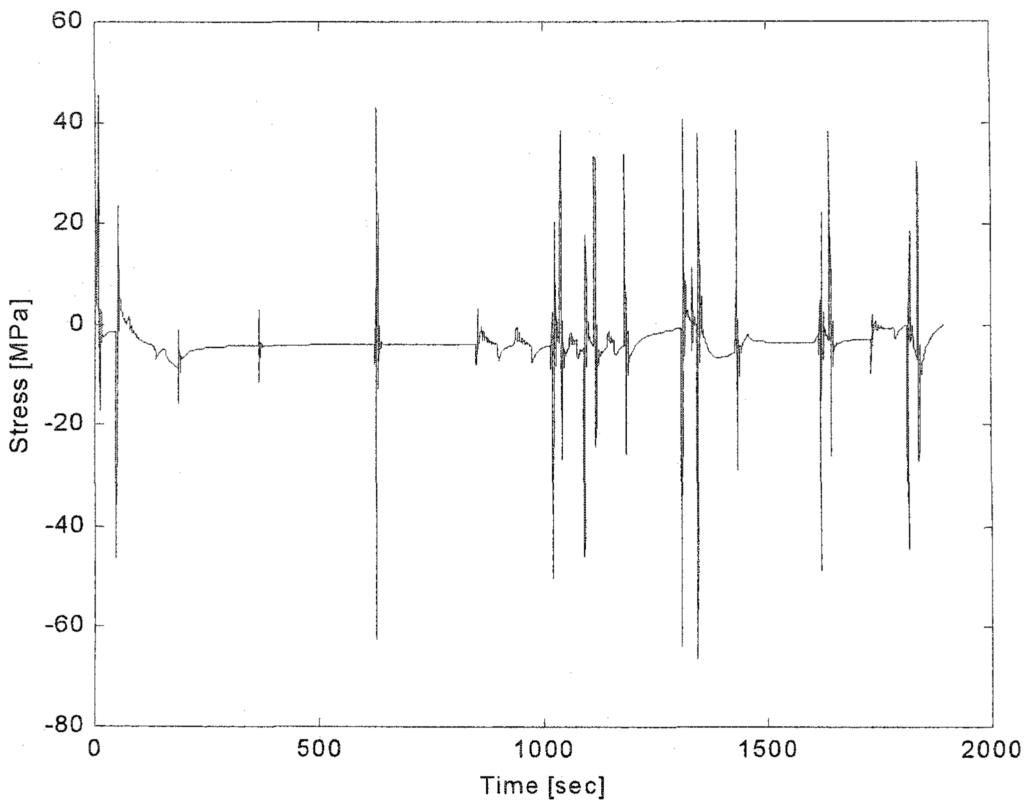

Figure 6.17 Stress Response of The Wing for the Nominal Mission Profile

where, E denotes modulus of elasticity, and x-z denote typical structural axes with x representing distance along the spar and z representing transversal spar deflection. The calculated stress of spar at 150 *in* is shown in Figure 6.17.

Note that the intermediate points between two peaks have no effect on fatigue crack growth. Only the peak points effect the crack growth. The rainfall method[5] is employed to pickup the peak points of the stress response shown in Figure 6.17. As a result of this process, the original stress response consisting of approximately 190,000 points is reduced to about 270 data points. The result is displayed in Figure 6.18.

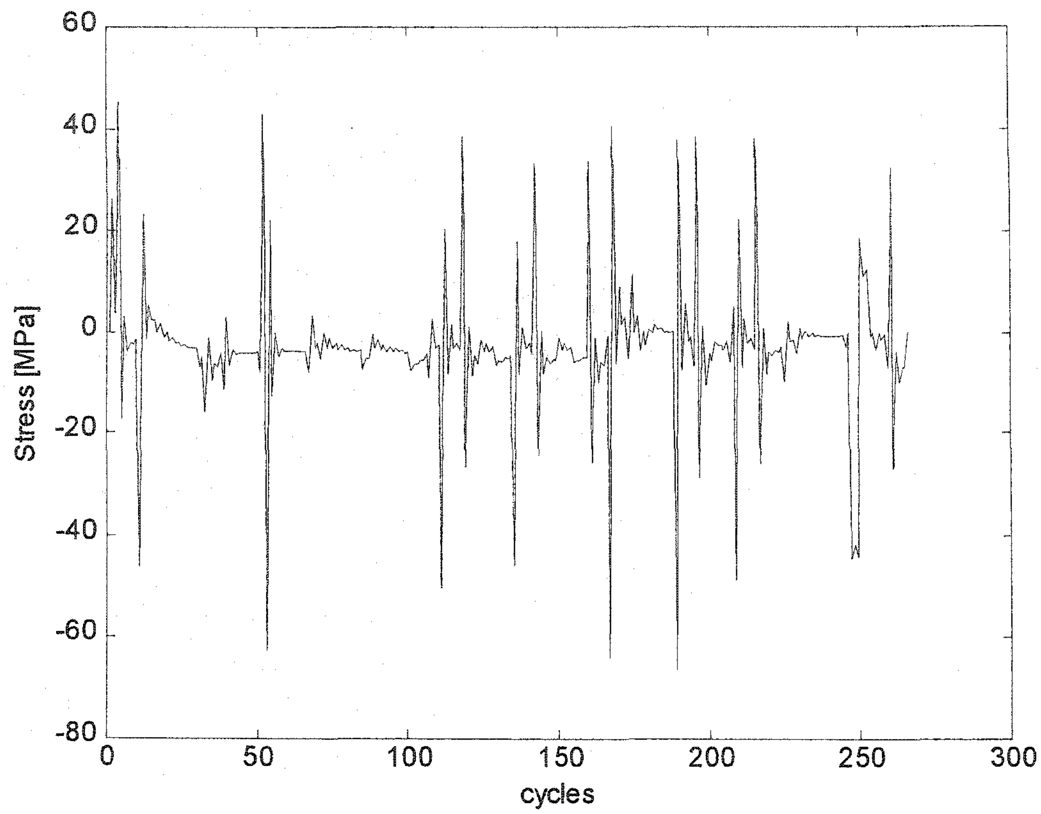

Figure 6.18 Stress Response of the Nominal Mission Profile – Peak Stress Only

The peak stress data is now processed in two steps. The negative stress which represent compression are moved to 0 *MPa*. Note the compression stress have minor effect on crack growth. Also, the dynamic crack model used is not capable to process negative stress values. The last step is the elimination of continuous zero data points. After all the negative data points are moved to zero, there are bands of continuous zero data points which have no effect but slowing the crack growth simulation. Each series of zero points is reduced to a single zero point, and the result is shown in Figure 6.19. This load data is used as input for the crack growth model.

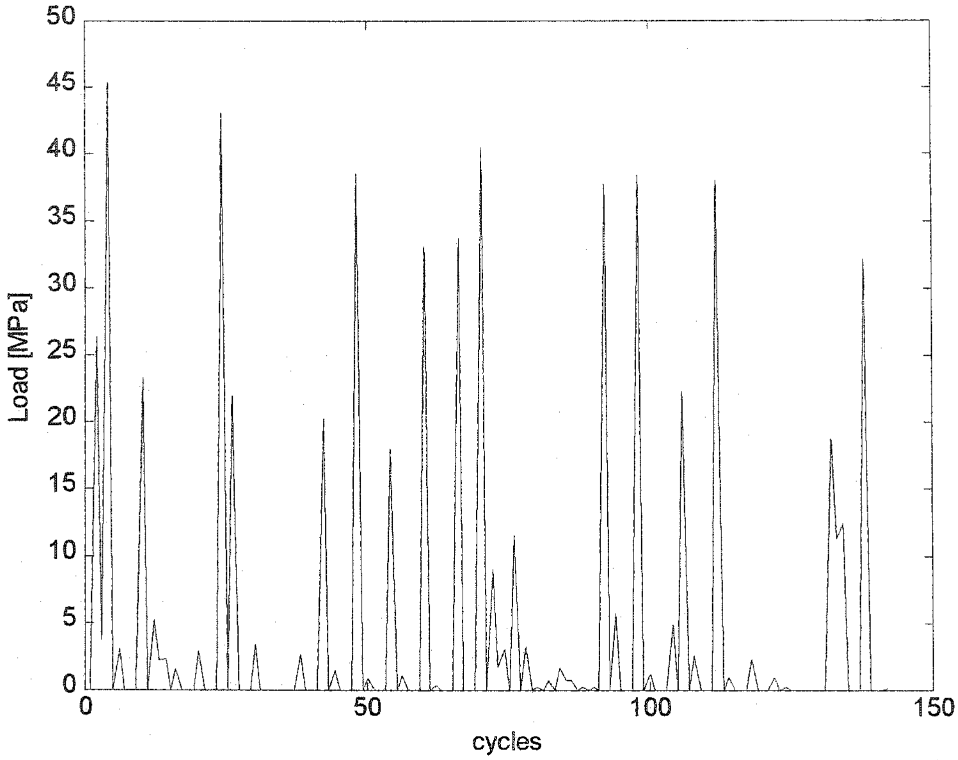

Figure 6.19 Load of the Nominal Mission Profile

CHAPTER 7

DEVELOPMENT OF LIFE EXTENDING CONTROL LOGIC

7.1 Description of Life Extending Control Logic

This chapter discusses LEC (Life Extending Control) logic and LEC activating logic which engages/disengages the LEC logic. A brief description of the overall logic is shown in Figure 7.1. The LEC logic changes the control parameter of FCS when the activating logic engages the LEC logic. The activating logic lying outside of LEC logic will be discussed shortly. The LEC logic consists of two parts. The first part is the optimal overload stress calculation logic, and the second part is the required maneuver level determination logic. The first part of the LEC, the optimal overload determination logic, gives the optimal or sub-optimal load that can reduce crack growth. The maneuver

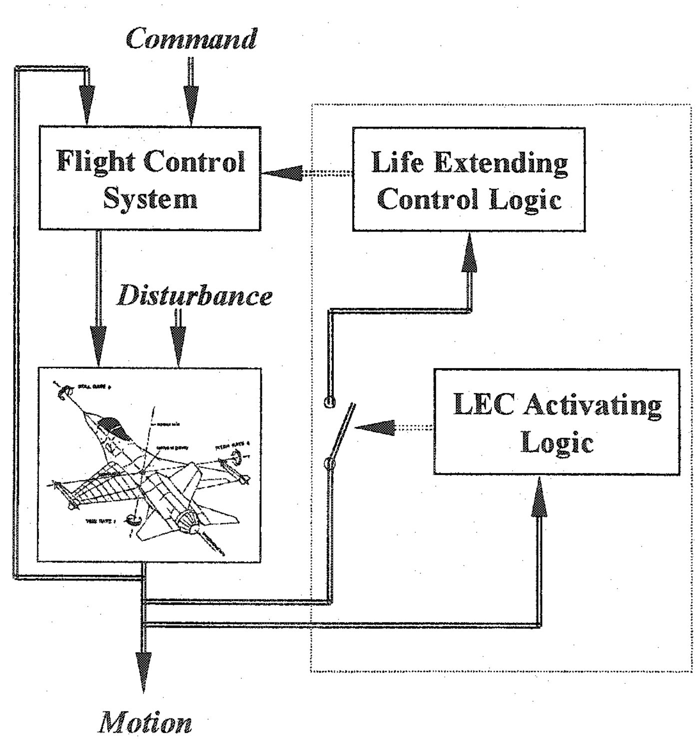

Figure 7.1 Schematic View of Overall Vehicle and LEC System

level determination logic computes and issues appropriate control authority to tailor the vehicle motion in order to result the optimal or sub-optimal load.

For the first part of LEC logic, the optimal load conditions can be obtained from Equation (3.28) when the overload interval is specified. Determination of appropriate overload interval is discussed shortly. The second part of the LEC logic requires a nonlinear mapping from control parameters such as control gain or additional control input to stress of wing structural components of vehicle. In this research, control gain is employed as a leverage to result the desired motion behavior. Through simulations, it is found that the bending stress of the wing spar is dominated by the pitch motion of the vehicle. Such a low contribution of lateral directional motion on the stress is because of the moderate lateral directional motion due to the limited capability of the autopilot system. Note the autopilot system does not utilize full control authorities available from the vehicle but only the minimum control authorities are considered. Effective control leverage to result desired pitch motion which generates desired stress level is also discussed in the next section.

The nonlinear mapping implies that the control parameter-stress relationship should be identified for determining appropriate maneuver level for the desired stress level. Because the vehicle model and flight control system are nonlinear, the control input and resulting motion behavior also have nonlinear relationship. On the other hand, the stress generated from the linear wing structural model and control authority have nonlinear functionality each other because the intermediate system, vehicle model, is nonlinear. Therefore, a number of simulations are conducted to establish nonlinear functionality between control gain and corresponding stress. Since this research is trying to identify the feasibility of direct implementation of benefits of crack retardation phenomenon to the flight control system using LEC logic, only longitudinal motion of the vehicle was simulated and the corresponding data is stored. In order to verify the feasibility of the overall LEC logic, the vehicle simulation was conducted in a large area of flight envelope implying that series of simulation for different flight conditions that are lists of different altitude and Mach number was conducted.

The LEC activating logic has two important functions. One of the functions is to determine LEC activating time, and the other is to provide the average level of nominal high stress which is denoted as σ_{max1} in Chapter 2 and Chapter 3. The LEC activating logic performs these functions through monitoring the critical motion behavior of the vehicle. The nonlinear functionality table mentioned above provides both connection from control gain to critical vehicle state and the connection from the vehicle state to the stress level of the wing. The LEC activating logic monitors the critical vehicle state to predict and estimate the stress level of each longitudinal maneuver using the nonlinear functionality table. When the critical state indicates occurrence of high wing stress that can give considerable effect on crack growth, the stress level is computed, and this stress is regarded as nominal high stress. From the last LEC activating cycle, the nominal high stress is accumulated. The number of cycles from the last overload occurrence is counted, and provided as the number of nominal high stress for the LEC logic. The LEC logic is activated when the number of nominal high stress reaches to the overload interval. Because the optimal stress calculation using Equation (3.28) requires the nominal high stress level, the mean value of the stored nominal high stress is also computed and made available for the LEC logic.

Now, determining when the overload will be applied is considered. Recall that the overload application interval is called overload interval, and this is counted in *cycle* which does not directly reflect *time*. Figure 7.2 shows the concept of overload interval for

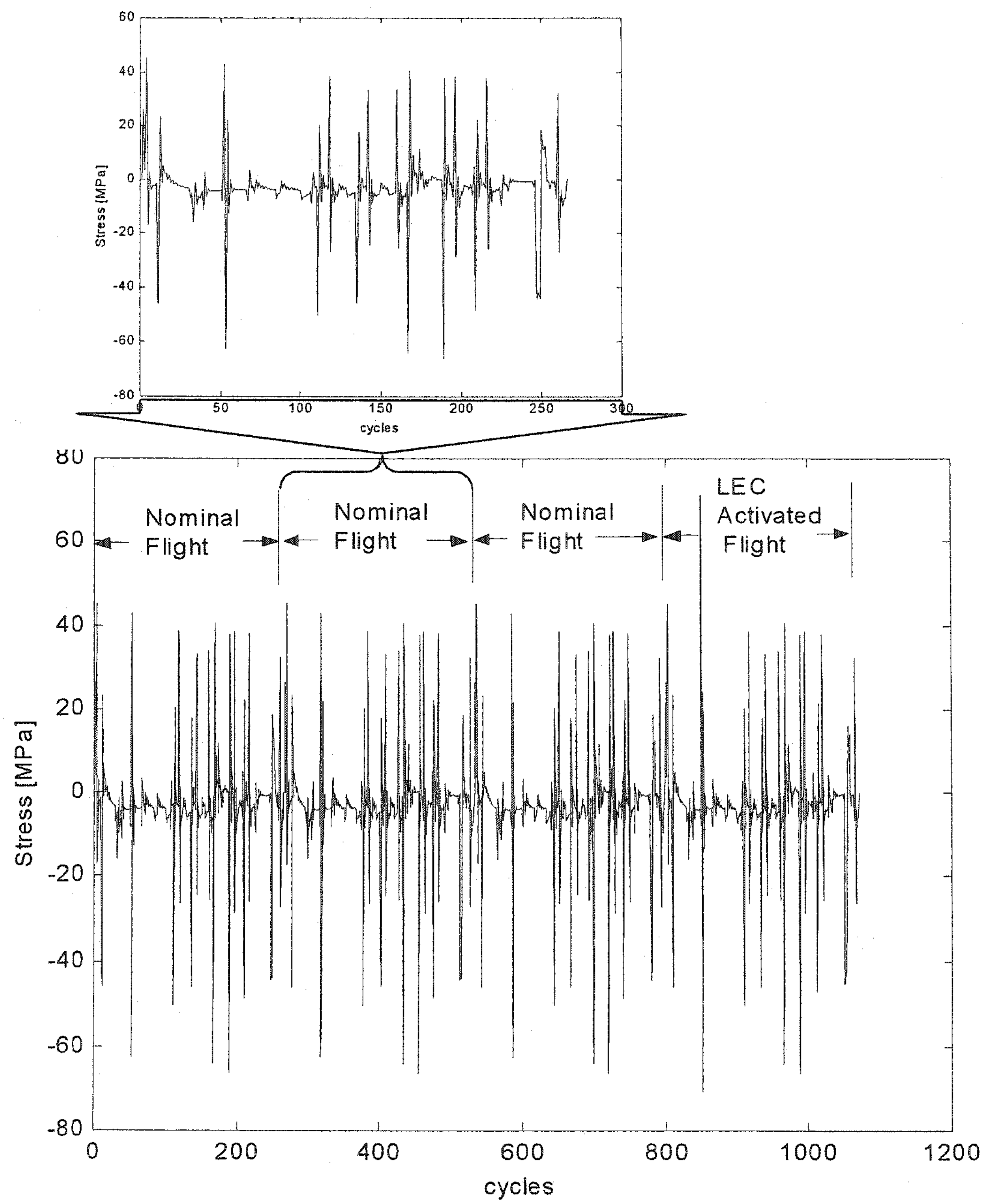

Figure 7.2 Stress of Multiple Missions with Additional LEC Activated Mission

continuous service. Nominal flight will be repeated until the number of nominal high stress cycles reaches the pre-defined overload interval. Although application of overload in every overload interval results in maximum structural life, it is unrealistic to expect that the natural occurrence interval of overload is close to the pre-defined fixed overload interval. During each overload interval, tens of flights are expected depending on number of nominal high stress experienced in each flight.

Two possible cases can be considered. The first case is the vehicles that experience near periodic stress history concerning lone term usage of the vehicle. The aircrafts in this sorts can be commercial passenger vehicles and cargo vehicles. In this case, the overload interval can be assumed to be fixed. Based on the natural overload occurrence interval, the overload interval can be estimated. The second case is the vehicles that experience non-periodic stress history. For the vehicles in the second case, variable overload interval can be considered, and the optimal overload ratio is calculated every time overload is naturally experienced. The aircrafts in this sort can be fighter airplanes or other military vehicles which is under various mission requirements. By generating the optimal overload at the naturally experienced overload interval, the structural life of the component of interest can be still dramatically increased although the overload interval is varied. This argument is based on the cumulative damage concept. Note occurrence of multiple overloads within very short interval is not considered in this dissertation. Overload interval in this research is pre-defined as 1,000 *cyc* since the mission developed in Chapter 6 is assumed to be repeated over the lifetime of the aircraft. In actual implementation of LEC logic, the overload interval should be determined considering the actual overload application interval of the vehicle mission and flying environment.

Recall from Chapter 2 that the load for the crack model can be simply represented as a combination of nominal high stress σ_{max1} and overload stress σ_{max2} as shown in Figure 7.3. Also from Chapter 1 that the nominal high stress σ_{max1} represents frequently generated high stress during nominal missions. For example, σ_{max1} can be a highest stress of relatively high pitch maneuver which is quite frequent during flight. The overload σ_{max2} represents an occasional high stress due to emergency maneuvers or unexpected air conditions, etc. Overload is uncommon when considered on a per flight basis, but quite common when considering overall lifetime of aircraft structures. Applying the optimal overload σ_{max2}^* with appropriate overload interval produces maximum structural life.[29,85,86] Note, the stresses that are significantly higher dominate the crack propagation.

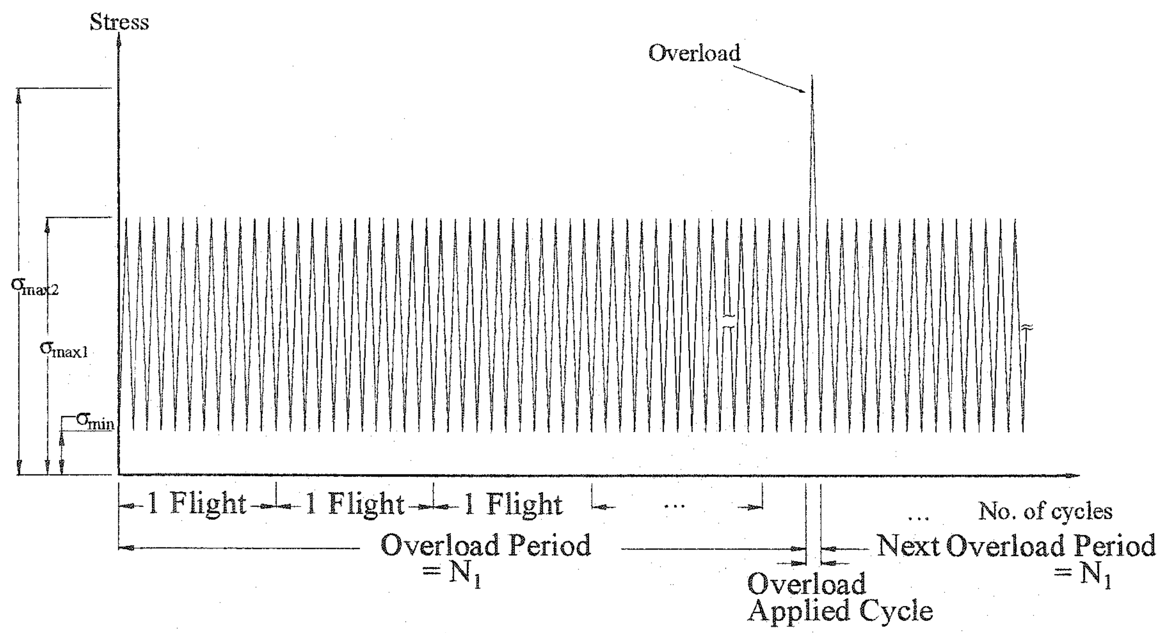

Figure 7.3 Definition of Overload and Overload Interval

On the other hand, relatively and considerably lower stress can be neglected when considering only the dominating part of stress response. Through applying this to Figure 7.3, one can observe that the stresses near 40 *MPa* dominate the crack growth, and stresses that are significantly smaller than 40 *MPa* have minor effect on crack growth. Note this behavior is usually more significant for random stress application such as the stress response in Figure 7.3. This fact can be found in any fatigue crack related literature.[1,5,11]

Now, determination of the overload magnitude which can be expressed as overload ratio is considered. Recall the overload ratio is defined as overload stress magnitude σ_{max2} divided by nominal high stress σ_{max1}. Overload ratio R_o is expressed as

$$R_o = \frac{\sigma_{\max 2}}{\sigma_{\max 1}} \tag{7.1}$$

Recall the optimal overload ratio R_o^* depends upon overload interval I_o. The optimal overload ratio R_o^*, can be computed from Eq. (3.28) from Chapter 2. Considering fixed overload interval I_o^{fixed}, optimal overload ratio is expressed as

$$R_o^* = 0.49 \times \log_{10} I_o^{fixed} + 0.93 \tag{7.2}$$

Eq. (7.2) allows the calculation of R_o^* at given I_o. The fixed overload interval I_o^{fixed} is pre-defined considering the R_o^* and I_o relationship. R_o^* usually lies between 2-3 depending on I_o, and the maximum structural life at R_o^* also varies due to the value of I_o. Using Equation (7.2), the optimal overload value can be calculated for the corresponding overload interval. Also, sub-optimal overload value can be defined when the optimal overload level is not feasible considering vehicle stability and performance.

7.2 Construction of a Stress-Maneuver Relationship Table

A stress-maneuver relationship is established in this section. When the vehicle motion command is given from the pilot - which is replaced by autopilot here-, the LEC logic should be able to compute the control gain that can achieve the desired stress level. In practice, the LEC logic needs to identify the stress level that will be generated by each gain using the pre-identified maneuver-stress relationship table, so the LEC logic can compute the appropriate command level to drive the vehicle motion. In order to establish the nonlinear relationship between the gain and resulting stress/load of the aircraft structures, a number of vehicle motion response curves need to be generated from simulation of many different maneuvers.

Consider the stress-maneuver relationship of longitudinal motion. Through simulation, lateral directional motion showed considerably lower contribution to the stress, implying minor contribution to the crack growth. This fact can be derived from the motion and stress response in Figures 6.3 - 6.17. This is because the autopilot system relies only on aileron and differential deflection of horizontal tail for lateral directional motion not using elevator to accelerate the lateral motion. Simulation results also show that climb/descent rate (vertical velocity of the vehicle) does not have a significant effect on the stress. In other words, resulted wing stress does not change significantly as climb/descent rate is changed. Besides, acceleration rate of altitude change showed significant contribution to the resulted wing stress.

Observation of the motion response and resulting stress also indicate that the pitch rate has significant contribution to the stress response. The stress is significantly high when Q is significantly high. Figure 7.4 and 7.5 give clear observation of the relationship between these two parameters. Note, when stress is near 40 *MPa*, pitch rate Q is near 4 *deg/s* while stress is about 45 *MPa* when Q is 4.5 *deg/s*. This shows that the pitch rate Q can be an indicator of resulting stress if the nonlinear functionality between pitch rate and stress is identified. This is based on the concept that the pitch maneuver can be idealized to the standard maneuver type such as Figure 7.6 (a)-(d) for roll maneuver.[7] The flight record of different roll maneuvers were stored, and plotted on the same figure, Figure 7.6 (a). After some processing, such as normalization of time, taking mean values, smoothing, and normalization of amplitude, the recorded roll rate can be illustrated as a series of similar curves as shown in Figure 7.6 (b). Figure 7.6 (c) shows the idealized roll maneuver, and Figure 7.6 (d) illustrates final curve representing roll maneuver.

The Stress of the structural component for the standard maneuver can be calculated, and this implies that it is possible to assume that a particular maneuver such as roll or pitch can be considered as a standard maneuver, and the resulting stress of the standard maneuver can be also considered as a standard stress in the similar manner. Simulation result also indicate that pitch rate and stress relationship may vary depending upon flight condition such as altitude and speed of the vehicle. Therefore, a set of simulations for different altitude and speed should be conducted in order to establish the nonlinear relationship between pitch rate Q and stress. Because pitch rate Q is not an independent state but an induced state depending upon the command input, the effective means to control Q should be available for LEC logic. So, the LEC logic can issue the command input to influence FCS in order to drive the vehicle to the desired motion behavior.

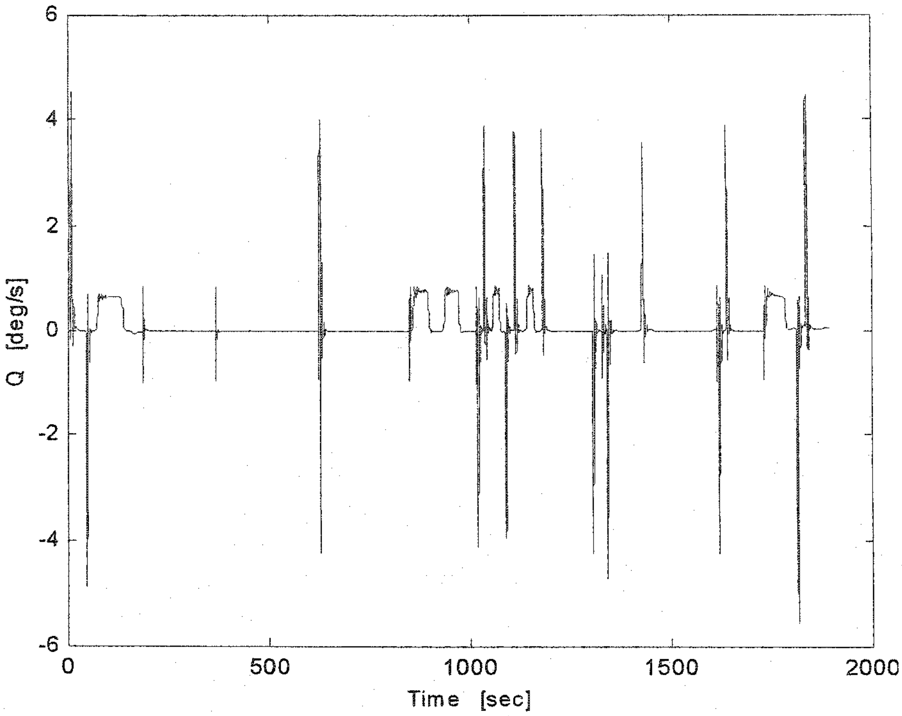

Figure 7.4 Q Response of Nominal Flight

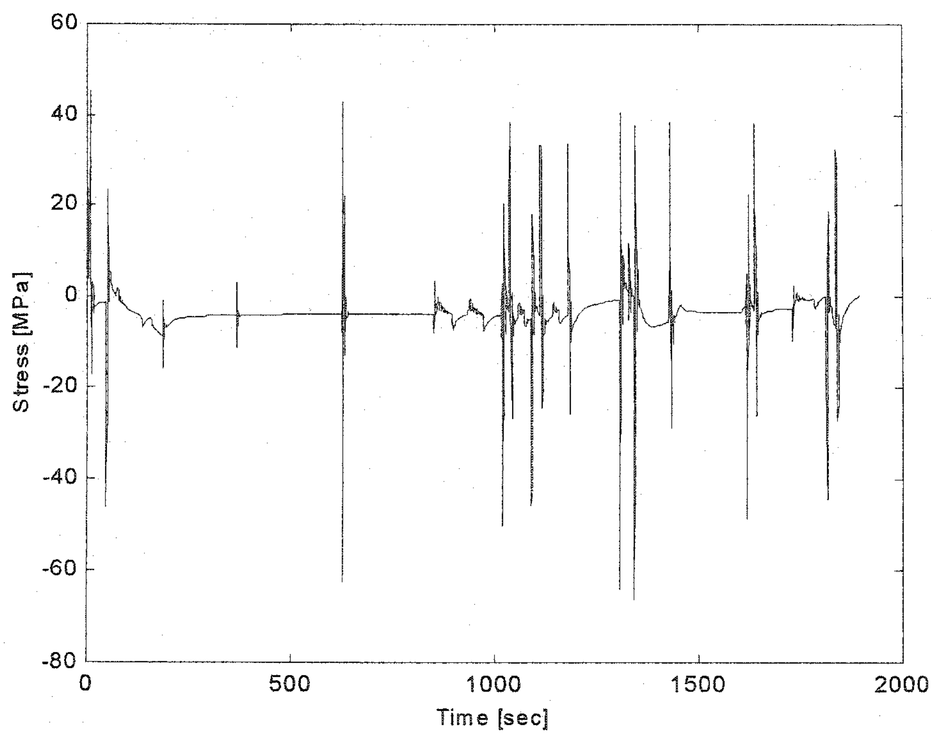

Figure 7.5 Stress Response of Nominal Flight

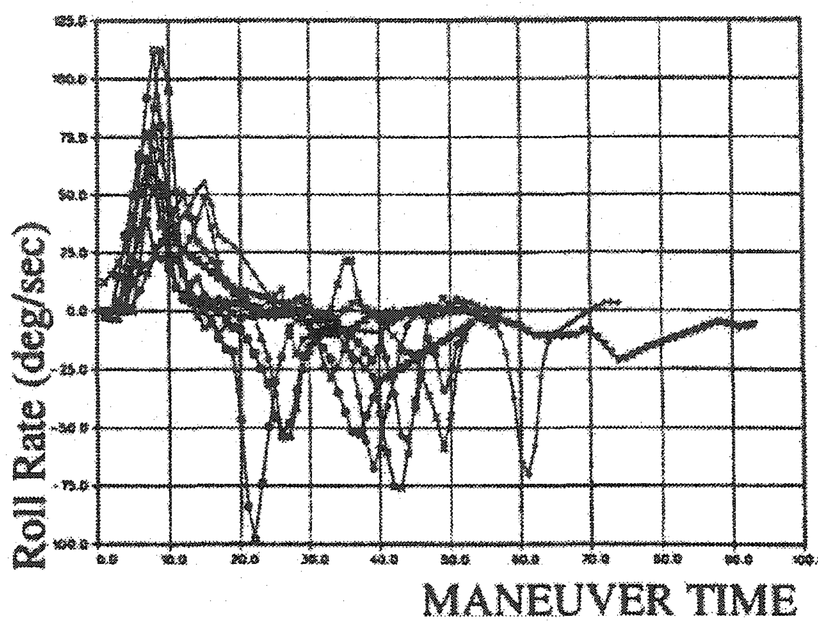

Figure 7.6 (a) Recorded Operational Parameter – Roll Rate[7]

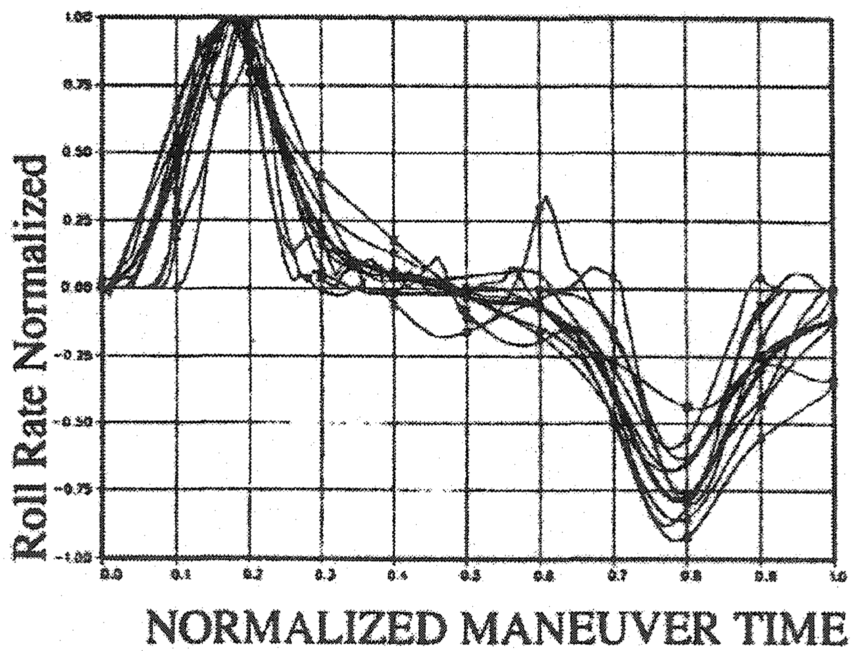

Figure 7.6 (b) Normalized Record of Roll Rate[7]

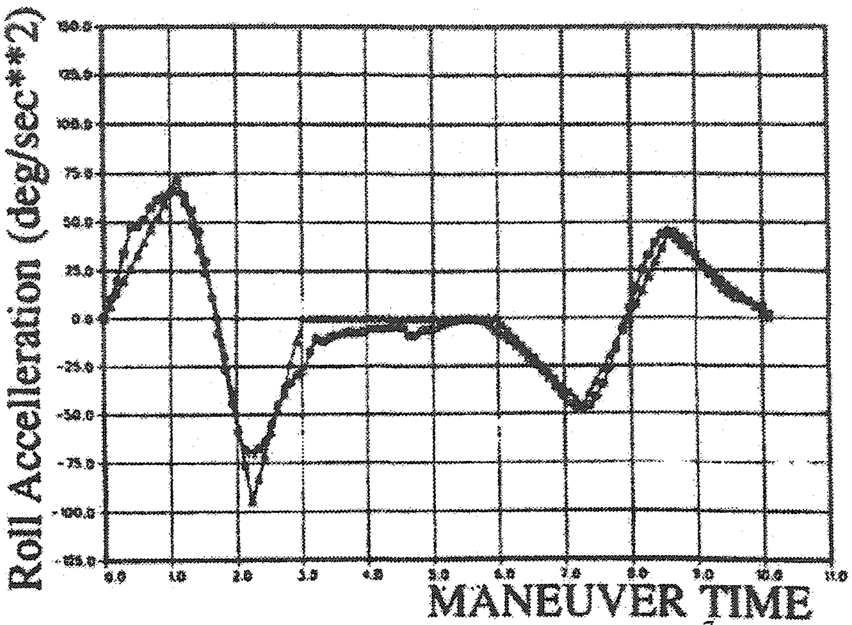

Figure 7.6 (c) Idealized Record of Roll Rate[7]

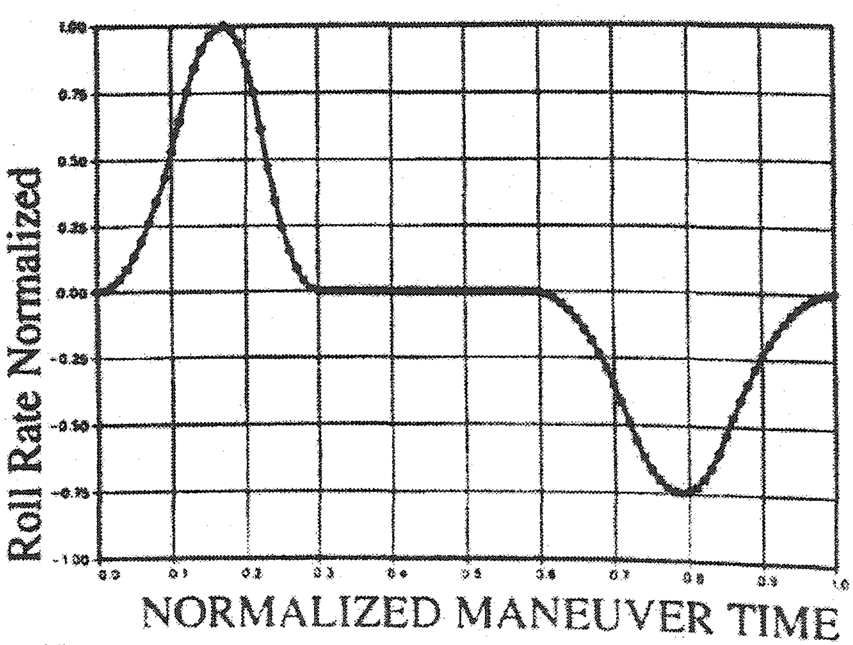

Figure 7.6 (d) Operational Roll Rate Time Histories for Standard Maneuver Type[7]

It is found that the Q level can be adjusted by placing additional control gain in as shown in Figure 7.7. Recall the acceleration rate of pitch maneuver has significant effect on stress. Placing the gain value K_{Fe} in F_e loop can have a similar influence as acceleration rate change. Through modifying gain value K_{Fe}, large variation of Q can be obtained. Therefore, the stress-maneuver relationship should be constructed in terms of nonlinear functionality between K_{Fe} and load instead of functionality between Q and load. Table 7.1 shows the simulated cases. 14 different gain values for 42 different flight conditions are simulated. Simulated flight conditions are 7 different altitudes and 6 different speeds as shown in Table 7.1. In each altitude, the vehicle starts from the listed altitude and climbs 1,500 *ft*. The resulting motion behavior and stress response are recorded. In selecting altitudes for simulation, the mission start altitude, cruise altitude, and highest altitude of the mission are taken account as well as at every 5,000 *ft* altitude increment. Simulated speed is also primarily based on the velocity range of the developed mission. In each of 42 different flight conditions, the gain K_{Fe} was changed from 1 to 2.3

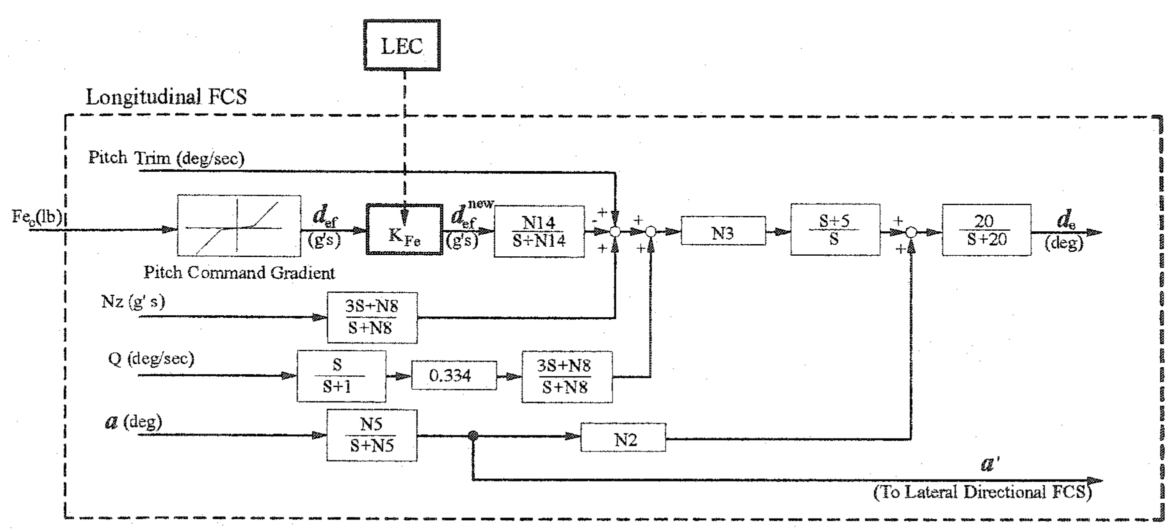

Figure 7.7 Modified Longitudinal FCS with K_{Fe}

Table 7.1 Simulated Cases

Speed \ Altitude		1,000 [*ft*]	5,000 [*ft*]	7,000 [*ft*]	10,000 [*ft*]	15,000 [*ft*]	20,000 [*ft*]	22,000 [*ft*]
200 [*knot*]	*A*	✓	×	×	×	×	×	×
	B	×	×	×	×	×	×	×
250 [*knot*]	*A*	✓	✓	✓	×	×	×	×
	B	✓	✓	✓	×	×	×	×
300 [*knot*]	*A*	✓	✓	✓	✓	✓	✓	×
	B	✓	✓	✓	✓	✓	×	×
350 [*knot*]	*A*	✓	✓	✓	✓	✓	✓	✓
	B	✓	✓	✓	✓	✓	✓	✓
400 [*knot*]	*A*	✓	✓	✓	✓	✓	✓	✓
	B	✓	✓	✓	✓	✓	✓	✓
440 [*knot*]	*A*	✓	✓	✓	✓	✓	✓	✓
	B	×	✓	✓	✓	✓	✓	✓

✓ : Simulated Case
× : Not Simulated Case

by 0.1. First seven values (K_{Fe} = 1-1.6) are denoted as case *A* in Table 7.1, and second seven values (K_{Fe} = 1.7-2.3) are denoted as *B* in Table 7.1. Note, the flight envelope of lower right corner and top left corner are less stable than other area as found in literatures.[9,98] Therefore, simulation of some flight conditions is not possible because the instability of the vehicle increases as gain increases although the particular flight condition is stable with nominal gain values (K_{Fe} = 1). This explains the blanks of Table 7.1. The vehicle motion response of each gain in each flight condition is applied to the wing structural model, and stress response is generated. Stress of each maneuver is computed, and shown in Table 7.2. Table 7.2 is the modified version of Table 7.1 showing the computed value of the table. Table 7.2 shows the gain values and corresponding highest stress of each pitch maneuver.

Table 7.2 Gain-Stress Relationship Table

Speed (Altitude)	K_{Fe}	Stress at 1,000 *ft* [*MPa*]	Stress at 5,000 *ft* [*MPa*]	Stress at 7,000 *ft* [*MPa*]	Stress at 10,000 *ft* [*MPa*]	Stress at 15,000 *ft* [*MPa*]	Stress at 20,000 *ft* [*MPa*]	Stress at 22,000 *ft* [*MPa*]
200 [*knot*]	*1.0*	47.5648	0	0	0	0	0	0
	1.1	50.5601	0	0	0	0	0	0
	1.2	53.3462	0	0	0	0	0	0
	1.3	55.9817	0	0	0	0	0	0
	1.4	58.7531	0	0	0	0	0	0
	1.5	61.4117	0	0	0	0	0	0
	1.6	64.4641	0	0	0	0	0	0
	1.7	0	0	0	0	0	0	0
	1.8	0	0	0	0	0	0	0
	1.9	0	0	0	0	0	0	0
	2.0	0	0	0	0	0	0	0
	2.1	0	0	0	0	0	0	0
	2.2	0	0	0	0	0	0	0
	2.3	0	0	0	0	0	0	0
250 [*knot*]	*1.0*	42.5411	47.4335	50.1438	0	0	0	0
	1.1	45.0691	50.1936	53.1060	0	0	0	0
	1.2	47.3546	53.0608	55.9951	0	0	0	0
	1.3	49.7861	55.7219	58.9373	0	0	0	0
	1.4	52.1401	58.1790	61.6887	0	0	0	0
	1.5	54.3401	60.4756	64.2515	0	0	0	0
	1.6	56.3877	63.0421	66.6276	0	0	0	0
	1.7	58.2846	65.4852	68.8221	0	0	0	0
	1.8	60.0975	67.8061	71.3804	0	0	0	0
	1.9	62.2046	70.0058	73.8282	0	0	0	0
	2.0	64.2246	72.0857	76.1664	0	0	0	0
	2.1	66.1584	74.0466	78.3960	0	0	0	0
	2.2	68.0064	75.8896	80.5179	0	0	0	0
	2.3	69.7693	77.6157	82.5329	0	0	0	0
300 [*knot*]	*1.0*	41.4317	45.6238	47.8409	78.3543	58.3858	66.8043	0
	1.1	42.9952	47.5134	50.0526	78.3543	61.6294	70.9217	0
	1.2	44.8840	49.8627	52.5795	78.3543	65.0410	74.7705	0
	1.3	46.9924	51.9673	54.9975	78.3543	68.1750	78.2844	0
	1.4	48.9733	54.3845	57.2319	78.3543	71.0476	82.1189	0
	1.5	50.7610	56.6419	59.7619	78.3543	74.2678	85.7529	0
	1.6	52.6651	58.7262	62.1397	67.0493	77.3166	89.1753	0
	1.7	54.6579	60.6410	64.3677	69.6749	80.1957	92.3884	0
	1.8	56.5334	62.3898	66.4480	72.1735	82.9069	95.3941	0
	1.9	58.2926	64.5396	68.3826	74.5460	85.4515	98.1943	0
	2.0	59.9364	66.6091	70.1731	76.7939	87.8312	100.7914	0
	2.1	61.4658	68.5824	72.0488	78.9181	90.0466	104.2558	0
	2.2	62.8818	70.4606	74.1834	80.9195	92.1772	111.8752	0
	2.3	64.1854	72.2446	76.2375	82.7993	94.7830	120.3606	0
350 [*knot*]	*1.0*	41.1779	45.6622	48.1049	51.9911	59.0230	67.5129	79.8541
	1.1	42.0686	46.3805	48.6598	52.3659	59.1529	67.0133	70.6066
	1.2	43.6361	48.1555	50.4708	54.4901	61.9079	70.2310	74.3021
	1.3	45.2437	50.1607	52.6654	56.8930	64.6088	73.8270	77.8091
	1.4	47.1467	52.0900	54.5975	59.2521	67.4427	77.1590	81.5627
	1.5	48.8618	54.2330	56.8773	61.3702	70.3106	80.2303	85.0837
	1.6	50.3925	56.2051	59.0295	63.7543	72.9747	83.0444	88.3740

Table 7.2 Gain-Stress Relationship Table (Continued)

	1.7	52.2673	58.0085	61.0145	66.1310	75.4389	86.2456	91.4362
	1.8	54.0626	59.6454	62.8344	68.3596	77.7069	89.3770	94.2725
	1.9	55.7452	61.5825	64.4912	70.4412	79.9981	92.3545	97.1773
	2.0	57.3162	63.5479	66.4731	72.3773	82.6185	95.1790	100.3786
	2.1	58.7766	65.4163	68.4973	74.1692	85.1262	97.8516	103.4490
	2.2	60.1275	67.1882	70.4275	75.8182	87.5222	100.3738	106.3899
	2.3	61.3701	68.8642	72.2643	77.7003	89.8077	102.7468	109.2024
400 [*knot*]	*1.0*	40.8782	45.1414	47.6563	51.7931	59.3075	68.0950	73.1714
	1.1	41.1364	45.5938	47.9648	51.7931	58.4075	66.7592	73.1714
	1.2	42.5960	46.9495	49.3185	53.0702	59.9373	67.8541	73.1714
	1.3	44.0857	48.6357	51.0321	54.9810	62.4287	70.7526	74.3705
	1.4	45.3052	50.3586	52.9722	57.2014	64.7567	73.9222	77.8041
	1.5	46.3333	51.9621	54.6697	59.2935	67.4235	76.8233	81.0535
	1.6	47.9086	53.8648	56.7010	61.1604	70.0052	79.4589	84.0525
	1.7	49.6715	55.6046	58.6616	63.3673	72.3911	82.3750	86.8062
	1.8	51.3155	57.1838	60.4679	65.5497	74.5835	85.3525	89.5558
	1.9	52.8428	58.8381	62.1220	67.5940	76.5847	88.1715	92.6750
	2.0	54.2546	60.7450	63.6257	69.5015	78.9323	90.8330	95.6523
	2.1	55.5529	62.5579	65.4938	71.2736	81.3581	93.3389	98.4892
	2.2	56.7386	64.2776	67.4006	72.9116	83.6743	95.6915	101.1872
	2.3	58.0006	65.9042	69.2218	74.4168	85.8813	97.8927	103.7477
440 [*knot*]	*1.0*	49.5283	45.3747	47.1183	51.7931	58.7918	79.5368	89.6848
	1.1	58.9846	45.1773	47.4874	51.7931	58.1919	79.5368	89.6848
	1.2	56.6226	46.8169	48.5330	52.1441	58.8147	79.5368	89.6848
	1.3	54.7165	48.2213	50.2451	53.9667	60.8305	79.5368	89.6848
	1.4	53.8571	49.3168	51.6519	55.8024	63.2533	79.5368	89.6848
	1.5	51.0768	50.1167	52.8421	57.5381	65.4906	79.5368	89.6848
	1.6	47.7398	51.4198	54.4812	59.5810	67.6506	79.5368	89.6848
	1.7	0	53.1778	56.5042	61.4337	70.1665	79.9000	84.3518
	1.8	0	54.7920	58.3948	63.1797	72.5181	82.2353	87.0374
	1.9	0	56.4074	60.1520	65.3502	74.7071	84.8306	89.5119
	2.0	0	58.3369	61.7795	67.4083	76.7354	87.5959	91.7774
	2.1	0	60.1850	63.2776	69.3555	78.6046	90.2304	94.6566
	2.2	0	61.9530	64.6495	71.1923	80.3165	92.7348	97.4482
	2.3	0	63.6422	66.1939	72.9197	82.4535	95.1100	100.1216

7.3 LEC and LEC Activating Logic

7.3.1) Concept of LEC Activating Logic

There are two major roles for LEC activating logic. The first role is to determine the nominal high stress level using the load history of the vehicle structure. Second is to determine when the LEC logic should be activated. In order to achieve these roles, the LEC activating logic must store peak stresses of selected maneuvers when the critical vehicle state is beyond the threshold value. As discussed in Chapter 1, the LEC logic is suggested to be developed focusing on structural life of selected structural components, and the effect of this LEC logic on other non-selected components will also be investigated. This implies that the stress of selected components or multiple components should be available for LEC activating logic. Three options are suggested. One way is to directly measure the stress of the selected components. This option may be the best to acquire the exact stress of the components, but requires large amount of direct cost and labor. Also, this option is not available for this research. Another option is to simulate the stress response of the selected vehicle components. This simulation takes a bit of time which is critical for computing appropriate commands for LEC logic since the architecture of stress determination logic will also be included in LEC logic. The last option is to predict the stress level through establishing the relationship between state of the vehicle and stress through a set of simulations before the actual application of LEC logic.

The third option is selected. Recall from Section 7.2 that Q can be the indicator of level of load. Once the relationship between K_{Fe} and load is identified in Section 7.2, the

Table 7.3 Pitch Rate-Stress Relationship Table

Speed	K_{Fe}	Q at 1,000 *ft* [*rad*]	Q at 5,000 *ft* [*rad*]	Q at 7,000 *ft* [*rad*]	Q at 10,000 *ft* [*rad*]	Q at 15,000 *ft* [*rad*]	Q at 20,000 *ft* [*rad*]	Q at 22,000 *ft* [*rad*]
200 [*knot*]	*1.0*	0.1248	0	0	0	0	0	0
	1.1	0.1344	0	0	0	0	0	0
	1.2	0.1436	0	0	0	0	0	0
	1.3	0.1527	0	0	0	0	0	0
	1.4	0.1664	0	0	0	0	0	0
	1.5	0.1944	0	0	0	0	0	0
	1.6	0.2199	0	0	0	0	0	0
	1.7	0	0	0	0	0	0	0
	1.8	0	0	0	0	0	0	0
	1.9	0	0	0	0	0	0	0
	2.0	0	0	0	0	0	0	0
	2.1	0	0	0	0	0	0	0
	2.2	0	0	0	0	0	0	0
	2.3	0	0	0	0	0	0	0
250 [*knot*]	*1.0*	0.0969	0.0999	0.1027	0	0	0	0
	1.1	0.1015	0.1076	0.1109	0	0	0	0
	1.2	0.1087	0.1153	0.1189	0	0	0	0
	1.3	0.1157	0.1228	0.1266	0	0	0	0
	1.4	0.1226	0.1301	0.1342	0	0	0	0
	1.5	0.1293	0.1373	0.1415	0	0	0	0
	1.6	0.1359	0.1443	0.1488	0	0	0	0
	1.7	0.1424	0.1512	0.1558	0	0	0	0
	1.8	0.1487	0.1579	0.1627	0	0	0	0
	1.9	0.1550	0.1645	0.1695	0	0	0	0
	2.0	0.1611	0.1710	0.1780	0	0	0	0
	2.1	0.1671	0.1782	0.1932	0	0	0	0
	2.2	0.1730	0.1920	0.2082	0	0	0	0
	2.3	0.1789	0.2074	0.2251	0	0	0	0
300 [*knot*]	*1.0*	0.0877	0.0902	0.0916	0.0940	0.0983	0.1066	0
	1.1	0.0842	0.0878	0.0902	0.0941	0.1015	0.1103	0
	1.2	0.0895	0.0940	0.0967	0.1010	0.1090	0.1185	0
	1.3	0.0951	0.1001	0.1031	0.1077	0.1163	0.1264	0
	1.4	0.1007	0.1062	0.1093	0.1143	0.1234	0.1341	0
	1.5	0.1062	0.1121	0.1154	0.1207	0.1304	0.1417	0
	1.6	0.1116	0.1178	0.1215	0.1271	0.1372	0.1491	0
	1.7	0.1169	0.1235	0.1274	0.1333	0.1439	0.1563	0
	1.8	0.1221	0.1291	0.1332	0.1393	0.1505	0.1634	0
	1.9	0.1273	0.1346	0.1388	0.1453	0.1569	0.1742	0
	2.0	0.1323	0.1400	0.1445	0.1512	0.1632	0.1897	0
	2.1	0.1373	0.1453	0.1500	0.1570	0.1695	0.2061	0
	2.2	0.1422	0.1506	0.1554	0.1626	0.1764	0.2223	0
	2.3	0.1470	0.1557	0.1608	0.1683	0.1900	0.2596	0
350 [*knot*]	*1.0*	0.0802	0.0825	0.0838	0.0857	0.0895	0.0942	0.0962
	1.1	0.0777	0.0797	0.0809	0.0828	0.0866	0.0921	0.0952
	1.2	0.0780	0.0809	0.0825	0.0856	0.0916	0.0991	0.1024
	1.3	0.0828	0.0860	0.0878	0.0912	0.0979	0.1059	0.1095
	1.4	0.0875	0.0911	0.0931	0.0968	0.1040	0.1126	0.1164
	1.5	0.0922	0.0961	0.0982	0.1023	0.1100	0.1191	0.1231
	1.6	0.0968	0.1010	0.1033	0.1076	0.1159	0.1255	0.1298

Table 7.3 Pitch Rate-Stress Relationship Table

	1.7	0.1012	0.1058	0.1082	0.1129	0.1216	0.1317	0.1362
	1.8	0.1056	0.1105	0.1131	0.1181	0.1273	0.1379	0.1426
	1.9	0.1098	0.1151	0.1179	0.1232	0.1329	0.1439	0.1488
	2.0	0.1139	0.1197	0.1226	0.1282	0.1383	0.1498	0.1549
	2.1	0.1179	0.1241	0.1272	0.1331	0.1437	0.1557	0.1610
	2.2	0.1219	0.1285	0.1318	0.1379	0.1490	0.1614	0.1669
	2.3	0.1258	0.1328	0.1363	0.1427	0.1542	0.1670	0.1743
400 [*knot*]	*1.0*	0.0798	0.0763	0.0771	0.0789	0.0823	0.0862	0.0881
	1.1	0.0778	0.0743	0.0750	0.0766	0.0799	0.0838	0.0858
	1.2	0.0760	0.0729	0.0735	0.0754	0.0797	0.0853	0.0880
	1.3	0.0790	0.0775	0.0782	0.0803	0.0851	0.0913	0.0942
	1.4	0.0831	0.0820	0.0828	0.0852	0.0904	0.0972	0.1003
	1.5	0.0870	0.0864	0.0873	0.0899	0.0956	0.1029	0.1062
	1.6	0.0908	0.0906	0.0917	0.0945	0.1008	0.1085	0.1120
	1.7	0.0944	0.0948	0.0960	0.0991	0.1058	0.1141	0.1178
	1.8	0.0979	0.0987	0.1001	0.1035	0.1107	0.1195	0.1234
	1.9	0.1013	0.1026	0.1042	0.1078	0.1155	0.1248	0.1289
	2.0	0.1045	0.1064	0.1081	0.1120	0.1203	0.1300	0.1343
	2.1	0.1076	0.1100	0.1119	0.1162	0.1249	0.1352	0.1397
	2.2	0.1106	0.1135	0.1156	0.1202	0.1295	0.1403	0.1449
	2.3	0.1135	0.1169	0.1192	0.1242	0.1341	0.1453	0.1501
440 [*knot*]	*1.0*	0.1586	0.1111	0.0778	0.0747	0.0772	0.0810	0.0827
	1.1	0.1723	0.1059	0.0762	0.0729	0.0752	0.0789	0.0806
	1.2	0.1615	0.1066	0.0740	0.0707	0.0728	0.0771	0.0792
	1.3	0.1536	0.1067	0.0771	0.0753	0.0777	0.0825	0.0849
	1.4	0.1500	0.1065	0.0812	0.0798	0.0825	0.0878	0.0904
	1.5	0.1475	0.1069	0.0852	0.0841	0.0872	0.0930	0.0958
	1.6	0.1630	0.1067	0.0889	0.0883	0.0918	0.0981	0.1011
	1.7	0	0.1063	0.0927	0.0924	0.0963	0.1031	0.1063
	1.8	0	0.1057	0.0962	0.0963	0.1007	0.1080	0.1114
	1.9	0	0.1038	0.0996	0.1001	0.1050	0.1128	0.1164
	2.0	0	0.1052	0.1029	0.1038	0.1092	0.1175	0.1213
	2.1	0	0.1080	0.1060	0.1074	0.1133	0.1222	0.1261
	2.2	0	0.1105	0.1091	0.1108	0.1173	0.1267	0.1309
	2.3	0	0.1129	0.1121	0.1142	0.1212	0.1313	0.1356

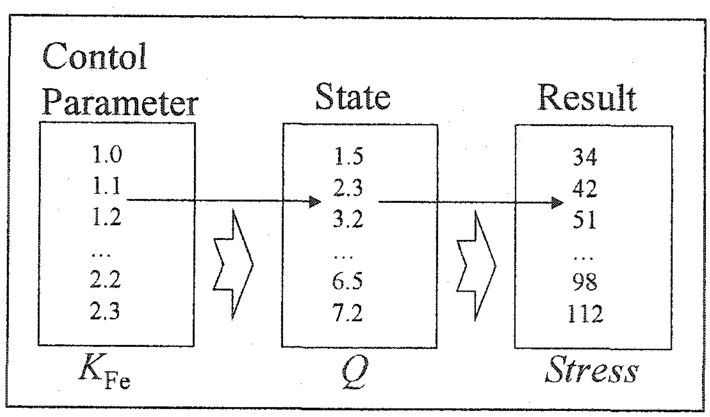

Figure 7.8 Control Gain, State, and Stress Relationship

vehicle state Q in each case can be monitored, and the relationship between Q and load can also be identified as shown in Table 7.3. Figure 7.8 shows concept of this nonlinear mapping. Therefore, through monitoring Q, the resulting stress level can be approximately predicted. The LEC activating logic uses this relationship as reference table to determine stress level. When the value of Q reaches above threshold value Q_{cr}, activating logic starts to store the Q values of the particular maneuver, and the highest Q of the maneuver is identified. Once the highest maneuver is identified, the corresponding stress is calculated using linear interpolation of Q-stress table. Note, the threshold value of Q is set to 1.5 *deg/sec*.

Highest stress of the stress response is calculated, and the computed stress is the nominal high stress of the maneuver. This nominal high stress is stored every time the maneuver is harsh enough to push Q above threshold value Q_{cr}. Each time nominal high stress of the vehicle is computed and stored, the LEC activating logic also compares the length of stored nominal high stress and pre-defined overload interval. When the number of nominal high stress cycle is equal to the pre-defined overload interval, LEC activating logic activates LEC logic. Also, the mean value of nominal high stress is computed, and made available for LEC logic as σ_{max1}.

7.3.2) Concept of LEC Logic

The LEC logic consists of two parts. The first part is the optimal overload stress σ_{max2}^* calculation logic, and the second part is the required gain K_{Fe} determination logic. Recall from Chapter 3 that two parameters needed to calculate optimal overload stress are optimal overload ratio R_o^* and nominal high stress σ_{max1}. As mentioned in the beginning of this chapter, the optimal overload ratio R_o^* can be described as function of overload interval I_o. Since the overload interval is pre-defined, the optimal overload ratio R_o^* is also fixed. In addition, the nominal high stress σ_{max1} is provided from the LEC activating logic. Therefore, the optimal overload stress σ_{max2}^* can be calculated using Equation (7.3).

$$\sigma_{max2}^* = R_o^* \cdot \sigma_{max1} \tag{7.3}$$

Now, the control gain for the resulting desired stress is computed from the gain and stress relationship table, Table 7.2. Linear interpolation logic is used for calculating the appropriate gain value. The location of desired stress σ_{max2}^* on the table is identified for the current altitude and speed of the vehicle. Once the desired stress is located on the table, the corresponding control gain, K_{Fe} is calculated. The computed K_{Fe} is now applied to the FCS as shown in Figure 7.7. When the control gain is calculated, the same K_{Fe} gain value is maintained during the LEC activated maneuver is executed.

In reality, although the LEC activating logic activates the LEC logic, the overload stress of desired level is not always possible to achieve through gain variation concerning current flight condition of the vehicle and available value of the relationship table. Two methods are employed for the feasible application of LEC logic. First, The LEC logic also calculates sub-optimal overload stress. Sub-optimal overload value is calculated by dividing the optimal value with sub-optimal weight R_{Sub}. The sub-optimal weight R_{Sub} is set to be 1.5 for the results shown below.

$$\sigma_{max2}^{Sub} = \frac{\sigma_{max2}^*}{R_{Sub}} \tag{7.4}$$

The second method is to leave LEC logic open until desired stress level is achievable. As observed in Table 7.2, the flight condition of the vehicle determines the maximum available stress of the pitch maneuver. The LEC logic computes the maximum available stress of the flight condition, and determines whether the LEC gain should be applied in this maneuver or should wait for the next maneuver. If the maximum available stress of the current flight condition is above the optimal or sub-optimal overload stress (depending on the setting and mission), the LEC gain is calculated, and applied to the FCS. If the maximum available stress is below the optimal or sub-optimal overload stress, LEC logic does not apply the LEC gain to FCS, and leaves the LEC logic activated until the maximum available stress is above the optimal or sub-optimal overload stress.

7.3.3) Detail of Overall LEC and LEC Activating Logic

Overall LEC and LEC activating logic is illustrated as a flow chart in Figure 7.9. The logic lying within the dotted line is the LEC logic, and remainder is LEC activating logic. The logic first checks current pitch rate Q. If Q is over the critical pitch rate Q_{cr}, the increment ik is increased. Also, the Q value of the current time step is recorded as a variable named Q_{accm}. Note, Q_{accm} denotes accumulated pitch rate Q of the maneuver while pitch rate stays above Q_{cr}. When a pitch maneuver is applied, Q value is gradually increased, and the logic starts recording the Q value if Q is greater than Q_{cr}. The logic keeps accumulation until Q decades below Q_{cr}. As soon as Q falls below Q_{cr}, the maximum pitch rate Q_{max} of the pitch maneuver is computed. Note this is the case when Q is less than or equal to Q_{cr}, and ik is non-zero value. Now, the logic runs the function

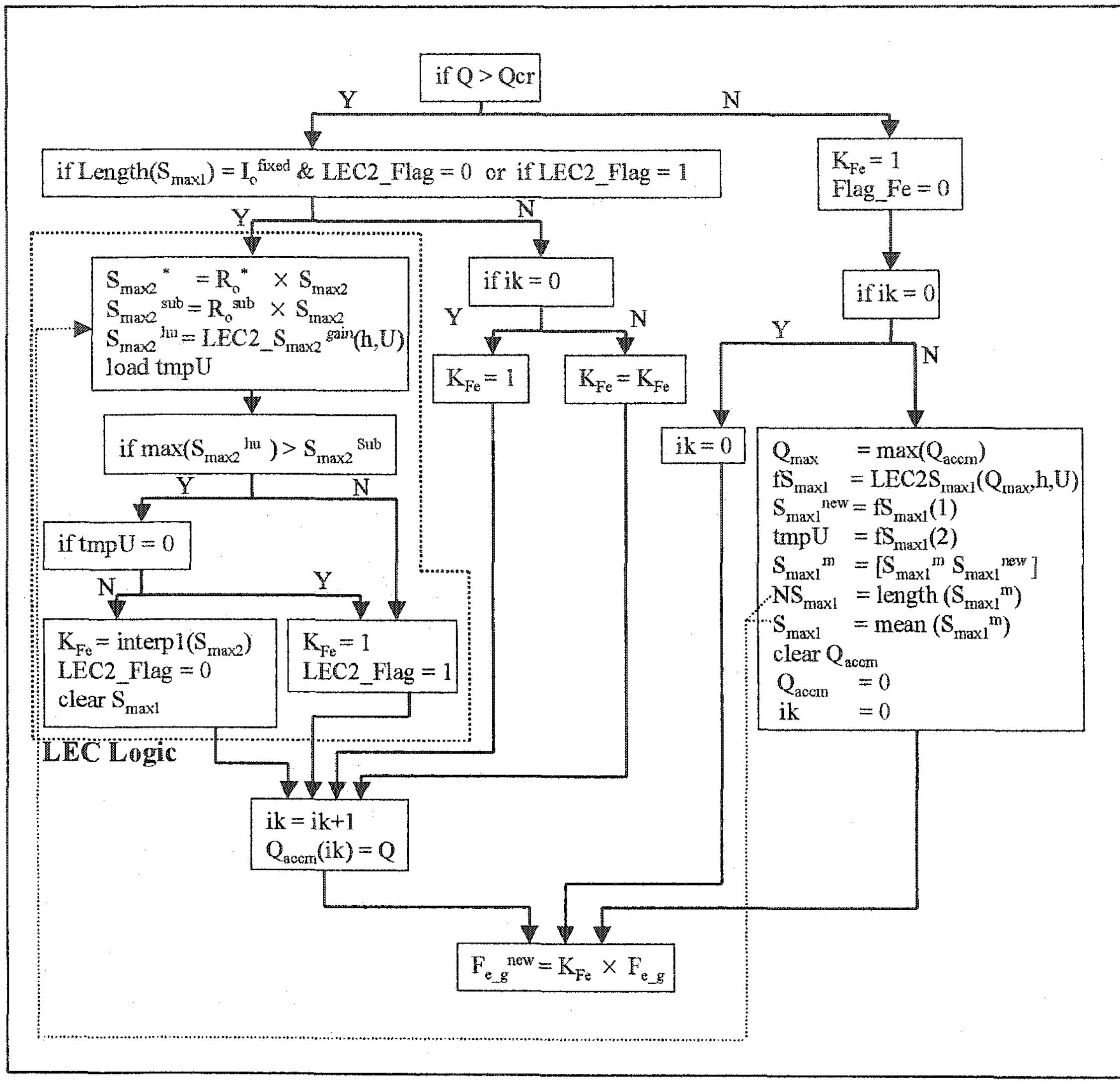

Figure 7.9 Overall LEC and LEC Activating Logic

named $LEC2S_{max1}$ which primary computes nominal high stress S_{max1}^{new}. $LEC2S_{max1}$ takes inputs that are current altitude and speed, and provides two outputs that are S_{max1}^{new} and *tmpU*. In the function $LEC2S_{max1}$, the stress corresponding to Q_{max} of the maneuver is computed using the Q-stress relationship table (Table 7.3), and the computed stress is denoted as S_{max1}^{new}. The indicator value *tmpU* becomes *0* when the current flight condition, h and U, are located outside the range of simulated cases of the table, and otherwise becomes *1*. After S_{max1}^{new} is calculated, this new nominal high stress S_{max1}^{new} is added to the previously accumulated nominal high stress S_{max1}^{m}, and this process of accumulating the nominal high stress is repeated every time Q exceeds Q_{cr} until the LEC logic is activated at the pre-defined overload interval I_o. Note, the critical pitch rate Q_{cr} can be set as a value that results S_{max1}^{new} that can give significant contribution to the crack growth. Note, the logic measures the length of S_{max1}^{m} where the length indicates the number of nominal high stress NS_{max1}, and takes mean value of S_{max1}^{m} which is nominal high stress S_{max1} for LEC logic. This way, S_{max1} of the maneuver is determined and stored. Next, Q_{accm} and *ik* are cleared, and set to initial value *0*.

When Q is greater than Q_{cr}, there are two cases activating LEC logic. The first case is when the length of S_{max1} is equal to I_o^{fixed} and *LEC_Flag* is equal to *0* at the same time. Another case to activate LEC logic is when *LEC2_Flag* is equal to *1*. *LEC2_Flag* is the indicator which is *1* when the overload stress of desired level cannot be obtained in current flight condition, so LEC is left activated while *LEC _Flag* is set to be *0* when the overload stress of desired level is available in current flight condition. Once the LEC logic is activated, optimal value S_{max2}^{*} and sub optimal value S_{max2}^{Sub} are computed from Equations (7.3) and (7.4). Function *LEC2_* S_{max2}^{gain} computes an available stress vector S_{max2}^{hu}. The vector is a series of stresses of each simulated gain values at the current flight condition. S_{max2}^{hu} is computed in following process. From Table 7.2, the new column for the current altitude is computed using linear interpolation of two nearest tested altitude values. Next, a set of stress of various gains for the current speed is also computed using linear interpolation of nearest two speed values. Now, a set of stress values for various gains is provided as $S_{max2}{}^{hu}$. From $S_{max2}{}^{hu}$, the gain K_{Fe} corresponding to the desired S_{max2} is computed.

Now, LEC determines if the desired stress is available in the current maneuver. If maximum value of vector $S_{max2}{}^{hu}$ is greater than $S_{max2}{}^{sub}$, at least sub-optimal overload is available. If not, the overload stress of desired level is not available from the table for the current flight condition, and application of the overload should be delayed until the desired overload is available. In this case, K_{Fe} is set to be default value *1*, and *LEC2_Flag* is set to be *1* indicating LEC must be activated whenever the pitch rate Q is over Q_{cr}. When maximum value of $S_{max2}{}^{hu}$ is greater than $S_{max2}{}^{sub}$, LEC logic checks if *tmpU* is equal to *0*. The indicator *tmpU* is 0 when the optimal or sub-optimal overload can be achieved in current flight condition. K_{Fe} of corresponding overload S_{max2} is computed when *tmpU* is not equal to *0*, and *LEC2_Flag* is set to be *0* and S_{max1} is cleared. If *tmpU* is equal to *0*, K_{Fe} is set to be *1*, and *LEC2_Flag* is set to be *1*.

If LEC is not activated and Q is greater than Q_{cr}, there are two cases. When LEC is activated, the gain value should be computed only one time, and the gain should be consistently applied during the pitch maneuver until Q falls down to Q_{cr}. Now, *ik* is checked. If *ik* is non-zero value, this indicates that the overload application maneuver is on the way, so K_{Fe} is consistently maintained as the computed value from LEC. If *ik* is equal to *0*, K_{Fe} is set to its default value *1*. When Q is greater than Q_{cr} and *ik* is equal to *0*, this time step does not have significant pitch maneuver neither in prior time step nor in this time step. When *ik* is not equal to *0*, the significant pitch maneuver ($Q > Q_{cr}$) has just finished.

7.4 Result of Life Extending Control

As a demonstration, simulation results of the LEC activated mission are shown in Figures 7.10-7.21. This can be compared with the nominal mission response in Figures 6.3-6.14. Since both the nominal and LEC activated missions perform the same mission, all the motion response is same except for the LEC influenced pitch maneuver 1,429 *sec* after the mission starts. Clear observation of this new pitch motion can be found in the middle figure of Figure 7.20. Note a high spike of elevator deflection angle δ_h observed at 1,429 *sec*. Motion response of all other points except for this LEC activated moment is same as the motion response of nominal mission since both cases are performing the same mission. In each nominal mission, 30 *cyc* of nominal high stress is recorded. Considering overload interval of 1,000 *cyc*, it takes 34 missions until the number of nominal high stress σ_{max1} reaches the overload interval. The number of nominal high stress cycles keep increasing until the overload interval is reached, and LEC is activated.

As shown in Chapter 6 for the nominal mission case, the motion response variables such as *P*, *Q*, *L*, and *M* were fed into the flexible wing structural model, and the model generated the stress response of the wing main spar. Figures 7.22 and 7.23 show the stress response of wing main spar at 10 *in* from the wing root in nominal and LEC activated case, respectively. Similarly, Figures 7.24-7.31 show the stress response of nominal and LEC activated mission for wing station 50, 100, 150, and 180, respectively. Note that the LEC logic is designed primary to extend structural life of wing station 150. The stress response of wing station 150 and 180 show significant difference between nominal and LEC activated cases. However, minor difference is observed in wing station 10, 50, and 100.

Now, the stress responses in Figures 7.22-7.31 are processed to be the appropriate input form for the dynamic crack growth model. The process includes extraction of peak values and elimination of negative data as discussed in Section 6.2. After the process, the load is fed into the crack growth model, and the result of crack growth in each case is plotted in Figures 7.32-7.36. Each figure shows structural life of the nominal mission only case as a dotted line and the LEC activated mission case as a solid line. Crack growth of multiple structural components, wing station 10, 50, 100, 150, and 180 are shown in the figures.

Significant life extension is observed in wing station 150 and 180 where the structural components are exposed to high stress. However, structural life of wing station 50 is even decreased. The structural life of wing station 50 is two order of magnitude longer than other components that are experiencing high stress; therefore structural life of this wing station is of less concern than the high stress region. In wing station 10 and 100, approximately the same structural life is observed, showing minor influence of LEC logic. Therefore, structural life of multiple components can be significantly extended by employing LEC logic. However, careful consideration is needed when applying the LEC logic because the structural life of some component can be decreased as observed in wing station 50.

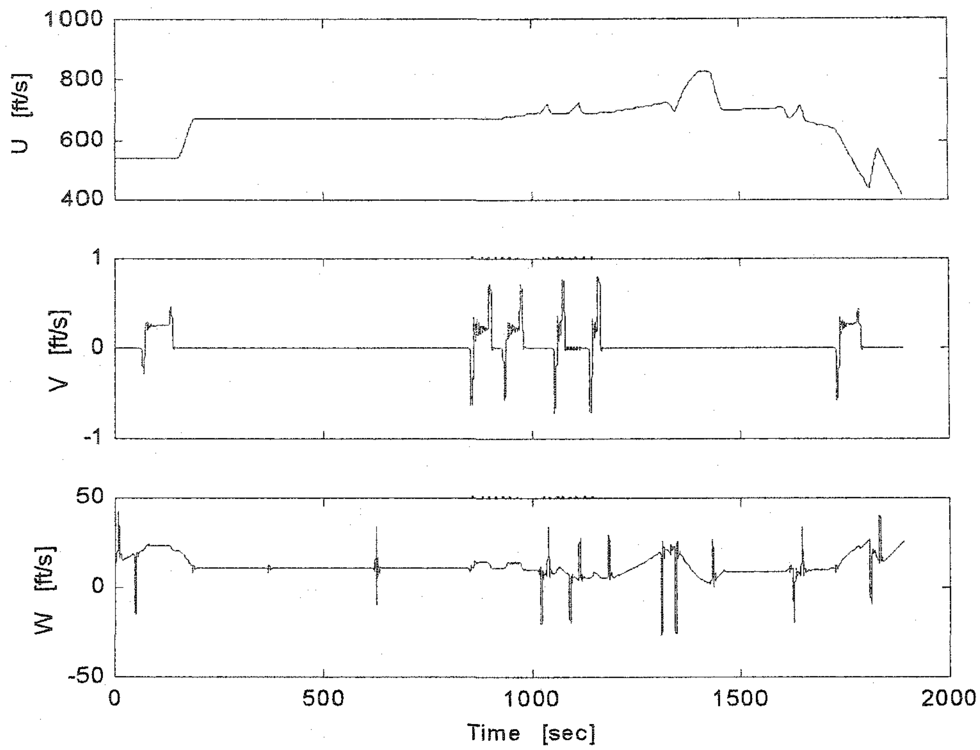

Figure 7.10 *U, V,* and *W* Response

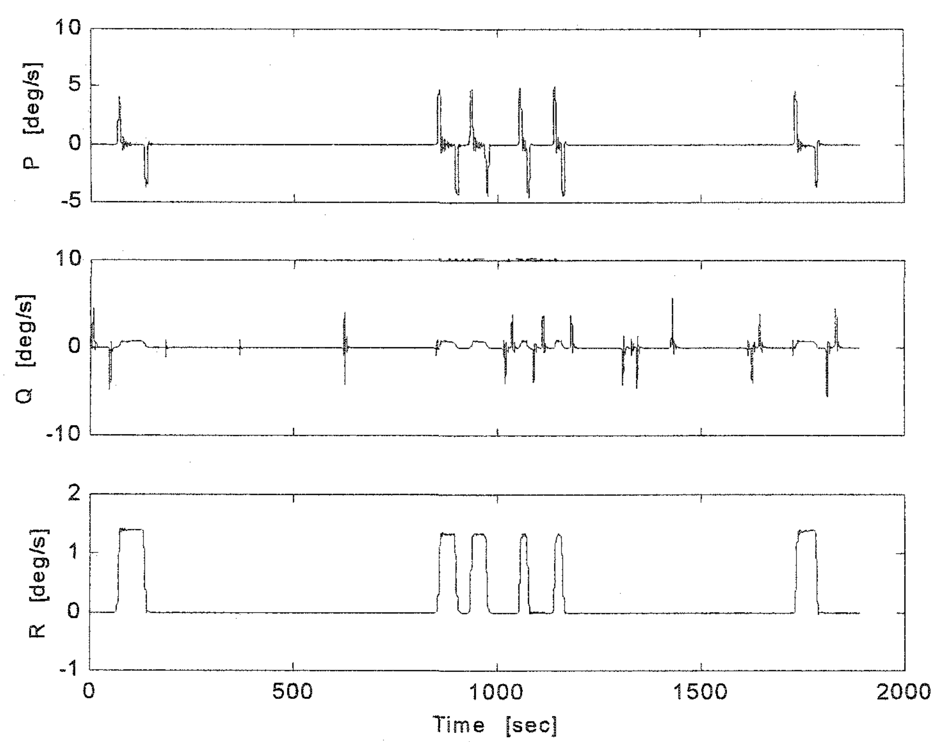

Figure 7.11 *P, Q,* and *R* Response

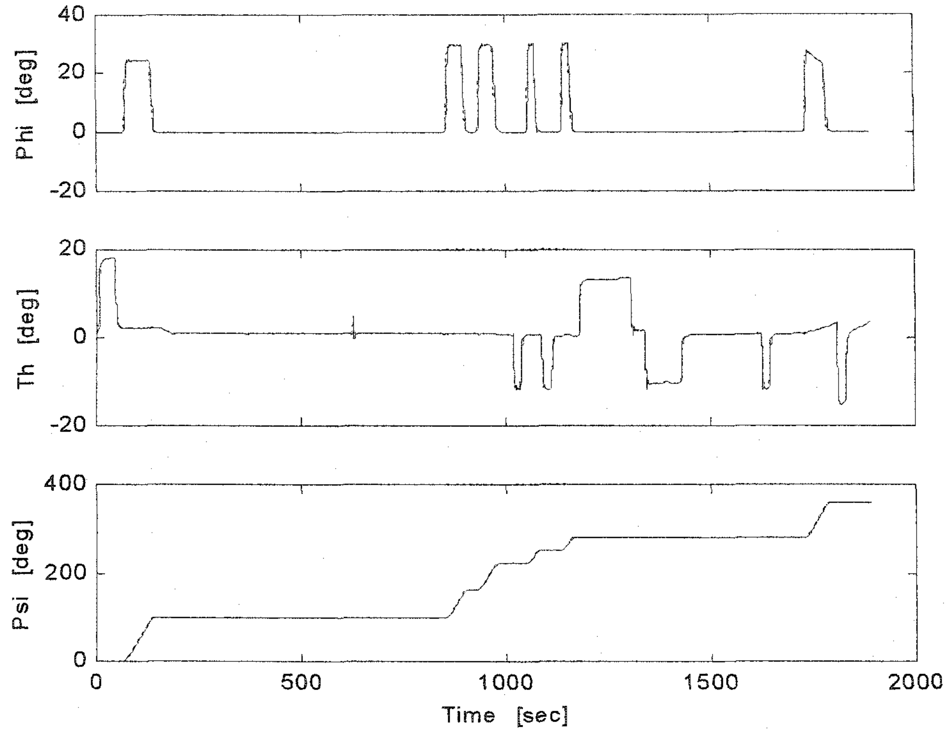

Figure 7.12 ϕ, θ, and φ Response

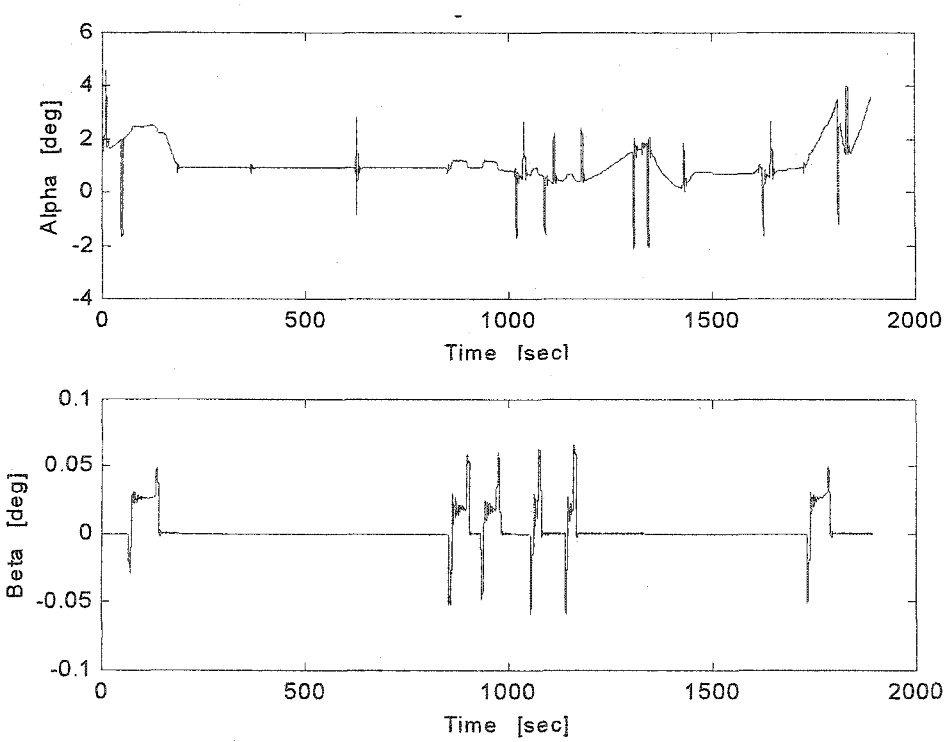

Figure 7.13 α and β Response

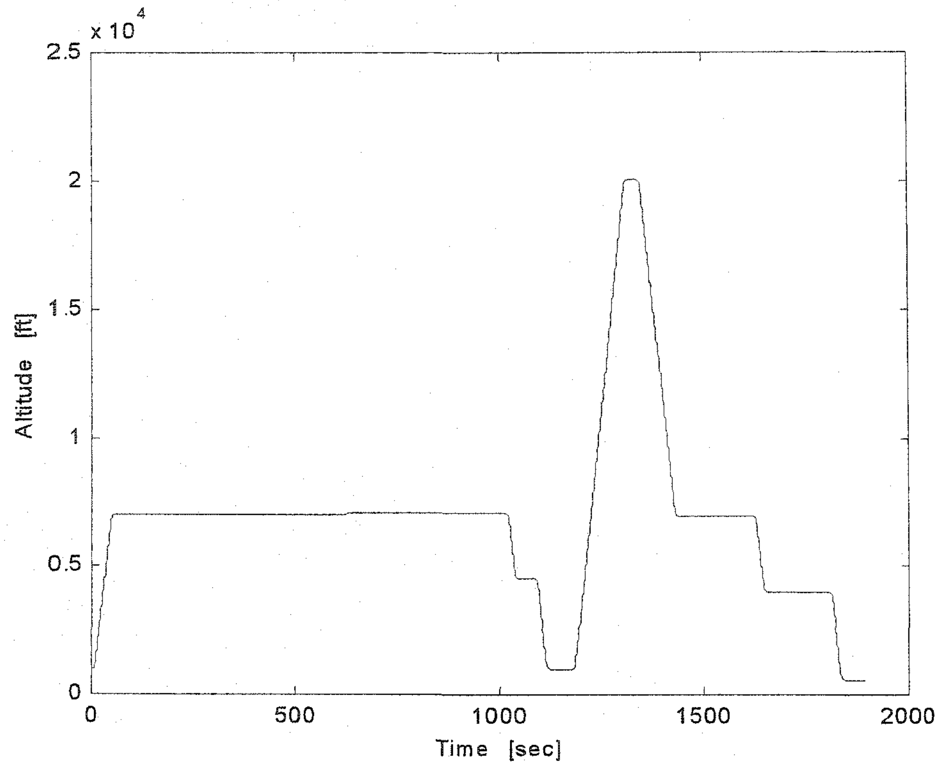

Figure 7.14 Altitude of the Aircraft (h)

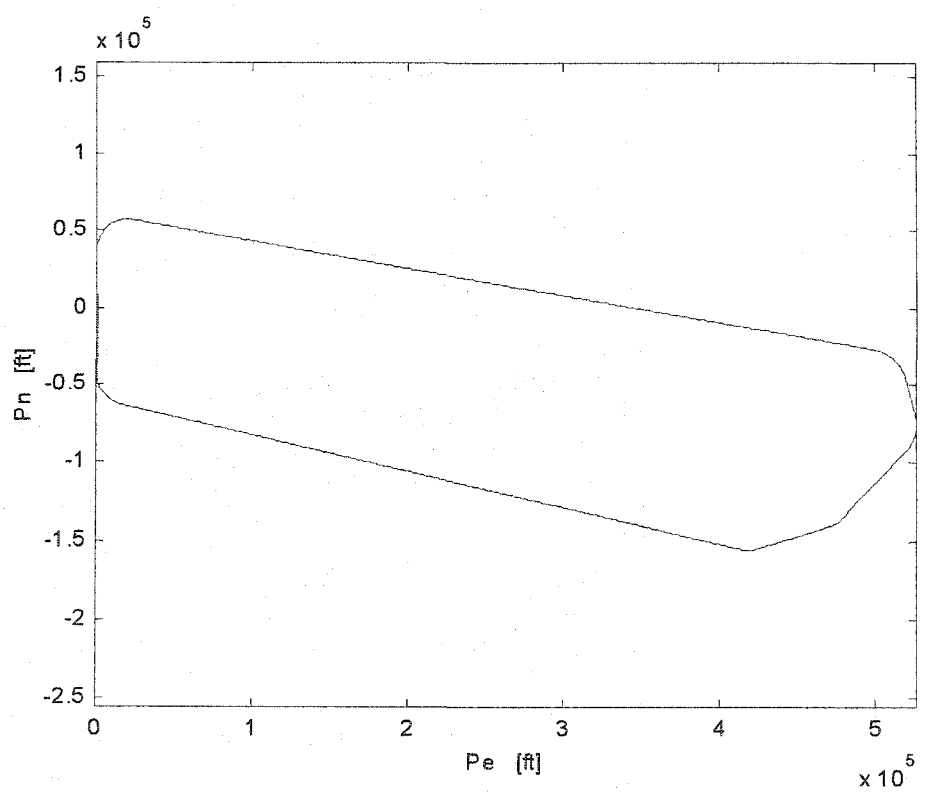

Figure 7.15 Plan View of Aircraft Motion (P_e and P_n)

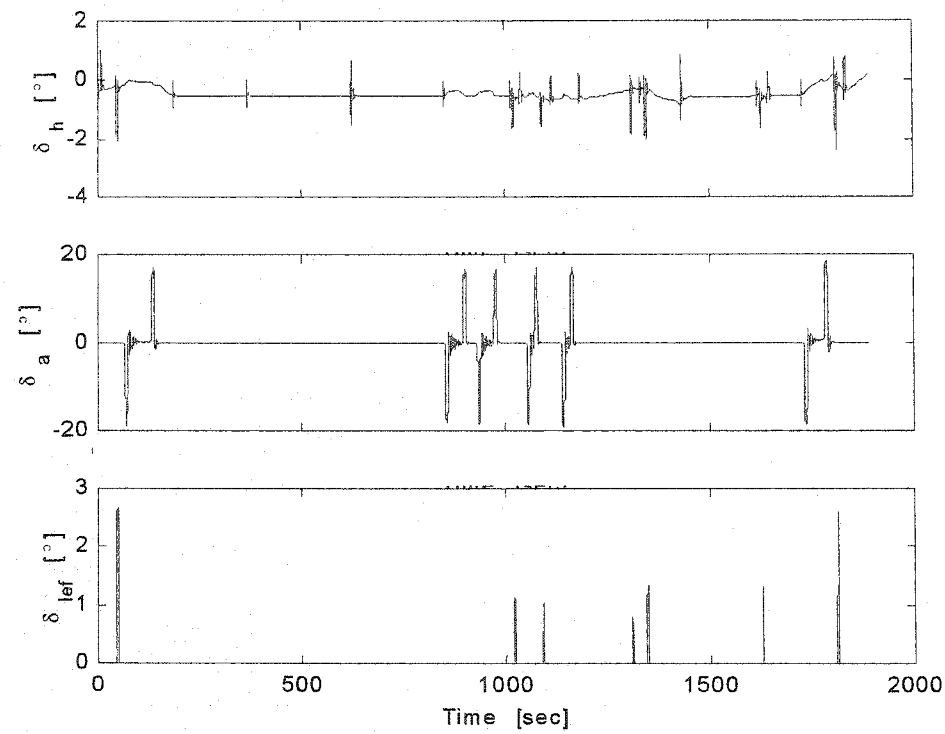

Figure 7.16 δ_h , δ_a , and δ_{lef} Response

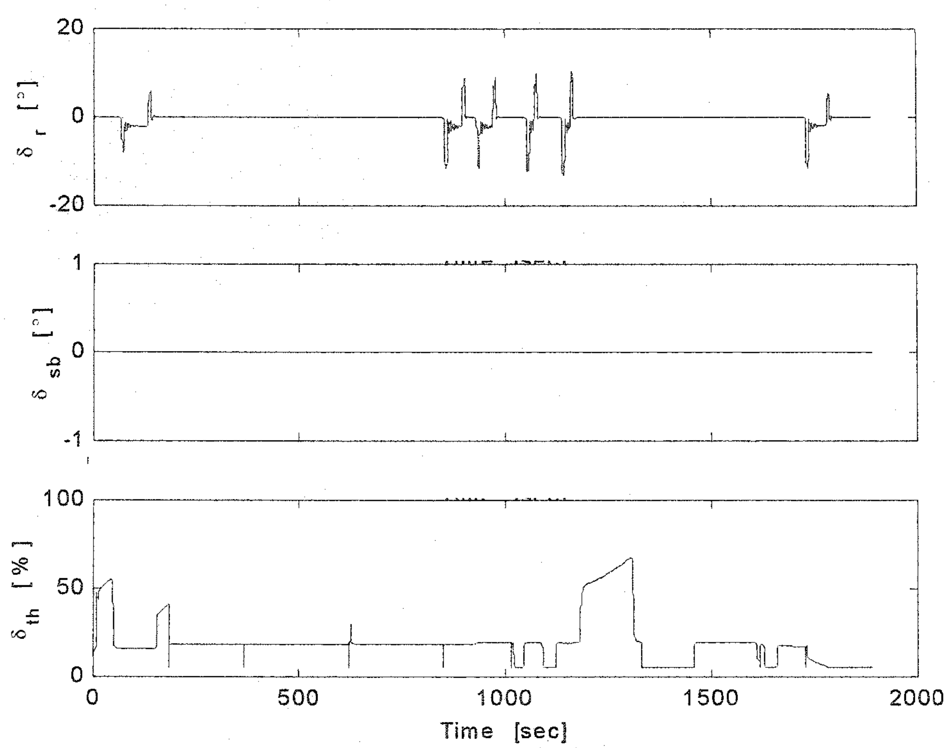

Figure 7.17 δ_r , δ_{sb} , and δ_{th} Response

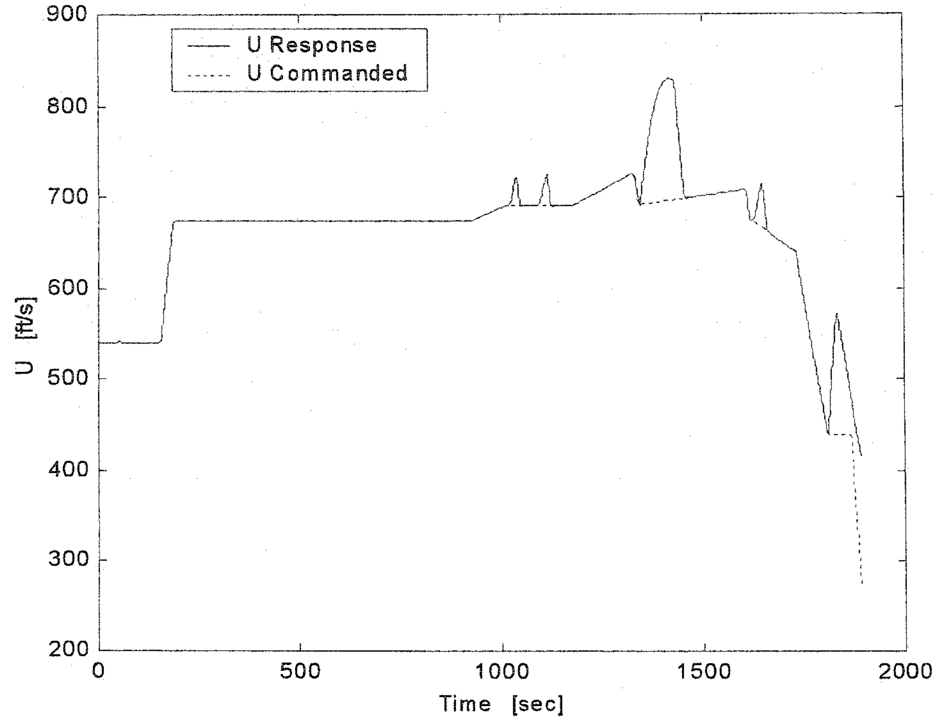

Figure 7.18 Desired Velocity Uc and U Response

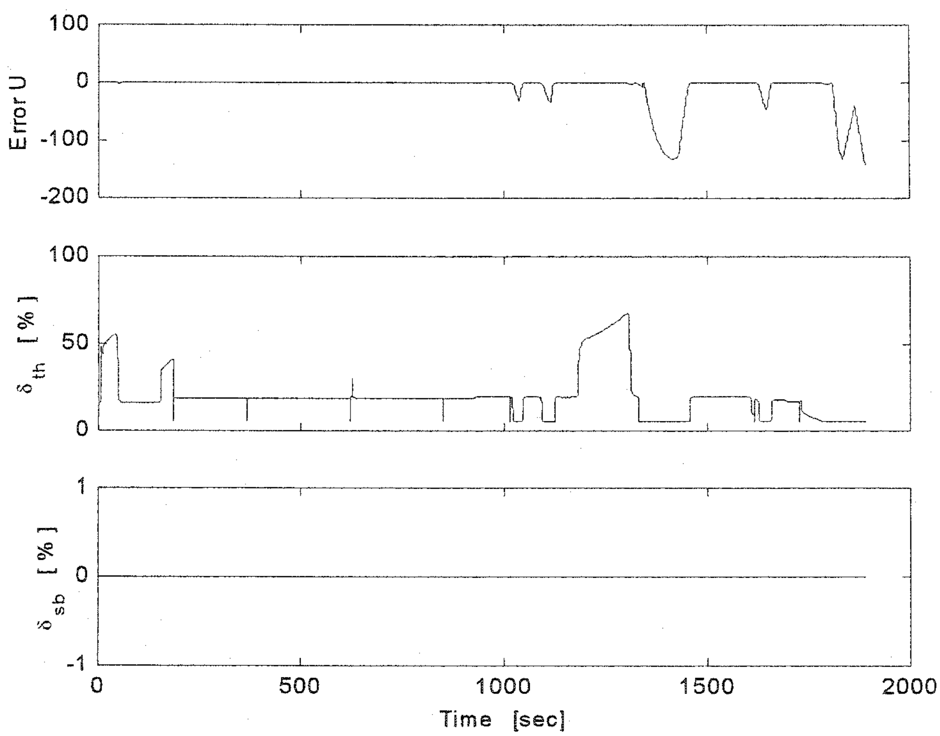

Figure 7.19 U_{error}, δ_{th}, and δ_{sb}, Response

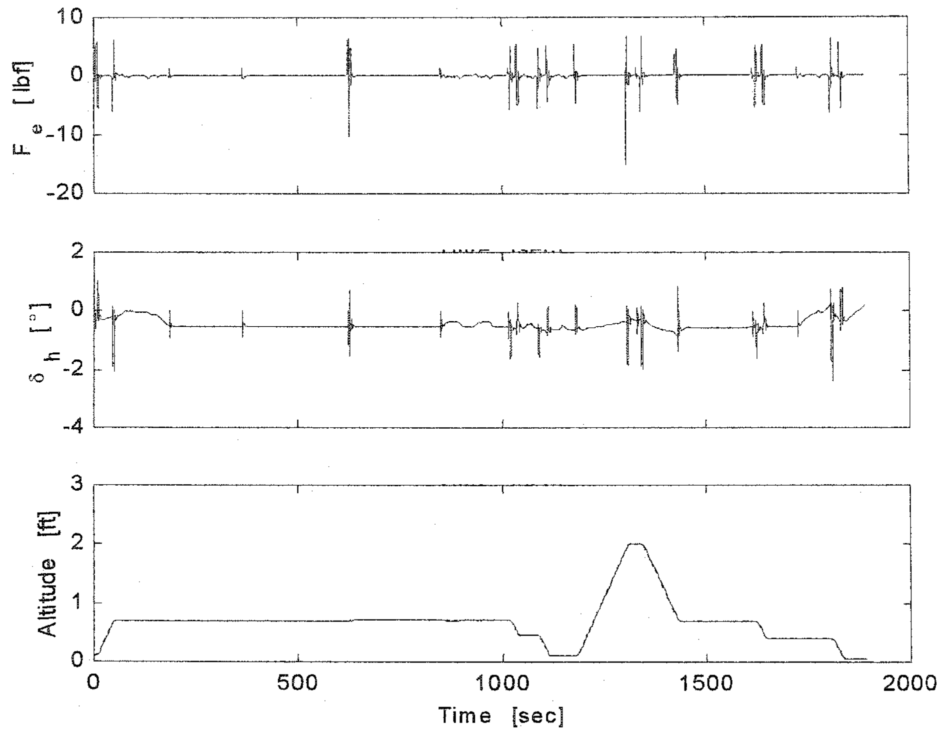

Figure 7.20 Altitude h, F_e, and δ_e Response

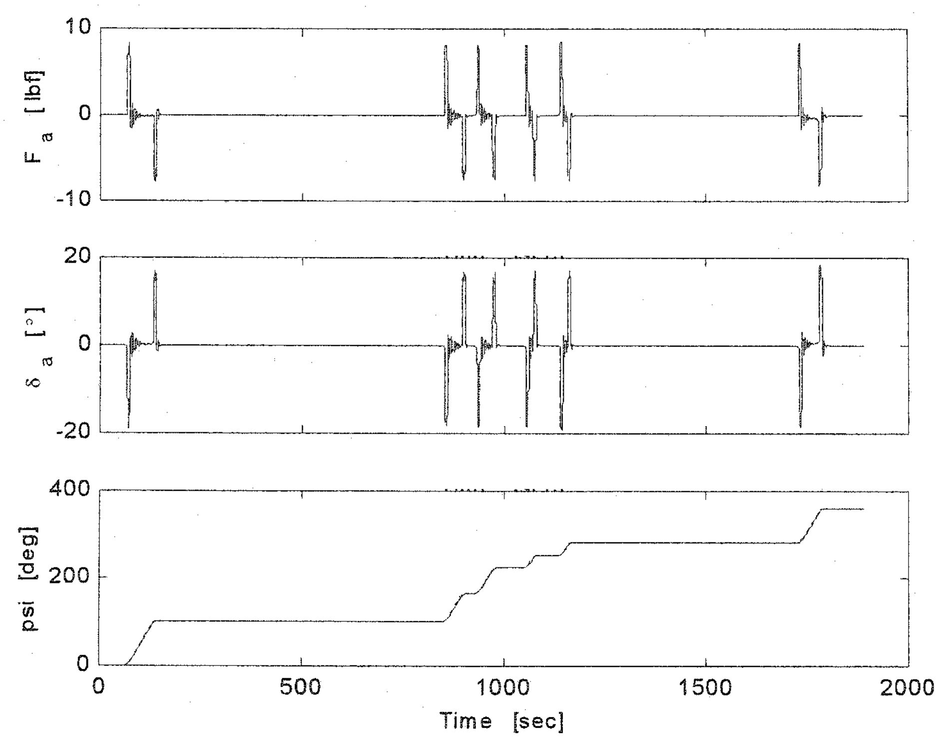

Figure 7.21 Heading Angle ψ, F_a, and δ_a Response

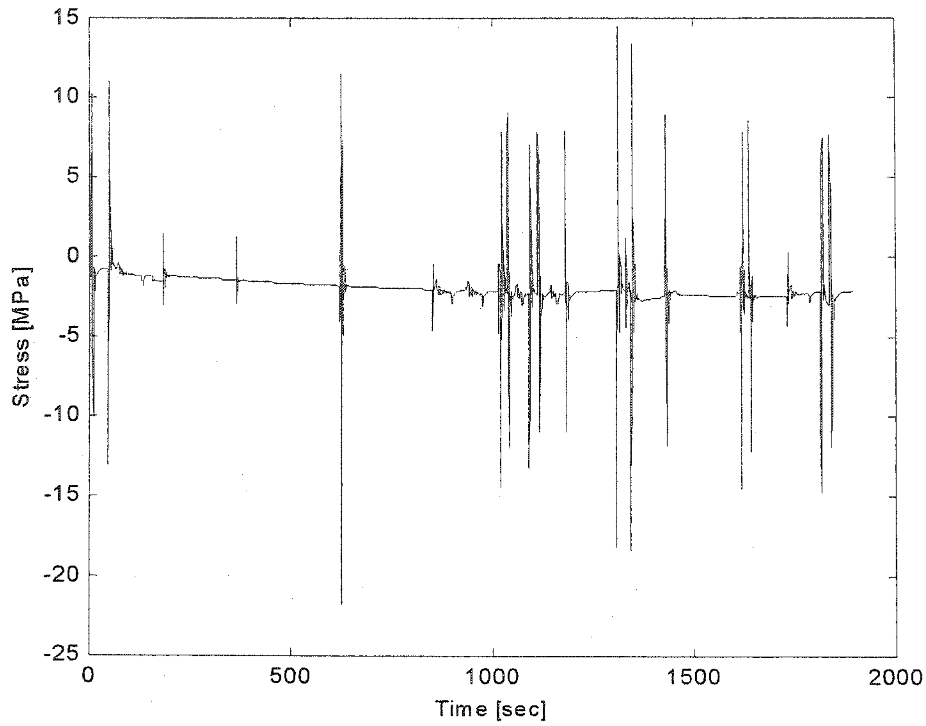

Figure 7.22 Stress Response of Wing Station 10 for Nominal Mission

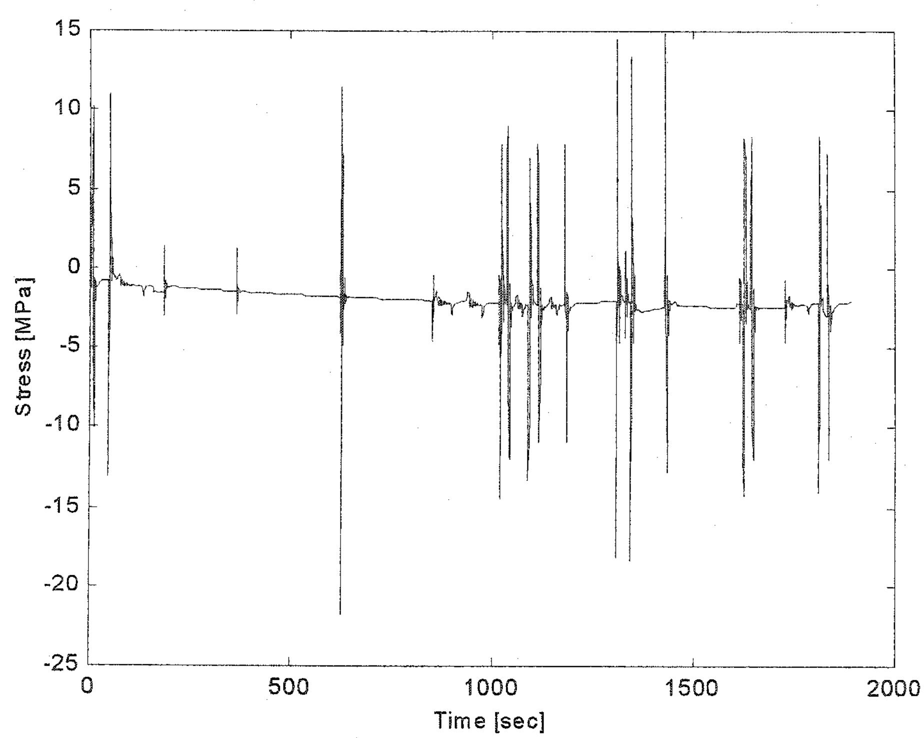

Figure 7.23 Stress Response of Wing Station 10 for LEC Activated Mission

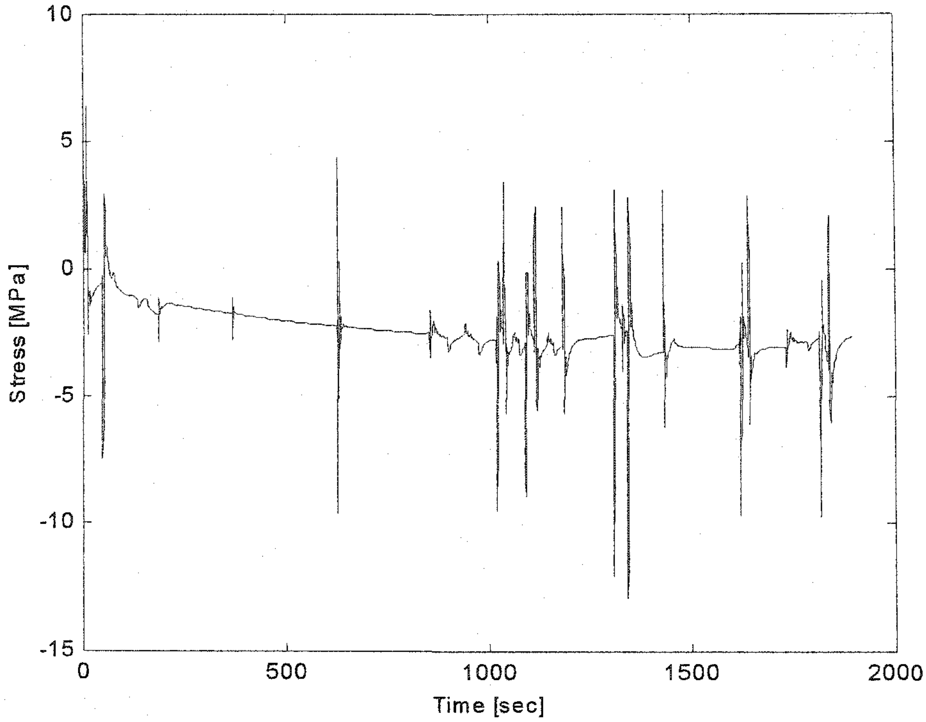

Figure 7.24 Stress Response of Wing Station 50 for Nominal Mission

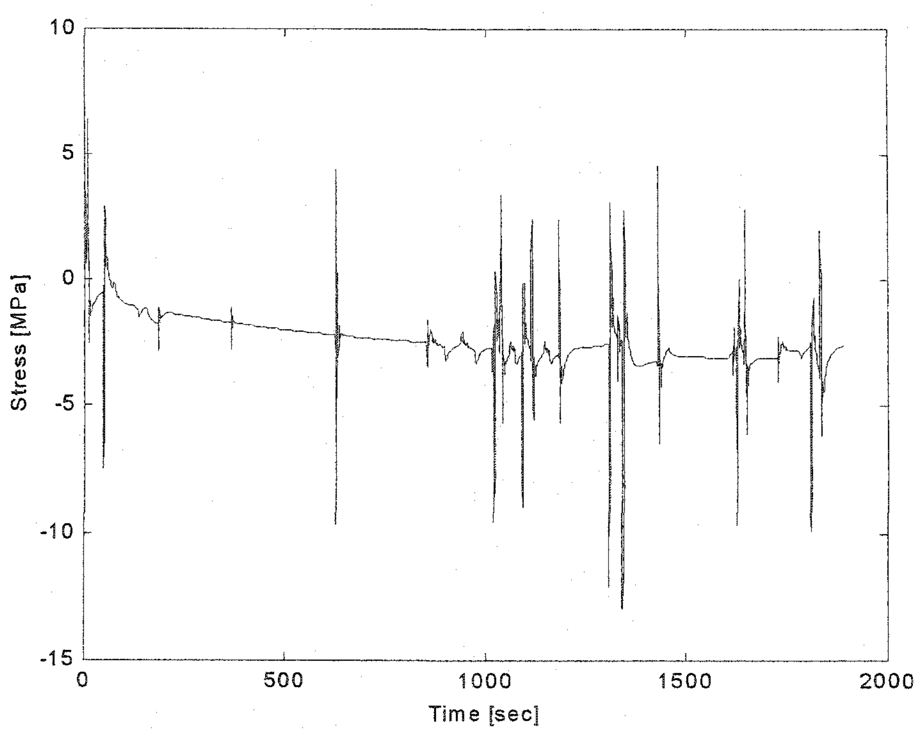

Figure 7.25 Stress Response of Wing Station 50 for LEC Activated Mission

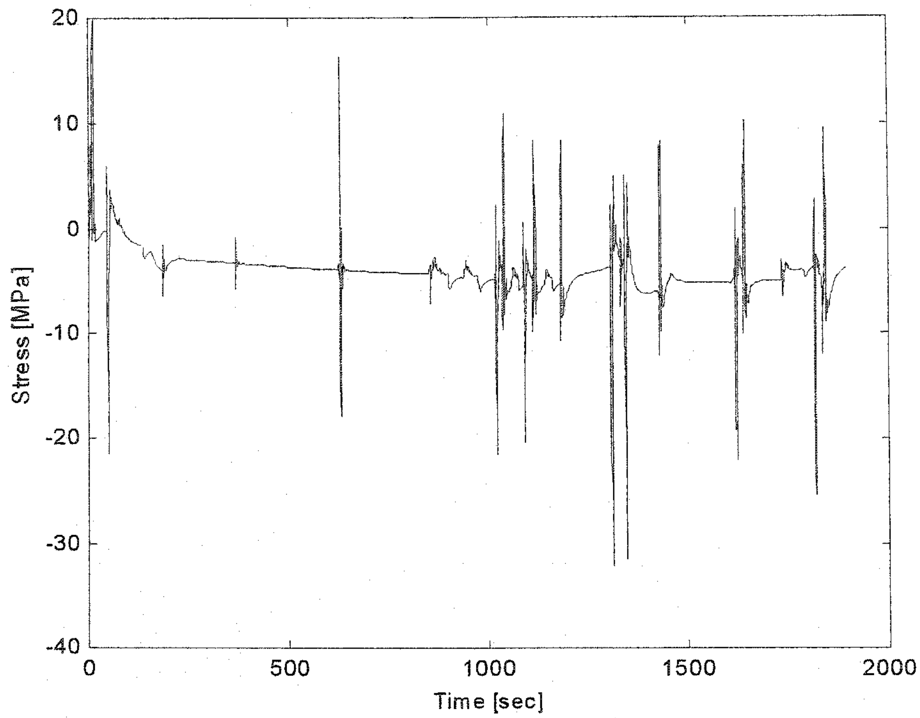

Figure 7.26 Stress Response of Wing Station 100 for Nominal Mission

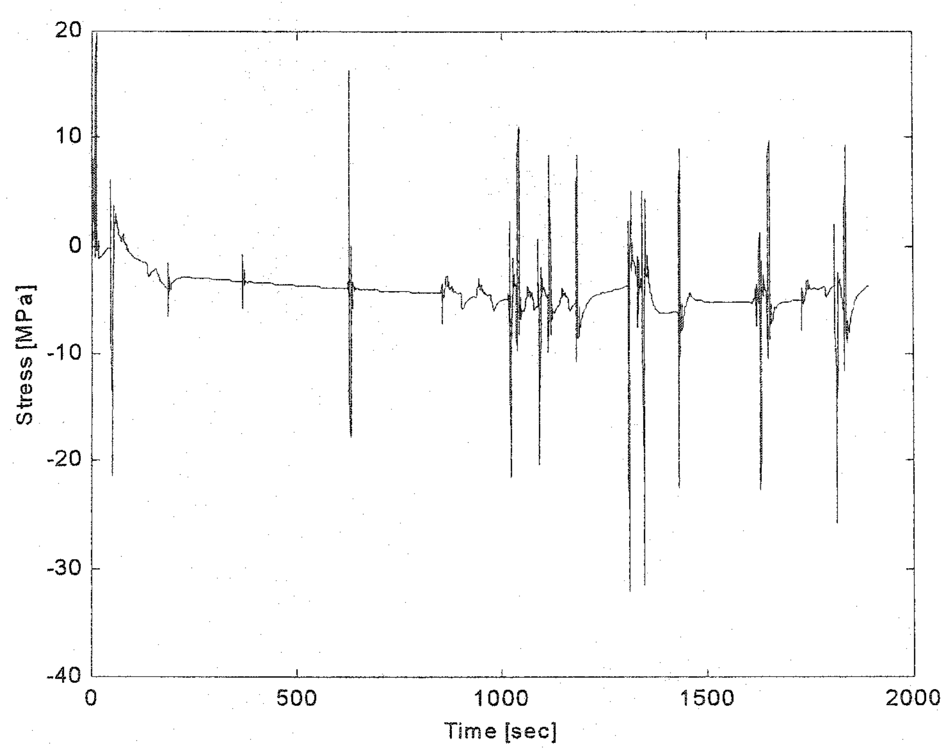

Figure 7.27 Stress Response of Wing Station 100 for LEC Activated Mission

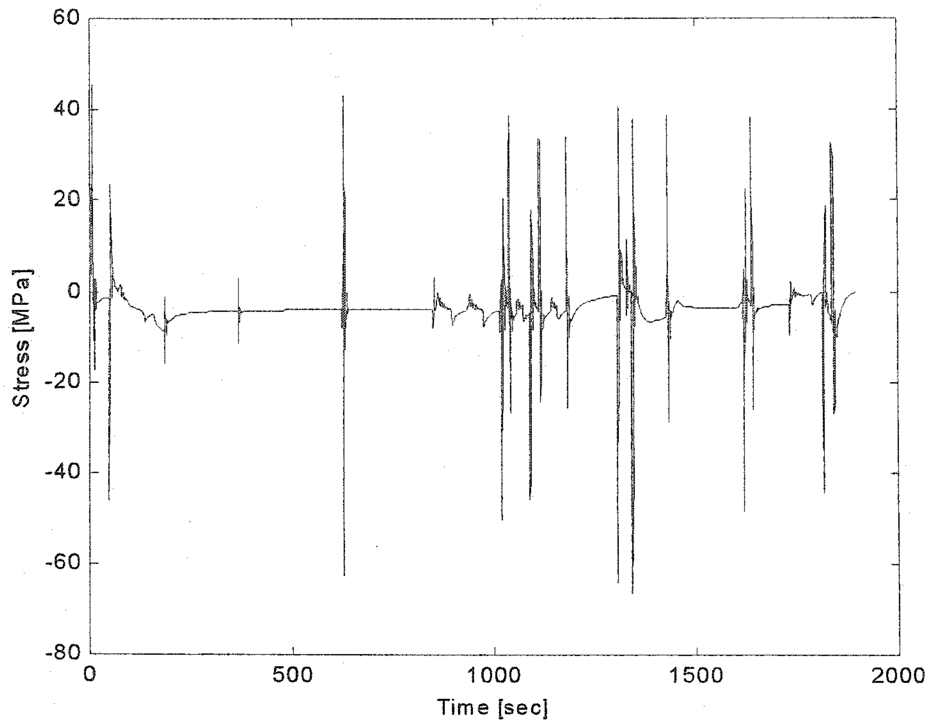

Figure 7.28 Stress Response of Wing Station 150 for Nominal Mission

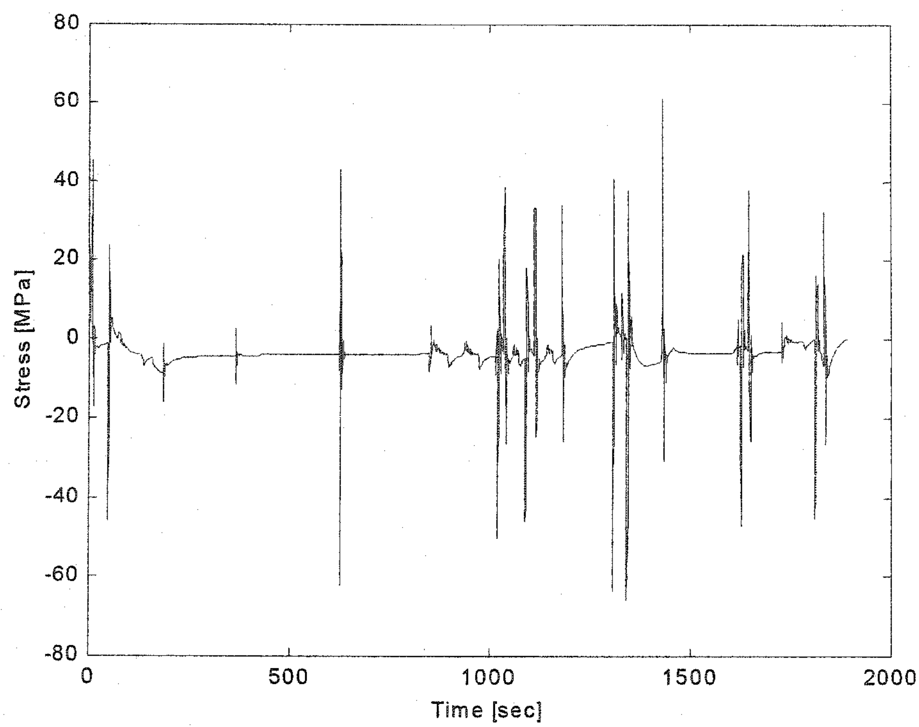

Figure 7.29 Stress Response of Wing Station 150 for LEC Activated Mission

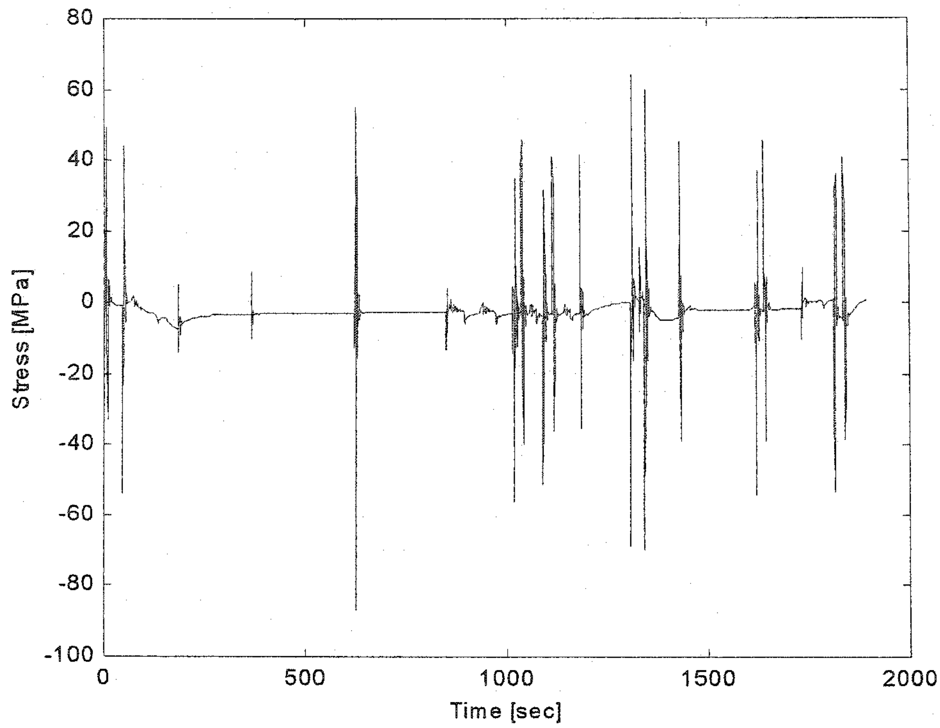

Figure 7.30 Stress Response of Wing Station 180 for Nominal Mission

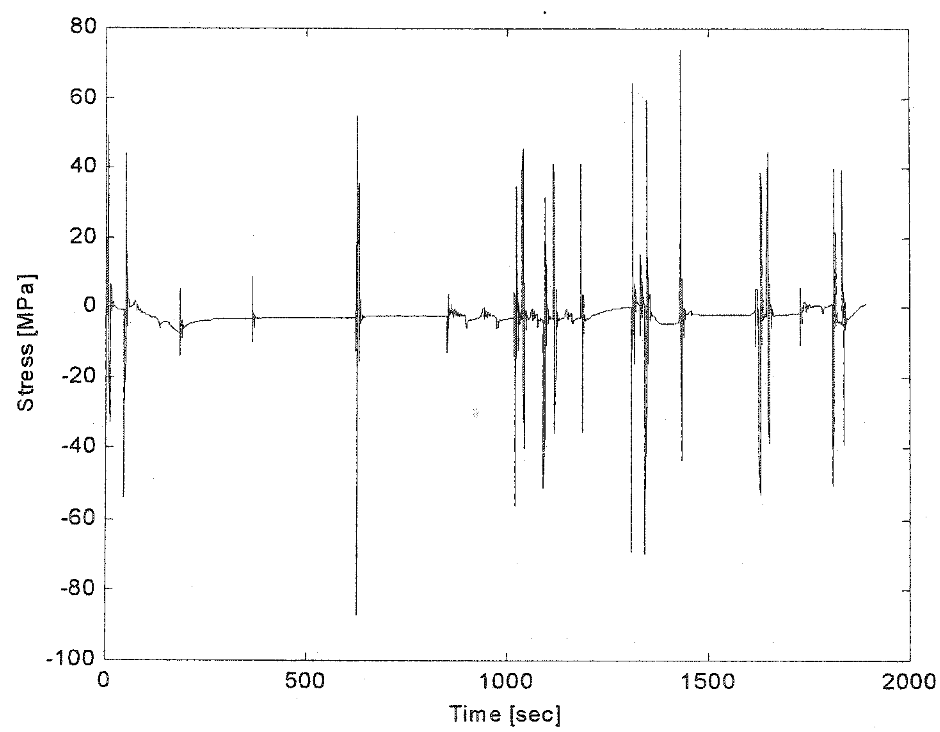

Figure 7.31 Stress Response of Wing Station 180 for LEC Activated Mission

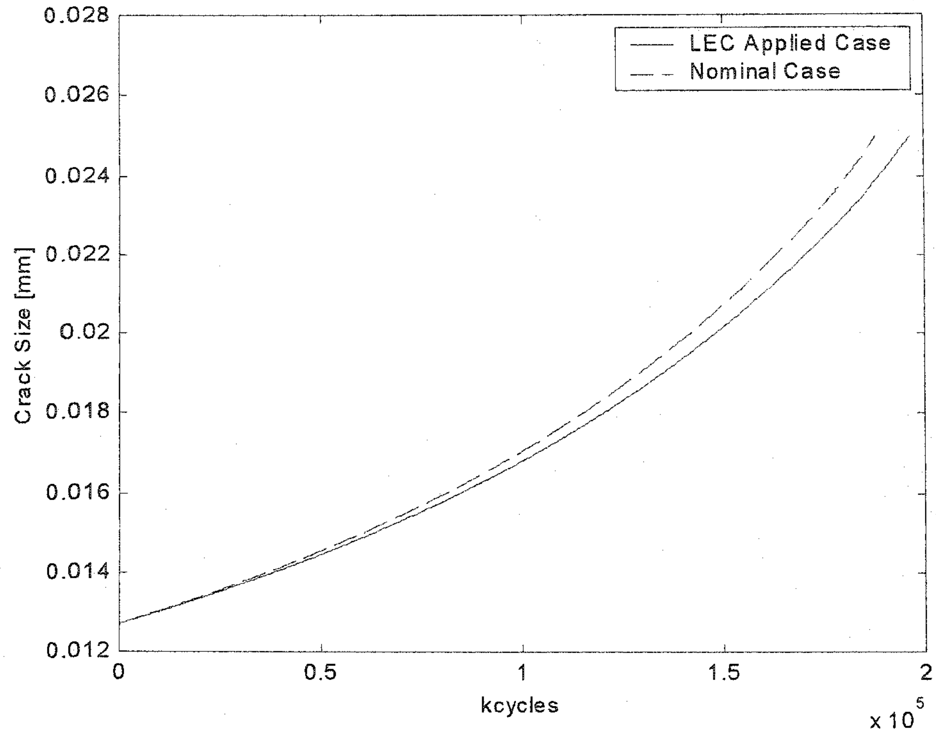

Figure 7.32 Crack Growth of Wing Station 10

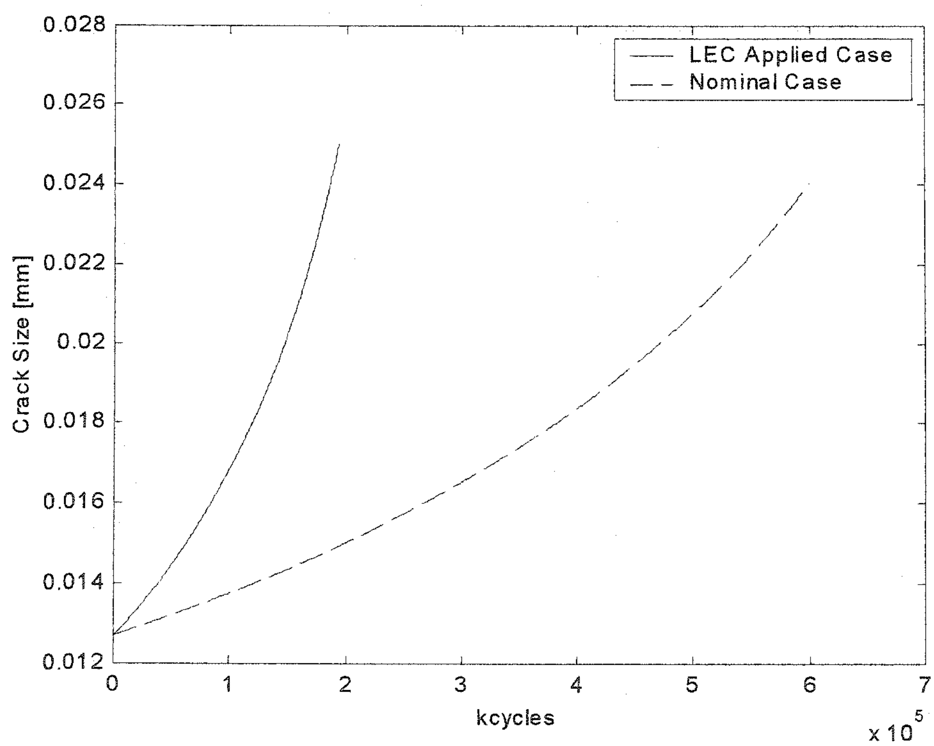

Figure 7.33 Crack Growth of Wing Station 50

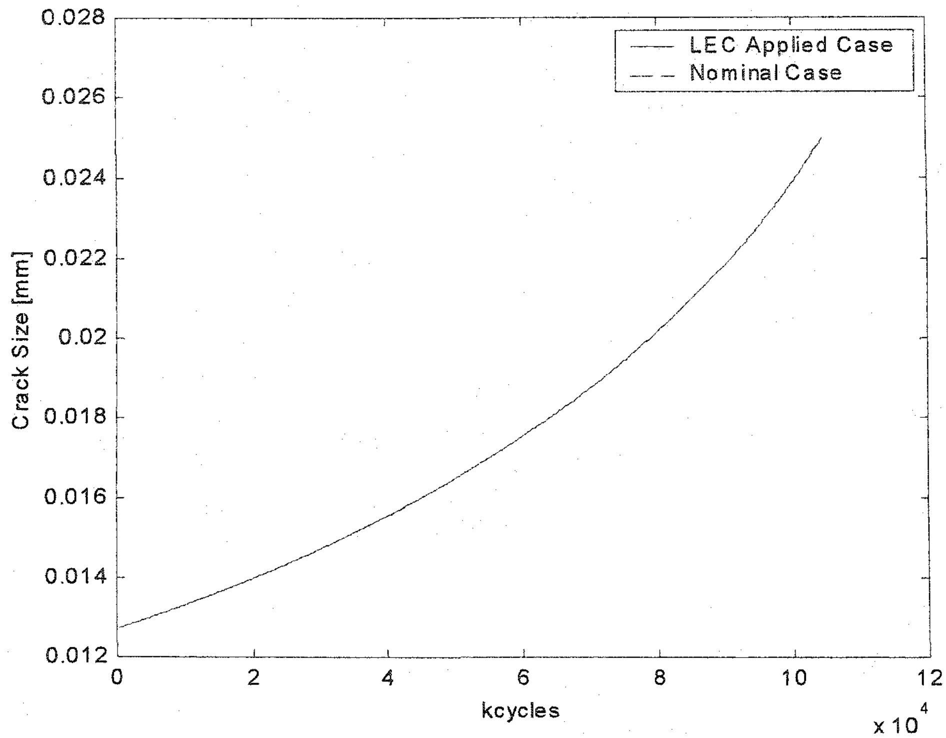

Figure 7.34 Crack Growth of Wing Station 100

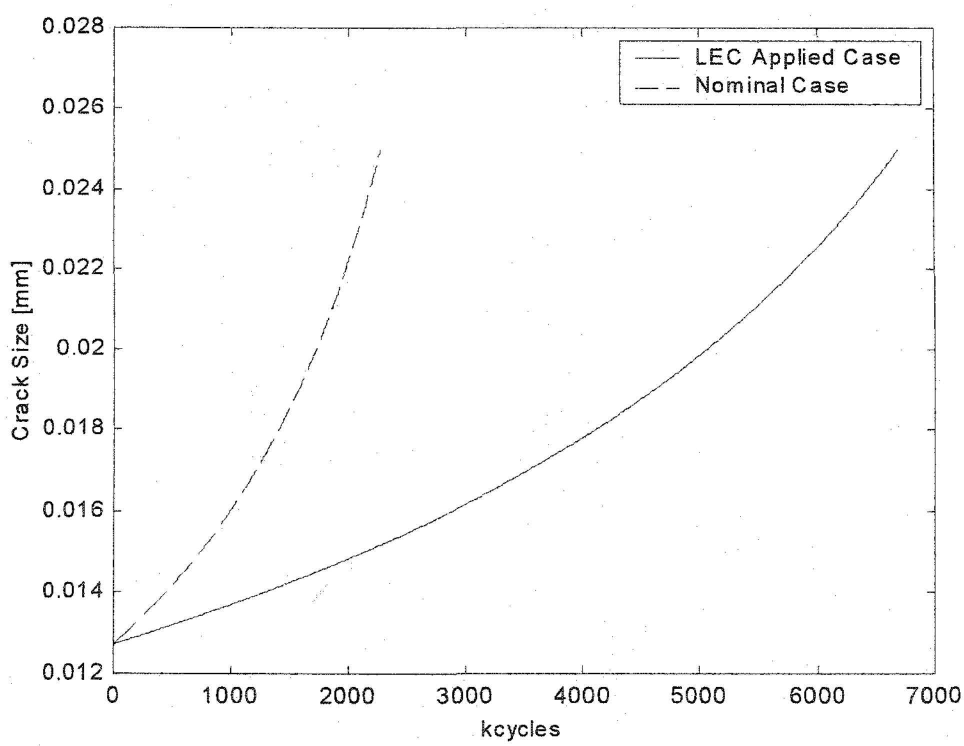

Figure 7.35 Crack Growth of Wing Station 150 – Target Station

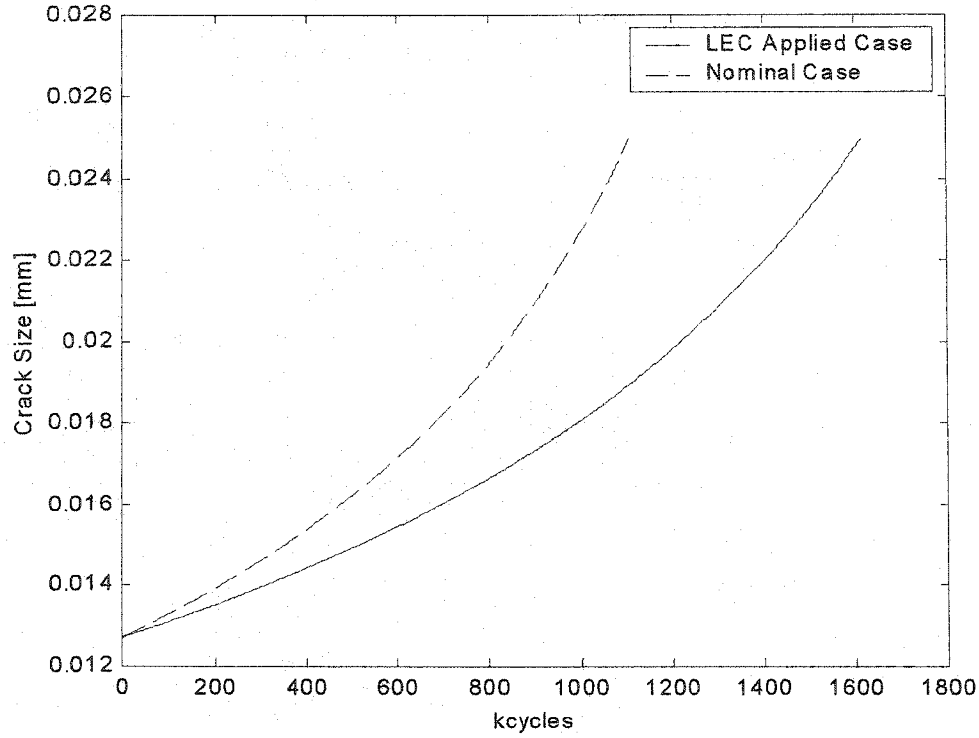

Figure 7.36 Crack Growth of Wing Station 180

CHAPTER 8

CONCLUSIONS

Life Extending Control (LEC) logic for a highly maneuverable aircraft is developed. This research demonstrates that significant life extension can be achieved through simply adding LEC logic to the current flight control system (FCS) of aircraft without significant modification of the original FCS. The LEC logic monitors critical motion behavior of the vehicle, and determines when the LEC logic should be engaged. When necessary, LEC logic issues commands to the FCS in order to achieve optimal or sub-optimal structural life. A nonlinear model of the F-16 aircraft, a corresponding FCS, and an autopilot system are developed as well as a realistic mission profile. The rigid-body motion excites the flexible wing model of F-16 aircraft, and the result out stress is fed into the nonlinear dynamic model of the crack growth.

LEC logic is designed for extending structural life of a selected component, and influence of LEC on multiple structural components is monitored. Simulation results indicate that significant life extension is obtained when using LEC logic for the structural components of interest, and other high-stress area. However, some components under lower stress were observed to have reduced structural life although the component is of less concern because the overall life of the component two orders of magnitude longer. The results imply that significant life extension is possible by employing LEC logic, but careful consideration is necessary when applying LEC logic to the aircraft FCS.

REFERENCES

1 Choudhury, A., *Metallergical Failure Analysis*, CR Brooks, McGraw Hill, 1993

2 Chapra, S. C., Canale, R. P., *Numerical Method for Engineers*, McGraw-Hill, Singapore, 1988.

3 Todd Curtis, "Average Fleet Age for Selected U.S. Carriers," Airsafe.com, http://www.airsafe.com/events/airlines/fleetage.htm, Accessed on June 4, 2003.

4 "Mainline Airline Fleet," Delta Airline, http://www.delta.com/inside/investors/annual_reports/2000b_annual/01_insidefrontcover.html, Accessed on March, 2003.

5 Dowling, N. E., *Mechanical Behavior of Materials*, Prentice-Hall, Upper Saddle River, New Jersey, 1999.

6 Liebowitz, H., "Fracture Mechanics of Aircraft Structures", AGARD-AG-176, NATO Advisory Group for Aerospace Research and Development, Technical Editing and Reproduction LTD, London, England, January, 1974.

7 Simpson, D. L., "Structures and Materials Panel Working Group 27 on Evaluation of Loads from Operational Flight Maneuvers - Final Working Group Report," AGARD-AR-340, NATO Advisory Group for Aerospace Research and Development, 7 Rue Ancelle, 92200 Neuilly-Sur-Senie, France, 1996.

8 Anderson, T. L., *Fracture Mechanics Fundamentals and Applications*, CRC Press, Boca Raton, Florida, 1995.

9 Blakelock, J. H., *Automatic Control of Aircraft and Missile*, Wiley-Interscience, New York, New York, 1991.

10 McLean, D., *Automatic Flight Control Systems, Series in Systems and Control Engineering*, Prentice Hall, New York, New York, 1990.

11 Stephens, R. I., Fatemi, A., Stephens, R. R., Fuchs, H. O., *Metal Fatigue in Engineering*, 2nd Edition, Wiley Inter-Science, Third Avenue, New York, New York, 2001.

12 Ewing, J. A. and Humfrey, J. C. W., *The Fracture of Metals Under Repeated Alterations of Stress*, Phil. Trans. Roy. Soc., London, Vol. CC, 1903, P. 241

13 Basquin, O. H., "The Experimental Law of Endurance Tests," *Processing of ASTM*, Vol. 10, Part II, 1910, P. 625

14 Bruhn, E. F., *Analysis and Design of Flight Vehicle Structures*, Jacobs Publishing, Indianapolis, Indiana, 1973.

15 Timoshenko, S. P. and Goodier, J. N., *Theory of Elasticity*, McGraw Hill, New York, New York, 1970.

16 Savin, G. N., *Stress Concentration Near Holes*, Pergemon Press, New York, New York, 1961.

17 Irwin, G. R., "Analysis of Stresses and Strains Near the End of a Crack Traversing a Plate", *Journal of Applied Mechanics*, Transactions of the ASME, 1957.

18 Irwin, G. R., *Fracture*, Handbuch der Physik, Vol. VI, Springer, Berlin, Germany, 1958.

19 Wells, A. A., "Notched Bar Tests, Fracture Mechanics and Strength of Welded Structures," *British Welding Journal*, Vol. 12, No.1, 1965.

20 Burdekin, F. M. and Stone, D. E., "The Crack Opening Displacement Approach to Fracture in Yielding Materials," *Journal of Strain Analysis*, Vol. 1, No. 2, 1966.

21 Patankar, R., Ray, A. and Lakhtakia, A., "A State-Space Model of Fatigue Crack Growth," *International Journal of Fracture*, Vol. 90, No. 3, 1998, pp. 235-249.

22 Paris, P. C., "The Growth of Cracks Due to Variations in Loads," Ph.D. Dissertation, Lehigh University, Bethlehem, Pennsylvania, 1962.

23 Paris, P. C. and Erdogan, F., "A Critical Analysis of Crack Growth Propagation Laws," *Journal of Basic Engineering*, Transactions of the ASME, Series D, Vol. 85, 1963.

24 Johnson, H. H. and Paris, P. C., "Sub-Critical Flaw Growth," *Engineering Fracture Mechanics,* Vol. 1, No. 1, 1968.

25 Ibrahim, F. K., Thompson, J. C. and Topper, T. H., "A Study of t he Effect of Mechanical Variables on Fatigue Crack Closure and Propagation," *International Journal of Fatigue*, Vol. 8, No. 3, July, 1986, pp. 135-142.

26 Porter, T. R., "Method of Analysis and Prediction for Variable Amplitude Fatigue Crack Growth," *Engineering Fracture Mechanics*, Vol. 4, No. 4, December, 1972, pp. 717-736.

27 McMillan, J. C. and Pelloux, R. M. N., "Fatigue Crack Propagation Under Program and Random Loading," *Fatigue Crack Propagation,* ASTM-STP-415, American Society for Testing and Materials, Philadelphia, Pennsylvania, 1967, pp. 505-535.

28 Shijve, J. and Broek, D., "Crack Propagation Tests Based on a Gust Spectrum with Variable Amplitude Loading," *Aircraft Engineering,* Vol. 34, 1962, pp. 314-316.

29 Dawicke, D. S., "Overload and Underload Effects on the Fatigue Crack Growth Behavior of the 2024-T3 Aluminum Alloy," NASA-CR-201668, Langley Research Center, Hampton, Virginia, March, 1997.

30 Elber, W., *The Significance of Fatigue Crack Closure, Damage Tolerance in Aircraft Structures*, ASTM-STP-486, American Society for Testing and Materials, Philadelphia, Pennsylvania, 1971, pp. 230-242.

31 Newman, J. C., Jr., "A Crack-Closure Model for Predicting Fatigue-Crack Growth under Aircraft Spectrum Loading," NASA TM-81941, January, 1981

32 Newman, J. C., Jr., "Finite-Element Analysis of Fatigue Crack Propagation—Including the Effects of Crack Closure," Ph.D. Thesis, Virginia Polytechnic Institute and State University, Blacksburg, Virginia., May, 1974.

33 Dugdale, D. S., *Journal of the Mechanics and Physics of Solids 8,* P. 100-104, 1960

34 Newman, J. C., Jr., A, "Crack Opening Stress Equation for Fatigue Crack Growth," *International Journal of Fatigue*, Martinus Nijhoff Publishers, The Hague, Netherlands, Vol. 24, R. 131-135.

35 Zhang, H., Ray, A. and Phoha, S., "Hybrid Damage-Mitigating Control of Mechanical Systems," *Proceedings of the AACC American Control Conference,* Philadelphia, Pennsylvania, June, 1998, pp. 254-258.

36 Ray, A., "Stochastic Modeling of Fatigue Crack Dynamics for Risk Analysis and Remaining Life Prediction," *Proceedings of the AACC American Control Conference*, Philadelphia, Pennsylvania, June, 1998, pp. 2591-2595.

37 Lorenzo, C. F., Holmes, M. S. and Ray, A., "Nonlinear Control of a Reusable Rocket Engine for Life Extension," *Proceedings of the AACC American Control Conference*, Philadelphia, Pennsylvania, June, 1998, pp. 2922-2926.

38 Blakelock, J. H., *Automatic Control of Aircraft and Missile*, Wiley-Interscience, New York, New York, 1991.

39 McLean, D., *Automatic Flight Control Systems, Series in Systems and Control Engineering*, Prentice Hall, New York, New York, 1990.

40 Ray, J. K., Carlin, C. M., and Lambregts, A. A., "High-Speed Civil Transport Flight- and Propulsion-Control Technological Issues," NASA-CR-186015, Dryden Flight Research Facility, Edwards, California, March, 1992.

41 McCarty, C. A., Feather, J. B., Dykman, J. R., Page, M. A., Hodgkinson, J., "Design and Analysis Issues of Integrated Control Systems for High-Speed Civil Transports," NASA-CR-186022, Dryden Flight Research Facility, Edwards, California, May, 1992.

42 Nyquist, H., "Regeneration Theory," *Bell Systems Technical Journal*, Vol. 11, January, 1932, pp. 126-147.

43 Bode, H. W., *Network Analysis and Feedback Amplifier Design*, Van Nostrand, New York, New York, 1945.

44 James, H. M., Nichols, N. B. and Phillips, R. S., *Theory of Servomechanisms*, McGraw-Hill, New York, New York, 1947.

45 Evans, W. R., "Control System Synthesis by Root Locus Method," *AIEE Transactions Part II*, Vol. 69, 1950, pp. 66-69.

46 Ogata, K., *Modern Control Engineering*, Prentice-Hall, Englewood Cliffs, New Jersey, 1970.

47 D'Azzo, J. J. and Houpis, C. H., *Linear Control System Analysis and Design: Conventional and Modern*, McGraw-Hall, New York, New York, 1988.

48 Maciejowski, J. M., *Multivariable Feedback Design*, Addison-Wesley, Workingham, England, 1989.

49 MacFarlane, A. G. J., "Multivariable Nyquist-Bode and Multivariable Root-Locus Techniques," *Proceedings of the IEEE Conference on Decision and Control*, Clearwater, Florida, December, 1976, pp. 342-347.

50 MacFarlane, A. G. J. and Kouvaritakis, B., "A Design Technique for Linear Multivariable Feedcack System," *International Journal of Control*, Vol. 25, No. 6, June, 1977, pp. 837-874.

51 MacFarlane, A. G. J. and Postlethwaite, I., "The Generalized Nyquist Stability Criterion and Multivariable Root Loci," *International Journal of Control*, Vol. 25, No. 1, January, 1977, pp. 81-127.

52 Horowitz, I., "Quantitative Synthesis of Uncertain Multiple Input-Output Feedback Systems," *International Journal of Control*, Vol. 30, No. 1, July, 1979, pp. 81-106.

53 Kwakernaak, H. and Sivan, R., *Linear Optimal Control Systems*, Wiley-Interscience, New York, New York, 1972.

54 Doyle, J. C. and Stein, G., "Multivariable Feedback Design: Concepts for a Classical/Modern Synthesis," *Transactions on Automatic Control,* Vol. AC-26, No. 1, February, 1981, pp. 4-16.

55 Doyle, J. C., Glover, K., Khargonekar, P. P. and Francis, B. A., "State-Space Solutions to Standard and Control Problems," *Transactions on Automatic Control,* Vol. AC-34, No. 8, 1989, pp. 831-847.

56 Hyde, R. A., *Aerospace Control Design: A VSTOL Flight Application*, Springer-Verlag, London, England, 1995.

57 Sobel, K. M., and Shapiro, E. Y., "Eigenstructure Assignment for Design of Multimode Flight Control Systems," *IEEE Control System*, May, 1985, pp. 9-14.

58 Kreindler, E., and Rothschild, D., "Model-Following in Linear Quadratic Optimization," *AIAA Journal*, Vol. 14, No. 7, July, 1976, pp. 835-842.

59 Swaim, R. L., "Aeroelastic Interactions with Flight Control (A Survey Paper)", *Proceedings of the Guidance and Control Conference*, Gatlinburg, Tennessee, August, 1983, pp. 404-411.

60 Dempster, J. B. and Arnold, J. I., "Flight Test Evaluation of an Advanced Stability Augmentation System for the B-52 Aircraft", *Journal of Aircraft*, Vol. 6, No. 4, July-August, 1969, pp. 343-348.

61 Hargrove, W. J., "The C-5A Active Lift Distribution Control System", *Advanced Control Technology and its Potential for Future Transport Aircraft*, NASA-TM-X-3409, Dryden Flight Research Facility, Edwards, California, August, 1976, pp. 325-351.

62 Bendixen, G. E., O'Connell, R. F. and Siegert, C. D., "Digital Active Control System for Load Alleviation for the Lockheed L-1011", *Aeronautical Journal*, Vol. 85, No. 430, November, 1981, pp. 430-436.

63 Burris, P. M., and Bender, M. A., "Aircraft Load Alleviation and Mode Stabilization (LAMS)," AFFDL-TR-68-158, Air Force Flight Dynamics Laboratory, Wright-Patterson AFB, Ohio, April, 1969.

64 Anderson, D. C., Berger, R. L. and Hess, J. R., "Maneuver Load Control and Relaxed Static Stability Applied to a Contemporary Fighter Aircraft," *Journal of Aircraft*, Vol. 10, No. 2, February, 1973, pp. 112-119.

65 White, R. J., "Improving the Airplane Efficiency by Use of Wing Maneuver Load Alleviation," *Journal of Aircraft*, Vol. 8, No. 10, October, 1971, pp. 769-775.

66 Arnold, J. I. and Murphy, F. B., "B-52 Control Configured Vehicles: Flight Test Results," *Advanced Control Technology and its Potential for Future Transport Aircraft*, NASA-TM-X-3409, Dryden Flight Research Facility, Edwards, California, August, 1976, pp. 75-89.

67 Wykes, J. H. and Mori, A. S., "An Analysis of Flexible Aircraft Structural Mode Control," AFFDL-TR-65-190, Part 1, Air Force Flight Dynamics Laboratory, Wright Patterson AFB, Ohio, June, 1966.

68 Wykes, J. H., "Structural Dynamic Stability Augmentation and Gust Alleviation of Flexible Aircraft," AIAA Paper No. 68-1067, *AIAA 5th Annual Meeting and Technology Display*, Philadelphia, Pennsylvania, October, 1968.

69 Wykes, J. H. and Knight, R. J., "Progress Report on a Gust Alleviation and Structural Dynamic Stability Augmentation System (GASDSAS) Design Study,"

AIAA Paper No. 66-999, *Proceedings of AIAA 3rd Annual Meeting*, Boston, Massachusetts, November, 1966.

70 Edinger, L. D., "Design of Elastic Mode Suppression Systems for Ride Quality Improvement," *Journal of Aircraft*, Vol. 5, No. 2, March-April, 1968, pp. 161-168.

71 Wykes, J. H., Moris, A. S. and Borland, C. J., "B-1 Structural Mode Control Systems," AIAA Paper No. 72-772, *AIAA Aircraft Design, Flight Test and Operations Meeting*, Stanford, California, August, 1972.

72 Newman, B. and Schmidt, D. K., "Aeroelastic Vehicle Multivariable Control Synthesis with Analytical Robustness Evaluation," *Journal of Guidance, Control and Dynamics*, Vol. 17, No. 6, November-December, 1994, pp. 1145-1153.

73 Hess, R. A. and Henderson, D. K., "Flexible Vehicle Control Using Quantitative Feedback Theory," *Journal of Guidance, Control and Dynamics*, Vol. 18, No. 5, September-October, 1995, pp. 1062-1067.

74 Newman, B. and Buttrill, C., "Conventional Flight Control for an Aeroelastic, Relaxed Static Stability High-Speed Transport," *Proceedings of the AIAA Guidance, Navigation and Control Conference*, Baltimore, Maryland, August, 1995, pp. 717-726.

75 Hanel, M., "Integrated Flight and Aeroelastic Control of a Flexible Transport Aircraft," *Proceedings of the AIAA Guidance, Navigation and Control Conference*, Boston, Massachusetts, August, 1998, pp. 1002-1011.

76 Chan, S. Y., Cheng, P. Y., Myers, T. T., Klyde, D. H., Magdaleno, R. E. and McRuer, D. T., "Advanced Aeroservoelastic Stabilization Techniques for

Hypersonic Flight Vehicles," NASA-CR-189702, Langley Research Center, Hampton, Virginia, November, 1992.

77 Ray, A., Dai, X., Wu, M-K., Carpino, M., and Lorenzo, C. F., "Damage-Mitigating Control of a Reusuable Rocket Engine," *AIAA Journal of Propulsion and Power*, Vol. 10, No. 2, March/April, 1994C, pp. 225-234

78 Kallapa, P. T., Holmes, M., and Ray, A., "Life Extending Control of Fossil Power Plants for Structural Durability and High Performance," *Automatica*, Vol. 33, No. 6, June, 1997.

79 Rozak, J. H., "Impact of Robust Control on Handling Qualities and Fatigue Damage of Rotorcraft," Doctoral Thesis, The Pennsylvania State University, University Park, PA, 1995.

80 Rozak, J. H., and Ray, A., "Robust Multivariable Control of Rotorcraft in Forward Flight," *Journal of the American Helicopter Society*, Vol. 42, No. 2, April 1997, pp. 149-160.

81 Ray, A. and Caplin, J., "Life Extending Control of Aircraft: Trade-off between Flight Performance and Structural Durability," *The Aeronautical Journal*, Vol. 104, No. 1039, September, 2000, pp. 397-408.

82 Caplin, J., "Damage-Mitigating Control of Aircraft for High Performance and Life Extension," Doctoral Thesis, The Pennsylvania State University, University Park, PA, December, 1998.

83 Robinson, P. A., "The Use of Predictive Lidar Measurements in Alleviating Turbulence Induced Disturbances of Aircraft in Flight," *SPIE AeroSense Conference*, Air Traffic Control Technologies II, pp. 86-97, April, 1996.

84 Gatt, P., Shald, S., Robinson, P., and Newman, B., "Feed-Forward Turbulence Mitigation with Coherent Doppler Lidar," Phase II SBIR Final Report, Contract NAS4-01007, NASA Langley Research Center, March, 2003.

85 Yu, S., Newman, B., "Age Dependency of the Optimal Overload Ratio on Fatigue Crack Growth of Aircraft Structures," *Proceedings of 44th AIAA/ASME/ASCE/AHS Structures, Structural Dynamics, and Materials Conference*, Norfolk, Virginia, April, 2003.

86 Yu, S. and Newman, B., "Load and Control Effects on Crack Growth in Flexible Aircraft," *Journal of Aircraft*, Vol. 39, No. 1, January-February, 2002, pp. 148-157.

87 Yu, S. "Long-Term Aircraft Structural Integrity Prediction Under the Influence of Feedback Control," Masters Thesis, Old Dominion University, Norfolk, Virginia, December, 1999.

88 Luat T., Marilyn E., William P., Kemper S., Philip W., and Perry L., "Simulation Study of Stall/Post-Stall Characteristics of a Fighter Airplane with Relaxed Longitudinal Static Stability," NASA Technical Paper 1538, NASA Langley Research Center, Hampton, Virginia, 1979.

89 Pendleton, E., Lee, M., "An Application of the Active Flexible Wing Concept to an F-16 Derivative Wing Model," *Proceedings of AIAA/ASME/ASCE/AHS/ASC 32nd Structures, Structural Dynamics, and Materials Conference*, April, 1991.

90 Miller, G., "Active Flexible Wing (AFW) Technology," AFWAL-TR-3096, Feburary, 1988.

91 *The NASTRAN User's Manual*, Level 17.5, December 1978.

92 Spick, M., *The Great Book of Modern War Planes*, Asalamander Book, 8 Blenheim Court, Brewery Road, London, United Kingdom, 2000.

93 Pendleton, E., Lee, M., and Wasserman, L., *Design and Wind Tunnel Tests of an F-16 Derivative Low Speed Flexible Model Applying the Active Flexible Wing Concept*, Presented to the Aerospace Flutter and Dynamic Council, Seattle, Washington, April, 1990.

94 Roark, R. J., *Formulas for Stress and Strain,* McGraw Hill, 1965

95 Kassan, Mark W., "F-16 Simulation for Man-in-the-Loop Testing of Aircraft Control System," Thesis, Air Force Institute of Technology, Wright -Patterson Air Force Base, Ohio, December, 1987.

96 HQ ACC/DOT (Maj. Michael K. Updike), *Multi Command Handbook 11-F16*, Vol. 5, Air Combat Command (ACC), Air Education and Training Command (AETC), National Guard Bureau (NGB), Pacific Air Forces (PACAF), United States Air Forces in Europe (USAFE), Effective Date: May 10, 1996.

97 Louie, G., Blankenship, S., *Falcon 4.0 Manual*, Micro Prose, December, 2001.

98 Stevens, B. L., Lewis, F. L., *Aircraft Control and Simulation*, Wiley Interscience, USA, 1992.

99 Elber, W., *Damage Tolerance in Aircraft Structures*, STP 486, American Society for Testing and Materials, Philadelphia, 1971, P. 230-242

100 Lomax, T. L. *Structural Loads Analysis for Commercial Transport Aircraft: Theory and Practice*, American Institute of Aeronautics and Astronautics, Reston, Virginia, 1996.

101 Waszak, M. R., Davidson, J. B. and Schmidt, D. K., "A Simulation Study of the Flight Dynamics of Elastic Aircraft," NASA-CR-4102, Langley Research Center, Hampton, Virginia, December, 1987.

102 Waszak, M. R. and Schmidt, D. K., "Flight Dynamics of Aeroelastic Vehicles," *Journal of Aircraft*, Vol. 25, No. 6, June, 1988, pp. 563-571.

103 "FAA Directive Target Boeing 737s, 747s," *Aviation Week & Space Technology*, McGraw Hill, January 13, 1997.

104 Yu, S. and Newman, B., "Flight Control Leverage on Crack Growth in a Flexible Aircraft – Part 1 & Part 2," *Proceedings of the AIAA Guidance, Navigation, and Control Conference*, Denver, Colorado, August, 2000.

105 "Boeing Commercial Airplane Prices," The Boeing Company, Seattle, Washington, http://www.boeing.com/commercial/prices/index.html, Accessed on June 2, 2003.

106 Caplin, J., Ray, A., and Joshi, S. M., "Damage-Mitigating Control of Aircraft for Enhanced Structural Durability," *IEEE Transactions on Aerospace end Electronic Systems,* Vol. 37, No. 3, July, 2001, pp. 849-862.

APPENDIX I

Dynamic Crack Growth Model

```
%State-space Model for Fatigue crack growth under Variable stress amplitude
%   All dimensions in MKS inits (i.e., lengths in meters and and stresses in MPa)
%
%
%                          TECHNICAL BACKGROUND
%
% Constant Amplitude Crack Growth Model is:
%
%              dC/dN = cons(delta_Keff)^nexp
%              delta_Keff = (SMAX-SO)*sqrt(pi*C)/sqrt(cos(0.5*pi*C/w))
%
%For cpnstant amplitude load SO=SoSS, where SoSS is given by Newman (1984)
%
%Specifications of constants and parameters for the material and test specimens under
study
%%%%%%%%%%%%%%%%%%%%%%%%%%%%%%%%%%%%%%%%%%%%%%%%%%%%%%%%%%%%
%
% This program assumes center-cracked specimens.  For other types (e.g., compact
specimens),
%     the program requires monor modifications.
%
%The following parameters are set for the 7075-T6 Aluminum alloy based on center-cracked
specimens based on
%     the single overload data of Porter (1972)
%
 cons = 7e-11;              % Constant
 nexp = 3.8                   % exponent
 E = 69600;           %elastic limit
 yield= 520;             %yield strength
 ult= 575;            %ultimate tensile strength
  t= 1.016e-3;        %thickness
  w= 76.2E-3;         %halfwidth
 ALP = 1.7               %Plane stress/strain factor
                                 % ALP=1 for plane stress; ALP =3 for plane strain,
normally between 1.1-1.8
%
%%%%%%%%%%%%%%%%%%%%%%%%%%%%%%%%%%%%%%%%%%%%%%%%%%%%%%%%%%%%%%%%%%%%%%%%%%%%%%%%%%%%%%%%%%%%
%%
%If variable ALP is desired, specify rate_mat= [log(rate1) alp1 log(rate2) alp2]
%For example: rate_mat= [ log(5E-10)   1.8   log(5E-9)   1.2]
%
% If an alternative look-up function {Newman (1992)] is desired,
%    set the following parameters for crack growth rate
%
%lookK=log([1.43 2.42 3.3 4.4 5.5 11 27.5 49.5 ]');
%lookup=log([3.56E-10 3.05E-9 6.1E-9 1.52E-8 4.06E-8 4.32E-7 1.78E-5 2.54E-4]');
%slope_1=(lookup(2)-lookup(1))/(lookK(2)-lookK(1));
%%%%%%%%%%%%%%%%%%%%%%%%%%%%%%%%%%%%%%%%%%%%%%%%%%%%%%%%%%%%%%%%%%%%%%%%%%%%%%%%%%%%%%%%%%%%
%%
%
cSTART= 12.7E-3          %Initial crack length
cFINAL= 25E-3         %Final crack length
eta=2.5e-4;        %Constant for the crack opening stress equation
                           %   (can be assumed to beidentical for all metallic
materials)
eta_spec= .8e-5;      %constant for a specimen
 %                             (may vary slightly from specimen to specimen)
                   %eta_spec determines the amount of crack arrest
                   %It can be best estimated from single overload data with
                   %crack arrest in an identical specimen.
%%%%%%%%%%%%%%%%%%%%%%%%%%%%%%%%%%%%%%%%%%%%%%%%%%%%%%%%%%%%%%%%%%%%%%%%%%%%%%%%%%%%%%%%%%%%
%%%
%
% Load specification in matrix form  -  This could also be done by loading a mat-file
```

```
%Each row is a block of loading. There are three coloumns
%coloumn1= SMAX , coloumn2= SMIN, coloumn3= Number of cycles of this block
%
LOAD=[68.9 .345 17000; 137.8 .345 1;68.9 .345 40000]
[p,q]=size(LOAD);
SFLOW=(ult+yield)/2;
CYC=0;
C=cSTART;
CRACK(1)=C;
SMIN_OLD=LOAD(1,2);
SMIN=LOAD(1,2);
SMAX=LOAD(1,1);

%estimation of starting value of crack opening stress SO
if SMAX <= 0
            RATIO=0.0;
            A0=0.0;
            A1=0.0;
            A2=0.0;
            A3=0.0;
else
            R=SMIN/SMAX;
            Z=SMAX/SFLOW;
            A0=(0.825-0.34*ALP+0.05*ALP^2)*(cos(pi*Z/2))^(1/ALP);
            A1=(0.415-0.071*ALP)*Z;
            if R >= 0.0
                A3=2*A0+A1-1;
                A2=1-A0-A1-A3;
            else
                A2=0.0;
                A3=0.0;
            end;
            RATIO=(A0+A1*R+A2*R^2+A3*R^3);
            if RATIO < R
                RATIO=R;
            end;
end;
SO=RATIO*SMAX;          %STARTING SO
                                %If the initial value SO of the crack opening stress is
known,
                                %  specify it here to over-ride the estimation
OPENSTR(1)=SO;

while (C < cFINAL),
for level=1:p,
      SMIN=LOAD(level,2);
      SMAX=LOAD(level,1);
   for i=1:LOAD(level,3),
      CYC=CYC+1;
      geo_F=sqrt(1/cos(0.5*pi*C/w)); %Elastic boundary correction for center crack
%
% crack growth equation

%Uncomment this section if using look up table instead of crack growth equation
%       if SMAX > SO
%        dKeff=geo_F*(SMAX-SO)*sqrt(pi*C);
%   if log(dKeff) < lookK(1)
%        log_dcdn=lookup(1)-slope_1*(lookK(1)-log(dKeff));
%   else
%           %Interpolating on log scale.
%        log_dcdn=interp1(lookK,lookup,log(dKeff));
%   end;
%   dcdn=exp(log_dcdn);
%        C=C+dcdn;
%       end;

%Comment out this loop if using look up table
      if SMAX > SO
        dKeff=geo_F*(SMAX-SO)*sqrt(pi*C);
    dcdn= cons*dKeff^nexp;
        C=C+dcdn;
```

```
        end;

%Uncomment the following equations for variable ALP
%        ALP=rate_mat(4)+rate_const*(log(dcdn)-rate_mat(3));
%        if ALP > rate_mat(2)
%         ALP=rate_mat(2);
%        elseif ALP < rate_mat(4)
%         ALP=rate_mat(4);
%        end;

      SMIN_mod=(SMIN+ALP*SMIN_OLD)/(1+ALP); %SMIN_mod was weighted by alpha for sequence
effects

% Newman's equation [Newman, 1981] for constant amplitude crack opening stress SoSS
      if SMAX <= 0
            RATIO=0.0;
            A0=0.0;
            A1=0.0;
            A2=0.0;
            A3=0.0;
      else
            R=SMIN_mod/SMAX;
            Z=SMAX*geo_F/SFLOW;
            A0=(0.825-0.34*ALP+0.05*ALP^2)*(cos(pi*Z/2))^(1/ALP);
            A1=(0.415-0.071*ALP)*Z;
            if R >= 0.0
                A3=2*A0+A1-1;
                A2=1-A0-A1-A3;
            else
                A2=0.0;
                A3=0.0;
            end;
            RATIO=(A0+A1*R+A2*R^2+A3*R^3);
         if RATIO < R
                RATIO=R;
            end;
    end;
      SoSS=RATIO*SMAX;

%Dynamic crack opening stress (SO) equation under variable-amplitude stress uses SoSS
      if SO >= SoSS
                if SO > SMAX
                    PULSE = SoSS*eta_spec;
                   SO=(SO+PULSE)/(eta_spec+1);
                else
                   PULSE = SoSS*eta;
                   SO=(SO+PULSE)/(eta+1);
                end;
      else
                lambda=(1+exp(2*t/(C-w)))*(SMAX-SMIN_mod)/(SMAX-SMIN_OLD);
                    PULSE=(SoSS*(1+eta)-SO)*lambda+SoSS*eta;
                SO=(SO+PULSE)/(eta+1);
      end;

% storing data at every 1000 cycles for printing
%
      if (rem(CYC,1000)==0)
            index=fix(CYC/1000)+1;
            CRACK(index)=C;
           OPENSTR(index)=SO;
%
%Comment out the matrix on the line to stop ecoingon the screen
%
            [index,C*1000,SO,SMAX]
      end;

      SMIN_OLD=SMIN;
   end;
end;
end
plot(CRACK);
```

```
%grid;
title('CRACK vs. Kcycles');
save temp OPENSTR CRACK;            % the data is stored in temp.mat
```

APPENDIX II

Nonlinear Aerodynamic Data of F-16 Aircraft

II.1. Geometric Data

Total Weight : 20,500 [lb_f]

Vehicle Moment of Inertia
I_x = 9,496 [$slug\ ft^2$]
I_y = 55,814 [$slug\ ft^2$]
I_z = 63,100 [$slug\ ft^2$]
I_{xz} = 982 [$slug\ ft^2$]

Wing Geometry
Wing Span : 30 [ft]
Wing Area : 300 [ft^2]
Mean Aerodynamic Chord : 11.32 [ft]

Engine Angular Momentum : 160 [$slug\ ft^2/sec$]

Center of Mass
Xcg_ref = .35

II.2. Thrust Data

$T_{idle}(h, M)$

Mach \ h	Thrust Value [$lb\ ft/sec^2$] at an Altitude, ft, of 0	10,000	20,000	30,000	40,000	50,000
0.2000	635	425	690	1,010	1,330	1,700
0.4000	60	25	345	755	1,130	1,525
0.6000	-1,020	-710	-300	350	910	1,360
0.8000	-2,700	-1,900	-1,300	-247	600	1,100
1.0000	-3,600	-1,400	-595	-342	-200	700

$T_{mil}(h, M)$

Mach \ h	Thrust Value [$lb\ ft/sec^2$] at an Altitude, ft, of 0	10,000	20,000	30,000	40,000	50,000
0.2000	12,680	9,150	6,313	4,040	2,470	1,400
0.4000	12,610	9,312	6,610	4,290	2,600	1,560
0.6000	12,640	9,839	7,090	4,660	2,840	1,660
0.8000	12,390	10,176	7,750	5,320	3,250	1,930
1.0000	11,680	9,848	8,050	6,100	3,800	2,310

$T_{max}(h, M)$

Mach \ h	Thrust Value [$lb\ ft/sec^2$] at an Altitude, ft, of 0	10,000	20,000	30,000	40,000	50,000
0.2000	21,420	15,700	11,225	7,323	4,435	2,600
0.4000	22,700	16,860	12,250	8,154	5,000	2,835
0.6000	24,240	18,910	13,760	9,285	5,700	3,215
0.8000	26,070	21,075	15,975	11,115	6,860	3,950
1.0000	28,886	23,319	18,300	13,484	8,642	5,057

II.3. x_b Directional Aerodynamic Force Coefficient Data

$C_x(\alpha, \beta, \delta_n = -25)$

α [°] \ β [°]	-30	-25	-20	-15	-10	-8	-6
-20	-0.1837	-0.1953	-0.1904	-0.1899	-0.1949	-0.1914	-0.1872
-15	-0.1714	-0.1765	-0.1792	-0.1827	-0.1816	-0.1834	-0.1852
-10	-0.1531	-0.1627	-0.1692	-0.1718	-0.1695	-0.1693	-0.1707
-5	-0.1151	-0.1232	-0.1276	-0.1317	-0.1390	-0.1415	-0.1420
0	-0.0907	-0.0985	-0.1043	-0.1093	-0.1120	-0.1115	-0.1122
5	-0.0514	-0.0567	-0.0603	-0.0640	-0.0653	-0.0661	-0.0668
10	-0.0079	-0.0108	-0.0099	-0.0101	-0.0074	-0.0070	-0.0078
15	0.0354	0.0358	0.0388	0.0402	0.0477	0.0503	0.0535
20	0.0740	0.0756	0.0746	0.0745	0.0867	0.0888	0.0924
25	0.1092	0.1124	0.1102	0.1067	0.1101	0.1121	0.1126
30	0.0915	0.1010	0.0975	0.1079	0.1188	0.1333	0.1399
35	0.1079	0.1137	0.1198	0.1278	0.1402	0.1425	0.1478
40	0.1306	0.1437	0.1350	0.1441	0.1574	0.1585	0.1601
45	0.1535	0.1603	0.1605	0.1604	0.1637	0.1671	0.1664
50	0.1471	0.1584	0.1646	0.1671	0.1712	0.1712	0.1676
55	0.1554	0.1615	0.1568	0.1661	0.1778	0.1769	0.1765
60	0.1501	0.1599	0.1647	0.1525	0.1664	0.1662	0.1704
70	0.1501	0.1536	0.1569	0.1420	0.1573	0.1595	0.1788
80	0.1685	0.1615	0.1559	0.1520	0.1521	0.1521	0.1535
90	0.1712	0.1651	0.1608	0.1648	0.1676	0.1660	0.1686

α [°] \ β [°]	-4	-2	0	2	4	6	8
-20	-0.1860	-0.1860	-0.1868	-0.1899	-0.1902	-0.1900	-0.1896
-15	-0.1853	-0.1877	-0.1875	-0.1898	-0.1876	-0.1868	-0.1848
-10	-0.1735	-0.1772	-0.1787	-0.1769	-0.1729	-0.1711	-0.1706
-5	-0.1425	-0.1437	-0.1432	-0.1425	-0.1422	-0.1410	-0.1397
0	-0.1124	-0.1130	-0.1132	-0.1129	-0.1119	-0.1110	-0.1102
5	-0.0675	-0.0690	-0.0693	-0.0686	-0.0680	-0.0664	-0.0650
10	-0.0090	-0.0116	-0.0120	-0.0123	-0.0106	-0.0088	-0.0083
15	0.0553	0.0538	0.0537	0.0533	0.0536	0.0527	0.0509
20	0.0941	0.0948	0.0951	0.0975	0.0939	0.0913	0.0867
25	0.1129	0.1123	0.1111	0.1122	0.1125	0.1136	0.1115
30	0.1422	0.1443	0.1435	0.1431	0.1407	0.1379	0.1359
35	0.1570	0.1623	0.1663	0.1667	0.1664	0.1637	0.1560
40	0.1682	0.1726	0.1739	0.1711	0.1699	0.1655	0.1611
45	0.1639	0.1674	0.1659	0.1649	0.1650	0.1625	0.1597
50	0.1644	0.1656	0.1693	0.1714	0.1728	0.1749	0.1725
55	0.1749	0.1762	0.1804	0.1743	0.1666	0.1677	0.1724
60	0.1710	0.1719	0.1718	0.1728	0.1730	0.1734	0.1721
70	0.1715	0.1738	0.1695	0.1710	0.1712	0.1730	0.1720
80	0.1585	0.1566	0.1598	0.1573	0.1563	0.1586	0.1558
90	0.1667	0.1669	0.1660	0.1672	0.1662	0.1664	0.1711

α [°] \ β [°]	10	15	20	25	30
-20	-0.1883	-0.1833	-0.1838	-0.1787	-0.1771
-15	-0.1841	-0.1852	-0.1817	-0.1790	-0.1739
-10	-0.1698	-0.1721	-0.1695	-0.1630	-0.1534
-5	-0.1372	-0.1299	-0.1258	-0.1214	-0.1133
0	-0.1092	-0.1065	-0.1015	-0.0957	-0.0879
5	-0.0649	-0.0631	-0.0594	-0.0558	-0.0505
10	-0.0080	-0.0107	-0.0105	-0.0114	-0.0085
15	0.0485	0.0410	0.0394	0.0366	0.0362
20	0.0824	0.0702	0.0703	0.0713	0.0697
25	0.1075	0.1041	0.1076	0.1098	0.1066
30	0.1323	0.1214	0.1110	0.1145	0.1050
35	0.1460	0.1336	0.1236	0.1195	0.1137
40	0.1567	0.1434	0.1343	0.1430	0.1299
45	0.1573	0.1540	0.1541	0.1539	0.1471
50	0.1730	0.1537	0.1457	0.1435	0.1362
55	0.1761	0.1722	0.1347	0.1448	0.1442
60	0.1688	0.1471	0.1462	0.1486	0.1460
70	0.1686	0.1474	0.1567	0.1557	0.1545
80	0.1572	0.1410	0.1410	0.1467	0.1538
90	0.1677	0.1531	0.1493	0.1549	0.1624

$C_x(\alpha,\ \beta,\ \delta_h = -10)$

α [°] \ β [°]	C_x						
	-30	-25	-20	-15	-10	-8	-6
-20	-0.1362	-0.1351	-0.1419	-0.1386	-0.1374	-0.1330	-0.1268
-15	-0.1216	-0.1245	-0.1235	-0.1208	-0.1176	-0.1176	-0.1170
-10	-0.1018	-0.1066	-0.1068	-0.1071	-0.1061	-0.1068	-0.1072
-5	-0.0655	-0.0706	-0.0746	-0.0771	-0.0836	-0.0864	-0.0876
0	-0.0483	-0.0509	-0.0532	-0.0544	-0.0578	-0.0589	-0.0597
5	-0.0118	-0.0106	-0.0096	-0.0102	-0.0142	-0.0148	-0.0155
10	0.0268	0.0328	0.0367	0.0399	0.0412	0.0417	0.0408
15	0.0735	0.0800	0.0887	0.0934	0.0983	0.1006	0.1024
20	0.1222	0.1275	0.1258	0.1249	0.1326	0.1347	0.1350
25	0.1374	0.1474	0.1466	0.1454	0.1465	0.1485	0.1485
30	0.1056	0.1261	0.1297	0.1437	0.1500	0.1619	0.1655
35	0.1075	0.1154	0.1299	0.1377	0.1523	0.1581	0.1722
40	0.1335	0.1412	0.1365	0.1456	0.1597	0.1622	0.1725
45	0.1521	0.1486	0.1517	0.1520	0.1608	0.1613	0.1597
50	0.1346	0.1410	0.1422	0.1486	0.1561	0.1570	0.1538
55	0.1375	0.1367	0.1251	0.1336	0.1467	0.1472	0.1475
60	0.1316	0.1360	0.1355	0.1154	0.1285	0.1289	0.1336
70	0.1171	0.1174	0.1185	0.1108	0.1161	0.1187	0.1376
80	0.1201	0.1161	0.1136	0.1124	0.1158	0.1148	0.1149
90	0.1287	0.1241	0.1214	0.1221	0.1265	0.1256	0.1257

α [°] \ β [°]	C_x						
	-4	-2	0	2	4	6	8
-20	-0.1249	-0.1222	-0.1223	-0.1246	-0.1247	-0.1252	-0.1257
-15	-0.1177	-0.1184	-0.1188	-0.1185	-0.1187	-0.1182	-0.1178
-10	-0.1083	-0.1094	-0.1147	-0.1095	-0.1084	-0.1077	-0.1063
-5	-0.0887	-0.0889	-0.0893	-0.0885	-0.0875	-0.0859	-0.0842
0	-0.0606	-0.0613	-0.0617	-0.0611	-0.0603	-0.0595	-0.0577
5	-0.0161	-0.0177	-0.0172	-0.0178	-0.0167	-0.0156	-0.0141
10	0.0413	0.0404	0.0399	0.0399	0.0409	0.0415	0.0414
15	0.1034	0.1033	0.1027	0.1031	0.1027	0.1018	0.1008
20	0.1349	0.1325	0.1322	0.1332	0.1338	0.1343	0.1310
25	0.1453	0.1429	0.1407	0.1418	0.1443	0.1457	0.1442
30	0.1660	0.1663	0.1651	0.1640	0.1643	0.1624	0.1615
35	0.1789	0.1801	0.1795	0.1793	0.1804	0.1782	0.1749
40	0.1762	0.1798	0.1798	0.1810	0.1771	0.1710	0.1702
45	0.1671	0.1667	0.1671	0.1664	0.1653	0.1629	0.1597
50	0.1511	0.1515	0.1544	0.1549	0.1547	0.1560	0.1538
55	0.1465	0.1462	0.1488	0.1433	0.1361	0.1370	0.1405
60	0.1351	0.1372	0.1383	0.1356	0.1320	0.1387	0.1323
70	0.1312	0.1353	0.1328	0.1301	0.1263	0.1270	0.1281
80	0.1194	0.1177	0.1211	0.1195	0.1195	0.1225	0.1204
90	0.1236	0.1248	0.1247	0.1262	0.1256	0.1256	0.1297

α [°] \ β [°]	C_x				
	10	15	20	25	30
-20	-0.1282	-0.1294	-0.1327	-0.1259	-0.1270
-15	-0.1184	-0.1216	-0.1243	-0.1253	-0.1224
-10	-0.1069	-0.1079	-0.1076	-0.1074	-0.1026
-5	-0.0812	-0.0747	-0.0722	-0.0682	-0.0631
0	-0.0561	-0.0527	-0.0515	-0.0492	-0.0466
5	-0.0133	-0.0093	-0.0087	-0.0106	-0.0127
10	0.0412	0.0399	0.0367	0.0328	0.0268
15	0.0983	0.0934	0.0887	0.0800	0.0735
20	0.1298	0.1231	0.1230	0.1247	0.1194
25	0.1439	0.1428	0.1440	0.1448	0.1348
30	0.1593	0.1530	0.1390	0.1354	0.1149
35	0.1678	0.1529	0.1451	0.1306	0.1227
40	0.1659	0.1518	0.1427	0.1474	0.1397
45	0.1569	0.1481	0.1478	0.1447	0.1482
50	0.1544	0.1469	0.1405	0.1393	0.1329
55	0.1431	0.1300	0.1215	0.1331	0.1339
60	0.1310	0.1179	0.1380	0.1385	0.1341
70	0.1268	0.1215	0.1292	0.1281	0.1278
80	0.1177	0.1143	0.1155	0.1180	0.1220
90	0.1257	0.1213	0.1206	0.1233	0.1279

$C_x(\alpha, \beta, \delta_n = 0)$

α [°] \ β [°]	Cx -30	-25	-20	-15	-10	-8	-6
-20	-0.1072	-0.1061	-0.1129	-0.1096	-0.1084	-0.1040	-0.0978
-15	-0.1006	-0.1035	-0.1025	-0.0998	-0.0966	-0.0966	-0.0960
-10	-0.0853	-0.0901	-0.0903	-0.0906	-0.0896	-0.0903	-0.0901
-5	-0.0546	-0.0597	-0.0637	-0.0662	-0.0727	-0.0755	-0.0767
0	-0.0355	-0.0381	-0.0404	-0.0416	-0.0450	-0.0461	-0.0469
5	-0.0012	0	-0.0010	-0.0004	-0.0036	-0.0042	-0.0049
10	0.0359	0.0491	0.0458	0.0490	0.0503	0.0508	0.0499
15	0.0780	0.0845	0.0932	0.0979	0.1028	0.1051	0.1069
20	0.1183	0.1236	0.1219	0.1210	0.1287	0.1308	0.1311
25	0.1267	0.1367	0.1359	0.1347	0.1358	0.1378	0.1378
30	0.0941	0.1146	0.1182	0.1322	0.1385	0.1504	0.1540
35	0.0885	0.0964	0.1109	0.1187	0.1333	0.1391	0.1532
40	0.1089	0.1166	0.1119	0.1210	0.1351	0.1376	0.1479
45	0.1232	0.1197	0.1228	0.1231	0.1319	0.1324	0.1308
50	0.1135	0.1185	0.1184	0.1171	0.1243	0.1279	0.1279
55	0.1137	0.1195	0.1146	0.1161	0.1209	0.1211	0.1211
60	0.1037	0.1090	0.1094	0.1049	0.1109	0.1123	0.1181
70	0.0857	0.0858	0.0857	0.0796	0.0851	0.0919	0.1150
80	0.0842	0.0807	0.0787	0.0778	0.0791	0.0793	0.0805
90	0.0847	0.0813	0.0798	0.0824	0.0843	0.0843	0.0853

α [°] \ β [°]	Cx -4	-2	0	2	4	6	8
-20	-0.0959	-0.0932	-0.0933	-0.0956	-0.0957	-0.0962	-0.0967
-15	-0.0967	-0.0974	-0.0978	-0.0975	-0.0977	-0.0972	-0.0968
-10	-0.0918	-0.0929	-0.0982	-0.0930	-0.0919	-0.0912	-0.0898
-5	-0.0778	-0.0780	-0.0784	-0.0776	-0.0766	-0.0750	-0.0733
0	-0.0478	-0.0485	-0.0489	-0.0483	-0.0475	-0.0467	-0.0449
5	-0.0055	-0.0071	-0.0066	-0.0072	-0.0061	-0.0050	-0.0035
10	0.0509	0.0497	0.0490	0.0490	0.0500	0.0506	0.0505
15	0.1079	0.1078	0.1072	0.1076	0.1072	0.1063	0.1053
20	0.1310	0.1286	0.1283	0.1293	0.1299	0.1304	0.1271
25	0.1346	0.1322	0.1300	0.1311	0.1336	0.1350	0.1335
30	0.1545	0.1548	0.1536	0.1525	0.1528	0.1509	0.1500
35	0.1599	0.1611	0.1605	0.1603	0.1614	0.1592	0.1559
40	0.1516	0.1552	0.1552	0.1564	0.1525	0.1464	0.1456
45	0.1332	0.1378	0.1382	0.1375	0.1364	0.1340	0.1308
50	0.1258	0.1257	0.1281	0.1258	0.1228	0.1221	0.1186
55	0.1195	0.1183	0.1200	0.1185	0.1153	0.1160	0.1152
60	0.1184	0.1170	0.1147	0.1141	0.1126	0.1129	0.1129
70	0.1087	0.1089	0.1025	0.1022	0.1007	0.1012	0.0994
80	0.0846	0.0808	0.0821	0.0802	0.0799	0.0826	0.0800
90	0.0841	0.0858	0.0864	0.0857	0.0828	0.0817	0.0857

α [°] \ β [°]	Cx 10	15	20	25	30
-20	-0.0992	-0.1004	-0.1037	-0.0969	-0.0980
-15	-0.0974	-0.1006	-0.1033	-0.1043	-0.1014
-10	-0.0904	-0.0914	-0.0911	-0.0909	-0.0861
-5	-0.0703	-0.0638	-0.0613	-0.0573	-0.0522
0	-0.0433	-0.0399	-0.0387	-0.0364	-0.0388
5	-0.0027	0.0013	0.0019	0	-0.0021
10	0.0503	0.0490	0.0458	0.0419	0.0359
15	0.1028	0.0979	0.0932	0.0845	0.0780
20	0.1259	0.1182	0.1191	0.1208	0.1155
25	0.1332	0.1321	0.1333	0.1341	0.1241
30	0.1478	0.1415	0.1275	0.1239	0.1034
35	0.1485	0.1339	0.1261	0.1116	0.1037
40	0.1413	0.1272	0.1181	0.1228	0.1151
45	0.1280	0.1192	0.1189	0.1158	0.1193
50	0.1180	0.1108	0.1121	0.1122	0.1072
55	0.1135	0.1087	0.1072	0.1121	0.1063
60	0.1109	0.1049	0.1094	0.1090	0.1037
70	0.0952	0.0897	0.0958	0.0959	0.0958
80	0.0709	0.0756	0.0765	0.0785	0.0820
90	0.0816	0.0797	0.0771	0.0786	0.0820

$C_x(\alpha, \beta, \delta_h = 10)$

β[°] / α [°]	C_x						
	-30	-25	-20	-15	-10	-8	-6
-20	-0.1023	-0.1012	-0.1080	-0.1047	-0.1035	-0.0991	-0.0929
-15	-0.1038	-0.1067	-0.1057	-0.1030	-0.0998	-0.0998	-0.0992
-10	-0.0963	-0.1011	-0.1013	-0.1016	-0.1006	-0.1013	-0.1017
-5	-0.0664	-0.0715	-0.0755	-0.0780	-0.0845	-0.0873	-0.0885
0	-0.0472	-0.0498	-0.0521	-0.0533	-0.0567	-0.0578	-0.0586
5	-0.0146	-0.0134	-0.0124	-0.0130	-0.0170	-0.0176	-0.0183
10	0.0182	0.0242	0.0281	0.0313	0.0326	0.0331	0.0322
15	0.0537	0.0602	0.0689	0.0736	0.0785	0.0808	0.0826
20	0.0871	0.0924	0.0907	0.0898	0.0975	0.0996	0.0999
25	0.0916	0.1016	0.1008	0.0996	0.1007	0.1027	0.1027
30	0.0509	0.0714	0.0750	0.0890	0.0953	0.1072	0.1108
35	0.0481	0.0560	0.0705	0.0783	0.0929	0.0987	0.1128
40	0.0664	0.0741	0.0694	0.0785	0.0926	0.0951	0.1054
45	0.0846	0.0811	0.0842	0.0845	0.0933	0.0938	0.0922
50	0.0908	0.0985	0.1011	0.0999	0.1063	0.1061	0.1018
55	0.0842	0.0869	0.0790	0.0882	0.1025	0.1010	0.0993
60	0.0749	0.0823	0.0849	0.0794	0.0831	0.0841	0.0896
70	0.0504	0.0500	0.0504	0.0467	0.0813	0.0811	0.0972
80	0.0421	0.0380	0.0355	0.0397	0.0420	0.0417	0.0424
90	0.0433	0.0404	0.0395	0.0467	0.0495	0.0492	0.0499

β[°] / α [°]	C_x						
	-4	-2	0	2	4	6	8
-20	-0.0910	-0.0884	-0.0884	-0.0907	-0.0908	-0.0913	-0.0918
-15	-0.0999	-0.1006	-0.1010	-0.1007	-0.1009	-0.1004	-0.1000
-10	-0.1028	-0.1039	-0.1092	-0.1040	-0.1029	-0.1022	-0.1008
-5	-0.0896	-0.0898	-0.0902	-0.0894	-0.0884	-0.0868	-0.0851
0	-0.0595	-0.0602	-0.0606	-0.0600	-0.0592	-0.0584	-0.0566
5	-0.0189	-0.0205	-0.0200	-0.0206	-0.0195	-0.0184	-0.0169
10	0.0327	0.0320	0.0313	0.0313	0.0323	0.0329	0.0328
15	0.0836	0.0835	0.0829	0.0833	0.0829	0.0820	0.0810
20	0.0998	0.0974	0.0971	0.0981	0.0987	0.0992	0.0959
25	0.0995	0.0971	0.0949	0.0960	0.0985	0.0999	0.0984
30	0.1113	0.1116	0.1104	0.1093	0.1096	0.1077	0.1068
35	0.1195	0.1207	0.1201	0.1199	0.1210	0.1188	0.1155
40	0.1091	0.1127	0.1127	0.1139	0.1100	0.1039	0.1031
45	0.0946	0.0992	0.0996	0.0989	0.0978	0.0954	0.0922
50	0.0996	0.1021	0.1071	0.1071	0.1064	0.1070	0.1036
55	0.0980	0.0991	0.1030	0.0972	0.0897	0.0914	0.0969
60	0.0908	0.0915	0.0914	0.0908	0.0893	0.0895	0.0889
70	0.0950	0.1075	0.1190	0.1101	0.1001	0.0967	0.0958
80	0.0478	0.0473	0.0519	0.0484	0.0465	0.0489	0.0472
90	0.0484	0.0500	0.0504	0.0495	0.0463	0.0457	0.0510

β[°] / α [°]	C_x				
	10	15	20	25	30
-20	-0.0943	-0.0955	-0.0988	-0.0920	-0.0931
-15	-0.1006	-0.1038	-0.1065	-0.1075	-0.1046
-10	-0.1014	-0.1024	-0.1021	-0.1019	-0.0971
-5	-0.0821	-0.0756	-0.0731	-0.0691	-0.0640
0	-0.0550	-0.0516	-0.0504	-0.0481	-0.0455
5	-0.0161	-0.0121	-0.0115	-0.0134	-0.0155
10	0.0326	0.0313	0.0281	0.0242	0.0182
15	0.0785	0.0736	0.0689	0.0602	0.0537
20	0.0947	0.0870	0.0879	0.0896	0.0843
25	0.0981	0.0910	0.0982	0.0990	0.0980
30	0.1046	0.0983	0.0843	0.0807	0.0602
35	0.1081	0.0935	0.0857	0.0712	0.0633
40	0.0988	0.0847	0.0756	0.0803	0.0726
45	0.0894	0.0806	0.0803	0.0772	0.0807
50	0.1032	0.0968	0.0980	0.0954	0.0877
55	0.1015	0.0872	0.0780	0.0859	0.0832
60	0.0868	0.0831	0.0886	0.0860	0.0786
70	0.0931	0.0585	0.0622	0.0618	0.0622
80	0.0450	0.0427	0.0385	0.0410	0.0451
90	0.0482	0.0454	0.0382	0.0391	0.0420

$C_x(\alpha,\ \beta,\ \delta_h = 25)$

α [°] \ β [°]	-30	-25	-20	-15	-10	-8	-6
-20	-0.1068	-0.1102	-0.1160	-0.1176	-0.1291	-0.1289	-0.1244
-15	-0.1122	-0.1180	-0.1227	-0.1292	-0.1365	-0.1397	-0.1406
-10	-0.1102	-0.1212	-0.1319	-0.1359	-0.1403	-0.1427	-0.1454
-5	-0.0911	-0.1027	-0.1093	-0.1144	-0.1244	-0.1304	-0.1316
0	-0.0811	-0.0889	-0.0955	-0.0996	-0.1015	-0.1037	-0.1056
5	-0.0575	-0.0588	-0.0631	-0.0676	-0.0671	-0.0694	-0.0715
10	-0.0183	-0.0188	-0.0211	-0.0241	-0.0226	-0.0254	-0.0291
15	0.0195	0.0186	0.0204	0.0186	0.0194	0.0181	0.0154
20	0.0494	0.0626	0.0562	0.0477	0.0323	0.0279	0.0289
25	0.0699	0.0695	0.0627	0.0557	0.0366	0.0316	0.0263
30	0.0207	0.0324	0.0323	0.0293	0.0304	0.0404	0.0419
35	0.0211	0.0282	0.0309	0.0263	0.0307	0.0334	0.0437
40	0.0386	0.0462	0.0331	0.0339	0.0365	0.0407	0.0394
45	0.0460	0.0438	0.0341	0.0311	0.0348	0.0373	0.0362
50	0.0394	0.0479	0.0513	0.0447	0.0538	0.0528	0.0483
55	0.0336	0.0411	0.0380	0.0471	0.0543	0.0508	0.0471
60	0.0158	0.0284	0.0361	0.0335	0.0487	0.0443	0.0442
70	-0.0186	-0.0121	-0.0057	-0.0070	0.0410	0.0451	0.0655
80	-0.0242	-0.0267	-0.0277	-0.0200	-0.0215	-0.0224	-0.0223
90	-0.0208	-0.0271	-0.0135	-0.0229	-0.0156	-0.0165	-0.0141

α [°] \ β [°]	-4	-2	0	2	4	6	8
-20	-0.1158	-0.1137	-0.1141	-0.1164	-0.1192	-0.1200	-0.1240
-15	-0.1416	-0.1442	-0.1450	-0.1448	-0.1428	-0.1408	-0.1440
-10	-0.1480	-0.1520	-0.1633	-0.1518	-0.1482	-0.1457	-0.1438
-5	-0.1320	-0.1333	-0.1337	-0.1340	-0.1322	-0.1309	-0.1280
0	-0.1065	-0.1077	-0.1075	-0.1072	-0.1061	-0.1045	-0.1024
5	-0.0739	-0.0775	-0.0785	-0.0787	-0.0744	-0.0704	-0.0688
10	-0.0333	-0.0370	-0.0336	-0.0345	-0.0326	-0.0283	-0.0247
15	0.0162	0.0198	0.0212	0.0157	0.0131	0.0136	0.0158
20	0.0263	0.0204	0.0187	0.0173	0.0255	0.0183	0.0165
25	0.0207	0.0160	0.0198	0.0165	0.0218	0.0244	0.0228
30	0.0404	0.0385	0.0381	0.0374	0.0379	0.0389	0.0417
35	0.0466	0.0458	0.0479	0.0495	0.0495	0.0487	0.0467
40	0.0411	0.0407	0.0418	0.0431	0.0426	0.0392	0.0405
45	0.0335	0.0338	0.0363	0.0325	0.0340	0.0342	0.0356
50	0.0441	0.0444	0.0472	0.0488	0.0497	0.0507	0.0487
55	0.0445	0.0450	0.0484	0.0442	0.0383	0.0410	0.0471
60	0.0432	0.0451	0.0460	0.0451	0.0433	0.0435	0.0438
70	0.0604	0.0655	0.0641	0.0677	0.0701	0.0702	0.0636
80	-0.0180	-0.0202	-0.0173	-0.0046	0.0281	0.0311	0.0053
90	-0.0184	-0.0173	-0.0173	-0.0168	-0.0185	-0.0183	-0.0130

α [°] \ β [°]	10	15	20	25	30
-20	-0.1243	-0.1128	-0.1112	-0.1054	-0.1020
-15	-0.1397	-0.1324	-0.1259	-0.1212	-0.1154
-10	-0.1419	-0.1375	-0.1335	-0.1228	-0.1118
-5	-0.1243	-0.1143	-0.1092	-0.1026	-0.0910
0	-0.1003	-0.0984	-0.0943	-0.0877	-0.0799
5	-0.0669	-0.0674	-0.0624	-0.0586	-0.0573
10	-0.0236	-0.0251	-0.0221	-0.0198	-0.0193
15	0.0179	0.0171	0.0189	0.0171	0.0180
20	0.0119	0.0273	0.0358	0.0422	0.0290
25	0.0214	0.0405	0.0475	0.0543	0.0547
30	0.0446	0.0435	0.0465	0.0466	0.0349
35	0.0434	0.0390	0.0436	0.0409	0.0338
40	0.0381	0.0355	0.0347	0.0478	0.0402
45	0.0338	0.0301	0.0331	0.0428	0.0450
50	0.0495	0.0478	0.0525	0.0476	0.0376
55	0.0522	0.0432	0.0272	0.0347	0.0315
60	0.0416	0.0363	0.0397	0.0340	0.0246
70	0.0546	0.0033	0.0020	-0.0005	0.0058
80	-0.0210	-0.0288	-0.0312	-0.0240	-0.0152
90	-0.0157	-0.0237	-0.0323	-0.0246	-0.0150

$C_{x,lef}(\alpha, \beta)$

α [°] \ β [°]	-30	-25	-20	-15	-10	-8	-6
-20	-0.0277	-0.0285	-0.0318	-0.0256	-0.0184	-0.0156	-0.0159
-15	-0.0314	-0.0310	-0.0259	-0.0191	-0.0161	-0.0157	-0.0162
-10	-0.0295	-0.0298	-0.0260	-0.0233	-0.0209	-0.0215	-0.0214
-5	-0.0148	-0.0153	-0.0163	-0.0150	-0.0167	-0.0173	-0.0185
0	-0.0136	-0.0149	-0.0143	-0.0136	-0.0168	-0.0178	-0.0182
5	-0.0029	-0.0010	-0.0003	-0.0005	-0.0004	-0.0006	-0.0017
10	0.0085	0.0104	0.0116	0.0121	0.0131	0.0125	0.0122
15	0.0145	0.0168	0.0196	0.0218	0.0225	0.0231	0.0238
20	0.0165	0.0170	0.0205	0.0226	0.0252	0.0245	0.0236
25	0.0138	0.0172	0.0157	0.0178	0.0226	0.0251	0.0264
30	0.0092	0.0122	0.0129	0.0165	0.0202	0.0253	0.0279
35	0.0099	0.0134	0.0162	0.0149	0.0208	0.0229	0.0273
40	0.0206	0.0202	0.0236	0.0246	0.0289	0.0293	0.0290
45	0.0257	0.0274	0.0266	0.0236	0.0266	0.0283	0.0236

α [°] \ β [°]	-4	-2	0	2	4	6	8
-20	-0.0162	-0.0174	-0.0181	-0.0179	-0.0167	-0.0168	-0.0156
-15	-0.0173	-0.0189	-0.0193	-0.0186	-0.0186	-0.0170	-0.0155
-10	-0.0224	-0.0230	-0.0224	-0.0220	-0.0217	-0.0213	-0.0205
-5	-0.0189	-0.0193	-0.0196	-0.0192	-0.0185	-0.0179	-0.0178
0	-0.0188	-0.0197	-0.0202	-0.0196	-0.0188	-0.0180	-0.0172
5	-0.0027	-0.0033	-0.0033	-0.0033	-0.0024	-0.0014	-0.0004
10	0.0119	0.0104	0.0099	0.0096	0.0106	0.0117	0.0126
15	0.0238	0.0231	0.0224	0.0224	0.0226	0.0227	0.0223
20	0.0232	0.0233	0.0221	0.0232	0.0241	0.0250	0.0267
25	0.0274	0.0271	0.0278	0.0275	0.0271	0.0267	0.0249
30	0.0295	0.0296	0.0301	0.0309	0.0306	0.0278	0.0261
35	0.0286	0.0303	0.0305	0.0286	0.0307	0.0292	0.0259
40	0.0320	0.0317	0.0328	0.0314	0.0305	0.0289	0.0281
45	0.0298	0.0268	0.0309	0.0307	0.0280	0.0238	0.0284

α [°] \ β [°]	10	15	20	25	30
-20	-0.0153	-0.0225	-0.0287	-0.0254	-0.0246
-15	-0.0154	-0.0184	-0.0252	-0.0303	-0.0307
-10	-0.0199	-0.0223	-0.0250	-0.0288	-0.0285
-5	-0.0162	-0.0155	-0.0168	-0.0158	-0.0153
0	-0.0160	-0.0144	-0.0151	-0.0149	-0.0144
5	-0.0004	-0.0013	-0.0011	-0.0002	-0.0021
10	0.0127	0.0117	0.0112	0.0100	0.0081
15	0.0222	0.0215	0.0193	0.0165	0.0142
20	0.0276	0.0250	0.0229	0.0212	0.0189
25	0.0252	0.0203	0.0183	0.0198	0.0164
30	0.0247	0.0200	0.0174	0.0167	0.0137
35	0.0253	0.0194	0.0207	0.0179	0.0144
40	0.0262	0.0219	0.0209	0.0175	0.0179
45	0.0254	0.0244	0.0254	0.0262	0.0245

α [°]	$\Delta C_{x,sb}(\alpha)$	$C_{x_q}(\alpha)$	$\Delta C_{x_q,lef}(\alpha)$
-20	-0.0101	0.9530	-1.2200
-15	-0.0101	0.9530	-1.2200
-10	-0.0101	0.9530	-1.2200
-5	-0.0101	1.5500	-1.6600
0	-0.0101	1.9000	-1.6200
5	-0.0358	2.4600	-1.5800
10	-0.0790	2.9200	-1.9600
15	-0.1227	3.3000	-2.5100
20	-0.1827	2.7600	-2.0400
25	-0.1892	2.0500	-1.6400
30	-0.1988	1.5000	-0.8240
35	-0.2000	1.4900	-0.8170
40	-0.1874	1.8300	-1.1000
45	-0.1673	1.2100	-0.5500
50	-0.1476	1.3300	
55	-0.1310	1.6100	
60	-0.1279	0.9100	
70	-0.1325	3.4300	
80	-0.1250	0.6170	
90	-0.1250	0.2730	

II.4. z_b Directional Aerodynamic Force Coefficient Data

$C_z(\alpha, \beta, \delta_h = -25)$

β[°] / α [°]	-30	-25	-20	-15	-10	-8	-6
-20	1.1940	1.2720	1.3110	1.3560	1.3960	1.3470	1.3390
-15	0.9960	1.0570	1.0900	1.1210	1.1280	1.1290	1.1310
-10	0.7930	0.8320	0.8410	0.8560	0.8870	0.8880	0.8990
-5	0.4100	0.4100	0.4200	0.4250	0.4510	0.4640	0.4740
0	0.1800	0.1550	0.1350	0.1300	0.1410	0.1490	0.1540
5	-0.0900	-0.1300	-0.1600	-0.1800	-0.1840	-0.1860	-0.1820
10	-0.3400	-0.4050	-0.4600	-0.4980	-0.5110	-0.5180	-0.5260
15	-0.6100	-0.6650	-0.7200	-0.7700	-0.8060	-0.8180	-0.8370
20	-0.8700	-0.9500	-1.0150	-1.0800	-1.1220	-1.1370	-1.1490
25	-1.1700	-1.2350	-1.2950	-1.3550	-1.4060	-1.4050	-1.4290
30	-1.3150	-1.3800	-1.4450	-1.5150	-1.5810	-1.6710	-1.6970
35	-1.5200	-1.5700	-1.6350	-1.7100	-1.7880	-1.8180	-1.8380
40	-1.6000	-1.6700	-1.7300	-1.8100	-1.8910	-1.9070	-1.9110
45	-1.5600	-1.6150	-1.6850	-1.7200	-1.8540	-1.9910	-2.0330
50	-1.3000	-1.4800	-1.6000	-1.7200	-1.8800	-1.9240	-1.9130
55	-1.7050	-1.7950	-1.8250	-1.8500	-1.9380	-1.9590	-2.0120
60	-1.7000	-1.7400	-1.7300	-1.8950	-1.9330	-1.8800	-1.9070
70	-1.6900	-1.7400	-1.7350	-1.8300	-1.8130	-1.8640	-2.0040
80	-1.9350	-1.9500	-1.9450	-1.9200	-1.8720	-1.8380	-1.9080
90	-1.9600	-1.9350	-1.8500	-1.8700	-1.9530	-2.0360	-2.0130

β[°] / α [°]	-4	-2	0	2	4	6	8
-20	1.3140	1.3210	1.3150	1.3370	1.3320	1.3400	1.3380
-15	1.1430	1.1580	1.1710	1.1770	1.1420	1.1480	1.1310
-10	0.9090	0.9150	0.9250	0.9100	0.8920	0.8890	0.8810
-5	0.4720	0.4740	0.4690	0.4600	0.4540	0.4470	0.4460
0	0.1530	0.1510	0.1550	0.1540	0.1510	0.1470	0.1380
5	-0.1870	-0.1870	-0.1890	-0.1930	-0.1910	-0.1930	-0.1950
10	-0.5350	-0.5340	-0.5300	-0.5320	-0.5250	-0.5200	-0.5210
15	-0.8490	-0.8510	-0.8560	-0.8540	-0.8550	-0.8550	-0.8360
20	-1.1540	-1.1560	-1.1690	-1.1510	-1.1480	-1.1460	-1.1350
25	-1.4410	-1.4460	-1.4460	-1.4520	-1.4490	-1.4550	-1.4400
30	-1.7140	-1.7190	-1.7170	-1.7200	-1.7090	-1.6840	-1.6700
35	-1.8890	-1.9100	-1.9090	-1.9090	-1.8930	-1.8910	-1.8460
40	-1.9830	-2.0160	-2.0370	-1.9320	-1.9900	-1.9690	-1.8360
45	-1.9390	-2.0030	-1.9850	-2.0200	-2.0400	-1.9130	-1.9180
50	-1.8660	-1.8790	-1.9590	-1.9920	-2.0170	-2.0300	-1.9420
55	-1.9990	-1.9690	-2.0100	-1.9650	-1.8470	-1.8950	-1.9280
60	-1.8980	-1.8920	-1.9160	-1.9360	-1.8770	-1.9330	-1.9520
70	-1.9500	-1.9250	-1.9570	-1.9050	-1.8330	-1.9320	-1.9520
80	-1.9490	-1.8260	-1.8160	-1.8370	-1.7550	-1.8480	-1.8580
90	-1.9680	-1.9900	-1.9780	-1.9570	-1.9560	-1.9620	-2.0480

β[°] / α [°]	10	15	20	25	30
-20	1.2940	1.2350	1.1850	1.1400	1.1000
-15	1.1370	1.1300	1.1000	1.0600	1.0050
-10	0.8750	0.8350	0.8210	0.8150	0.7800
-5	0.4400	0.4240	0.4050	0.3940	0.4030
0	0.1290	0.1190	0.1370	0.1230	0.1590
5	-0.1940	-0.1870	-0.1710	-0.1330	-0.0990
10	-0.5150	-0.4980	-0.4650	-0.4020	-0.3410
15	-0.8270	-0.8010	-0.7380	-0.6640	-0.6020
20	-1.1290	-1.0770	-0.9940	-0.9430	-0.8730
25	-1.4150	-1.3560	-1.2880	-1.2170	-1.1670
30	-1.6510	-1.5800	-1.4770	-1.4630	-1.3890
35	-1.8400	-1.7210	-1.6400	-1.5900	-1.5310
40	-1.9180	-1.8390	-1.7550	-1.6710	-1.6300
45	-1.9460	-1.9110	-1.8240	-1.6890	-1.6630
50	-2.0020	-1.8700	-1.7380	-1.6230	-1.4470
55	-1.9650	-1.7550	-1.6970	-1.7060	-1.6180
60	-1.9150	-1.7800	-1.7500	-1.7500	-1.6880
70	-1.8930	-1.8000	-1.8530	-1.7990	-1.7910
80	-1.7740	-1.8100	-1.8640	-1.8850	-1.8340
90	-1.9700	-1.8950	-1.8900	-1.9690	-1.9700

$C_z(\alpha, \beta, \delta_h = -10)$

α [°] \ β [°]	C_z -30	-25	-20	-15	-10	-8	-6
-20	1.1490	1.2140	1.2640	1.2940	1.3270	1.2830	1.2660
-15	0.9480	0.9950	1.0210	1.0470	1.0430	1.0400	1.0370
-10	0.7550	0.7780	0.7770	0.7880	0.8010	0.7990	0.8030
-5	0.3200	0.3200	0.3270	0.3320	0.3500	0.3650	0.3700
0	0.0860	0.0610	0.0410	0.0390	0.0520	0.0560	0.0620
5	-0.1920	-0.2320	-0.2620	-0.2790	-0.2800	-0.2840	-0.2810
10	-0.4550	-0.5220	-0.5750	-0.6110	-0.6240	-0.6320	-0.6410
15	-0.7140	-0.7840	-0.8460	-0.8980	-0.9330	-0.9490	-0.9670
20	-1.0050	-1.0880	-1.1610	-1.2230	-1.2630	-1.2840	-1.2990
25	-1.3130	-1.3780	-1.4450	-1.5090	-1.5600	-1.5660	-1.5830
30	-1.4180	-1.4980	-1.5780	-1.6630	-1.7460	-1.8250	-1.8480
35	-1.5420	-1.6290	-1.7190	-1.8190	-1.9190	-1.9770	-2.0330
40	-1.6710	-1.7680	-1.8620	-1.9670	-2.0740	-2.0770	-2.1510
45	-1.6150	-1.5770	-1.7700	-1.9630	-2.1300	-2.2170	-2.1840
50	-1.4060	-1.5920	-1.7160	-1.9440	-2.0260	-2.0810	-2.0810
55	-1.6880	-1.7380	-1.7210	-1.8090	-2.0140	-2.0480	-2.1120
60	-1.7240	-1.7930	-1.8000	-1.7560	-1.9490	-1.9230	-1.9750
70	-1.7430	-1.7540	-1.8110	-1.7810	-1.8390	-1.8970	-2.0040
80	-1.9350	-1.9930	-1.9790	-1.9910	-1.9280	-1.8770	-1.9310
90	-1.9900	-2.0090	-1.9500	-1.9790	-2.0060	-2.0850	-2.0190

α [°] \ β [°]	C_z -4	-2	0	2	4	6	8
-20	1.2450	1.2340	1.2280	1.2580	1.2570	1.2680	1.2650
-15	1.0420	1.0500	1.0590	1.0660	1.0480	1.0510	1.0400
-10	0.8040	0.8120	0.8150	0.8130	0.8050	0.8040	0.8000
-5	0.3720	0.3570	0.3560	0.3520	0.3490	0.3430	0.3370
0	0.0620	0.0610	0.0640	0.0620	0.0610	0.0580	0.0530
5	-0.2870	-0.2870	-0.2870	-0.2890	-0.2910	-0.2890	-0.2910
10	-0.6470	-0.6500	-0.6500	-0.6510	-0.6460	-0.6420	-0.6380
15	-0.9760	-0.9770	-0.9800	-0.9800	-0.9780	-0.9770	-0.9630
20	-1.3060	-1.3020	-1.3060	-1.2920	-1.2890	-1.2870	-1.2790
25	-1.5900	-1.5950	-1.5940	-1.5970	-1.5950	-1.5950	-1.5840
30	-1.8610	-1.8610	-1.8630	-1.8630	-1.8560	-1.8360	-1.8160
35	-2.0640	-2.0790	-2.0900	-2.0810	-2.0750	-2.0670	-2.0340
40	-2.1840	-2.1990	-2.2160	-2.1920	-2.1940	-2.0840	-2.1100
45	-2.2160	-2.3060	-2.2630	-2.3040	-2.3040	-2.2420	-2.2350
50	-2.0330	-2.0310	-2.0970	-2.1180	-2.1310	-2.1420	-2.0620
55	-2.1000	-2.0580	-2.0880	-2.0670	-1.9720	-2.0160	-2.0190
60	-1.9900	-2.0050	-2.0510	-2.0210	-1.9140	-1.9560	-1.9980
70	-1.9990	-1.9860	-2.0270	-1.9430	-1.8350	-1.9250	-1.9930
80	-1.9810	-1.8920	-1.9160	-1.9380	-1.8560	-1.9430	-1.9470
90	-2.0070	-2.0190	-1.9980	-1.9900	-2.0040	-2.0360	-2.1020

α [°] \ β [°]	C_z 10	15	20	25	30
-20	1.2360	1.1960	1.1540	1.1090	1.0630
-15	1.0530	1.0510	1.0310	0.9990	0.9550
-10	0.7970	0.7760	0.7690	0.7650	0.7470
-5	0.3280	0.3170	0.3090	0.2950	0.3060
0	0.0470	0.0350	0.0490	0.0440	0.0760
5	-0.2930	-0.2920	-0.2750	-0.2440	-0.2050
10	-0.6350	-0.6220	-0.5870	-0.5240	-0.4630
15	-0.9510	-0.9230	-0.8640	-0.7900	-0.7170
20	-1.2660	-1.2200	-1.1460	-1.0900	-1.0050
25	-1.5660	-1.5050	-1.4450	-1.3740	-1.3070
30	-1.7950	-1.7350	-1.6130	-1.5570	-1.4700
35	-1.9890	-1.8960	-1.8000	-1.6960	-1.6130
40	-2.1110	-1.9960	-1.9000	-1.7870	-1.7020
45	-2.2100	-2.1210	-1.8910	-1.6540	-1.6960
50	-2.1290	-2.0470	-1.8190	-1.6950	-1.5090
55	-2.0250	-1.8200	-1.7320	-1.7490	-1.6690
60	-1.9850	-1.7920	-1.8360	-1.8290	-1.7600
70	-1.9210	-1.8630	-1.8930	-1.8360	-1.8250
80	-1.8480	-1.9110	-1.8990	-1.9130	-1.8550
90	-2.0030	-1.9760	-1.9470	-2.0060	-1.9870

$C_z(\alpha, \beta, \delta_h = 0)$

α [°] \ β [°]	-30	-25	-20	-15	-10	-8	-6
-20	1.0910	1.1400	1.2030	1.2150	1.2390	1.2010	1.1710
-15	0.9050	0.9390	0.9590	0.9800	0.9670	0.9600	0.9540
-10	0.7130	0.7180	0.7060	0.7110	0.7050	0.6990	0.6960
-5	0.2650	0.2650	0.2700	0.2750	0.2880	0.3050	0.3060
0	-0.0060	-0.0300	-0.0500	-0.0500	-0.0360	-0.0350	-0.0280
5	-0.2750	-0.3150	-0.3450	-0.3600	-0.3590	-0.3640	-0.3620
10	-0.5500	-0.6200	-0.6700	-0.7050	-0.7190	-0.7270	-0.7370
15	-0.8250	-0.9100	-0.9800	-1.0350	-1.0690	-1.0890	-1.1050
20	-1.1150	-1.2000	-1.2800	-1.3400	-1.3790	-1.4050	-1.4210
25	-1.3750	-1.4400	-1.5100	-1.5750	-1.6260	-1.6350	-1.6500
30	-1.5200	-1.6150	-1.7100	-1.8100	-1.9100	-1.9770	-1.9970
35	-1.5550	-1.6650	-1.7700	-1.8850	-1.9980	-2.0730	-2.1520
40	-1.7150	-1.8300	-1.9450	-2.0650	-2.1880	-2.1830	-2.3010
45	-1.6250	-1.5700	-1.7850	-2.0000	-2.1780	-2.2720	-2.2100
50	-1.5700	-1.7350	-1.9000	-2.0500	-2.1650	-2.2540	-2.2880
55	-1.7750	-1.9000	-1.9700	-2.0550	-2.1760	-2.1840	-2.2230
60	-1.9000	-1.9350	-1.9600	-1.9950	-2.1280	-2.1110	-2.1730
70	-1.9300	-1.9450	-1.9400	-1.9200	-1.9290	-2.0210	-2.1610
80	-2.0000	-2.0450	-2.0750	-2.0800	-2.0450	-1.9940	-2.0480
90	-1.9600	-1.9500	-1.9000	-2.0100	-2.0600	-2.1580	-2.1120

α [°] \ β [°]	-4	-2	0	2	4	6	8
-20	1.1570	1.1220	1.1160	1.1560	1.1600	1.1750	1.1720
-15	0.9510	0.9530	0.9590	0.9660	0.9640	0.9650	0.9590
-10	0.6870	0.6970	0.6920	0.7050	0.7080	0.7100	0.7100
-5	0.3110	0.2850	0.2870	0.2860	0.2850	0.2800	0.2710
0	-0.0270	-0.0270	-0.0250	-0.0280	-0.0280	-0.0290	-0.0310
5	-0.3680	-0.3680	-0.3670	-0.3680	-0.3720	-0.3680	-0.3700
10	-0.7410	-0.7470	-0.7500	-0.7500	-0.7460	-0.7440	-0.7360
15	-1.1110	-1.1110	-1.1120	-1.1120	-1.1080	-1.1060	-1.0980
20	-1.4310	-1.4220	-1.4180	-1.4080	-1.4050	-1.4030	-1.3960
25	-1.6550	-1.6590	-1.6580	-1.6600	-1.6580	-1.6550	-1.6460
30	-2.0060	-2.0020	-2.0080	-2.0060	-2.0010	-1.9810	-1.9610
35	-2.1710	-2.1820	-2.2000	-2.1860	-2.1860	-2.1740	-2.1490
40	-2.3100	-2.3140	-2.3280	-2.3550	-2.3210	-2.1560	-2.2810
45	-2.2640	-2.3580	-2.3110	-2.3530	-2.3500	-2.2990	-2.2900
50	-2.2580	-2.2580	-2.3260	-2.3120	-2.2900	-2.2770	-2.1840
55	-2.2110	-2.1960	-2.2520	-2.2350	-2.1450	-2.1820	-2.1650
60	-2.1830	-2.1810	-2.2080	-2.1900	-2.0940	-2.1310	-2.1500
70	-2.1600	-2.1200	-2.1340	-2.0850	-2.0110	-2.1080	-2.1250
80	-2.0920	-1.9920	-2.0040	-2.0190	-1.9300	-2.0140	-2.0180
90	-2.1170	-2.1450	-2.1400	-2.1130	-2.1070	-2.1010	-2.1690

α [°] \ β [°]	10	15	20	25	30
-20	1.1610	1.1450	1.1150	1.0700	1.0150
-15	0.9780	0.9800	0.9700	0.9450	0.9100
-10	0.7090	0.7100	0.7100	0.7100	0.7100
-5	0.2600	0.2510	0.2510	0.2340	0.2470
0	-0.0340	-0.0480	-0.0370	-0.0330	-0.0060
5	-0.3730	-0.3770	-0.3600	-0.3350	-0.2920
10	-0.7350	-0.7250	-0.6890	-0.6260	-0.5640
15	-1.0830	-1.0530	-0.9990	-0.9240	-0.8400
20	-1.3820	-1.3360	-1.2710	-1.2100	-1.1130
25	-1.6310	-1.5700	-1.5130	-1.4420	-1.3670
30	-1.9390	-1.8880	-1.7990	-1.6510	-1.5500
35	-2.1040	-2.0020	-1.8970	-1.7600	-1.6630
40	-2.2310	-2.0950	-1.9910	-1.8600	-1.7470
45	-2.2550	-2.1570	-2.0020	-1.6480	-1.7020
50	-2.2390	-2.1090	-1.9860	-1.8480	-1.6490
55	-2.1520	-2.0250	-1.9650	-1.9310	-1.8000
60	-2.1140	-1.9900	-1.9860	-1.9620	-1.8760
70	-2.0630	-1.9700	-2.0160	-1.9470	-1.9240
80	-1.9190	-2.0000	-2.0340	-2.0320	-1.9580
90	-2.0730	-2.0740	-2.0380	-2.0880	-2.0600

$C_z(\alpha, \beta, \delta_n = 10)$

α [°] \ β [°]	-30	-25	-20	-15	-10	-8	-6
	C_z						
-20	1.0210	1.0660	1.1160	1.1260	1.1390	1.1080	1.1030
-15	0.8150	0.8380	0.8460	0.8630	0.8540	0.8480	0.8440
-10	0.6220	0.6180	0.6030	0.6090	0.6060	0.6020	0.5990
-5	0.1810	0.1760	0.1790	0.1840	0.1980	0.2120	0.2130
0	-0.0690	-0.1000	-0.1250	-0.1310	-0.1220	-0.1200	-0.1140
5	-0.3390	-0.4000	-0.4440	-0.4740	-0.4800	-0.4800	-0.4810
10	-0.5850	-0.6300	-0.7150	-0.7680	-0.8060	-0.8100	-0.8240
15	-0.8430	-0.9470	-1.0310	-1.0790	-1.1330	-1.1470	-1.1670
20	-1.1040	-1.2000	-1.2870	-1.3560	-1.4040	-1.4310	-1.4460
25	-1.3620	-1.4580	-1.5600	-1.6550	-1.7410	-1.7710	-1.7710
30	-1.5200	-1.6300	-1.7400	-1.8540	-1.9680	-2.0370	-2.0700
35	-1.6900	-1.8560	-2.0690	-2.1360	-2.2520	-2.2550	-2.2600
40	-1.8490	-1.9490	-2.0540	-2.1690	-2.2900	-2.3610	-2.3430
45	-1.5900	-1.4840	-1.7410	-2.0000	-2.1930	-2.2790	-2.1860
50	-1.7070	-1.8910	-2.0130	-2.2550	-2.1410	-2.2000	-2.2040
55	-1.7350	-1.8380	-1.8440	-1.9040	-2.1330	-2.1590	-2.2170
60	-1.7990	-1.8890	-1.9170	-1.9420	-2.0970	-2.0650	-2.1120
70	-1.7530	-1.7520	-1.7970	-1.7790	-1.9870	-2.0480	-2.1570
80	-2.0670	-2.1230	-2.1070	-2.1450	-2.0530	-1.9110	-1.9740
90	-2.0080	-2.0200	-1.9550	-2.0760	-2.0260	-2.1160	-2.0610

α [°] \ β [°]	-4	-2	0	2	4	6	8
	C_z						
-20	1.0700	1.0410	1.0390	1.0710	1.0760	1.0890	1.0860
-15	0.8410	0.8460	0.8490	0.8560	0.8520	0.8530	0.8480
-10	0.5920	0.6000	0.5960	0.6050	0.6070	0.6090	0.6090
-5	0.2150	0.2020	0.2050	0.2020	0.1980	0.1920	0.1830
0	-0.1120	-0.1150	-0.1140	-0.1170	-0.1170	-0.1210	-0.1230
5	-0.4860	-0.4870	-0.4900	-0.4900	-0.5040	-0.4960	-0.4910
10	-0.8330	-0.8440	-0.8490	-0.8510	-0.8420	-0.8460	-0.8310
15	-1.1750	-1.1820	-1.1770	-1.1710	-1.1760	-1.1750	-1.1710
20	-1.4530	-1.4450	-1.4420	-1.4350	-1.4300	-1.4340	-1.4280
25	-1.7820	-1.7940	-1.7890	-1.7870	-1.7910	-1.7750	-1.7750
30	-2.0810	-2.0830	-2.0820	-2.0800	-2.0700	-2.0540	-2.0390
35	-2.3260	-2.3170	-2.3080	-2.3550	-2.3410	-2.3020	-2.2590
40	-2.3750	-2.2840	-2.4110	-2.4190	-2.4020	-2.3450	-2.3330
45	-2.2620	-2.3950	-2.3060	-2.3730	-2.3690	-2.2950	-2.2930
50	-2.1650	-2.1790	-2.2610	-2.2830	-2.2810	-2.2940	-2.1820
55	-2.2090	-2.1840	-2.2310	-2.1860	-2.0680	-2.1150	-2.1450
60	-2.1230	-2.1400	-2.1850	-2.1640	-2.0650	-2.1070	-2.1420
70	-2.1490	-2.0480	-2.2680	-2.1780	-2.0640	-2.1420	-2.1610
80	-2.0240	-1.9260	-1.9400	-1.9670	-1.8910	-1.9780	-1.9760
90	-2.0570	-2.0730	-2.0570	-2.0340	-2.0330	-2.0300	-2.0950

α [°] \ β [°]	10	15	20	25	30
	C_z				
-20	1.0780	1.0700	1.0460	1.0070	0.9570
-15	0.8630	0.8630	0.8560	0.8410	0.8200
-10	0.6090	0.6070	0.6070	0.6110	0.6190
-5	0.1800	0.1650	0.1630	0.1550	0.1690
0	-0.1260	-0.1340	-0.1220	-0.1090	-0.0750
5	-0.4930	-0.4830	-0.4580	-0.4120	-0.3540
10	-0.8250	-0.8010	-0.7520	-0.6760	-0.5950
15	-1.1580	-1.1200	-1.0470	-0.9540	-0.8640
20	-1.4140	-1.3570	-1.2860	-1.2150	-1.1100
25	-1.7600	-1.6460	-1.5820	-1.4730	-1.3700
30	-2.0160	-1.9290	-1.7900	-1.6730	-1.5630
35	-2.2190	-2.0810	-1.9380	-1.7600	-1.6790
40	-2.3030	-2.1630	-2.0650	-1.9710	-1.8780
45	-2.2620	-2.1750	-1.9930	-1.5550	-1.6610
50	-2.2180	-2.1780	-1.9360	-1.8140	-1.6300
55	-2.1800	-1.9510	-1.8910	-1.8850	-1.7820
60	-2.1210	-1.9660	-1.9410	-1.9130	-1.8230
70	-2.1020	-1.8940	-1.9120	-1.8670	-1.8680
80	-1.8720	-1.9640	-1.9260	-1.9420	-1.8860
90	-1.9960	-2.0460	-1.9250	-1.9900	-1.9780

$C_z(\alpha, \beta, \delta_h = 25)$

α [°] \ β [°]	-30	-25	-20	-15	-10	-8	-6
-20	0.7230	0.7250	0.7440	0.7440	0.7110	0.7090	0.6970
-15	0.5120	0.4950	0.4610	0.4650	0.4700	0.4700	0.4710
-10	0.2490	0.2120	0.1860	0.1950	0.2030	0.2050	0.2020
-5	0.1000	0.0900	0.0900	0.0950	0.1110	0.1220	0.1220
0	-0.1500	-0.1900	-0.2200	-0.2350	-0.2320	-0.2240	-0.2240
5	-0.3850	-0.4600	-0.5150	-0.5880	-0.5660	-0.5630	-0.5660
10	-0.6200	-0.6900	-0.7600	-0.8300	-0.8920	-0.8910	-0.9100
15	-0.8650	-0.9900	-1.0900	-1.1700	-1.2080	-1.2150	-1.2390
20	-1.0550	-1.1950	-1.3200	-1.4300	-1.5190	-1.5500	-1.5640
25	-1.3600	-1.4600	-1.5700	-1.6700	-1.7630	-1.7970	-1.7940
30	-1.5200	-1.6350	-1.7500	-1.8700	-1.9890	-2.0580	-2.0950
35	-1.6150	-1.7500	-1.8750	-1.9950	-2.1110	-2.1540	-2.2000
40	-1.7750	-1.8750	-1.9800	-2.0950	-2.2160	-2.2870	-2.2690
45	-1.7400	-1.8450	-1.9250	-2.0000	-2.1300	-2.2510	-2.2860
50	-1.5700	-1.7400	-1.9000	-2.0500	-2.1560	-2.2160	-2.2030
55	-1.7000	-1.8100	-1.8800	-1.9500	-2.0430	-2.1700	-2.1840
60	-1.7950	-1.8950	-1.9600	-2.0200	-2.1130	-2.0940	-2.1240
70	-1.7800	-1.7850	-1.7900	-1.8100	-1.8730	-1.9430	-2.0590
80	-1.9500	-1.9800	-1.9800	-1.9600	-1.9110	-1.8810	-1.9550
90	-1.9250	-1.9200	-1.8700	-1.8850	-1.9690	-2.0710	-2.0290

α [°] \ β [°]	-4	-2	0	2	4	6	8
-20	0.6970	0.6960	0.7100	0.7040	0.7150	0.7200	0.7210
-15	0.4670	0.4830	0.4760	0.4810	0.4720	0.4750	0.4730
-10	0.2030	0.2070	0.2050	0.2000	0.1940	0.1980	0.1980
-5	0.1220	0.1210	0.1250	0.1210	0.1140	0.1070	0.0970
0	-0.2210	-0.2270	-0.2280	-0.2310	-0.2320	-0.2390	-0.2410
5	-0.5710	-0.5720	-0.5780	-0.5780	-0.5990	-0.5880	-0.5770
10	-0.9240	-0.9390	-0.9460	-0.9490	-0.9360	-0.9450	-0.9240
15	-1.2500	-1.2690	-1.2530	-1.2400	-1.2550	-1.2550	-1.2570
20	-1.5580	-1.5550	-1.5540	-1.5630	-1.5490	-1.5770	-1.5780
25	-1.8060	-1.8200	-1.8140	-1.8110	-1.8160	-1.7980	-1.8000
30	-2.1070	-2.1120	-2.1080	-2.1060	-2.0940	-2.0790	-2.0660
35	-2.2400	-2.2420	-2.2480	-2.2610	-2.2550	-2.2310	-2.1980
40	-2.3010	-2.2100	-2.3370	-2.3450	-2.3280	-2.2710	-2.2590
45	-2.2700	-2.2390	-2.3270	-2.2890	-2.2880	-2.3120	-2.2820
50	-2.1580	-2.1750	-2.2610	-2.2660	-2.2620	-2.2550	-2.1530
55	-2.1110	-2.2040	-2.2310	-2.2030	-2.1020	-2.1350	-2.1730
60	-2.1240	-2.1340	-2.1740	-2.1770	-2.1030	-2.1530	-2.1750
70	-2.2740	-2.0000	-2.2590	-2.2110	-1.8850	-2.2210	-2.2120
80	-2.0050	-1.8940	-1.8990	-2.0090	-2.0140	-2.1010	-2.0140
90	-2.0390	-2.0700	-2.0690	-2.0260	-2.0050	-2.0000	-2.0850

α [°] \ β [°]	10	15	20	25	30
-20	0.7210	0.7500	0.7500	0.7400	0.7100
-15	0.4730	0.4650	0.4700	0.4900	0.5150
-10	0.2010	0.1850	0.1900	0.2100	0.2500
-5	0.1010	0.0810	0.0770	0.0770	0.0930
0	-0.2440	-0.2440	-0.2320	-0.2070	-0.1640
5	-0.5790	-0.5590	-0.5280	-0.4670	-0.3980
10	-0.9130	-0.8760	-0.8130	-0.7240	-0.6260
15	-1.2450	-1.1980	-1.1030	-0.9900	-0.8910
20	-1.5630	-1.4530	-1.3580	-1.2410	-1.0970
25	-1.7850	-1.6610	-1.5950	-1.4790	-1.3710
30	-2.0430	-1.9430	-1.8040	-1.6810	-1.5680
35	-2.1550	-2.0370	-1.9150	-1.7600	-1.6700
40	-2.2290	-2.0890	-1.9910	-1.8970	-1.8040
45	-2.2320	-2.0990	-2.0300	-1.9450	-1.8340
50	-2.2010	-2.1100	-1.9840	-1.8410	-1.6370
55	-2.1070	-1.9500	-1.8920	-1.8770	-1.7650
60	-2.1440	-2.0000	-1.9600	-1.9300	-1.8380
70	-2.1250	-1.9700	-1.9070	-1.8820	-1.8740
80	-1.8250	-1.8400	-1.8990	-1.9220	-1.8730
90	-2.0070	-1.9350	-1.9480	-1.9890	-1.9510

$C_{z,lef}(\alpha, \beta)$

α [°] \ β [°]	$C_{z,lef}$						
	-30	-25	-20	-15	-10	-8	-6
-20	1.1830	1.2460	1.2790	1.2900	1.3690	1.3640	1.2970
-15	0.9600	1.0180	1.0550	1.0930	1.0580	1.0390	1.0310
-10	0.7090	0.7100	0.7020	0.7040	0.7010	0.7100	0.7300
-5	0.2220	0.2160	0.2310	0.2270	0.2400	0.2430	0.2440
0	-0.0660	-0.0840	-0.0900	-0.1050	-0.1040	-0.0990	-0.1070
5	-0.3170	-0.3470	-0.3900	-0.4140	-0.4200	-0.4170	-0.4170
10	-0.5690	-0.6190	-0.6790	-0.7030	-0.7280	-0.7650	-0.7720
15	-0.8530	-0.9290	-1.0180	-1.0700	-1.0980	-1.1160	-1.1140
20	-1.1060	-1.1680	-1.2280	-1.3140	-1.3480	-1.3590	-1.3620
25	-1.3140	-1.4070	-1.4650	-1.5060	-1.5640	-1.5980	-1.6280
30	-1.4960	-1.5100	-1.5890	-1.6920	-1.7750	-1.8140	-1.8460
35	-1.5940	-1.6940	-1.8070	-1.8750	-1.9570	-1.9760	-2.0320
40	-1.6830	-1.7550	-1.9120	-1.9990	-2.1110	-2.1490	-2.1470
45	-1.6640	-1.7830	-1.8590	-1.9620	-2.0300	-2.1290	-1.9170

α [°] \ β [°]	$C_{z,lef}$						
	-4	-2	0	2	4	6	8
-20	1.2770	1.2760	1.2560	1.2810	1.2800	1.3120	1.3150
-15	1.0190	1.0250	1.0350	1.0330	1.0420	1.0430	1.0560
-10	0.7290	0.7290	0.7250	0.7290	0.7280	0.7280	0.7230
-5	0.2490	0.2490	0.2480	0.2480	0.2420	0.2390	0.2350
0	-0.0990	-0.0990	-0.1000	-0.1010	-0.1040	-0.1040	-0.1040
5	-0.4210	-0.4240	-0.4280	-0.4210	-0.4280	-0.4220	-0.4230
10	-0.7740	-0.7720	-0.7740	-0.7700	-0.7670	-0.7610	-0.7540
15	-1.1510	-1.1420	-1.1390	-1.1350	-1.1180	-1.1120	-1.1070
20	-1.3520	-1.3570	-1.3550	-1.3710	-1.3760	-1.3700	-1.3790
25	-1.6470	-1.6460	-1.6500	-1.6420	-1.6410	-1.6180	-1.5990
30	-1.8750	-1.8790	-1.8830	-1.8910	-1.8760	-1.8430	-1.8380
35	-2.0600	-2.0700	-2.0770	-2.0380	-2.0390	-2.0280	-2.0050
40	-2.2040	-2.2070	-2.2040	-2.2050	-2.1950	-2.1930	-2.1740
45	-2.1430	-2.0500	-2.2080	-2.2010	-2.1820	-2.0770	-2.2090

α [°] \ β [°]	$C_{z,lef}$				
	10	15	20	25	30
-20	1.3060	1.2270	1.2160	1.1830	1.1200
-15	1.0560	1.0910	1.0530	1.0160	0.9580
-10	0.7110	0.7140	0.7120	0.7200	0.7190
-5	0.2290	0.2160	0.2200	0.2050	0.2110
0	-0.1060	-0.1070	-0.0920	-0.0860	-0.0680
5	-0.4250	-0.4190	-0.3950	-0.3520	-0.3220
10	-0.7560	-0.7310	-0.7070	-0.6450	-0.5970
15	-1.0990	-1.0710	-1.0190	-0.9300	-0.8540
20	-1.3990	-1.3650	-1.2790	-1.2190	-1.1570
25	-1.5850	-1.5270	-1.4860	-1.4280	-1.3350
30	-1.8110	-1.7280	-1.6250	-1.5460	-1.5320
35	-1.9860	-1.9040	-1.8360	-1.7130	-1.6230
40	-2.1330	-2.0210	-1.9340	-1.7770	-1.7050
45	-2.1260	-2.0580	-1.9550	-1.8790	-1.7600

α [°]	$\Delta C_{z,sb}(\alpha)$	$C_{z_q}(\alpha)$	$\Delta C_{z_q,lef}(\alpha)$
-20	-0.3858	-23.9000	15.1000
-15	-0.3858	-23.9000	15.1000
-10	-0.3858	-23.9000	15.1000
-5	-0.3858	-29.5000	3.7000
0	-0.3858	-29.5000	0.6000
5	-0.2685	-30.5000	-1.3000
10	-0.3021	-31.3000	0.3000
15	-0.4248	-30.1000	-3.8000
20	-0.2094	-27.7000	-4.6000
25	-0.0969	-28.2000	-0.2000
30	0.4380	-29.0000	-2.7000
35	0.9470	-29.8000	-3.5000
40	0.0014	-38.3000	-1.3000
45	-0.0097	-35.3000	-0.6500
50	-0.0153	-32.3000	
55	-0.0520	-27.3000	
60	-0.0010	-25.2000	
70	-0.0202	-27.3000	
80	-0.0369	-9.3500	
90	-0.0369	-2.1600	

II.5. y_b Directional Aerodynamic Moment Coefficient Data

$C_m(\alpha, \beta, \delta_h = -25)$

α [°] \ β [°]	-30	-25	-20	-15	-10	-8	-6
	C_m						
-20	0.2509	0.1937	0.1918	0.1850	0.1692	0.1693	0.1770
-15	0.1698	0.1650	0.1733	0.1723	0.1533	0.1618	0.1639
-10	0.1426	0.1579	0.1807	0.1641	0.1533	0.1586	0.1595
-5	0.1620	0.1770	0.1530	0.1450	0.1380	0.1365	0.1329
0	0.1530	0.1540	0.1480	0.1450	0.1445	0.1438	0.1430
5	0.1470	0.1530	0.1560	0.1570	0.1586	0.1595	0.1585
10	0.1500	0.1620	0.1650	0.1700	0.1746	0.1758	0.1768
15	0.1670	0.1760	0.1910	0.1960	0.2000	0.2012	0.2041
20	0.1510	0.1700	0.1900	0.2020	0.2073	0.2098	0.2122
25	0.1200	0.1470	0.1750	0.1940	0.2043	0.2028	0.2028
30	0.1080	0.0670	0.0980	0.1500	0.1704	0.1930	0.1985
35	0.0820	0.0470	0.0680	0.0810	0.1174	0.1233	0.1522
40	0.1130	0.0500	0.0600	0.0870	0.1131	0.1279	0.1341
45	0.0930	0.0660	0.0650	0.0530	0.0734	0.0914	0.0968
50	-0.0150	-0.0110	-0.0250	0.0150	0.0663	0.0644	0.0498
55	0.0190	0.0170	-0.0860	-0.0040	0.0794	0.0494	0.0174
60	-0.0360	-0.0320	-0.0750	-0.0600	-0.0627	-0.0705	-0.0556
70	-0.3070	-0.3080	-0.2850	-0.3050	-0.2769	-0.2648	-0.1828
80	-0.3650	-0.3980	-0.4030	-0.3870	-0.3411	-0.3344	-0.3425
90	-0.5260	-0.5270	-0.5150	-0.5040	-0.4900	-0.5157	-0.4801

α [°] \ β [°]	-4	-2	0	2	4	6	8
	C_m						
-20	0.1746	0.1742	0.1750	0.1721	0.1758	0.1801	0.1826
-15	0.1607	0.1597	0.1584	0.1589	0.1615	0.1573	0.1534
-10	0.1629	0.1615	0.1590	0.1566	0.1534	0.1523	0.1489
-5	0.1269	0.1242	0.1216	0.1183	0.1212	0.1236	0.1267
0	0.1411	0.1412	0.1409	0.1410	0.1409	0.1403	0.1409
5	0.1577	0.1580	0.1580	0.1591	0.1584	0.1576	0.1572
10	0.1778	0.1833	0.1845	0.1840	0.1824	0.1811	0.1797
15	0.2062	0.2069	0.2087	0.2070	0.2066	0.2055	0.2022
20	0.2129	0.2137	0.2152	0.2133	0.2118	0.2109	0.2082
25	0.1991	0.1981	0.1978	0.1969	0.1957	0.1958	0.1948
30	0.2009	0.2022	0.2022	0.2021	0.2007	0.1972	0.1947
35	0.1713	0.1789	0.1814	0.1815	0.1799	0.1790	0.1703
40	0.1433	0.1483	0.1478	0.1291	0.1312	0.1245	0.1025
45	0.0848	0.0935	0.0922	0.0940	0.0838	0.0610	0.0491
50	0.0407	0.0521	0.0745	0.0670	0.0453	0.0373	0.0320
55	0.0530	0.0292	0.0713	0.0404	0.0007	-0.0024	0.0165
60	-0.0534	-0.0549	-0.0540	-0.0618	-0.0674	-0.0828	-0.0849
70	-0.2115	-0.2032	-0.2244	-0.2264	-0.2195	-0.2054	-0.2203
80	-0.3455	-0.3254	-0.3389	-0.3522	-0.3187	-0.3262	-0.3283
90	-0.4970	-0.4831	-0.4723	-0.4830	-0.4818	-0.4911	-0.5074

α [°] \ β [°]	10	15	20	25	30
	C_m				
-20	0.1912	0.2070	0.2140	0.2160	0.2270
-15	0.1464	0.1650	0.1670	0.1580	0.1630
-10	0.1493	0.1580	0.1750	0.1530	0.1380
-5	0.1303	0.1373	0.1444	0.1679	0.1538
0	0.1414	0.1448	0.1453	0.1523	0.1513
5	0.1573	0.1568	0.1557	0.1540	0.1472
10	0.1784	0.1750	0.1701	0.1663	0.1547
15	0.2000	0.1958	0.1901	0.1755	0.1668
20	0.2061	0.1991	0.1878	0.1618	0.1479
25	0.1953	0.1877	0.1687	0.1406	0.1330
30	0.1901	0.1696	0.1186	0.0889	0.1270
35	0.1459	0.1124	0.0962	0.0757	0.1132
40	0.1028	0.0745	0.0495	0.0406	0.1024
45	0.0420	0.0208	0.0343	0.0338	0.0600
50	0.0397	-0.0114	-0.0514	-0.0371	-0.0408
55	0.0281	-0.0562	-0.1373	-0.0343	-0.0335
60	-0.1004	-0.0976	-0.1117	-0.0599	-0.0714
70	-0.2191	-0.2479	-0.2276	-0.2518	-0.2503
80	-0.3285	-0.3763	-0.3923	-0.3857	-0.3532
90	-0.4863	-0.5001	-0.5124	-0.5227	-0.5219

$C_m(\alpha, \beta, \delta_h = -10)$

α [°] \ β [°]	Cm -30	-25	-20	-15	-10	-8	-6
-20	0.1469	0.1272	0.1210	0.1075	0.0798	0.0756	0.0800
-15	0.1087	0.0956	0.0947	0.0885	0.0581	0.0549	0.0505
-10	0.0784	0.0743	0.0852	0.0619	0.0390	0.0344	0.0290
-5	0.0570	0.0620	0.0440	0.0320	0.0170	0.0160	0.0120
0	0.0520	0.0540	0.0430	0.0390	0.0420	0.0410	0.0420
5	0.0520	0.0420	0.0500	0.0530	0.0560	0.0530	0.0540
10	0.0280	0.0350	0.0400	0.0400	0.0470	0.0480	0.0500
15	0.0430	0.0400	0.0530	0.0600	0.0630	0.0630	0.0670
20	0.0270	0.0250	0.0400	0.0500	0.0570	0.0560	0.0580
25	0.0100	0.0080	0.0230	0.0380	0.0470	0.0480	0.0480
30	0.0150	-0.0350	-0.0170	0.0030	0.0200	0.0400	0.0470
35	0.0160	-0.0270	-0.0340	-0.0240	-0.0060	0.0040	0.0160
40	0.0680	0.0190	-0.0160	-0.0130	-0.0080	-0.0070	-0.0060
45	0.0250	-0.0210	-0.0270	-0.0540	-0.0500	-0.0390	-0.0530
50	-0.0111	0	-0.0070	-0.0105	0.0073	-0.0085	-0.0371
55	0.0002	0.0043	-0.0936	-0.0425	0.0359	0.0134	-0.0110
60	-0.0879	-0.0315	-0.0384	-0.1757	-0.0962	-0.1050	-0.0912
70	-0.3429	-0.3579	-0.3430	-0.3564	-0.3520	-0.3363	-0.2691
80	-0.4294	-0.4715	-0.4877	-0.4833	-0.4315	-0.4235	-0.4238
90	-0.6208	-0.6173	-0.6028	-0.5959	-0.5532	-0.5881	-0.5617

α [°] \ β [°]	Cm -4	-2	0	2	4	6	8
-20	0.0827	0.0853	0.0864	0.0782	0.0811	0.0821	0.0847
-15	0.0427	0.0378	0.0328	0.0353	0.0426	0.0481	0.0499
-10	0.0249	0.0177	0.0041	0.0169	0.0227	0.0280	0.0311
-5	0.0080	0.0100	0.0076	0.0070	0.0080	0.0100	0.0110
0	0.0430	0.0430	0.0430	0.0420	0.0430	0.0370	0.0380
5	0.0530	0.0520	0.0501	0.0520	0.0510	0.0510	0.0510
10	0.0500	0.0510	0.0553	0.0520	0.0530	0.0520	0.0520
15	0.0690	0.0720	0.0706	0.0710	0.0700	0.0700	0.0680
20	0.0600	0.0650	0.0674	0.0690	0.0660	0.0620	0.0550
25	0.0460	0.0480	0.0492	0.0460	0.0470	0.0440	0.0430
30	0.0490	0.0510	0.0528	0.0480	0.0480	0.0450	0.0400
35	0.0240	0.0310	0.0278	0.0280	0.0250	0.0120	0.0130
40	-0.0050	-0.0060	-0.0094	-0.0220	-0.0220	-0.0440	-0.0380
45	-0.0540	-0.0390	-0.0411	-0.0470	-0.0580	-0.0720	-0.0750
50	-0.0519	-0.0379	-0.0129	-0.0221	-0.0455	-0.0542	-0.0594
55	-0.0169	-0.0113	0.0202	-0.0131	-0.0553	-0.0602	-0.0424
60	-0.0857	-0.0794	-0.0708	-0.0887	-0.1045	-0.1247	-0.1264
70	-0.3005	-0.2924	-0.3137	-0.3113	-0.3001	-0.2868	-0.3076
80	-0.4321	-0.4110	-0.4236	-0.4445	-0.4185	-0.4268	-0.4231
90	-0.5859	-0.5773	-0.5718	-0.5728	-0.5618	-0.5680	-0.5878

α [°] \ β [°]	Cm 10	15	20	25	30
-20	0.0965	0.1240	0.1376	0.1439	0.1631
-15	0.0524	0.0820	0.0891	0.0898	0.1002
-10	0.0357	0.0505	0.0820	0.0707	0.0752
-5	0.0120	0.0270	0.0390	0.0580	0.0520
0	0.0370	0.0430	0.0450	0.0570	0.0500
5	0.0510	0.0510	0.0490	0.0430	0.0520
10	0.0510	0.0430	0.0420	0.0380	0.0300
15	0.0630	0.0590	0.0530	0.0400	0.0420
20	0.0520	0.0460	0.0360	0.0200	0.0220
25	0.0430	0.0340	0.0190	0.0020	0.0050
30	0.0330	0.0160	-0.0005	-0.0240	0.0280
35	0.0030	-0.0210	-0.0260	-0.0200	0.0230
40	-0.0410	-0.0470	-0.0500	-0.0130	0.0330
45	-0.0810	-0.0850	-0.0560	-0.0510	-0.0060
50	-0.0515	-0.0693	-0.0658	-0.0588	-0.0699
55	-0.0319	-0.1104	-0.1614	-0.0635	-0.0676
60	-0.1414	-0.2209	-0.0836	-0.0767	-0.1331
70	-0.3124	-0.3168	-0.3034	-0.3182	-0.3033
80	-0.4175	-0.4693	-0.4737	-0.4575	-0.4154
90	-0.5702	-0.5789	-0.5858	-0.6003	-0.6038

$C_m(\alpha, \beta, \delta_n = 0)$

α [°] \ β [°]	C_m -30	-25	-20	-15	-10	-8	-6
-20	0.0978	0.0719	0.0621	0.0430	0.0054	-0.0023	-0.0006
-15	0.0560	0.0357	0.0264	0.0163	-0.0240	-0.0372	-0.0472
-10	0.0342	0.0167	0.0194	-0.0089	-0.0410	-0.0510	-0.0608
-5	-0.0240	-0.0240	-0.0390	-0.0550	-0.0758	-0.0773	-0.0802
0	-0.0550	-0.0460	-0.0590	-0.0640	-0.0660	-0.0660	-0.0639
5	-0.0460	-0.0640	-0.0550	-0.0520	-0.0514	-0.0507	-0.0509
10	-0.0670	-0.0620	-0.0560	-0.0530	-0.0495	-0.0484	-0.0467
15	-0.0670	-0.0770	-0.0680	-0.0590	-0.0536	-0.0514	-0.0489
20	-0.0570	-0.0710	-0.0620	-0.0520	-0.0478	-0.0518	-0.0498
25	-0.0640	-0.0880	-0.0770	-0.0670	-0.0548	-0.0539	-0.0530
30	-0.0450	-0.0105	-0.0920	-0.0920	-0.0782	-0.0608	-0.0529
35	-0.0220	-0.0720	-0.0920	-0.0880	-0.0738	-0.0639	-0.0594
40	0.0450	0.0050	-0.0520	-0.0610	-0.0662	-0.0729	-0.0739
45	-0.0010	-0.0520	-0.0600	-0.0920	-0.0927	-0.0861	-0.1056
50	-0.0090	-0.0130	-0.0170	-0.0350	-0.0780	-0.0713	-0.0774
55	-0.0510	-0.0180	-0.0650	-0.0530	-0.0477	-0.0520	-0.0583
60	-0.1830	-0.1480	-0.1730	-0.1720	-0.1512	-0.1428	-0.1118
70	-0.3830	-0.3980	-0.3820	-0.3870	-0.3869	-0.3637	-0.2706
80	-0.4830	-0.5180	-0.5280	-0.5060	-0.4850	-0.4785	-0.4804
90	-0.6330	-0.6300	-0.6160	-0.6160	-0.6067	-0.6366	-0.6053

α [°] \ β [°]	C_m -4	-2	0	2	4	6	8
-20	0.0062	0.0114	0.0127	0.0001	0.0023	0.0006	0.0033
-15	-0.0590	-0.0674	-0.0755	-0.0712	-0.0600	-0.0460	-0.0393
-10	-0.0700	-0.0813	-0.1025	-0.0793	-0.0673	-0.0576	-0.0500
-5	-0.0802	-0.0774	-0.0744	-0.0774	-0.0782	-0.0784	-0.0782
0	-0.0615	-0.0605	-0.0598	-0.0600	-0.0606	-0.0608	-0.0617
5	-0.0501	-0.0499	-0.0498	-0.0500	-0.0518	-0.0526	-0.0532
10	-0.0457	-0.0444	-0.0437	-0.0448	-0.0458	-0.0480	-0.0490
15	-0.0456	-0.0419	-0.0407	-0.0410	-0.0422	-0.0432	-0.0447
20	-0.0463	-0.0384	-0.0342	-0.0329	-0.0366	-0.0426	-0.0532
25	-0.0520	-0.0499	-0.0507	-0.0501	-0.0506	-0.0526	-0.0539
30	-0.0500	-0.0471	-0.0459	-0.0510	-0.0520	-0.0542	-0.0612
35	-0.0572	-0.0567	-0.0605	-0.0605	-0.0625	-0.0729	-0.0747
40	-0.0789	-0.0820	-0.0835	-0.0917	-0.0971	-0.1252	-0.1071
45	-0.0966	-0.0862	-0.0923	-0.0975	-0.1080	-0.1168	-0.1209
50	-0.0890	-0.0913	-0.0826	-0.0898	-0.1112	-0.1201	-0.1277
55	-0.0663	-0.0830	-0.0738	-0.0851	-0.1053	-0.1050	-0.0988
60	-0.1094	-0.1266	-0.1414	-0.1436	-0.1437	-0.1521	-0.1459
70	-0.2967	-0.2944	-0.3216	-0.3252	-0.3199	-0.3123	-0.3385
80	-0.4869	-0.4605	-0.4678	-0.4883	-0.4620	-0.4774	-0.4792
90	-0.6281	-0.6217	-0.6184	-0.6163	-0.6022	-0.6073	-0.6281

α [°] \ β [°]	C_m 10	15	20	25	30
-20	0.0177	0.0550	0.0740	0.0840	0.1100
-15	-0.0287	0.0110	0.0220	0.0310	0.0460
-10	-0.0424	-0.0100	0.0180	0.0140	0.0320
-5	-0.0770	-0.0572	-0.0400	-0.0251	-0.0260
0	-0.0621	-0.0606	-0.0587	-0.0484	-0.0517
5	-0.0537	-0.0545	-0.0564	-0.0619	-0.0651
10	-0.0498	-0.0534	-0.0555	-0.0619	-0.0658
15	-0.0484	-0.0536	-0.0609	-0.0715	-0.0613
20	-0.0555	-0.0620	-0.0705	-0.0800	-0.0660
25	-0.0560	-0.0649	-0.0761	-0.0888	-0.0633
30	-0.0680	-0.0847	-0.0849	-0.0971	-0.0364
35	-0.0804	-0.0930	-0.0974	-0.0775	-0.0279
40	-0.1116	-0.1057	-0.0979	-0.0402	0.0022
45	-0.1243	-0.1234	-0.0897	-0.0820	-0.0294
50	-0.1222	-0.1220	-0.0852	-0.0648	-0.0624
55	-0.1000	-0.1076	-0.1152	-0.0589	-0.1047
60	-0.1530	-0.1709	-0.1741	-0.1475	-0.1841
70	-0.3487	-0.3486	-0.3445	-0.3593	-0.3444
80	-0.4821	-0.5022	-0.5242	-0.5145	-0.4788
90	-0.6115	-0.6209	-0.6210	-0.6351	-0.6381

$C_m(\alpha, \beta, \delta_h = 10)$

α [°] \ β[°]	-30	-25	-20	-15	-10	-8	-6
-20	0.0200	-0.0036	-0.0107	-0.0334	-0.0778	-0.0944	-0.0926
-15	-0.0153	-0.0385	-0.0525	-0.0743	-0.1233	-0.1376	-0.1466
-10	-0.0549	-0.0792	-0.0932	-0.1226	-0.1521	-0.1609	-0.1688
-5	-0.1120	-0.1240	-0.1520	-0.1680	-0.1830	-0.1880	-0.1910
0	-0.1170	-0.1270	-0.1520	-0.1590	-0.1600	-0.1600	-0.1590
5	-0.1050	-0.1330	-0.1440	-0.1550	-0.1550	-0.1550	-0.1550
10	-0.0970	-0.1120	-0.1220	-0.1350	-0.1420	-0.1420	-0.1510
15	-0.0970	-0.1180	-0.1330	-0.1510	-0.1520	-0.1500	-0.1550
20	-0.0620	-0.0830	-0.0970	-0.1060	-0.1340	-0.1420	-0.1380
25	-0.0750	-0.1030	-0.1130	-0.1080	-0.1370	-0.1440	-0.1530
30	-0.0880	-0.1680	-0.1650	-0.1720	-0.1710	-0.1550	-0.1500
35	-0.1050	-0.1611	-0.1862	-0.2095	-0.1951	-0.1760	-0.1514
40	-0.0438	-0.1079	-0.1281	-0.1485	-0.1405	-0.1272	-0.1301
45	-0.1448	-0.0931	-0.1319	-0.1793	-0.1518	-0.1264	-0.1053
50	-0.1530	-0.1330	-0.1280	-0.1470	-0.1077	-0.1030	-0.1111
55	-0.0760	-0.0630	-0.1520	-0.0570	-0.0075	-0.0460	-0.0865
60	-0.1710	-0.1200	-0.1350	-0.1400	-0.1588	-0.1634	-0.1455
70	-0.4001	-0.4044	-0.3789	-0.4050	-0.3419	-0.3364	-0.2610
80	-0.5082	-0.5338	-0.5333	-0.5253	-0.4877	-0.4848	-0.4902
90	-0.6368	-0.6326	-0.6174	-0.6217	-0.5909	-0.6214	-0.5906

α [°] \ β[°]	-4	-2	0	2	4	6	8
-20	-0.0855	-0.0815	-0.0835	-0.0955	-0.0930	-0.0943	-0.0881
-15	-0.1551	-0.1663	-0.1719	-0.1683	-0.1568	-0.1437	-0.1371
-10	-0.1774	-0.1880	-0.2153	-0.1839	-0.1738	-0.1648	-0.1594
-5	-0.1920	-0.1890	-0.1888	-0.1900	-0.1930	-0.1930	-0.1981
0	-0.1570	-0.1620	-0.1610	-0.1620	-0.1630	-0.1670	-0.1620
5	-0.1550	-0.1580	-0.1606	-0.1610	-0.1620	-0.1570	-0.1570
10	-0.1530	-0.1570	-0.1548	-0.1550	-0.1520	-0.1530	-0.1450
15	-0.1550	-0.1520	-0.1452	-0.1480	-0.1550	-0.1550	-0.1570
20	-0.1340	-0.1300	-0.1264	-0.1260	-0.1260	-0.1510	-0.1610
25	-0.1540	-0.1540	-0.1530	-0.1550	-0.1500	-0.1500	-0.1600
30	-0.1470	-0.1440	-0.1440	-0.1450	-0.1460	-0.1530	-0.1570
35	-0.1444	-0.1427	-0.1411	-0.1450	-0.1513	-0.1565	-0.1627
40	-0.1367	-0.1555	-0.1450	-0.1543	-0.1595	-0.1527	-0.1644
45	-0.1575	-0.1807	-0.1411	-0.1635	-0.1655	-0.1635	-0.1815
50	-0.1154	-0.1161	-0.1008	-0.1060	-0.1254	-0.1273	-0.1228
55	-0.0614	-0.0976	-0.0679	-0.0922	-0.1253	-0.1221	-0.0972
60	-0.1444	-0.1512	-0.1556	-0.1653	-0.1719	-0.1866	-0.1859
70	-0.2714	-0.2201	-0.1983	-0.2363	-0.2655	-0.2695	-0.2844
80	-0.4970	-0.4677	-0.4721	-0.4929	-0.4669	-0.4776	-0.4787
90	-0.6146	-0.6099	-0.6083	-0.6080	-0.5958	-0.5979	-0.6109

α [°] \ β[°]	10	15	20	25	30
-20	-0.0743	-0.0265	-0.0040	0.0034	0.0268
-15	-0.1295	-0.0798	-0.0589	-0.0445	-0.0241
-10	-0.1525	-0.1225	-0.0931	-0.1276	-0.0548
-5	-0.1830	-0.1680	-0.1520	-0.1250	-0.1120
0	-0.1620	-0.1620	-0.1530	-0.1260	-0.1170
5	-0.1560	-0.1560	-0.1450	-0.1330	-0.1180
10	-0.1460	-0.1400	-0.1260	-0.1170	-0.1040
15	-0.1520	-0.1510	-0.1340	-0.1180	-0.0960
20	-0.1660	-0.1370	-0.1260	-0.1150	-0.0940
25	-0.1640	-0.1330	-0.1380	-0.1290	-0.0990
30	-0.1560	-0.1590	-0.1520	-0.1550	-0.0750
35	-0.1705	-0.1836	-0.1611	-0.1363	-0.0815
40	-0.1682	-0.1791	-0.1553	-0.1362	-0.0744
45	-0.1872	-0.2206	-0.1644	-0.1320	-0.1935
50	-0.1052	-0.1442	-0.1253	-0.1286	-0.1498
55	-0.0797	-0.1301	-0.2255	-0.1358	-0.1481
60	-0.1985	-0.1808	-0.1758	-0.1621	-0.2116
70	-0.2833	-0.3734	-0.3473	-0.3728	-0.3685
80	-0.4779	-0.5155	-0.5235	-0.5240	-0.4984
90	-0.5865	-0.6173	-0.6130	-0.6282	-0.6324

$C_m(\alpha,\ \beta,\ \delta_h = 25)$

α [°] \ β [°]	-30	-25	-20	-15	-10	-8	-6
-20	-0.0818	-0.1023	-0.1060	-0.1334	-0.1866	-0.2149	-0.2128
-15	-0.1160	-0.1432	-0.1646	-0.2020	-0.2635	-0.2792	-0.2868
-10	-0.1527	-0.1845	-0.2168	-0.2480	-0.2740	-0.2816	-0.2874
-5	-0.1770	-0.2000	-0.2370	-0.2520	-0.2630	-0.2698	-0.2734
0	-0.1740	-0.1970	-0.2340	-0.2470	-0.2487	-0.2486	-0.2493
5	-0.1640	-0.1920	-0.2190	-0.2430	-0.2429	-0.2425	-0.2441
10	-0.1280	-0.1620	-0.1880	-0.2160	-0.2297	-0.2289	-0.2391
15	-0.1160	-0.1480	-0.1810	-0.2150	-0.2186	-0.2174	-0.2272
20	-0.0680	-0.0930	-0.1240	-0.1540	-0.2203	-0.2311	-0.2272
25	-0.0750	-0.1090	-0.1320	-0.1330	-0.1882	-0.2123	-0.2264
30	-0.0970	-0.1860	-0.1860	-0.1980	-0.1989	-0.1828	-0.1798
35	-0.1040	-0.1600	-0.1850	-0.2080	-0.1936	-0.1746	-0.1503
40	-0.0250	-0.0840	-0.1120	-0.1300	-0.1248	-0.1157	-0.1182
45	-0.0570	-0.0680	-0.0880	-0.1260	-0.1157	-0.1018	-0.1055
50	-0.1080	-0.0930	-0.0930	-0.0870	-0.0745	-0.0894	-0.1198
55	-0.1250	-0.1150	-0.2070	-0.1030	-0.0588	-0.0831	-0.1095
60	-0.1430	-0.0820	-0.0850	-0.0910	-0.1251	-0.1492	-0.1507
70	-0.4220	-0.4380	-0.4250	-0.4330	-0.3390	-0.3231	-0.2373
80	-0.4500	-0.5000	-0.5240	-0.5140	-0.4633	-0.4648	-0.4746
90	-0.5600	-0.5920	-0.5130	-0.5930	-0.5674	-0.6030	-0.5774

α [°] \ β [°]	-4	-2	0	2	4	6	8
-20	-0.2055	-0.2030	-0.2093	-0.2204	-0.2176	-0.2185	-0.2077
-15	-0.2906	-0.3059	-0.3079	-0.3052	-0.2933	-0.2816	-0.2750
-10	-0.2952	-0.3025	-0.3391	-0.2988	-0.2907	-0.2825	-0.2794
-5	-0.2737	-0.2738	-0.2741	-0.2761	-0.2782	-0.2785	-0.2756
0	-0.2489	-0.2539	-0.2527	-0.2524	-0.2524	-0.2532	-0.2517
5	-0.2476	-0.2540	-0.2562	-0.2589	-0.2581	-0.2482	-0.2428
10	-0.2519	-0.2626	-0.2554	-0.2599	-0.2530	-0.2501	-0.2367
15	-0.2283	-0.2258	-0.2157	-0.2184	-0.2297	-0.2305	-0.2310
20	-0.2205	-0.2205	-0.2165	-0.2182	-0.2138	-0.2589	-0.2705
25	-0.2304	-0.2337	-0.2325	-0.2322	-0.2269	-0.2243	-0.2382
30	-0.1762	-0.1751	-0.1740	-0.1732	-0.1782	-0.1855	-0.1875
35	-0.1433	-0.1416	-0.1401	-0.1440	-0.1502	-0.1555	-0.1616
40	-0.1245	-0.1400	-0.1320	-0.1411	-0.1463	-0.1532	-0.1523
45	-0.1203	-0.1230	-0.1113	-0.1232	-0.1304	-0.1350	-0.1445
50	-0.1388	-0.1366	-0.1234	-0.1254	-0.1416	-0.1463	-0.1508
55	-0.0791	-0.1189	-0.0929	-0.1186	-0.1533	-0.1523	-0.1304
60	-0.1570	-0.1589	-0.1584	-0.1689	-0.1773	-0.1947	-0.1982
70	-0.2547	-0.2277	-0.2303	-0.3505	-0.1931	-0.1880	-0.2371
80	-0.4862	-0.4621	-0.4716	-0.4474	-0.3916	-0.4082	-0.4299
90	-0.6021	-0.5938	-0.5886	-0.5839	-0.5673	-0.5700	-0.5885

α [°] \ β [°]	10	15	20	25	30
-20	-0.1946	-0.1330	-0.1060	-0.1020	-0.0820
-15	-0.2717	-0.2080	-0.1730	-0.1510	-0.1230
-10	-0.2734	-0.2460	-0.2150	-0.1830	-0.1500
-5	-0.2632	-0.2527	-0.2370	-0.2002	-0.1772
0	-0.2491	-0.2491	-0.2359	-0.1983	-0.1748
5	-0.2427	-0.2434	-0.2199	-0.1939	-0.1612
10	-0.2330	-0.2220	-0.1938	-0.1664	-0.1338
15	-0.2190	-0.2175	-0.1838	-0.1502	-0.1195
20	-0.2751	-0.2111	-0.1811	-0.1482	-0.1227
25	-0.2465	-0.1828	-0.1848	-0.1595	-0.1250
30	-0.1852	-0.1824	-0.1732	-0.1478	-0.0814
35	-0.1694	-0.1825	-0.1603	-0.1356	-0.0808
40	-0.1562	-0.1636	-0.1432	-0.1159	-0.0582
45	-0.1488	-0.1618	-0.1188	-0.1003	-0.0933
50	-0.1421	-0.1550	-0.1585	-0.1588	-0.1771
55	-0.1158	-0.1580	-0.2612	-0.1702	-0.1812
60	-0.2150	-0.1808	-0.1737	-0.1719	-0.2333
70	-0.2701	-0.3635	-0.3563	-0.3697	-0.3534
80	-0.4593	-0.5113	-0.5202	-0.4961	-0.4460
90	-0.5696	-0.5961	-0.6158	-0.5951	-0.5634

$C_{m,lef}(\alpha, \beta)$

β[°] / α [°]	$C_{m,lef}$ -30	-25	-20	-15	-10	-8	-6
-20	0.0922	0.0559	0.0525	-0.0338	-0.0518	-0.0650	-0.0574
-15	0.0372	0.0062	-0.0067	-0.0217	-0.0702	-0.0860	-0.1001
-10	0.0251	0.0006	0.0014	-0.0229	-0.0536	-0.0634	-0.0654
-5	-0.0006	-0.0193	-0.0234	-0.0321	-0.0386	-0.0389	-0.0385
0	-0.0273	-0.0246	-0.0230	-0.0231	-0.0259	-0.0255	-0.0286
5	-0.0319	-0.0272	-0.0204	-0.0170	-0.0152	-0.0148	-0.0145
10	-0.0446	-0.0368	-0.0266	-0.0166	-0.0127	-0.0113	-0.0092
15	-0.0682	-0.0587	-0.0425	-0.0197	0	0.0026	0.0078
20	-0.0947	-0.0851	-0.0642	-0.0536	-0.0308	-0.0293	-0.0275
25	-0.1090	-0.1235	-0.0938	-0.0777	-0.0674	-0.0648	-0.0607
30	-0.0135	-0.0857	-0.0907	-0.1013	-0.0875	-0.0983	-0.0951
35	-0.0202	-0.0510	-0.0891	-0.1086	-0.1018	-0.1014	-0.1105
40	-0.0116	-0.0639	-0.0971	-0.1156	-0.1170	-0.1142	-0.1182
45	-0.0023	-0.0164	-0.0417	-0.0987	-0.0985	-0.0975	-0.1278

β[°] / α [°]	$C_{m,lef}$ -4	-2	0	2	4	6	8
-20	-0.0554	-0.0550	-0.0530	-0.0521	-0.0483	-0.0459	-0.0404
-15	-0.1000	-0.1002	-0.1012	-0.0974	-0.0939	-0.0839	-0.0837
-10	-0.0656	-0.0652	-0.0647	-0.0653	-0.0659	-0.0654	-0.0631
-5	-0.0386	-0.0388	-0.0387	-0.0389	-0.0387	-0.0388	-0.0392
0	-0.0271	-0.0271	-0.0267	-0.0266	-0.0272	-0.0280	-0.0267
5	-0.0138	-0.0127	-0.0128	-0.0133	-0.0141	-0.0149	-0.0157
10	-0.0057	-0.0033	-0.0016	-0.0017	-0.0025	-0.0038	-0.0049
15	0.0158	0.0243	0.0323	0.0328	0.0290	0.0189	0.0120
20	-0.0234	-0.0188	-0.0161	-0.0141	-0.0136	-0.0154	-0.0180
25	-0.0558	-0.0526	-0.0455	-0.0471	-0.0479	-0.0530	-0.0563
30	-0.0913	-0.0902	-0.0871	-0.0865	-0.0896	-0.0962	-0.0997
35	-0.1117	-0.1127	-0.1151	-0.1167	-0.1230	-0.1301	-0.1387
40	-0.1160	-0.1178	-0.1206	-0.1280	-0.1347	-0.1436	-0.1512
45	-0.1042	-0.1156	-0.0979	-0.1122	-0.1225	-0.1444	-0.1340

β[°] / α [°]	$C_{m,lef}$ 10	15	20	25	30
-20	-0.0373	-0.0193	0.0670	0.0704	0.1067
-15	-0.0759	-0.0274	-0.0124	0.0005	0.0315
-10	-0.0570	-0.0263	-0.0020	-0.0028	0.0217
-5	-0.0386	-0.0321	-0.0234	-0.0193	-0.0006
0	-0.0270	-0.0242	-0.0241	-0.0257	-0.0284
5	-0.0164	-0.0182	-0.0216	-0.0287	-0.0331
10	-0.0085	-0.0124	-0.0224	-0.0326	-0.0404
15	0.0061	-0.0136	-0.0364	-0.0526	-0.0621
20	-0.0273	-0.0501	-0.0607	-0.0816	-0.0912
25	-0.0610	-0.0713	-0.0874	-0.1171	-0.1026
30	-0.1060	-0.1198	-0.1092	-0.1042	-0.0320
35	-0.1402	-0.1470	-0.1275	-0.0894	-0.0142
40	-0.1516	-0.1502	-0.1317	-0.0985	-0.0462
45	-0.1461	-0.1463	-0.0893	-0.0640	-0.0499

α [°]	$\Delta C_{m,sb}(\alpha)$	$\Delta C_{m}(\alpha)$	$C_{m_q}(\alpha)$	$\Delta C_{m_{q}def}(\alpha)$
-20	-0.0034	0.0190	6.8400	-0.3670
-15	-0.0034	0.0190	6.8400	-0.3670
-10	-0.0034	0.0190	6.8400	-0.3670
-5	-0.0034	0.0190	3.4200	2.8800
0	-0.0034	0.0190	5.4800	0.2500
5	0.0289	0.0190	5.4500	0.2700
10	0.0215	0.0200	6.0200	-0.2100
15	0.0122	0.0400	6.7000	0.3600
20	0.0241	0.0400	5.6900	-1.2600
25	0.0263	0.0500	6.0000	-2.5100
30	-0.0163	0.0600	6.2000	-1.6600
35	-0.0428	0.0600	6.4000	-1.7200
40	-0.0704	0.0600	6.6000	-1.2000
45	-0.0844	0.0600	6.0000	-0.6000
50	-0.0789	0.0600	5.5500	
55	-0.0603	0.0600	5.0000	
60	-0.0450	0.0600	4.5000	
70	-0.0578	0.0600	3.5000	
80	-0.0107	0.0600	5.6000	
90	-0.0107	0.0600	4.0400	

δ_h	-25	-10	0	10	25
$\eta_{\delta h}$	1.0000	1.0000	1.0000	1.0000	0.9500

$\Delta C_{m,sb}(\alpha)$

δ_h [°] / α [°]	$\Delta C_{m,sb}$						
	-25	-10	0	10	15	20	25
-20	0	0	0	0	0	0	0
-15	0	0	0	0	0	0	0
-10	0	0	0	0	0	0	0
-5	0	0	0	0	0	0	0
0	0	0	0	0	0	0	0
5	0	0	0	0	0	0	0
10	0	0	0	0	0	0	0
15	0	0	0	0	0	0	0
20	0	0	0	0	0	0	0
25	0	0	0	0	0	0	0
30	0	0	0	0	0	0	0
35	0	0	0	0	-0.0113	-0.0132	0
40	0	0.0100	0.0100	0.0200	0.0041	0.0297	0.0254
45	0.0480	0.0570	0.0640	0.0700	0.0706	0.0506	0.0407
50	0.0390	0.0540	0.1050	0.0750	0.0792	0.0747	0.0822
55	0	0.0250	0.0750	0.0400	0.0416	0.0500	0.0583
60	0.0840	0.0800	0.1060	0.1000	0.0886	0.0776	0.0785
70	0.0990	0.0750	0.1320	0.0200	0.0288	0.0361	0.0468
80	0.0200	0.0100	0.0500	0	0.0218	-0.0251	-0.0210
90	0	0.0100	0.0400	0	-0.0345	-0.0378	-0.0378

II.6. y_b Directional Aerodynamic Force Coefficient Data

$C_y(\alpha, \beta)$

α [°] \ β [°]	-30	-25	-20	-15	-10	-8	-6
-20	0.3677	0.3070	0.2460	0.1844	0.1062	0.0850	0.0677
-15	0.4019	0.3220	0.2651	0.1964	0.1332	0.1039	0.0753
-10	0.4367	0.3823	0.3185	0.2462	0.1513	0.1156	0.0760
-5	0.5538	0.4778	0.3758	0.2818	0.1833	0.1449	0.1055
0	0.6218	0.5258	0.4208	0.3088	0.2014	0.1553	0.1138
5	0.6544	0.5514	0.4294	0.3124	0.2028	0.1607	0.1133
10	0.6255	0.5185	0.4225	0.3065	0.2016	0.1597	0.1131
15	0.5885	0.4665	0.3755	0.2875	0.1837	0.1473	0.1069
20	0.5783	0.4633	0.3383	0.2563	0.1814	0.1504	0.1116
25	0.5005	0.4195	0.3005	0.2295	0.1643	0.1409	0.1029
30	0.3751	0.3161	0.2291	0.1411	0.0927	0.1057	0.0911
35	0.3292	0.2952	0.2112	0.1472	0.0857	0.0581	0.0651
40	0.4470	0.3885	0.3025	0.2135	0.0748	0.0531	0.0303
45	0.1634	0.0894	0.0444	0.0894	0.0782	0.0612	0.0458
50	0.1366	0.1036	0.0916	0.1556	0.0866	0.0785	0.0555
55	0.1735	0.1355	0.1795	0.1725	0.1104	0.0926	0.0663
60	0.2233	0.1713	0.2083	0.1883	0.1230	0.1051	0.0788
70	0.2609	0.2279	0.1739	0.1469	0.1074	0.0941	0.0765
80	0.3055	0.2595	0.2165	0.1635	0.1096	0.0871	0.0753
90	0.3078	0.2498	0.1998	0.1568	0.1089	0.0843	0.0658

α [°] \ β [°]	-4	-2	0	2	4	6	8
-20	0.0380	0.0186	0	-0.0232	-0.0467	-0.0747	-0.1078
-15	0.0442	0.0175	0	-0.0188	-0.0402	-0.0681	-0.1004
-10	0.0434	0.0161	0	-0.0124	-0.0430	-0.0792	-0.1171
-5	0.0662	0.0325	0	-0.0420	-0.0763	-0.1177	-0.1575
0	0.0726	0.0371	0	-0.0394	-0.0764	-0.1191	-0.1674
5	0.0767	0.0331	0	-0.0383	-0.0819	-0.1233	-0.1705
10	0.0748	0.0345	0	-0.0383	-0.0786	-0.1204	-0.1668
15	0.0652	0.0298	0	-0.0383	-0.0770	-0.1200	-0.1642
20	0.0703	0.0332	0	-0.0248	-0.0558	-0.0984	-0.1366
25	0.0654	0.0343	0	-0.0335	-0.0677	-0.1028	-0.1369
30	0.0630	0.0297	0	-0.0306	-0.0647	-0.0906	-0.1159
35	0.0563	0.0264	0	-0.0214	-0.0513	-0.0806	-0.0971
40	0.0360	0.0123	0	-0.0320	-0.0484	-0.0664	-0.0958
45	0.0398	0.0279	0	-0.0868	-0.1048	-0.1365	-0.1541
50	0.0399	0.0302	0	-0.0178	-0.0791	-0.1060	-0.1177
55	0.0460	0.0424	0	-0.0087	-0.0718	-0.1065	-0.1225
60	0.0546	0.0474	0	-0.0048	-0.0571	-0.0840	-0.1047
70	0.0564	0.0371	0	-0.0113	-0.0300	-0.0477	-0.0715
80	0.0498	0.0212	0	-0.0203	-0.0361	-0.0655	-0.0804
90	0.0446	0.0203	0	-0.0263	-0.0418	-0.0611	-0.0836

α [°] \ β [°]	10	15	20	25	30
-20	-0.1421	-0.2221	-0.2861	-0.3461	-0.4081
-15	-0.1317	-0.1930	-0.2540	-0.3190	-0.3980
-10	-0.1542	-0.2482	-0.3212	-0.3842	-0.4382
-5	-0.2072	-0.3041	-0.4001	-0.5013	-0.5794
0	-0.2134	-0.3198	-0.4315	-0.5369	-0.6400
5	-0.2173	-0.3257	-0.4430	-0.5506	-0.6514
10	-0.2171	-0.3204	-0.4347	-0.5313	-0.6371
15	-0.2056	-0.3091	-0.3966	-0.4868	-0.6100
20	-0.1729	-0.2479	-0.3280	-0.4542	-0.5698
25	-0.1692	-0.2337	-0.3044	-0.4241	-0.5030
30	-0.1353	-0.1841	-0.2743	-0.3600	-0.4189
35	-0.1022	-0.1632	-0.2282	-0.3141	-0.3488
40	-0.1075	-0.1539	-0.1575	-0.1807	-0.2242
45	-0.1830	-0.1940	-0.1506	-0.1951	-0.2662
50	-0.1508	-0.2201	-0.1565	-0.1679	-0.2008
55	-0.1468	-0.2090	-0.2153	-0.1709	-0.2107
60	-0.1242	-0.1885	-0.2077	-0.1719	-0.2099
70	-0.0859	-0.1266	-0.1534	-0.2078	-0.2421
80	-0.1027	-0.1554	-0.2075	-0.2495	-0.2954
90	-0.1068	-0.1547	-0.1986	-0.2474	-0.3047

$C_{y,lef}(\alpha, \beta)$

β[°] / α [°]	$C_{y,lef}$						
	-30	-25	-20	-15	-10	-8	-6
-20	0.3692	0.2991	0.2417	0.1692	0.1078	0.0874	0.0837
-15	0.4368	0.3797	0.3249	0.2636	0.1826	0.1456	0.1068
-10	0.5000	0.4441	0.3671	0.2896	0.1871	0.1475	0.1096
-5	0.5683	0.4913	0.3913	0.2943	0.1926	0.1490	0.1125
0	0.6293	0.5313	0.4173	0.3053	0.2024	0.1582	0.1116
5	0.6397	0.5367	0.4267	0.3097	0.2042	0.1630	0.1174
10	0.6132	0.5192	0.4302	0.3142	0.2080	0.1631	0.1187
15	0.5416	0.4876	0.4126	0.3066	0.2023	0.1576	0.1168
20	0.4750	0.3750	0.2950	0.2300	0.1576	0.1254	0.0919
25	0.4878	0.3708	0.2508	0.1578	0.1176	0.1174	0.0893
30	0.3436	0.3226	0.2286	0.1396	0.0825	0.0801	0.0757
35	0.2437	0.2267	0.1757	0.1307	0.0776	0.0602	0.0535
40	0.1976	0.1776	0.1566	0.1286	0.0906	0.0737	0.0593
45	0.1741	0.1251	0.1201	0.1321	0.1110	0.0854	0.0550

β[°] / α [°]	$C_{y,lef}$						
	-4	-2	0	2	4	6	8
-20	0.0572	0.0260	0	-0.0258	-0.0592	-0.0863	-0.1209
-15	0.0701	0.0336	0	-0.0337	-0.0702	-0.1100	-0.1500
-10	0.0757	0.0377	0	-0.0339	-0.0708	-0.1108	-0.1513
-5	0.0723	0.0369	0	-0.0363	-0.0765	-0.1169	-0.1644
0	0.0729	0.0374	0	-0.0374	-0.0776	-0.1223	-0.1712
5	0.0775	0.0394	0	-0.0352	-0.0785	-0.1189	-0.1689
10	0.0784	0.0370	0	-0.0378	-0.0774	-0.1228	-0.1664
15	0.0718	0.0377	0	-0.0368	-0.0784	-0.1194	-0.1636
20	0.0590	0.0282	0	-0.0313	-0.0670	-0.1023	-0.1374
25	0.0585	0.0286	0	-0.0301	-0.0566	-0.0925	-0.1126
30	0.0549	0.0287	0	-0.0289	-0.0527	-0.0724	-0.0939
35	0.0407	0.0181	0	-0.0214	-0.0537	-0.0808	-0.1009
40	0.0505	0.0188	0	-0.0286	-0.0516	-0.0737	-0.0938
45	0.0339	0.0183	0	-0.0544	-0.0929	-0.1312	-0.1581

β[°] / α [°]	$C_{y,lef}$				
	10	15	20	25	30
-20	-0.1504	-0.2106	-0.2836	-0.3396	-0.4106
-15	-0.1902	-0.2712	-0.3332	-0.3882	-0.4452
-10	-0.1949	-0.2978	-0.3758	-0.4528	-0.5078
-5	-0.2132	-0.3148	-0.4118	-0.5130	-0.5889
0	-0.2158	-0.3196	-0.4308	-0.5443	-0.6426
5	-0.2150	-0.3218	-0.4364	-0.5448	-0.6496
10	-0.2153	-0.3196	-0.4353	-0.5237	-0.6177
15	-0.2096	-0.3143	-0.4223	-0.4947	-0.5499
20	-0.1710	-0.2452	-0.3089	-0.3869	-0.4880
25	-0.1321	-0.1714	-0.2647	-0.3850	-0.5025
30	-0.1136	-0.1694	-0.2589	-0.3511	-0.3742
35	-0.1226	-0.1766	-0.2208	-0.2714	-0.2901
40	-0.1132	-0.1503	-0.1791	-0.1996	-0.2195
45	-0.1766	-0.1977	-0.1859	-0.1900	-0.2385

α [°]	$C_{y_R}(\alpha)$	$\Delta C_{y_R,lef}(\alpha)$	$C_{y_P}(\alpha)$	$\Delta C_{y_P,lef}(\alpha)$
-20	1.4400	-0.5580	0.0333	-0.1410
-15	1.4400	-0.5580	0.0333	-0.1410
-10	1.4400	-0.5580	0.0333	-0.1410
-5	1.0500	-0.1980	-0.1770	0.0690
0	0.9810	-0.1070	0.0055	-0.1970
5	0.9390	0.0270	0.0679	0.0601
10	0.9990	-0.0850	0.3100	-0.1210
15	0.9810	-0.0460	0.2340	-0.0520
20	0.8190	0.3310	0.3440	0.0750
25	0.4830	0.2150	0.3620	0.1060
30	0.5900	0.4300	0.6110	-0.0770
35	1.2100	-0.0600	0.5290	-0.6420
40	-0.4930	-0.3740	0.2980	-0.2550
45	-1.0400	-0.1870	-2.2700	-0.1280
50	-1.2100		0.9710	
55	-1.5800		1.0200	
60	-1.3700		2.9000	
70	-0.0259		0.4510	
80	-0.1270		-0.2940	
90	0.1930		-0.2610	

$C_{y,\delta_a=20°}(\alpha,\beta)$

α [°] \ β [°]	$C_{y,\delta_a=20°}$ -30	-25	-20	-15	-10	-8	-6
-20	0.3747	0.3113	0.2855	0.2184	0.1376	0.1109	0.0919
-15	0.3972	0.3293	0.2807	0.2110	0.1468	0.1207	0.0914
-10	0.4252	0.3679	0.3145	0.2356	0.1679	0.1287	0.0939
-5	0.6008	0.5148	0.4158	0.3148	0.2050	0.1656	0.1276
0	0.6628	0.5668	0.4528	0.3338	0.2168	0.1837	0.1428
5	0.7024	0.6094	0.4894	0.3584	0.2246	0.1894	0.1486
10	0.6715	0.5855	0.4715	0.3535	0.2293	0.1934	0.1492
15	0.6465	0.5355	0.4395	0.3285	0.2189	0.1786	0.1375
20	0.5873	0.4973	0.4013	0.3133	0.2083	0.1673	0.1319
25	0.4995	0.4185	0.3215	0.2495	0.1705	0.1496	0.1162
30	0.3789	0.3202	0.2295	0.1481	0.0986	0.1119	0.1010
35	0.3286	0.2712	0.1966	0.1350	0.0709	0.0509	0.0626
40	0.1812	0.1670	0.1194	0.0923	0.0535	0.0353	0.0269
45	0.1054	0.0775	0.0595	0.0456	0.0346	0.0039	0.0015
50	0.0947	0.0717	0.0668	0.0668	0.0340	0.0321	0.0133
55	0.1264	0.1026	0.1346	0.1186	0.0546	0.0359	0.0249
60	0.1655	0.1444	0.1574	0.1305	0.0734	0.0424	0.0329
70	0.2561	0.2250	0.1688	0.1169	0.0820	0.0536	0.0358
80	0.2946	0.2500	0.2010	0.1397	0.0941	0.0753	0.0500
90	0.2833	0.2290	0.1788	0.1498	0.0986	0.0765	0.0565

α [°] \ β [°]	$C_{y,\delta_a=20°}$ -4	-2	0	2	4	6	8
-20	0.0626	0.0409	0.0190	-0.0063	-0.0245	-0.0503	-0.0785
-15	0.0638	0.0383	0.0157	-0.0035	-0.0242	-0.0501	-0.0849
-10	0.0618	0.0315	0.0160	-0.0001	-0.0307	-0.0636	-0.0997
-5	0.0880	0.0509	0.0152	-0.0162	-0.0540	-0.0889	-0.1320
0	0.1001	0.0611	0.0235	-0.0128	-0.0490	-0.0919	-0.1312
5	0.1064	0.0665	0.0288	-0.0087	-0.0423	-0.0880	-0.1306
10	0.1093	0.0660	0.0284	-0.0093	-0.0472	-0.0885	-0.1318
15	0.0978	0.0578	0.0222	-0.0138	-0.0504	-0.0951	-0.1347
20	0.0903	0.0480	0.0181	-0.0047	-0.0357	-0.0736	-0.1120
25	0.0842	0.0470	0.0141	-0.0168	-0.0489	-0.0834	-0.1190
30	0.0749	0.0431	0.0143	-0.0146	-0.0445	-0.0763	-0.1024
35	0.0577	0.0316	0.0067	-0.0154	-0.0407	-0.0679	-0.0868
40	0.0312	0.0149	0.0005	-0.0191	-0.0426	-0.0615	-0.0918
45	-0.0117	-0.0198	-0.0250	-0.0668	-0.1326	-0.1557	-0.1745
50	-0.0110	-0.0257	-0.0412	-0.0597	-0.1052	-0.1322	-0.1279
55	-0.0136	-0.0270	-0.0544	-0.0589	-0.1026	-0.1340	-0.1419
60	-0.0080	-0.0224	-0.0497	-0.0553	-0.0866	-0.1117	-0.1291
70	0.0065	-0.0132	-0.0208	-0.0512	-0.0601	-0.0694	-0.0907
80	0.0411	0.0101	-0.0081	-0.0439	-0.0617	-0.0783	-0.0985
90	0.0339	0.0099	-0.0060	-0.0332	-0.0488	-0.0782	-0.1001

α [°] \ β [°]	$C_{y,\delta_a=20°}$ 10	15	20	25	30
-20	-0.1040	-0.1851	-0.2531	-0.2791	-0.3431
-15	-0.1166	-0.1810	-0.2510	-0.2990	-0.3690
-10	-0.1352	-0.2018	-0.2802	-0.3362	-0.3912
-5	-0.1738	-0.2843	-0.3859	-0.4843	-0.5669
0	-0.1783	-0.2962	-0.4152	-0.5288	-0.6256
5	-0.1756	-0.2977	-0.4281	-0.5479	-0.6396
10	-0.1832	-0.2989	-0.4277	-0.5401	-0.6267
15	-0.1814	-0.2914	-0.4032	-0.4977	-0.6021
20	-0.1514	-0.2563	-0.3433	-0.4383	-0.5262
25	-0.1575	-0.2363	-0.3079	-0.4062	-0.4874
30	-0.1254	-0.1749	-0.2563	-0.3473	-0.4057
35	-0.1076	-0.1717	-0.2333	-0.3079	-0.3653
40	-0.1074	-0.1483	-0.1712	-0.2184	-0.2338
45	-0.1943	-0.2057	-0.1814	-0.2160	-0.2853
50	-0.1826	-0.2161	-0.2142	-0.2175	-0.2434
55	-0.1784	-0.2409	-0.2557	-0.2224	-0.2454
60	-0.1527	-0.2123	-0.2423	-0.2233	-0.2445
70	-0.1136	-0.1456	-0.1930	-0.2491	-0.2794
80	-0.1221	-0.1673	-0.2253	-0.2766	-0.3206
90	-0.1216	-0.1747	-0.2165	-0.2584	-0.3185

$C_{y,\delta_a=20°,lef}(\alpha,\beta)$

α [°] \ β [°]	-30	-25	-20	-15	-10	-8	-6
-20	0.3744	0.3091	0.2661	0.1722	0.1174	0.1099	0.0935
-15	0.4225	0.3583	0.3168	0.2510	0.1890	0.1557	0.1197
-10	0.4773	0.4065	0.3506	0.2736	0.1981	0.1627	0.1230
-5	0.6313	0.5463	0.4403	0.3313	0.2102	0.1768	0.1372
0	0.6663	0.5753	0.4543	0.3373	0.2131	0.1779	0.1399
5	0.6707	0.5837	0.4637	0.3397	0.2209	0.1848	0.1448
10	0.6522	0.5692	0.4652	0.3432	0.2262	0.1900	0.1453
15	0.5976	0.5446	0.4646	0.3376	0.2223	0.1856	0.1413
20	0.4910	0.4140	0.3430	0.2750	0.1837	0.1542	0.1180
25	0.5028	0.3738	0.2828	0.1918	0.1354	0.1314	0.1043
30	0.3466	0.3296	0.2386	0.1466	0.0865	0.0877	0.0796
35	0.2987	0.2557	0.1647	0.1167	0.0601	0.0575	0.0556
40	0.2026	0.1575	0.1446	0.1206	0.0718	0.0541	0.0509
45	0.1161	0.0661	0.0831	0.0791	0.0597	0.0353	0.0159

α [°] \ β [°]	-4	-2	0	2	4	6	8
-20	0.0642	0.0382	0.0131	-0.0183	-0.0450	-0.0761	-0.1055
-15	0.0849	0.0507	0.0156	-0.0182	-0.0527	-0.0887	-0.1295
-10	0.0890	0.0558	0.0217	-0.0149	-0.0503	-0.0857	-0.1218
-5	0.0933	0.0578	0.0195	-0.0139	-0.0545	-0.0908	-0.1333
0	0.0960	0.0568	0.0212	-0.0176	-0.0549	-0.0961	-0.1344
5	0.1039	0.0586	0.0237	-0.0157	-0.0522	-0.0933	-0.1377
10	0.1027	0.0634	0.0236	-0.0159	-0.0510	-0.0969	-0.1390
15	0.1026	0.0581	0.0227	-0.0147	-0.0507	-0.0922	-0.1362
20	0.0806	0.0496	0.0192	-0.0126	-0.0459	-0.0806	-0.1120
25	0.0784	0.0446	0.0118	-0.0153	-0.0423	-0.0693	-0.0953
30	0.0604	0.0385	0.0114	-0.0127	-0.0449	-0.0655	-0.0854
35	0.0456	0.0247	0.0112	-0.0193	-0.0431	-0.0778	-0.0926
40	0.0241	0.0104	-0.0101	-0.0308	-0.0584	-0.0725	-0.0938
45	-0.0119	-0.0251	-0.0470	-0.0915	-0.1466	-0.1588	-0.1820

α [°] \ β [°]	10	15	20	25	30
-20	-0.1364	-0.1906	-0.2846	-0.3276	-0.3926
-15	-0.1672	-0.2282	-0.2952	-0.3362	-0.4002
-10	-0.1621	-0.2398	-0.3138	-0.3718	-0.4408
-5	-0.1793	-0.2978	-0.4071	-0.5128	-0.5965
0	-0.1799	-0.3046	-0.4230	-0.5434	-0.6341
5	-0.1857	-0.3044	-0.4281	-0.5467	-0.6335
10	-0.1890	-0.3064	-0.4250	-0.5321	-0.6136
15	-0.1806	-0.2950	-0.4221	-0.5009	-0.5527
20	-0.1515	-0.2420	-0.3106	-0.3811	-0.4585
25	-0.1166	-0.1715	-0.2606	-0.3523	-0.4822
30	-0.0991	-0.1580	-0.2483	-0.3394	-0.3555
35	-0.1215	-0.1778	-0.2236	-0.2611	-0.3046
40	-0.1158	-0.1628	-0.1862	-0.1979	-0.2432
45	-0.2127	-0.2315	-0.2354	-0.2172	-0.2687

$C_{y,\delta_r=30°}(\alpha,\beta)$

α [°] \ β [°]	-30	-25	-20	-15	-10	-8	-6
-20	0.4105	0.3419	0.2886	0.2323	0.1815	0.1736	0.1669
-15	0.4387	0.3684	0.3134	0.2471	0.2072	0.1971	0.1732
-10	0.4771	0.4196	0.3728	0.3013	0.2258	0.2034	0.1718
-5	0.6048	0.5388	0.4738	0.3628	0.2599	0.2259	0.1889
0	0.6388	0.5698	0.4998	0.3838	0.2736	0.2445	0.2017
5	0.6674	0.6064	0.5234	0.4034	0.2880	0.2574	0.2112
10	0.7015	0.6015	0.5295	0.4135	0.2963	0.2462	0.2034
15	0.6695	0.5555	0.4755	0.3615	0.2584	0.2353	0.1984
20	0.6703	0.5583	0.4533	0.3643	0.2524	0.2316	0.2094
25	0.5815	0.4915	0.4035	0.3185	0.2299	0.2239	0.2040
30	0.4141	0.3541	0.2781	0.2061	0.1323	0.1569	0.1737
35	0.3632	0.3442	0.2822	0.2202	0.1321	0.1160	0.1219
40	0.2365	0.2465	0.2035	0.1755	0.1214	0.0887	0.0909
45	0.2134	0.1434	0.1134	0.1274	0.0965	0.0849	0.0798
50	0.1606	0.1156	0.1116	0.1286	0.0946	0.0929	0.0803
55	0.1895	0.1495	0.1905	0.1755	0.1235	0.0999	0.0769
60	0.2183	0.1833	0.2173	0.1683	0.1375	0.1067	0.0846
70	0.2689	0.2289	0.1989	0.1729	0.1163	0.0968	0.0850
80	0.2915	0.2445	0.2045	0.1515	0.1075	0.0867	0.0696
90	0.2988	0.2398	0.1898	0.1568	0.1042	0.0772	0.0616

α [°] \ β [°]	-4	-2	0	2	4	6	8
-20	0.1355	0.1173	0.0854	0.0681	0.0447	0.0229	-0.0109
-15	0.1405	0.1144	0.0900	0.0732	0.0522	0.0271	-0.0107
-10	0.1350	0.1043	0.0869	0.0717	0.0478	0.0128	-0.0291
-5	0.1516	0.1180	0.0815	0.0510	0.0146	-0.0267	-0.0715
0	0.1610	0.1240	0.0859	0.0530	0.0185	-0.0259	-0.0750
5	0.1690	0.1264	0.0923	0.0574	0.0175	-0.0244	-0.0741
10	0.1629	0.1207	0.0851	0.0511	0.0161	-0.0335	-0.0800
15	0.1582	0.1181	0.0834	0.0477	0.0121	-0.0348	-0.0785
20	0.1608	0.1334	0.0936	0.0626	0.0352	-0.0026	-0.0385
25	0.1753	0.1364	0.0994	0.0661	0.0347	-0.0045	-0.0405
30	0.1599	0.1358	0.1071	0.0709	0.0419	0.0115	-0.0247
35	0.1340	0.1121	0.0885	0.0731	0.0471	0.0180	-0.0115
40	0.0821	0.0781	0.0749	0.0468	0.0304	-0.0005	-0.0242
45	0.0855	0.0669	0.0387	-0.0412	-0.0713	-0.0954	-0.1275
50	0.0511	0.0476	0.0251	-0.0120	-0.0441	-0.0836	-0.1146
55	0.0407	0.0366	0.0122	-0.0079	-0.0639	-0.0920	-0.1252
60	0.0442	0.0311	0.0066	-0.0041	-0.0551	-0.0762	-0.0722
70	0.0543	0.0272	0.0061	-0.0101	-0.0256	-0.0408	-0.0609
80	0.0543	0.0293	0.0175	-0.0069	-0.0276	-0.0570	-0.0747
90	0.0470	0.0240	0.0052	-0.0124	-0.0335	-0.0646	-0.0841

α [°] \ β [°]	10	15	20	25	30
-20	-0.0556	-0.1061	-0.1621	-0.2141	-0.2821
-15	-0.0476	-0.0870	-0.1420	-0.1970	-0.2670
-10	-0.0713	-0.1482	-0.2192	-0.2662	-0.3232
-5	-0.1190	-0.2225	-0.3339	-0.4012	-0.4692
0	-0.1271	-0.2369	-0.3526	-0.4212	-0.4912
5	-0.1258	-0.2407	-0.3594	-0.4316	-0.5026
10	-0.1319	-0.2388	-0.3564	-0.4285	-0.5295
15	-0.1251	-0.2295	-0.3411	-0.4215	-0.5365
20	-0.0760	-0.1859	-0.2758	-0.3857	-0.4947
25	-0.0782	-0.1668	-0.2536	-0.3505	-0.4475
30	-0.0619	-0.1347	-0.2078	-0.2859	-0.3459
35	-0.0395	-0.1278	-0.1904	-0.2618	-0.2808
40	-0.0593	-0.1122	-0.1415	-0.1866	-0.1779
45	-0.1447	-0.1735	-0.1591	-0.1897	-0.2583
50	-0.1370	-0.1726	-0.1533	-0.1553	-0.2004
55	-0.1448	-0.1972	-0.2129	-0.1698	-0.2095
60	-0.1282	-0.1790	-0.2092	-0.1737	-0.2095
70	-0.0872	-0.1442	-0.1702	-0.2018	-0.2416
80	-0.1027	-0.1484	-0.2013	-0.2457	-0.2924
90	-0.1016	-0.1539	-0.1873	-0.2374	-0.3009

II.7. z_b Directional Aerodynamic Moment Coefficient Data

$C_n(\alpha,\ \beta,\ \delta_n = -25)$

α [°] \ β[°]	-30	-25	-20	-15	-10	-8	-6
-20	-0.0633	-0.0667	-0.0565	-0.0418	-0.0175	-0.0093	-0.0006
-15	-0.0621	-0.0579	-0.0454	-0.0285	-0.0181	-0.0133	-0.0067
-10	-0.0678	-0.0588	-0.0493	-0.0393	-0.0242	-0.0167	-0.0098
-5	-0.0850	-0.0761	-0.0639	-0.0478	-0.0354	-0.0263	-0.0184
0	-0.0995	-0.0869	-0.0795	-0.0528	-0.0375	-0.0280	-0.0193
5	-0.1044	-0.0824	-0.0691	-0.0521	-0.0352	-0.0280	-0.0193
10	-0.0981	-0.0759	-0.0631	-0.0478	-0.0358	-0.0283	-0.0201
15	-0.0976	-0.0618	-0.0475	-0.0447	-0.0339	-0.0267	-0.0190
20	-0.0677	-0.0506	-0.0290	-0.0276	-0.0259	-0.0216	-0.0151
25	-0.0488	-0.0351	-0.0163	-0.0128	-0.0155	-0.0115	-0.0072
30	-0.0102	0.0155	0.0287	0.0256	0.0294	0.0067	0.0040
35	-0.0028	0.0314	0.0572	0.0712	0.0545	0.0537	0.0413
40	-0.0037	0.0167	0.0770	0.0803	0.0573	0.0433	0.0292
45	-0.0120	0.0027	0.0397	0.0577	0.0399	0.0304	0.0200
50	-0.0373	-0.0274	-0.0096	0.0216	0.0319	0.0296	0.0298
55	-0.0449	-0.0324	0.0102	-0.0077	-0.0161	-0.0090	-0.0057
60	-0.0055	0.0068	0.0374	0.0119	0.0234	0.0127	-0.0016
70	0.0232	0.0280	0.0203	0.0127	0.0007	-0.0031	-0.0070
80	0.0236	0.0237	0.0161	0.0116	0.0099	0.0110	0.0108
90	0.0319	0.0199	0.0108	0.0018	0.0079	0.0062	0.0039

α [°] \ β[°]	-4	-2	0	2	4	6	8
-20	0.0047	0.0034	0	-0.0048	-0.0106	-0.0074	-0.0015
-15	-0.0010	0.0010	0	0.0004	0.0028	0.0071	0.0151
-10	-0.0022	0.0022	0	0.0047	0.0096	0.0163	0.0245
-5	-0.0114	-0.0055	0	0.0054	0.0112	0.0189	0.0290
0	-0.0118	-0.0053	0	0.0055	0.0122	0.0208	0.0302
5	-0.0121	-0.0050	0	0.0056	0.0132	0.0210	0.0301
10	-0.0125	-0.0054	0	0.0054	0.0131	0.0225	0.0309
15	-0.0114	-0.0045	0	0.0055	0.0129	0.0223	0.0304
20	-0.0088	-0.0040	0	-0.0022	0.0021	0.0099	0.0161
25	-0.0037	-0.0016	0	0.0013	0.0047	0.0085	0.0132
30	0.0046	0.0038	0	-0.0042	-0.0050	-0.0069	-0.0090
35	0.0254	0.0145	0	-0.0104	-0.0162	-0.0223	-0.0312
40	0.0184	0.0068	0	-0.0048	-0.0115	-0.0233	-0.0332
45	0.0147	0.0062	0	-0.0145	-0.0356	-0.0442	-0.0580
50	0.0157	0.0104	0	-0.0082	-0.0255	-0.0441	-0.0619
55	-0.0065	-0.0040	0	-0.0019	-0.0152	-0.0275	-0.0315
60	-0.0120	-0.0029	0	0.0052	0.0057	-0.0101	-0.0215
70	-0.0137	-0.0168	0	0.0028	0.0133	0.0138	0.0083
80	0.0087	0.0059	0	-0.0013	0.0035	-0.0054	-0.0069
90	0.0029	0.0018	0	-0.0064	-0.0051	-0.0098	-0.0097

α [°] \ β[°]	10	15	20	25	30
-20	0.0052	0.0297	0.0443	0.0545	0.0510
-15	0.0200	0.0303	0.0473	0.0602	0.0641
-10	0.0320	0.0473	0.0572	0.0666	0.0754
-5	0.0392	0.0516	0.0680	0.0800	0.0886
0	0.0393	0.0547	0.0706	0.0891	0.1034
5	0.0383	0.0553	0.0721	0.0858	0.1075
10	0.0391	0.0512	0.0668	0.0798	0.1018
15	0.0372	0.0480	0.0509	0.0647	0.0909
20	0.0210	0.0226	0.0241	0.0460	0.0627
25	0.0157	0.0132	0.0162	0.0347	0.0487
30	-0.0115	-0.0214	-0.0218	0.0055	0.0417
35	-0.0506	-0.0670	-0.0536	-0.0276	0.0069
40	-0.0492	-0.0762	-0.0727	-0.0125	0.0079
45	-0.0698	-0.0900	-0.0704	-0.0336	-0.0191
50	-0.0788	-0.0693	-0.0384	-0.0217	-0.0120
55	-0.0305	-0.0386	-0.0564	-0.0137	-0.0017
60	-0.0221	-0.0263	-0.0358	-0.0055	0.0066
70	0.0018	-0.0100	-0.0173	-0.0251	-0.0207
80	-0.0054	-0.0075	-0.0117	-0.0192	-0.0191
90	-0.0101	-0.0038	-0.0072	-0.0159	-0.0277

$C_n(\alpha,\ \beta,\ \delta_h = 0)$

α [°] \ β[°]	C_n -30	-25	-20	-15	-10	-8	-6
-20	-0.0551	-0.0588	-0.0496	-0.0406	-0.0219	-0.0145	-0.0075
-15	-0.0561	-0.0527	-0.0456	-0.0333	-0.0248	-0.0179	-0.0127
-10	-0.0666	-0.0637	-0.0545	-0.0468	-0.0297	-0.0233	-0.0145
-5	-0.0902	-0.0812	-0.0664	-0.0523	-0.0366	-0.0277	-0.0194
0	-0.1058	-0.0916	-0.0749	-0.0578	-0.0413	-0.0317	-0.0226
5	-0.1074	-0.0916	-0.0754	-0.0587	-0.0415	-0.0329	-0.0227
10	-0.0981	-0.0798	-0.0718	-0.0568	-0.0416	-0.0326	-0.0232
15	-0.0812	-0.0592	-0.0537	-0.0513	-0.0375	-0.0301	-0.0212
20	-0.0684	-0.0491	-0.0290	-0.0321	-0.0308	-0.0262	-0.0179
25	-0.0528	-0.0411	-0.0223	-0.0229	-0.0240	-0.0188	-0.0129
30	-0.0300	0.0002	0.0115	0.0164	0.0091	-0.0037	-0.0024
35	-0.0098	0.0168	0.0392	0.0514	0.0396	0.0340	0.0163
40	-0.0025	0.0054	0.0683	0.0744	0.0506	0.0351	0.0207
45	-0.0111	0.0010	0.0294	0.0612	0.0451	0.0369	0.0293
50	-0.0256	-0.0136	0.0058	0.0287	0.0254	0.0231	0.0233
55	-0.0302	-0.0228	0.0130	0.0140	0.0040	0.0027	0.0023
60	-0.0188	-0.0075	0.0211	0.0080	-0.0061	-0.0100	-0.0174
70	0.0296	0.0316	0.0210	0.0092	0.0003	-0.0062	-0.0128
80	0.0264	0.0351	0.0254	0.0180	0.0133	0.0126	0.0107
90	0.0274	0.0128	0.0118	0.0059	0.0051	0.0044	0.0031

α [°] \ β[°]	C_n -4	-2	0	2	4	6	8
-20	-0.0012	0.0002	0	-0.0009	0.0012	0.0059	0.0099
-15	-0.0057	-0.0018	0	0.0025	0.0058	0.0111	0.0180
-10	-0.0079	-0.0031	0	0.0028	0.0075	0.0150	0.0221
-5	-0.0117	-0.0055	0	0.0063	0.0127	0.0214	0.0297
0	-0.0138	-0.0066	0	0.0061	0.0135	0.0225	0.0324
5	-0.0145	-0.0064	0	0.0061	0.0148	0.0231	0.0335
10	-0.0146	-0.0062	0	0.0063	0.0147	0.0240	0.0332
15	-0.0121	-0.0052	0	0.0063	0.0141	0.0243	0.0334
20	-0.0102	-0.0042	0	0.0018	0.0068	0.0152	0.0233
25	-0.0072	-0.0029	0	0.0033	0.0088	0.0147	0.0216
30	0.0009	0.0025	0	-0.0029	-0.0023	-0.0013	-0.0003
35	0.0103	0.0069	0	-0.0097	-0.0147	-0.0157	-0.0189
40	0.0131	0.0052	0	-0.0071	-0.0136	-0.0216	-0.0329
45	0.0201	0.0116	0	-0.0237	-0.0375	-0.0460	-0.0565
50	0.0105	0.0078	0	-0.0063	-0.0217	-0.0355	-0.0456
55	0.0070	0.0043	0	0.0028	-0.0058	-0.0172	-0.0239
60	-0.0219	-0.0079	0	0.0075	0.0103	0.0043	-0.0013
70	-0.0193	-0.0187	0	0.0039	0.0151	0.0163	0.0116
80	0.0079	0.0055	0	-0.0001	0.0060	-0.0033	-0.0069
90	0.0027	0.0017	0	-0.0018	-0.0023	-0.0031	-0.0048

α [°] \ β[°]	C_n 10	15	20	25	30
-20	0.0141	0.0333	0.0425	0.0516	0.0477
-15	0.0238	0.0330	0.0450	0.0521	0.0553
-10	0.0302	0.0474	0.0552	0.0646	0.0674
-5	0.0398	0.0553	0.0693	0.0843	0.0933
0	0.0414	0.0579	0.0746	0.0914	0.1055
5	0.0421	0.0594	0.0762	0.0914	0.1079
10	0.0427	0.0579	0.0727	0.0809	0.0995
15	0.0404	0.0541	0.0566	0.0622	0.0840
20	0.0296	0.0309	0.0279	0.0479	0.0674
25	0.0258	0.0251	0.0242	0.0429	0.0547
30	-0.0019	-0.0097	-0.0042	0.0069	0.0370
35	-0.0295	-0.0415	-0.0291	-0.0068	0.0194
40	-0.0440	-0.0677	-0.0622	0.0012	0.0202
45	-0.0694	-0.0847	-0.0530	-0.0246	-0.0126
50	-0.0548	-0.0574	-0.0346	-0.0161	-0.0046
55	-0.0258	-0.0361	-0.0355	0.0014	0.0073
60	-0.0019	-0.0156	-0.0284	0.0004	0.0110
70	0.0059	-0.0023	-0.0141	-0.0246	-0.0228
80	-0.0075	-0.0130	-0.0198	-0.0242	-0.0209
90	-0.0048	-0.0054	-0.0111	-0.0121	-0.0163

$C_n(\alpha,\ \beta,\ \delta_h = 25)$

α [°] \ β [°]	C_n -30	-25	-20	-15	-10	-8	-6
-20	-0.0488	-0.0515	-0.0442	-0.0428	-0.0215	-0.0136	-0.0046
-15	-0.0499	-0.0463	-0.0402	-0.0324	-0.0201	-0.0154	-0.0095
-10	-0.0574	-0.0534	-0.0477	-0.0424	-0.0277	-0.0208	-0.0134
-5	-0.0758	-0.0714	-0.0617	-0.0507	-0.0368	-0.0290	-0.0208
0	-0.0919	-0.0818	-0.0694	-0.0560	-0.0402	-0.0311	-0.0233
5	-0.0860	-0.0749	-0.0659	-0.0531	-0.0406	-0.0322	-0.0223
10	-0.0821	-0.0723	-0.0653	-0.0534	-0.0403	-0.0328	-0.0233
15	-0.0671	-0.0516	-0.0486	-0.0496	-0.0357	-0.0289	-0.0195
20	-0.0398	-0.0355	-0.0237	-0.0284	-0.0311	-0.0270	-0.0183
25	-0.0273	-0.0210	-0.0132	-0.0148	-0.0219	-0.0196	-0.0159
30	-0.0116	0.0142	0.0273	0.0242	0.0111	-0.0066	-0.0063
35	0.0018	0.0282	0.0499	0.0550	0.0430	0.0382	0.0193
40	0.0003	-0.0193	0.0698	0.0788	0.0534	0.0372	0.0252
45	-0.0149	-0.0007	0.0226	0.0569	0.0455	0.0363	0.0288
50	-0.0219	-0.0174	-0.0077	0.0171	0.0310	0.0307	0.0328
55	-0.0518	-0.0435	-0.0053	-0.0307	-0.0231	-0.0108	-0.0022
60	-0.0270	-0.0207	0.0042	-0.0137	-0.0137	-0.0138	-0.0173
70	0.0158	0.0270	0.0252	0.0117	-0.0010	-0.0039	-0.0068
80	0.0106	0.0182	0.0182	0.0117	0.0081	0.0096	0.0099
90	0.0118	0.0101	0.0117	0.0036	0.0060	0.0053	0.0041

α [°] \ β [°]	C_n -4	-2	0	2	4	6	8
-20	-0.0018	0.0001	0	-0.0005	-0.0003	0.0048	0.0084
-15	-0.0029	-0.0013	0	0.0005	0.0031	0.0093	0.0145
-10	-0.0073	-0.0025	0	0.0018	0.0075	0.0140	0.0222
-5	-0.0128	-0.0061	0	0.0064	0.0139	0.0222	0.0304
0	-0.0141	-0.0065	0	0.0069	0.0147	0.0230	0.0319
5	-0.0127	-0.0047	0	0.0042	0.0124	0.0221	0.0323
10	-0.0135	-0.0061	0	0.0049	0.0126	0.0218	0.0310
15	-0.0107	-0.0048	0	0.0038	0.0108	0.0208	0.0306
20	-0.0091	-0.0035	0	0.0028	0.0052	0.0178	0.0268
25	-0.0089	-0.0033	0	0.0043	0.0103	0.0179	0.0264
30	-0.0020	0.0009	0	-0.0010	-0.0006	0.0018	0.0039
35	0.0099	0.0069	0	-0.0086	-0.0126	-0.0154	-0.0181
40	0.0169	0.0073	0	-0.0084	-0.0147	-0.0248	-0.0362
45	0.0188	0.0089	0	-0.0252	-0.0403	-0.0511	-0.0621
50	0.0189	0.0120	0	-0.0058	-0.0251	-0.0408	-0.0543
55	-0.0016	0.0065	0	-0.0026	-0.0085	-0.0223	-0.0257
60	-0.0203	-0.0071	0	0.0093	0.0138	0.0067	-0.0028
70	-0.0132	-0.0159	0	-0.0039	0.0110	0.0088	0.0084
80	0.0081	0.0056	0	-0.0010	0.0042	-0.0043	0.0016
90	0.0035	0.0021	0	-0.0002	0.0008	0.0008	-0.0008

α [°] \ β [°]	C_n 10	15	20	25	30
-20	0.0143	0.0356	0.0369	0.0441	0.0425
-15	0.0195	0.0319	0.0398	0.0459	0.0492
-10	0.0277	0.0421	0.0476	0.0534	0.0572
-5	0.0399	0.0536	0.0645	0.0742	0.0787
0	0.0408	0.0565	0.0693	0.0824	0.0924
5	0.0415	0.0567	0.0694	0.0786	0.0892
10	0.0400	0.0531	0.0649	0.0718	0.0814
15	0.0381	0.0510	0.0499	0.0532	0.0684
20	0.0332	0.0305	0.0259	0.0374	0.0417
25	0.0311	0.0239	0.0224	0.0302	0.0362
30	0.0018	-0.0111	-0.0146	-0.0012	0.0244
35	-0.0288	-0.0456	-0.0402	-0.0185	0.0071
40	-0.0480	-0.0733	-0.0641	-0.0052	0.0051
45	-0.0712	-0.0804	-0.0480	-0.0247	-0.0207
50	-0.0664	-0.0530	-0.0292	-0.0187	-0.0151
55	-0.0244	-0.0171	-0.0424	-0.0042	0.0031
60	-0.0073	-0.0072	-0.0254	-0.0008	0.0056
70	0.0069	-0.0059	-0.0191	-0.0209	-0.0104
80	-0.0035	-0.0112	-0.0135	-0.0135	-0.0058
90	-0.0008	0.0014	-0.0068	-0.0054	-0.0072

$C_{n,lef}(\alpha, \beta)$

β[°] / α [°]	$C_{n,lef}$ -30	-25	-20	-15	-10	-8	-6
-20	-0.0541	-0.0563	-0.0461	-0.0495	-0.0296	-0.0208	-0.0173
-15	-0.0678	-0.0728	-0.0658	-0.0539	-0.0358	-0.0282	-0.0204
-10	-0.0780	-0.0773	-0.0629	-0.0555	-0.0370	-0.0289	-0.0218
-5	-0.0881	-0.0851	-0.0753	-0.0556	-0.0402	-0.0308	-0.0254
0	-0.1060	-0.0929	-0.0754	-0.0593	-0.0420	-0.0319	-0.0222
5	-0.1051	-0.0877	-0.0728	-0.0573	-0.0410	-0.0324	-0.0225
10	-0.0926	-0.0797	-0.0731	-0.0580	-0.0424	-0.0327	-0.0235
15	-0.0632	-0.0670	-0.0653	-0.0549	-0.0414	-0.0316	-0.0223
20	-0.0359	-0.0191	-0.0173	-0.0230	-0.0216	-0.0174	-0.0076
25	-0.0342	-0.0208	-0.0017	0.0063	-0.0059	-0.0094	-0.0061
30	-0.0265	-0.0047	0.0128	0.0249	0.0198	0.0114	0.0055
35	0.0138	0.0391	0.0533	0.0553	0.0434	0.0397	0.0263
40	0.0302	0.0357	0.0675	0.0645	0.0445	0.0330	0.0214
45	0.0003	-0.0038	0.0214	0.0400	0.0326	0.0261	0.0199

β[°] / α [°]	$C_{n,lef}$ -4	-2	0	2	4	6	8
-20	-0.0100	-0.0043	0	0.0037	0.0076	0.0121	0.0186
-15	-0.0126	-0.0058	0	0.0057	0.0125	0.0206	0.0288
-10	-0.0142	-0.0068	0	0.0069	0.0141	0.0224	0.0301
-5	-0.0141	-0.0067	0	0.0067	0.0144	0.0234	0.0328
0	-0.0135	-0.0062	0	0.0066	0.0143	0.0234	0.0340
5	-0.0140	-0.0061	0	0.0062	0.0149	0.0229	0.0336
10	-0.0154	-0.0064	0	0.0064	0.0150	0.0243	0.0330
15	-0.0135	-0.0059	0	0.0055	0.0143	0.0232	0.0325
20	-0.0058	-0.0015	0	0.0030	0.0087	0.0159	0.0227
25	-0.0029	-0.0012	0	0.0008	0.0038	0.0069	0.0078
30	0.0057	0.0030	0	-0.0032	-0.0077	-0.0117	-0.0201
35	0.0206	0.0119	0	-0.0090	-0.0134	-0.0190	-0.0263
40	0.0156	0.0065	0	-0.0060	-0.0136	-0.0155	-0.0266
45	0.0130	0.0047	0	-0.0170	-0.0369	-0.0464	-0.0533

β[°] / α [°]	$C_{n,lef}$ 10	15	20	25	30
-20	0.0231	0.0428	0.0393	0.0494	0.0468
-15	0.0364	0.0539	0.0658	0.0730	0.0683
-10	0.0387	0.0572	0.0645	0.0715	0.0794
-5	0.0430	0.0586	0.0785	0.0872	0.0913
0	0.0429	0.0595	0.0759	0.0938	0.1066
5	0.0423	0.0589	0.0747	0.0877	0.1069
10	0.0425	0.0579	0.0730	0.0796	0.0925
15	0.0417	0.0533	0.0656	0.0673	0.0635
20	0.0279	0.0292	0.0237	0.0253	0.0421
25	0.0034	-0.0088	-0.0008	0.0183	0.0317
30	-0.0276	-0.0332	-0.0209	-0.0034	0.0188
35	-0.0328	-0.0444	-0.0427	-0.0279	-0.0021
40	-0.0330	-0.0532	-0.0561	-0.0240	0.0014
45	-0.0611	-0.0681	-0.0495	-0.0245	-0.0280

α [°]	$C_{n_\beta}(\alpha)$	$\Delta C_{n_\beta}(\alpha)$	$\Delta C_{n_{\delta_a}}(\alpha)$	$\Delta C_{n_\beta,lef}(\alpha)$	$C_{n_p}(\alpha)$	$\Delta C_{n_p,lef}(\alpha)$
-20	-0.5170	0	0	0.1370	-0.0006	0.0615
-15	-0.5170	0	0	0.1370	-0.0006	0.0615
-10	-0.5170	0	0	0.1370	-0.0006	0.0615
-5	-0.4610	0	0	0.0980	0.0242	0.0091
0	-0.4140	0	0.0010	0.0370	-0.0075	0.0610
5	-0.3970	0	0.0008	0.0160	-0.0214	0.0129
10	-0.3730	0	0.0016	0.0070	-0.0320	0.0439
15	-0.4550	0	0.0010	0.0140	-0.0320	0.0512
20	-0.5500	0	0	0.1030	0.0500	-0.0294
25	-0.5820	-0.0008	0	0.0980	0.1500	0.0017
30	-0.5950	0.0010	0	0.3100	0.1300	0.0584
35	-0.6370	0	0	0.4370	0.1580	0.2110
40	-1.2000	0	0	0.1670	0.2400	0.3920
45	-0.8400	0	0	0.0840	0.1500	0.1960
50	-0.5410	0	0		0	
55	-0.3500	0	0		-0.2000	
60	-0.3500	0	0		-0.3000	
70	-0.0700	0	0		0.1500	
80	-0.1500	0	0		0	
90	-0.1500	0	0		0	

$C_{n,\delta_a=20°}(\alpha,\beta)$

β[°] / α [°]	$C_{n,\delta_a=20°}$						
	-30	-25	-20	-15	-10	-8	-6
-20	-0.0639	-0.0628	-0.0616	-0.0550	-0.0359	-0.0267	-0.0188
-15	-0.0619	-0.0554	-0.0490	-0.0384	-0.0336	-0.0279	-0.0232
-10	-0.0679	-0.0599	-0.0544	-0.0465	-0.0396	-0.0322	-0.0254
-5	-0.1080	-0.0994	-0.0838	-0.0677	-0.0460	-0.0398	-0.0321
0	-0.1234	-0.1094	-0.0915	-0.0721	-0.0498	-0.0448	-0.0377
5	-0.1245	-0.1100	-0.0939	-0.0730	-0.0496	-0.0440	-0.0360
10	-0.1118	-0.1020	-0.0894	-0.0690	-0.0486	-0.0440	-0.0349
15	-0.0967	-0.0807	-0.0737	-0.0628	-0.0472	-0.0416	-0.0379
20	-0.0670	-0.0561	-0.0505	-0.0472	-0.0358	-0.0269	-0.0198
25	-0.0353	-0.0316	-0.0201	-0.0243	-0.0175	-0.0130	-0.0079
30	-0.0187	0.0091	0.0230	0.0196	0.0132	0.0026	0.0021
35	0.0070	0.0357	0.0548	0.0658	0.0468	0.0383	0.0219
40	0.0056	0.0322	0.0831	0.0881	0.0563	0.0395	0.0271
45	0.0046	0.0141	0.0404	0.0642	0.0513	0.0416	0.0319
50	-0.0109	-0.0043	0.0157	0.0385	0.0386	0.0357	0.0282
55	-0.0100	-0.0124	0.0256	0.0303	0.0237	0.0233	0.0166
60	0.0047	-0.0008	0.0281	0.0257	0.0165	0.0169	0.0115
70	0.0470	0.0426	0.0308	0.0301	0.0253	0.0186	0.0160
80	0.0410	0.0414	0.0368	0.0314	0.0251	0.0248	0.0233
90	0.0320	0.0287	0.0237	0.0165	0.0165	0.0153	0.0151

β[°] / α [°]	$C_{n,\delta_a=20°}$						
	-4	-2	0	2	4	6	8
-20	-0.0119	-0.0093	-0.0089	-0.0081	-0.0071	-0.0043	-0.0004
-15	-0.0174	-0.0137	-0.0098	-0.0066	-0.0042	0.0002	0.0088
-10	-0.0193	-0.0139	-0.0091	-0.0055	-0.0007	0.0047	0.0120
-5	-0.0248	-0.0176	-0.0111	-0.0054	0.0008	0.0074	0.0159
0	-0.0277	-0.0193	-0.0120	-0.0056	0.0015	0.0092	0.0175
5	-0.0265	-0.0176	-0.0105	-0.0037	0.0024	0.0109	0.0194
10	-0.0267	-0.0171	-0.0090	-0.0020	0.0047	0.0132	0.0220
15	-0.0234	-0.0136	-0.0066	-0.0003	0.0069	0.0158	0.0231
20	-0.0111	-0.0029	0.0001	0.0015	0.0052	0.0121	0.0204
25	-0.0037	0.0012	0.0045	0.0072	0.0106	0.0159	0.0217
30	0.0056	0.0082	0.0065	0.0039	0.0022	0.0030	0.0055
35	0.0178	0.0138	0.0099	0.0011	-0.0052	-0.0082	-0.0098
40	0.0187	0.0127	0.0044	-0.0009	-0.0060	-0.0131	-0.0224
45	0.0252	0.0164	0.0097	-0.0062	-0.0283	-0.0386	-0.0475
50	0.0229	0.0196	0.0130	0.0071	-0.0140	-0.0211	-0.0198
55	0.0132	0.0193	0.0167	0.0175	0.0025	-0.0042	-0.0060
60	0.0092	0.0207	0.0182	0.0236	0.0195	0.0158	0.0112
70	0.0206	0.0190	0.0154	0.0245	0.0216	0.0283	0.0218
80	0.0184	0.0156	0.0138	0.0154	0.0133	0.0101	0.0075
90	0.0155	0.0138	0.0125	0.0133	0.0110	0.0101	0.0101

β[°] / α [°]	$C_{n,\delta_a=20°}$				
	10	15	20	25	30
-20	0.0020	0.0211	0.0277	0.0289	0.0300
-15	0.0134	0.0182	0.0288	0.0352	0.0417
-10	0.0186	0.0255	0.0334	0.0389	0.0469
-5	0.0246	0.0463	0.0624	0.0780	0.0866
0	0.0268	0.0491	0.0685	0.0864	0.1004
5	0.0285	0.0519	0.0728	0.0889	0.1034
10	0.0318	0.0522	0.0726	0.0852	0.0950
15	0.0328	0.0484	0.0593	0.0663	0.0823
20	0.0273	0.0387	0.0420	0.0476	0.0585
25	0.0277	0.0345	0.0303	0.0418	0.0455
30	0.0045	-0.0019	-0.0053	0.0086	0.0364
35	-0.0174	-0.0364	-0.0254	-0.0063	0.0224
40	-0.0328	-0.0646	-0.0578	-0.0087	0.0179
45	-0.0583	-0.0712	-0.0474	-0.0211	-0.0116
50	-0.0452	-0.0451	-0.0223	-0.0023	0.0043
55	-0.0183	-0.0249	-0.0202	0.0178	0.0154
60	0.0039	-0.0053	-0.0077	0.0212	0.0157
70	0.0156	0.0108	0.0101	-0.0017	-0.0061
80	0.0081	0.0018	-0.0036	-0.0082	-0.0078
90	0.0117	0.0117	0.0045	-0.0005	-0.0038

$C_{n,\delta_a=20°,lef}(\alpha,\beta)$

α [°] \ β [°]	-30	-25	-20	-15	-10	-8	-6
-20	-0.0683	-0.0615	-0.0556	-0.0519	-0.0393	-0.0314	-0.0264
-15	-0.0733	-0.0702	-0.0663	-0.0551	-0.0437	-0.0372	-0.0301
-10	-0.0775	-0.0683	-0.0610	-0.0527	-0.0434	-0.0385	-0.0301
-5	-0.1149	-0.1067	-0.0898	-0.0716	-0.0482	-0.0429	-0.0359
0	-0.1225	-0.1106	-0.0909	-0.0722	-0.0482	-0.0428	-0.0359
5	-0.1162	-0.1030	-0.0873	-0.0677	-0.0465	-0.0406	-0.0328
10	-0.1024	-0.0944	-0.0827	-0.0658	-0.0450	-0.0401	-0.0307
15	-0.0799	-0.0816	-0.0789	-0.0608	-0.0433	-0.0378	-0.0286
20	-0.0364	-0.0285	-0.0304	-0.0355	-0.0273	-0.0233	-0.0167
25	-0.0370	-0.0163	-0.0025	-0.0028	-0.0087	-0.0105	-0.0071
30	-0.0169	0.0037	0.0210	0.0303	0.0211	0.0133	0.0096
35	0.0213	0.0543	0.0602	0.0659	0.0515	0.0439	0.0311
40	0.0189	0.0463	0.0803	0.0786	0.0519	0.0392	0.0287
45	0.0055	0.0045	0.0224	0.0432	0.0419	0.0355	0.0274

α [°] \ β [°]	-4	-2	0	2	4	6	8
-20	-0.0199	-0.0140	-0.0096	-0.0054	-0.0029	0.0019	0.0074
-15	-0.0233	-0.0170	-0.0108	-0.0046	0.0017	0.0082	0.0159
-10	-0.0240	-0.0175	-0.0108	-0.0040	0.0027	0.0089	0.0161
-5	-0.0267	-0.0188	-0.0113	-0.0050	0.0024	0.0093	0.0186
0	-0.0256	-0.0170	-0.0099	-0.0027	0.0042	0.0121	0.0197
5	-0.0240	-0.0145	-0.0077	-0.0008	0.0055	0.0134	0.0222
10	-0.0224	-0.0137	-0.0056	0.0015	0.0079	0.0164	0.0251
15	-0.0201	-0.0104	-0.0037	0.0024	0.0080	0.0159	0.0249
20	-0.0106	-0.0056	-0.0026	0.0004	0.0045	0.0095	0.0164
25	-0.0049	-0.0019	-0.0006	0.0004	0.0024	0.0041	0.0055
30	0.0100	0.0081	0.0043	-0.0005	-0.0044	-0.0078	-0.0155
35	0.0236	0.0178	0.0068	0.0002	-0.0047	-0.0096	-0.0195
40	0.0209	0.0127	0.0062	-0.0017	-0.0079	-0.0105	-0.0161
45	0.0202	0.0141	0.0069	-0.0105	-0.0321	-0.0375	-0.0468

α [°] \ β [°]	10	15	20	25	30
-20	0.0124	0.0251	0.0293	0.0354	0.0421
-15	0.0230	0.0343	0.0455	0.0497	0.0528
-10	0.0236	0.0327	0.0407	0.0479	0.0575
-5	0.0278	0.0511	0.0689	0.0856	0.0932
0	0.0292	0.0533	0.0720	0.0915	0.1034
5	0.0316	0.0539	0.0729	0.0888	0.1024
10	0.0345	0.0550	0.0719	0.0838	0.0917
15	0.0341	0.0513	0.0697	0.0721	0.0683
20	0.0229	0.0312	0.0260	0.0242	0.0323
25	0.0015	-0.0098	-0.0050	0.0089	0.0307
30	-0.0240	-0.0318	-0.0242	-0.0066	0.0139
35	-0.0275	-0.0419	-0.0361	-0.0298	0.0029
40	-0.0221	-0.0486	-0.0497	-0.0155	0.0116
45	-0.0536	-0.0549	-0.0344	-0.0164	-0.0174

$C_{n,\delta_r=30°}(\alpha,\beta)$

α [°] \ β [°]	-30	-25	-20	-15	-10	-8	-6
-20	-0.0787	-0.0815	-0.0741	-0.0656	-0.0620	-0.0627	-0.0616
-15	-0.0758	-0.0745	-0.0708	-0.0610	-0.0623	-0.0658	-0.0649
-10	-0.0850	-0.0833	-0.0828	-0.0749	-0.0670	-0.0685	-0.0657
-5	-0.1422	-0.1270	-0.1170	-0.0932	-0.0774	-0.0745	-0.0671
0	-0.1576	-0.1381	-0.1181	-0.0981	-0.0791	-0.0783	-0.0693
5	-0.1591	-0.1406	-0.1216	-0.1026	-0.0819	-0.0793	-0.0696
10	-0.1520	-0.1350	-0.1170	-0.0990	-0.0816	-0.0779	-0.0690
15	-0.1306	-0.1091	-0.1026	-0.0906	-0.0752	-0.0759	-0.0694
20	-0.1271	-0.1071	-0.0866	-0.0836	-0.0677	-0.0685	-0.0676
25	-0.1041	-0.0925	-0.0738	-0.0683	-0.0542	-0.0600	-0.0620
30	-0.0598	-0.0295	-0.0183	-0.0098	-0.0049	-0.0281	-0.0422
35	-0.0467	-0.0201	0.0061	0.0186	0.0159	0.0123	-0.0085
40	-0.0289	-0.0111	0.0386	0.0484	0.0321	0.0145	0.0013
45	-0.0243	-0.0129	0.0213	0.0447	0.0325	0.0248	0.0140
50	-0.0395	-0.0247	-0.0063	0.0177	0.0196	0.0149	0.0082
55	-0.0364	-0.0305	0.0088	0.0067	0.0006	-0.0018	-0.0075
60	-0.0162	-0.0127	0.0181	0.0026	-0.0084	-0.0121	-0.0195
70	0.0267	0.0297	0.0177	0.0069	-0.0016	-0.0081	-0.0156
80	0.0223	0.0261	0.0215	0.0167	0.0109	0.0084	0.0050
90	0.0089	0.0077	0.0068	0.0014	-0.0036	-0.0044	-0.0057

α [°] \ β [°]	-4	-2	0	2	4	6	8
-20	-0.0551	-0.0520	-0.0481	-0.0494	-0.0486	-0.0465	-0.0396
-15	-0.0580	-0.0522	-0.0484	-0.0465	-0.0437	-0.0395	-0.0298
-10	-0.0590	-0.0520	-0.0476	-0.0447	-0.0407	-0.0338	-0.0238
-5	-0.0599	-0.0522	-0.0449	-0.0401	-0.0337	-0.0258	-0.0147
0	-0.0610	-0.0527	-0.0451	-0.0389	-0.0323	-0.0230	-0.0116
5	-0.0610	-0.0520	-0.0450	-0.0388	-0.0311	-0.0220	-0.0100
10	-0.0600	-0.0513	-0.0441	-0.0382	-0.0309	-0.0200	-0.0083
15	-0.0605	-0.0517	-0.0446	-0.0386	-0.0320	-0.0201	-0.0088
20	-0.0628	-0.0543	-0.0475	-0.0431	-0.0404	-0.0321	-0.0230
25	-0.0589	-0.0527	-0.0483	-0.0451	-0.0411	-0.0333	-0.0254
30	-0.0475	-0.0474	-0.0494	-0.0510	-0.0514	-0.0504	-0.0437
35	-0.0243	-0.0363	-0.0449	-0.0527	-0.0571	-0.0607	-0.0583
40	-0.0103	-0.0243	-0.0328	-0.0405	-0.0449	-0.0496	-0.0570
45	0.0047	-0.0053	-0.0162	-0.0410	-0.0545	-0.0617	-0.0697
50	0.0022	0.0003	0.0081	0.0166	0.0300	-0.0438	-0.0558
55	-0.0075	0.0004	-0.0040	-0.0012	-0.0089	-0.0203	-0.0289
60	-0.0193	-0.0082	-0.0012	0.0066	0.0096	0.0046	-0.0033
70	-0.0203	-0.0152	0.0015	0.0015	0.0143	0.0157	0.0094
80	0.0016	-0.0002	-0.0061	-0.0055	-0.0089	-0.0096	-0.0105
90	-0.0010	-0.0009	-0.0024	-0.0042	-0.0047	-0.0054	-0.0058

α [°] \ β [°]	10	15	20	25	30
-20	-0.0310	-0.0270	-0.0191	-0.0113	-0.0143
-15	-0.0202	-0.0216	-0.0117	-0.0082	-0.0069
-10	-0.0125	-0.0046	0.0033	0.0043	0.0056
-5	-0.0045	0.0152	0.0352	0.0498	0.0598
0	0	0.0190	0.0389	0.0584	0.0784
5	0.0009	0.0215	0.0405	0.0594	0.0794
10	0.0031	0.0207	0.0381	0.0550	0.0725
15	0.0019	0.0173	0.0289	0.0349	0.0569
20	-0.0047	0.0012	0.0043	0.0249	0.0447
25	-0.0179	-0.0042	0.0013	0.0197	0.0317
30	-0.0367	-0.0325	-0.0242	-0.0130	0.0180
35	-0.0585	-0.0611	-0.0451	-0.0228	0.0104
40	-0.0659	-0.0824	-0.0726	-0.0227	-0.0053
45	-0.0784	-0.0912	-0.0672	-0.0332	-0.0222
50	-0.0655	-0.0632	-0.0394	-0.0202	-0.0058
55	-0.0318	-0.0383	-0.0401	-0.0011	0.0051
60	-0.0048	-0.0163	-0.0317	-0.0012	0.0026
70	0.0049	-0.0035	-0.0148	-0.0263	-0.0236
80	-0.0114	-0.0172	-0.0225	-0.0268	-0.0233
90	-0.0057	-0.0109	-0.0157	-0.0170	-0.0181

II.8. x_b Directional Aerodynamic Moment Coefficient Data

$C_l(\alpha,\ \beta,\ \delta_h = -25)$

α [°] \ β [°]	-30	-25	-20	-15	-10	-8	-6
-20	-0.0060	0.0065	0.0133	0.0217	0.0268	0.0238	0.0219
-15	-0.0048	0.0059	0.0178	0.0242	0.0187	0.0157	0.0130
-10	-0.0033	0.0095	0.0173	0.0184	0.0128	0.0100	0.0088
-5	0.0298	0.0245	0.0233	0.0211	0.0178	0.0144	0.0113
0	0.0276	0.0285	0.0262	0.0225	0.0189	0.0151	0.0112
5	0.0390	0.0337	0.0329	0.0282	0.0240	0.0195	0.0142
10	0.0562	0.0558	0.0540	0.0455	0.0346	0.0285	0.0218
15	0.0737	0.0670	0.0629	0.0568	0.0439	0.0361	0.0272
20	0.0761	0.0708	0.0654	0.0551	0.0454	0.0377	0.0284
25	0.0910	0.0713	0.0627	0.0513	0.0397	0.0331	0.0261
30	0.0743	0.0429	0.0101	0.0110	0.0025	0.0152	0.0180
35	0.0704	0.0530	0.0453	0.0184	0.0067	0.0020	0.0017
40	0.0665	0.0605	0.0353	0.0132	0.0077	0.0092	0.0156
45	0.0788	0.0563	0.0344	0.0234	0.0150	0.0140	0.0091
50	0.0605	0.0568	0.0469	0.0340	0.0169	0.0146	0.0129
55	0.0453	0.0323	0.0257	0.0140	0.0003	0.0024	0.0042
60	0.0610	0.0413	0.0336	0.0230	0.0137	0.0122	0.0106
70	0.0713	0.0603	0.0501	0.0191	0.0221	0.0190	0.0124
80	0.0614	0.0507	0.0405	0.0309	0.0202	0.0167	0.0167
90	0.0601	0.0460	0.0363	0.0253	0.0213	0.0183	0.0147

α [°] \ β [°]	-4	-2	0	2	4	6	8
-20	0.0179	0.0121	0	-0.0096	-0.0167	-0.0210	-0.0239
-15	0.0106	0.0061	0	-0.0059	-0.0101	-0.0146	-0.0162
-10	0.0056	0.0027	0	-0.0047	-0.0077	-0.0118	-0.0136
-5	0.0072	0.0030	0	-0.0039	-0.0081	-0.0123	-0.0149
0	0.0075	0.0035	0	-0.0035	-0.0075	-0.0114	-0.0151
5	0.0096	0.0049	0	-0.0047	-0.0094	-0.0138	-0.0188
10	0.0147	0.0067	0	-0.0068	-0.0143	-0.0219	-0.0282
15	0.0185	0.0091	0	-0.0087	-0.0183	-0.0286	-0.0367
20	0.0185	0.0093	0	-0.0101	-0.0180	-0.0293	-0.0369
25	0.0175	0.0088	0	-0.0089	-0.0174	-0.0263	-0.0347
30	0.0126	0.0091	0	-0.0066	-0.0124	-0.0160	-0.0194
35	0.0028	0.0011	0	-0.0018	-0.0009	-0.0003	-0.0030
40	0.0096	0.0048	0	-0.0077	-0.0117	-0.0123	-0.0150
45	0.0089	0.0037	0	-0.0052	-0.0082	-0.0124	-0.0135
50	0.0089	0.0055	0	-0.0022	-0.0065	-0.0090	-0.0170
55	0.0025	0.0025	0	-0.0064	-0.0130	-0.0176	-0.0280
60	0.0064	0.0048	0	-0.0026	-0.0049	-0.0095	-0.0132
70	0.0097	0.0057	0	-0.0066	-0.0102	-0.0143	-0.0153
80	0.0078	0.0067	0	-0.0039	-0.0075	-0.0124	-0.0156
90	0.0091	0.0056	0	-0.0006	-0.0012	-0.0086	-0.0152

α [°] \ β [°]	10	15	20	25	30
-20	-0.0245	-0.0196	-0.0107	-0.0039	-0.0118
-15	-0.0189	-0.0245	-0.0179	-0.0060	0.0048
-10	-0.0158	-0.0220	-0.0140	-0.0060	0.0069
-5	-0.0188	-0.0221	-0.0241	-0.0253	-0.0209
0	-0.0187	-0.0223	-0.0260	-0.0283	-0.0274
5	-0.0230	-0.0292	-0.0339	-0.0349	-0.0398
10	-0.0343	-0.0447	-0.0531	-0.0546	-0.0550
15	-0.0433	-0.0568	-0.0626	-0.0672	-0.0736
20	-0.0448	-0.0542	-0.0642	-0.0694	-0.0743
25	-0.0411	-0.0525	-0.0637	-0.0724	-0.0797
30	-0.0225	-0.0308	-0.0350	-0.0628	-0.0943
35	-0.0100	-0.0017	-0.0281	-0.0358	-0.0533
40	-0.0130	-0.0180	-0.0403	-0.0656	-0.0716
45	-0.0178	-0.0274	-0.0370	-0.0579	-0.0804
50	-0.0200	-0.0371	-0.0500	-0.0599	-0.0636
55	-0.0173	-0.0316	-0.0433	-0.0499	-0.0629
60	-0.0141	-0.0234	-0.0340	-0.0417	-0.0614
70	-0.0172	-0.0292	-0.0466	-0.0568	-0.0678
80	-0.0190	-0.0297	-0.0393	-0.0495	-0.0602
90	-0.0191	-0.0231	-0.0341	-0.0438	-0.0579

$C_l(\alpha, \beta, \delta_h = 0)$

β[°] / α [°]	C_l						
	-30	-25	-20	-15	-10	-8	-6
-20	-0.0153	-0.0028	0.0091	0.0188	0.0234	0.0173	0.0106
-15	-0.0132	-0.0028	0.0077	0.0145	0.0104	0.0084	0.0060
-10	-0.0102	-0.0013	0.0094	0.0134	0.0107	0.0102	0.0081
-5	0.0087	0.0153	0.0186	0.0194	0.0183	0.0156	0.0125
0	0.0157	0.0190	0.0199	0.0207	0.0185	0.0153	0.0110
5	0.0318	0.0307	0.0296	0.0272	0.0219	0.0180	0.0132
10	0.0510	0.0510	0.0496	0.0422	0.0328	0.0271	0.0207
15	0.0732	0.0679	0.0638	0.0574	0.0433	0.0357	0.0274
20	0.0895	0.0815	0.0692	0.0579	0.0453	0.0354	0.0270
25	0.0884	0.0785	0.0665	0.0536	0.0400	0.0326	0.0254
30	0.0820	0.0505	0.0234	0.0143	0.0064	0.0189	0.0196
35	0.0790	0.0610	0.0390	0.0095	0.0037	0.0029	0.0150
40	0.0721	0.0573	0.0302	0.0087	0.0050	0.0104	0.0174
45	0.0744	0.0576	0.0331	0.0248	0.0170	0.0179	0.0163
50	0.0534	0.0411	0.0262	0.0238	0.0147	0.0144	0.0130
55	0.0587	0.0422	0.0320	0.0261	0.0176	0.0151	0.0117
60	0.0650	0.0481	0.0387	0.0301	0.0229	0.0192	0.0155
70	0.0663	0.0538	0.0422	0.0307	0.0245	0.0220	0.0160
80	0.0683	0.0554	0.0430	0.0325	0.0208	0.0149	0.0126
90	0.0701	0.0534	0.0410	0.0293	0.0205	0.0188	0.0163

β[°] / α [°]	C_l						
	-4	-2	0	2	4	6	8
-20	0.0090	0.0041	0	-0.0031	-0.0064	-0.0084	-0.0128
-15	0.0039	0.0025	0	-0.0029	-0.0050	-0.0080	-0.0086
-10	0.0060	0.0011	0	-0.0004	-0.0048	-0.0071	-0.0091
-5	0.0088	0.0043	0	-0.0038	-0.0087	-0.0126	-0.0158
0	0.0071	0.0033	0	-0.0030	-0.0067	-0.0107	-0.0147
5	0.0089	0.0043	0	-0.0037	-0.0081	-0.0126	-0.0173
10	0.0139	0.0056	0	-0.0065	-0.0137	-0.0207	-0.0266
15	0.0187	0.0090	0	-0.0088	-0.0188	-0.0284	-0.0369
20	0.0171	0.0076	0	-0.0085	-0.0177	-0.0271	-0.0365
25	0.0181	0.0081	0	-0.0082	-0.0165	-0.0258	-0.0330
30	0.0133	0.0071	0	-0.0057	-0.0118	-0.0165	-0.0205
35	0.0143	0.0097	0	-0.0016	-0.0003	-0.0018	-0.0017
40	0.0124	0.0062	0	-0.0075	-0.0108	-0.0131	-0.0145
45	0.0191	0.0115	0	-0.0042	-0.0108	-0.0148	-0.0156
50	0.0091	0.0056	0	-0.0051	-0.0123	-0.0152	-0.0212
55	0.0065	0.0045	0	-0.0040	-0.0081	-0.0133	-0.0187
60	0.0094	0.0063	0	-0.0029	-0.0055	-0.0111	-0.0163
70	0.0128	0.0073	0	-0.0050	-0.0069	-0.0120	-0.0165
80	0.0036	0.0045	0	-0.0045	-0.0086	-0.0134	-0.0159
90	0.0110	0.0066	0	0	-0.0001	-0.0067	-0.0124

β[°] / α [°]	C_l				
	10	15	20	25	30
-20	-0.0171	-0.0120	-0.0022	0.0097	0.0225
-15	-0.0116	-0.0160	-0.0090	0.0015	0.0119
-10	-0.0102	-0.0135	-0.0094	0.0013	0.0108
-5	-0.0186	-0.0199	-0.0189	-0.0157	-0.0095
0	-0.0182	-0.0204	-0.0196	-0.0187	-0.0154
5	-0.0209	-0.0263	-0.0288	-0.0299	-0.0310
10	-0.0322	-0.0418	-0.0486	-0.0501	-0.0501
15	-0.0430	-0.0567	-0.0624	-0.0663	-0.0714
20	-0.0440	-0.0569	-0.0682	-0.0804	-0.0884
25	-0.0403	-0.0538	-0.0669	-0.0788	-0.0882
30	-0.0248	-0.0327	-0.0418	-0.0687	-0.1003
35	-0.0011	-0.0034	-0.0326	-0.0547	-0.0726
40	-0.0148	-0.0185	-0.0399	-0.0671	-0.0815
45	-0.0206	-0.0285	-0.0364	-0.0608	-0.0778
50	-0.0222	-0.0313	-0.0337	-0.0486	-0.0609
55	-0.0201	-0.0286	-0.0346	-0.0448	-0.0613
60	-0.0188	-0.0260	-0.0346	-0.0440	-0.0609
70	-0.0220	-0.0282	-0.0397	-0.0513	-0.0638
80	-0.0186	-0.0303	-0.0408	-0.0532	-0.0661
90	-0.0154	-0.0242	-0.0359	-0.0483	-0.0650

$C_l(\alpha, \beta, \delta_h = 25)$

α [°] \ β [°]	C_l						
	-30	-25	-20	-15	-10	-8	-6
-20	-0.0138	-0.0009	0.0106	0.0227	0.0248	0.0145	0.0112
-15	-0.0061	0.0033	0.0140	0.0209	0.0157	0.0105	0.0066
-10	0	0.0074	0.0131	0.0151	0.0139	0.0108	0.0088
-5	0.0171	0.0196	0.0186	0.0204	0.0181	0.0142	0.0111
0	0.0267	0.0261	0.0245	0.0215	0.0188	0.0147	0.0105
5	0.0427	0.0376	0.0355	0.0285	0.0220	0.0180	0.0138
10	0.0622	0.0596	0.0551	0.0454	0.0331	0.0266	0.0208
15	0.0776	0.0696	0.0623	0.0544	0.0435	0.0372	0.0303
20	0.0830	0.0794	0.0694	0.0558	0.0427	0.0332	0.0243
25	0.0892	0.0760	0.0635	0.0524	0.0306	0.0214	0.0174
30	0.0791	0.0452	0.0194	0.0041	-0.0046	0.0112	0.0109
35	0.0751	0.0563	0.0348	0.0071	-0.0030	-0.0077	-0.0002
40	0.0673	0.0583	0.0297	0.0050	-0.0002	0.0031	0.0106
45	0.0778	0.0625	0.0411	0.0326	0.0187	0.0163	0.0141
50	0.0619	0.0519	0.0393	0.0326	0.0192	0.0177	0.0151
55	0.0476	0.0336	0.0258	0.0149	0.0016	0.0045	0.0066
60	0.0611	0.0428	0.0321	0.0263	0.0219	0.0165	0.0161
70	0.0654	0.0502	0.0358	0.0224	0.0185	0.0175	0.0130
80	0.0638	0.0506	0.0380	0.0287	0.0179	0.0138	0.0134
90	0.0607	0.0486	0.0407	0.0305	0.0211	0.0180	0.0165

α [°] \ β [°]	C_l						
	-4	-2	0	2	4	6	8
-20	0.0050	0.0031	0	-0.0033	-0.0081	-0.0077	-0.0160
-15	0.0060	0.0027	0	-0.0024	-0.0049	-0.0075	-0.0090
-10	0.0034	0.0008	0	-0.0006	-0.0051	-0.0076	-0.0096
-5	0.0081	0.0039	0	-0.0035	-0.0071	-0.0109	-0.0141
0	0.0058	0.0026	0	-0.0029	-0.0065	-0.0108	-0.0152
5	0.0099	0.0065	0	-0.0061	-0.0111	-0.0143	-0.0186
10	0.0146	0.0074	0	-0.0067	-0.0158	-0.0221	-0.0271
15	0.0213	0.0112	0	-0.0110	-0.0219	-0.0303	-0.0379
20	0.0172	0.0079	0	-0.0102	-0.0202	-0.0215	-0.0294
25	0.0136	0.0061	0	-0.0077	-0.0142	-0.0202	-0.0221
30	0.0061	0.0031	0	-0.0038	-0.0072	-0.0107	-0.0128
35	0.0085	0.0016	0	-0.0004	-0.0006	0.0005	0.0029
40	0.0053	0.0055	0	-0.0054	-0.0077	-0.0099	-0.0058
45	0.0165	0.0115	0	-0.0021	-0.0079	-0.0105	-0.0134
50	0.0103	0.0062	0	-0.0047	-0.0115	-0.0151	-0.0230
55	0.0046	0.0035	0	-0.0078	-0.0157	-0.0215	-0.0244
60	0.0102	0.0071	0	-0.0042	-0.0081	-0.0142	-0.0190
70	0.0112	0.0064	0	-0.0064	-0.0097	-0.0146	-0.0181
80	0.0050	0.0052	0	-0.0028	-0.0052	-0.0101	-0.0147
90	0.0116	0.0070	0	-0.0008	-0.0017	-0.0198	-0.0130

α [°] \ β [°]	C_l				
	10	15	20	25	30
-20	-0.0186	-0.0167	-0.0044	0.0074	-0.0256
-15	-0.0134	-0.0193	-0.0123	-0.0017	0.0081
-10	-0.0130	-0.0140	-0.0123	-0.0065	0.0008
-5	-0.0175	-0.0203	-0.0184	-0.0194	-0.0174
0	-0.0188	-0.0215	-0.0247	-0.0263	-0.0269
5	-0.0228	-0.0293	-0.0358	-0.0378	-0.0425
10	-0.0332	-0.0441	-0.0534	-0.0573	-0.0597
15	-0.0454	-0.0560	-0.0637	-0.0708	-0.0783
20	-0.0394	-0.0520	-0.0653	-0.0753	-0.0784
25	-0.0277	-0.0493	-0.0605	-0.0732	-0.0864
30	-0.0156	-0.0241	-0.0391	-0.0649	-0.0989
35	0.0086	-0.0013	-0.0291	-0.0503	-0.0691
40	-0.0068	-0.0120	-0.0367	-0.0654	-0.0741
45	-0.0149	-0.0288	-0.0375	-0.0588	-0.0738
50	-0.0258	-0.0392	-0.0459	-0.0585	-0.0685
55	-0.0232	-0.0365	-0.0474	-0.0552	-0.0692
60	-0.0211	-0.0255	-0.0313	-0.0420	-0.0603
70	-0.0209	-0.0290	-0.0424	-0.0568	-0.0720
80	-0.0194	-0.0302	-0.0395	-0.0521	-0.0653
90	-0.0150	-0.0244	-0.0346	-0.0425	-0.0546

$C_{l,lef}(\alpha, \beta)$

β[°] / α [°]	$C_{l,lef}$ -30	-25	-20	-15	-10	-8	-6
-20	-0.0205	-0.0170	-0.0076	0.0047	0.0150	0.0134	0.0008
-15	-0.0060	-0.0042	-0.0007	0.0033	0.0006	-0.0002	0.0022
-10	-0.0081	-0.0061	-0.0001	0.0018	0.0034	0.0022	0.0016
-5	0.0106	0.0102	0.0104	0.0103	0.0093	0.0073	0.0052
0	0.0238	0.0232	0.0224	0.0204	0.0168	0.0134	0.0098
5	0.0390	0.0361	0.0353	0.0315	0.0248	0.0202	0.0149
10	0.0485	0.0463	0.0430	0.0347	0.0263	0.0213	0.0155
15	0.0462	0.0462	0.0450	0.0420	0.0297	0.0241	0.0172
20	0.0480	0.0335	0.0290	0.0209	0.0158	0.0141	0.0095
25	0.0731	0.0573	0.0371	0.0221	0.0233	0.0203	0.0175
30	0.0752	0.0632	0.0428	0.0235	0.0106	0.0133	0.0138
35	0.0528	0.0479	0.0422	0.0190	0.0078	0.0069	0.0117
40	0.0555	0.0435	0.0339	0.0173	0.0094	0.0156	0.0193
45	0.0500	0.0493	0.0351	0.0306	0.0179	0.0158	0.0128

β[°] / α [°]	$C_{l,lef}$ -4	-2	0	2	4	6	8
-20	0.0013	0.0027	0	-0.0012	-0.0031	-0.0054	-0.0051
-15	0.0039	0.0019	0	-0.0015	-0.0030	-0.0039	-0.0028
-10	0.0006	0	0	-0.0003	-0.0008	-0.0011	-0.0020
-5	0.0030	0.0012	0	-0.0010	-0.0027	-0.0044	-0.0065
0	0.0060	0.0029	0	-0.0027	-0.0058	-0.0094	-0.0134
5	0.0100	0.0049	0	-0.0049	-0.0100	-0.0149	-0.0206
10	0.0100	0.0046	0	-0.0048	-0.0015	-0.0175	-0.0227
15	0.0113	0.0052	0	-0.0056	-0.0123	-0.0187	-0.0248
20	0.0058	0.0005	0	-0.0060	-0.0117	-0.0175	-0.0183
25	0.0120	0.0061	0	-0.0058	-0.0128	-0.0183	-0.0186
30	0.0094	0.0075	0	-0.0063	-0.0095	-0.0110	-0.0101
35	0.0070	0.0022	0	0.0014	-0.0057	-0.0076	-0.0077
40	0.0110	0.0110	0	-0.0074	-0.0126	-0.0194	-0.0213
45	0.0077	0.0019	0	-0.0118	-0.0124	-0.0150	-0.0173

β[°] / α [°]	$C_{l,lef}$ 10	15	20	25	30
-20	-0.0054	0.0036	0.0159	0.0256	0.0297
-15	-0.0003	-0.0024	0.0023	0.0052	0.0072
-10	-0.0026	-0.0007	0.0007	0.0071	0.0093
-5	-0.0087	-0.0100	-0.0103	-0.0102	-0.0106
0	-0.0164	-0.0200	-0.0220	-0.0228	-0.0234
5	-0.0250	-0.0317	-0.0355	-0.0363	-0.0392
10	-0.0278	-0.0360	-0.0443	-0.0476	-0.0498
15	-0.0304	-0.0369	-0.0399	-0.0411	-0.0411
20	-0.0203	-0.0250	-0.0335	-0.0378	-0.0521
25	-0.0260	-0.0248	-0.0398	-0.0610	-0.0758
30	-0.0151	-0.0280	-0.0473	-0.0677	-0.0797
35	-0.0091	-0.0203	-0.0435	-0.0492	-0.0541
40	-0.0253	-0.0332	-0.0498	-0.0594	-0.0714
45	-0.0214	-0.0341	-0.0386	-0.0528	-0.0535

α [°]	$C_{l_{\delta_a}}(\alpha)$	$\Delta C_{l_\beta}(\alpha)$	$\Delta C_{l_{\delta_a},lef}(\alpha)$	$C_{l_p}(\alpha)$	$\Delta C_{l_p,lef}(\alpha)$
-20	-0.1550	0	0.0290	-0.3660	0.0060
-15	-0.1550	0	0.0290	-0.3660	0.0060
-10	-0.1550	0	0.0290	-0.3660	0.0060
-5	-0.2010	0	0.1750	-0.3770	0.0180
0	-0.0024	0	0.0665	-0.3450	-0.1000
5	0.0880	0	0.0360	-0.4340	0.0200
10	0.2050	0	0.0070	-0.4080	0.0580
15	0.2200	0.0070	0.0660	-0.3880	0.0870
20	0.3190	0.0050	0.2010	-0.3290	0.0270
25	0.4370	0.0030	0.0060	-0.2940	-0.0560
30	0.6800	0	-0.0680	-0.2300	-0.0820
35	0.1000	0	-0.5370	-0.2100	0.3620
40	0.4470	0	-0.7870	-0.1200	0.1940
45	-0.3300	0	-0.3940	-0.1000	0.0970
50	-0.0680	0		-0.1000	
55	0.1180	0		-0.1200	
60	0.0802	0		-0.1400	
70	0.0529	0		-0.1000	
80	0.0868	0		-0.1500	
90	-0.0183	0		-0.2000	

$C_{l,\delta_a=20^\circ}(\alpha,\beta)$

β[°] / α [°]	$C_{l,\delta_a=20^\circ}$						
	-30	-25	-20	-15	-10	-8	-6
-20	-0.0514	-0.0340	-0.0199	-0.0128	-0.0038	-0.0074	-0.0140
-15	-0.0492	-0.0362	-0.0231	-0.0148	-0.0196	-0.0227	-0.0262
-10	-0.0455	-0.0342	-0.0275	-0.0248	-0.0253	-0.0262	-0.0270
-5	-0.0343	-0.0302	-0.0257	-0.0229	-0.0241	-0.0269	-0.0300
0	-0.0403	-0.0371	-0.0326	-0.0301	-0.0322	-0.0341	-0.0372
5	-0.0245	-0.0250	-0.0235	-0.0246	-0.0291	-0.0328	-0.0372
10	-0.0029	-0.0024	-0.0025	-0.0089	-0.0183	-0.0233	-0.0299
15	0.0159	0.0146	0.0122	0.0064	-0.0067	-0.0134	-0.0213
20	0.0072	0.0043	0.0036	0.0061	0.0024	-0.0055	-0.0139
25	0.0298	0.0260	0.0239	0.0159	0.0048	-0.0023	-0.0103
30	0.0402	0.0079	-0.0151	-0.0076	-0.0198	-0.0107	-0.0124
35	0.0411	0.0228	0.0122	-0.0144	-0.0121	-0.0144	-0.0070
40	0.0448	0.0282	0.0070	-0.0154	-0.0125	-0.0032	-0.0015
45	0.0573	0.0412	0.0175	0.0104	0.0029	0.0013	-0.0006
50	0.0408	0.0297	0.0203	0.0187	0.0065	0.0054	0.0039
55	0.0472	0.0296	0.0244	0.0185	0.0088	0.0059	0.0018
60	0.0517	0.0350	0.0294	0.0209	0.0116	0.0073	0.0022
70	0.0418	0.0409	0.0299	0.0197	0.0083	0.0083	-0.0022
80	0.0598	0.0465	0.0369	0.0275	0.0143	0.0109	0.0073
90	0.0716	0.0532	0.0410	0.0327	0.0192	0.0153	0.0115

β[°] / α [°]	$C_{l,\delta_a=20^\circ}$						
	-4	-2	0	2	4	6	8
-20	-0.0131	-0.0185	-0.0226	-0.0257	-0.0286	-0.0346	-0.0367
-15	-0.0264	-0.0300	-0.0327	-0.0336	-0.0357	-0.0382	-0.0365
-10	-0.0295	-0.0340	-0.0328	-0.0330	-0.0352	-0.0374	-0.0404
-5	-0.0333	-0.0367	-0.0401	-0.0439	-0.0479	-0.0510	-0.0540
0	-0.0413	-0.0450	-0.0481	-0.0509	-0.0535	-0.0569	-0.0594
5	-0.0419	-0.0466	-0.0511	-0.0548	-0.0580	-0.0612	-0.0647
10	-0.0364	-0.0435	-0.0499	-0.0555	-0.0606	-0.0663	-0.0715
15	-0.0312	-0.0400	-0.0491	-0.0575	-0.0655	-0.0728	-0.0779
20	-0.0230	-0.0324	-0.0418	-0.0517	-0.0608	-0.0691	-0.0786
25	-0.0200	-0.0285	-0.0372	-0.0452	-0.0534	-0.0615	-0.0684
30	-0.0195	-0.0246	-0.0308	-0.0364	-0.0431	-0.0458	-0.0495
35	-0.0113	-0.0173	-0.0256	-0.0252	-0.0271	-0.0259	-0.0241
40	-0.0028	-0.0088	-0.0166	-0.0247	-0.0281	-0.0318	-0.0317
45	-0.0016	-0.0024	-0.0122	-0.0176	-0.0204	-0.0249	-0.0242
50	0	-0.0024	-0.0076	-0.0136	-0.0225	-0.0256	-0.0309
55	-0.0021	-0.0043	-0.0095	-0.0138	-0.0199	-0.0232	-0.0278
60	-0.0016	-0.0043	-0.0092	-0.0128	-0.0166	-0.0208	-0.0250
70	-0.0047	-0.0054	-0.0075	-0.0133	-0.0143	-0.0194	-0.0237
80	0.0030	0.0009	-0.0041	-0.0087	-0.0154	-0.0158	-0.0203
90	0.0086	0.0047	0.0022	-0.0025	-0.0052	-0.0090	-0.0123

β[°] / α [°]	$C_{l,\delta_a=20^\circ}$				
	10	15	20	25	30
-20	-0.0407	-0.0317	-0.0246	-0.0105	0.0069
-15	-0.0402	-0.0450	-0.0367	-0.0236	-0.0106
-10	-0.0436	-0.0441	-0.0414	-0.0347	-0.0234
-5	-0.0554	-0.0566	-0.0538	-0.0493	-0.0452
0	-0.0623	-0.0644	-0.0619	-0.0574	-0.0542
5	-0.0679	-0.0724	-0.0735	-0.0720	-0.0725
10	-0.0769	-0.0863	-0.0927	-0.0928	-0.0923
15	-0.0854	-0.0985	-0.1043	-0.1067	-0.1080
20	-0.0865	-0.0902	-0.0877	-0.0884	-0.0913
25	-0.0761	-0.0872	-0.0952	-0.0973	-0.1011
30	-0.0503	-0.0628	-0.0550	-0.0780	-0.1103
35	-0.0222	-0.0199	-0.0465	-0.0571	-0.0754
40	-0.0310	-0.0281	-0.0505	-0.0717	-0.0883
45	-0.0317	-0.0392	-0.0463	-0.0700	-0.0861
50	-0.0304	-0.0426	-0.0442	-0.0536	-0.0647
55	-0.0291	-0.0388	-0.0447	-0.0499	-0.0675
60	-0.0269	-0.0362	-0.0447	-0.0503	-0.0670
70	-0.0257	-0.0371	-0.0473	-0.0583	-0.0672
80	-0.0243	-0.0375	-0.0469	-0.0565	-0.0698
90	-0.0160	-0.0295	-0.0378	-0.0500	-0.0684

$C_{l,\delta_a=20°,lef}(\alpha,\beta)$

α [°] \ β [°]	-30	-25	-20	-15	-10	-8	-6
-20	-0.0536	-0.0402	-0.0309	-0.0204	-0.0147	-0.0228	-0.0244
-15	-0.0467	-0.0455	-0.0445	-0.0424	-0.0378	-0.0356	-0.0333
-10	-0.0492	-0.0481	-0.0412	-0.0414	-0.0387	-0.0366	-0.0380
-5	-0.0413	-0.0441	-0.0422	-0.0401	-0.0440	-0.0452	-0.0463
0	-0.0293	-0.0290	-0.0305	-0.0311	-0.0352	-0.0385	-0.0408
5	-0.0163	-0.0186	-0.0172	-0.0202	-0.0269	-0.0314	-0.0362
10	0.0036	0.0005	-0.0038	-0.0210	-0.0191	-0.0233	-0.0289
15	-0.0058	-0.0057	-0.0052	-0.0078	-0.0145	-0.0184	-0.0254
20	0.0088	-0.0020	-0.0015	-0.0031	-0.0133	-0.0143	-0.0168
25	0.0311	0.0247	0.0081	-0.0099	-0.0018	-0.0003	-0.0083
30	0.0396	0.0318	0.0165	0.0032	-0.0064	-0.0023	-0.0095
35	0.0291	0.0248	0.0227	0.0010	-0.0062	-0.0094	-0.0048
40	0.0373	0.0282	0.0154	0.0024	-0.0030	0.0058	0.0025
45	0.0448	0.0399	0.0299	0.0212	0.0077	0.0046	0.0038

α [°] \ β [°]	-4	-2	0	2	4	6	8
-20	-0.0228	-0.0227	-0.0233	-0.0231	-0.0256	-0.0288	-0.0303
-15	-0.0288	-0.0289	-0.0312	-0.0329	-0.0333	-0.0344	-0.0353
-10	-0.0385	-0.0396	-0.0404	-0.0408	-0.0411	-0.0417	-0.0444
-5	-0.0487	-0.0502	-0.0518	-0.0527	-0.0531	-0.0544	-0.0560
0	-0.0448	-0.0484	-0.0510	-0.0539	-0.0566	-0.0597	-0.0621
5	-0.0412	-0.0472	-0.0525	-0.0572	-0.0616	-0.0659	-0.0703
10	-0.0341	-0.0401	-0.0444	-0.0491	-0.0541	-0.0588	-0.0637
15	-0.0310	-0.0367	-0.0436	-0.0478	-0.0515	-0.0573	-0.0632
20	-0.0216	-0.0258	-0.0297	-0.0350	-0.0413	-0.0437	-0.0473
25	-0.0141	-0.0193	-0.0258	-0.0303	-0.0366	-0.0414	-0.0438
30	-0.0132	-0.0196	-0.0222	-0.0317	-0.0356	-0.0360	-0.0338
35	-0.0107	-0.0179	-0.0204	-0.0242	-0.0259	-0.0298	-0.0297
40	0.0027	0.0008	-0.0143	-0.0160	-0.0273	-0.0351	-0.0410
45	0.0007	-0.0049	-0.0110	-0.0147	-0.0219	-0.0223	-0.0283

α [°] \ β [°]	10	15	20	25	30
-20	-0.0318	-0.0259	-0.0151	-0.0052	0.0087
-15	-0.0362	-0.0318	-0.0289	-0.0277	-0.0258
-10	-0.0451	-0.0432	-0.0430	-0.0352	-0.0341
-5	-0.0572	-0.0608	-0.0585	-0.0573	-0.0597
0	-0.0649	-0.0694	-0.0697	-0.0705	-0.0702
5	-0.0748	-0.0817	-0.0838	-0.0839	-0.0856
10	-0.0686	-0.0771	-0.0842	-0.0884	-0.0913
15	-0.0688	-0.0750	-0.0784	-0.0776	-0.0772
20	-0.0483	-0.0584	-0.0595	-0.0589	-0.0702
25	-0.0461	-0.0383	-0.0482	-0.0654	-0.0817
30	-0.0341	-0.0442	-0.0573	-0.0726	-0.0801
35	-0.0295	-0.0370	-0.0585	-0.0606	-0.0648
40	-0.0414	-0.0468	-0.0597	-0.0728	-0.0817
45	-0.0284	-0.0429	-0.0511	-0.0611	-0.0650

$C_{l,\delta_r=30°}(\alpha,\beta)$

α [°] \ β [°]	-30	-25	-20	-15	-10	-8	-6
-20	-0.0115	0.0042	0.0163	0.0276	0.0350	0.0349	0.0321
-15	-0.0078	0.0048	0.0176	0.0233	0.0242	0.0247	0.0255
-10	-0.0057	0.0055	0.0169	0.0209	0.0237	0.0252	0.0265
-5	0.0261	0.0317	0.0343	0.0331	0.0311	0.0312	0.0290
0	0.0292	0.0329	0.0339	0.0330	0.0294	0.0299	0.0262
5	0.0416	0.0436	0.0436	0.0400	0.0336	0.0320	0.0277
10	0.0640	0.0640	0.0626	0.0552	0.0442	0.0401	0.0343
15	0.0821	0.0771	0.0731	0.0654	0.0519	0.0482	0.0411
20	0.1088	0.0928	0.0808	0.0708	0.0530	0.0474	0.0412
25	0.0932	0.0838	0.0718	0.0611	0.0449	0.0427	0.0369
30	0.0818	0.0503	0.0234	0.0168	0.0045	0.0240	0.0269
35	0.0742	0.0652	0.0432	0.0135	0.0084	0.0065	0.0201
40	0.0613	0.0606	0.0389	0.0117	0.0076	0.0121	0.0172
45	0.0819	0.0629	0.0399	0.0313	0.0223	0.0194	0.0223
50	0.0529	0.0439	0.0295	0.0243	0.0157	0.0155	0.0149
55	0.0585	0.0435	0.0330	0.0265	0.0166	0.0148	0.0125
60	0.0627	0.0475	0.0377	0.0297	0.0209	0.0184	0.0157
70	0.0669	0.0563	0.0453	0.0343	0.0242	0.0219	0.0175
80	0.0662	0.0552	0.0432	0.0323	0.0201	0.0165	0.0098
90	0.0670	0.0542	0.0400	0.0279	0.0184	0.0166	0.0112

α [°] \ β [°]	-4	-2	0	2	4	6	8
-20	0.0301	0.0236	0.0201	0.0144	0.0139	0.0127	0.0085
-15	0.0227	0.0197	0.0176	0.0152	0.0133	0.0105	0.0093
-10	0.0243	0.0202	0.0184	0.0169	0.0128	0.0110	0.0095
-5	0.0253	0.0205	0.0154	0.0112	0.0073	0.0032	-0.0009
0	0.0221	0.0182	0.0146	0.0112	0.0079	0.0036	-0.0009
5	0.0236	0.0189	0.0144	0.0103	0.0062	0.0014	-0.0039
10	0.0280	0.0209	0.0137	0.0073	0.0006	-0.0069	-0.0136
15	0.0329	0.0228	0.0135	0.0047	-0.0044	-0.0142	-0.0238
20	0.0313	0.0225	0.0137	0.0056	-0.0032	-0.0122	-0.0233
25	0.0309	0.0230	0.0147	0.0051	-0.0030	-0.0116	-0.0210
30	0.0244	0.0213	0.0126	0.0080	0.0010	-0.0054	-0.0094
35	0.0223	0.0178	0.0114	0.0109	0.0102	0.0092	0.0087
40	0.0169	0.0158	0.0059	0.0023	-0.0024	-0.0044	-0.0059
45	0.0230	0.0133	0.0007	0.0011	-0.0062	-0.0097	-0.0115
50	0.0117	0.0080	0.0026	-0.0042	-0.0081	-0.0144	-0.0150
55	0.0086	0.0069	0.0019	-0.0034	-0.0064	-0.0133	-0.0156
60	0.0104	0.0075	0.0015	-0.0028	-0.0051	-0.0113	-0.0145
70	0.0125	0.0052	0.0008	-0.0010	-0.0064	-0.0112	-0.0152
80	0.0100	0.0045	-0.0023	-0.0063	-0.0083	-0.0126	-0.0180
90	0.0099	0.0079	0.0018	-0.0020	-0.0041	-0.0064	-0.0122

α [°] \ β [°]	10	15	20	25	30
-20	-0.0010	0.0064	0.0176	0.0296	0.0450
-15	0.0050	0.0060	0.0134	0.0259	0.0424
-10	0.0044	0.0073	0.0112	0.0227	0.0340
-5	-0.0046	-0.0067	-0.0078	-0.0049	0.0007
0	-0.0053	-0.0086	-0.0092	-0.0079	-0.0043
5	-0.0081	-0.0146	-0.0177	-0.0177	-0.0199
10	-0.0199	-0.0307	-0.0381	-0.0395	-0.0395
15	-0.0319	-0.0453	-0.0529	-0.0569	-0.0619
20	-0.0326	-0.0503	-0.0600	-0.0721	-0.0801
25	-0.0300	-0.0464	-0.0569	-0.0688	-0.0782
30	-0.0167	-0.0293	-0.0360	-0.0627	-0.0941
35	0.0069	0.0017	-0.0277	-0.0498	-0.0588
40	-0.0081	-0.0114	-0.0397	-0.0612	-0.0619
45	-0.0180	-0.0269	-0.0355	-0.0584	-0.0777
50	-0.0202	-0.0286	-0.0339	-0.0486	-0.0577
55	-0.0189	-0.0276	-0.0342	-0.0449	-0.0595
60	-0.0175	-0.0263	-0.0348	-0.0443	-0.0597
70	-0.0196	-0.0295	-0.0407	-0.0516	-0.0623
80	-0.0191	-0.0310	-0.0419	-0.0540	-0.0652
90	-0.0146	-0.0237	-0.0358	-0.0503	-0.0628

VITA

Si-bok Yu was born in Seoul, South Korea on January 15, 1975. He graduated from University of Ulsan in February 1997 with Bachelor of Science degree in Aerospace Engineering. He began to pursue his Master of Science degree in Aerospace Engineering at Old Dominion University in the fall of 1997. Fatigue crack reduction using flight control system was investigated for his master's research. He continued his Ph.D. study in Aerospace Engineering at Old Dominion University from the spring of 1999. He graduated with his Master of Science degree in December 1999. He completed his Ph.D. degree in December 2003. His master's research continued in Ph.D. Design of life extending control system which can be directly implemented to the current flight control system was investigated for his Ph.D. dissertation.